Image Guided Prostate Cancer Treatments

Robert L. Bard
Jurgen Fütterer
Dan Sperling
Editors

Springer

Image Guided Prostate Cancer Treatments

Robert L. Bard • Jurgen J. Fütterer
Dan Sperling
Editors

Image Guided Prostate Cancer Treatments

Springer

Editors
Robert L. Bard, MD
Bard Cancer Center
Biofoundation for Angiogenesis
Research and Development
New York, NY
USA

Dan Sperling, MD
Sperling Prostate Center, Alpha 3T MRI
New York, NY
USA

Jurgen J. Fütterer, MD, PhD
Department of Radiology
Radboud University Nijmegen
Medical Centre
HB Nijmegen
The Netherlands

ISBN 978-3-642-40428-3 ISBN 978-3-642-40429-0 (eBook)
DOI 10.1007/978-3-642-40429-0
Springer Heidelberg New York Dordrecht London

© Springer-Verlag Berlin Heidelberg 2014
This work is subject to copyright. All rights are reserved by the Publisher, whether the whole or part of the material is concerned, specifically the rights of translation, reprinting, reuse of illustrations, recitation, broadcasting, reproduction on microfilms or in any other physical way, and transmission or information storage and retrieval, electronic adaptation, computer software, or by similar or dissimilar methodology now known or hereafter developed. Exempted from this legal reservation are brief excerpts in connection with reviews or scholarly analysis or material supplied specifically for the purpose of being entered and executed on a computer system, for exclusive use by the purchaser of the work. Duplication of this publication or parts thereof is permitted only under the provisions of the Copyright Law of the Publisher's location, in its current version, and permission for use must always be obtained from Springer. Permissions for use may be obtained through RightsLink at the Copyright Clearance Center. Violations are liable to prosecution under the respective Copyright Law.
The use of general descriptive names, registered names, trademarks, service marks, etc. in this publication does not imply, even in the absence of a specific statement, that such names are exempt from the relevant protective laws and regulations and therefore free for general use.
While the advice and information in this book are believed to be true and accurate at the date of publication, neither the authors nor the editors nor the publisher can accept any legal responsibility for any errors or omissions that may be made. The publisher makes no warranty, express or implied, with respect to the material contained herein.

Printed on acid-free paper

Springer is part of Springer Science+Business Media (www.springer.com)

To my patients, whose courage showed me possibility
To my wife, Loreto, whose vision generated reality

Foreword

With an estimated 238,590 new cases in 2013, prostate cancer is the most common cancer in men in the USA. One in 6 men will be diagnosed with this disease in his lifetime. It is, at the same time, the second biggest killer in men, with an estimated 29,720 deaths in 2013 in the USA.

As for other cancers in the past, the science of prostate cancer has changed tremendously during the last 10 years. Premalignant conditions have been described leading to an extremely active search for genomic signatures of prostate cell transformation. Cohort studies are ongoing. The diagnosis of prostate cancer has become more sophisticated with the introduction of newer criteria, outside of the classical Gleason classification, that could predict an individual's tumor aggressiveness, with the hope of better and more personalized tailored therapeutic strategies.

Among them, "watchful follow-up" is more widely accepted and fewer patients are getting an unnecessary prostatectomy, that, due to the widely increased use of PSA screening that occurred during the last decade, was the reason for some real concerns, both in term of individual risk as well as for the economy of cancer.

All the tools that constituted the classical armamentarium in the management of prostate cancer have had an impressive evolution toward high sophistication and better indication: Surgery with the unquestionable benefit of the robotic technologies. Radiotherapy with the IMRT and endo-brachytherapy and ARC Therapy. Hormonal treatment with two newly approved medicines such Abiraterone and Anzalutamide and others in clinical developments. Chemotherapy also with Docetaxel and Cabazitaxel.

Finally, prostate cancer, which was for years a disease with very few options, and not really well understood, is now a field of great change, evolving knowledge and the focus of ongoing basic and translational research.

There is another field of particular attention regarding prostate cancer: this is the diagnostic procedures. Anatomical imaging, functional imaging as well as molecular imaging appear today as useful tools that as an oncologist one needs to know and understand.

Acquiring this knowledge and these skills in order to improve the management of patients is a real challenge. This is where Robert L. Bard and his colleagues have contributed tremendously, through this fantastic book, to help us in decoding what is significant prostate cancer and offering revolutionary treatments.

Each chapter of this book is a kind of bible where all existing information in the different scopes ultimately define the everlasting, so rapidly evolving field of prostate cancer.

Rarely has so much useful data been put together with such efficient communication style as in *Image Guided Prostate Cancer Treatments*.

I already advised all my assistants to read it carefully as I am sure that it will certainly help to improve our patient's outcome worldwide.

Paris, France David Khayat, MD, PhD

Acknowledgments

I thank Loreto Bard, Executive Director of the Biofoundation for Angiogenesis Research and Development, for her assistance in coordinating international multidisciplinary medical exchanges that advanced the concepts developed in this book. I wish to thank members of the Prostate Cancer Research Institute Drs. Duke Bahn, Stanley Brosman, Arthur Lurvey, Mark Scholz and Charles Myers; members of the Catholic University Hospital in Rome, Italy, Drs. Giuseppe Brisinda, Federica Cadeddu and Giorgio Maria; members of the Mayo Clinic Foundation, Drs. Thayne Larson, Benjamin Larson and Lance Mynderse; members of the Academic Hospital of Bicetre, Drs. Francois Cornud and Francoise Giuliano; members of The Prostatitis Foundation, Drs. Susan Keay and John Warren; members of the NY Roentgen Society, Drs. Richard Stock, Lincoln Pao, Michael Zelefsky, Shalom Kalnicki; members of the Societe Francaise de Radiologie, Drs. Guy Frija, Olivier Helenon, JF Moreau, Olivier Rouviere and J-M Correas; members of the Radiologia Policlinico Umberto I, Rome, Drs. Roberto Passariello and Vito Cantisani: members of the Groupe Hospitalier Necker-Enfants Malades, Paris, France, Drs. Bertrand Dufour, N. Thiounn and Y. Chretien; members of the Imperial College of Medicine, London, Dr. David Cosgrove and Sir Richard Sykes; members of the American Urological Association, Drs. William DeWolf, Edward Messing, Louis Denis, Eric Rovner, Ernest Sosa, Alexis Te, Michael Manyak, Michael Marberger, Joseph Smith, Jr., Harris Nagler, J. Fracchia, Peter Scardino, M. Droller, P. Schlegel, S. Kaplan, H. Lepor, M. Grasso, N. Romas, A. Melman, I. Grunberger, R. Macchia, M. Choudhury and Patrick Walsh; members of the New York Cancer Society, Drs. Marvin Rotman, Patrick Fratellone and Howard Hochster. I thank Dr. Jelle Barentsz, President of the International Cancer Imaging Society, for developing lymph node detection technology and disseminating awareness throughout the medical profession. Special thanks to Drs. Catherine Roy, Francois Cornud, Olivier Helenon and Peter Scardino whose books have provided new hope for cancer victims and further advanced medical knowledge. Finally, input from Jerry Calosa and Dr. Mark Liebeskind and support from members of my staff Niurka Achury, Aimee Arceo, Mary Ann Sta. Rita and Karen Barrie were indispensable in the timely publication of this book.

Preamble

The practice of medicine is a commitment to lifetime learning applied in the service of patients. For any of us who practice, the simple truths that we learned in medical school have been found no longer simple and no longer true. The advances in oncologic analysis, imaging, and treatment options with respect to prostate cancer have shown great expansion in the last 40 years, and the authors have taken pains to make the details of these advances accessible to generalists and specialists of all stripes.

Initially, the identification of prostate cancer was limited by the ability of the probing finger to feel that part of the prostate that was accessible. Often the first identification of the cancer was the appearance of the spread to bone at a time that the rectal examination was still normal. The development of the PSA test helped identify patients that required more aggressive investigation, but the variety of benign conditions producing PSA elevations resulted in often unnecessary invasive biopsies. Early imaging was crude and the inherent errors did not dissuade the urologist from pursuing biopsy or help him in guiding the biopsy in the areas of greatest likelihood of malignant disease.

The improvement of imaging techniques with power Doppler ultrasound, sonographic elastography, high-resolution MRI, and the organization of these techniques into a multimodal approach has dramatically changed the field of prostate cancer diagnosis. No longer is every PSA elevation an obligation to biopsy nor are the appropriate biopsies blindly directed. Judgments of the severity of disease allow many patients to be followed expectantly, confident that changes in the underlying condition will be identified soon enough to change course. Furthermore, when those changes are identified, the biopsy can be directed to the specific area of concern.

These improvements in diagnostic techniques have been paralleled by the development of more focused modalities of treatment. Therapeutic ultrasound, laser, and photodynamic therapies are being actively investigated to ascertain their roles in the spectrum of prostate malignancies. We are at an exciting time in the development of knowledge in the identification and treatment of prostate cancer, and the authors are leaders in these fields and this volume brings the reader up to speed on these developments.

May 2013

John E. Postley, MD, FACP
College of Physicians and Surgeons
Columbia University
New York, NY, USA

Contents

Part I Basic Principles

1 **Current Scope of Prostate Cancer** 3
Robert L. Bard

2 **Diagnostic Ultrasound Imaging of the Prostate** 11
Robert L. Bard

3 **Advanced Ultrasound: Prostate Elastography and Photoacoustic Imaging** 31
Stephen Rosenzweig, Richard Bouchard, Thomas Polascik, Liang Zhai, and Kathryn Nightingale

4 **Contrast-Enhanced Ultrasound in Prostate Cancer** 47
F. Cornelis, Y. Le Bras, G. Rigou, J.M. Correas, and N. Grenier

5 **Power Doppler Imaging of Prostate Cancer** 55
Jean-Luc Sauvain

6 **Doppler Histogram Vessel Density Analysis** 71
Robert L. Bard

7 **MR Imaging of the Prostate** 83
Jurgen J. Fütterer

8 **MR Imaging Localization of Prostate Tumors** 91
Jurgen J. Fütterer

9 **Diffusion-Weighted Whole-Body Imaging: Tumor Staging Applications** 97
Dan Sperling and Robert L. Bard

10 **MRI-Guided Biopsy** 107
Jurgen J. Fütterer

11 **MRI-Ultrasound Fusion Imaging** 115
Dan Sperling

Part II Clinical Applications

12 Clinical Applications of Ultrasound, Doppler Ultrasound, MRI, and DCE-MRI 127
Robert L. Bard

13 Intraprostatic Cancer 145
Robert L. Bard

14 Focal Tumors: Extraprostatic 149
Robert L. Bard

15 Metastatic Disease 165
Robert L. Bard

16 Diagnosing, Treating, and Reversing Prostate Cancers with Hormonal and Nutritional Intervention 187
Robert L. Bard, Arthur Bartunek, and Eugene Shippen

17 Imaging Detection of Regression and Recurrence 207
Robert L. Bard

Part III Advanced Image Guided Procedures

18 Laser Principles 219
Arif Aslam and David J. Goldberg

19 Focal Laser Ablation of the Prostate 227
Dan Sperling and Robert L. Bard

20 Focal Therapy for Prostate Cancer Using Irreversible Electroporation 235
Gary Onik

21 Photodynamic Therapy 243
Ashley J. Ridout and Caroline M. Moore

22 High-Intensity Focused Ultrasound for the Treatment of Prostate Cancer 255
John C. Rewcastle and Inderbir S. Gill

Index 263

Part I

Basic Principles

Current Scope of Prostate Cancer

1

Robert L. Bard

1.1 Introduction

Prostate cancer statistics and ambivalence about screening challenge our profession to enlarge our array of clinical practices in order to better serve patients' needs. The diagnostic and treatment conventions that dominated urologic practice at the turn of the millennium are rapidly evolving toward an image-guided target-and-manage approach to the disease. Advances in imaging coupled with biomarkers enable more informed decisions about the timing and utilization of diagnostic and treatment interventions. In addition to advanced imaging technologies, complementary and alternative medicine also offer hope for preventing, managing, and overcoming prostate cancer.

1.2 The Changing Scope of Prostate Cancer

The revered Ewing's textbook of pathology *Neoplastic Diseases* (Ewing 1940) mentioned that prostate cancer was a rare disease comprising about 0.27 % of overall male cancers. We now know this is not the case. In fact, prostate cancer (PCa) is the most common cancer in North America. It is an expensive disease, representing 11 % of the costs for the treatment of all cancers in the USA with a per-patient cost from diagnosis to death of $81,658 for a total of $8 billion annually (Racioppi et al. 2012). While the price tag of a single preferred treatment may limit a patient's access to it, the costs strain the overall economics of private and public healthcare administration.

A less public but perhaps more poignant burden is borne by the patient and his family. The burden contains varying contents depending on the individual patient: whether or not to screen, TRUS biopsy with its attendant flaws and risks, treatment cost/benefits analysis, seeking second opinions and conducting extensive internet research, decision-making, undergoing treatment, recovery issues, and impact on quality of life. As recently as three decades ago, many patients were paying an even higher price in terms of late-stage diagnosis, radical localized treatments with high comorbidity rates despite the increased odds of undetected metastatic disease, suffering from late-stage systemic disease, and death. Thankfully, a simple blood test for prostate-specific antigen (PSA) reversed the damages of late-stage diagnosis, but it also sparked a downward trend in age at the time of diagnosis and created new complications from overtreatment of low-grade indolent cancers.

The identification of prostate-specific antigen (PSA) as a possible prostate cancer (PCa) marker resulted from the work of various researchers

---

R.L. Bard, MD
Bard Cancer Center, Biofoundation for Angiogenesis
Research and Development, 121 E. 60th St,
New York, NY 10022, USA
e-mail: rbard@cancerscan.com

R.L. Bard et al. (eds.), *Image Guided Prostate Cancer Treatments*,
DOI 10.1007/978-3-642-40429-0_1, © Springer-Verlag Berlin Heidelberg 2014

throughout the 1960s and 1970s. In 1986, the FDA approved the PSA blood test to monitor the progression of prostate cancer (PCa) in men already diagnosed with the disease. Though the FDA did not approve the use of this test, in conjunction with the digital rectal exam, to screen asymptomatic men until 1994, the 6 years from 1986 to 1992 saw a doubling of incidence of PCa in the male population and a sharp shift of the diagnosis to a younger age group.

1.2.1 The Prostate Cancer Screening Dilemma

With widespread screening and increased grassroots awareness, there occurred a significant trend toward detection of clinical stage T1c prostate cancer (from 2.1 to 36.4 %) while those with palpable clinical stage T3 decreased from 23.5 to 6.5 % (Amling et al. 1998). Thus, there were far fewer cases of metastases at diagnosis. In the USA over the past 20 years, prostate cancer death rates have been reduced by close to 40 % without substantial changes in surgical or radiation treatment strategies. Some models suggest that more than 50 % of this reduction is due to early detection (Scosyrev and Messing 2013).

In addition to earlier detection, a demographic shift occurred. While the overall prostate cancer incidence rate was stable from 2001 to 2007, rates significantly increased among men aged 40–49 years and decreased among men aged 70–79+ years. In addition, about 42 % of localized prostate cancers diagnosed from 2004 to 2007 were poorly differentiated (Li et al. 2012).

Therefore, the apparent increase in survival advantage due to screening and the raised stakes for younger patients who may have aggressive disease would seem to warrant continued screening despite its imperfections.

On the other hand, in 2012, the U.S. Preventive Services Task Force (USPSTF) recommended against routine PSA screening for prostate cancer due to the risk of overdiagnosis and overtreatment with most prostate cancer remaining asymptomatic. The panel concluded that the potential benefit of testing did not outweigh the risk of harm, arguing against continued screening except for those with known risk factors and a life expectancy greater than 10 years.

Mixed reviews came in from the European Randomized Study of Screening for Prostate Cancer (ERSSPC). The study concluded that while PSA-based screening indeed reduced the rate of death from prostate cancer by an estimated 20 %, it was associated with a high risk of overdiagnosis (diagnosis in men who would not have clinical symptoms in their lifetime) (Schröder et al. 2009). In fact, overdiagnosis, overtreatment, and its concomitant comorbidities are likely the most important adverse effects of screening and are significantly more common than in screening for breast, colorectal, or cervical cancer (Hakama and Auvinen 2008). Knowing this, a younger PCa patient might be deterred from screening by the risk of posttreatment erectile dysfunction.

To screen or not to screen? The approach-avoidance dilemma over this issue is understandable if PSA, DRE, and TRUS biopsy are the only tools available to physicians and patients. However, advances in imaging and precision tumor ablation are spurring clinicians to adopt new practice models that overlap and integrate urology and radiology.

1.3 Limitations of PSA Testing and an Alternate Paradigm

Modern thinking regarding prostate cancer screening is shaped by major US and British studies pointing to a need for a better diagnostic test than random biopsies for men with elevated PSA. Prostate cancer is currently the only malignancy that is diagnosed using a nonspecific blood test leading to a random set of biopsies of the entire organ. Since only 3 % of prostate cancer is lethal, a new paradigm for diagnosing and treating prostate cancer has evolved based on the following assumptions:

1. Gleason 3+3 tumors do not metastasize (Lepor 2013) and have a 1 % overall mortality at 15 years, meaning curative radical treatment may be replaced by more conservative approaches.

2. Metastatic lesions appear to be attributable to a single clone of cells that form a significant or dominant lesion.
3. Imaging modalities such as high-resolution sonography and advanced MR imaging protocols usually find the dominant tumor.
4. Focal dominant cancers may be ablated under image guidance of ultrasound (US) and/or MRI.
5. Untreated patients will live as long as treated patients.
6. Focal treatment is a targeted therapy with a reduced economic burden and less risk of injury to the periprostatic structures of the neurovascular bundles, rectum, bladder, and urinary sphincter. Focal ablation is an alternative to active surveillance/watchful waiting and radical prostatectomy/radiation therapies.

1.3.1 Prostate Imaging: Resolving the Screening Dilemma?

Advanced imaging may provide a fundamentally organic solution to the screening dilemma by both avoiding unnecessary biopsies and also minimizing the burdens associated with overtreatment.

1. Is a biopsy warranted? When biomarkers raise a suspicion of PCa, imaging can identify a region of interest (ROI) to help determine if a biopsy is warranted. Thus, imaging abrogates the rush to a randomized, systematic biopsy, which entails risks of minor complications (60–79 %) and sampling challenges in all zones (Carroll and Shinohara 2008).
2. Is a focal treatment reasonable for clinically qualified patients? Precise image-guided ablation of all known lesions can "favorably alter the natural history of the cancer without impacting health-related quality of life and allows for safe retreatment with repeated focal therapy or whole-gland approaches if necessary" (Mearini and Porena 2011).
3. Is active surveillance a viable option for men with early-stage, low-risk disease? Imaging provides a way to monitor for disease progression, allowing a patient to defer the treatment decision and maintain, or even improve, quality of life and health through lifestyle changes that may also help manage his cancer.

1.3.2 Active Surveillance

Ninety-seven percent of men with tumors will die from other causes, calling into question the rush to treat biopsy-demonstrated PCa. Patients with early-stage, low-risk disease are often considered candidates for what was historically termed watchful waiting (WW). Today's preferred nomenclature is active surveillance (AS), since lifestyle changes and antioxidant treatments bring dynamism to this option that addresses both the overdiagnosis caused by PSA screening and the potential side effects of the standard treatments of radical prostatectomy (impotence and incontinence) and radiation therapy (bladder and gastrointestinal toxicity) (Wei et al. 2002).

Men with organ-confined disease that is low risk and who can tolerate the anxiety of deferring standard treatment are candidates. The initial definition of insignificant prostate cancer 4 (Stamey et al. 1993) was Gleason grade <7, PSA < 10 ng/ml, and physical disease volume of 0.5 cc. This has been generally replaced by the definition of significant cancer as volume >1.3 cc, Gleason score >6, and a dominant lesion imaged by high-resolution Doppler ultrasound and/or multiparametric MRI (Sauvain et al. 2013).

Since the accuracy of PSA for prostate cancer detection is 2 %, one must reflect upon its potential accuracy for predicting treatment failures. It is the author's opinion that recurrent disease or treatment failure must be documented by imaging using one of three existing technologies: 3-D power Doppler ultrasound (3D PDS), contrast-enhanced ultrasound (CEUS), or dynamic contrast-enhanced MRI (DCE-MRI) (Bard 2009).

1.3.3 Active Surveillance Protocols

Patients with minor degrees of extracapsular disease, early seminal vesicle involvement, and Gleason 7 disease of small volume who have considered disease progression, anxiety levels, life expectancy, and comorbidities may elect a variety of therapy options. Treatment efficacy is traditionally measured by PSA fluctuation, serial digital rectal exams, and prostate biopsies.

This approach may account for the high dropout rate of men switching from their therapy to radical treatments despite lack of evidence of disease progression (Klotz 2005; Martin et al. 2006). Monitoring by serial 3D PDS and DCE-MRI coupled with professional antianxiety counseling may lead to better adherence to active surveillance.

1.4 Rationale for Focal Therapy

Minimally invasive focal ablation (MIAT) takes advantage of the lead time advantage of serial PSA monitoring by destroying significant index lesions. Even though prostate cancer is a multifocal disease in up to 87 % of cases, patients with multiple tumors less than 0.5 cc had a better survival rate than those with a significant index lesion (Bott et al. 2010). Identifying and characterizing the index lesion is currently performed by biopsy and multimodality MRI. In many university settings, MRI is performed before the biopsy since hemorrhage can mask or mimic malignant findings over a post-biopsy period up to 4 months. In clinical practice, since men need staging following a positive biopsy, accurate results have been obtained by DCE-MRI and 3D PDS in patients 10 days after 12-core biopsy sampling.

1.5 Modalities for Focal Therapy

Currently used focal treatments include cryotherapy, photodynamic therapy (PDT), high-intensity focused ultrasound (HIFU), radiofrequency ablation (RFA), irreversible electroporation (IRE), histotripsy, and focal laser ablation (FLA). Microwave thermal ablation is used in some countries outside the USA. This is a whole-gland treatment and not considered a focal therapy.

(a) Cryotherapy involves placing cryoprobes under ultrasound guidance into the area of interest or the entire gland.
(b) PDT involves intravenous administration of a photosensitizer followed by laser fiber insertion creating a light source.
(c) HIFU uses focused ultrasound to generate thermal damage via a transrectal approach.
(d) RFA uses ultrasound-guided fibers to heat abnormal areas.
(e) IRE is a new technology that electrocutes tumor cells.
(f) Histotripsy is an experimental modality using intense pulses of ultrasound.
(g) FLA uses MRI or ultrasound guidance to insert laser fibers into a lesion.

FDA-approved technologies are cryotherapy, RFA, and FLA. These treatments require follow-up at the same clinical intervals as do standard therapies. The posttreatment gland is best evaluated by DCE-MRI, 3D PDS, and CEUS.

1.6 Clinical Trial and Anecdotal Observation

There are two important phrases in classic scientific methodology: clinical trial and anecdotal observation. Clinical trial is evidence accumulated based on an assumption of a possible mechanism of therapy to be investigated. Anecdotal observation means that a treatment worked once or twice, and the mechanism may not be readily understood at that time.

The following example illustrates how the interplay between formal clinical study and anecdotal evidence can drive medicine forward. The drug finasteride (Proscar®) was developed 15 years ago as a miracle cure for progressive urinary symptoms of an enlarged prostate. Initial clinical trials showed it was useful and Proscar rapidly received FDA approval. Early studies also suggested that it might reduce prostate cancer risk. Anecdotal reports that it was only minimally effective began to appear and increase in number. New data also suggested men were developing serious cancers while on the medication. Finally, a critique of a large study recently concluded, surprisingly, that while the drug was somewhat useful in alleviating the symptoms of benign prostatic hypertrophy and there was an overall 25 % decrease in prostate cancer prevalence, there was a 68 % increase in the frequency of high-grade killing prostate cancers in the treated group (Walsh 2004). This report underscores the interaction between clinical trials and anecdotal reports. The wonder drug appeared to produce fewer nonlethal tumors but stimulated more aggressive killing cancers. Clearly more research must focus on the controversial area of cancers being aggravated by prescription medications.

The story does not end here. Since the evidence did not fit the theory, the facts were reinterpreted in the last few years. It is now felt that the increase in significant tumors was due to the shrinking of the enlarged prostate that made the more dangerous cancer easier to detect. The jury is still out in this trial and we need more data to come to a definitive conclusion. A major study on breast cancer demonstrated 10 % of proven cancers disappeared after 6 years without treatment. Remember, the breast and prostate are both glands. We see prostate cancers resolve without traditional medical treatments and this deserves further clinical study.

David Hess (Hess 1999) quotes the following from medical scholar Robert Houson:

> The FDA requires a convincing mechanism to obtain approval for clinical trials, and I think this is a completely unnecessary requirement. If there are clear indications of benefit in humans or animals, that should bypass the whole issue of mechanism. The point is that the investigators do not have to know the mechanism in order to corroborate the effect that is occurring. In cancer, case studies have a greater degree of validity than in other diseases. In cancer the rate of spontaneous remission is extremely low, so low that it is virtually zero. Therefore, if you have just a few cases, even only two cases, you have something that is significant and most likely meaningful. So, I consider what is being dismissed as anecdotal evidence, to be in cancer, actually an impressive proof of success because you can have much more detail in the case studies than you can in a clinical trial.

The same principle of anecdotal observation applies to advances in disease detection through imaging. In the 1980s, when the state-of-the-art sonogram equipment showed that doctors could see malignant lymph nodes, I started a protocol with Cabrini Medical Center in New York City under the famed breast surgeon, Dr. Henry Leis. We scanned patients with breast cancer to see if the underarm lymph nodes were involved by tumor. Detection of these cancerous glands meant surgery was not indicated, since abnormal glands showed the cancer had spread too far for a local operation to be useful. The results of our investigation spared selected patients unnecessary surgery. The project broke new ground and showed that the sonograms could alter surgical planning. This technology has evolved to the imaging of 3 mm cancer deposits in nodes affected by prostate, breast, and melanoma skin cancers using high-resolution 3D PDS and DCE-MRI. Thus, clinical trial and anecdotal observation are illuminating the path to new image-guided treatments.

When Dr. Bertrand Guillonneau introduced the laparoscopic radical prostatectomy (LRP) procedure in Paris in 1995, he was considered radical for wanting to alter the existing established treatment. His student, Dr. Arnon Krongrad, brought this laser surgical technique to the USA in 1999 and was initially outcast by the local medical community. Later, the LRP was superseded by the robot-assisted radical prostatectomy (RRP) and robot-assisted laser prostatectomy (RALP). Debate continues as to whether a surgeon's own hands in a patient's body would or would not be more accurate than robotically manipulated instruments guided by extreme visual magnification as discussed by Dr. Herbert Lepor at the 2013 NYU Medical Center MIAT conference.

When a traditional method offers fewer rewards than an innovation does, is it not time to start questioning the norm? Acceptance of new ideas occurs slowly, and its transformation into action as distinct new protocols is frequently glacial. The information presented in this book is not new, is not hidden, and is not controversial. The majority of concepts in this book have been in use internationally for over 30 years, for example, laser ablation of liver tumors in some

European medical centers have been performed for 32 years. The same way that the radical mastectomy was phased out by the breast lumpectomy, so may the traditional radical prostatectomy pass into history as a treatment that no longer serves the good of most patients. Already the standard surgical treatment for improving urine flow in men with enlarged prostates (the transurethral resection of the prostate or TURP) is becoming less popular among younger urologists in training programs. Indeed, the green light laser accomplishes the same effect with less blood loss and is done as an outpatient procedure. Alternatively, oral medications that relax the urinary sphincter muscle have reduced the need for any surgery by 60 % in men with obstructive symptoms from an enlarged gland.

Change does not just come from doctors. Our patients also play a key part in propelling progress in medical practice. Patients who could drive home a few days after surgery helped increase the demand for this growing new standard of care. Less invasive prostatectomy, with its speedy recovery and lower side effect profile, is a positive trend for patients. But it is essential to ask ourselves: how many patients even require surgical prostate removal? Today's patients are not passive. Educated patients want what does work rather than what should work. Educated men are asking their doctors hard questions, yet most of their physicians are not prepared to address them to their patients' satisfaction.

1.7 Dualistic vs. Integrative Thinking

When we come face to face with a problem, it's tempting to oversimplify the solution as "either this or that." The name for this type of thinking is false dichotomy, meaning there are many more ways to resolve the situation but we have reduced ourselves to only two. Prostate cancer patients are all too familiar with the side effect risks that accompany conventional whole-gland treatments. Unless they are aware of a broad spectrum of choices, their options are limited to only two: Either it is *conventional treatment* or it is *no treatment*.

1.8 Complementary and Alternative Medical Therapies

Thankfully, there is an entire array of therapeutic choices in the world of complementary and alternative medicine (CAM). Complementary and alternative medical techniques may be seen as a middle ground between no treatment and standard conventional medicine. Perhaps each of the four options identified in this introduction (no treatment, conventional treatment, focal treatment, CAM) has something to recommend it. In fact, while the idea of no treatment may seem unacceptable, we have yet to fully understand the mysterious inconsistencies of cancer and when no treatment may be a preferred option. The 2008 *Archives of Internal Medicine* featured a large study of breast cancer patients in which some of the tumors disappeared spontaneously after being observed over a 6-year period. Dr. Robert Kaplan from UCLA and Dr. Franz Porzsolt from the University Cancer Center in Ulm, Germany, analyzed the data and suggested a reevaluation of breast cancer research and treatment be considered. Proven breast cancers had regressed after no treatment.

1.9 Varieties of CAM Practices

The National Institutes of Health (NIH) defines conventional medicine as medicine practiced by licensed healthcare professionals to treat diseases using drugs, radiation, or surgery. This is also termed Western, modern, mainstream, or orthodox medicine. Professional schools that train students in conventional medicine award degrees that include MD (Doctor of Medicine) and DO (Doctor of Osteopathy) as well as degrees in nursing, pharmacy, and practical therapies. In contrast, the NIH loosely defines CAM as a group of diverse healthcare systems, practices, and products that are not presently considered to be part of conventional medicine. CAM practices include:

- Mind-body medicine such as meditation, prayer, imaging, and art therapy to enhance the mind's capacity to alter bodily function
- Biologically based practices like herbs, botanicals, and dietary supplements found in nature

but not yet scientifically proven to be efficacious

- Manipulative practices including massage and chiropractic employing manipulation of the spine and other body parts
- Energy medicine, which is divided into biofield therapies as Qigong, Reiki, and acupuncture that manipulate the body to affect the "energy fields," and bioelectromagnetic therapies like magnetic therapy, sound energy therapy, and light therapy that use electromagnetic fields to produce health benefits.

In practice, CAM is categorized into complementary medicine, which is used alongside Western medicine, and alternative medicine, which is used in place of potentially harmful conventional medicine. History has shown that numerous CAM therapies over time have become incorporated into standard practices.

1.10 Prostate Cancer Statistics

The big picture statistics for prostate cancer challenge our profession to serve patients' needs by enlarging our array of clinical choices.

According to the 2012 Cancer Facts and Figures (ACS 2012), over 240,000 cases of prostate cancer are expected to be diagnosed in a single year. An estimated 28,170 men will die of this disease. Findings reported by the Centers for Disease Control and Prevention and the National Cancer Institute in collaboration with the North American Association of Central Cancer Registries show the leading type of cancer causing death among men is lung cancer; however, prostate cancer is the most common form of non-skin cancer diagnosed in men in the USA.

Prostate cancer facts:

- One in 6 men will get prostate cancer.
- About 1 man in 36 will die of prostate cancer.
- More than 90 % of all prostate cancers are found when the disease is confined to the prostate and nearby organs.
- A man is 33 % more likely to develop prostate cancer than a woman is to develop breast cancer.
- As baby boomer men reach the target zone for prostate cancer, beginning at age 50, the number of new cases is projected to increase dramatically.
- 99 % of men diagnosed with prostate cancer are expected to live at least 5 years after diagnosis.
- By 2015, there will be more than 300,000 new prostate cancer cases each year, an increase of one third.
- Prostate cancer death rates have been decreasing since the early 1990s in both African Americans and whites. Although death rates have decreased more rapidly among African American than white men, rates in African Americans remain more than twice as high as those in whites.
- Prostate cancer death rates decreased 3.0 % per year in white men and 3.5 % per year in African American men from 2004 to 2008.

In contrast, there have been dramatic decreases in the death rate for other diseases, for example:

- Pneumonia decreased 54 %.
- Strokes decreased 68 %.
- Heart disease decreased 58 %.

The lifetime probability of a man in the USA developing cancer is 50 %. A breakdown of this data shows the lifetime cancer probability for:

(a) Prostate 17 %
(b) Lung 8 %
(c) Colon 6 %
(d) Bladder 6 %
(e) Lymphoma 2 %
(f) Melanoma 3 %
(g) Leukemia 2 %
(h) Mouth 1 %
(i) Kidney 1 %
(j) Stomach 1 %

Of this list, prostate cancer is the most common and most rapidly increasing cancer. A nonsmoking man is more likely to develop prostate cancer than he is to develop colon, bladder, melanoma, lymphoma, and kidney cancers combined. Without improvements in diagnosis and treatment, dire outcomes are projected:

1. In 2015, the number of new prostate cancer cases will increase by a third.
2. In 2020, the number of prostate cancer deaths per year will increase by 44 %.
3. In 2030, 80,000 men will lose their lives to prostate cancer (Prostate Cancer Foundation 2004).
4. In 2037, there will be over 400,000 new prostate cancer cases per year.

These are sobering statistics. It is incumbent upon us, as physicians and healers, to continue to scrutinize current practices, ask critical questions, seek out technologies that are successfully used elsewhere, and develop new diagnostic and treatment modalities to promote the health and quality of life of our patients.

References

American Cancer Society. Cancer Facts & Figures 2012. Atlanta, GA: American Cancer Society; 2012.

Amling CL, Blute ML, Lerner SE, Bergstralh EJ, Bostwick DG, Zincke H. Influence of prostate-specific antigen testing on the spectrum of patients with prostate cancer undergoing radical prostatectomy at a large referral practice. Mayo Clin Proc. 1998;73(5):401–6.

Bard R. DCE-MRI of prostate cancer. Berlin: Springer; 2009. p. 88.

Bott SR, Ahmed HU, Hindley RG, Abdul-Rahman A, Freeman A, Emberton M. The index lesion and focal therapy: an analysis of the pathological characteristics of prostate cancer. BJU Int. 2010;106(11):1607–11.

Carroll P and Shinohara K. Transrectal ultrasound guided biopsy. UCSF Patient Guide 2008 http://urology2008-2012.ucsf.edu/patientGuides/pdf/uroOnc/Prostate_Biopsy.pdf

Ewing J. Neoplastic diseases: a textbook on tumors. 4th ed. Philadelphia: Saunders; 1940. p. 844.

Hakama M, Auvinen A. Cancer screening. In: Heggenhougen K, Quah SR, editors. International encyclopedia of public health. San Diego: Academic; 2008. p. 464–80.

Hess D. Evaluating alternative cancer therapies. Edited collection of interviews of leaders of the CAM cancer therapy movement. New Brunswick: Rutgers University Press; 1999.

Klotz L. Active surveillance with selective delayed intervention is the way to manage 'good-risk' prostate cancer. Nat Clin Pract Urol. 2005;2(3):136–42; quiz 131 p following 149.

Lepor H. Is targeted minimally invasive therapies (MIAT) ready for prime time? Presented In: Advances in prostate imaging and focal ablative treatment of prostate cancer conference, New York, University Langone Medical Center; 2013.

Li J, Djenaba J, et al. Recent trends in prostate cancer incidence by age, cancer stage, and grade, the United States, 2001–2007. Prostate Cancer. 2012. Article ID 691380, 8 pages. doi:10.1155/2012/691380.

Martin RM, Gunnell D, Hamdy F, Neal D, Lane A, Donovan J. Continuing controversy over monitoring men with localized prostate cancer: a systematic review of programs in the prostate specific antigen era. J Urol. 2006;176(2):439–49.

Mearini L, Porena M. Pros and cons of focal therapy for localized prostate cancer. Prostate Cancer. 2011. Article ID 584784, 8 pages. doi:10.1155/2011/584784.

Prostate Cancer Foundation. Eliminating cancer as a cause of death by 2015. Panel discussion presented during the 2004 Global Conference; Los Angeles, CA: 2004.

Racioppi M, Palermo G, et al. Hot topics in urological health economics: a mini review. Arch Ital Urol Androl. 2012;84(2):47–52.

Sauvain J, Sauvain E, Rohmer P, et al. Role of Doppler ultrasound in detection of low risk prostate cancers. Diagn Interv Radiol. 2013;94:60.

Schröder F, Hugosson J, et al. Screening and prostate-cancer mortality in a randomized European study. N Engl J Med. 2009;360:1320–8.

Scosyrev E, Messing EM. Reply to prostate-specific antigen screening for prostate cancer and the risk of overt metastatic disease at presentation: analysis of trends over time. Cancer. 2013;119(5):1113–4.

Stamey TA, Freiha FS, McNeal JE, Redwine EA, Whittemore AS, Schmid HP. Localized prostate cancer. Relationship of tumor volume to clinical significance for treatment of prostate cancer. Cancer. 1993;71(3 Suppl):933–8.

Walsh PC. The influence of finasteride on the development of prostate cancer [ed. comment]. J Urol. 2004; 171:506–7.

Wei JT, Dunn RL, Sandler HM, et al. Comprehensive comparison of health-related quality of life after contemporary therapies for localized prostate cancer. J Clin Oncol. 2002;20(2):557–66.

Diagnostic Ultrasound Imaging of the Prostate

2

Robert L. Bard

2.1 History of Ultrasound and Sonography

Sonograms use ultrasound. In fact, the terms are clinically identical. The physical principle of ultrasound, the piezoelectric effect where sound is created from electrical energy, was discovered by Pierre and Marie Curie 10 years before the recognition of the x-ray.

After the sinking of the TITANIC steamship, sound waves were used to alert the ship's captain to the presence of icebergs below the visible waterline. The French military developed sonar to detect submarines during the First World War. Modern sonar was invented by American industrialists for checking metal flaws in railroad ties. It was later perfected by the US military for navigational use and underwater scanning. Early medical uses included imaging disorders of the eye, heart, and the developing fetus. As computers grew in sophistication, so did the applications of ultrasound, and now it is often used as the first diagnostic test for many medical disorders. Doppler sonar created in 1972 gives pictures of flow movement in the human body in the same way it shows motion of storms and tornadoes in the weather patterns (Doppler radar) that one sees on television weather reports. Doppler technology has been around for years. In fact, it was reported that Doppler radar designed and built missiles for the US Army at the White Sands Proving Grounds in New Mexico in the 1950s were so sensitive that they had to be continually modified and toned down; an air conditioner turned on a mile away could trigger a missile's detection system to arm and prepare to fire—once, a missile actually launched towards a moving train and followed it along the Santa Fe railroad tracks.

Urologists in Japan, oncologists in England, surgeons in the Netherlands, chemotherapists in Belgium, ultrasonographers in Scandinavia, and radiologists in France, seeing the success of sonograms in diagnosing malignant tumors in the breast, turned their attention to the study of the prostate. They concluded that the vascular pattern shown by the Doppler technique held the key to the degree of malignancy. Thirteen years ago, German surgeons at the University of Ulm, the largest bone tumor center in Europe, showed that highly malignant bone cancers had high blood flows. The standard treatment for bone cancer is amputation of the entire limb. Bone tumors that demonstrate no vascularity or low blood flows are now watched or treated more conservatively. The current clinical use of this technique in Europe thus prevents unnecessary amputations.

Dr. Nathalie Lassau, an interventional radiologist at the Institut de Cancérologie Gustave-Roussy, an internationally known cancer center in Paris, published similar findings on the deadly

---

R.L. Bard, MD
Bard Cancer Center, Biofoundation for Angiogenesis Research and Development, 121 E. 60th St,
New York, NY 10022, USA
e-mail: rbard@cancerscan.com

R.L. Bard et al. (eds.), *Image Guided Prostate Cancer Treatments*,
DOI 10.1007/978-3-642-40429-0_2, © Springer-Verlag Berlin Heidelberg 2014

skin cancer, melanoma. Her research revealed lethal skin cancers to be highly vascular and skin cancers that could be watched were not vascular (Lassau et al. 2002). Dr. Lassau is currently investigating medicines and performing curative treatments to reduce blood flows to cancers in hope of lessening their malignant consequences and has presented this work at numerous international meetings. Her finding that 3D Doppler sonography correlates best with the pathologic process was highlighted at the 2012 Journees Francaises de Radiologie Meeting in Paris. Newer MRI protocols are currently being fine-tuned based on the proven high accuracy of the color and power of Doppler sonography data.

2.1.1 Blood Flow: A Detectable Sign of Tumor Activity?

Is there a way to determine whether a cancer is part of the natural aging process to be watched or whether the malignancy has potential deadly consequences, as with interval cancers? In 1985, a prominent British radiologist and physician, David Cosgrove, published a paper in the *American Journal of Radiology* demonstrating the presence of blood flows in breast cancers. After reading his article, I hopped on a plane and visited the Radiology Department at Hammersmith Hospital in London. There I observed the test firsthand and envisioned future potential uses. I noted the new generation of sonogram equipment now had the capability to show pictures of blood vessels. The arteries and veins supplying a tumor could be clearly imaged. Moreover, the actual flowing blood in the cancer could be seen and the velocity of flow of blood in the vessels accurately measured. By the mid- to late 1990s, there were great advances in this area. At an international conference in Italy in 1997, Dr. Rodolfo Campani, an Italian radiologist specializing in studying the blood flows of cancers at the University of Pavia Medical Center, identified the criteria to differentiate vessels supplying blood to malignancies from those attached to benign tumors (Campani 1997). Benign vessels are few in number, smoothly outlined, follow straight courses, and branch regularly. Malignant vessels are many in number, irregularly outlined, irregular in course, and crooked in branching patterns.

These findings have been confirmed by other investigators at the 2013 World Congress of Interventional Oncology and 2013 Annual Convention of the American Institute of Ultrasound in Medicine. Malignant blood vessels may be accurately and noninvasively detected by newer Doppler sonography techniques and advanced blood flow MRI protocols. Studies of tissue density or hardness have been perfected and also guide the assessment of tumor aggression. The harder or denser a tumor is, the more likely it is to be malignant. Ultrasound elastic measurements and MRI diffusion (hardness) data now quantify tumor aggression and are complementary with the blood flow technologies. This wealth of diagnostic input assists patients and doctors in decision making.

The blood flow patterns depicted by Doppler sonography provide a way to quantitatively measure and serially monitor the severity of malignancy throughout the treatment course. Blood flow analysis can reveal treatment response, since the size and number of tumor vessels decrease with successful therapies. Although this concept was described in the early 1990s in Europe, it was first mentioned in the American literature in 1996 at the American Roentgen Ray Society Annual Meeting. Dr. E. Louvar from Henry Ford Hospital (Detroit, MI) combined radiology and pathology studies to determine that the power Doppler flows in malignancies were correlated to the vessels that feed aggressive tumors (Louvar et al. 1996). Significantly higher Gleason scores were seen in cancer biopsies of high Doppler flow areas compared to cancers with no Doppler flows. Dr. D. Downey at John Robarts Research Institute (University Hospital, Ontario, Canada) has looked at vascular imaging techniques and 3D imaging of blood vessels. Blood vessels can be rendered in 3D with angiography (high-intensity dye injected into arteries), CT scanning (medium-intensity dye), MR angiography (low-intensity dye), contrast-enhanced ultrasound (low-intensity dye not FDA approved), 3D color Doppler imaging (no injection or dye), and 3D power Doppler imaging (no injection or dye). Downey noted that power Doppler was better able to delineate abnormal vessel architecture in prostate cancers than color Doppler techniques (Downey and Fenster 1995). Since then we now use even more sensitive Doppler modalities with better computer analysis of tumor vessel concentrations.

Dr. Miroslav Zalesky, a urologist from Prague, Czechoslovakia, delivered a paper in 2003 at the 98th AUA Annual Meeting in Chicago. He noted that blood vessels observed by the 3D PDS technology in the prostate determined extracapsular spread with 89 % accuracy in a series of 282 patients. The spread of abnormal vessels from the gland through the capsule was highly significant and best demonstrated using the 3D capability for interpretation (Moyer 2003). Dr. Zalesky felt that 3D reconstruction enables physicians to biopsy areas of suspicious neovascularization (new abnormal arteries and veins) that would be missed by the standard sextant biopsy. In a response, Dr. Michael Brawer, a urologist not involved in the study, and quoted in the April 30, 2003, issue of *Doctor's Guide* on the Internet, commented: "It is uncertain at this point whether the new modality can detect the fine vessels that are typical of the neovascularization found in cancer…The problem is that the size of the vessel delineated with Doppler is larger than the vessels found in malignancies. Are our imaging modalities sensitive enough to identify the small vessels characteristic of cancer? I don't know" (Moyer 2003). While Dr. Brawer may be correct, he may also be missing the point that we do not need to see the small vessels associated with cancer to identify tumors, but can assume that growing malignancy needs nourishment by larger vessels easily seen on the Doppler to distribute blood to the smaller intratumor arteries.

2.1.2 Using Doppler Technologies

A 2004 newsletter from the Prostate Cancer Research Institute reported that hormone therapy may change the way the pathologist interprets a cancer (Bostwick 2004). A pathologist looks at a frozen picture of a cell that may or may not be indicative of the cells' current activity. For this reason, functional imaging using blood flow technologies assists in determining tumor aggression. Androgen deprivation therapy (ADT) makes it more difficult to grade the tumor with the microscope. Men who have been on ADT should have a Doppler sonogram study to confirm the absence of residual disease. If there are areas of abnormal blood vessels, biopsy may be considered. Many patients who have been treated for cancer accept the presence of abnormal blood flows as proof of recurrence and choose treatments accordingly without further biopsies. Most patients use the amount of decrease in number of the visible blood vessels to represent the degree of success. Dr. Pam Unger, a prostate cancer pathology specialist at Mount Sinai Hospital in New York, mentioned in a personal communication that radiation changes also caused difficulties in reading the microscopic slides. Furthermore, pathologists generally don't look for blood vessels and thus do not routinely evaluate the vascular pattern in the specimens they interpret. Another problem with biopsy interpretation is the over-the-counter herbal medicine market. Many of the products for prostate health have some hormonal effects that shrink the prostate and improve symptoms. However, no one has determined if the pharmacologic properties of these alternative health treatments change the cells of the prostate to mimic cancer when the pathologist studies them under a glass slide. Today, one must also consider the possible toxic effects on the prostate of medicines and supplements made by foreign companies.

2.1.3 Medical Progress and Government Regulation

In 1999, at the University of California, San Diego, a French medical student, Dr. Olivier Lucidarme developed a highly sensitive technique to improve Doppler ultrasound. Special bubbles injected intravenously greatly improved imaging of small vessels. To date, our FDA has not approved this technology and Dr. Lucidarme now practices this methodology in Paris. Italian researchers Drs. Vito Cantisani and Francesco Drudi have demonstrated that this technology can show cancers unsuspected by other means. Advanced MRI scans performed in Europe are not available in the USA, nor are certain sophisticated radioactive bone scans allowed in the states at this writing.

In addition to government approval processes, other factors influence which treatment a doctor may recommend to a patient. If you have an ulcer, an internist will give you pills, a psychiatrist will offer psychotherapy, and a surgeon will recommend an operation. The cancer treatment field likewise provides a host of traditional and nontraditional options.

Metastases is the most dreaded word for patients since it indicates their primary tumor has spread to remote parts of their body and hope for a cure is lost. In 2004, my colleague, Dr. Jelle Barentsz, head of Cancer Research at Nijmegen University Hospital in Holland, presented a paper at the International Congress of Radiology in which he described a new technique to evaluate cancer spreading to the lymph nodes. It uses MRI with a novel contrast agent called Combidex and the technique is termed MRL (Magnetic Resonance Lymphangiography). This technology is extremely important since MRI is the best way to image abnormal nodes that are hidden or inaccessible at surgery. The imaging shows the size and location of the lymph nodes as well as the presence of cancerous tissue as small as 3 mm. This critical piece of information that pinpoints cancer infiltration tells where the spread occurs and allows for accurate treatment planning. The current "gold standard" for lymph node evaluation is a surgery called *pelvic lymph node dissection*. Clearly this invasive exploratory operation, where the surgeon searches with his hand for hard lumps in the abdomen, cannot find all the tiny disease sites to which cancer spreads. The MRL exam is so accurate that a negative exam translates into a 96 % chance that there is no metastatic disease to the lymph nodes. In addition to sparing patients from the risk and pain of surgery, this methodology reduces healthcare costs.

However, imaging with lymph node-specific contrast agents using ultrasmall superparamagnetic particles of iron oxide (Combidex or USPIO) contrast was most promising but is not approved by the FDA and therefore not clinically available. An alternative contrast agent gadofosveset has shown a sensitivity and specificity of 85 and 97 % in detecting benign lymph nodes that enhance from cancerous nodes in patients with rectal carcinomas (Lambregts et al. 2013) and may have application in prostate cancer staging in distinguishing benign from malignant lymphadenopathy.

2.2 Principles of High-Frequency Ultrasound Scanning

2.2.1 Pulse-Echo Imaging

US technology is rapidly advancing to increase image quality and expand new fields of applications. The transducer is the essential part of the equipment that generates and receives returning echoes. The basis of ultrasound scanning is the "pulse-echo" method, which is a reflection of a portion of the transmitted ultrasound back towards its source as it strikes an object or interface. An interface occurs whenever there is a difference in acoustic impedance between two adjacent tissues that is related to the density of the tissue and the velocity of the interrogating sound wave.

Two main types of echoes are encountered clinically in the prostate depending on the structure of the reflecting surface. When the reflecting surface is smooth, like the prostate capsule, Snell's law for refraction and reflection is obeyed, returning the echoes at an angle equal to the angle of incidence. This property is called a specular or mirrorlike reflection. Specular reflectors return large signals back to the transmitter. This gives sharp images but also may produce and artifact whereby the mirrorlike returning energy is completely reflected allowing no passage of sound waves past the interface. This occurs in prostatic calculi and bladder stones. Sound waves encountering an irregular interface produce more

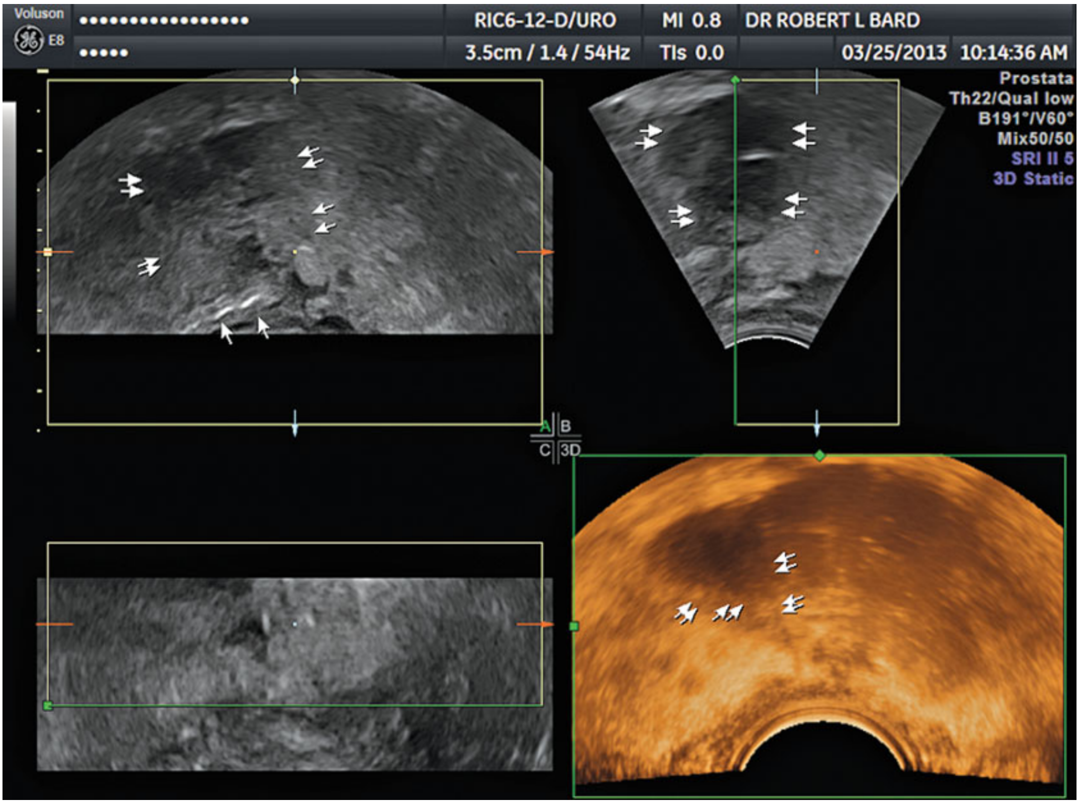

Fig. 2.1 Calculi (*single arrows*) cause dark acoustic shadow (*double arrows*)

scattering than reflection, giving weak returning signals and less defined images as one finds in the prostate parenchyma. This means that other windows of acoustic interrogation must be achieved to image the remainder of the gland that is blocked in one plane (Figs. 2.1 and 2.2a, b).

2.2.2 Attenuation

Attenuation is the loss of the energy as it undergoes continuous modification during its passage into and back from the tissues. This is a result of absorption, reflection, and scattering. Sound wave absorption is usually the dominant cause of decreased signal and occurs when the orderly particle movement characteristic of ultrasonic waveforms is converted to random vibration expressed as heat. Attenuation increases with increasing frequency and the ultrasound unit's time gain compensation adjusts for this loss of echo intensity in accurate image reproduction. The use of ceramic composite elements led to the application of short acoustic pulses and increased bandwidth, called broadband transducers, which allowed for improved axial resolution without loss of signal penetration due to attenuation of sound energy as it passes through the tissues. This is accomplished by a spectrum of frequencies within a single probe, which allows the change of scanning parameters to adjust to the area under investigation. An example of this would be to scan the prostate at 18 MHz on a 10–16 broadband probe and then lower the frequency to 8 MHz to image the more distant bladder and seminal vesicles. While reducing the width of the US beam increases contrast and spatial resolution, focusing the beam is electronic and further adjusts and improves image quality. Spatial compounding and harmonic capabilities are standard on most new systems and further improve image quality.

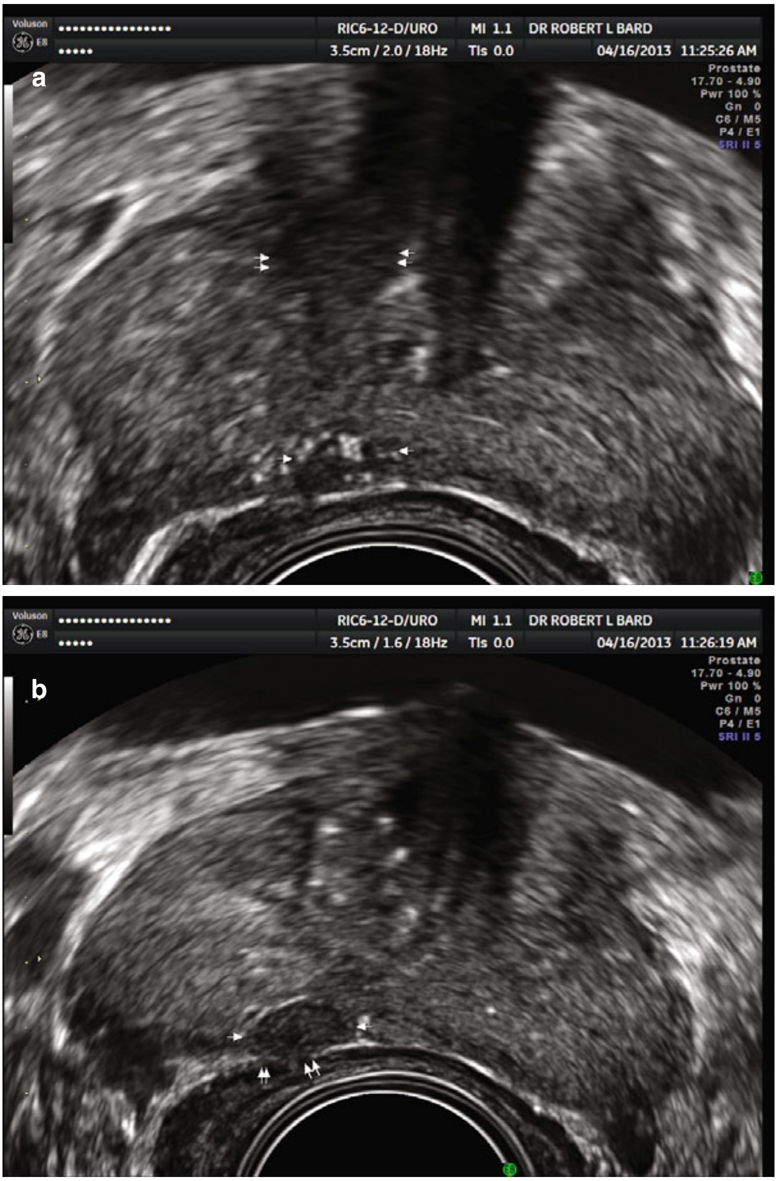

Fig. 2.2 (**a**) Presence of tumor microcalculi (*arrows*) scattered sound waves producing poor penetration and impaired resolution of anterior lesions (*double arrows*). (**b**) Shifting scan plane produces less attenuation and images posterior capsule erosion better (*double arrows*)

2.2.3 Imaging Artifacts

If the sonic beam travels in a straight line going to a reflective interface and returning to the probe, at a constant velocity, and the beam width is uniform and extremely thin, then artifacts will not occur. While artifactual distortion may degrade the image, understanding of its true nature often serves as an alert and assists the experienced sonographer in refocusing on the area of pathology.

Specular echoes are faithfully and maximally returned when the interface is 90° to the insonating beam. This means that an interface at 0° or parallel to the beam may be not imaged. Most pelvic organ tissue interfaces are a mixture of specular and scattering surfaces so that diagnostic information will be returned at beam angles greater than 20° off the perpendicular axis.

Slice thickness artifacts occur when reflecting objects at the side of a beam profile appear as centrally positioned and may produce low-level echoes in cystic structures. These artifacts may cause trouble during biopsy and image-guided procedures if not recognized.

Reverberation artifacts from strong specular reflectors may be re-reflected and create a duplicate image or images at a deeper depth. This is common in cystic lesions where the ever-weakening signals are parallel to the initial surface and of a constant interval of distance with respect to each other. In the prostate, this occurs in the presence of metallic objects or gas bubbles and has the appearance of a bright streak of echoes. This descriptive picture has been referred to as the “comet tail sign” which often occurs when air-filled catheters are present in the urethra.

Velocity artifacts occur when the insonated region is different from normal tissues of fat, glands, cystic, or solid lesions. A specific case is the presence of silicone or similar filler used in augmentation that conducts sound waves half the speed of soft tissue. The returning images appear twice as deep as expected.

Shadowing and enhancement artifacts are commonly encountered in pelvic imaging. Acoustic shadowing occurs in three forms and is due to reduced or absent sound transmission through an overlying object. The most frequently encountered is reflective shadowing or sonic shadowing produced by an interface reflecting most or all of the transmitted beam and is produced by gas (air) or dense, extensive calcification which is often encountered following healed prostatitis. Microcalcifications, which occur in 5 % of prostate malignancies, often will be imaged without creating a sonic shadow artifact. Periurethral calcifications are centrally located and have an Eiffel Tower triangular appearance. These are usually readily distinguished as such and rarely cause diagnostic problems.

Absorptive shadowing (also called attenuative sonic shadowing) has a different mechanism due to the strong attenuation of sound by fibrotic tissue or desmoplastic tumor tissues. This is uncommon in prostate imaging but must be considered in postoperative glands or in the presence of highly malignant anaplastic tumors. Edge shadowing produces lateral shadowing around some solid masses but is not expected to occur in most prostate lesions.

Doppler artifacts, common in pulse wave spectral technologies, are not seen with the current formats of color, power, and angio Doppler in modern units. Pulse wave analysis may be used to interrogate postoperative arteriovenous fistulae, but will not be further discussed in the text. Color Doppler, which is directional (showing blood flow towards and away from the transducer), has largely been replaced by the nondirectional and more sensitive power and angio Doppler systems.

2.2.4 Scan Planes

Sonographic evaluation of the prostate and bladder may be performed via the transabdominal, transperineal, or transrectal approach. The transabdominal approach through distended urinary bladder gives an accurate measurement of the gland but lacks fine prostatic anatomic detail. Transperineal imaging may be applied when the transrectal approach is not feasible or when specific biopsy methods are entailed.

The transrectal approach is the most common today and transrectal US is commonly abbreviated as TRUS. This sonographic window allows for excellent imaging of the peripheral zone of the gland where 70 % of tumors occur as well as permitting ease of sonographically guided biopsy techniques. Before inserting the rectal probe, a visual inspection for hemorrhoids and a digital examination must be performed with a lubricated glove. Easier insertion of the covered transducer may be obtained when the patient is asked to either bear down or relax after a deep inhalation. There are biplane and end-fire probes available. The biplane probe allows imaging in both the transverse and sagittal planes, whereas the end-fire probe scans in one plane that is an oblique transverse plane between the true coronal and transverse planes. To obtain a sagittal view, the probe must be rotated 90°. The scan angle is important since a 180–195° opening will show the entire transverse or craniocaudal aspect of the gland. Many commercial units today have a 145° angle which may necessitate scanning both sides separately.

2.3 Gray-Scale Appearance of Prostate Cancer

Current prostate ultrasound imaging can accurately diagnose a large variety of common pathologies by using frequencies between 5 and 9 MHz with specially designed and focused end-fire one-plane or biplane (end-fire plus perpendicular fire) transducers. The prostate and adjacent structures are small and superficial in location and so are best examined with probes of high frequency. The higher the scanning frequency, the lower the sound penetration. For example, in measuring axial resolution, the discrimination between two points in the y-axis is 0.3 mm at 5 MHz, 0.15 mm at 10 MHz, 0.12 mm at 13 MHz, and 0.06 mm at 18 MHz. This results in improved resolution, but the loss of distal information may occur when scanning deeper structures such as the enlarged median lobe (central and transitional zone) or periprostatic lymph nodes.

Cysts or fluid-filled areas are without internal echoes and are called echo-free. Solid regions have internal echoes and are classified as echo poor or hypoechoic if there are few internal echoes. The term echogenic or hyperechoic is used if there are many internal echoes. Isoechoic means the lesion has the same echo pattern as the adjacent tissue. The colon mucosa appears highly echogenic as do the bony structures. Bone, air, foreign bodies, and calcification stop the transmission of sound waves producing a "sonic shadow" which is a dark region distal to the echogenic obstructing region. The term acoustical shadowing is also used to describe the low or absent echoes associated with these lesions. Acoustic window refers to an optimal placing of the transducers so that the areas of interest are clearly imaged and areas of artifact and shadowing (such as large areas of corpora amylacea, also known as prostatic microcalculi) are avoided. Acoustic windows are aided by the use of adequate gel inside and outside the prophylactic sheath covering the transducer and further maintained by water inflatable balloons designed to couple the rectal mucosa with the transducer.

Due to the presence of high anal tone, difficulty may occur in inserting the transducer. Insertion of the probe as the patient exhales is useful. If the insertion remains painful, instillation of lidocaine-permeated ultrasound gel by a specially designed syringe with blunt tip serves the dual purpose of adequately lubricating the mucosa and anesthetizing the adjacent tissues. If biopsy is considered or other image-guided treatment, 10 cc of lidocaine or Marcaine may be injected on both sides of the lateral pericapsular nerve bundles. Since the nerve bundles may be diffusely placed, moving the needle in an arc may be advantageous.

2.4 Color and Power Doppler Applications

Conventional pulsed and continuous wave Doppler exams are used to demonstrate and quantify blood flow velocities. However, these tests are extremely time consuming, highly operator dependent, and relatively insensitive. Color Doppler uses computer coding to demonstrate directional blood flows in a clinically useful manner. Power Doppler sonography (PDS), also called power Doppler imaging (PDI), is a new feature of blood flow analysis that is proportional to the total number of moving scatterers. This allows low flow states and minute vascular structures to be investigated. Advantages of PDS over color Doppler include:

(a) Lack of aliasing artifact
(b) Two to five times greater sensitivity to flow imaging
(c) Information preservation with increasing perpendicularity of angle of beam incidence (Rizzato et al. 1995)

Current clinical PDS applications are the neovascular regions found in healing fractures, resolving hematomas, inflammatory tenosynovitis, and the detection of tumor vascularity that is associated with arteriovenous shunting, arterial malformations in size and caliber, increased vessel density, and various other vessel irregularities (Adler 1996; Campani 1997; Bard 1996). A 2002 major study on cancer imaging including sarcomas showed PDS to be useful in surgical planning decisions when a tumor was shown to be more or less aggressive than clinically suspected (Shulte 2000).

2.5 Prostate Cancer Diagnosis

Diagnosis of the most common cancer in the American male population has traditionally depended on digital rectal examination, PSA test, and TRUS (transrectal ultrasound) and, more recently, MRI. Digital rectal exam examines the periphery of the prostate, missing more centrally located lesions and extreme lateral tumors. Also, large areas of microcalculi, scars and fibrosis, or corpora amylacea may simulate a mass. PSA blood tests have been known to be falsely elevated in the presence of prostatitis and have been recently shown to be unable to definitively exclude prostate cancer. Indeed, the study of 3916 biopsies in 326 patients with PSA and TRUS showed that of the 127 patients with proven cancer, standard gray-scale TRUS correctly predicted cancer in 48 % of 326 patients studied while combined gray-scale TRUS with color Doppler imaging correctly predicted cancer in 64 %. A high PSA falsely predicted cancer in 30 % of men without malignancy. Using a threshold of 4 ng/ml, serum PSA correctly predicted cancer in 113 of 127 patients but falsely predicted cancer in 131 of 199 patients (Barish 1999).

These findings suggest the need for improved accuracy, which appears in the newer techniques of power Doppler imaging (PDS) and 3D TRUS imaging. A British study using 3D imaging to stage clinically localized prostate cancer where standard TRUS exams were 3 dimensionally reconstructed showed a 22 % increase in accuracy compared to standard TRUS when findings were compared with surgical and pathologic specimens. The technique was only useful in patients where the cancer was visible on conventional TRUS (Garg 1999) (Fig. 2.3).

Color Doppler imaging and power Doppler sonographic imaging are able to investigate cancers that do not appear clearly on standard gray-scale TRUS. Indeed, review of Doppler exams gives the physician a second look at areas initially determined to be unremarkable. Limitations of standard end-fire or biplane TRUS include misdiagnosis of cancers that are isoechoic and not imaged and false-positive diagnosis of hypoechoic areas. Approximately 25 % of malignancies are isoechoic (Alexander 1995).

A recent study showed that color Doppler imaging of 256 patients out of which 100 had biopsy-proven cancer showed tumors as the only modality in 16 %. These patients had Gleason scores of ranging between 5 and 8 with a mean of 6.4. However, it was found that 9 % of cancers (some of which were significant in size) were not discovered by either gray-scale TRUS or color Doppler imaging which used a low-velocity high-sensitivity color setting with a color filter optimized for low-velocity flow visualization of small vessels. The color window size was adjusted to cover the peripheral zone posteriorly allowing for a right and left comparison as well as deep enough to image most of the central and transitional zones (Lavoipierre et al. 1998).

Power Doppler sonography, with its higher sensitivity counterpart power angio Doppler, has been shown to differentiate between benign hypertrophy and malignant disease (Okihara et al. 1997). The sensitivity for malignancy diagnosis varies between 86 and 90 % (Cho et al. 1998). In a study of malignant disease, 22 patients with positive PDS findings were operated revealing 18 proven cancers and four false positives. Two cases were missed by PDS. The sensitivity was 90 % and the specificity was 75 % (Sakarya et al. 1998). This study underlines the necessity of proper imaging parameters so as not to be overly sensitive nor to be undersensitive in imaging blood flows.

The general consensus among imaging physicians is that a lack of blood flow in a suspicious area means the area is free of tumor or that the

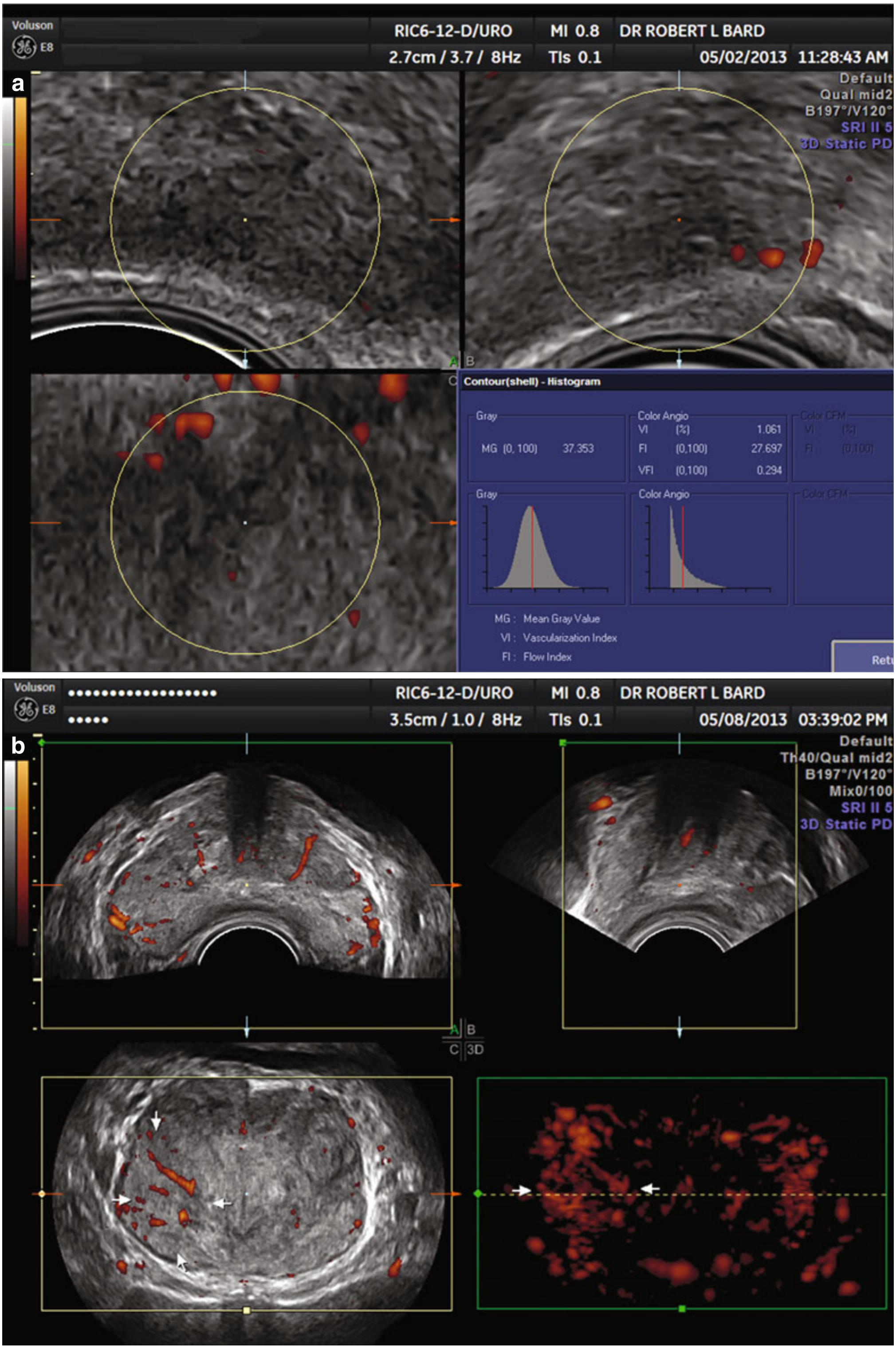

Contour(shell) - Histogram

Gray
MG (0, 100) 37.353

Color Angio
VI (%) 1.061
FI (0,100) 27.697
VFI (0,100) 0.294

Color CFM
VI (%)
FI (0,100)

MG : Mean Gray Value
VI : Vascularization Index
FI : Flow Index

Fig. 2.3 (**a**) Low-grade cancer. Note absent flows and tumor is isoechoic. (**b**) High-grade cancer. Note high flows and tumor is isoechoic cancer is of low grade. A large study over 6 years using color Doppler imaging demonstrated that 24 out of 25 patients with cancer having low blood flows are free from biochemical relapse (rising PSA) after a mean of 31 months' follow-up. Patients with high cancer blood vessel flow density were 10 times more likely to relapse following treatments (Ismail et al. 1997).

Benign tumor vessels usually start from a single vascular pedicle and have regular caliber arterial vessels with regular course and regular vascular distribution. Functional Doppler pressure flow parameters show one kind of flow in the tumor, that is, arterial blood flows with high to medium resistance. There is the absence of fresh small vessels. Malignant masses often have at least two or more feeding vascular pedicles that tend to penetrate the cancer at a more or less right angle. These arterial vessels have irregular caliber, course, and canalization. Fresh thin microvessels are noted. Arteriovenous shunts are demonstrable. Rapid changes of course with sharp angulations are present. A rich peripheral and slightly less dense internal vascularization is present unless there is central internal degeneration or necrosis. In this case peripheral neovascularization will be present and central vessels will be absent. This distinction is important for biopsy sampling, since a core from a necrotic area will not be diagnostically useful to the pathologist. Therefore, targeting the more vascular region will lead to more useful pathologic data analysis.

Functional Doppler shows vessels with variable resistance and variable velocity. Different types of flow are often noted within the same tumor (Campani 1995). The pathologist may use this same concept with the microscope. Microvessel tumor density is now being evaluated by immunohistochemical staining of blood vessels (Factor VIII-related antigen). Blood vessel density is an objective measurement of angiogenesis. Digital image analysis of the stained blood vessels may be quantified and put into an algorithm that predicts the probability of prostate cancer spread versus the probability of localized disease. This algorithm is called optimized microvessel tumor density, and it has now been used on over 10,000 patients nationwide on their biopsy specimens to provide appropriate patient management (Strum 1998).

Intense effort to discover new ways to demonstrate prostate cancer neovascularity is currently ongoing around the world. The use of contrast agents by injection has been shown in Europe to produce a 50 % increase in detection of abnormal blood vessels (Gajonova 1999). These agents are not yet approved by the FDA in the USA after a 10-year successful trial in European medical centers.

The normal prostate has thin arc-like vessels at the periphery (capsular region) and at the demarcation between the peripheral zone and the central zone. Central periurethral vessels are often noted and best imaged in longitudinal planes although these are rarely confused with tumor vessels. The vessels are symmetric and have regular course and slightly tapering caliber as it progresses distally along the urethra. Median lobe enlargement of benign nature and benign prostatic hypertrophy show enlargement of the vessels between the central zone and the peripheral zone. These vessels are symmetric and have regular course and caliber. Prostatitis has normal to slightly increased caliber vessels with high flow states. The vessels are widely separated by the edematous parenchyma. Cancers of low grade show increased number of vessels with some vessel caliber irregularity. There may be multiple feeding vessels of tortuous configuration in larger tumors. Cancers of high grade show increased vessel density, enlarged gross caliber, and course irregularity including sharp angulations of vessel trajectory. Malignancies with massive central internal necrosis caused by the tumor outgrowing its blood supply will show a rich peripheral neovascularization without vessels extending into or through the center of the mass. Cancers that have been treated successfully by radiation, cryosurgery, HIFU (high-intensity focused ultrasound), laser ablation, or certain nonsurgical methodologies may show an echogenic irregular region of fibrotic tissue conforming to the general region of the previously noted active malignancy. Extreme caution must be taken to avoid the brightly echogenic and color-producing regions of stones, corpora amylacea, or microcalculi. The gray-scale b scan must be checked before any region of abnormal blood flows is finally documented. Spectral PW (pulsed wave) Doppler in these regions will show the absence of arterial or venous flows and the presence of staccato-like reverberation artifacts distinctly different from true vessels and abnormal vessel configurations.

The blood supply to the prostate originates from the branch of the common iliac artery called the hypogastric artery. Branches from the anterior trunk give rise to the superior vesical, middle vesical, inferior vesical, middle hemorrhoidal, obturator, internal pudendal, and inferior gluteal arteries. The prostate is mainly supplied normally by the inferior vesical and middle hemorrhoidal arteries. These arteries surround the capsule and then travel linearly centrally to supply the interior of the gland in a central manner. The arteries have a specific functional component called pulsatility index (PI) related to the systolic and diastolic blood flows. It has been noted that breast cancer (the prostate and breast are both glands and have similar histologic features) local feeding blood vessels have greater flow volumes than the contralateral or normal vessels (Hollerweger 1997). A recent study showed the possibility of studying the regional prostatic vasculature by example of the breast cancer analogy demonstrating that the lateral thoracic artery in breast malignancies showed a significantly elevated PI difference in the cancerous breast (Obwegeser et al. 1999).

It is probable, in a similar manner, that new information evolving from the study of the major feeding prostatic blood vessels will lead to important diagnostic and prognostic possibilities. A further clinical application now being investigated is to selectively destroy the cancer by embolizing the feeding blood vessels via an arterial catheter or deliver high doses of chemotherapies via the same route. At this point a technical note of great importance must be introduced. As sensitive as PDS is to low flow states, excessive use of probe pressure will effectively reduce blood perfusion to undetectable states. This hemodynamic fact may be used in the case of significant post-biopsy hemorrhage. There are reports of uncontrolled rectal bleed post prostate biopsy being controlled and stopped by application of the biopsy probe to compress the ruptured vessels. Anecdotal reports and case studies cite the need to continue pressure for 60 min.

A simple method of maintaining sound wave contact through the transducer with respect to the prostate is the use of copious amounts of ultrasound gel to produce a bath of gel around the transducer tip. Another method is the use of a water bath that is filled up by a syringe adjacent to the transducer handle. This setup is commonly found in biplane systems. Again, the balloon effect to maintain contact with the rectal wall must be sufficiently mild so as not to adversely affect the flow of blood in the prostate gland. This problem was first recognized in breast cancer detection some 5 years ago using PDI. Whereas the prostate is more deeply seated, the peripheral zone may still be pressure sensitive to transducer application. It is incumbent on the examining physician to recognize the iatrogenically produced low flow states and attempt to improve flow status by reducing probe pressure during the exam to see if a change in flow status is observed. Special prelubricated probe covers are available for the larger diameter 3D transducers.

2.6 Tumor Angiogenesis

The early basic pathophysiologic work in tumor angiogenesis emanates mainly from Japan. Improvements in gray-scale ultrasound technologies, power Doppler imaging, and contrast agent science will allow us to appreciate far more detail of tumor neovascularization and its associated tissue changes in the near future. Tumor neovascularization is a process that is essentially similar in all organs. Most cancers would never grow larger than 2 mm in diameter without the ability to recruit new blood vessels (Blood and Zetter 1990). Tumor neovascularization is initiated from a starting vessel at the level of a terminal arteriole. This new vessel anastomoses with host capillaries resulting in a rich network of tumor vessels (Hori et al. 1981). The normal blood pressure in the vessel increases up to 4 times with neoplastic growth and the existing postcapillaries become deformed and dilated decreasing blood pressure.

Neovascularization proceeds at the periphery of the tumor while low-pressure vessels are reduced and occluded resulting in central necrosis (Hori et al. 1990) producing a partly cystic center within the tumor or semisolid liquefied region.

The usual pathologic process of cancer neovascularization produces most vessels at the periphery and fewest in the interior of the tumor. In general, arteries are not invaded by tumor growth. However, tumor angiogenetic factors affect the fibrous tissues surrounding the vessels causing encasement and tortuosity with possible obstruction of the arteries. As well as different degrees of vascularization, angiographic studies have shown characteristic patterns in the periphery and in the center of a tumor. Centrally located are dilated capillaries with varying diameter from 50 to 500 μm (micromillimeters) that are irregular in shape. Blood flow is stagnant due to low pressure and low resistance and the associated high resistance of draining veins. At present, these low flow states cannot be imaged by color flow imaging or PDS. Future developments using OCT (optical coherence tomography) and photoacoustic imaging (lasers produce sonic reverberations received and imaged by a transducer) are now seeing 50 μm vessels within a 2–4 mm depth of tissue.

The feeding vessels at the periphery of malignant tumors enter at right angles together with the drainage veins. The feeding arteries are usually encased and somewhat obstructed and the often noted early venous drainage on angiography results from arteriovenous shunts at the periphery.

Morphologic assessment of tumor neovascularity is qualitative at this time with standard urologic 2D ultrasound systems. Earlier investigators thought vascularity in a tumor implied malignancy; however, slowly expanding benign tumors commonly have a new blood supply detected with newer imaging systems. While feeding arteries to malignant tumors enter at approximately right angles, supplying arteries to benign masses tend to course along the peripheral surface of the lesion. The demonstration of a penetrating artery with encasement and irregularity due to surrounding tumoral tissues is indicative of cancer. Some feeding arteries become tumor vessels, whereas others pass through the tumor. The correlate in the prostate is the benign prostatic enlargement demonstrating smoothly coursing symmetric vessels at the periphery of the hypertrophic median lobe with occasional vessels of normal caliber passing through the enlarged region. Aggressive cancers show tortuous, penetrating, and encased vessels.

Compressibility of vessels may be evaluated by pressure on the examining probe to detect the decrease in size of the luminal walls of the feeding arteries and draining veins. Highly malignant tumors appear to have greater amounts of desmoplastic reaction resulting in perivascular fibrotic tissue that prevents deformity by external pressure (Tsunoda-Shimizu 1991). The presence of Doppler flow signals following compression is an area to be further studied in the prostate since the work in this area was performed in breast cancers showing a poor prognosis in women with highly vascular tumors (Maeda 1977).

2.7 Tumor Metastases

Prostate cancers spread locally by direct growth and distantly by lymphatic and vascular metastases. The possibility of tumor metastases is increased in the presence of capsular erosion (Fig. 2.4a, b) and may also be measured by the degree of tumor neovascularity.

Two major methods of assessing tumor vascularity are microvessel density on a microscopic level and Doppler sonography on a macroscopic level. When microvessel density exceeds 80 vessels per 250x microscopic field, the tumors were likely to be demonstrated by Doppler imaging (Sterns et al. 1996). A recent study of breast cancers showed that PDS was a potentially noninvasive method to assess the presence or absence of lymph node metastases. This investigation showed a high correlation of lymph node involvements with 93 % sensitivity in vascular tumors although the specificity was only 32 %. This means that tumors with no vascularity on PDS had a 90 % chance of no lymph node spread. Tumors spread to lymph nodes either by lymphatic drainage or by a hematogenous route, thus the rationale for investigating tumor neovascularity for lymph node involvement (Mehta and Raza 1999).

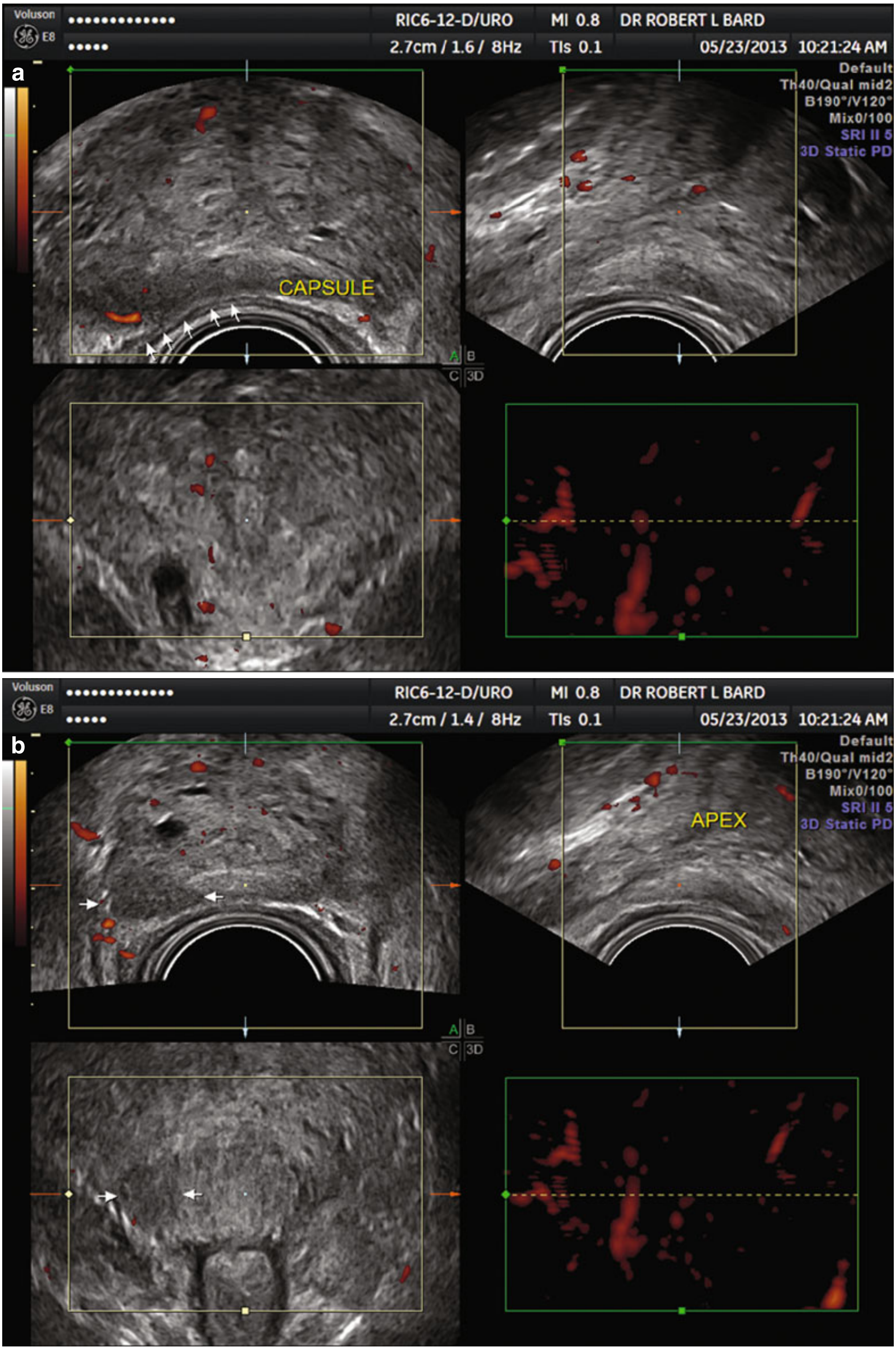

Fig. 2.4 (**a**) Loss of right pseudocapsule is evident in comparison to left highly echogenic border. (**b**) Right-sided tumor present in region of capsular abnormality

2.8 Ultrasound Contrast Agents

To best understand the rationale for the use of contrast agents, it is important to understand the limits of spatial resolution and Doppler flow sensitivities. One needs only to image the superficial small vessels first with gray-scale b mode and then with power Doppler imaging to see that blood flows are easily detectable even though the vessels themselves are no longer imaged even by very-high-frequency probes. The limit of Doppler imaging is the point at which the velocity of flow needed to produce the Doppler shift is distinguishable from that produced by the surrounding adjacent normal motion of tissues. The limit of spatial resolution for gray-scale ultrasound is the received intensity of the backscattered return signal that is greater than the acoustic and electrical noise of the system. Higher-frequency ultrasound is useful in both respects since the Doppler shift actually increases proportionally to the transmitted sound frequency. Also, the backscattered intensity (resolution) increases to the fourth power of transmitted frequency. In the case of the prostate, probes between the frequencies of 5–9 MHz are used currently with broadband technology and the potential for higher-frequency probes may be feasible if one were to focus on the peripheral zone of the prostate that is closest to the transducer where most of the cancers occur.

Contrast agents should be introducible into the vascular system and can act either by selective uptake in the tissues or by their presence in the vascular system. Although the concept of contrast was introduced in cardiac work in 1968, current usage is of free or encapsulated gas bubbles, colloidal suspensions, emulsions, and aqueous solutions. As mentioned earlier, the FDA has not approved its use in prostate examination.

2.9 Harmonic Imaging

Since units capable of harmonic imaging are now in routine clinical use, brief mention will be made for future reference. The actual effect of ultrasound contrast is to decrease image contrast between blood and soft tissue. This in turn allows detection of contrast agent in solid tissue; for example, the myocardium is currently being investigated in the USA. It also provides a new means for suppression of Doppler clutter caused by the Doppler shift inherent in soft tissues, which is a determinant of flow detection in small vessels.

Backscattered sound from contrast agent appears to show harmonic type peaks. This permits creating contrast particles of a certain size to maximize a specific peak. A consequence of this dynamic property is to induce nonlinear oscillations in particles, which greatly magnifies the backscatter effect. This means that small amounts of properly sized contrast agent particles will produce a large return echo when insonated at specific frequencies even if the amount of contrast agent is small. The sound emitted or backscattered from the contrast bubble also has harmonic multiples like in music. This creates the possibility of a new type of imaging based on second and third harmonics of sound vibrations. Thus tumor vessels not imaged by current systems may be detected by this new variant in sonar detection (Wells 1994) and by phase inversion or intermittent imaging techniques that allow contrast buildup in the denser tissue since it is clear that the vascular supply in malignant prostatic tissue is different from normal prostate (Halpern and Strup 2000).

2.10 Doppler Flow Imaging

The American College of Radiology has recommended color Doppler imaging to be used as a guideline for hypervascular regions to biopsy in the Standards of the College for the Performance of Prostate Ultrasound since the year 2000 (Prostate Ultrasound Standards 1999–2000). Areas of increased flows on power Doppler imaging are 4.7 times as likely to contain cancer than adjacent tissue without flow (Halpern et al. 2000). Indeed, the negative predictive value is 99 % suggesting that this may be used to avoid biopsies on patients with falsely elevated PSA levels (Okihara et al. 2000). Clinicians who feel that cancers of low grade may be followed and not biopsied suggest that tumors without high blood flows require half yearly observation rather than intervention (Cosgrove 2000). Indeed, the response of tumor vascularity to nonsurgical treatment may be assessed serially. If the blood supply diminishes, treatment may be considered efficacious. On the contrary, if vascularity fails to decrease, alternative methods of therapy should be considered (Cornud et al. 2000).

While every patient responds to treatment differently, persistent neovascularity after 4 months indicates treatment failure, especially in cases of chemotherapy, antioxidant, radiation, watchful waiting/active surveillance, and photodynamic therapies. Immediate disappearance of abnormal vessels is expected in ablative therapies such as surgery, cryotherapy, HIFU (high-intensity focused ultrasound), and focal laser ablation.

Hypervascular areas may be preferentially biopsied under ultrasound guidance (Hricak 2000). Postradiation PSA elevations may be evaluated as to tumor recurrence or to inflammatory presence. Repeat biopsies may be avoided in the absence of demonstrable focal neovascularity. Due to the difficulty in the accuracy of determining Gleason scores, PDS may become a prime indicator of prognosis (O'Dowd et al. 2001). A 1992 Swedish study published in the Journal of the American Medical Association evaluated 223 men with an average age of 72 years who had early-stage prostate cancer but received no initial treatment. Ten years later, only 19 of them (8.5 %) had died of the disease, whereas more than five times as many (105) had died of other causes (Harvard Medical School Pamphlet 2001). In the author's own experience of 4000 biopsy-proven cases from Gleason 6 to Gleason 9, the vast majority have had the cancer controlled by nonsurgical means as demonstrated by diminished or complete reversal of neovascular areas (Bard 2001). Tumor hypervascularity correlates well with metastatic potential (Lassau et al. 2002; Lee 2002; Bahn 2002).

Prostate Doppler sonography has an accuracy of 97 % in the peripheral zone using 18 MHz transducers. The development of MRI, diffusion-weighted MRI, and DCE-MRI was accelerated by comparing the MRI exam with the high-resolution Doppler sonogram. In the USA and Canada, men are reluctant to have prostatectomies, so the proven modality of PDS was used to develop and improve MRI technologies in the absence of the whole mount pathologic specimens.

Early experience with color Doppler by Sudakoff et al. (1996) showed that color Doppler imaging (CDI) could differentiate posttreatment radical prostatectomy tumor recurrence in the face of a rising PSA from distant metastases. In his study of 23 patients, CDI showed a specificity of 100 % as compared with the standard ultrasound specificity of 89 %. The conclusion was that CDI added to transrectal sonography improved the detection of early recurrent or residual prostate cancer. CDI actually detected foci not visible on standard TRUS.

The technology of Doppler imaging has evolved continuously from the early color Doppler work. Cornud has demonstrated that color Doppler sonography (CDS) correlates well with pathology. He reported his results with a group of 94 patients with non-suspicious findings on DRE who were imaged before radical prostatectomy. There were 42 hypoechoic and hypervascular tumors that had Gleason tumor grades of 4 or 5 as opposed to the 52 hypovascular tumors that gave a Gleason grade of 3 and, in some cases, were of insignificant tumor volume. The study conclusion was that TRUS and CDS were useful in differentiating low-risk invisible tumors from high-risk visible and hypervascular tumors.

In 2003, Sauvain et al. did a study of 323 patients with power Doppler sonography (now called PDS), which is more sensitive than color Doppler although loss of directional flow occurs. The specificity of the cancer diagnosis was 72 % as compared with 57 % for TRUS. More important, the negative predictive value was 81 % (Sauvain et al. 2003). Targeting the area of abnormal blood flow allowed biopsy of isoechoic areas that would have been missed by standard TRUS, thus improving the sampling rate.

PDS allowed the location of flow in three areas: (a) peripheral prostatic capsular vessels, (b) parenchymal vessels, and (c) vessels anastamosing with the extraprostatic vessels.

Where a tumor nodule was found, the presence or absence of posterior prostatic margin flow was assessed and searched around the lesion for mass effect delineated by displaced vessels or a gap in the expected symmetric vascular diffusion pattern observed.

Using 3D PDS technology, three vascular types were demonstrated and confirmed by histology following operative prostatectomy:

Type A Vascular perfusion of the prostatic posterior margin was absent and effaced by the tumor mass effect, and a regular hypoechoic margin with a 1–2 mm thickness was noted behind the most posterior peripheral detected vessel. This was found to be typical of cancer without measurable blood flow.

Type B Vascular perfusion of the posterior margin is absent; however, the marginal rim is thinned and irregular. No detectable anastomosis with the peripheral extraprostatic vascular system is noted. In this type the possibility of extracapsular extension is possible.

Type C Vascular perfusion of the posterior margin is present and anastomotic connection with the extracapsular vessel system is noted. The posterior margin is thinned in some areas and absent in other areas. There is a presumption of extracapsular spread. In this type the specificity for extracapsular tumor spread was 94.4 % while the sensitivity was 59.3 % and the accuracy was 79.3 %.

The 3D technology allows the depiction of mass effect with draping vessels visualized more easily than with 2D imaging. Optimal delineation of mass effect is better when the prostate has no evidence of inflammation or previous biopsy. The 3D volumetric capability allows for vessel density measurement in pathologic conditions.

This paper concluded that the PDS imaging accuracy was insufficient to avoid biopsies in suspected patients. A follow-up paper 10 years later by the same team (Sauvain et al. 2013) evaluated the risk of low-risk prostate cancer or prostate cancer that may benefit from active surveillance in patients with a PSA level less than 10 ng/ml, a normal DRE, and an unremarkable PDS. 243 consecutive patients in this category were biopsied under PDS with 12–15 samples taken systematically and targeted in suspicious areas. The PDS results were rated from 1 to 4 as follows:

1. Normal
2. Slightly hypoechoic (echo poor) (hypoechogenic) avascular area in which the echogenicity increases (hypoechogenicity decreases) after compression by transducer probe
3. Hypoechoic (echo poor) (hypoechogenic) avascular region
4. Hypoechoic (echo poor) (hypoechogenic) vascular region

Patients in the 3 and 4 categories were considered pathologic. The PDS was rated true positive if at least one biopsy was positive in the same sextant as the suspect image. D'Amico's criteria were used to assess the risk of a biologic recurrence after treatment. The criteria of Dall'Era were used to select the patients that would benefit from active surveillance.

Results showed 65 % of patients with normal PDS exams. In that group there was a 96 % probability of not having a high-risk cancer. With an abnormal PDS, there was at least one positive biopsy in 57 % of cases. In that group the probability of having a significant cancer was 30 % according to the criteria of Dall'Era.

The conclusion was that the above criteria may be used to put off the indication for biopsies in order to reduce the number as well as the risks of overtreatment for a latent or clinically insignificant cancer. In the PSA range of 4–10 ng/ml, there was 64 % likelihood that active surveillance (AS) would be appropriate. PDS has less value in the central/anterior/transitional zones (as do all the MRI modalities) than in the peripheral zone, although the delayed diagnosis in this area often results in higher PSA value than 10 ng/ml (Sauvain et al. 2013).

The compression of abnormal tissue with the probe to increase echogenicity may be replaced by the expanding use of elastography. It is felt that the presence of edematous or inflammatory parenchyma permits compression by external force suggesting that it is not cancerous, since malignant tissue tends to be incompressible tissue. Both inflammation and edema increase the water content of the tissues, reducing the echo density. Increased sonic transmission is characteristic of benign noncancerous tissues. Probe pressure also has the added benefit of eliciting pain in the edematous or vascular inflamed segment under visual control to confirm the presence of inflammation as opposed to edema.

Another way to differentiate inflammation from edema by mechanical pressure is to observe the vascular density, which is elevated in acute inflammatory diseases and may minimally decrease as outside force is applied. Edematous tissue will have fewer visible vessels that will disappear upon moderate peripheral probe pressure. We have observed that high altitude, such as recent air travel, may produce mild enlargement of the gland without discernable neovascular findings.

Since the Doppler flow findings are so important in the clinical decisions regarding the prostate, let us briefly examine the accuracy of this technology in other organ systems to prove that aggression verified by blood flow is predictable in all organ systems and not limited to the prostate. Areas that have been studied extensively are breast cancer, nodal metastases, choroid/retinal melanoma, melanoma skin cancer, and uterine cancer with special attention to the endometrium.

A study was conducted to show the clinical usefulness of 3D PDS for the diagnosis of endometrial carcinoma at endometrial volume and vessel density indices. 84 women with proven endometrial hyperplasia or endometrial cancer were evaluated by endometrial biopsy and showed a specificity of 81 % using the PDS indices of vascularization index (VI), flow index, and vascularization-flow index (VFI). Additionally, the vascular resistive index (RI) was documented to be lower in cases of high histologic grade (Mercé et al. 2007).

Three-dimensional (3D) sonography and power Doppler angiography show the whole vascular supply of the endometrium which is evaluated from 3D power Doppler mapping. The following vascularity indices are calculated automatically: the vascularization index (VI), flow index (FI), and vascularization-flow index (VFI). This calibration software provides numbers that can be used to follow treatment success or failure in a quantitative manner. Doppler indices (VI, FI, and VFI) are significantly increased in endometrial carcinoma. Histologic grade and lymph node metastases were noted proportional to the decrease in intratumoral RI.

Other confirmed clinical uses of Doppler ultrasound are in the fields of ophthalmology, skin cancer, hepatology, breast cancer, sarcoma of soft tissue, and bone and lymph node imaging.

To appreciate the value of 3D imaging in prostate transrectal scans, a study by the innovator, Dr. Michael Mitterberger (Mitterberger et al. 2007), of this technology was performed on 180 patients who underwent radical prostatectomy providing histologic confirmation of volumetric scanning. This was undertaken because the presence of undetected extracapsular extension might result in incomplete tumor excision and increased risk of treatment failure (Damber and Khatami 2005). Apparently, the standard methods of local staging (PSA, DRE, TRUS, axial CT, and endorectal MRI) lack sensitivity and can understage up to half of cancers (Aus et al. 2005). 3D TRUS was developed out of the need for a more accurate, less subjective, and relatively inexpensive means of staging prostate cancer (Mehta et al. 2004; Strasser et al. 1996, 2004).

To ensure high-quality volumetric multiplanar imaging, the patient and the sonographer must avoid any movement. A useful method is for both the patient and examiner to hold their breath during the 3–5 s scan. Once the initial scan is obtained, the computer program displays three sections in the horizontal (transverse/usual 2D display) as well as the sagittal and coronal planes, which are 90° to one another. Scan angle varies with units; however, a minimum angle of 145° is necessary for proper display of the capsular symmetry. Greater angles up to 200° afford better assessment of the pericapsular fat and paracapsular lymph nodes although a minor loss of resolution is involved as a tradeoff to obtain a wider field of view.

Suspicion of extracapsular extension (ECE) is seen as an interruption of the pseudocapsule, which is the periprostatic fat layer that is juxtaposed to a hypoechoic lesion. This is often most clearly delineated in the coronal view. The full extent of the seminal vesicles is difficult to image in some patients. Dividing the field to encompass each vesicle individually with a narrower angle may be efficacious.

Suspicion of seminal vesicle invasion (SVI) is noted as obliteration of the angle between the seminal vesicle (SV) and the base of the prostate. Another more positive finding is the continuation of the hypoechoic mass into the seminal vesicle with accompanying expansion. If PDS is available, confirmation of the tumor vascularity into the abnormal seminal vesicle corroborates the initial observation. While TRUS was invented in 1971 by Watanabe (Watanabe et al. 1971), continuing improvements now allow the imaging of perirectal lymph nodes with a different type of endorectal circumferential scanner. This is important because the presence of perirectal adenopathy is highly suggestive of true metastatic adenopathy. A periprostatic adenopathy search should be attempted by the sonographer; however, this area is usually best studied by the 3 T MRI. In this study the pathologic capsular penetration was accurate in 96 % with an 88 % sensitivity and a specificity of 97 %. The detection of SVI had an overall accuracy of 96 %.

With today's higher-resolution equipment (18 MHz probe as contrasted with the study's 7.5–10 MHz transducer) and the addition of blood flow imaging, the detection of ECE and SVI has improved although there are no major series published to date with better accuracy than the present example. Currently, we can detect capsular bulging and erosion that precede the full picture of ECE. The data set obtained makes comparison with the MRI easier and each 90° plane can be matched with the similar MRI plane, remembering that the TRUS transverse or horizontal plane may be different from the MRI planes due to patient position and probe positions. In general, there is good correlation. The fusion of TRUS and MRI is now clinically available and is being used for image-guided biopsies by the urologist who has more familiarity with the sonogram procedure than the multiple MRI options.

References

Adler R. Power Doppler applications in musculoskeletal ultrasound. In: Presented at 6th annual conference of Musculoskeletal Ultrasound, Montreal, 1996.

Alexander AA. To color Doppler image the prostate or not. Radiology. 1995;195(1):11–3.

Aus G, Abbou CC, et al. European Association of Urology. Eur Urol. 2005;48(4):546–51.

Bahn D. Proc Inst Prostate Cancer Res. 2002;5(1). See also Bahn D. Color Doppler and tissue harmonic ultrasound in the early detection and staging of prostate cancer. PCRI Insights. 2002;5(2). Found online at http://prostate-cancer.org/color-doppler-and-tissue-harmonic-ultrasound-in-the-early-detection-and-staging-of-prostate-cancer/.

Bard R. The blizzard sign of intramuscular healing hematoma. In: Presented at 6th annual conference of Musculoskeletal Ultrasound, Montreal, 1996.

Bard R. Department of Urology College of Physicians and Surgeons at Columbia Presbyterian Medical Center. Grand Rounds Presentation, 2001.

Barish MA. Relative value of PSA and TRUS findings in predicting prostate cancer. In: Proceedings 99th annual ARRS meeting, New Orleans, 1999.

Blood CH, Zetter BR. Tumor interactions with the vasculature: angiogenesis and tumor metastasis. Biochim Biophys Acta. 1990;1032:89–118.

Bostwick D. Does finasteride alter the pathology of the prostate and cancer grading? PCRI Insights. 2004;7(1):67.

Burns PN. Mezzi di contrasto per ecografia nella diagnostica radiologica. La Radiologia Medica 1994;87(5):71–82.

Campani R. Sonography of soft tissue malignancies. In: Presented at AIUM annual conference, Inst Ultrasound Medicine Rapallo, Italy, 1995.

Campani R. Ultrasonic contrast agents. In: Presented at 7th annual conference of Musculoskeletal Ultrasound, Portofino, 1997.

Cho JY, Seung HK, Sang EL. Diffuse prostatic lesions: role of color Doppler and power Doppler ultrasonography. J Ultrasound Med. 1998;17:283–7.

Cornud F, Hamida K, et al. Endorectal color Doppler sonography and endorectal MR imaging features of nonpalpable prostate cancer: correlation with radical prostatectomy findings. AJR Am J Roentgenol. 2000; 175(4):1161–8.

Cosgrove D. Microbubble vascular sonography. Diagn Imaging. 2000;7:69.

Damber JE, Khatami A. Surgical treatment of localized prostate cancer. Acta Oncol. 2005;44(6):599–604.

Downey D, Fenster A. Vascular imaging with a three-dimensional power Doppler system. Am J Radiol. 1995;165:665–8.

Gajonova VY. 3D power Doppler enhanced sonography in detection of prostate cancer neovascularity following Levovist injection. European Congress of Radiology. Vienna, Austria, 1999.

Garg S. Staging of prostate cancer using 3D transrectal ultrasound images. In: Proceedings 99th annual ARRS meeting, New Orleans, 1999.

Halpern E, Strup S. Using gray-scale and color and power Doppler sonography to detect prostatic cancer. AJR Am J Roentgenol. 2000;174(3):623–7.

Halpern E, Verkh L, et al. Initial experience with contrast-enhanced sonography of the prostate. AJR Am J Roentgenol. 2000;174(6):1575–80.

Harvard Medical School Pamphlet. Protect your prostate. Boston. 2001.

Hollerweger A. New signs of breast cancer: high resistance flow and variations in resistive indices evaluation by color Doppler sonography. Ultrasound Med Biol. 1997;23(6):851–6.

Hori K, Suzuki M, et al. New technique for measurement of microvascular pressure in normal and tumor vessels of rats. Invasion Metastasis. 1981;1(4):248–60.

Hori K, Suzuki M, et al. Development of the angioarchitecture and microcirculatory characteristics in rat tumor. Japan J Cancer Chemo. 1990;17(3 Pt 2):554–63.

Hricak H. Prostate Doppler biopsy imaging. In: NY Roentgen Society conference, New York Roentgen Ray Annual Meeting NYC, 2000.

Ismail M, Petersen RO, et al. Color Doppler imaging in predicting the biologic behavior of prostate cancer: correlation with disease-free survival. Urology. 1997;50(6):906–12.

Lambregts DM, Heijnen LA, et al. Gadofosveset-enhanced MRI for the assessment of rectal cancer lymph nodes: predictive criteria. Abdom Imaging. 2013;38(4):720–7. doi: 10.1007/s00261-012-9957-4.

Lassau N, Koscielny S, et al. Prognostis value of angiogenesis evaluated with high-frequency and color Doppler sonography for preoperative assessment of melanomas. AJR Am J Roentgenol. 2002;178(6): 1547–51.

Lavoipierre A, Snow R, et al. Prostatic cancer: role of color Doppler imaging in transrectal sonography. AJR Am J Roentgenol. 1998;171(1):205–10.

Lee F. Prostate Mayo Clinic Foundation Commerce, MI. 2002.

Louvar E, Littrup P, et al. Correlation of color Doppler flow in the prostate with tissue vascularity. In: First presented at the 96th annual meeting of the American Roentgen Ray Society, San Diego, 5–10 May 1996.

Maeda M. Angiography of the breast. Nippon Acta Radiol. 1977;37(12):1101–8.

Mehta T, Raza S. Power Doppler sonography of breast cancer: does vascularity correlate with node status or lymphatic vascular invasion? AJR Am J Roentgenol. 1999;173(2):303–7.

Mehta SS, Azzouzi AR, Hamdy FC. Three dimensional ultrasound and prostate cancer. World J Urol. 2004; 22:339–45.

Mercé LT, Alcázar J, et al. Clinical usefulness of 3-dimensional sonography and power Doppler angiography for diagnosis of endometrial carcinoma. J Ultrasound Med. 2007;26:1279–87.

Mitterberger M, Pinggera GM, et al. The value of three-dimensional transrectal ultrasonography in staging prostate cancer. BJU Int. 2007;100(1):47–50.

Moyer P. Power Doppler, 3D vascular US may aid diagnosis, staging of prostate cancer. DG News, 30 April 2003. Online at http://www.docguide.com/power-doppler-3d-vascular-us-may-aid-diagnosis-staging-prostate-cancer-presented-aua?tsid=5.

Obwegeser R, et al. Ultrasound-imaging of lateral thoracic arteries to detect breast cancer. Lancet. 1999; 353(9168):1938.

O'Dowd G, Veltri R, et al. The Gleason score: a significant biological manifestation of prostate cancer aggressiveness on biopsy. PCRI Insights. 2001;4(1) [page numbers not available].

Okihara K, Kojima M, et al. Ultrasonic power Doppler imaging for prostatic cancer: a preliminary report. Tohoku J Exp Med. 1997;182(4):277–81.

Okihara K, Kojima M, et al. Transrectal power Doppler imaging in the detection of prostate cancer. BJU Int. 2000;85(9):1053–7.

Prostate Ultrasound Standards: American College of Radiology Standards 2000;39:617–19.

Rizzato G, et al. Bone and callus. In: Solbiati L, Rizzatto G, editors. Ultrasound of superficial structures. New York: Churchill Livingstone; 1995. p. 377–82.

Sakarya ME, Arslan H, et al. The role of power Doppler ultrasonography in the diagnosis of prostate cancer: a preliminary study. Br J Urol. 1998;82(3):386–8.

Sauvain JL, Palascak P, et al. Value of power Doppler and #D vascular sonography as a method for diagnosis and staging of prostate cancer. Eur Urol. 2003;44(1): 21–30.

Sauvain JL, Sauvain E, et al. Value of transrectal power Doppler sonography in the detection of low-risk prostate cancers. Diagn Interv Imaging. 2013;94(1): 60–7.

Shulte M. Color Duplex sonography in staging of malignant primary bone tumors. In: Proceedings at 5th international congress of Musculoskeletal Ultrasound, Prague, 2000.

Sterns E, SenGupta S, et al. Vascularity demonstrated by Doppler ultrasound and immunohistochemistry in invasive ductal carcinoma of the breast. Breast Cancer Res Treat. 1996;40(2):197–203.

Strasser H, Janetschek G, et al. Prostate zones in three-dimensional transrectal ultrasound. Urology. 1996; 47(4):485–90.

Strasser H, Pinggera GM, et al. Three-dimensional transrectal ultrasound of the male urethral rhabdosphincter. World J Urol. 2004;22(5):335–8.

Strum S. Optimized microvessel density in prostate cancer localization. Proc Institute of Prostate Cancer Research, Los Angeles CA, 1998.

Sudakoff G, Smith R, et al. Color Doppler imaging and transrectal sonography of the prostatic fossa following radical prostatectomy: early experience. AJR Am J Roentgenol. 1996;167:883–8.

Tsunoda-Shimizu H. Correlation of color Doppler imaging with B mode ultrasound in breast cancer. Jpn Soc Ultrasound Med Proc. 1991;18(353):17–27.

Watanabe H, Kaiho H, et al. Diagnostic application of ultrasonotomography to the prostate. Invest Urol. 1971;8(5):548–59.

3

Advanced Ultrasound: Prostate Elastography and Photoacoustic Imaging

Stephen Rosenzweig, Richard Bouchard, Thomas Polascik, Liang Zhai, and Kathryn Nightingale

3.1 Introduction

Conventional B-mode transrectal ultrasound (TRUS) is used extensively to aid in visualizing the prostate gland and needle during biopsy. However, TRUS has limited sensitivity and specificity for prostate cancer detection (Nelson et al. 2007; Correas et al. 2013), and therefore advanced ultrasonic methods are currently being investigated to improve prostate cancer detection.

Generally, cancer has increased vascularity as compared to the surrounding tissue, and therefore, multiple studies have investigated using either color or power Doppler imaging in conjunction with standard B-mode TRUS during biopsy (Nelson et al. 2007; Correas et al. 2013; Kamoi et al. 2008). Although some of the studies showed improved sensitivity or specificity, they concluded that performing guided biopsies with Doppler imaging could not replace standard 6 or 12 core biopsies (Nelson et al. 2007; Kamoi et al. 2008; Ito 2003).

Similar to using Doppler ultrasound to visualize increased blood flow, contrast-enhanced ultrasound (CEUS) is currently under evaluation to determine its utility to detect prostate cancer. CEUS involves injecting microbubbles into the vasculature then utilizing specialized ultrasonic pulse sequences to localize the bubbles. Studies have shown that guided biopsies targeting regions of increased microbubble density have a higher yield than systematic biopsy (Mitterberger et al. 2010; Tang et al. 2007; Halpern et al. 2012).

Another characteristic of prostate cancer is a change in the cell structure, which can cause a change in the backscatter characteristics of the ultrasound signal. By analyzing the radiofrequency spectrum of the received data on a calibrated system, it is possible to detect these changes in the backscatter echoes (Lizzi et al. 1983). Recent work has focused on using more advanced methods of detecting these changes, such as artificial neural networks that account for multiple parameters, which have yielded very promising results (Feleppa et al. 2004a, b; Feleppa et al. 2011).

S. Rosenzweig (✉)
Department of Biomedical Engineering,
Duke University, Durham, NC, USA
e-mail: stephen.rosenzweig@duke.edu

R. Bouchard, PhD
Department of Imaging Physics,
The University of Texas MD
Anderson Cancer Center, Houston, TX, USA
e-mail: rrbouchard@mdanderson.org

T. Polascik, MD
Department of Urology,
Duke University Medical Center,
Durham, NC, USA
e-mail: polas001@mc.duke.edu

L. Zhai, PhD
Ultrasound Business Unit,
Siemens Healthcare, Mountain View, CA, USA
e-mail: liang.zhai@siemens.com

K. Nightingale, PhD
Department of Biomedical Engineering,
Duke University, Durham, NC, USA
e-mail: kathy.nightingale@duke.edu

R.L. Bard et al. (eds.), *Image Guided Prostate Cancer Treatments*,
DOI 10.1007/978-3-642-40429-0_3, © Springer-Verlag Berlin Heidelberg 2014

An ultrasound-based imaging modality that has the potential to take advantage of both the increased blood density and the cell structure changes is photoacoustic (PA) imaging, which utilizes laser light to excite the tissue and a standard TRUS transducer to detect the resulting photoacoustic signal (Gusev et al. 1993; Oraevsky and Karabutov 2003). PA imaging can provide spectroscopic images to assess blood content and oxygenation state (Wang et al. 2010) and to monitor changes in cell structure and growth in prostate cancer by using targeted nanoscale contrast agents (Kim et al. 2007).

In addition to increased blood flow and cell structure changes, prostate cancer normally presents as stiffer than the surrounding tissue; the digital rectal exam (DRE) has traditionally been utilized to detect this change in stiffness to diagnose prostate cancer (Hoyt et al. 2008; Zhai et al. 2010a). Ultrasound elastography generates qualitative or quantitative stiffness images, allowing for detection of stiff regions throughout the entire gland. Recent advancements in commercially available elastography tools have encouraged many studies, most of which demonstrated significant increases in sensitivity and specificity (60–90 %) for cancer detection (Parker et al. 2011; Correas et al. 2013; Pallwein et al. 2008a).

This chapter will focus on the current state-of-the-art and new advances in two of the aforementioned areas, ultrasound elastography and PA imaging of the prostate.

3.2 Prostate Elastography

3.2.1 Introduction

The digital rectal exam (DRE) is used extensively to diagnose prostate cancer; however, this technique is limited to palpation of the posterior region of the prostate. Elastography extends the idea of palpation by portraying stiffness variations throughout the tissue. Elastographic imaging techniques introduce a mechanical excitation and use either MRI or ultrasound to monitor the tissue response, thereby creating an image of the tissue stiffness. Elastographic methods that have been used to visualize structures in the prostate are strain imaging (Kamoi et al. 2008; Miyanaga et al. 2006; Pallwein et al. 2008a; Eggener et al. 2010), acoustic radiation force impulse (ARFI) imaging (Zhai et al. 2008, 2010a, b, 2012), shear wave imaging (Zhai et al. 2009; Ahmad et al. 2013), vibration elastography imaging (Salcudean et al. 2006; Mahdavi et al. 2011), and vibration amplitude sonoelastography (Castaneda et al. 2009; Hoyt et al. 2008; Taylor et al. 2005).

Although there are a multitude of elastographic techniques, they are all based on the same concept of applying a force and imaging the resulting tissue response. Common forces include compressing the tissue, using a vibrating piston or other mechanical actuator, or using acoustic radiation force. The tissue response has been monitored with both ultrasound and magnetic resonance imaging (MRI). The induced tissue deformation, or displacement, is related to the mechanical properties of the tissue through the principles of elasticity. There are two general types of elastographic images, qualitative and quantitative. Qualitative images portray the relative stiffness, strain, or displacement response of the tissue, whereas quantitative images utilize the principles of elasticity to derive the underlying elastic material properties of the tissue. The quality of the images depends on the imaging modality being used, the magnitude and type of force being applied, the signal processing of the data, and the validity of the assumptions used to reconstruct the images.

3.2.2 Governing Principles of Elasticity

To appreciate elastography images and the data that they contain, a brief overview of the governing principles of elasticity is necessary. Elastographic imaging methods measure the displacement (u) or strain (ε) of the tissue in response to an applied force (or stress, σ). The strain is the spatial gradient of the displacement $\varepsilon = \mathrm{du/dx}$ and represents the change in displacement with depth (i.e., how tissue compresses). Strain is related both to the applied

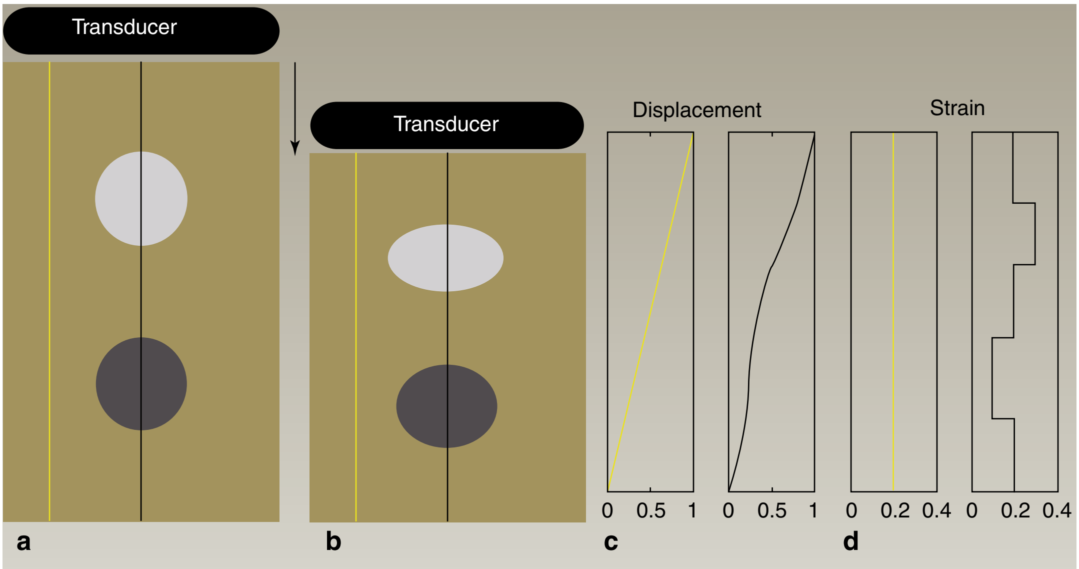

Fig. 3.1 Schematic representation of tissue with a soft circular inclusion (top, *light gray*) and stiff circular inclusion (bottom, *dark gray*) prior to compression (**a**), post-compression (**b**), the induced displacements (**c**), and the computed strain (**d**). The background has linearly varying displacement throughout depth due to the applied force at the top of the tissue and fixed bottom boundary; thus, the background has constant strain, as represented by the *yellow line*. The displacement in the region with the two inclusions is piecewise linear, with different slopes in the lesions and the background. The soft lesion displaces more than the background, and the stiff inclusion displaces less than the background; thus, the strain provides information about the relative stiffness of the lesions and background

stress (σ, i.e., force per unit area) and the inherent tissue mechanical properties (E, the elastic, or Young's modulus), and under simplifying assumptions is described by the equation:

$$\varepsilon = \frac{\sigma}{E} \tag{3.1}$$

The elastic modulus describes the stiffness of tissue; stiffer tissues have a higher elastic modulus than softer tissues. Since strain is inversely proportional to the elastic modulus, for a given stress, stiffer structures exhibit smaller strain, or displacement, and softer tissues exhibit larger strains (Fig. 3.1). Both MRI and ultrasound can be used to measure tissue motion; thus, in elastographic imaging methods, tissue displacement in response to an applied stress is measured, and images of tissue displacement or strain are generated that reflect relative differences in tissue stiffness.

In addition to compressing the tissue, it is possible to generate shear waves in the tissue. These shear waves propagate in a direction orthogonal to the applied stress and are in concept similar to the ripples that propagate away from a pebble dropped in water. The spatial and temporal behavior of a shear wave in tissue is governed by the wave equation:

$$\nabla^2 u = \frac{1}{c_s^2}\frac{\delta^2 u}{\delta t^2}, \tag{3.2}$$

where u is the displacement of the tissue, c_s is the wave speed, and ∇ is the Laplacian operator.

Equation 3.2 relates the spatial behavior of the wave, the left side of the equation, to the temporal behavior of the wave, the right side of the equation. Additionally, there is a constant of proportionality c_s, which is known as the shear wave speed. The shear wave speed can be related to the shear modulus through assumptions of linear elasticity and homogeneity, such that $\mu = \rho c_s^2$ where μ is the shear modulus and ρ is the density. Furthermore, under the assumption of incompressibility, which is considered reasonable in soft tissues such as the prostate, the shear modulus is directly proportional to the Young's modulus, such that $E = 3\mu = 3\rho c_s^2$. Therefore, if the shear wave speed is measured using elastographic techniques, it is possible to directly estimate the corresponding shear and Young's moduli, which represent the inherent material elastic properties of the tissue.

3.2.3 Elastic Properties of the Prostate

In addition to empirical evidence that prostate cancer is stiffer than normal prostate tissue (i.e., the digital rectal exam), multiple studies have been published that quantify the stiffness. Zhang et al. performed a study on ex vivo prostates and found that the Young's moduli of normal posterior and cancerous prostatic tissue were 15.9 ± 5.9 *kPa* and 40.4 ± 15.7 *kPa*, respectively (Zhang et al. 2008). Zhai et al. utilized quantitative shear wave-based elastography methods in ex vivo samples and reported that the Young's moduli of normal peripheral zone and cancerous prostatic tissues were 12.3 ± 2.4 *kPa* and 30 ± 3.0 *kPa*, respectively (Zhai et al. 2009). Although the stiffness differed between the studies, both found that there is approximately a 2.5x increase in the stiffness of the cancerous regions as compared to the prostatic peripheral zone tissue.

3.2.4 Elastographic Methods in Prostate

Strain Imaging

The vast majority of prostate elastography clinical studies have employed strain imaging (i.e., compression elastography) because this method is commercially available (Kamoi et al. 2008; Cochlin et al. 2002; Miyagawa et al. 2009; Nelson et al. 2007; Pallwein et al. 2008a, b, c; Parker et al. 2011; Salomon et al. 2008; Tsutsumi et al. 2007). Strain imaging requires the user to obtain a B-mode image of the prostate, then compress the organ, and obtain a second B-mode image. The tissue displacement is estimated using correlation-based techniques, and the strain between the two states is then computed (Parker et al. 2011; Ophir 1991).

Strain imaging assumes that the operator applies a uniform stress across the prostate. Stiffer regions can then be identified by their relatively low strain compared to the surrounding tissue as shown in Fig. 3.1. Elastography is typically performed as a freehand technique with the operator gently compressing the prostate with the ultrasound transducer. A skilled technician is needed to obtain adequately uniform compression, which can be challenging. Some recent studies have used inflatable balloons that surround the endorectal transducer and can be filled or emptied by the operator, thereby generating a more uniform stress on the prostate (Parker et al. 2011; Kapoor et al. 2011; Tsutsumi and Miyagawa 2010).

Researchers have also investigated the potential use of strain imaging to obtain quantitative information about the tissue. To accomplish this, the inverse problem is solved using models of the tissue structure and displacement data. While this method holds promise, it has not been used clinically to date due to challenges with implementation (Barbone and Gokhale 2004; Fehrenbach 2007).

Transrectal ultrasound (TRUS) is widely used for visualization during systematic prostate biopsies, but it is not typically used for biopsy guidance since tumors may not be visualized (Pallwein et al. 2008b). The primary use of strain imaging investigated in the clinical literature is for biopsy guidance. As will be reviewed below, many studies have employed conventional biopsy techniques and then used elastography to identify and target additional regions (Kamoi et al. 2008; Cochlin et al. 2002; Miyagawa et al. 2009; Nelson et al. 2007; Tsutsumi et al. 2007; Kapoor et al. 2011). Some studies have acquired elastography data and retrospectively compared suspicious regions with those that were biopsied (Pallwein et al. 2008a) or with whole-mount histology after the prostate is excised (Salomon et al. 2008).

Cochlin et al. demonstrated a significant improvement using strain imaging as compared to TRUS for prostate cancer (PCa) biopsy guidance. The authors studied 100 patients and using elastography identified five cancers that would not have otherwise been biopsied. Additionally, of these five cancerous regions, three were in patients whose other biopsies showed no cancer; thus, cancer detection was only achieved through the use of elastography. For elastography, the reported sensitivity and specificity for PCa were 51 and 83 %, respectively (Cochlin et al. 2002).

Nelson et al. in 2007 studied targeting biopsies using TRUS, color Doppler, and elastography in addition to the traditional sextant biopsy. The authors concluded that color Doppler and elastography both improve cancer detection, but that the detection is not sufficient to replace the standard sextant biopsy. Additionally, the authors showed that cancer detections in grayscale ultrasound, color Doppler, and elastography images are all correlated with Gleason score (Nelson et al. 2007).

Kamoi et al. studied 107 patients using both power Doppler ultrasound and elastography, indicating that elastography had 68 % sensitivity and 81 % specificity for PCa. The authors report that elastography is more successful at detection of high Gleason score tumors, with 100 % of the tumors with a Gleason score 8 being detected. The authors indicated that their primary difficulty with elastography was the image quality variability between users due to the user-dependent nature of compression (Kamoi et al. 2008).

Although the previous studies used both Doppler ultrasound and strain imaging, other groups have evaluated exclusively strain imaging. A 311 patient study by Miyagawa et al. reported a 90 % diagnostic sensitivity for PCa using the combination of TRUS and elastography. The authors reported that elastography was most successful in detecting cancer in the anterior prostate. They also noted that the sensitivity of elastography decreased as prostate volume increased, which they attributed to the confounding effects of BPH (Miyagawa et al. 2009).

The observation that the diagnostic utility of elastography differs in various regions of the prostate was expanded upon by Tsutsumi et al. The authors divided the prostate into three regions, anterior, middle, and posterior and analyzed the utility of elastography for prostate cancer detection. While elastography improved cancer detection in all regions of the prostate, the largest benefit was seen with anterior tumors, with decreasing improvement for middle and posterior tumors (Tsutsumi et al. 2007).

Pallwein et al. studied 492 patients, who had elastograms of the prostate recorded prior to receiving a systematic 10-core biopsy. The urologist performing the biopsy was blinded to the results of the elastography study. The authors found a whole organ sensitivity of 86 % and specificity of 72 % in the retrospective analysis of suspicious regions in the elastograms. Cancer detection in the basal region was compromised due to high false-positive rates associated with chronic inflammation and atrophy. A representative series of elastograms is reproduced from their work in Fig. 3.2 (Pallwein et al. 2008a).

Kapoor et al. performed a 50-patient study specifically focused on determining the utility of elastography in targeting biopsies. The authors reported the sensitivity and specificity of 91.7 and 86.8 %, respectively, as compared to their reported sensitivity and specificity of TRUS: 16.7 and 89 %, respectively. They noted that the primary challenges in using elastography are the inability to differentiate between cancer and prostatitis, very large prostates, and lack of operator experience (Kapoor et al. 2011).

Salomon et al. studied prostate elastography in 109 patients undergoing radical prostatectomy, in which the preoperative elastography data was correlated with whole-mount histology data. The authors reported 75 % sensitivity and 77 % specificity for elastography. The authors found that elastography detection of PCa was positively correlated with Gleason score (Salomon et al. 2008).

One of the common challenges reported for strain imaging of the prostate is achieving uniform compression of the organ. To address this challenge, Tsutsumi et al. inflated a water balloon surrounding the transducer to compress the tissue, which reduced the operator dependence of the image quality. Using this method, the authors detected 71 % of histology confirmed prostate cancer lesions (Tsutsumi and Miyagawa 2010).

Overall, the multitude of studies performed using strain imaging has demonstrated great promise for guidance of targeted biopsies. The primary benefits have been reported for detecting PCa in the peripheral zone, where approximately 80 % of cancers are located (Pallwein et al. 2008b). Although the studies have demonstrated higher sensitivity than with TRUS alone, challenges have

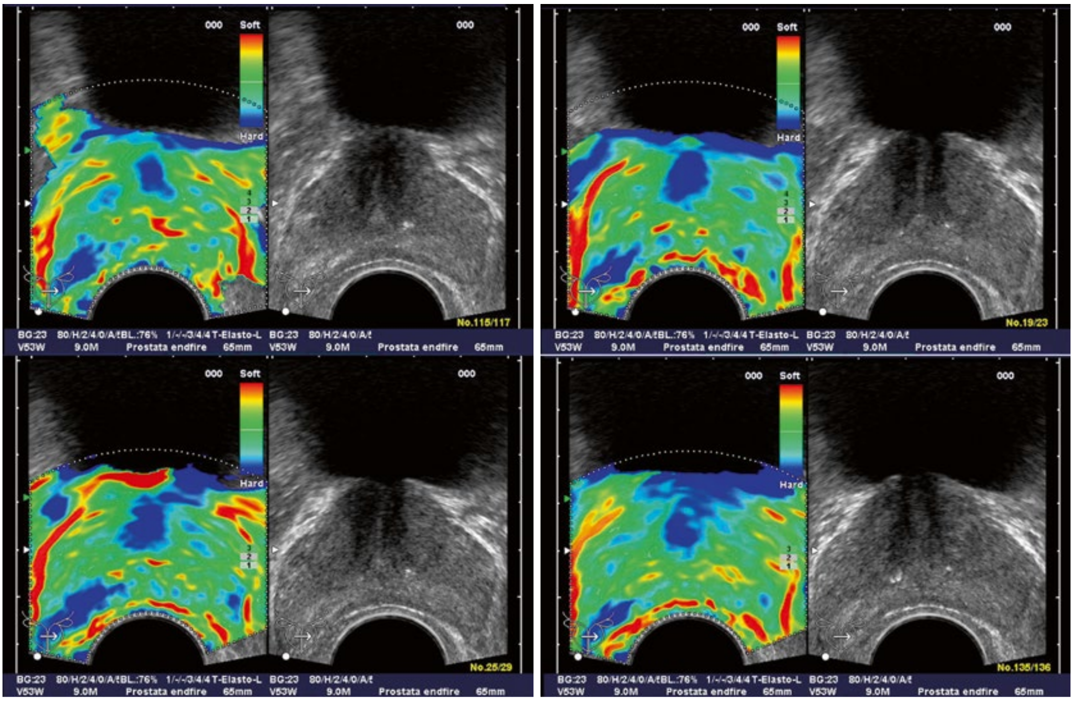

Fig. 3.2 Patient (picture series) with histologically confirmed prostate cancer in the right mid-gland of prostate. The elastographic examination showed a well-defined lesion with low strain (*dark blue*). The peripheral zone on the patient left side showed normal stiffness (Figure reproduced with permission Pallwein et al. (2008a))

also been identified. The studies using freehand compression noted that an experienced operator was needed to obtain high-quality images. Additionally, many studies demonstrated a high false-positive rate due to the confounding effects of BPH, which looks similar to cancer in strain images. Finally, the studies determined that targeted biopsies are not sufficient and that standard sextant or 10-core biopsies are necessary in addition to elastography-targeted biopsies.

Acoustic Radiation Force Impulse (ARFI) Imaging

Although strain imaging has been the most widely used elastographic imaging technique in the prostate to date, many other methods are currently under investigation. One promising area is the use of an acoustic radiation force impulse (ARFI) excitation rather than transrectal compression. The primary benefit of ARFI excitation is the ability to apply the force directly within the tissue, reducing the operator dependence of image quality (Torr 1984).

ARFI imaging applies short duration (<1 ms)-focused ultrasound pushing pulses that displace the tissue on the order of 10 μm; the displacement response is then measured with the same ultrasonic transducer. Regions of decreased displacement are assumed to represent stiffer tissues in the same way that regions of decreased strain represent stiffer tissues in strain imaging (Nightingale et al. 2002).

ARFI imaging has been used in preliminary feasibility studies to detect prostate cancer. Zhai et al. have acquired three-dimensional volumes of ARFI data and correlated their results to whole-mount histology in both ex vivo and in vivo studies. The initial ex vivo studies demonstrated that ARFI images portrayed zonal anatomy, BPH, and prostate cancer with considerably higher contrast than matched B-mode images (Zhai et al. 2010a).

In a follow-up study of 19 patients, the same group acquired three-dimensional volumes in vivo using an end-fire endocavity transducer prior to radical prostatectomy. The images were then

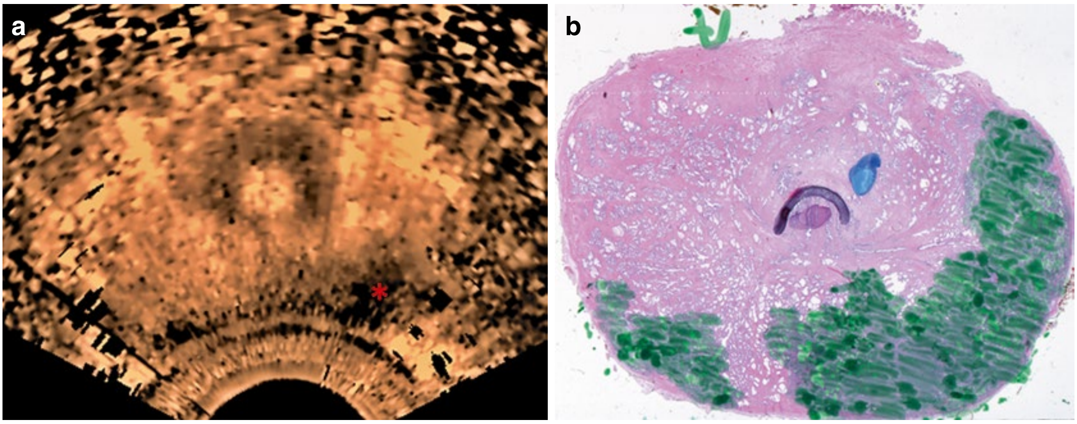

Axial ARFI image

Axial histology slide

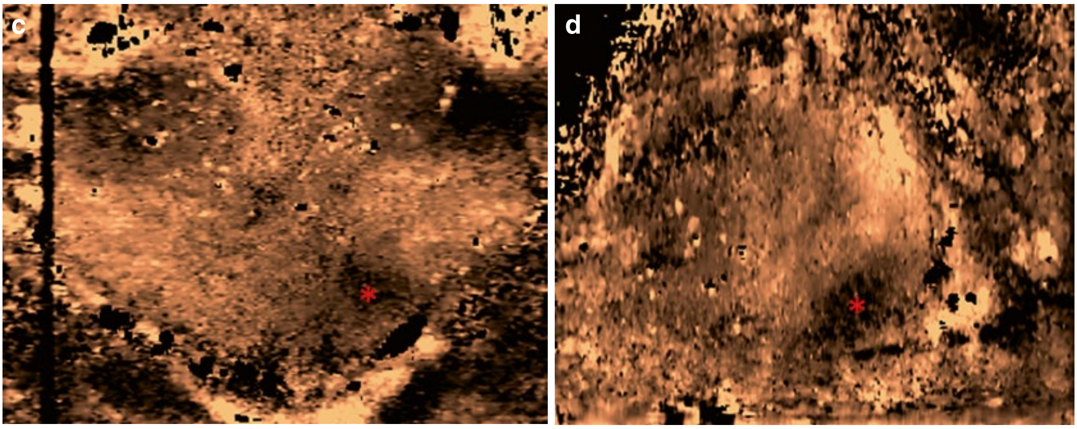

Coronal ARFI image

Saggital ARFI image

Fig. 3.3 Axial (**a**), coronal (**c**), and sagittal (**d**) sections of ARFI images in vivo and the corresponding histological slide (**b**). The basal area of the prostate is at the *top* of the coronal image, and the apex is at the *bottom*; the *red asterisk* indicates where the orthogonal views intersect. Images were obtained in vivo immediately prior to radical prostatectomy surgery. In the histological slide, cancerous regions were masked in *green* by a pathologist. The stiff structure (*dark*) in the right apex region shown in the ARFI image corresponds to the large cancerous region

correlated with histological results. As with strain imaging, when visible, cancers appeared as stiffer regions, corresponding to decreased displacement in the ARFI images. In addition, regions of BPH within the central gland were well visualized with a nodular appearance. Representative ARFI images and corresponding histology slide are shown in Fig. 3.3 (Zhai et al. 2008, 2012).

Shear Wave Elastography

Shear wave imaging is an elastography technique in which the tissue stiffness is interrogated by exciting a shear wave and monitoring the speed of propagation away from the excitation, thus obtaining c_s, as given in Eq. 3.2. To generate a shear wave in vivo, acoustic radiation force impulse excitations are used, either with a single focus or in a multifocal "supersonic" configuration (Bercoff et al. 2004); an image of the tissue is then generated by estimating the shear wave speed in small regions that are assumed to be uniform (Parker et al. 2011).

Although shear wave imaging has been used to image the breast (Tanter et al. 2008), muscles (Gennisson et al. 2010), and liver (Muller et al. 2009), it has only recently been translated to imaging prostates in vivo (Correas et al. 2013). In a single-center study, Ahmad et al. imaged and biopsied 50 patients, 33 of which had at least one positive biopsy core. Based on this work, they found that cancer was approximately 50 % stiffer than the benign tissue and that they were able to detect cancer with high sensitivity and specificity (0.9 and 0.88, respectively) (Ahmad et al. 2013).

Vibro-elastography

Vibro-elastography is an elastography technique that uses external vibratory actuators to excite the tissue at many frequencies simultaneously. The displacement of the tissue is then monitored using ultrasound, and the biomechanical properties of the tissue are calculated from the induced displacement. This method is equivalent to a strain image but is calibrated to the frequency and amplitude of motion, and therefore it can be used to obtain quantitative values for stiffness, density, and viscosity (Turgay et al. 2006).

Vibro-elastography has been used in a pilot study by Salcudean et al. to demonstrate the potential utility in detecting prostate cancer and brachytherapy seed placement. The tissue is excited using a mechanical actuator coupled to a transrectal ultrasound transducer to generate displacements within the tissue, which are subsequently observed using correlation-based techniques. The authors showed the ability to generate repeatable, operator-independent images that revealed stiff regions in the prostates they studied (Salcudean et al. 2006; Mahdavi et al. 2011).

Vibration Amplitude Sonoelastography

Another ultrasound-based elastographic method that has been used to evaluate prostate cancer in vivo is vibration amplitude sonoelastography. Two external mechanical actuators positioned beneath the patient's pelvis vibrate at low frequency (70–200 Hz) generating vibrations within the prostate. These vibrations are monitored using a specially designed ultrasound Doppler processing mode. Regions of decreased amplitude are associated with stiffer structures in the tissue (Castaneda et al. 2009; Hoyt et al. 2008; Taylor et al. 2005; Parker et al. 2011).

Castaneda et al. imaged 10 patients prior to radical prostatectomy and correlated the results with whole-mount histology. Twelve of 19 cancerous lesions were identified (average diameters: 7.4 mm visualized, 3.8 mm missed), and 12 false-positive regions were identified, 6 of which corresponded to BPH. The primary challenges associated with this method are the inability to detect small tumors and difficulty in coupling enough vibration energy into the tissue (Castaneda et al. 2009; Hoyt et al. 2008).

3.2.5 Conclusions

Empirical evidence and quantitative experiments have demonstrated that cancerous regions in the prostate can be stiffer than healthy tissue. Strain imaging, which is available on multiple commercial ultrasound scanners, has been investigated for targeted biopsy guidance. Reports generally indicate improved sensitivity (70–90 %) and specificity (72–87 %) for prostate cancer as compared to TRUS alone using compression elastography. However, several challenges have been identified, including operator-dependent image quality; difficulty in differentiating between BPH, prostatitis, atrophy, and prostate cancer; reduced image quality in larger prostates; and limitations of cancer sensitivity in the basal region of the prostate. Given the promising initial findings, techniques that have the potential to overcome some of these challenges are under development. If successful, elasticity imaging could find application for guidance of targeted biopsy procedures, guidance of prostatic focal therapies, and facilitating watchful waiting and monitoring therapeutic treatment response.

3.3 Photoacoustic Imaging of the Prostate

3.3.1 Introduction

Much like elastography, photoacoustic (PA) imaging has the potential to give clinicians more than just anatomical information. PA imaging is able to provide an image of the optical absorption of tissue constituents and nanoscale contrast agents. Such an ability allows for powerful functional and molecular imaging approaches that could lead the way to improved cancer screening, diagnosis, and therapy monitoring.

Although the PA effect was first discovered in 1880 by Alexander Graham Bell, only in the last few decades has this powerful phenomenon been leveraged for medical imaging pursuits, which have tended to be relegated to the preclinical arena (i.e., small animal models). In recent years, however, there has been a significant push to translate PA imaging technologies into the clinic. Given the reasonable access afforded to the prostate with transrectal imaging, the prostate – along with a few other "accessible" organs (e.g., breast) – is being pursued as a target for clinical PA imaging.

3.3.2 Governing Principles of Photoacoustic Imaging

Photoacoustic imaging is achieved with the irradiation of a region of interest (ROI) by nanosecond pulses of laser light. The processes of optical absorption and thermoelastic expansion result in the irradiated volume producing broadband ultrasound (US) waves. The optical absorption of the ROI can then be imaged by detecting and spatially resolving the generated US waves with an US transducer. Because PA imaging generally cannot provide the level of soft tissue contrast afforded by US imaging, both imaging modalities are frequently implemented with the same US array to provide co-registered photoacoustic-ultrasonic (PAUS) images.

Much like US imaging, PA imaging relies on three steps: transmission of energy into tissue, interaction of this energy with tissue, and reception of the generated (or scattered, in the case of US imaging) energy. The reception of acoustic energy is very similar (often almost identical) to what occurs in US imaging. What distinguishes PA imaging from US imaging is its initial irradiation of tissue with light as opposed to insonification with sound. As a result of the PA effect, irradiating the tissue with narrow pulse width laser light generates local acoustic sources at regions of increased optical absorption. The magnitude of these acoustic sources can then be imaged to provide a map of local optical absorption with high contrast and with resolution similar to that afforded by US imaging. The penetration depth of PA imaging – often multiple centimeters – far outperforms that typical of other optically mediated imaging approaches.

Generally, the initial pressure generated by a PA transient can be estimated by (Oraevsky and Karabutov 2003; Gusev et al. 1993)

$$p_o = \frac{\beta c^2}{c_p} \mu_a F, \tag{3.3}$$

where $\beta[\mathrm{K}^{-1}]$ is the thermal coefficient of volume expansion, $\mathrm{c} = [\mathrm{m/s}]$ is the speed of sound through tissue, $\mathrm{c}_p = [\mathrm{J}/kgK]$ is the heat capacity at constant pressure, $\mu_a[\mathrm{cm}^{-1}]$ is the optical absorption coefficient, and $\mathrm{F} = [J/cm^2]$ is the local laser fluence. Temperature increases resulting from PA irradiation are typically <0.1 K (Wang 2009).

Because of their ability to spectroscopically probe the absorption properties of tissue constituents, PA imaging applications include the assessment and monitoring of tissue properties (e.g., oxygen saturation or anemia monitoring) or presence of blood (e.g., ischemia or angiogenesis assessment) and real-time imaging of nanoscale contrast agents in vivo. Unlike US imaging, PA imaging does not require flow to image blood; the mere presence of the optically absorbing hemoglobin molecule provides imaging contrast. For the purpose of prostate imaging, perhaps the two most promising advantages of PA imaging are its capacity to visualize nanoscale contrast agents, which can penetrate the endothelial layer of vessels, and its ability to image spectroscopically, which provides powerful molecular/cellular characterization potential. Both dye-based contrast agents and gold nanoparticles have shown potential for prostate cancer imaging (Malugin and Ghandehari 2010). To increase the specific accumulation of a contrast agent at a tumor site, the agent can be conjugated to a targeting moiety specific to an overexpressed cell surface receptor. Kim et al. used this concept when they conjugated an FDA-approved indocyanine-green-based contrast agent with the HER-2 antibody to create a PA imaging agent capable of targeting prostate cancer (Kim et al. 2007).

PA imaging derives its spectroscopic capabilities from its ability to utilize a tunable laser source. By obtaining the resulting PA images generated by discrete wavelengths, one is able to able to classify photoabsorbers based on their unique absorption spectra. Through spectroscopic PA imaging of hemoglobin, which has an absorption spectrum that depends on its oxygenation state, one is able to characterize oxygen saturation to differentiate between hyperoxia, normoxia, and hypoxia (Zhang et al. 2007). “Optoacoustic imaging” is another commonly used term for PA imaging and is similarly limited to the visible (400–750 nm) and near-infrared (NIR; 750–1,800 nm) ranges.

3.3.3 Preclinical Applications of Photoacoustic Imaging in the Prostate

Although PA imaging is starting to make its way into the clinic, most notably in the case of breast imaging, to date prostate PA research has been conducted in the preclinical realm, focusing on imaging tissue-mimicking prostate phantoms, in vitro preparations of prostate cancer cells, and murine models of prostate cancer. Perhaps the earliest work investigating PA imaging in the prostate was conducted in 2003 with a PA imaging system consisting of a 32-element arc array transducer and a laser operating at 757 and 1,064 nm (Andreev et al. 2003). By imaging a circular phantom consisting of chicken breast encased in gelatin with included blood targets, Spirou et al. demonstrated that PA imaging could image at depths up to 5 cm, which should allow for interrogation of most prostates (Spirou et al. 2004). Through results of the study, PA imaging was found to provide good contrast of the hemoglobin targets and visualization of a thermal ablation lesion created in the chicken breast inclusion.

Following proof-of-concept PA imaging in phantom preparations, investigators focused on imaging prostate cancer cells in vitro using targeted nanoparticles and spectroscopic imaging techniques. LNCaP prostate cancer cells, known to overexpress the transmembrane receptor Her-2/neu, were targeted with gold nanorods conjugated to a monoclonal antibody designed specifically for the Her-2/neu antigen (Agarwal et al. 2007). Upon PA imaging in vitro, Agarwal et al. observed that an order of magnitude higher concentration of targeted nanoparticles were endocytosed by the prostate cancer cells compared to the non-targeted nanoparticle control. This specific accumulation has similarly been demonstrated on LNCaP prostate cancer cells in vitro with gold nanoparticles targeting the prostate-specific membrane antigen (Fleron et al. 2007). Using PA spectroscopy, Harvey et al. were able to differentiate between the LNCaP, PC-3, PNT2C2, and BPH prostate cancer cell lines in vitro with principal component analysis (Harvey et al. 2007).

On the heels of promising in vitro results, investigators began pursuing preclinical in vivo applications, focusing on murine and canine imaging. By using a mouse window model (i.e., transparent window implanted on a subcutaneous tumor to mitigate optical scattering) of PC-3 human prostate cancer, investigators were able to image microvasculature, map local oxygen saturation, and identify hemorrhaging of developing prostate tumors (Bauer et al. 2010, 2011). Using a transgenic adenocarcinoma mouse prostate (TRAMP) model, Patterson et al. achieved impressive tumor contrast using PA imaging at 775 nm, with a contrast ratio of 3.5 obtained when comparing to the surrounding healthy tissue (Patterson et al. 2010). In a similar study, Kumon et al. utilized frequency-domain analysis of PA imaging data to differentiate metastatic anaplastic tumor able to disseminate to lymph nodes and lung (MAT-LyLu) subcutaneous tumors from adjacent normal flank tissue in a murine model (Kumon et al. 2011).

To test the feasibility of PAUS imaging in a clinical setting, Wang et al. imaged an in vivo canine prostate with a linear array placed directly on the animal’s gland through a midline vertical incision; images from this study are presented in Fig. 3.4 (Wang et al. 2010). Results from this study demonstrate that PA imaging provides

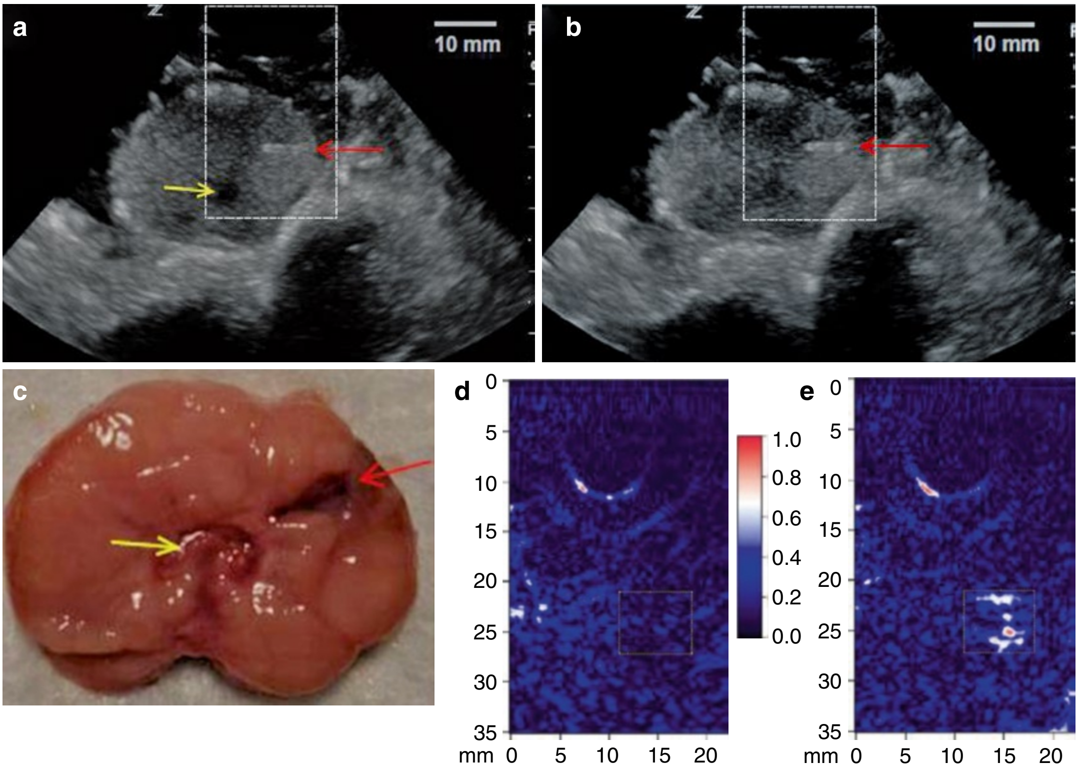

Fig. 3.4 In vivo PAUS dual-modality imaging of a canine prostate with a subsurface lesion induced. Grayscale US images of the prostate acquired (**a**) before and (**b**) after the generation of the lesion (0.1 mL of injected blood). The red arrow indicates the plastic cannula inserted into the prostate for the injection of blood; the yellow arrow indicates the urethra. (**c**) Anatomical photograph of the imaged cross section in the prostate with the lesion marked. PA images of the prostate right lobe acquired (**d**) before and (**e**) after the generation of the lesion (0.1 mL of injected blood), where the image intensities are demonstrated with an image color bar. The PA imaging plane is the same as that in US images, where the reconstructed area is indicated with the *dashed rectangles* in the US images in (a) and (b) (Used with permission from Wang et al. (2010b))

good sensitivity and a high contrast-to-noise ratio in visualizing deep, blood-rich lesions that mimic prostate tumors, while US imaging provides important morphological features. In a similar canine study that utilized more clinically relevant transrectal imaging, Yaseen et al. were able to clearly visualize an induced blood-laden prostate lesion in the PA image (757 nm), while this same lesion was not apparent in US image (Yaseen et al. 2010). Additionally, with PAUS imaging of an excised canine prostate, Ke et al. were able to clearly visualize the gland's ductal structure (Ke et al. 2011).

In addition to its diagnostic potential, PA imaging (and/or its associated contrast agents) can also be utilized for improved therapy guidance and localized therapy in the prostate. Recently, PAUS imaging has shown potential in providing real-time visualization of radioactive brachytherapy seeds during implantation in the prostate (Su et al. 2011; Harrison and Zemp 2011; Kuo et al. 2012); an example of a PAUS image of a brachytherapy seed in bovine prostate is provided in Fig. 3.5. With the high contrast of metallic objects afforded by PA imaging and the anatomical context of the prostate provided by US imaging, PAUS imaging may be able to provide real-time dosimetric evaluation and permit adaptive seed implantation (Mitcham et al. 2013a). Furthermore, targeted gold nanoparticles have the potential of providing localized and specific radiation dose enhancement during external beam radiation therapy. In an in

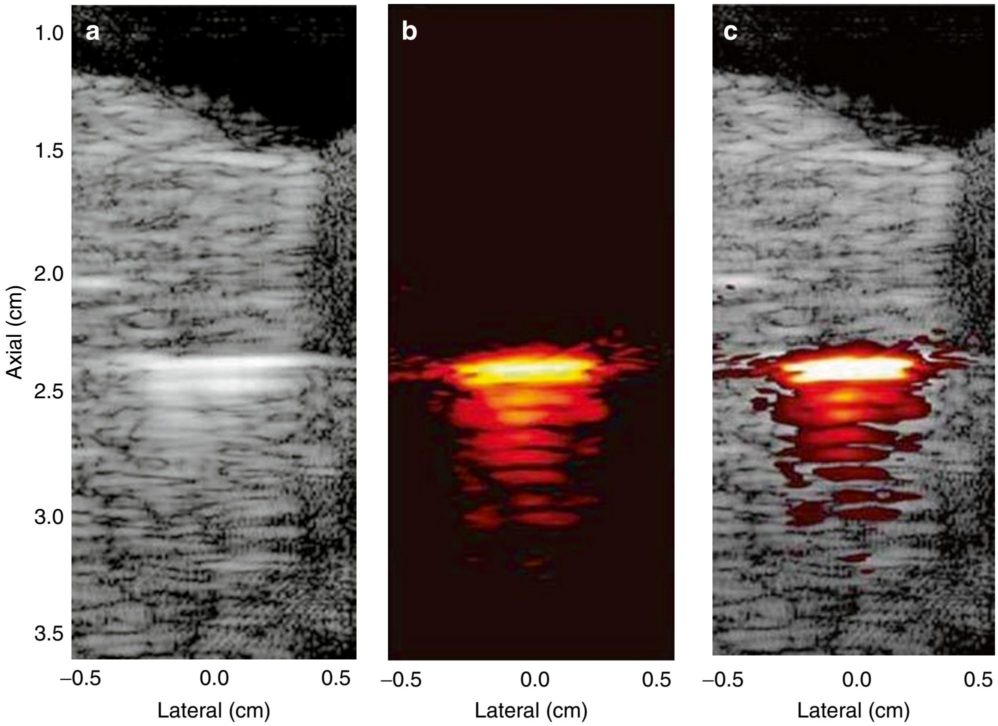

Fig. 3.5 US B-mode (**a**), PA (**b**), and combined PAUS (**c**) images of a seed embedded in a bovine prostate sample in the long-axis orientation. PA image was acquired at 870 nm and is displayed with 35-dB dynamic range; B-mode image is displayed with 55-dB range (Used with permission from Su et al. (2011))

vitro study of human prostate carcinoma DU-145 cells, functional glucose-bound gold nanoparticles enhanced irradiation cytotoxicity by up to twofold over the control (Zhang et al. 2008).

3.3.4 Conclusion

Given the promising phantom and preclinical results thus far, the next likely step for PA imaging in the prostate will be full clinical translation. Yet, as with any new imaging modality, there are technical and regulatory boundaries that must first be overcome before successful translation. Although NIR irradiation encounters significantly less scattering through tissue than visible light, achieving a sufficient fluence throughout the prostate with transrectal illumination could still present a challenge for safe surface fluences to be maintained. One potential solution to this problem could be through the use of cylindrical diffuse irradiation in the urethra to improve the local signal-to-noise ratio (SNR) at the prostate's distal margins (Xie et al. 2012). A similar light delivery system could be utilized for PA-guided prostate biopsies, whereby an interstitial laser source would provide local irradiation along biopsy needle tracts to permit spectroscopic characterization of surrounding tissue and guide subsequent biopsy sampling locations (Mitcham et al. 2013b). Improved imaging penetration depths could also be achieved with an US transducer capable of receiving acoustic transmissions with improved sensitivity. Recently, a two-dimensional capacitive micromachined ultrasonic transducer (CMUT) array was constructed that can provide endoscopic PA imaging capabilities at depths of up to 5 cm with an SNR of about 35 dB and lateral and axial resolutions of 360 and 500 μm, respectively (Kothapalli et al. 2012). For very specific applications, it might also be possible to image PA contrast outside of the body but after it has interacted with cancer cells in the bloodstream. Establishing the proof-of-concept for such an approach, Viator et al. tagged PC-3 cancer cells with gold nanoparticles and imaged them with spectroscopic (470–570 nm) PA flowmetry, which is designed to detect circulating tumor cells in blood samples (Viator et al. 2010).

Despite some of the technical limitations that must first be overcome, PA imaging's promise of facilitating molecular and cellular imaging capabilities throughout the prostate will likely continue to drive this exciting new modality closer to the clinic. Just like the laser irradiation that makes it possible, PA imaging appears to have a bright future in providing improved cancer screening, diagnosis, and therapy monitoring options in the prostate.

Conclusion

Although conventional B-mode TRUS has been used extensively to visualize the prostate gland and needle during biopsy, its limited sensitivity and specificity for cancer has led to advanced ultrasonic methods being investigated. Doppler ultrasound, contrast-enhanced ultrasound, tissue characterization, elasticity imaging, and PA imaging have all shown promise in preclinical and clinical settings and could soon be utilized for cancer screening, guidance of targeted biopsy procedures and focal therapies, and facilitating watchful waiting.

References

Agarwal A, Huang SW, et al. Targeted gold nanorod contrast agent for prostate cancer detection by photoacoustic imaging. J Appl Physics. 2007;102(6):64701–4.

Ahmad S, Cao R, et al. Transrectal quantitative shear wave elastography in the detection and characterisation of prostate cancer. Surg Endosc. 2013;27(9):3280–7.

Andreev VG, Ponomarev AE, et al. Detection of prostate cancer with opto-acoustic tomography. In: Biomedical Optics 2003. International Society for Optics and Photonics, San Jose, CA, 2003, p. 45–57.

Barbone PE, Gokhale NH. Elastic modulus imaging: on the uniqueness and nonuniqueness of the elastography inverse problem in two dimensions. Inverse Probl. 2004;20(1):283–96.

Bauer DR, Olafsson R, et al. *In vivo* multi-modality photoacoustic and pulse echo tracking of prostate tumor growth using a window chamber. In: BiOS. International Society for Optics and Photonics, San Francisco, CA, 2010, p. 75643B–75643B–10.

Bauer DR, Olafsson R, et al. 3-D photoacoustic and pulse echo imaging of prostate tumor progression in the mouse window chamber. J Biomed Opt. 2011;16(2):26010–2.

Bercoff J, Tanter JM, Fink M. Supersonic shear imaging: a new technique for soft tissue elasticity mapping. IEEE Trans Ultrason Ferroelectr Freq Control. 2004;51(4):396–409.

Castaneda B, Hoyt K, et al. Performance of three-dimensional sonoelastography in prostate cancer detection: A comparison between *ex vivo* and *in vivo* experiments. In: 2009 IEEE International Ultrasonics symposium, Rome, Italy, Sept 2009, p. 519–22.

Cochlin D, Ganatra R, Griffiths D. Elastography in the Detection of Prostatic Cancer. Clin Radiol. 2002;57(11):1014–20.

Correas J-M, Tissier AM, et al. Ultrasound elastography of the prostate. State of the art. Diagn Interv Imaging. 2013;94(5):551–60.

Eggener S, Salomon G, et al. Focal therapy for prostate cancer: possibilities and limitations. Eur urology. 2010;58(1):57–64.

Fehrenbach J. Influence of Poisson's ratio on elastographic direct and inverse problems. Phys Med Biol. 2007;52(3):707–16.

Feleppa EJ, Ketterling JA, et al. Ultrasonic tissue-type imaging (TTI) for planning treatment of prostate cancer. Med Imaging. 2004a;5373:223–30.

Feleppa EJ, et al. Quantitative ultrasound in cancer imaging. Semin Oncol. 2011;38(1):136–50.

Feleppa EJ, Porter CR, et al. Recent Developments in Tissue-Type Imaging (TTI) for Planning and Monitoring Treatment of Prostate Cancer. Ultrason Imaging. 2004b;26(3):163–72.

Fleron M, Schol D, et al. Optoacoustic specific detection of prostate cancer using functionalized gold nanorods. Poster presentation. 2007.

Gennisson JL, Deffieux T, et al. Viscoelastic and Anisotropic Mechanical Properties of *in vivo* Muscle Tissue Assessed by Supersonic Shear Imaging. Ultrasound Med Biol. 2010;36(5):789–801.

Gusev VE, Karabutov AA, Hendzel K. Laser optoacoustics. New York: American Institute of Physics; 1993.

Halpern EJ, Gomella LG, et al. Contrast enhanced transrectal ultrasound for the detection of prostate cancer: a randomized, double-blind trial of dutasteride pretreatment. J Urol. 2012;188(5):1739–45.

Harrison T, Zemp RJ. Coregistered photoacoustic-ultrasound imaging applied to brachytherapy. J Biomed Opt. 2011;16(8):80502.

Harvey TJ, Henderson A, et al. Discrimination of prostate cancer cells by reflection mode FTIR photoacoustic spectroscopy. Analyst. 2007;132(4):292–5.

Hoyt K, Castaneda B, et al. Tissue elasticity properties as biomarkers for prostate cancer. Cancer Biomark. 2008;4(4–5):213–25.

Ito H. Visualization of prostate cancer using dynamic contrast-enhanced MRI: comparison with transrectal power Doppler ultrasound. Br J Radiol. 2003; 76(909):617–24.

Kamoi K, Okihara K, et al. The utility of transrectal real-time elastography in the diagnosis of prostate cancer. Ultrasound Med Biol. 2008;34(7):1025–32.

Kapoor A, Kapoor A, et al. Real-time elastography in the detection of prostate cancer in patients with raised PSA level. Ultrasound Med Biol. 2011;37(9): 1374–81.

Ke H, Guo Z, et al. Photoacoustic and thermoacoustic tomography of dog prostates. In: SPIE BiOS. International Society for Optics and Photonics, San Francisco, CA, 2011, p. 789936–789938.

Kim G, Huang SW, et al. Indocyanine-green-embedded PEBBLEs as a contrast agent for photoacoustic imaging. J Biomed Opt. 2007;12(4):044020.

Kothapalli S, Ma TJ, et al. Deep Tissue Photoacoustic Imaging Using a Miniaturized 2-D Capacitive Micromachined Ultrasonic Transducer Array. IEEE Trans Biomed Eng. 2012;59(5):1199–204.

Kumon RE, Deng CX, Wang X. Frequency-domain analysis of photoacoustic imaging data from prostate adenocarcinoma tumors in a murine model. Ultrasound Med Biol. 2011;37(5):834–9.

Kuo N, Kang HJ, et al. Real-time photoacoustic imaging of prostate brachytherapy seeds using a clinical ultrasound system. J Biomed Opt. 2012;17(6):660051–7.

Lizzi FL, Greenebaum M, et al. Theoretical framework for spectrum analysis in ultrasonic tissue characterization. J Acoust Soc Am. 1983;73(4):1366.

Mahdavi S, Moradi M, et al. Evaluation of visualization of the prostate gland in vibro-elastography images. Med Image Anal. 2011;15(4):589–600.

Malugin A, Ghandehari H. Cellular uptake and toxicity of gold nanoparticles in prostate cancer cells: a comparative study of rods and spheres. J Appl Toxicol. 2010;30(3):212–7.

Mitcham T, Homan K, et al. Modulation of Photoacoustic Signal Generation from Metallic Surfaces. J Biomed Opt. Prague, Czech Republic, 2013a;18(5):56008.

Mitcham T, Marques T, et al. Transrectal photoacoustic-ultrasonic imaging enhancement through interstitial irradiation and targeted nanoparticles. In: Proceedings of the 2013 IEEE Ultrasonics symposium, Prague, Czech Republic, 2013b.

Mitterberger MJ, Aigner F, et al. Comparative efficiency of contrast-enhanced colour Doppler ultrasound targeted versus systematic biopsy for prostate cancer detection. Eur Radiol. 2010;20(12):2791–6.

Miyagawa T, Tsutsumi M, et al. Real-time elastography for the diagnosis of prostate cancer: evaluation of elastographic moving images. Japanese J Clin Oncol. 2009;39(6):394–8.

Miyanaga N, Akaza H, et al. Tissue elasticity imaging for diagnosis of prostate cancer: a preliminary report. Int J Urol. 2006;13(12):1514–8.

Muller M, Gennisson JL, et al. Quantitative Viscoelasticity Mapping of Human Liver Using Supersonic Shear Imaging: Preliminary *in vivo* Feasibility Study. Ultrasound Med Biol. 2009;35(2):219–29.

Nelson ED, Slotoroff CB, et al. Targeted biopsy of the prostate: the impact of color Doppler imaging and elastography on prostate cancer detection and Gleason score. Urology. 2007;70(6):1136–40.

Nightingale KR, Soo M, et al. Acoustic radiation force impulse imaging: *In vivo* demonstration of clinical feasibility. Ultrasound Med Biol. 2002;28:227–35.

Ophir O. Elastography: A quantitative method for imaging the elasticity of biological tissues. Ultrasonic Imaging. 1991;13(2):111–34.

Oraevsky A, Karabutov A. Optoacoustic tomography. In: Vo-Dinh T, editor. Biomedical photonics handbook. Boca Raton: CRC Press; 2003. p. 31–4.

Pallwein L, Aigner F, et al. Prostate cancer diagnosis: value of real-time elastography. Abdom Imaging. 2008a;33(6):729–35.

Pallwein L, Mitterberger M, et al. Ultrasound of prostate cancer: recent advances. Eur Radiol. 2008b;18(4):707–15.

Pallwein L, Mitterberger M, et al. Sonoelastography of the prostate: comparison with systematic biopsy findings in 492 patients. Eur J Radiol. 2008c;65(2):304–10.

Parker KJ, Doyley MM, Rubens DJ. Imaging the elastic properties of tissue: the 20 year perspective. Phys Med Biol. 2011;56(2):513.

Patterson MP, Arsenault M, et al. Optoacoustic imaging of an animal model of prostate cancer. In: BiOS. International Society for Optics and Photonics, San Francisco, CA, 2010, p. 75641B–75641B–5.

Salcudean SE, French D, et al. Viscoelasticity modeling of the prostate region using vibro-elastography. Medical image computing and computer-assisted intervention : MICCAI. In: International conference on Medical Image Computing and Computer-Assisted Intervention. 2006:9(Pt 1):389–96.

Salomon G, Kollerman J, et al. Evaluation of prostate cancer detection with ultrasound real-time elastography: a comparison with step section pathological analysis after radical prostatectomy. Euro Urol. 2008;54(6): 1354–62.

Spirou GM, Vitkin IA, et al. Development and testing of an optoacoustic imaging system for monitoring and guiding prostate cancer therapies. In: Biomed Optics 2004. International Society for Optics and Photonics, San Jose, CA, 2004, p. 44–56.

Su JL, Bouchard RR, et al. Photoacoustic imaging of prostate brachytherapy seeds. Biomed Opt Exp. 2011;2(8):2243.

Tang J, Yang J, Li Y. Peripheral zone hypoechoic lesions of the prostate evaluation with contrast-enhanced gray scale transrectal ultrasonography. J Ultrasound Med. 2007;26(12):1671–9.

Tanter M, Bercoff J, et al. Quantitative assessment of breast lesion viscoelasticity: initial clinical results using supersonic shear imaging. Ultrasound Med Biol. 2008;34(9):1373–86.

Taylor LS, Rubens DJ, et al. Prostate cancer: three-dimensional sonoelastography for in vitro detection. Radiology. 2005;237(3):981–5.

Torr GR. The acoustic radiation force. Am J Phys. 1984;52:402–8.

Tsutsumi M, Miyagawa T. Real-time balloon inflation elastography for prostate cancer detection and initial evaluation of clinicopathologic analysis. Am J Roentgenol. 2010(6);471–6.

Tsutsumi M, Miyagawa T, et al. The impact of real-time tissue elasticity imaging (elastography) on the detection of prostate cancer: clinicopathological analysis. Int J Clin Oncol. 2007;12(4):250–5.

Turgay E, Salcudean S, Rohling R. Identifying the mechanical properties of tissue by ultrasound strain imaging. Ultrasound Med Biol. 2006;32(2):221–35.

Viator JA, Gupta S, et al. Gold nanoparticle mediated detection of prostate cancer cells using photoacoustic flowmetry with optical reflectance. J Biomed Nanotechnol. 2010;6(2):187–91.

Wang L. Photoacoustic imaging and spectroscopy, vol. 144. CRC Press, Boca Raton, FL; 2009.

Wang X, Roberts WW, et al. Photoacoustic tomography: a potential new tool for prostate cancer. Biomed Opt Exp. 2010;1(4):1117.

Xie W, Li L, et al. Photoacoustic imaging of prostate cancer using cylinder diffuse radiation. In: Photonics Asia. International Society for Optics and Photonics, Beijing, China, 2012, p. 85532V–85532V–6.

Yaseen MA, Ermilov SA, et al. Optoacoustic imaging of the prostate: development toward image-guided biopsy. J Biomed Opt. 2010;15(2):21310–8.

Zhai L, Dahl J, et al. Three-dimensional acoustic radiation force impulse (ARFI) imaging of human prostates *in vivo*. In: 2008 IEEE Ultrasonics symposium, Beijing, China, Nov 2008, p. 540–3.

Zhai L, Madden J, et al. Characterizing stiffness of human prostates using acoustic radiation force. Ultrason Imaging. 2010a;32(4):201–13.

Zhai L, Madden J, et al. Acoustic radiation force impulse imaging of human prostates *ex vivo*. Ultrasound Med Biol. 2010b;36(4):576–88.

Zhai L, Madden J, et al. Correlation between SWEI and ARFI image findings in *ex vivo* human prostates. In: Ultrasonics Symposium (IUS) IEEE International, Rome, Italy, 2009, p. 523–6.

Zhai L, Polascik TJ, et al. Acoustic radiation force impulse imaging of human prostates: initial *in vivo* demonstration. Ultrasound Med Biol. 2012;38(1):50–61.

Zhang HF, Maslov K, et al. Imaging of hemoglobin oxygen saturation variations in single vessels *in vivo* using photoacoustic microscopy. Appl Phys Letters. 2007; 90(5):53901–3.

Zhang M, Nigwekar P, Castaneda B. Quantitative characterization of viscoelastic properties of human prostate correlated with histology. Ultrasound Med Biol. 2008; 34(7):1033–42.

Contrast-Enhanced Ultrasound in Prostate Cancer

4

F. Cornelis, Y. Le Bras, G. Rigou, J.M. Correas, and N. Grenier

4.1 Introduction

Prostatic carcinoma (PCa) remains the third main cause of mortality in men and now accounts for 25 % of all new male cancers diagnosed in Europe (Jemal et al. 2009). Diagnosis is based on biopsy in patients with abnormal digital rectal examination and/or elevated PSA levels. Biopsy allows the establishment of the histological grade of the tumor according to the Gleason score. However, when the serum PSA levels are between 4 and 20 ng/ml, the sextant approach yields approximately a 25 % cancer detection rate. Subsequently men frequently require more than two sets of biopsies for diagnosis with an increased risk of complications (mainly bleeding and/or infection).

Therefore, to decrease the rate of repeat biopsies, an increased number of cores have been proposed to improve the detection of prostate cancer (Heidenreich et al. 2008; Cookson et al. 1997). While increasing the number of biopsies remains controversial since it was first proposed, the completion of 12 sextant biopsies is now considered as an acceptable compromise, in particular for a first series of biopsies (Scattoni et al. 2003). However, guiding biopsies to areas most suspicious could improve their diagnostic value.

For guiding biopsies, transrectal ultrasound (TRUS) using transducer frequencies from 7 to 12 MHz has been primarily proposed and is now considered as reference (Heidenreich et al. 2008; Cookson et al. 1997; Scattoni et al. 2003). TRUS enables a detailed visualization of the prostate. The first set of biopsies should focus first on the peripheral zone (PZ), especially if ultrasound abnormalities have been observed. The signs for malignancy are not specific because cancer in the peripheral zone may correspond to a nodule or a hypoechoic (60 % of cases), isoechoic (40 %), or hyperechoic area (5 %), vesicular asymmetry, and capsular irregularity. However, only 11–35 % of the malignancies are visible on gray-scale TRUS. Furthermore, of all hypoechoic lesions seen with TRUS, malignancy is present only in 17–57 % of the cases.

Nowadays, these biopsies are sensitive (sensitivity of 85 %) with high negative predictive value (sensitivity of 85 %) but with a low specificity and positive predictive value (30 %) (Scattoni et al. 2003). For lesions less than 1 cm in diameter, it has been showed that biopsies do not permit diagnosis in 24 % of cases (Djavan et al. 2000). As performed with nontargeted biopsies, repeated biopsies can be performed if the first set of biopsies is negative. Therefore, the detection rate varies between 10 and 35 % (Djavan et al. 2000).

Subsequently, to increase the detection rate of prostate cancer with TRUS-guided biopsy, some authors have proposed to use contrast-enhanced

F. Cornelis, MD (✉) • Y. Le Bras, MD • G. Rigou, MD
N. Grenier, MD
Department of Radiology, Pellegrin Hospital, Place
Amélie Raba Léon, 33076 Bordeaux, France
e-mail: francois.cornelis@chu-bordeaux.fr

J.M. Correas, MD
Department of Radiology, Necker Hospital, 149 rue
de Sèvres, 75743 Paris, France

R.L. Bard et al. (eds.), *Image Guided Prostate Cancer Treatments*,
DOI 10.1007/978-3-642-40429-0_4, © Springer-Verlag Berlin Heidelberg 2014

ultrasound (CEUS) due to the hypervascular nature of prostate cancer compared to surrounding healthy tissue.

4.2 CEUS Detection of Prostate Carcinoma

4.2.1 Ultrasonic Contrast Agents

Several ultrasonic contrast agents (UCA) are currently available. They are composed of tiny bubbles of an injectable gas in a supporting shell. Injected intravenously in a small bolus, they are confined to the vascular lumen until they dissolve, thus improving flow detection. The microbubbles will remain in systemic circulation for a certain period of time depending on the US technique used. The diameter of these microbubbles is in the order of micrometers, smaller than red blood cells. Gas, which composes the microbubbles (perfluorocarbon, nitrogen), is eliminated by the lungs through the alveolar barrier, while the stabilizing elements (shells, surfactants) are removed by the liver and kidney. Today, the ultrasonic contrast agents have very good general tolerance, equivalent to MRI contrast agents. Contrast in the USA is approved only for myocardial imaging; however, "off label" use is practiced at several centers. Microbubble contrast agents are not nephrotoxic, and the incidence of allergic reactions is very low (= 1/50,000 patients). The injections can be repeated after a short delay of a few minutes.

4.2.2 Technical Considerations

The microbubbles oscillate in response to the acoustic compression of the high-frequency sonic energy field and the then-enhanced US signal. Initially proposed to enhance the Doppler signal, contrast-specific softwares have been recently developed on ultrasound equipment, allowing for new possibilities of microbubble detection. After suppression of the signal from the background tissue, these techniques are capable of detecting only the signal issue from the intravascular microbubbles. Therefore, it is possible to visualize exclusively the blood flow in the microvasculature. Several different methods have been proposed, such as harmonic imaging, pulse inversion, cadence contrast-pulse sequence (CPS), and power modulation. A microbubble contrast-only image can be obtained due to the differentiation between the nonlinear signals reflected by the microbubbles and the linear signals from the tissue. For example, a CPS US technique based on the reflections of a series of US pulses allows an optimized contrast-to-tissue ratio (Fig. 4.1). While linear reflectors, such as normal tissue, produce no net signal with the summation of pulses, microbubbles which have nonlinear properties produce echoes that are asymmetric and do not sum to zero. In addition, with the development of techniques with low mechanical index (MI) for transmission of US, the microbubble population is preserved and subsequently may be observed for longer periods.

4.3 CEUS Examination of the Prostate

While contrast-enhanced ultrasound is mainly used for perfusion measurement of the heart and for the detection of liver malignancies, CEUS into the prostate has been proposed because prostate cancer tissue is associated with an increased microvessel density due to the proliferation of neovessels. US contrast agents enable improved detection of low-volume blood flow by increasing the signal-to-noise ratio, while conventional color/power Doppler US imaging cannot visualize microvessels (Fig. 4.2). Therefore, contrast agents, such as Sonovue® (sulfur hexafluoride), Definity® (perflutren lipid microspheres), or Sonazoid® (perflubutane), allow real-time visualizing of the contrast enhancement of the whole prostate which differentiates between normal prostate, adenoma, and carcinoma.

4.4 CEUS-Guided Biopsies

By improving sensitivity, CEUS has been shown to increase the detection of prostate cancer during the first set of biopsies. However, false-positive findings may result if the difference in specificity

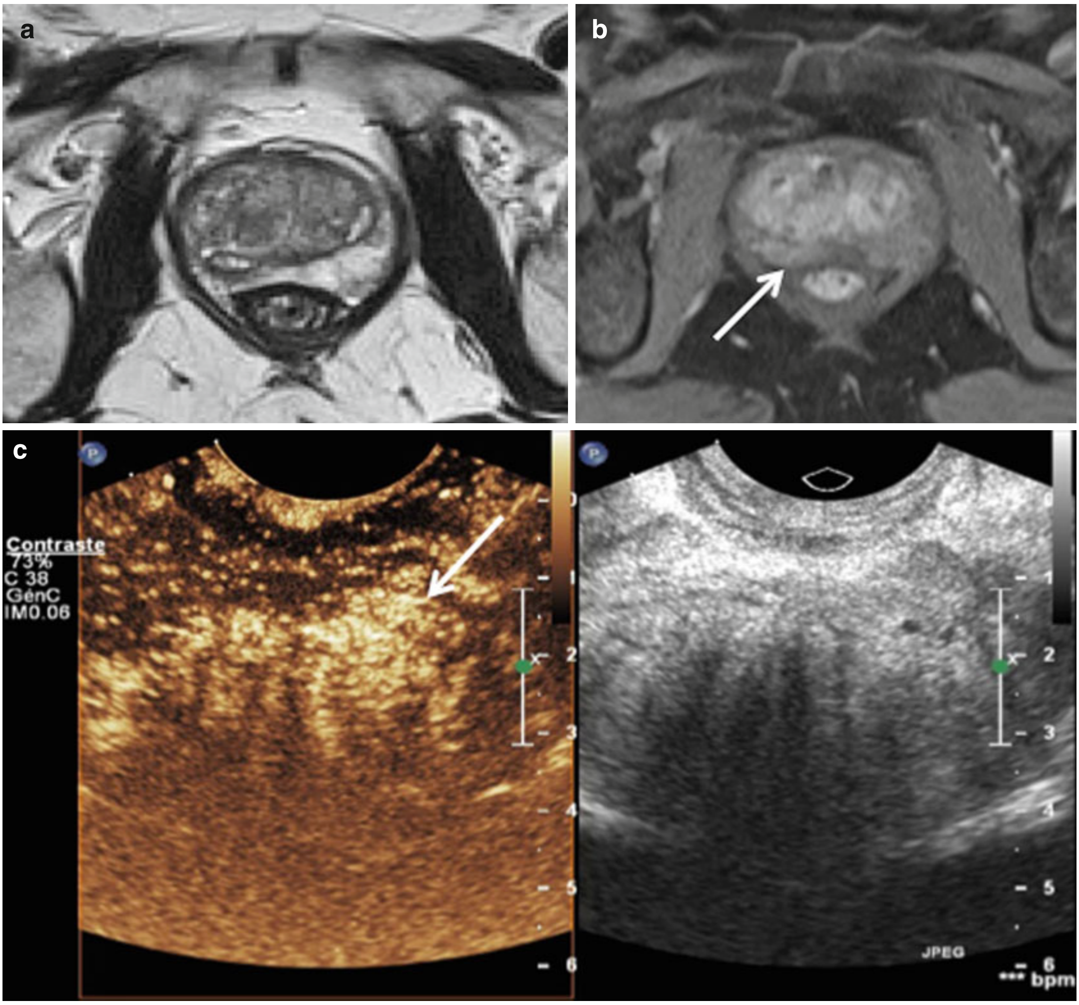

Fig. 4.1 (**a**) Axial T2-weighted spin echo image (TE: 116/TR: 6450) showing no suspicious low signal intensity area in the peripheral zone in a 63-year-old man with PSA level at 7.2 and history of two negative sets of biopsy. (**b**) Dynamic axial T1-weighted gradient echo sequences (TE: 1.46/TR: 3.77/10°) with fat suppression show an early enhancement, whereas the surrounding PZ shows no enhancement (*white arrow*). (**c**) Axial TRUS after contrast injection shows the corresponding hypervascular area on the CPS-mode images (*white arrow*). Histopathologic examination revealed a prostate carcinoma Gleason 6 (3 + 3) on targeted biopsies only

is not evident (Mitterbetger et al. 2010) due to flow abnormalities resulting from prostatitis or hyperplasia in the TZ. Several studies have been published on the topic and have confirmed the preliminary results of ultrasound-guided conventional gray-scale and/or color Doppler biopsies. These studies mainly compared contrast-enhanced US-targeted biopsy of the prostate with gray-scale US-guided systematic biopsy.

Ultrasound-guided color Doppler biopsies have been proposed. In the study of Frauscher et al. (2002), 230 patients were biopsied and cancer was found in 30 % patients (69/230), including 24.4 % (56/230) by contrast-enhanced targeted biopsy and in 22.6 % (52/230) by systematic biopsy. The detection rate for targeted biopsy cores (10.4 %) was significantly better than for systematic biopsy cores (5.3 %, $P<0.001$), and contrast-enhanced targeted biopsy in a patient with cancer was 2.6-fold more likely to detect prostate cancer than systematic US-guided biopsy. Similar results were reported by Pelzer et al. (2005), who observed that a contrast-enhanced targeted biopsy was 3.1-fold more likely to detect cancer than systematic

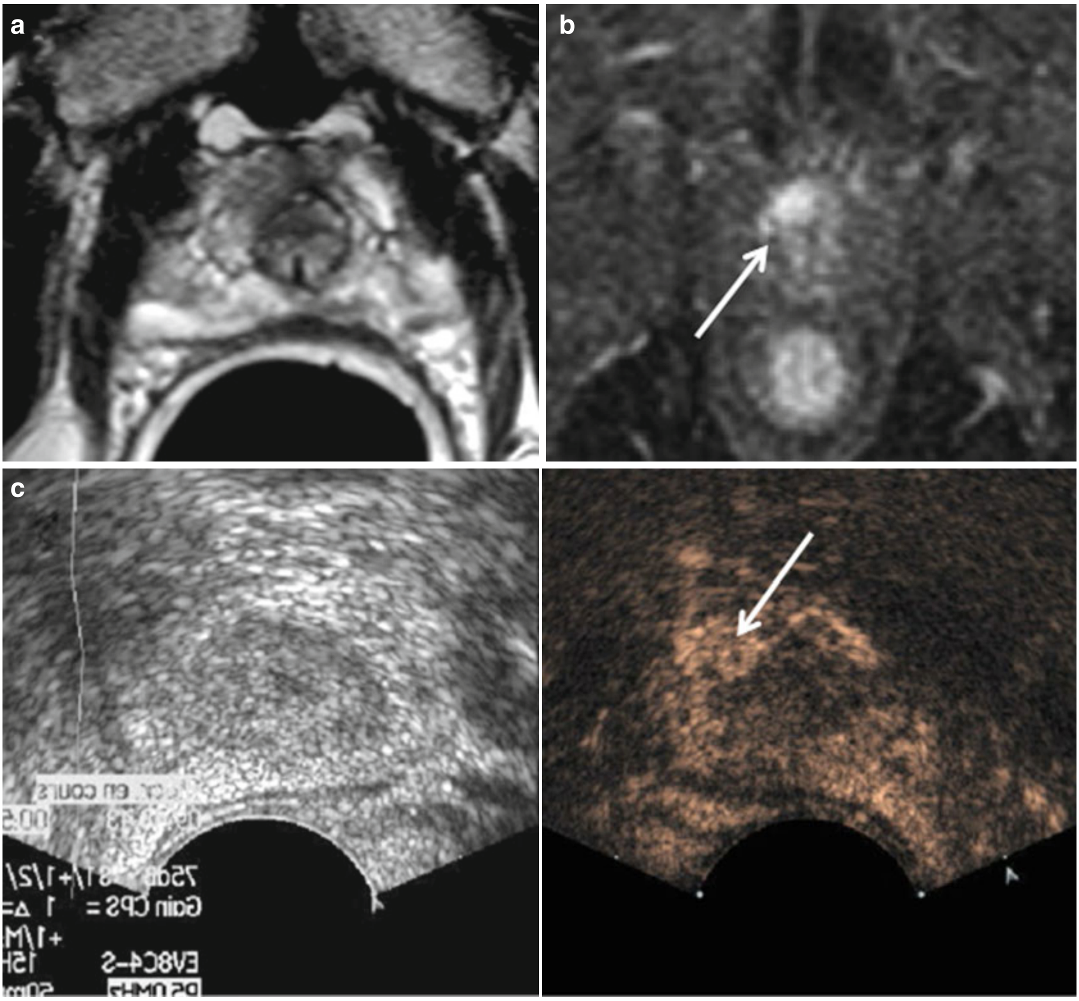

Fig. 4.2 (**a**) Axial T2-weighted spin echo image (TE: 116/TR: 6450) showing an anterior hypointense lesion suspicious for prostate cancer in a 68-year-old man with PSA level at 5.4 and history of 1 negative set of biopsy. (**b**) Dynamic axial T1-weighted gradient echo sequences (1.46/3.77/10°) with fat suppression show an early enhancement (*white arrow*), whereas the surrounding transition zone shows no enhancement. (**c**) Axial TRUS after contrast injection shows the corresponding hypervascular area on the CPS-mode images (*white arrow*). Pathological results concluded to a prostate carcinoma Gleason 7 (4 + 3) on targeted biopsies only

biopsy. However, the combined use of color Doppler-targeted and systematic biopsy allowed for maximal cancer detection with a detection rate of 37.6 % in patients with PSA 4–10 ng/ml. Based on Gleason score findings, Mitterberger et al. (2010) showed that contrast-enhanced biopsy detected significantly higher Gleason scores compared with systematic biopsy in a population of 690 patients. The Gleason score of all 180 cancers (26 %) detected by contrast-enhanced targeted biopsy was 6 or higher (mean 6.8) vs. a range from 4 to 8 (mean 5.4) for the 166 cancers (24 %) detected by systematic biopsy alone.

Based on a gray-scale harmonic CEUS evaluation, Matsumoto et al. (2010) compared radical prostatectomy specimens with the CEUS and were able to identify at least one tumor focus in 40 % of the cases (20/50 patients). When using CEUS alone, at least one tumor focus enhancement was seen in 62 % of the patients; when gray-scale and contrast-enhanced imaging were combined, identification of a tumor focus occurred in 80 % of the cases (40/50 patients). Moreover, Halpern et al. showed that cancer could be identified in 40 % of biopsies of 40 patients (Halpern et al. 2005). The same team confirmed this finding subsequently when authors compared contrast-enhanced harmonic imaging-targeted biopsies with systematic biopsies in 301 patients. In these studies, CEUS-guided biopsies were two times more likely to find cancer compared to systematic biopsy in patients with PCa. However, 20 % of cancers were missed with targeted biopsies and were detected on systematic biopsy alone. While the detection rate of carcinoma is higher with CEUS-guided biopsies, the authors concluded that systematic biopsies were still recommended. Sano et al. (2011) used harmonic imaging to perform 12-core systematic and targeted biopsies in 41 patients. In this study, significantly more cancers were found with CEUS-targeted biopsies compared with systematic biopsies (36.6 vs. 17.7 %).

4.5 Combining CEUS and MRI

A recent study (Cornelis et al. 2013) showed that similar results could be achieved by using a simple approach based on the combination of both advantages of magnetic resonance imaging (MRI) and CEUS (Fig. 4.3). In patients with a target identified on multiparametric (mp) MR imaging, performances of repeated mpMRI-CEUS-guided biopsies were equivalent (46.6 %, 83/178) to MR-guided biopsies and MRI/US fusion technique. Overall, 30.9 % of targeted biopsies and 5.9 % of random biopsies were positive for cancer. Further, 24 % of patients with prostate cancer (20/83) were detected by targeted biopsies only. These performances were independent of the number of previous biopsies, the location of the tumor (PZ vs. TZ) and the PSA level. However, this study also showed that random biopsies must be maintained because 24/83 cancer patients were detected by random biopsies alone. The discrepancy between MR imaging and CEUS, with 20 cases not enhancing on US was probably related to the difference in pharmacokinetics between both types of agents, as MRI diffuses within the interstitium of the prostate parenchyma and CEUS does not, since it is limited to the vasculature. This method has several advantages: no specific US platform is required except for the CEUS software; the biopsy technique remains the same; and about 10 min are required to complete both the 12 standard nontargeted biopsy cores and the CEUS-guided biopsy under local anesthesia.

4.6 Perspective

Additional developments such as replenishment technique (Hodge et al. 1989; Uemura et al. 2013) or use of 4D probes may improve the performances of CEUS. Moreover, targeted microbubbles for molecular imaging can be used with this method in the future, targeting the vascular endothelial growth factor receptors, as recently shown (Fischer et al. 2010; Pochon et al. 2010). These new perspectives will be convenient not only for targeted biopsy but also for US-guided focal therapy.

Conclusion

In summary, CEUS for guided biopsy can be a simple method for the detection of cancer at a higher rate per core than conventional random biopsy.

It improves the performance of the basic gray-scale or Doppler ultrasound for the detection of prostate cancer and the efficiency of targeted biopsy on enhanced zones. Moreover, the combination of mpMRI and CEUS-guided biopsy appears to be a simple and accurate method for the detection of prostate cancer in patients with previous negative biopsies, while prospective comparative studies with the alternative approaches using MR-guided biopsies or MRI/US fusion techniques would be worthwhile in the future. The limitations of the brevity of enhancement in the arterial phase should disappear with 4D volume acquisitions, and the quantitative functional imaging may provide objective evidence of the diagnosis of malignant lesions and aggressiveness, as well as for the evaluation of therapeutic response.

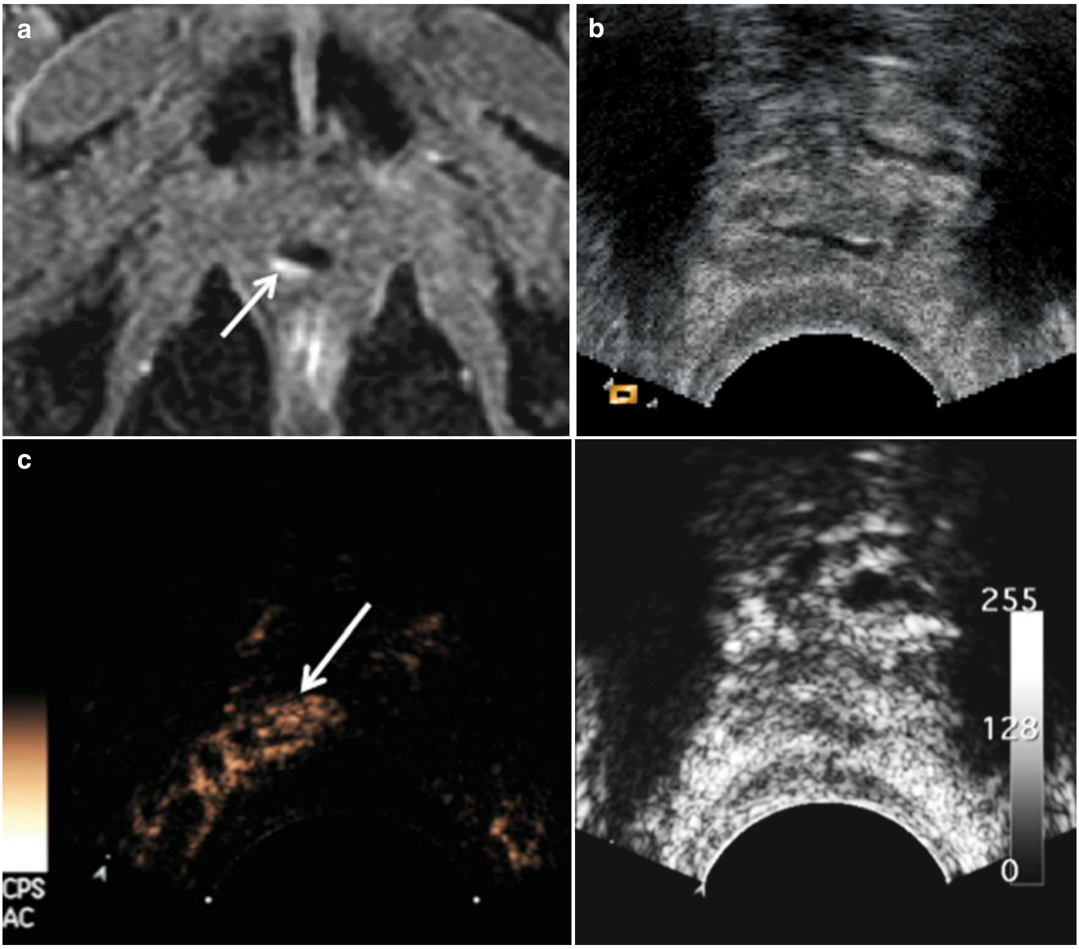

Fig. 4.3 (**a**) Dynamic axial T1-weighted gradient echo sequences (TE: 1.46/TR: 3.77/10°) with fat suppression show an early enhancement on right peripheral zone (*white arrow*), whereas the surrounding prostate shows no enhancement, suspicious for a recurrence of prostate cancer in a 65-year-old man with PSA level at 5.4 and history of radiotherapy and HIFU. (**b**) Axial TRUS before contrast injection shows no difference into the prostate. (**c**) Axial TRUS after contrast injection shows the corresponding hypervascular area on the CPS-mode images (*white arrow*). Pathological results concluded to a prostate carcinoma Gleason 8 (4+4) on targeted biopsies only

References

Cookson MS, Fleshner NE, Soloway SM, Fair WR. Correlation between Gleason score of needle biopsy and radical prostatectomy specimen: accuracy and clinical implications. J Urol. 1997;157(2):559–62.

Cornelis F, Rigou G, Le Bras Y, et al. Real-time contrast-enhanced transrectal US-guided prostate biopsy: diagnostic accuracy in men with previously negative biopsy results and positive MR imaging Findings. Radiology. 2013;269(1):159–66.

Djavan B, Zlotta AR, Ekane S, Remzi M, Kramer G, Roumeguere T, et al. Is one set of sextant biopsies enough to rule out prostate cancer? Influence of transition and total prostate volumes on prostate cancer yield. Eur Urol. 2000;38(2):218–24. PubMed PMID: 10895015. Epub 2000/07/15. eng.

Fischer T, Thomas A, Tardy I, Schneider M, Hunigen H, Custodis P, et al. Vascular endothelial growth factor receptor 2-specific microbubbles for molecular ultrasound detection of prostate cancer in a rat model. Investig Radiol. 2010;45(10):675–84.

Frauscher F, Klauser A, Volgger H, Halpern EJ, Pallwein L, Steiner H, et al. Comparison of contrast enhanced color Doppler targeted biopsy with conventional systematic biopsy: impact on prostate cancer detection. J Urol. 2002;167(4):1648–52.

Halpern EJ, Ramey JR, Strup SE, Frauscher F, McCue P, Gomella LG. Detection of prostate carcinoma with contrast-enhanced sonography using intermittent harmonic imaging. Cancer. 2005;104(11):2373–83.

Heidenreich A, Aus G, Bolla M, Joniau S, Matveev VB, Schmid HP, et al. EAU guidelines on prostate cancer. Eur Urol. 2008;53(1):68–80.

Hodge KK, McNeal JE, Terris MK, Stamey TA. Random systematic versus directed ultrasound guided transrectal core biopsies of the prostate. J Urol. 1989; 142(1):71–4.

Jemal A, Siegel R, Ward E, Hao Y, Xu J, Thun MJ. Cancer statistics, 2009. CA Cancer J Clin. 2009;59(4): 225–49.

Matsumoto K, Nakagawa K, Hashiguchi A, Kono H, Kikuchi E, Nagata H, et al. Contrast-enhanced ultrasonography of the prostate with Sonazoid. Jpn J Clin Oncol. 2010;40(11):1099–104.

Mitterbetger MJ, Aigner F, Horninger W, Ulmer H, Cavuto S, Halpern EJ, et al. Comparative efficiency of contrast-enhanced colour Doppler ultrasound targeted versus systematic biopsy for prostate cancer detection. Eur Radiol. 2010;20(12):2791–6.

Pelzer A, Bektic J, Berger AP, Pallwein L, Halpern EJ, Horninger W, et al. Prostate cancer detection in men with prostate specific antigen 4 to 10 ng/ml using a combined approach of contrast enhanced color Doppler targeted and systematic biopsy. J Urol. 2005;173(6):1926–9.

Pochon S, Tardy I, Bussat P, Bettinger T, Brochot J, von Wronski M, et al. BR55: a lipopeptide-based VEGFR2-targeted ultrasound contrast agent for molecular imaging of angiogenesis. Invest Radiol. 2010;45(2):89–95.

Sano F, Terao H, Kawahara T, Myoshi Y, Sasaki T, Noguchi K, et al. Contrast-enhanced ultrasonography of the prostate: various imaging findings that indicate prostate cancer. BJU Int. 2011;107(9):1404–10.

Scattoni V, Roscigno M, Raber M, Montorsi F, Da Pozzo L, Guazzoni G, et al. Multiple vesico-urethral biopsies following radical prostatectomy: the predictive roles of TRUS, DRE, PSA and the pathological stage. Eur Urol. 2003;44(4):407–14.

Uemura H, Sano F, Nomiya A, et al. Usefulness of perflubutane microbubble-enhanced ultrasound in imaging and detection of prostate cancer: phase II multicenter clinical trial. World J Urol. 2013;31(5):1123–8.

Power Doppler Imaging of Prostate Cancer

5

Jean-Luc Sauvain

5.1 Introduction

Prostatic tumors range from small slow-growing lesions to aggressive tumors that metastasize rapidly, and there is controversy about which screen-detected lesion will become clinically significant (Neal and Donovan 2000). Current methods of screening involve measurement of PSA followed by transrectal ultrasound scanning and biopsy.

Grayscale US is limited as a screening test (Resnick et al. 1981; Rifkin et al. 1993; Aarninck et al. 1998) and lacks adequate specificity and sensitivity. With grayscale ultrasonography, prostate cancer more often presents visible findings like a hypoechoic area or can sometimes appear echogenic, but cancer is also isoechoic and invisible (50 % of non-palpable tumor in some radical prostatectomy series). A hypoechoic area can be found in prostatitis lesions.

Color Doppler improves the echographic diagnostic predictive value and specificity in cancer by virtue of demonstration of abnormal blood flow (Kelly et al. 1993). Color Doppler sonography has also been shown to be an adjunct to grayscale US improving the accuracy of cancer detection especially for isoechoic cancer and cancer with elevated Gleason score and allowed more precise orientation and guidance of biopsies (Newmann et al. 1995; Bree 1997; Lavoipierre et al. 1998).

Power Doppler sonography (PDS) (Cornud et al. 1997, 2000; Halpern and Strup 2000; Sauvain et al. 1997) is more sensitive to slow flow and less angle dependent than color Doppler (Kuligowska et al. 2001). The result is that blood flow measurement allows a better analysis of intraprostatic vessels without variation in color or intensity according to flow orientations. Some authors suggested using power Doppler for targeted biopsies when the number of biopsies must be limited (Halpern and Strup 2000).

Power Doppler also allows three-dimensional reconstruction of blood flow.

The value of sonography combined with color Doppler explorations (CDS) and power Doppler explorations (PDS) in the detection of prostate cancer has given rise to a great many evaluations. Cornud et al. calculated that the risk of a positive biopsy was 11 % with a normal DRE (Digital Rectal Examination), a PSA level less than 10 ng/ml, and a normal CDS and that the CDS may be of use to distinguish avascular low-risk tumors from hypervascular high-risk tumors (Cornud et al. 1997, 2000).

The increasing use of individual screening and the increased number of biopsies have led to the early detection of increasingly small lesions. In view of these small lesions, the value of the PDS was low since a significant number of sometimes little differentiated cancers were non-palpable and not visible (Halpern and Strup 2000; Kuligowska et al. 2001). Sometimes large, anterior cancers as well as those of the transition area were not detectable in the sonography examination. The only

---

J.-L. Sauvain, MD
Imaging Medical Center, 6 passage Jules Didier,
70000 Vesoul, France
e-mail: jlfsauvain@aol.com

R.L. Bard et al. (eds.), *Image Guided Prostate Cancer Treatments*,
DOI 10.1007/978-3-642-40429-0_5, © Springer-Verlag Berlin Heidelberg 2014

known value of the PDS was that of directing the biopsies when a suspect area was detected.

Technical progress in Doppler sonography and a better understanding of its value and limits may help better integrate them in a diagnostic approach (Sauvain et al. 2003, 2006).

5.2 Prostate Vascular Anatomy

The prostate is supplied from two arterial sources: the prostatic arteries and the inferior vesical arteries, both arising from the internal iliac system. The prostatic arteries enter the prostate from an antero-lateral location on each side and give off capsular branches as well as urethral branches. Capsular arteries course along the lateral margin of the prostate and give off numerous perforating branches which penetrate the capsule and supply approximately two-thirds of the total glandular tissue. The areas of penetration into the capsule are commonly referred to as the neurovascular bundles. The inferior vesical arteries run along the inferior surface of the bladder and also provide urethral branches. In addition to supplying the central portion of the prostate, the inferior vesical arteries also give off branches which supply the bladder base, seminal vesicles, and distal ureters. Both the capsular and urethral branches can be visualized with power Doppler ultrasound (Fig. 5.1).

With PDS and 3D PDS, in normal subjects (Fig. 5.2a–c) at the level of the peripheral prostate and at the lateral edges, capsular arteries radially supplying the parenchymal branches were found in all the patients: on coronal section they were symmetrically distributed with a weak Doppler signal. There were no secondary division branches observed at the level of the intra-prostate parenchymal vessels. In 26 of the 41 referring subjects, a 1–2 mm thick posterior peripheral margin was identified that contained vessels of diverse origin: sagittally, medially, and laterally arranged vessels having their origin in the inferior vesical net; others having a periurethral origin; and finally, others originating at the lateral pedicular level. On 3-D PDS reconstruction, this group of vessels forms a marginal system that delimits the posterior surface of the prostate. In the normal state, there were no apparent anastomoses visualized on power Doppler sonography appearing between the vessels forming the marginal system and the intraparenchymal or extra-prostate vessels. Near the posterolateral border, identification of neurovascular bundles in this referring group was suggested on coronal scans on both sides of the prostate-like vessels giving branches to the posterior peripheral margin.

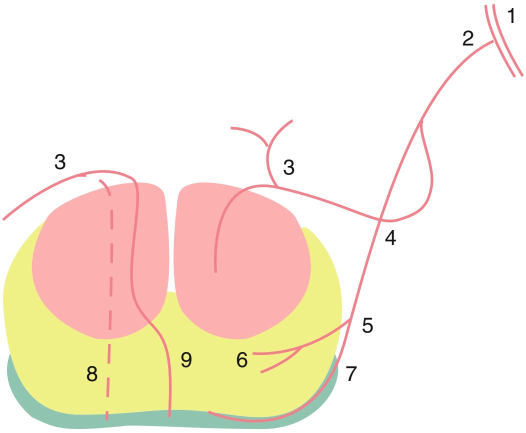

Fig. 5.1 Schema of normal intraprostatic and intracapsular blood supply. *1* Internal iliac artery, *2* prostatic vesical artery, *3* inferior vesical artery, *4* prostatic artery, *5* capsular artery, *6* parenchymal artery, *7* intracapsular artery (pedicular origin), *8* intracapsular artery (vesical origin), *9* intracapsular artery (urethral origin)

5.3 Equipment and Techniques

No specific patient preparation is required. The patient is placed in the left lateral decubitus position. A digital rectal examination is recommended prior to probe insertion to rule out any obstructing pathology and also to allow the examiner to evaluate the prostate by digital examination. The probe is covered with a condom into which coupling gel has been placed and the probe lubricated and gently inserted into the rectal canal.

5.3.1 Sonography Technique and Power Doppler Mode

Examination of the prostate by ultrasound requires a high-frequency (7.5–10 MHz) end-fire

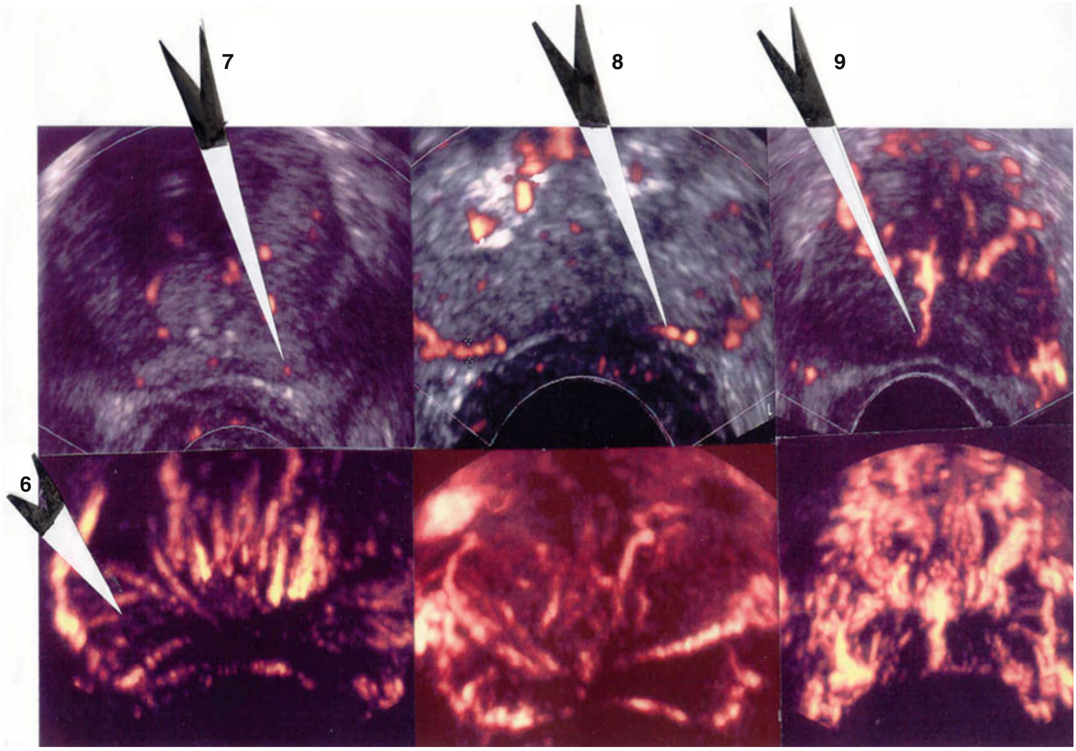

Fig. 5.2 (**a**) Axial section: Visualization of three vessels in posterior peripheral margin on axial section and placed symmetrically on 2D imaging. The capsule is raised in 3D by its vessels. (**b**) Axial section: posterior peripheral vessels of left and right pedicular origin on power Doppler and in 3D PDS. (**c**) Axial section: Anastomosis between periurethral and posterior peripheral vessels

or biplane transrectal transducer. We used Philips HDI 5000 power Doppler sonography instruments (Philips Ultrasound, Bothell, WA, USA) coupled with a C9-5 ICT endocavity probe and Toshiba Aplio MX (Toshiba MS, Nasu, Japan) coupled with a biplane PVT-770RT endocavity probe (5–10 MHz). Examination of the prostate by grayscale imaging is first performed and the length, width, and height of the gland measured. The prostatic volume is calculated based on the formula for a prolate ellipsoid (length × width × height × 0.523); this allows correlation of the measured PSA with a predicted PSA based on gland volume.

As a complement to the endorectal sonography, an exploration with the power Doppler mode was carried out in all patients. The Doppler increase was optimized in each patient so that there was no background noise at about 80 %. We privileged a low PRF that was adjusted to 500 Hz in standard value: the filtration and persistence were preset at their maximum level in order to limit the movement artifacts.

A weak compression with the end of the probe was systematically carried out in case of a hypoechogenic area in the search for a modification of its echostructure. The mean time for a Doppler sonography of the prostate was about 15 min.

Three-dimensional reconstruction with power Doppler of intraprostatic blood flow imaging (3D PDS) was performed for a better understanding of the prostate perfusion. 3D PDS was obtained with the capture of 11 power Doppler US images after scanning a suspicious volume. Then all these images were added in a three-dimensional reconstruction allowing us to make an angular movement of 15°. On the final image, only power Doppler acquisitions were present without grayscale data.

5.4 Value of Transrectal Power Doppler Sonography in Suspect Subjects of Cancer of the Prostate (PSA level > 4ng/ml or Abnormal DRE) Before a First Series of Biopsy

Prostate cancer is generally hypervascular when compared to normal prostatic tissue, and this is manifested as increased color encoding at sensitive instrument settings. 3D PDS looks for area or intraprostatic volume with an increase in the number of detectable vessels or asymmetry in the distribution of blood flow in each investigated case. A vascular density in the suspected area or volume was noted.

The criteria of analysis were: increase in number of intra-lesion vessels, disoriented vessels or verticalized vessels in peripheral gland, asymmetrical blood flow, mass effect on the intraprostate perilesional vessels and vessels in peripheral margins (Fig. 5.3a, b).

5.4.1 Ultrasound Semiology and Power Doppler (Sauvain et al. 2003, 2006)

In B mode, the peripheral area was in the normal state homogenous and more echogenic than the transition area.

The suspect ultrasonographic anomalies in the peripheral prostate area may be qualified as hypoechogenic, weakly hypoechogenic or subtle (Figs. 5.4a–c and 5.5a–c), and heterogenic. The power Doppler mode searched for the presence of tumor vessels in a suspect lesion in the B-mode sonography. A visible lesion in B mode was said to be hypervascularized if it included one or several vessels. The lesion was qualified as focal if it was less than 5 mm. However, this lesion was qualified as nodular if it was over 5 mm and confined to a single sextant, comprising vessels remaining strictly intralesional. If the zone hypoechogenic area involved three sextants or more and/or if the vessels extended beyond the hypoechogenic area, the lesion was qualified as infiltrating (Fig. 5.4). If the lesion was nodular or focal and associated with outer seats without real contiguity, the lesion was qualified as multifocal.

A minority of cribriform carcinomas can demonstrate punctate calcifications.

5.4.2 Four Classes for the Different Vascular Tumor Types (Sauvain et al. 2003)

The PDS results can be rated from 1 to 4 classes:

1. Normal
2. Slightly hypoechogenic avascular lesion in which the hypoechogenicity disappears after slight compression with the probe (Fig. 5.6)
3. Hypoechogenic avascular lesion (Fig. 5.7)
4. Weakly hypoechogenic hypervascularized lesion and isolated hypervascular lesion (Fig. 5.8) or hypervascularized hypoechogenic lesion (Fig. 5.9)

Classes 3 and 4 are considered to be pathological.

5.4.3 PDS and Tumor Location

The base and apical margins are the most important margins as they are the ones most frequently involved by infiltration of the cancer. Apical prostate cancer demands particular attention in terms of whether or not it is really organ confined. Some 80 % of apical prostate cancers are close to the apical capsule, and the cancers here are at risk of capsular penetration along apical nerve branches entering the prostate allowing the cancer to infiltrate (perineural infiltration) along these conduits out of the prostate (Fig. 5.10).

As an aside, this is not to say that all men who have clear base and apical margins to their prostate will remain free from disease forever, as some 10–15 % of men with localized or organ-confined disease will develop spread of their prostate cancer after radical surgical/robotic removal. It is unknown if the manipulation from radical surgery/robotics actually contributes to this problem of cancer spread or whether there are other factors involved.

The “apex” is the most frequent location of PCa, and there is a high false-negative rate from

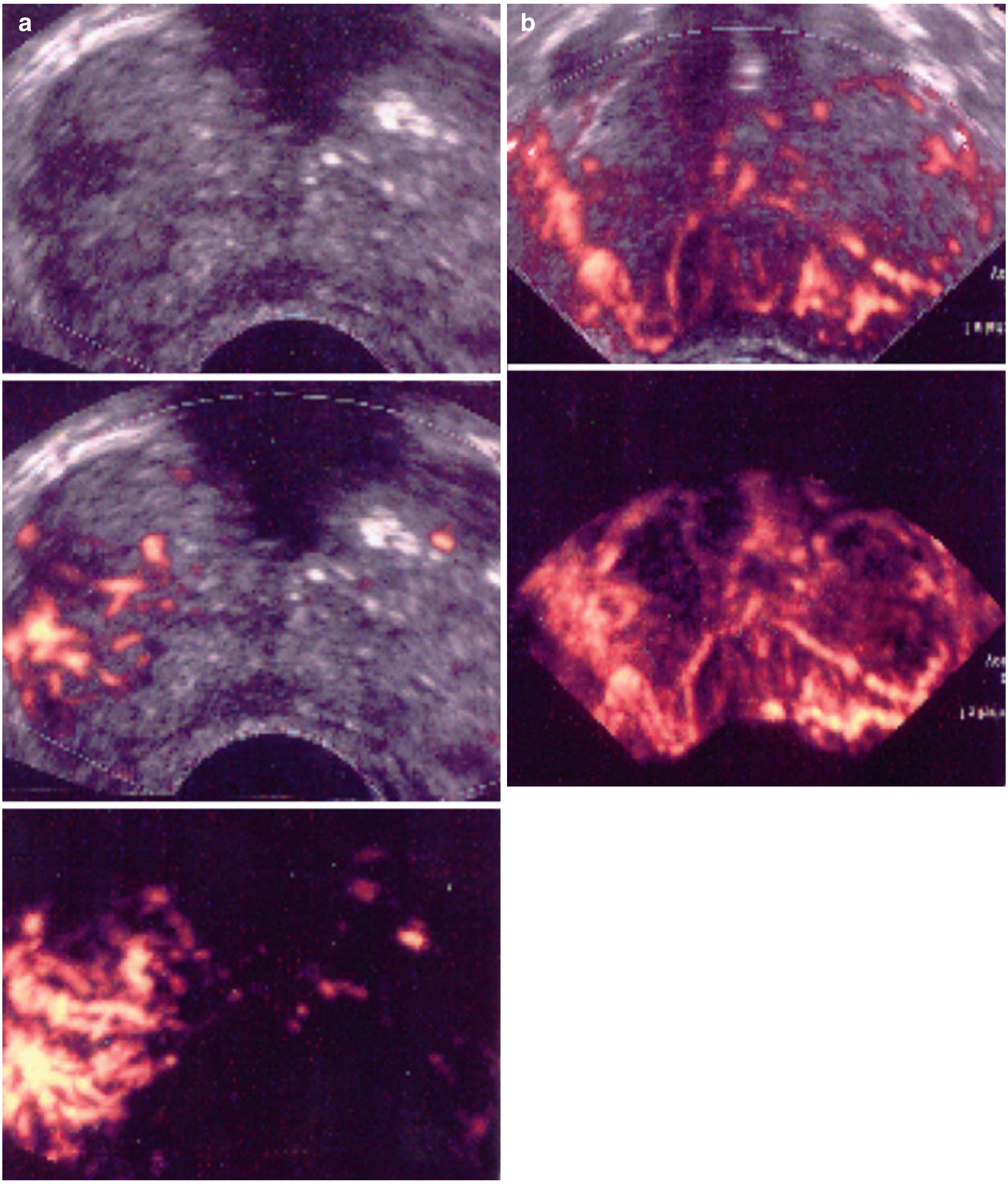

Fig. 5.3 (**a**) Prostate cancer with 3D PDS vascular asymmetry or irregular vessels in any part of the prostate. (**b**) Prostate cancer with 3D PDS vertically or disoriented parenchymal vessels

transrectal biopsy. It is difficult to predict apex cancer preoperatively using methods currently available.

Transrectal PDS allows one to localize a lesion in the apex or base area (Fig. 5.11a–c).

Transition zone tumors tend to behave in a clinically more benign manner because they are distant from sites of anatomical weakness and thus need to grow quite large before spreading outside of the gland. The main problem with the diagnosis of transition zone tumors is the heterogeneous echotexture of the normal transition zone. Power Doppler cannot play a role in the diagnosis of transition zone tumors by identifying areas of abnormal flow.

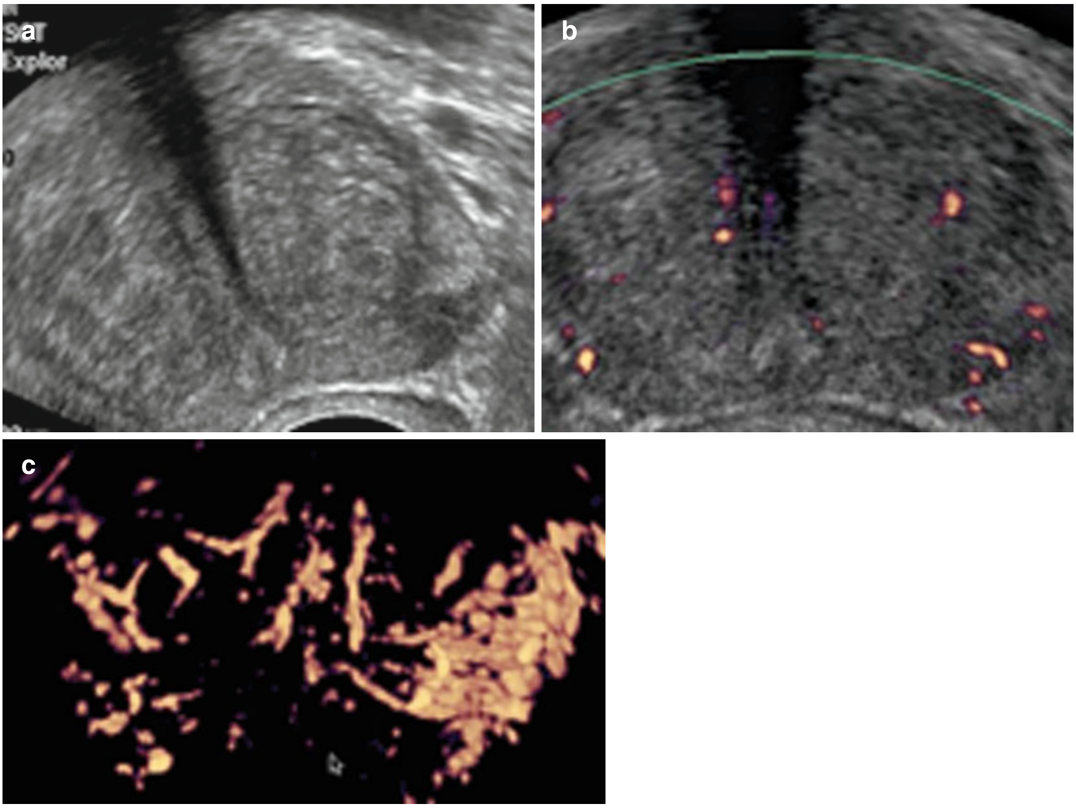

Fig. 5.4 Subtle hypoechoic and hypervascular lesion. (**a**) B mode: isoechoic lesion. (**b**) Increase in vessel number in left sextants. (**c**) 3D vascular reconstruction (PSA 10 ng/ml, 3 positive biopsies in left sextant, Gleason score 7(4+3), extraprostatic extension)

When we suspect a lesion in the transition zone, we conduct a multiparametric MRI before a transrectal PDS biopsy (Fig. 5.11).

5.4.4 PDS Results

We published a study in 2006 about a group of 579 patients with a serum PSA level greater than 3.5 ng/ml who underwent sextant biopsies (Sauvain et al. 2006). An echographic or vascular anomaly was detected in 335 patients; after biopsies, this anomaly corresponded to 260 cancers, 39 of which were not visible (false-negative Doppler results). The negative predictive value was 84 %, and there was no significant relation between PSA level and negative predictive value. After initial biopsies, if an abnormal Doppler signal was present, the risk of having positive additional biopsies was 83 %. Abnormal disoriented irregular vessels were present in 69 % of patients with a Gleason score of 7 or higher versus 31 % in patients with a Gleason score less than 7 ($p < 0.01$).

5.4.5 PDS and Extracapsular Extension (ECE)

In our study of 2006 (Sauvain et al. 2006), we have prospectively evaluated three vascular types of intracapsular and peripheral blood flow in the 63 patients who underwent a radical prostatectomy (Fig. 5.12).

- Type A: perfusion of prostatic posterior margin was absent, effaced by the tumor mass effect. A regular, hypoechogenic margin with a thickness of between 1 and 2 mm was found behind the most peripheral detectable vessel.

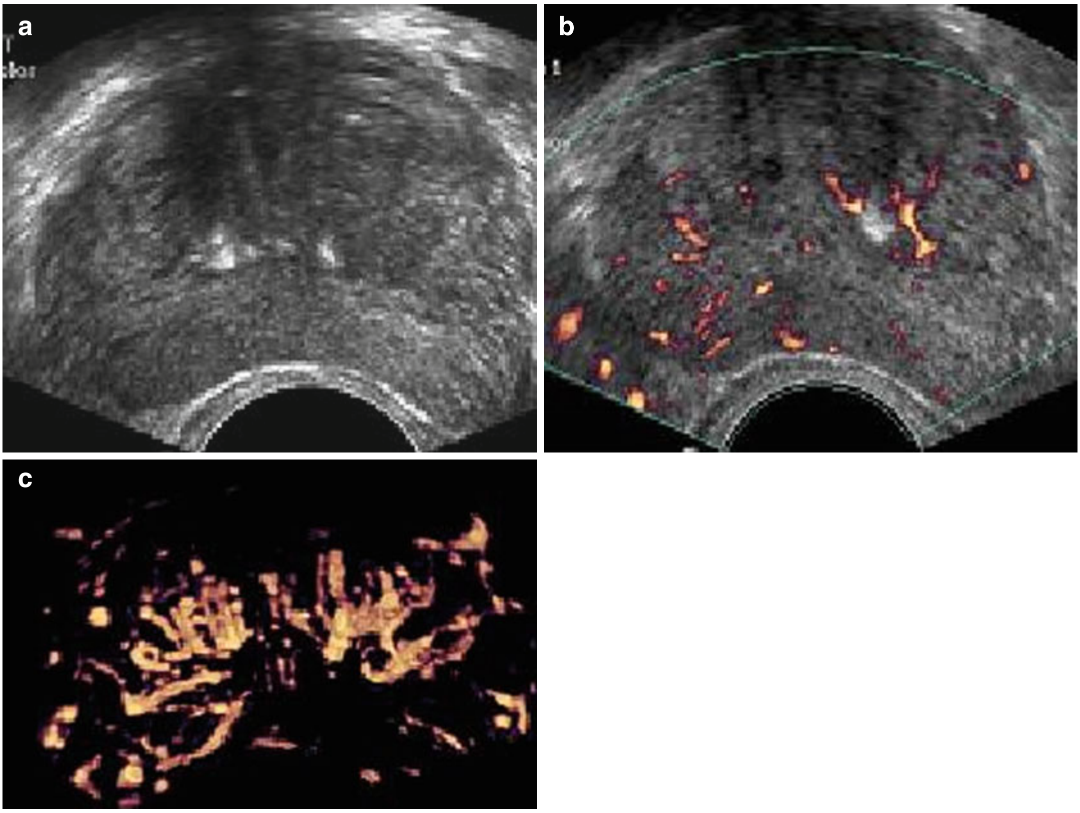

Fig. 5.5 Isoechoic and hypervascular lesion. (**a**) B mode: isoechoic lesion. (**b**) Increase in vessel number in right sextants. (**c**) 3D vascular reconstruction (PSA 10 ng/ml, 3 positive biopsies in right sextant, Gleason score 6, no extraprostatic extension)

Extracapsular involvement was presumed to be absent. Cancer without measurable blood flow was considered as Type A (Fig. 5.12).

- Type B: the perfusion in the posterior margin is also absent, but the margin was irregular and exhibits localized thinning. There was no detectable anastomosis with the extra-prostate vascular system with respect to the lesion. In this type, investigation of extraprostatic spread is difficult and could not be determined (Fig. 5.13).
- Type C: the posterior peripheral margin was absent in places, and the vessels having tumoral origin left the prostate gland to create direct anastomoses with the periprostatic vessels. In this lesion type, extracapsular involvement was presumed to be present (Fig. 5.14).

The risk of extracapsular extension in our cancer group with vascular Type C was 88 % and only 12 % in vascular Type A (44 % in vascular Type B).

The presence or the absence of vessels crossing the capsule to determine an extraprostatic tumor spread was a significant sign ($p<0.0001$) (sensitivity = 59.3 %, specificity = 94.4 %, PPV = 88.9 %, NPV = 75.6 %, and accuracy = 79.3 %).

5.5 Value of Transrectal Power Doppler Sonography in the Detection of Low-Risk Prostate Cancers (Sauvain et al. 2013)

The increasing use of individual screening and the increased number of biopsies have led to the early detection of increasingly small lesions. In view of these small lesions, the value of the PDS was low since a significant number of sometimes little differentiated cancers were non-palpable and not

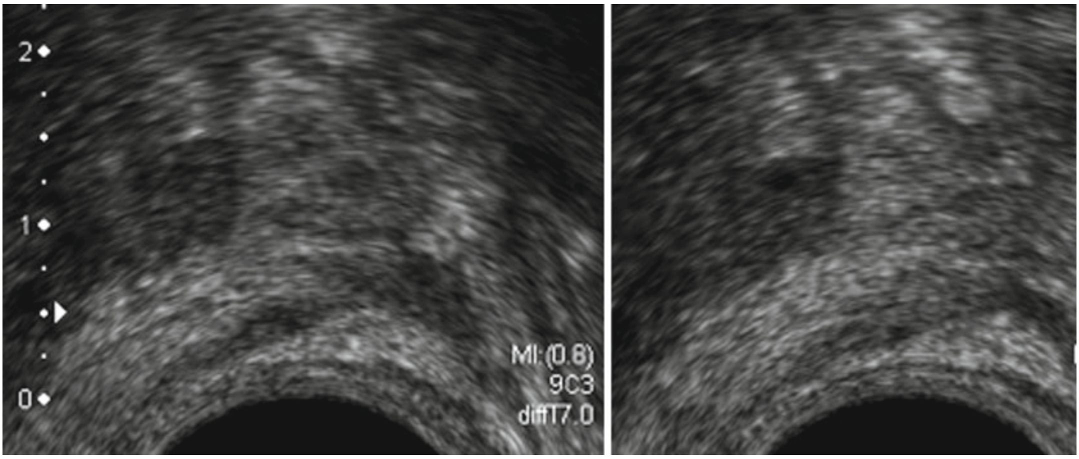

Fig. 5.6 Class 2. (**a**) (*Left*) Low hypoechoic lesion of peripheral prostate without vascular anomaly that disappears under compression. (**b**) (*Right*) PSA 6.2 ng/ml, negative biopsies

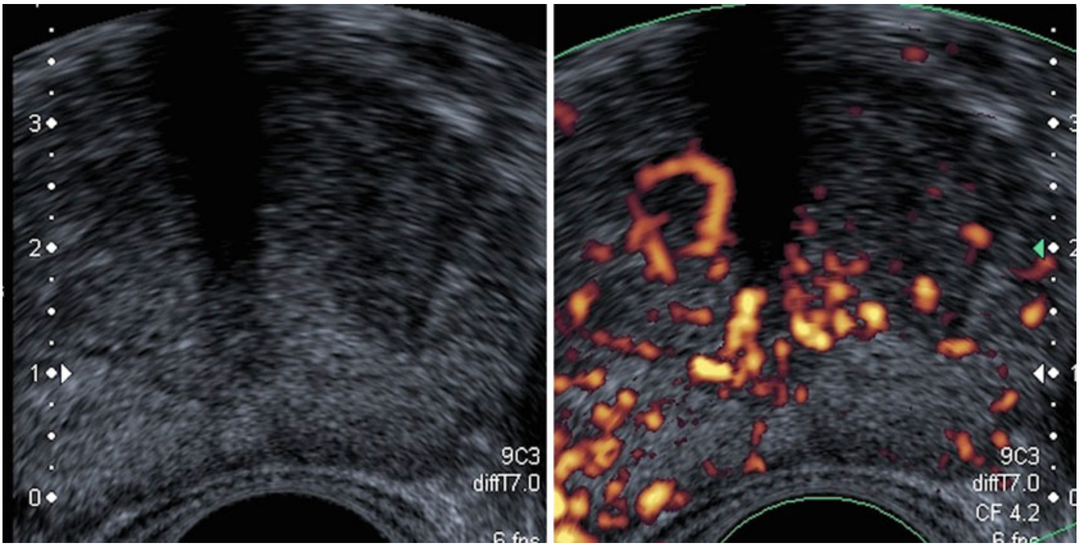

Fig. 5.7 Low hypoechoic lesion of peripheral prostate without anomaly (**a**) that does not disappear under compression (**b**)

visible. Among the small lesions thereby detected, some well-differentiated lesions may be qualified as latent, painless, or nonsignificant. They are at the origin of an overdiagnosis involving 40 % of the patients treated. The risk of an overdiagnosis and overtreatment of a lesion has until now been underestimated, and the active surveillance protocols proposed are probably not adapted to the psychological profile of each patient.

Also, the question of the probability of not having an evolving high-risk lesion in prostate biopsies in patients with a normal DRE, a PSA level between 4 and 10 ng/ml and a prostatic transrectal sonography with a normal PDS examination, was asked.

In our last published study (Sauvain et al. 2013), 243 consecutive patients with a PSA level less than 10 ng/ml and a DRE without anomaly had PDS-guided biopsies; 12–15 samples were systematically taken and echo guided in the suspect areas. The PDS results were rated from 1 to 4 as in the upper paragraph:

1. Normal
2. Slightly hypoechogenic avascular area in which the hypoechogenicity disappears after compression by probe

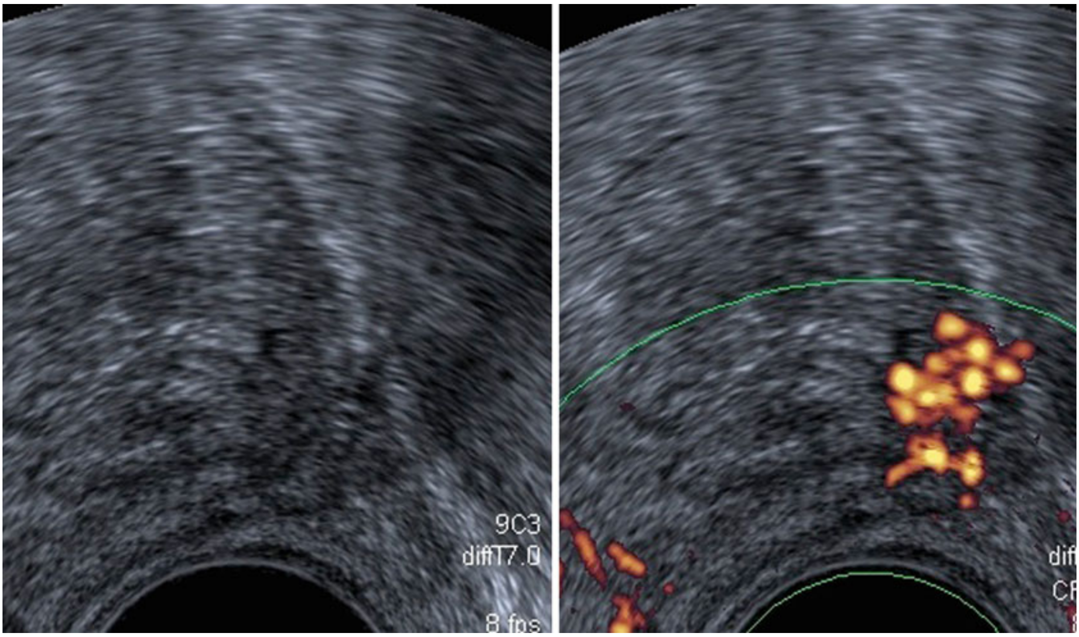

Fig. 5.8 Class 4. Low hypoechoic vascular lesion of peripheral prostate: 120 g, normal DRE, PSA: 9.6 ng/ml, Gleason 7 (3+4) score

3. Hypoechogenic avascular area
4. Hypoechogenic vascularized area with power Doppler sonography

Patients rated 3 or 4 were considered to be pathological. D'Amico's criteria (D'Amico et al. 2004) were used to assess the risk of a biological recurrence after treatment, and those of Dall'Era (Dall'Era et al. 2008) were used to select the patients that could benefit from active surveillance (AS) (Table 5.1). The PDS was considered to be a true positive if at least one biopsy was positive in the same sextant as the suspect image.

In a prospective manner, 106 cancers were diagnosed that could be qualified as low risk in 84 % of the cases (89 % with a normal PDS and 79 % with an abnormal PDS). Sixty-nine percent of the cases could be subject to AS (86 % of the normal PDS cases and 47 % of the abnormal PDS cases; $P < 0.001$). The PDS was normal in 159 of the 243 patients (65 %). With a normal PDS, there was a 96 % probability of not having a high-risk cancer. With an abnormal PDS, at least one biopsy was positive in 57 % of the cases, and the probability of having a significant cancer was 30 % according to the Dall'Era criteria. A significant reduction was noted with a normal PDS, to 36 and 5 %, respectively (VPN = 95 %) ($P = 0.015$).

The negative predictive value of the PDS may significantly modify the risk of having or not having an aggressive lesion and may weigh the statistical risk of the PSA level.

The negative predictive value of the MRI exceeds 90 % with an accuracy of 98 % in the diagnosis of significant cancers, independent of the fact that its high sensitivity also favors the overdiagnosis of a great many lesions under 0.5 cc.

D'Amico's criteria to assess the risks of biological recurrence after treatment have gained a wide consensus. The criteria proposed by Dall'Era are most often used in Europe and have been validated over long periods of time. Studies on cohorts of patients with clinically localized and non-treated prostate cancer have shown that the overall survival of patients with a Gleason score less than 7 is excellent (D'Amico et al. 1998). Therefore, after 20 years, the specific survival of the patients ranges from 70 to 90 % (Albertsen et al. 2005).

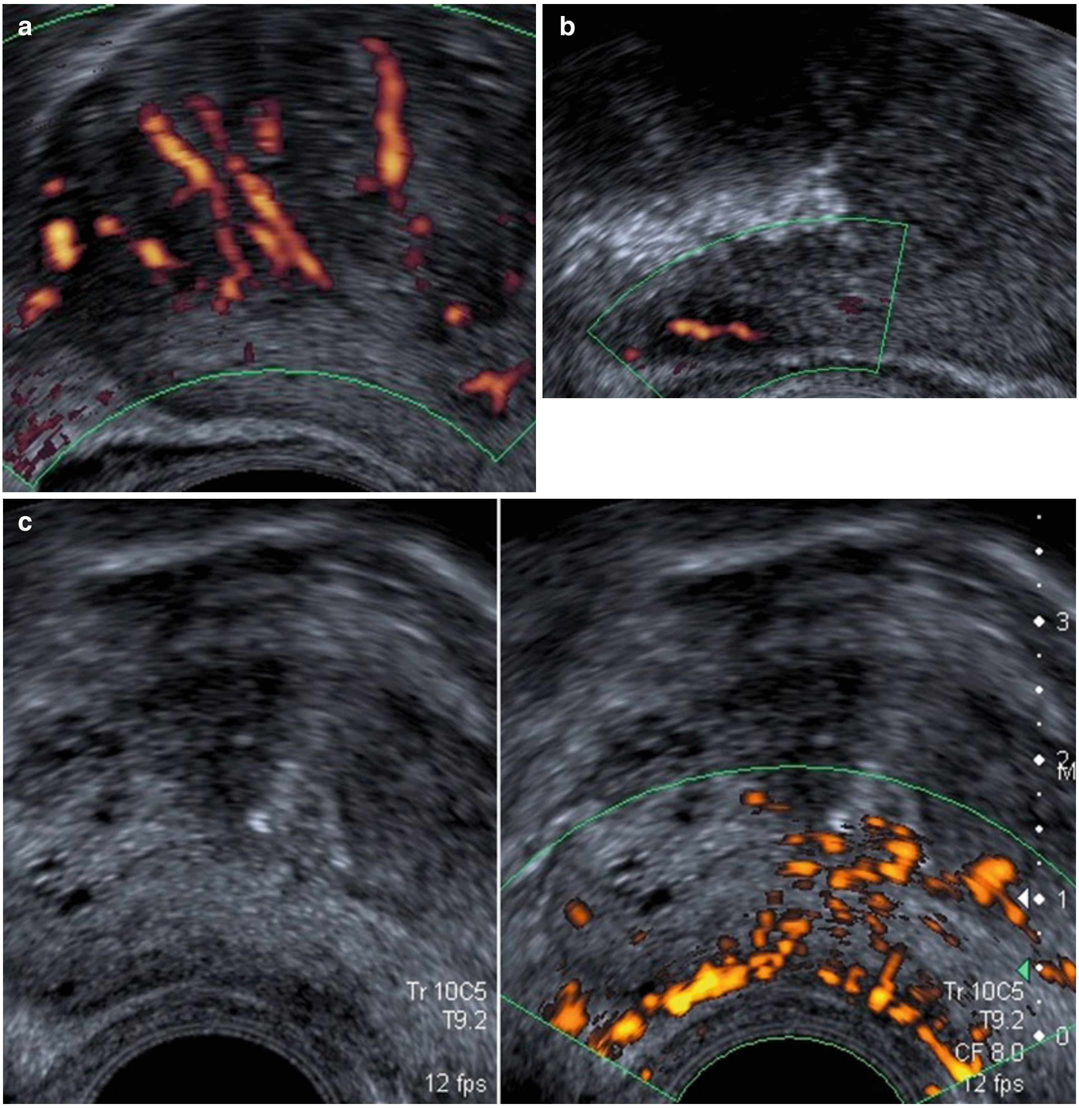

Fig. 5.9 Class 4. Non-palpable hypoechogenic and hypervascular lesions: (**a**) PSA 4.5 ng/ml, Gleason score 7 (4+3), one positive biopsy. (**b**) PSA 7.4 ng/ml, Gleason score 6 (3+3), two positive biopsies included on invaded greater than 50 %. (**c**) PSA: 6.2 ng/ml, Gleason score 6 (3+3): three positive biopsies

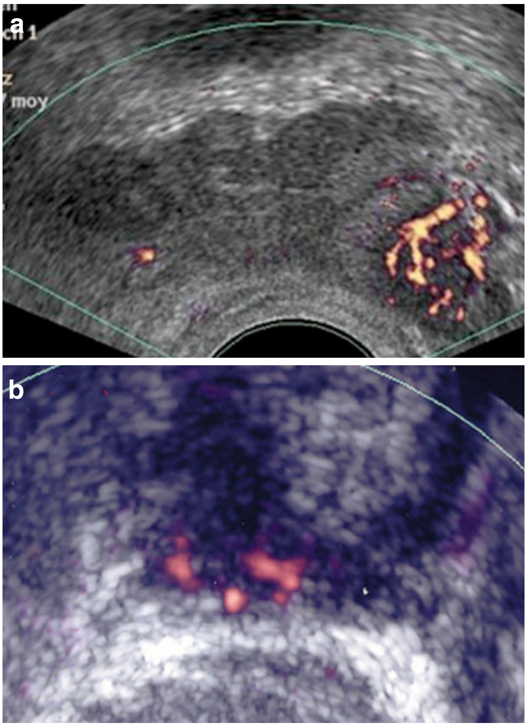

Fig. 5.10 (**a**) PCa in the left base. (**b**) Apical prostate cancer

5.6 PDS and Biopsy Decision

Areas with pathological PDS findings may be targeted for biopsy with increased positive biopsy rates compared to blinded sextant biopsies. It is controversial as to whether targeted biopsies using color or power Doppler alone can replace sextant biopsies.

Transrectal biopsy with PDS must be realized in the state of art: a team including urologic surgeons and trained radiologists must perform the biopsy samples with an ultrasound machine up to date (Fig. 5.15a, b).

Acute prostatitis (Fig. 5.16) is the main complication of prostatic biopsies (PB) and sometimes requires hospitalization and appropriate antibiotic therapy (Stoica et al. 2007) with incidence of 2–6 %.

Other complications can be also discussed: Hara et al. in their study (Hara et al. 2001) suggest that prostate biopsy might scatter prostate cells in the bloodstream especially in cases with high PSA and thus might contribute to tumor spreading in the cases of prostate cancer. However, further investigations are needed, and no studies can give a definitive response to this question. In 2008, the Diagnostic Center for Disease™ (Sarasota, Florida) identified a previously underestimated risk that routine prostate biopsy performed to evaluate for prostate cancer spreads cancer cells (Fig. 5.17) and may be the reason that men have a recurrence of disease many years after the prostate was removed successfully with clear surgical margins.

Also, it is probably legitimate to delay biopsies when an indolent lesion is suspected. In our last study (Sauvain et al. 2013), we concluded that the patients with a PSA level not exceeding 10 ng/ml, a normal clinical examination and a normal PDS had less than a 5 % risk of having a high-risk cancer.

The protocol with systematic extended number of biopsies must be discussed when clinical examination and PDS are pathological and a single target biopsy sufficient for the diagnosis.

5.7 Power Doppler of Prostatic Inflammatory Disease

Prostatitis can complicate transrectal biopsy. There are several etiologies of prostatitis, ranging from bacterial to nonbacterial causes. In the case of bacterial prostatitis, the offending organism is usually *Escherichia coli* or other urinary tract pathogens. Grayscale findings of acute prostatitis include a hypoechoic rim around the prostate or periurethral areas and low-level echogenic areas within the prostate. Power Doppler is useful in cases of diffuse bacterial prostatitis. The severity of the inflammatory reaction is mirrored by focal or

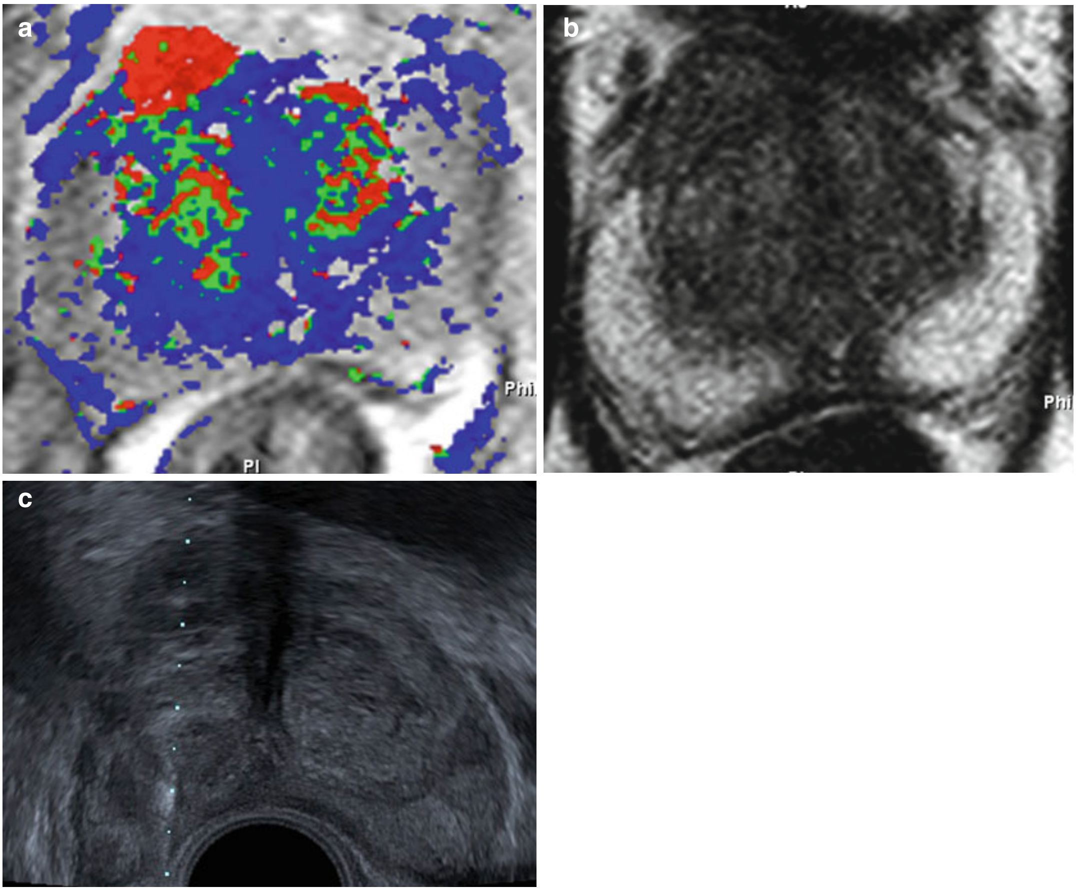

Fig. 5.11 (**a**–**c**) Patient with normal digital rectal examination and a PSA level of 16 ng/ml who underwent 12 initial negative randomized biopsies. No lesion in the peripheral prostate. After MRI, 1 positive echo-guided biopsy (Gleason score 8) in the anterior stroma

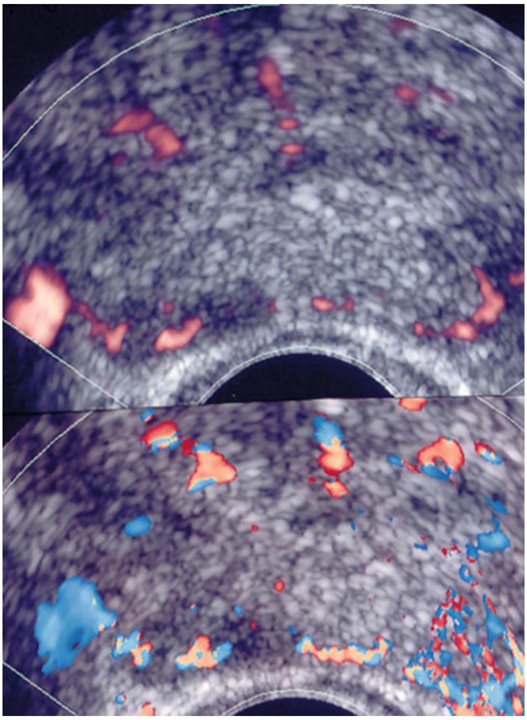

Fig. 5.12 Type A – Perfusion of prostatic posterior margin was absent, effaced by the tumor mass effect. A regular, hypoechogenic margin with a thickness of between 1 and 2 mm was found behind the most peripheral detectable vessel

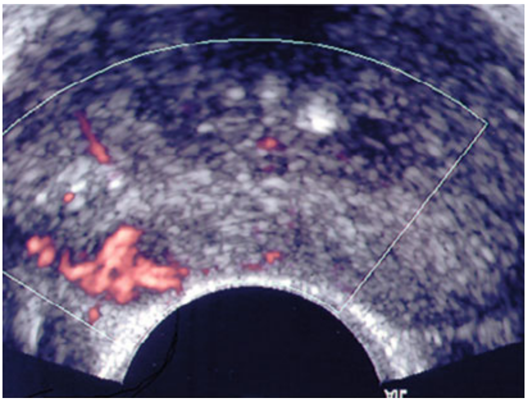

Fig. 5.13 Type B – The perfusion in posterior margin is also absent, but the margin was irregular and exhibits localized thinning

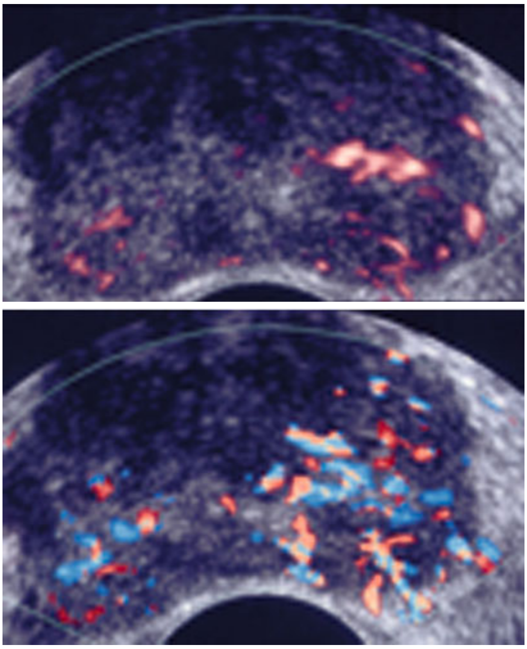

Fig. 5.14 Type C – The posterior peripheral margin was absent in places, and the vessels having tumoral origin left the prostate gland to create direct anastomoses with the periprostatic vessels

Table 5.1 Selection criteria for evolving low-risk prostate cancers according to D'Amico and Dall'Era

D'Amico et al. (1998)	PSA level < 10 ng/ml
	No grade 4 or 5
	Clinical stage not exceeding T2a
Dall'Era et al. (2008) (criteria most often used)	Clinical stage not exceeding T2a
	No grade 4 or 5
	PSA level < 10 ng/ml
	Kinetics of the PSA level stable
	<33 % positive biopsies
	<50 % cancer by biopsy

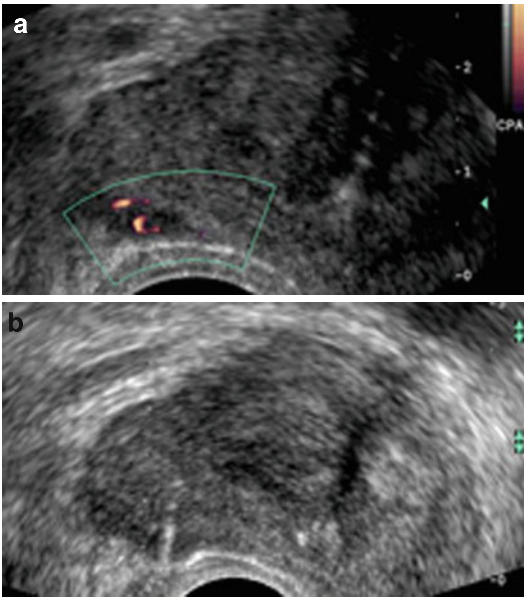

Fig. 5.15 Patient with normal digital rectal examination and et PSA level of 11 ng/ml who underwent 12 initial negative randomized biopsies. Pathologic hypervascularization on power Doppler is present (**a**). One positive echoguided biopsy (Gleason score 7) (**b**)

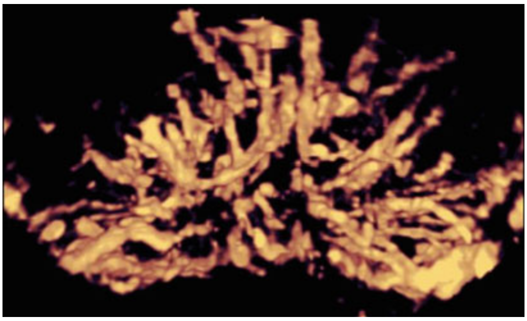

Fig. 5.16 Prostatitis – Color Doppler image of diffuse prostatitis demonstrates grossly increased flow throughout the gland. Vessels are more numerous and thicker with localized secondary division and hypertrophied intracapsular vessels. PDS signs decrease after appropriate antibiotic therapy

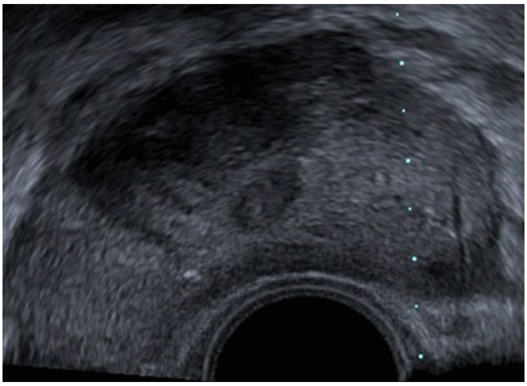

Fig. 5.17 After biopsy, a hole through capsule and parenchyma is visible on the left side in which blood cells and tumor cells can pass in the main blood circulation

diffuse increase in the color signal in the prostatic parenchyma. When focally increased color signals are seen in cases of prostatitis, there is no reliable noninvasive method to differentiate inflammation from tumor. However, cases of grossly increased flow spread diffusely throughout the gland should be considered prostatitis in the appropriate clinical setting. When the inflammatory process continues to suppurate, a prostatic abscess can develop. On ultrasound, this is seen as a cavity filled with low-level echoes from debris. Power Doppler may detect increased flow around the rim of the cavity.

Conclusions

Sonography coupled with the Doppler examination remains an examination that is easily accessible and cheap. Its performance may be improved by the rules of good practice that still have to be determined.

Power Doppler and three-dimensional vascular imaging improve the accuracy of echographic imaging in the diagnosis of significant cancer. In patients suspected with cancer with serum PSA level range 4–10 ng/ml combining a first set of sextant biopsies and targeted areas presenting abnormal blood flow, the use of PDS can increase in cancer detection with an optimized number of biopsy cores.

Power Doppler and three-dimensional vascular imaging contribute also to evaluate the risk of extracapsular involvement by the presence of vessels perforating the capsule. On the other hand, a mass effect exerted by a hypo- or hypervascular lesion on a regular peripheral margin where no blood flow is found behind this lesion can suggest a localized intraprostatic cancer.

Power Doppler sonography could have a great interest in the detection of low-risk prostate cancers. About 30 % of all cancers diagnosed are T1c cancers where the PSA level does not exceed 10 ng/ml and suspicious areas are not visible in the PDS. In our recent published study, 89 % of these cancers involved a low risk of biological recurrence, and 86 % of the cases could benefit from active surveillance according to the Dall'Era criteria after the biopsies. Patients with a PSA level not exceeding 10 ng/ml without a DRE anomaly and with a negative PDS (35 % of the subjects tested of our study) had less than a 5 % risk of having a high-risk cancer. In these patients, the biopsies probably could be differed and carried out on the basis of arguments other than only the initial assay of the PSA level in order to limit the number of useless biopsies and reduce the risks of overdiagnosis.

References

Aarninck RG, Beerlage HP, De La Rosette JJ, Debruyne FM, Wijkstra A. Transrectal ultrasound of the prostate: innovations and future applications. J Urol. 1998;159:1568–79.

Albertsen PC, Hanley JA, Fine J. 20-year outcomes following conservative management of clinically localized prostate cancer. JAMA. 2005;293:2095–101.

Bree RL. The role of color Doppler and staging biopsies in prostate cancer detection. Urology. 1997;49:31–4.

Cornud F, Belin X, Piron D, Chrétien Y, Flam T, Casanova JM, et al. Color Doppler-guided prostate biopsies in 591 patients with an elevated serum PSA level: impact on Gleason score for nonpalpable lesions. Urology. 1997;49(5):709–15.

Cornud F, Hamida K, Flam T, Hélénon O, Chrétien Y, Thiounn N, et al. Endorectal color doppler sonography and endorectal MR imaging features of nonpalpable prostate cancer: correlation with radical prostatectomy findings. AJR Am J Roentgenol. 2000;175(4):1161–8.

D'Amico AV, Whittington R, Malkowicz SB, Schultz D, Blank K, Broderick GA. Biochemical outcome after radical prostatectomy, external beam radiation therapy, or interstitial radiation therapy for clinically localized prostate cancer. JAMA. 1998;280:969–74.

D'Amico AV, Chen MH, Roehl KA, Catalona WJ. Preoperative PSA velocity and the risk of death from prostate cancer after radical prostatectomy. N Engl J Med. 2004;351:125–35.

Dall'Era MA, Konety BR, Cowan JE, Shinohara K, Stauf F, Cooperberg MR, et al. Active surveillance for the management of prostate cancer in a contemporary cohort. Cancer. 2008;112(12):2664–70.

Halpern EJ, Strup SE. Using gray-scale and color and power Doppler sonography to detect prostatic cancer. AJR. 2000;174:623–7.

Hara N, Kasahara T, Kawasaki T, Bilim V, Tomita Y, Obara K, Takahachi K. Frequency of PSA-mRNA-bearing cells in the peripheral blood of patients after prostate biopsy. Br J Cancer. 2001;85(4):557–62.

Kelly I, Lees W, Rickards D. Prostate cancer and the role of color Doppler US. Radiology. 1993;189:153–6.

Kuligowska E, Barish MA, Fenlon HM, Blake MA. Predictors of prostate carcinoma: accuracy of gray-scale and color Doppler US and serum markers. Radiology. 2001;220:757–64.

Lavoipierre AM, Snow RM, Frydenberg M, Gunter D, Reisner G, Royce PL, Lavoipierre GL. Prostatic cancer: role of color Doppler imaging in transrectal sonography. AJR. 1998;171(1):205–10.

Neal DE, Donovan JL. Prostate cancer: to screen or not to screen? Lancet Oncol. 2000;1(1):17–24.

Newmann JS, Bree RL, Rubin JM. Prostate cancer: diagnosis with color Doppler sonography with histological correlation of each biopsy site. Radiology. 1995; 195(1):86–90.

Resnick NI, Willard JW, Boyce WH. Ultrasonic evaluation of the prostatic nodule. J Urol. 1981;120:86–9.

Rifkin M, Sudakoff G, Alexander A. Prostate: techniques, results and potential applications of color Doppler US scanning. Radiology. 1993;186:509–13.

Sauvain JL, Palascak P, Bremon JM. Power Doppler ultrasonography and hypoechoic nodules of peripheral prostate: prospective and limitations. J Radiol. 1997;78:491–7.

Sauvain JL, Palascak P, Bourscheid D, Chabi C, Atassi A, Bremon JM, et al. Value of power doppler and 3D vascular sonography as a method for diagnosis and staging of prostate cancer. Eur Urol. 2003;44(1): 21–30.

Sauvain JL, Palascak P, Nader N, Gomez W, Bloqueau P, Bremon JM, et al. Echo-Doppler et cancer de la prostate: option ou nécessité? J Radiol. 2006;87(9): 1063–72.

Sauvain JL, Sauvain E, Rohmer P, Louis D, Nader N, Papavero R, Bremon JM, Jehl J. Value of transrectal power Doppler sonography in the detection of low-risk prostate cancers. Diagnostic and Interventional Imaging. 2013;94:60–7.

Stoica G, Cariou G, Colau A, Cortesse A, Hoffmann P, Schaetz A, Sellam R. Epidemiology and treatment of acute prostatitis after prostatic biopsy. Prog Urol. 2007;17(5):960–3.

Doppler Histogram Vessel Density Analysis

6

Robert L. Bard

6.1 Three-Dimensional Sonography and Power Doppler Angiography

Sonographic and 3-D Doppler examinations are performed with patients in the left lateral decubitus position. A system equipped with a multifrequency transrectal probe (10–18 MHz) is used as instructed by the manufacturer. Full-field B mode and color Doppler exploration of the prostate are initially carried out. Maximum prostate volume is measured in the midsagittal plane and 90° perpendicular interfaces. A power Doppler window is placed over the prostate. The same power Doppler characteristics have been applied in all our examinations: normal color quality, color gain of −3.4, a pulse repetition frequency of 600 Hz, and a wall motion filter of 50 Hz. The pulsed Doppler sample volume is moved over the most intense color signals to obtain the artery flow velocity waves. It is important to verify the color flow with spectral waveform analysis to ensure that the color-coded signal is not artifactual as is commonly noted with intraprostatic calculi (Figs. 6.1 and 6.2). The resistive index (RI) is calculated automatically (RI = systolic velocity – diastolic velocity/systolic velocity), with the lowest value taken as representative.

A sweeping angle of 195° (commercial units have sweep angles from 120 to 195°) allows for the greatest visual display permitting pathology not well imaged in one plane to be better depicted in other simultaneous planes.

6.2 Technique of Volume Analysis

The acquisition box of the 3D volume is placed over the power Doppler window. With the patient asked to remain as still as possible, volume acquisition is made during an interval varying from 5 to 20 s. Volume acquisition may be repeated if flash-type artifacts due to patient motion, respiratory, or intestinal movements appear on the screen. VOCAL can be computed on the ultrasound unit touch screen or the volumes stored and evaluated later in a personal computer or dedicated workstation to manipulate the data after the patient has left. With the VOCAL program, the abnormal area is evaluated manually in the transverse or coronal plane. By a rotational technique with a 6°, 9°, 15°, or 30° step, 12–30 slices are obtained to outline a volume. A 9° rotation is commonly used because it has previously been shown to have the best reproducibility for the 3D power Doppler indices (Bard 2013).

An initial volume is obtained, and the sonographer is queried if the data is accurate. If the region of interest is correct, the VOCAL program automatically calculates the three 3D power Doppler

---

R.L. Bard, MD
Bard Cancer Center, Biofoundation for Angiogenesis
Research and Development, 121 E. 60th St,
New York, NY 10022, USA
e-mail: rbard@cancerscan.com

R.L. Bard et al. (eds.), *Image Guided Prostate Cancer Treatments*,
DOI 10.1007/978-3-642-40429-0_6, © Springer-Verlag Berlin Heidelberg 2014

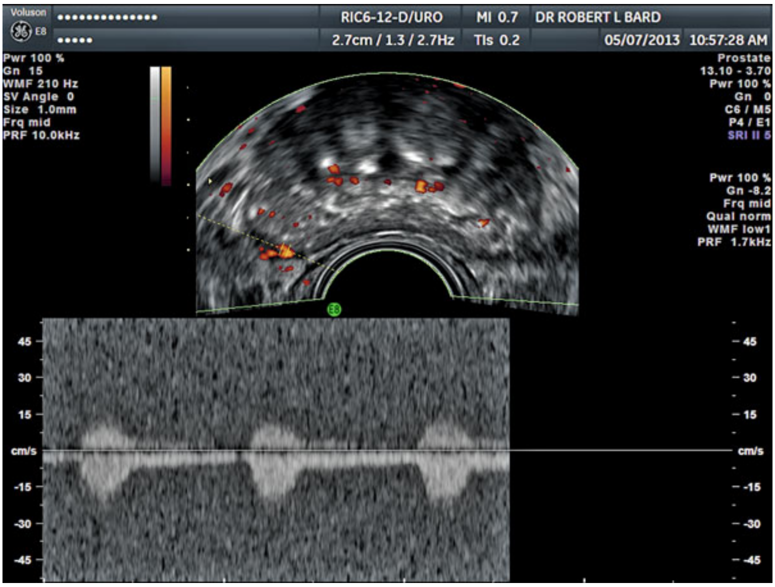

Fig. 6.1 Spectral waveform analysis with pulsed wave Doppler

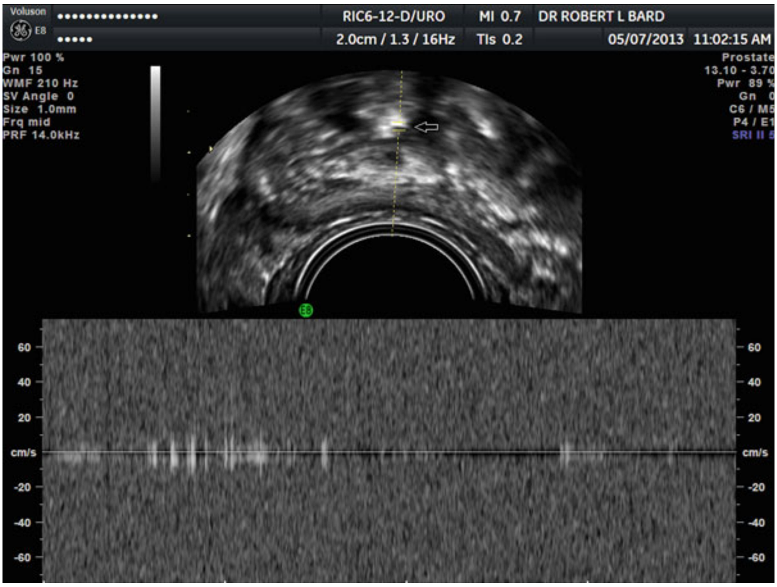

Fig. 6.2 Calculi creating color artifact-absent arterial or venous waveforms

indices: Vascular index (VI), flow index (FI), and vascular flow index (VFI). The VI measures the number of color voxels in the volume, representing the vessels in the tissue, and is expressed as a percentage. The FI is the mean color value in the color voxels, indicating the average intensity of blood flow, and is expressed as a number from 0 to 100. The VFI is the mean color value in all the voxels in the volume; therefore, it represents a composite of both the vascularization and the blood flow. It is also expressed as a number from 0 to 100 (Figs. 6.3 and 6.4).

6.3 Interpretation of Histogram Analysis

Differences between 3D power Doppler indices and the RI according to the tumor stage, the histologic grade, capsular disruption, and lymph node

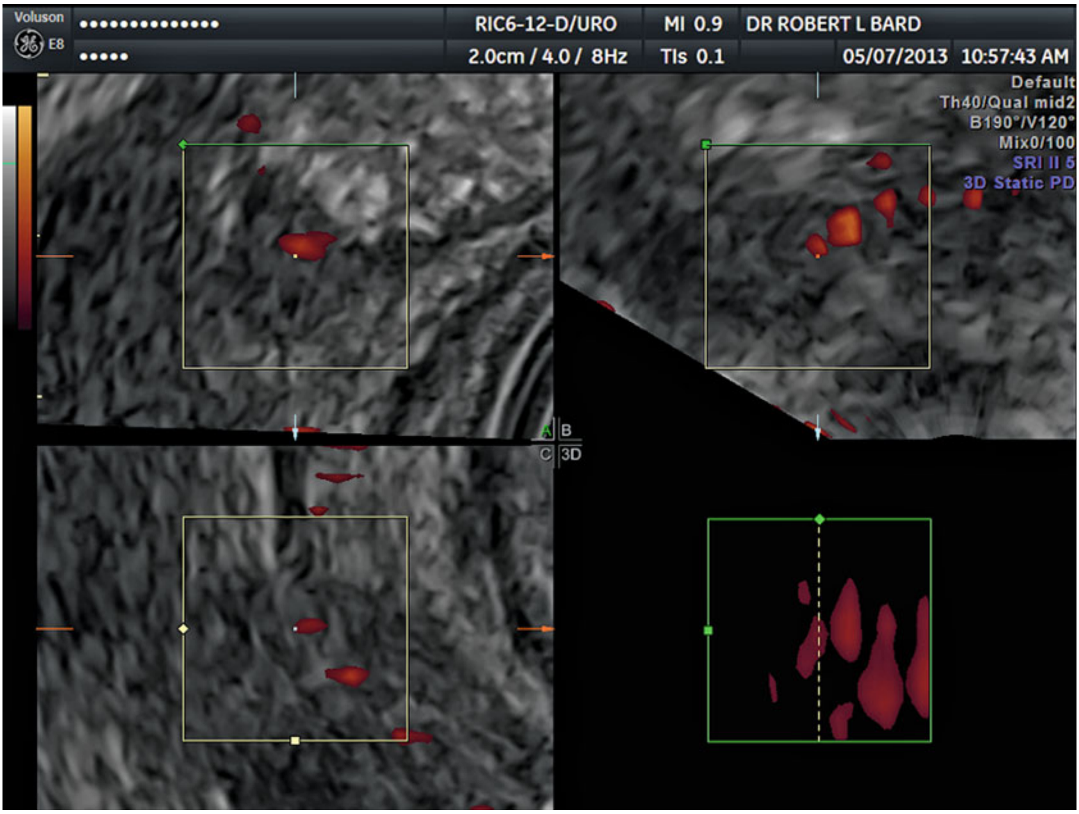

Fig. 6.3 Review of tumor flow region before VOCAL analysis

metastases are also evaluated. Histologic grade has been studied with this technology, and the following approximation has proven useful: low-grade tumor (Gleason 3+2, 3+3) has VI <5 %, medium-grade cancer (Gleason 3+4) has VI 5–9 %, and high-grade malignancies (Gleason 4+4, 4+5, 5+5) have VI >9 %. This does not exactly correlate with histologic Gleason grading since this is a current functional measure, while the microscopy is purely anatomical and may not represent current aggressive potential (Figs. 6.5 and 6.6).

Studies of the other indices are underway. Increased color Doppler mapping is also significantly associated with cancer. Nevertheless, color Doppler mapping shows some technique limitations that decrease its reliability. The power Doppler technique is based on the Doppler signal amplitude instead of the Doppler frequency. For this reason, it has high sensitivity for depicting blood flow with very low velocities. Moreover, a power Doppler image is independent of the insonation angle and does not show aliasing.

All these characteristics permit better visualization of irregular vessels. With this advantageous technology, some authors have shown that power Doppler mapping can discriminate between hyperplasia and carcinoma (Mitterberger et al. 2007). There is good correlation between intratumoral blood flow and the histologic grade. The results of this study show that the intratumoral RI can predict the histologic grade, capsule invasion, and lymph node metastases (Bard 2011).

6.4 Tumor Volume VOCAL Reconstruction

Three-dimensional sonography can assess the tumor volume (TV) by using the VOCAL program, which applies a rotational method. This software can quantify the number and intensity of

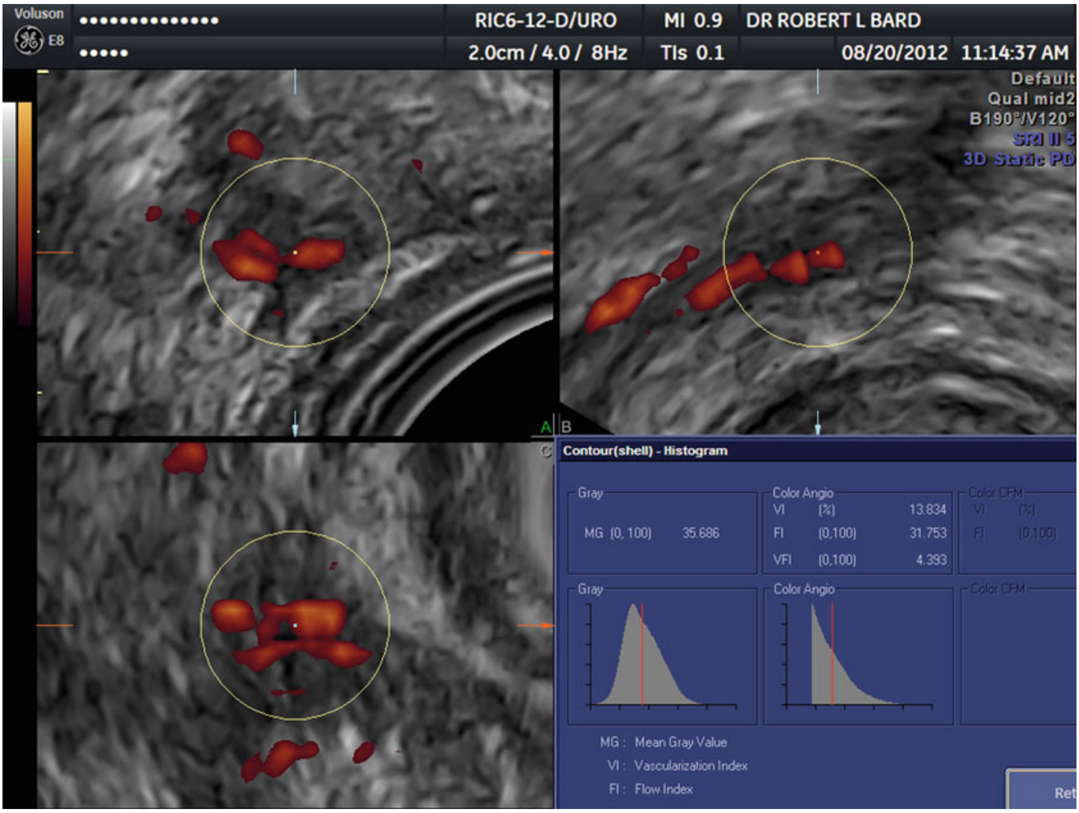

Contour(shell) - Histogram

Gray: MG (0, 100) 35.686

Color Angio: VI (%) 13.834; FI (0,100) 31.753; VFI (0,100) 4.393

Color CFM: VI (%); FI (0,100)

MG : Mean Gray Value
VI : Vascularization Index
FI : Flow Index

Fig. 6.4 VOCAL histogram showing VI = 13.8 % indicating high-grade tumor

power Doppler voxels and relate them to the grayscale B-mode voxels of the TV.

Our results showed that the TV and 3D power Doppler indices were significantly increased, and the intratumoral RI was decreased, in carcinoma when compared with benign hyperplasia. The ROC curves showed an area under the curve with a 95 % confidence interval lower limit of greater than 50 for all variables (Fig. 6.7a, b).

Tumor recurrence is better assessed when the vascular index increases significantly as compared to the previously treated volume of disease (Figs. 6.8a, b and 6.9a–c).

To assess tumors in the anterior prostate or central zone in enlarged glands, the focal plane is advanced to a more distal location, and VOCAL reconstruction proceeds with the volume box adjusted to the new position (Fig. 6.10a).

This is useful in pre-biopsy planning since a large tumor may be mostly low grade with a focus or several foci of high-grade regions. If the more aggressive tumor is anteriorly located, it may be out of range of the standard core biopsy needle length of 11 mm (Obek 2012). It is important to target the most vascular area for optimal tumor grading (Fig. 6.11a, b).

In conclusion, 3D sonography and power Doppler angiography are techniques that contribute new morphologic parameters and noninvasive functional tumoral angiogenic markers for

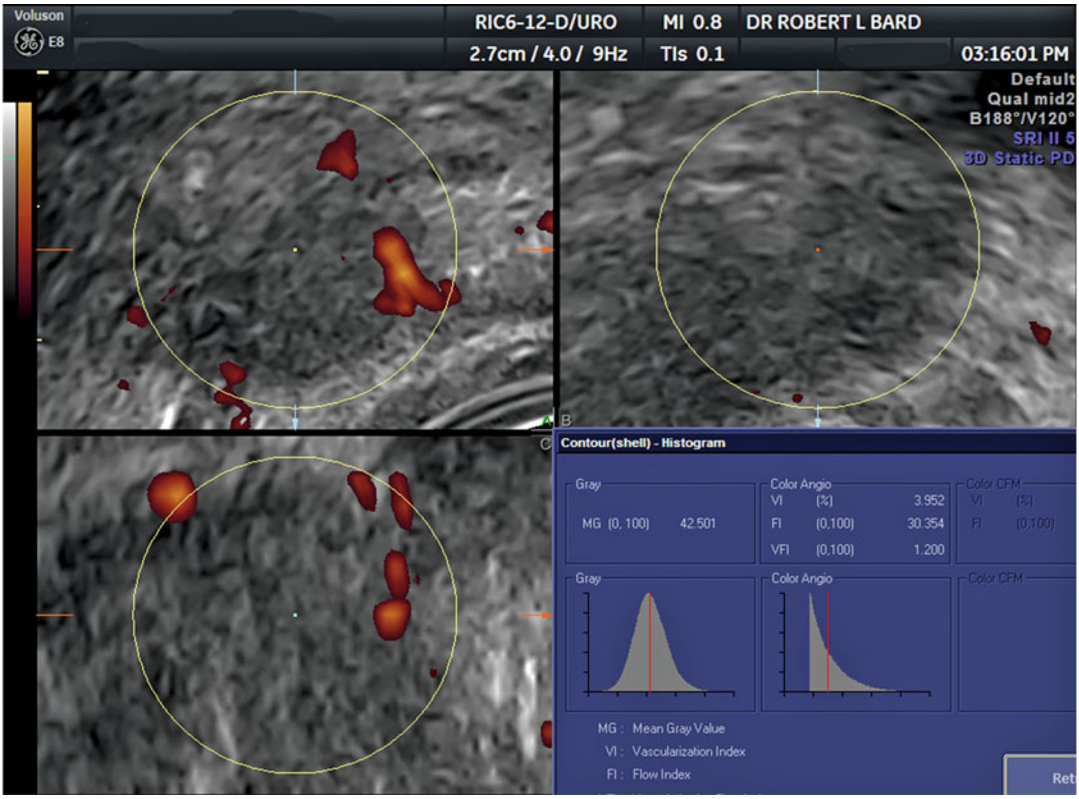

Gray
MG (0, 100) 42.501

Color Angio
VI (%) 3.952
FI (0,100) 30.354
VFI (0,100) 1.200

Color CFM
VI (%)
FI (0,100)

MG : Mean Gray Value
VI : Vascularization Index
FI : Flow Index

Fig. 6.5 Prostate cancer Gleason 3 + 4 VI = 3.9 %

evaluation and treatment follow-up of hyperplastic diseases and prostate cancers. 3D PDS has been proven to be of value in identifying extraprostatic tumor extension (Zalesky 2008). It is clinically useful in the detection and grading of breast cancer (Bard 2012a) and endometrial carcinoma (Merce et al. 2007). Density analysis of malignant melanoma serves as a guide to biopsy of a skin lesion, treatment in transit lesions by image-guided technologies, and follow-up of metastatic foci at later intervals (Bard 2012b). It has been applied in the characterization of bladder tumors which are occasionally imaged during the course of a TRUS (Bard et al. 2010). Abnormal, disoriented, irregular vessels in prostate cancer are present in 69 % of cases with Gleason 7 or greater tumors (Sauvain et al. 2006). External beam radical radiotherapy remains the primary treatment for patients with locally advanced or high-grade tumors in the United States as is associated with a 5-year failure rate of 35 % with Gleason scores of 6 or higher (Sartor 2002). The biochemical failure (BF) rate predicting tumor recurrence is less reliable than thought and may be replaced by other functional parameters such as DCE-MRI and tumor vascular endothelial growth factor (VEGF) expression (Green et al. 2007). The addition of in vivo real-time volume density measurements of tumor neovascularity may prove to be of value in determining the risk of tumor recurrence noninvasively.

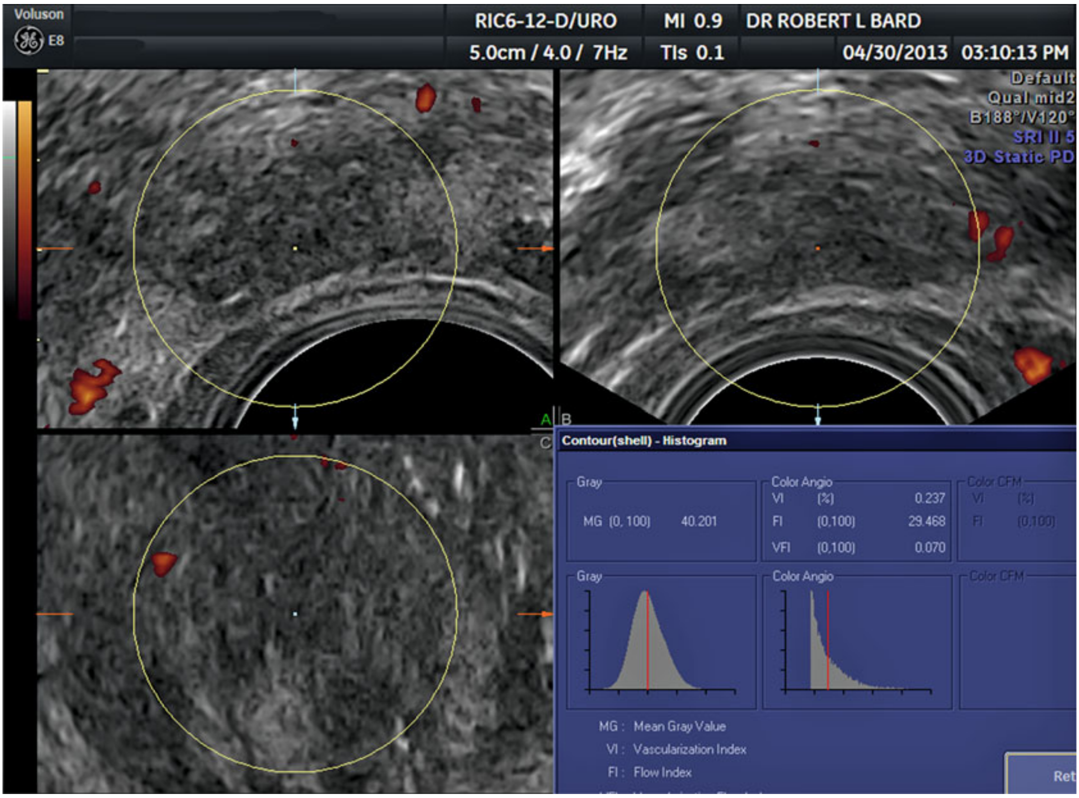

Gray
MG (0, 100) 40.201

Color Angio
VI (%) 0.237
FI (0,100) 29.468
VFI (0,100) 0.070

MG : Mean Gray Value
VI : Vascularization Index
FI : Flow Index

Fig. 6.6 Prostate cancer post-ablation VI = 0.2 %

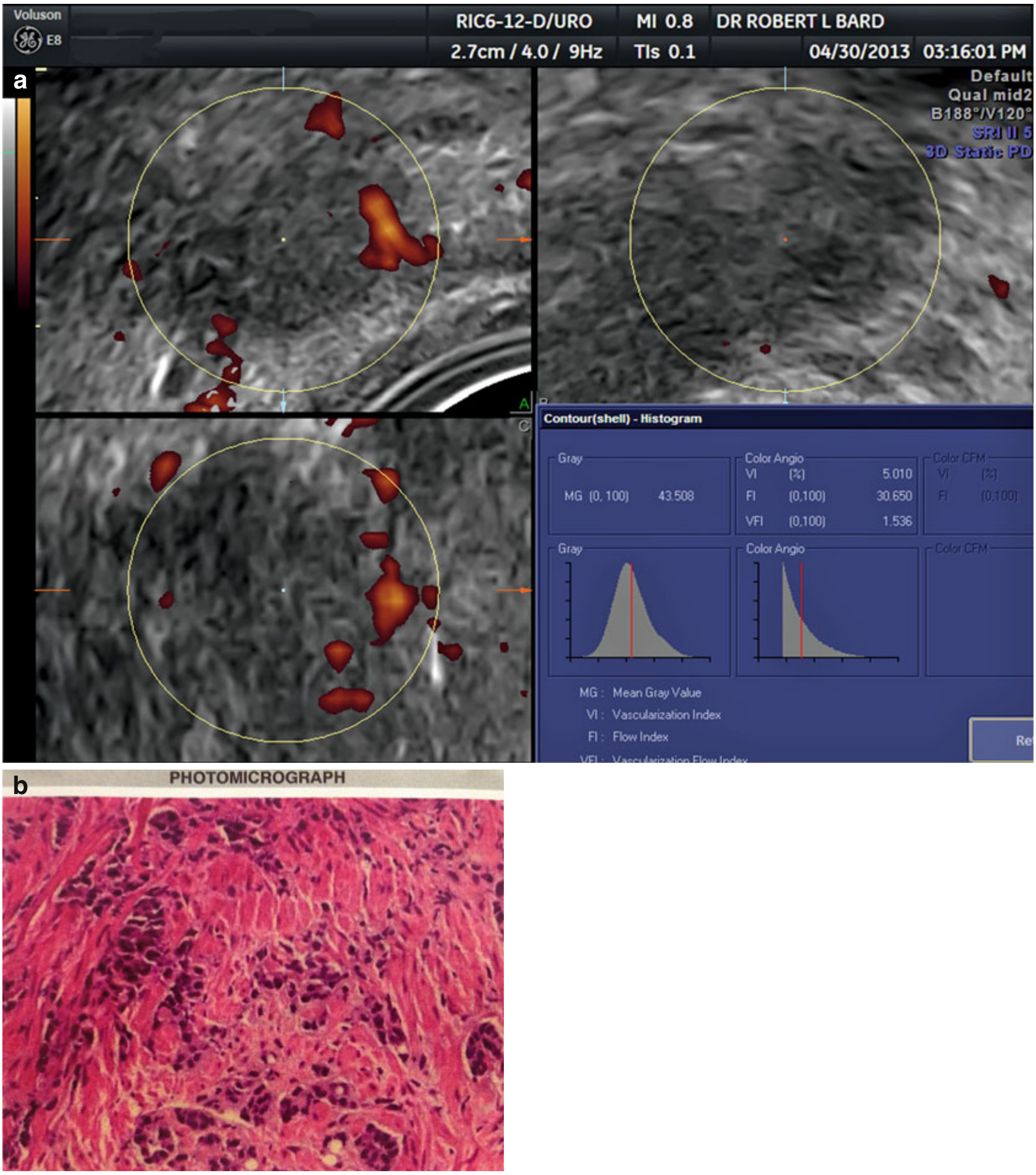

RIC6-12-D/URO MI 0.8 DR ROBERT L BARD
2.7cm / 4.0 / 9Hz TIs 0.1 04/30/2013 03:16:01 PM
Default
Qual mid2
B188°/V120°
SRI II 5
3D Static PD

Contour(shell) - Histogram

Gray
MG (0, 100) 43.508

Color Angio
VI (%) 5.010
FI (0,100) 30.650
VFI (0,100) 1.536

Color CFM
VI (%)
FI (0,100)

MG : Mean Gray Value
VI : Vascularization Index
FI : Flow Index
VFI : Vascularization Flow Index

Fig. 6.7 (**a**) Post-ablation follow-up with increased vessel density VI = 5 %. (**b**) Biopsy shows Gleason 4 + 4 disease corresponding to VI = 5 %

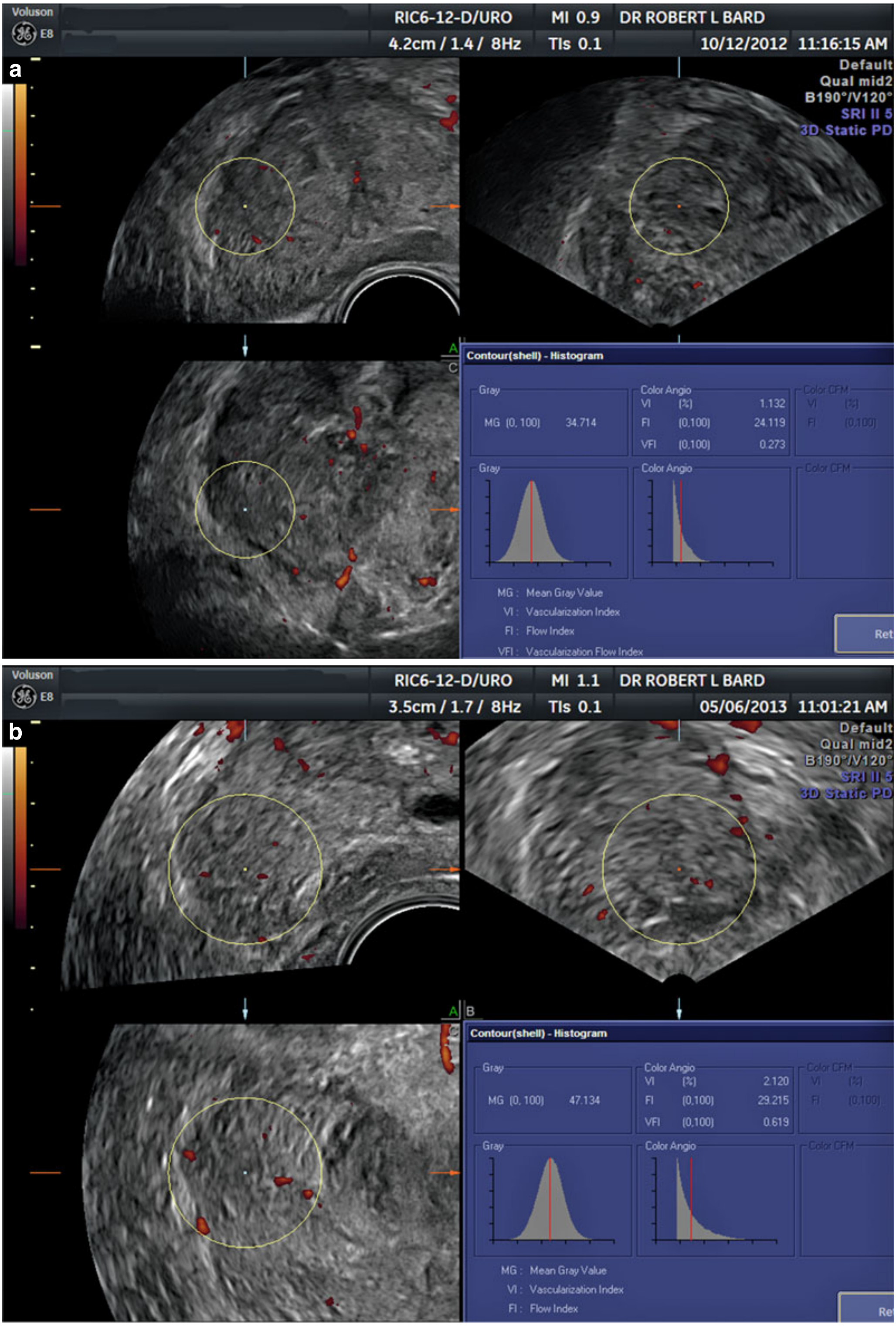

RIC6-12-D/URO MI 0.9 DR ROBERT L BARD
4.2cm / 1.4 / 8Hz TIs 0.1 10/12/2012 11:16:15 AM

Contour(shell) - Histogram
MG (0, 100) 34.714
VI (%) 1.132
FI (0,100) 24.119
VFI (0,100) 0.273
MG : Mean Gray Value
VI : Vascularization Index
FI : Flow Index
VFI : Vascularization Flow Index

RIC6-12-D/URO MI 1.1 DR ROBERT L BARD
3.5cm / 1.7 / 8Hz TIs 0.1 05/06/2013 11:01:21 AM

Contour(shell) - Histogram
MG (0, 100) 47.134
VI (%) 2.120
FI (0,100) 29.215
VFI (0,100) 0.619
MG : Mean Gray Value
VI : Vascularization Index
FI : Flow Index

Fig. 6.8 (**a**) Anterior Gleason 6 10–2012 VI = 1 %. (**b**) 7-month follow-up VI = 2 % (100 % doubling time)

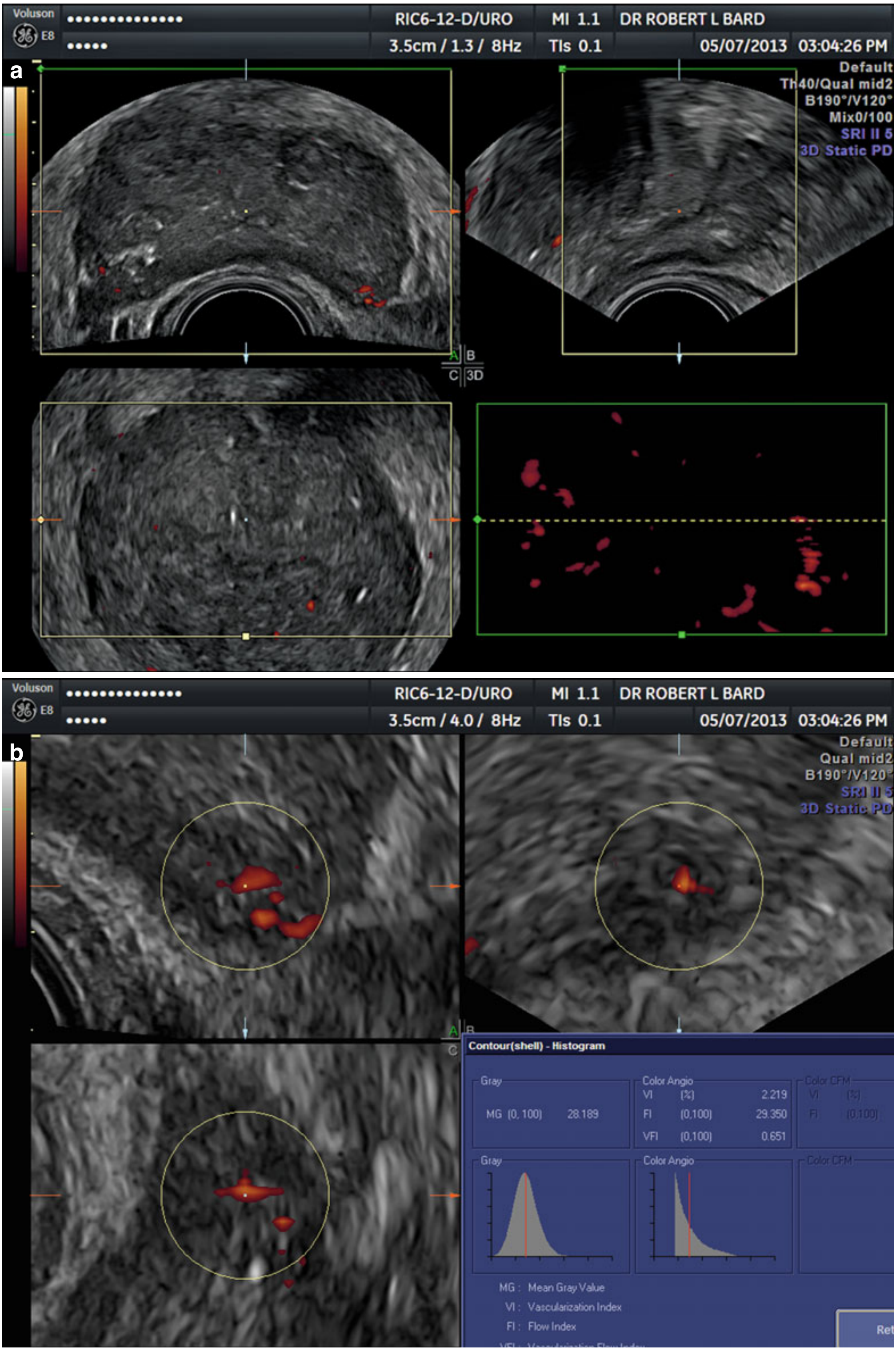

Gray
MG (0, 100) 28.189

Color Angio
VI (%) 2.219
FI (0,100) 29.350
VFI (0,100) 0.651

Color CFM
VI (%)
FI (0,100)

MG : Mean Gray Value
VI : Vascularization Index
FI : Flow Index

Fig. 6.9 (**a**) Postradiation treatment. Note loss of normal peripheral gland echoes. (**b**) Low-grade left recurrence. (**c**) Low-grade right recurrence with extracapsular disease

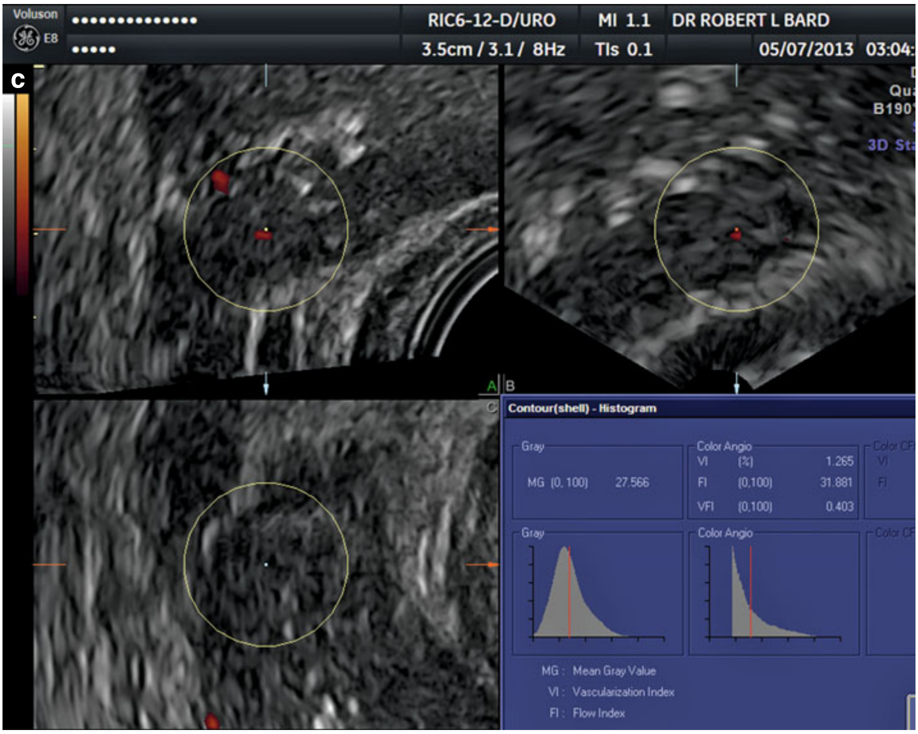

MG (0, 100) 27.566

VI (%) 1.265
FI (0,100) 31.881
VFI (0,100) 0.403

Fig. 6.9 (continued)

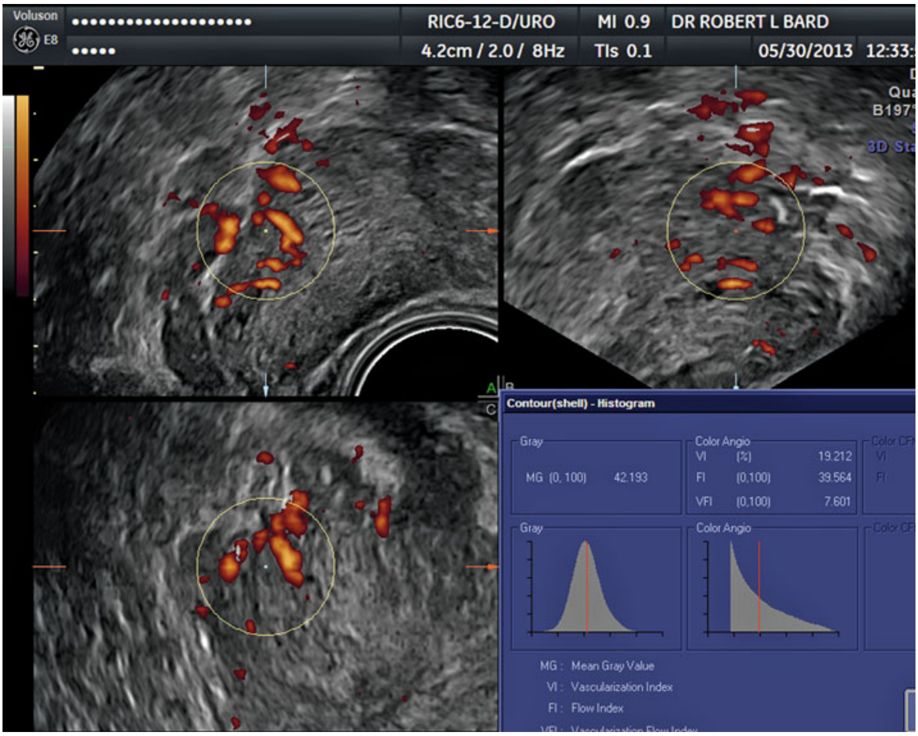

MG (0, 100) 42.193

VI (%) 19.212
FI (0,100) 39.564
VFI (0,100) 7.601

Fig. 6.10 Nonpalpable anterior Gleason 4+5 VI=19 %

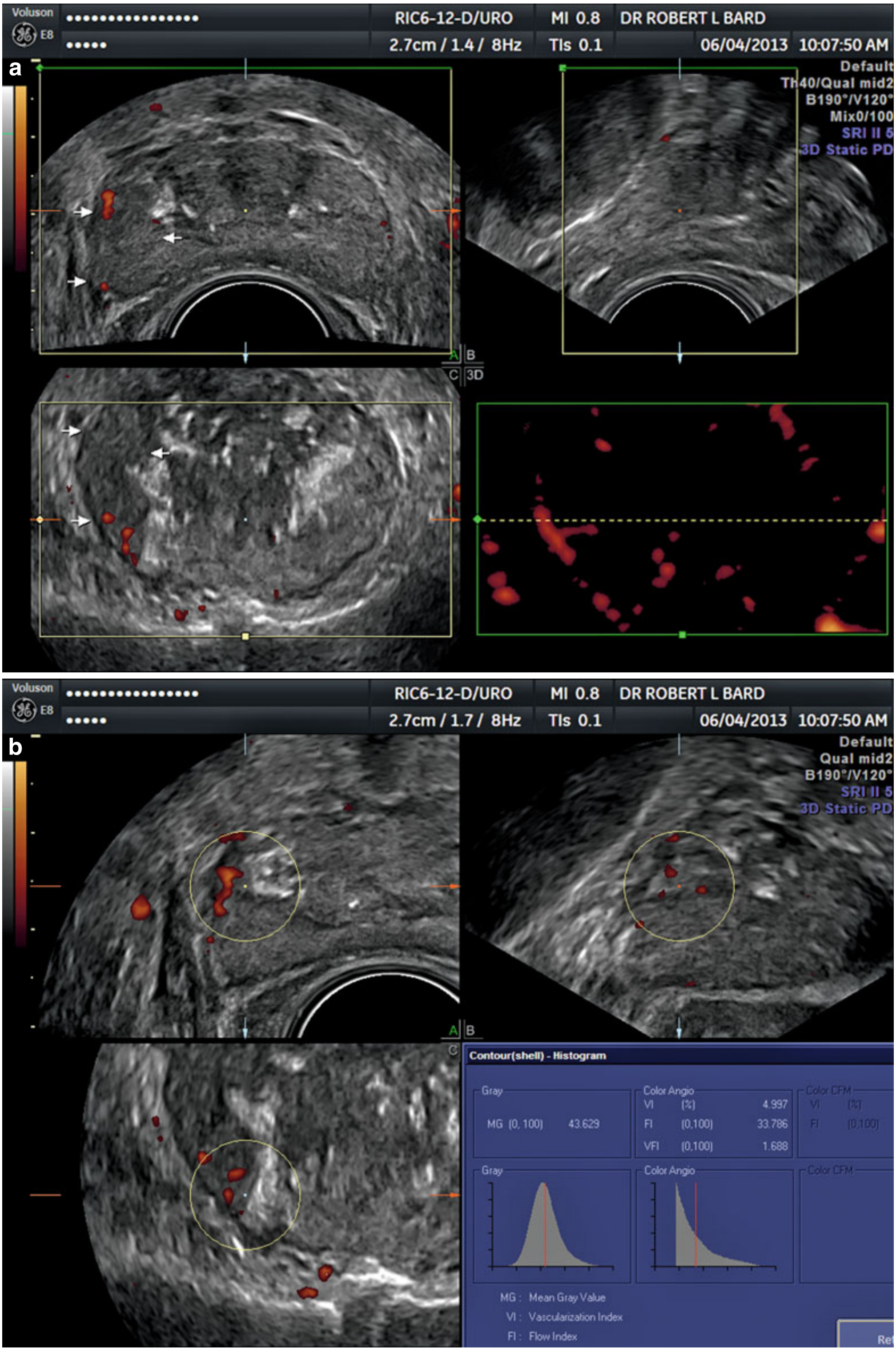

```
Contour(shell) - Histogram

Gray                      Color Angio                  Color CFM
                          VI    (%)         4.997      VI   (%)
MG (0, 100)   43.629      FI    (0,100)    33.786      FI   (0,100)
                          VFI   (0,100)     1.688

Gray                      Color Angio                  Color CFM

MG : Mean Gray Value
VI : Vascularization Index
FI : Flow Index
```

Fig. 6.11 (**a**) Low-grade tumor with focal high-grade region at 13 mm depth. (**b**) VI = 5 % High-grade region would be missed on standard biopsy needle throw of 11 mm

References

Bard R, Cantisani V, Barentsz J. Vascular imaging of bladder cancer. J Radiol. 2010;91(10):1479.

Bard R. Prostate cancer neovascular responses to antioxidant treatments. 59th Journees Francaises de Radiologie, Paris, 2011, p. 338.

Bard R. Vascular imaging of cancer in the dense breast. 60th Journees Francaises de Radiologie, Paris, 2012a, p. 416.

Bard R. Image guided cancer treatment. Advances in Medical and Surgical Dermatology, 15th Annual Mt Sinai Winter symposium, New York, 2012b.

Bard R. Prostate cancer 3-dimensional capsular erosion alert for bone metastases and lymphadenopathy evaluation. Annual Convention Am Inst Ultrasound Med NYC, New York, 2013, p. 134.

Green MM, Hiley CT, Shanks JH, et al. Expression of vascular endothelial growth factor in locally invasive prostate cancer is prognostic for radiotherapy outcome. Int J Radiat Oncol Biol Phys. 2007;67:84.

Merce L, Alcazar J, Lopez C, et al. Clinical usefulness of 3-dimensional sonography and power Doppler angiography for the diagnosis of endometrial carcinoma. J Ultrasound Med. 2007;26:1279.

Mitterberger M, Pingerra G, Horninger W, et al. Comparison of contrast enhanced ultrasound color targeted biopsy: impact on Gleason score. J Urol. 2007;178:464.

Obek C. Core needle biopsy length affects grading and staging. J Urol. 2012;187(6):2051.

Sartor O. Endpoints in prostate cancer clinical trials. Urology. 2002;60 (Suppl 1):101.

Sauvain JL, Palascak P, Nader N. Echo-Doppler et cancer de la prostate: option ou necessite? J Radiol. 2006;87:1063.

Zalesky M. Value of power Doppler sonography with 3D reconstruction in preoperative diagnostics of extraprostatic tumor extension in clinically localized prostate cancer. Int J Urol. 2008;15:68.

MR Imaging of the Prostate

7

Jurgen J. Fütterer

7.1 Introduction

The widespread use of prostate-specific antigen (PSA) as a screening test for prostate cancer resulted in earlier detection of high-grade prostate cancer at a curative stage. However, insignificant cancers are often detected which lead to overtreatment of low-risk disease (Krakowsky et al. 2010). The prevalence of prostate cancer increases with age; 34 % of men in the fifth decade of life and up to 70 % aged 80 years or older have histologic evidence of prostate cancer (Bonekamp et al. 2011).

In order to determine the treatment that optimally suits the individual patient, it is necessary to evaluate all patient and clinical characteristics. Most often, PSA level, the results of digital rectal examination, and transrectal ultrasound (TRUS)-guided biopsy findings (Gleason score) are used for this purpose. However, imaging plays an important role to detect, to localize, and to stage prostate cancer (Hoeks et al. 2011). This directly influences the diagnostic work-up and may lead to important changes in treatment strategy.

The clinical stage is identified using clinical variables (digital rectal examination, PSA, and Gleason score) and is expressed in the TNM staging classification. The Gleason score is a histopathological score that correlates with prostate cancer prognosis. In prostate cancer staging it is important to differentiate between T2 and T3 disease (intra- vs extracapsular disease). Curative therapy can be considered in cases of localized disease using radical prostatectomy or radical radiotherapy (i.e., external beam radiotherapy, low- or high-dose brachytherapy, and proton or electron beam therapy).

MR imaging plays an important role in the detection, localization, and staging of prostate cancer. Image-guided interventions and therapies are available permitting precise biopsies and targeted focal treatment.

7.1.1 MR Imaging

Although the introduction of MR scanners in the mid-1980s of the previous century resulted in initial moderate staging results due to lack of signal-to-noise ratio, the role of MR imaging was promising. The first publications were focused on characterization of the T2-weighted anatomical images (Hricak et al. 1987). Endorectal coils were introduced to improve the signal-to-noise ratio in the prostate (Schnall et al. 1989). Moderate local staging performance was found in the early 1990s (Tempany et al. 1994). Since the last 10 years, innovation in the MRI field resulted in improved prostate cancer detection, localization, and staging. Especially the introduction of 3 T MR scanners resulted in improved image quality (Bloch et al. 2004). The increase

---

J.J. Fütterer, MD, PhD
Department of Radiology, Radboud University
Nijmegen Medical Centre, 9101,
Nijmegen 6500 HB,
The Netherlands
e-mail: j.futterer@rad.umcn.nl

R.L. Bard et al. (eds.), *Image Guided Prostate Cancer Treatments*,
DOI 10.1007/978-3-642-40429-0_7, © Springer-Verlag Berlin Heidelberg 2014

signal-to-noise ratio obtained at 3 T compared to the 1.5 T scanners resulted in improved image quality. Many of the differences between imaging at 1.5 and 3 T are the direct result of MR physical properties related to magnetic field strength changes. The signal-to-noise ratio is approximately two times higher at 3 T compared to 1.5 T. Probably the most significant benefit is to decrease the acquisition time and/or increase the in-plane spatial resolution. The latter can be used to obtain enhanced anatomical details of the prostate. Potential drawbacks of clinical MR imaging at high field strengths are the shorter T2 and longer T1 relaxation times, increased susceptibility differences, dielectric effect, and the homogeneity of the magnetic field in the organ of interest. Increasing the spatial resolution at higher field could partially circumvent some of these issues.

7.2 MRI Technique

7.2.1 T1-Weighted MR Imaging

T1-weighted imaging has a limited role for prostate cancer detection. T1-weighted contrast in the prostate is very low. Therefore, the zonal anatomy cannot be discerned using T1-weighted MR imaging. The main usefulness of T1-weighted imaging is for the detection of TRUS-guided biopsy hemorrhage or artifacts. The latter can be a confounding factor on T2-weighted MR images (White et al. 1995).

7.2.2 Anatomic T2-Weighted MR Imaging

T2-weighted MR imaging is the most widely used MR sequence of prostate imaging. Anatomical T2-weighted MR imaging is the cornerstone for interpretation. The latter technique is helpful for zonal delineation and tumor detection. The prostate is divided in three zones, i.e., peripheral, central, and transition zone. High in-plane resolution T2-weighted fast or turbo spin echo sequences, performed with endorectal and/or external pelvic phased-array coils, are generally used to depict prostate anatomy (Hoeks et al. 2011). T2-weighted MR images have high spatial resolution and, thus, can clearly differentiate the normal intermediate- to high-signal-intensity peripheral zone from the low-signal-intensity central and transition zones in young male subjects (Hricak et al. 1983). The seminal vesicles demonstrated a high signal within the lumen. The seminal vesicle wall has a well-defined low-signal-intensity rim.

In the elderly male, owing to variable extension of the transition zone due to benign prostatic hyperplasia, the size and signal intensity of the prostate transition zone may vary. Benign nodular hyperplasia of the prostate gives rise to nodular adenomas in the transition zone, and with time these will compress the central zone which thus forms a pseudocapsule, thus occupying the complete central gland. The peripheral zone is almost never affected by BPH and will retain its own histological characteristics. Benign prostatic hyperplasia is a round or oval nodule with a well-defined low-signal-intensity rim (capsule-like). The nodule is inhomogeneous with (variable) intermediate signal intensity and a low-signal-intensity rim that surrounds the expanded transition zone (Hricak et al. 1983). The typical nodular appearance of BPH on T2-weighted imaging will help in discriminating benign prostatic hyperplasia from prostate cancer. Because of transition zone expansion, the remainder of the compressed central zone is often indefinable on MR images (Hoeks et al. 2011).

On T2-weighted images, prostate cancer can appear as an area of low-signal intensity within the high-signal intensity of a normal peripheral zone (Fig. 7.1). The degree of signal intensity on the T2-weighted MR image decrease may differ with the Gleason score (Wang et al. 2008). Higher Gleason score components 4 or 5 have shown lower signal intensities than do lower Gleason score components 2 or 3.

7.2.3 Diffusion-Weighted Imaging

Water molecules exhibit random motion in tissue, related to temperature (Brownian effect) (Lansberg et al. 2000). Diffusion-weighted MR imaging can

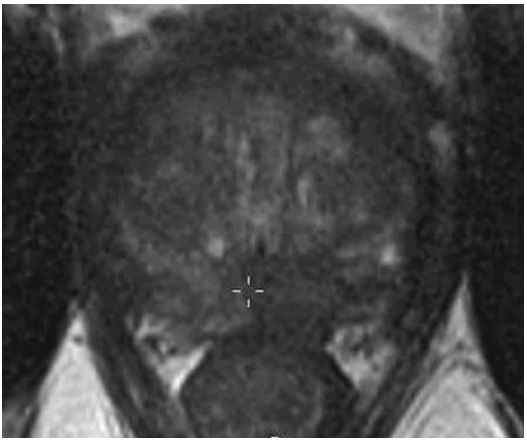

Fig. 7.1 T2-weighted MR imaging of prostate cancer. The image is obtained at the midprostate level. Lesion with low-signal intensity in the left peripheral zone with signs of extracapsular disease

quantify this water motion in an indirect manner (Stejskal and Tanner 1965). The DWI pulse sequence labels hydrogen nuclei in space, of which most will be part of water molecules at any moment, and determines the length of the path that water molecules travel over a short period of time. However, DWI is not able to determine the distance traveled by individual hydrogen nuclei, but is capable of estimating the mean distance traveled by all hydrogen nuclei in every voxel of imaged tissue. This quantification of proton diffusion properties in water is used to produce image contrast. Images that reflect proton diffusion are acquired by applying motion-encoding gradients, which cause phase shifts in moving protons, depending on the direction and quantity of their movement (Stejskal and Tanner 1965).

The greater the mean distance, the more self-diffusion of water molecules has taken place in a certain time interval (Bammer et al. 2005). The attenuation of the MR signal in DW imaging is expressed with the Stejskal–Tanner equation (Stejskal and Tanner 1965). The *b* value and the apparent diffusion coefficient (ADC) are components in this equation. In a volume of pure water, this self-diffusion is equal in all directions, hence isotropic, and not restricted by any barrier. As diffusion in tissue is limited by cellular structures, to establish a reliable estimate of this mean distance traveled by hydrogen nuclei, an ADC is acquired in at least three different orthogonal directions (Bammer et al. 2005; Basser 1995). This phenomenon of varying restriction of self-diffusion along different axes is called anisotropy and can also be used for tissue characterization, as in linear aligned tissue this anisotropy will be more pronounced as there will be one direction that contributes most to the ADC. While the *b* value expresses the amount of diffusion weighting, ADC reflects the movement of the water molecules within the interpulse time. Because ADC quantifies the flow as well as the distance a water molecule has moved, it represents both capillary perfusion and diffusion characteristics.

DWI has T2- and diffusion-weighted MR imaging characteristics. The signal intensity on the DWI represents a combination of signal on the $b=0$ image and the dephasing due to water motion in the presence of the diffusion gradients. At low *b* values, there is greater contribution from the $b=0$ image, and at higher *b* values, contrast is determined more by relative diffusion (Bammer 2003). DWI has to be obtained with at least two *b* values to correct for this T2-weighted effect in every diffusion-weighted sequence, which may be present in lesions with high T2 signal intensity. For differentiation between a lesion with a low ADC value and one that displays high T2 signal intensity, at least two *b* values have to be used and the images consequently subtracted, typically a low, $b=0$–50, and a high diffusion-weighted acquisition. For prostate cancer, *b* values between 500 and 800 s/mm^2 are typically used (Bonekamp et al. 2011). High *b* values, i.e., $\geq$1,000, may increase the accuracy of prostate cancer detection within the transition zone (Katahira et al. 2011). However, high *b* values are affected by lower signal-to-noise ratio. Image quality is dependent on gradient system and field strength. To minimize the influence of bulk motion as a distorting factor, typically a time to echo as short as possible is chosen for DWI sequences.

Healthy prostate tissue in the peripheral zone is rich in tubular structures. This will allow for abundant self-diffusion of water molecules in their contents and thus provides high ADC values (Fig. 7.2). Prostate cancer tissue destroys the normal glandular

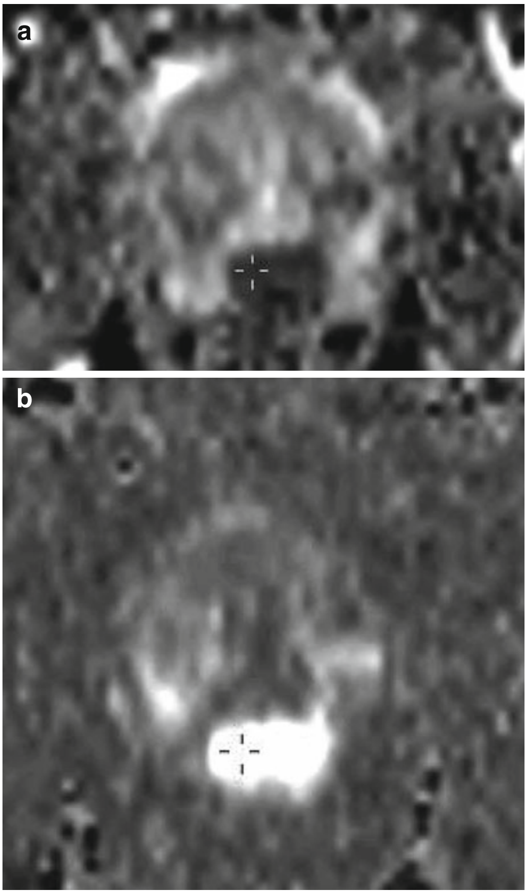

Fig. 7.2 DWI of prostate cancer. Axial ADC maps (3,200/78, $b=50$, and 800 s/mm^2) obtained at midprostate level in same patient as in Fig. 7.1. (**a**) Lesion with low ADC (mean ADC $=0.69\times10$–3 mm^2/s) is suspicious for cancer in left peripheral zone (*arrows*). This indicates intermediate to high cancer aggressiveness. (**b**) High *b* value MR image ($b=1{,}400$) shows an area of increased signal intensity

structure of the prostate and replaces ducts. It also has a higher cellular density than does healthy prostate peripheral zone tissue. In most cases, the peripheral zone can be easily discriminated from the transition zone on DWI, as it will display relative higher ADC values (Somford et al. 2008). On ADC maps, therefore, prostate cancer often shows lower ADCs in comparison to surrounding healthy peripheral zone prostate tissue (Kumar et al. 2007; Kim et al. 2007; Tamada et al. 2008).

BPH is defined by hyperplasia of all cells that constitute the transition zone, with glandular, muscular, and fibrous compartments more or less evenly involved. This nodular hyperplasia gives rise to inhomogeneous diffusion patterns, and as tubular structures often remain in place, the increased cellular density of hyperplasia, which is far less predominant than in prostate carcinoma, might explain the observed reduction in ADC levels of the central gland on DWI, due to decreased ratio of extracellular to intracellular volume. However, as BPH has inhomogeneous diffusion characteristics, an increase in ADC has been observed as well (Ren et al. 2008).

Chronic prostatitis is histopathological characterized by extracellular edema surrounding the involved prostatic cells with concomitant aggregation of lymphocytes, plasma cells, macrophages, and neutrophils in the prostatic stroma. This abundance in cells as compared to normal prostatic tissue may lead to a decreased ADC due to decreased extracellular to intracellular fluid volume ratio. Diffusion-weighted imaging is a noninvasive technique that shows differences between prostatitis and PCa in both the peripheral zone and central gland, although its usability in clinical practice is limited as a result of significant overlap in ADCs (Nagel et al. 2013).

7.2.4 DCE-MRI

For a tumor, one critical factor that affects development, growth, invasiveness, and progression into the metastatic form is the ability of the tumor to generate new blood vessels. Angiogenesis, the sprouting of new capillaries from existing blood vessels, and vasculogenesis, the de novo generation of new blood vessels, are the two primary methods of vascular expansion by which nutrient supply to tumor tissue is adjusted to match physiologic needs (Padhani et al. 2005). The importance of angiogenesis in prostate cancer is well established. A number of features are characteristic of malignant vasculature, many of which are amenable to study by DCE-MRI and DWI techniques. These include (a) spatial heterogeneity and chaotic structure; (b) poorly formed fragile vessels with high permeability to macromolecules due to the presence of large endothelial cell gaps, incomplete basement membrane, and relative lack of pericytes or smooth muscle association with endothelial cells; (c) arteriovenous shunting; (d) intermittent or unstable blood flow; and (e) extreme heterogeneity of vascular density, with areas of low vascular density mixed with regions of high angiogenic activity (Hambrock et al. 2006).

Dynamic contrast-enhanced MR imaging is a noninvasive method to probe tumor angiogenesis. Dynamic contrast-enhanced MR imaging consists of a series of fast T1-weighted sequences covering the entire prostate before and after rapid injection of a bolus of a low-molecular-weight gadolinium chelate. DCE-MRI following the administration of low-molecular-weight contrast media (<1 kDa) is the most common imaging method for evaluating human tumor vascular function in situ (Collins and Padhani 2004). Because the prostate as a whole is highly vascularized, a simple comparison of pre- and postgadolinium images is usually insufficient to discern prostate cancer (Huisman et al. 2001; Alonzi et al. 2007).

Assessment of signal intensity changes on T1-weighted dynamic contrast-enhanced MR images in order to estimate contrast agent uptake in vivo can be performed qualitatively, semiquantitatively, or quantitatively. Qualitative analysis of signal intensity changes can be achieved by assessing the shape of the signal intensity–time curve (Bonekamp et al. 2011; Hoeks et al. 2011).

The semiquantitative approach describing signal intensity changes by using a number of parameters such as (a) the onset time of the signal intensity curve (t0 = time from appearance in an artery to the arrival of contrast agent in the tissue of interest); (b) the slope and height of the enhancement curve (time to peak); (c) maximum signal intensity (peak enhancement); and (d) persistent delayed phase (type 1 enhancement curve), plateau delayed phase (type 2 enhancement curve), and washout delayed phase (type 3 enhancement curve) (Huisman et al. 2001) (Fig. 7.3).

The quantitative approach using pharmacokinetic modeling is usually applied to calculate changes in the contrast agent concentrations in tissue. Concentration–time curves are mathematically fitted by using one of many described pharmacokinetic models, and quantitative kinetic parameters are derived. These include (a) transfer constant of the contrast agent (Ktrans), (b) rate constant (Kep), and (c) interstitial extravascular extracellular space (Ve) (Huisman et al. 2001). The arterial input function used in the calculations also affects the reliability of the data obtained. In other words, robust methods for measuring the arterial input function are essential. Prostate cancer tends to enhance earlier and faster and to a greater extent and shows earlier contrast agent washout, as compared with healthy prostate tissue (Alonzi et al. 2007; Barentsz et al. 1999). Dynamic contrast-enhanced MR imaging is limited in the discrimination of cancer from prostatitis in the peripheral zone and from highly vascularized benign prostatic hyperplasia nodules in the transition zone.

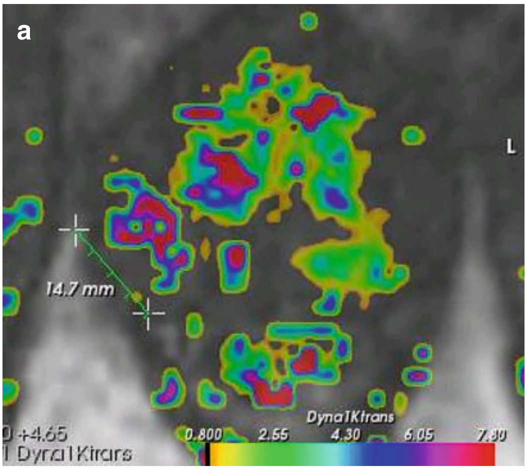

Fig. 7.3 DCE-MRI of prostate cancer. (**a**) Asymmetric and localized contrast uptake in the right peripheral zone. This finding was consistent with a Gleason 8 prostate cancer. (**b**) Relative gadolinium concentration (*y*-axis)–time (*x*-axis) curve of normal tissue shows a persistent delayed phase (type 1 enhancement curve). (**c**) Relative gadolinium concentration (*y*-axis)–time (*x*-axis) curve of plateau of low-grade prostate cancer shows a delayed phase (type 2 enhancement curve). (**d**) Relative gadolinium concentration (*y*-axis)–time (*x*-axis) curve of cancerous tissue shows a washout delayed phase (type 3 enhancement curve)

Fig. 7.3 (continued)

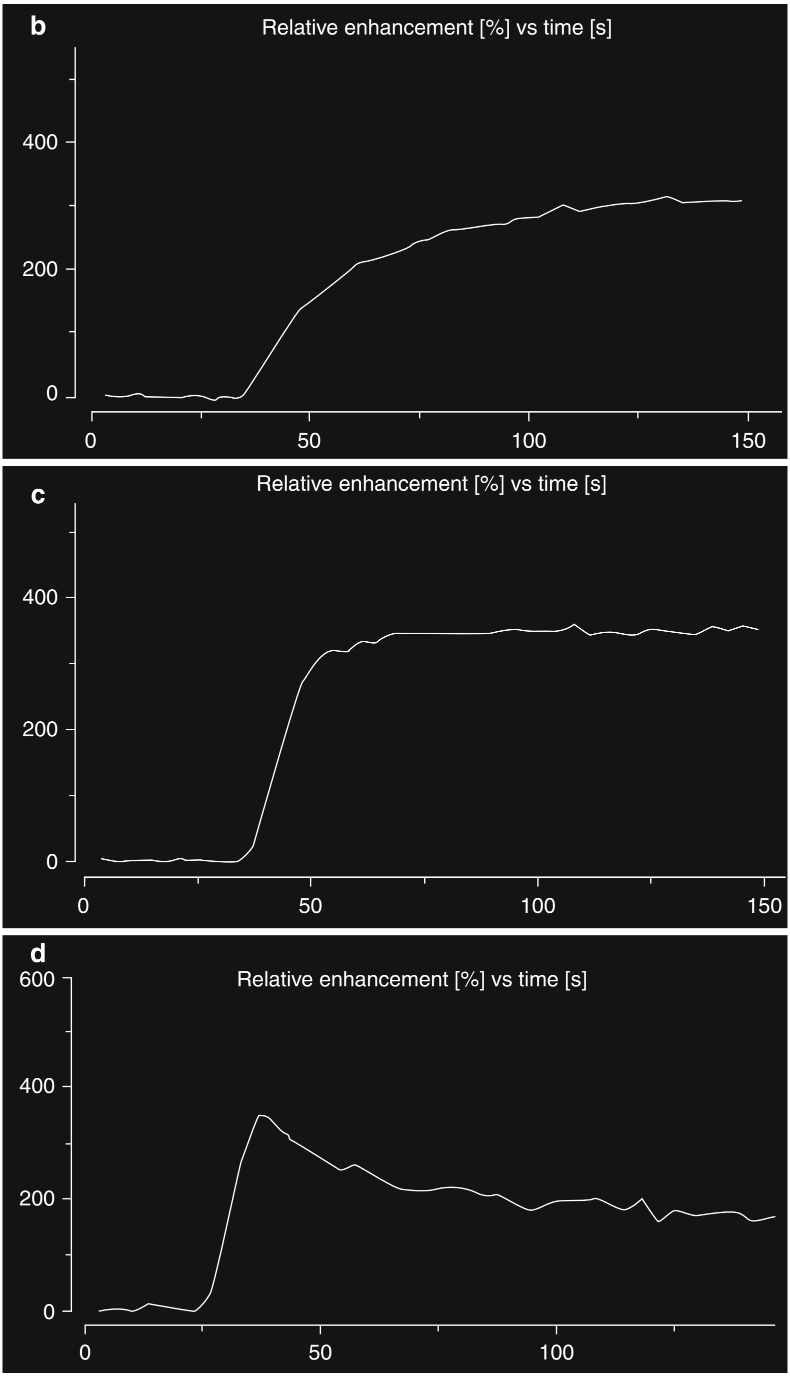

7.3 Multiparametric Prostate MR Imaging (mpMRI)

Prostate MR imaging can provide functional tissue information along with anatomic information. To increase the diagnostic accuracy, anatomic T2-weighted MR imaging and functional MR imaging techniques such as dynamic contrast agent–enhanced MR imaging and diffusion-weighted imaging should be combined in an integrated multiparametric MR imaging prostate examination. Each of the techniques has their strengths and shortcomings; however, the combination may overcome those shortcomings. The information obtained with the various techniques is combined and being interpreted in computer-aided diagnosis programs. The recommendation for the use of MRI in prostate cancer consists of multiparametric MRI. This includes a combination of high-resolution T2-weighted images and at least two functional MRI techniques, as these provide better characterization than T2WI with only one functional technique (Barentsz et al. 2012).

References

Alonzi R, Padhani AR, Allen C. Dynamic contrast enhanced MRI in prostate cancer. Eur J Radiol. 2007;63(3):335–50.

Bammer R. Basic principles of diffusion-weighted imaging. Eur J Radiol. 2003;45:169–84.

Bammer R, Skare S, Newbould R, et al. Foundations of advanced magnetic resonance imaging. NeuroRx. 2005;2:167–95.

Barentsz JO, Engelbrecht M, Jager GJ, et al. Fast dynamic gadolinium-enhanced MR imaging of urinary bladder and prostate cancer. J Magn Reson Imaging. 1999; 10(3):295–304.

Barentsz JO, Richenberg J, Clements R, et al. ESUR prostate MR guidelines 2012. Eur Radiol. 2012;22(4): 746–57.

Basser PJ. Inferring microstructural features and the physiological state of tissues from diffusion-weighted images. NMR Biomed. 1995;8:333–44.

Bloch BN, Rofsky NM, Baroni RH, et al. 3 Tesla magnetic resonance imaging of the prostate with combined pelvic phased-array and endorectal coils; initial experience(1). Acad Radiol. 2004;11(8):863–7.

Bonekamp D, Jacobs MA, El-Khouli R, Stoianovici D, Macura KJ. Advancements in MR imaging of the prostate: from diagnosis to interventions. Radiographics. 2011;31(3):677–703.

Collins DJ, Padhani AR. Dynamic magnetic resonance imaging of tumor perfusion. IEEE Eng Med Biol Mag. 2004;23:65–83.

Hambrock T, Padhani AR, Tofts PS, Vos P, Huisman HJ, Barentsz JO. Dynamic contrast-enhanced MR imaging in the diagnosis and management of prostate cancer. RSNA categorical course in diagnostic radiology. Genitourin Radiol. 2006;1:61–77.

Hoeks CM, Barentsz JO, Hambrock T, et al. Prostate cancer: multiparametric MR imaging for detection, localization, and staging. Radiology. 2011;261(1):46–66.

Hricak H, Williams RD, Spring DB, et al. Anatomy and pathology of the male pelvis by magnetic resonance imaging. AJR Am J Roentgenol. 1983;141(6):1101–10.

Hricak H, Dooms GC, Jeffrey RB, et al. Prostatic carcinoma: staging by clinical assessment, CT, and MR imaging. Radiology. 1987;162:331–6.

Huisman HJ, Engelbrecht MR, Barentsz JO. Accurate estimation of pharmacokinetic contrast-enhanced dynamic MRI parameters of the prostate. J Magn Reson Imaging. 2001;13(4):607–14.

Katahira K, Takahara T, Kwee TC, et al. Ultra-high-b-value diffusion-weighted MR imaging for the detection of prostate cancer: evaluation in 201 cases with histopathological correlation. Eur Radiol. 2011;21(1): 188–96.

Kim CK, Park BK, Lee HM, Kwon GY. Value of diffusion-weighted imaging for the prediction of prostate cancer location at 3T using a phased-array coil: preliminary results. Invest Radiol. 2007;42:842–7.

Krakowsky Y, Loblaw A, Klotz L. Prostate cancer death of men treated with initial active surveillance: clinical and biochemical characteristics. J Urol. 2010;184:131–5.

Kumar V, Jagannathan NR, Kumar R, et al. Apparent diffusion coefficient of the prostate in men prior to biopsy: determination of a cut-off value to predict malignancy of the peripheral zone. NMR Biomed. 2007;20:505–11.

Lansberg MG, Norbash AM, Marks MP, Tong DC, Moseley ME, Albers GW. Advantages of adding diffusion-weighted magnetic resonance imaging to conventional magnetic resonance imaging for evaluating acute stroke. Arch Neurol. 2000;57:1311–6.

Nagel KN, Schouten MG, Hambrock T, et al. Differentiation of prostatitis and prostate cancer by using diffusion-weighted MR imaging and MR-guided biopsy at 3 T. Radiology. 2013;267(1):164–72.

Padhani AR, Harvey CJ, Cosgrove DO. Angiogenesis imaging in the management of prostate cancer. Nat Clin Pract Urol. 2005;2:596–607.

Ren J, Huan Y, Wang H, et al. Diffusion-weighted imaging in normal prostate and differential diagnosis of prostate diseases. Abdom Imaging. 2008;33(6):724–8.

Schnall MD, Lenkinski RE, Pollack HM, Imai Y, Kressel HY. Prostate: MR imaging with an endorectal surface coil. Radiology. 1989;172:570–4.

Somford DM, Fütterer JJ, Hambrock T, Barentsz JO. Diffusion and perfusion MR imaging of the prostate. Magn Reson Imaging Clin N Am. 2008;16(4): 685–95.

Stejskal EO, Tanner JE. Spin diffusion measurements: spin echoes in the presence of a time-dependent field gradient. J Chem Phys. 1965;42(1):288–92.

Tamada T, Sone T, Toshimutsu S, et al. Age-related and zonal anatomical changes of apparent diffusion coefficient values in normal human prostatic tissues. J Magn Reson Imaging. 2008;27:552–6.

Tempany CM, Zhou X, Zerhouni EA, et al. Staging of prostate cancer: results of Radiology Diagnostic Oncology Group project comparison of three MR imaging techniques. Radiology. 1994;192:47–54.

White S, Hricak H, Forstner R, et al. Prostate cancer: effect of postbiopsy hemorrhage on interpretation of MR images. Radiology. 1995;195:385–90.

Wang L, Mazaheri Y, Zhang J, Ishill NM, Kuroiwa K, Hricak H. Assessment of biologic aggressiveness of prostate cancer: correlation of MR signal intensity with Gleason grade after radical prostatectomy. Radiology. 2008;246(1):168–76.

MR Imaging Localization of Prostate Tumors

8

Jurgen J. Fütterer

8.1 Introduction

Prostate cancer is the most common cancer in men and the second leading cause of cancer-related deaths in American men (Siegel et al. 2013). Prostate cancer is initially evaluated by PSA, digital rectal examination (clinical stage), and transrectal ultrasound-guided biopsy results. Treatment is based on life expectancy, potential side effects, comorbidity, and patient preference. The standard treatment of choice for organ-confined disease is curative surgery or radiotherapy. Active surveillance is suitable for early-stage and low-grade prostate cancer. Focal therapy is being currently investigated within multiple clinical trials. Accurate and detailed information of the tumor lesion, location (including extracapsular disease), and volume is needed before these image-guided interventions and therapies can be performed.

Prostate MR imaging is currently the modality of choice for tumor detection, localization, and staging. Anatomical T2-weighted MR imaging is the cornerstone of prostate imaging. Typically significant or index tumors present as low-signal-intensity lesions on T2-weighted MR imaging. Functional MR imaging techniques improve both tumor detection and localization. Diffusion-weighted imaging and dynamic contrast-enhanced MR imaging techniques are the most commonly used functional sequences in multiparametric MR imaging of the prostate (Barentsz et al. 2012). MR imaging is indicated for prostate cancer detection, localization, and local staging. Multiparametric prostate MR imaging has significantly increased the significant tumor detection rate and localization accuracy of prostate cancer. In most institutions, two functional MR techniques are added to the anatomical images. This is feasible for both 1.5 and 3 T MR scanners.

8.2 Detection

Males with palpable abnormalities or with rising or elevated PSA level typically undergo transrectal ultrasound-guided prostate biopsy (Smeenge et al. 2012). In males with an initial *negative* transrectal ultrasound-guided prostate session and a continuing clinical suspicion of prostate cancer, additional transrectal ultrasound-guided biopsy sessions are the current standard of care. Systematic transrectal ultrasound-guided biopsy has low sensitivity (39–53 %) but considerable specificity (80–82 %) in detecting prostate cancer (Pondman et al. 2008).

MR imaging can be used to detect and localize tumor suspicious areas. These areas can be targeted under imaging guidance. The accuracy

---

J.J. Fütterer, MD, PhD
Department of Radiology,
Radboud University Nijmegen Medical Centre,
9101, Nijmegen 6500 HB,
The Netherlands
e-mail: j.futterer@rad.umcn.nl

R.L. Bard et al. (eds.), *Image Guided Prostate Cancer Treatments*,
DOI 10.1007/978-3-642-40429-0_8, © Springer-Verlag Berlin Heidelberg 2014

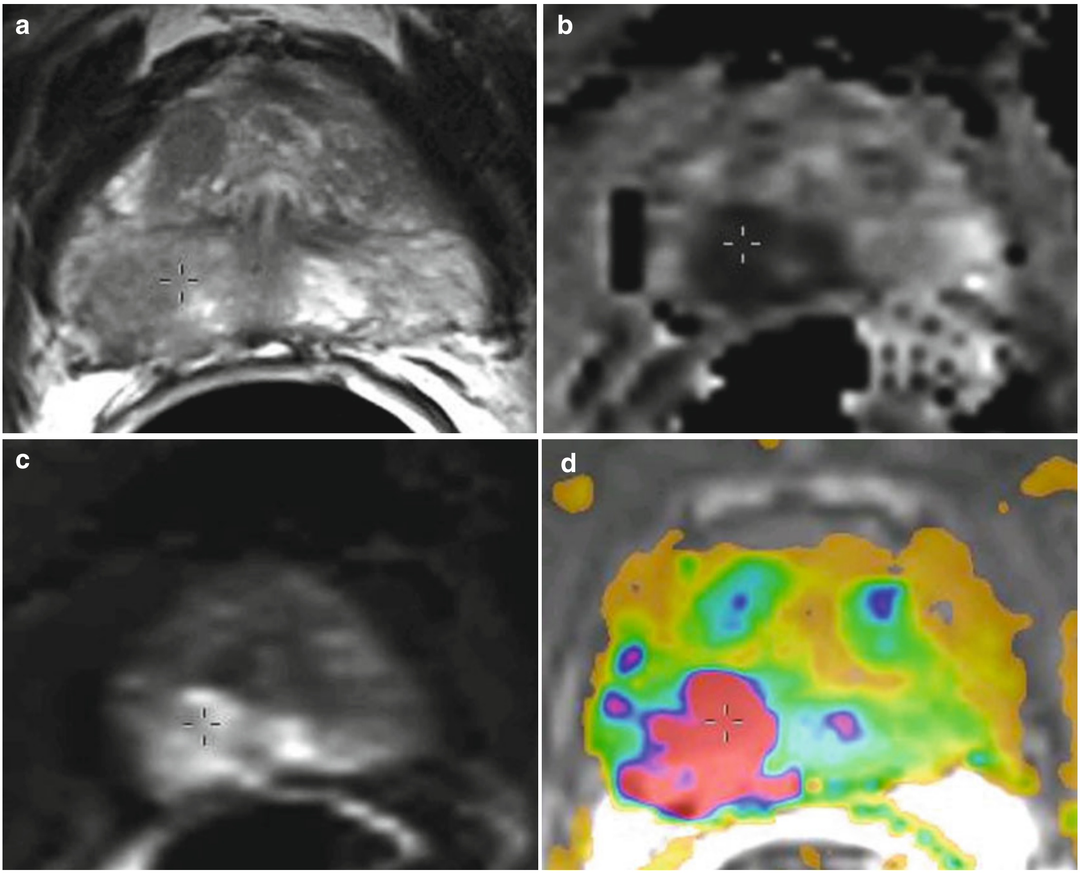

Fig. 8.1 Multiparametric prostate MRI. A 68-year-old male with biopsy-proven prostate cancer (Gleason 7 (3+4) and PSA 22 ng/mL). The axial T2-weighted anatomical MR image (**a**) shows a lesion in the right peripheral zone with extracapsular extension. This is confirmed on the ADC map showing restricted diffusion (**b**). The high b value (1,400) demonstrates high signal intensity within the lesion (**c**). The Ktrans map demonstrates an increased Ktrans compared to the contralateral site (**d**)

of tumor localization with T2-weighted MR imaging varies between 67 and 90 % in patients with biopsy-proven prostate cancer (Fütterer et al. 2006, 2007). The accuracy depends on the applied image interpretation criteria and the experience of the radiologist. Addition of functional MR imaging techniques to the T2-weighted MR sequence has improved prostate cancer localization (Fütterer et al. 2006; Haider et al. 2007; Delongchamps et al. 2011). Increasing the number of functional MR imaging sequence techniques improves tumor detection. Despite the increase in diagnostic accuracy, substantial variability in interpretation of prostate multiparametric MR imaging among radiologists and centers has hindered its widespread adoption (Rosenkrantz et al. 2013; Dickinson et al. 2013). Standardization of interpretation and reporting may lead to reduction in variability in interpretation. The PI-RADS entails explicit criteria that can be used to derive a score on a scale from 3 to 15 to stratify the likelihood that a focal prostatic abnormality represents tumor; such a system is intended to improve interreader reproducibility (Barentsz et al. 2012; Rosenkrantz et al. 2013).

A multiparametric MRI of the prostate consists of a T1- and T2-weighted MRI sequence combined with at least two functional MR imaging techniques (Fig. 8.1). The functional MR techniques have high specificity compared to the PSA test. This may prevent the unnecessary performance of untargeted biopsies. Furthermore,

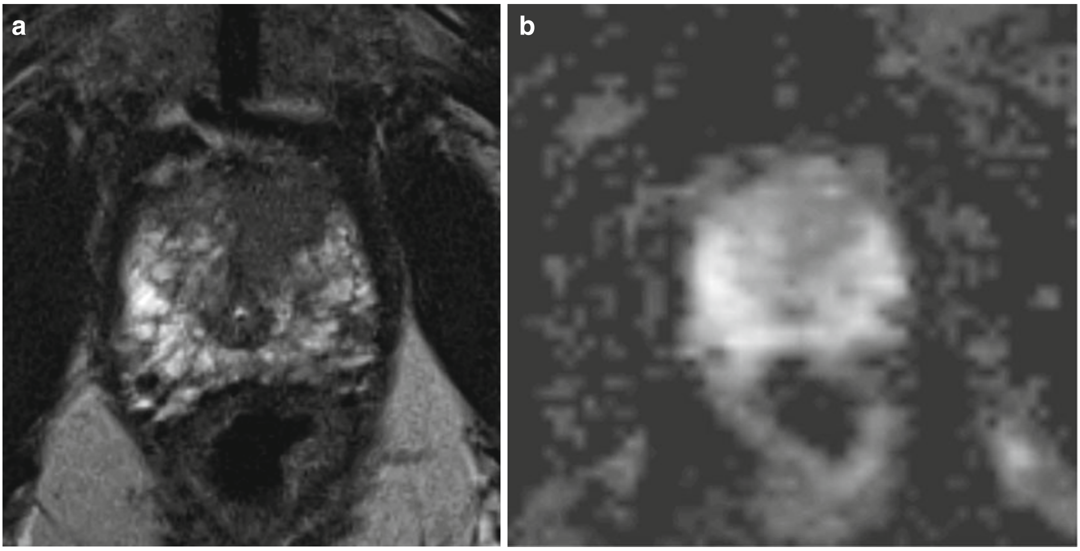

Fig. 8.2 A 70-year-old male with biopsy-proven prostate cancer in the left transition zone (Gleason 7 and PSA of 12). (**a**) A low-signal-intensity area in the left transition zone can be appreciated on the T2-weighted MR images. (**b**) The ADC map demonstrates reduced ADC in this area, however, not convincing for tumor. T2-weighted imaging is dominant in the transition zone for tumor localization

results of prospective separate functional MR imaging studies for prostate cancer detection are difficult to compare, since criteria for cancer detection, methods of analysis, sample sizes, and mean PSA levels of patient groups differ or are not always presented (Hoeks et al. 2011). The addition of dynamic contrast-enhanced MR imaging and/or diffusion-weighted MR imaging to anatomical T2-weighted MR imaging significantly improved prostate cancer detection sensitivity from 63 to 79 %–81 % in the peripheral zone, while maintaining a stable specificity (Delongchamps et al. 2011). In the transition zone, however, multiparametric MR imaging did not improve prostate cancer detection. The use of 3 T multiparametric MR imaging, consisting of anatomical T2-weighted imaging, diffusion-weighted MR imaging, and dynamic contrast-enhanced MR imaging, did not improve transition zone cancer detection and localization accuracy compared with T2-weighted imaging (Fig. 8.2). The addition of high-b-value diffusion-weighted imaging may improve localization accuracies; however, only a few papers have been published on this topic (Fig. 8.3) (Katahira et al. 2011). The combination of proton MR spectroscopic imaging with T2-weighted MR imaging resulted in higher sensitivity and comparable specificity for prostate cancer detection than was shown for T2-weighted MR imaging (sensitivity of 72–89 % vs. 57–84 %) (Villeirs et al. 2010; Casciani et al. 2007).

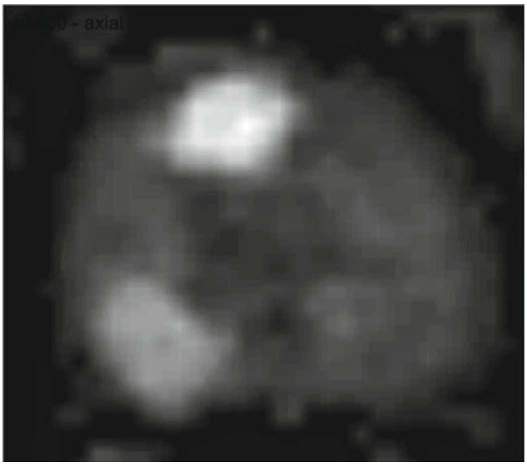

Fig. 8.3 A 62-year-old male with biopsy-proven prostate cancer in the right peripheral and transition zone (Gleason 8 and PSA of 2.1). The high-b-value MR image demonstrates high signal intensity in both right peripheral and transition zone. Histopathology revealed disease in both locations

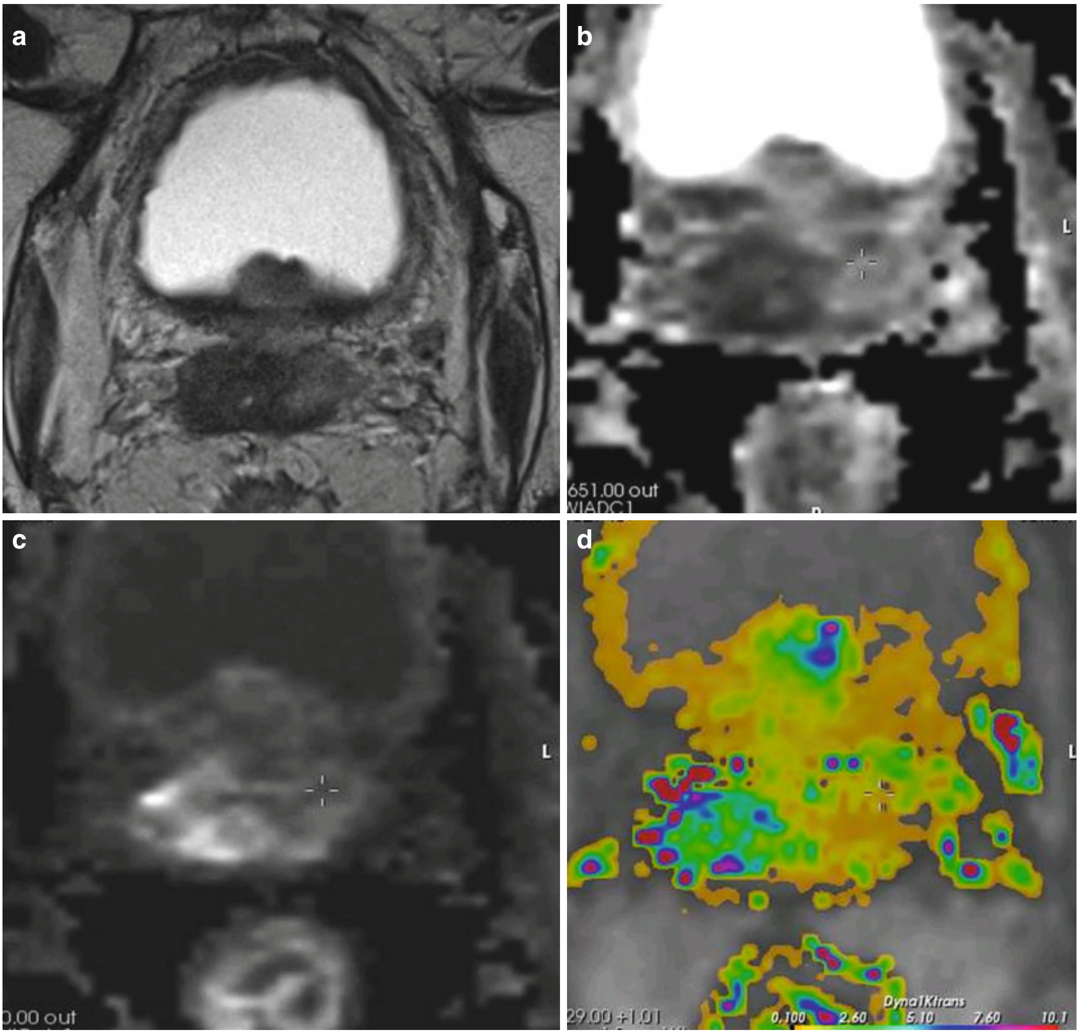

Fig. 8.4 A 56-year-old male with biopsy-proven prostate cancer (Gleason 7 (3+4) and PSA 16 ng/mL). (**a**) T2-weighted axial MR image demonstrate signal loss in the lumen of the seminal vesicle. (**b**) ADC map and the (**c**) high-b-value image confirm the findings on T2 with restriction and increased signal intensity. (**d**) Perfusion MR imaging demonstrates asymmetric enhancement

8.3 Localization and Staging

8.3.1 Tumor Localization

MR imaging with anatomical T2-weighted MR imaging has enabled the acquisition of MR images of the prostate and its surrounding tissues with high spatial resolution. State-of-the-art 1.5 T scanners with a 16-channel phased-array coil meet the minimal requirements for clinically acceptable prostate imaging (Barentsz et al. 2012). Localization of prostate cancer with anatomical MR imaging is significantly more accurate than digital rectal examination and systematic random biopsy results in the entire prostate except for the apex (Mullerad et al. 2005). Even with an eight-channel phased-array coil, diffusion-weighted imaging outperforms anatomical imaging for tumor localization (Miao et al. 2007). The localization accuracy of dynamic contrast-enhanced MR imaging in the peripheral zone is higher compared to the transition zone. Benign prostatic hyperplasia commonly presents as fast enhancing nodules with type 3 washout curves in the transition zone (Hoeks et al. 2013). This is often mistaken for prostate cancer. Perfusion MR imaging is a very sensitive technique for the transition zone and should always be interpreted in combination with the T2-weighted images. The erased charcoal sign in the transition zone is most commonly associated with a prostate cancer. In the peripheral zone, a very fast enhancing area with a type three curve and triangular or linear signal abnormality on T2-weighted images is a typical finding for prostatitis. Diffusion-weighted imaging shows differences between prostatitis and prostate cancer in both the peripheral zone and transition zone. However, there is a significant overlap in apparent diffusion coefficients, and as a consequence the clinical applicability is questionable (Nagel et al. 2013).

8.3.2 Tumor Staging

Although a relatively high spatial resolution can be achieved within a clinically acceptable examination time, reported staging accuracy ranges from 54 to 88 % (Casciani et al. 2007; Tempany et al. 1994; May et al. 2001; Jager et al. 1996; Hricak et al. 1994). The most reliable criteria for the detection of extracapsular extension of prostate carcinoma are asymmetry of the neurovascular bundle, obliteration of the rectoprostatic angle, tumor bulge into the periprostatic fat, broad tumor contact with the surface of the capsule, an extracapsular tumor, and the radiologist's overall impression (Schiebler et al. 1992; Outwater et al. 1994) (Fig. 8.4). Local staging of prostate cancer in the preoperative work-up of prostate cancer is cost effective and should be performed with a high-specificity reading. In attaining this specificity, however, a low sensitivity has to be considered (Jager et al. 2000). The use of dynamic contrast-enhanced MR imaging in local staging prostate cancer improves the performance of the less-experienced readers, whereas the experienced reader has no benefit (Mullerad et al. 2005). The same is true for diffusion-weighted imaging. The functional imaging technique draws the radiologist's attention to the affected area (Bard 2009), which may improve local staging accuracy. The anatomical T2-weighted MR imaging is the most important imaging sequence for local staging. Small lesions can be appreciated on the high-resolution images, whereas diffusion-weighted imaging, proton MR spectroscopy, and dynamic contrast-enhanced MR imaging are hampered by the in-plane spatial resolution.

References

Bard R. DCE-MRI atlas of prostate cancer. Springer-Verlag Berlin Heidelberg; 2009. p. 17–40.

Barentsz JO, Richenberg J, Clements R, et al. ESUR prostate MR guidelines 2012. Eur Radiol. 2012;22(4):746–57.

Casciani E, Polettini E, Bertini L, et al. Contribution of the MR spectroscopic imaging in the diagnosis of prostate cancer in the peripheral zone. Abdom Imaging. 2007;32(6):796–802.

Delongchamps NB, Rouanne M, Flam T, et al. Multiparametric magnetic resonance imaging for the detection and localization of prostate cancer: combination of T2-weighted, dynamic contrast-enhanced and diffusion-weighted imaging. BJU Int. 2011;107(9):1411–8.

Dickinson L, Ahmed HU, Allen C, et al. Scoring systems used for the interpretation and reporting of multiparametric MRI for prostate cancer detection, localization, and characterization: could standardization lead to improved utilization of imaging within the diagnostic pathway? J Magn Reson Imaging. 2013;37(1):48–58.

Fütterer JJ, Heijmink SW, Scheenen TW, et al. Prostate cancer localization with dynamic contrast-enhanced MR imaging and proton MR spectroscopic imaging. Radiology. 2006;241(2):449–58.

Fütterer JJ, Scheenen TW, Heijmink SW, et al. Standardized threshold approach using three-dimensional proton magnetic resonance spectroscopic imaging in prostate cancer localization of the entire prostate. Invest Radiol. 2007;42(2):116–22.

Haider MA, van der Kwast TH, Tanguay J, et al. Combined T2-weighted and diffusion-weighted MRI for localization of prostate cancer. AJR Am J Roentgenol. 2007;189(2):323–8.

Hoeks CM, Barentsz JO, Hambrock T, et al. Prostate cancer: multiparametric MR imaging for detection, localization, and staging. Radiology. 2011;261(1):46–66.

Hoeks CM, Hambrock T, Yakar D, et al. Transition zone prostate cancer: detection and localization with 3-T multiparametric MR imaging. Radiology. 2013;266(1):207–17.

Hricak H, White S, Vigneron D, et al. Carcinoma of the prostate gland: MR imaging with pelvic phased-array coils versus integrated endorectal-pelvic phased-array coils. Radiology. 1994;193:703–9.

Jager GJ, Ruijter ET, van de Kaa VA, et al. Local staging of prostate cancer with endorectal MR imaging: correlation with histopathology. AJR Am J Roentgenol. 1996;166(4):845–52.

Jager GJ, Severens JL, Thornbury JR, de La Rosette JJ, Ruijs SH, Barentsz JO. Prostate cancer staging: should MR imaging be used? – A decision analytic approach. Radiology. 2000;215(2):445–51.

Katahira K, Takahara T, Kwee TC, et al. Ultra-high-b-value diffusion-weighted MR imaging for the detection of prostate cancer: evaluation in 201 cases with histopathological correlation. Eur Radiol. 2011;21(1): 188–96.

May F, Treumann T, Dettmar P, Hartung R, Breul J. Limited value of endorectal magnetic resonance imaging and transrectal ultrasonography in the staging of clinically localized prostate cancer. BJU Int. 2001;87(1):66–9.

Miao H, Fukatsu H, Ishigaki T. Prostate cancer detection with 3-T MRI: comparison of diffusion-weighted and T2-weighted imaging. Eur J Radiol. 2007;61: 297–302.

Mullerad M, Hricak H, Kuroiwa K, et al. Comparison of endorectal magnetic resonance imaging, guided prostate biopsy and digital rectal examination in the preoperative anatomical localization of prostate cancer. J Urol. 2005;174(6):2158–63.

Nagel KN, Schouten MG, Hambrock T, et al. Differentiation of prostatitis and prostate cancer by using diffusion-weighted MR imaging and MR-guided biopsy at 3 T. Radiology. 2013;267(1):164–72.

Outwater EK, Petersen RO, Siegelman ES, Gomella LG, Chernesky CE, Mitchell DG. Prostate carcinoma: assessment of diagnostic criteria for capsular extension on endorectal coil images. Radiology. 1994; 193(2):333–9.

Pondman KM, Fütterer JJ, ten Haken B, et al. MR-guided biopsy of the prostate: an overview of techniques and a systematic review. Eur Urol. 2008;54(3):517–27.

Rosenkrantz AB, Kim S, Lim RP, et al. Prostate cancer localization using multiparametric MR imaging: Comparison of Prostate Imaging Reporting and Data System (PI-RADS) and Likert Scales. Radiology 122233. 2013 Jun 20. doi:10.1148/radiol.13122233

Schiebler ML, Yankaskas BC, Tempany C, et al. MR imaging in adenocarcinoma of the prostate: interobserver variation and efficacy for determining stage C disease. AJR Am J Roentgenol. 1992;158(3):559–62.

Siegel R, Naishadham D, Jemal A. Cancer statistics, 2013. CA Cancer J Clin. 2013;63(1):11–30.

Smeenge M, de la Rosette JJ, Wijkstra H. Current status of transrectal ultrasound techniques in prostate cancer. Curr Opin Urol. 2012;22(4):297–302.

Tempany CM, Zhou X, Zerhouni EA, et al. Staging of prostate cancer: results of radiology diagnostic oncology group project comparison of three MR imaging techniques. Radiology. 1994;192:47–54.

Villeirs GM, Oosterlinck W, Vanherreweghe E, De Meerleer GO. A qualitative approach to combined magnetic resonance imaging and spectroscopy in the diagnosis of prostate cancer. Eur J Radiol. 2010; 73(2):352–6.

9

Diffusion-Weighted Whole-Body Imaging: Tumor Staging Applications

Dan Sperling and Robert L. Bard

9.1 Development of Diffusion-Weighted Imaging for Magnetic Resonance Imaging

In the early-to-mid 1950s, researchers experimented with using magnetic pulses that generated detectable spin echoes as a way of measuring diffusion. This eventually led to the refinement of echo planar imaging (EPI) now commonly used in diffusion-weighted imaging with MRI (DWI-MR) (Stehling et al. 1991).

In the mid-1980s, DWI-MR was used to obtain intracranial information during neurologic studies. The first DWI-MR brain images of normal and diseased states were announced in 1985 (Le Bihan et al. 1985). The ability to evaluate brain tissue progressed to functional and anatomic neurologic applications, including assessing the severity and extent of stroke damage, measuring the activation of neuronal activity, diagnosing various neurologic disorders, and creating detailed anatomic characterization of white-matter tracts.

Since the early 1990s, advances in EPI, high-gradient amplitude multichannel coils, and parallel imaging have resulted in fewer motion artifacts (Kim et al. 2010). A notable contribution was the introduction of DWI with background body signal suppression (DWIBS) that allows for free-breathing MRI and suppression of signals from fat, which thereby enables screening of the complete body in 25 min (Takahara et al. 2004).

9.1.1 Whole-Body DWI (wbMRI)

Imaging applications have evolved to meet a range of oncologic needs: detection of tissue suspicious for malignancy, characterization of tumor aggressiveness, staging, prediction of progression risk, and monitoring treatment response. It is common to combine imaging technologies to gain information about an individual's disease (MRI, CT, ultrasound, conventional radiography, PET, and scintigraphy) when one modality alone is insufficient for both high sensitivity in tumor detection and high specificity in characterizing it (Lenz et al. 2011).

DWI offers several advantages:

(a) It is not dependent on contrast agents or radio markers.
(b) It does not involve ionizing radiation and can thus be used when multiple scans are used to monitor response to chemotherapy and/or radiotherapy.
(c) It can be performed in relatively less time than PET or CT.

D. Sperling, MD (✉)
Sperling Prostate Center, Alpha 3T MRI,
145 E. 32nd St, New York, NY 10016, USA
e-mail: dan.sperling@sperlingmedical.com

R.L. Bard, MD
Bard Cancer Center, Biofoundation for Angiogenesis
Research and Development, 121 E 60th St.,
New York, NY 10022, USA
e-mail: rbard@cancerscan.com

R.L. Bard et al. (eds.), *Image Guided Prostate Cancer Treatments*,
DOI 10.1007/978-3-642-40429-0_9, © Springer-Verlag Berlin Heidelberg 2014

(d) It is easy to repeat and allows assessment of the entire tumor, minimizing the need for invasive biopsy.
(e) It provides information about microscopic structures (e.g., cell density, necrosis) (Ohno et al. 2012).

Whole-body DWI (wbMRI) has been applied to the diagnosis and staging of extensive malignant disease such as non-small cell lung cancer, malignant lymphoma, multiple myeloma, bone marrow pathologies, and lesions in the liver, pancreas, and kidney (Lenz et al. 2011). Numerous studies have been published comparing DWI with PET scans involving injection of fludeoxyglucose F 18 (FDG-PET) or other radiotracers for tumor detection in malignancies typically identified under FDG-PET: pulmonary tumors (Yang et al. 2013; Ohno et al. 2012; Ohba et al. 2009), gastrointestinal malignancy (Soussan et al. 2012), and metastatic bone lesions (Luboldt et al. 2008; Goudarzi et al. 2010). These studies demonstrate that DWI compares favorably with PET for whole-body imaging and detection of metastases while offering the above-stated advantages.

Other studies report exploration into combining PET and DWI, either as two modalities done simultaneously (Buchbender et al. 2013) or as a fusion imaging process (Reiner et al. 2011). Just as co-registration of MRI and real-time ultrasound imaging is demonstrating value in prostate cancer detection, integrating DWI with PET or other technologies has the potential to improve detection, diagnosis, and posttreatment monitoring in extracranial applications.

9.2 Mechanisms

Diffusion causes random dephasing within each image element (voxel) and thereby attenuates signal from that voxel. Using gradient pulses, this effect can be imaged and a diffusion coefficient (*D*) can be calculated (Le Bihan et al. 1986). The coefficient is related to the size of the particles or molecules, the viscosity of the solvent or fluid medium, and the temperature (Pledger et al. 2011). Water molecule diffusion patterns can reveal microscopic details about both normal and pathological tissue states.

To obtain diffusion-weighted images, a pair of strong gradient pulses is added to the pulse sequence. The first pulse dephases the spins, and the second pulse rephases the spins if no net movement occurs. If net movement of spins occurs between the gradient pulses, signal attenuation occurs. The degree of attenuation depends on the magnitude of molecular translation and diffusion weighting. The amount of diffusion weighting is determined by the strength of the diffusion gradients, the duration of the gradients, and the time between the gradient pulses.

Diffusion imaging is performed optimally on a high-field (≥1.5 T) echo planar system. While scan time is decreased and signal to noise is increased at 3 T, imaging artifacts may be more noticeable.

The intensity of each image element (voxel) represents an estimate of the rate of water diffusion at that location. Due to the interplay of factors in tissues, the actual diffusion coefficient of water cannot be measured directly by MRI. Therefore the diffusion coefficient from orthogonal DWI in all three planes is obtained and is the apparent diffusion coefficient (ADC) which replaces the diffusion coefficient (*D*). Diffusion data can then be presented as an image map of the ADC or signal intensity (Kim et al. 2010). Calculation of the ADC requires two or more acquisitions with different diffusion weightings. ADC and signal intensity are inversely related: a low ADC corresponds to high signal intensity (restricted diffusion), and a high ADC to low signal intensity on DWI, thereby aiding in characterizing abnormal tissue.

9.3 DWI of Prostate Tumors

DWI can improve the detectability of malignant tissue in the prostate compared to T2-weighted images. Numerous studies have shown that based on lower ADC values of prostate carcinoma compared with normal tissue, DWI can distinguish between them, especially in the central parts of the gland. Malignant tissue is characterized by a more highly cellular environment that restricts water molecule movement in the extracellular spaces, resulting in decreased diffusion and therefore a low ADC (high signal intensity). Lower ADC values are associated with higher Gleason scores (Turkbey et al. 2011; Woodfield et al. 2010). The reported ADC values of prostate cancer in the peripheral zone range between 0.93 and 1.38×10^3 mm^2/s, and this variability may be related to the heterogeneous tissue composition of prostate cancer (Kim et al. 2007) (Fig. 9.1).

DWI is extensively covered in many chapters of prostate imaging as highly effective in both anatomic verification and grading of prostate tumors; however, DWI does not appear to accurately differentiate malignant tissue from benign prostatic hyperplasia (BPH) as this condition may also cause areas of restricted diffusion in the central parts of the prostate gland (Lenz et al. 2011).

9.4 WbDWI Imaging Metastases from Cancer

Metastatic disease spreads to the liver, lung, and bone hematogenously. Lymphadenopathy may be due to local invasion or by lymphatic drainage. Generally metastatic nodal disease from prostate cancer is small and usually not imaged by wbMRI. Metastatic involvement of local disease to the seminal vesicles, bladder, bowel, and pelvic side wall musculature is currently under study with this modality.

9.4.1 Liver Metastases

The tumor having the greatest metastatic potential is malignant melanoma. Indeed, clinicians would see a patient with an eye patch and enlarged liver and conclude that uveal melanoma was the etiology.

The literature on PET/CT imaging of hepatic metastases of uveal melanoma surprisingly shows poor imaging correlation, that is, metastatic disease may be easily undetected by this highly malignant disorder. A multitumor multicenter study including 11 patients with malignant melanoma studied by PET/CT and wbDWI showed a 100 % correlation by wbDWI at $b = 1{,}000$ with the 18 FDG images (Lichy et al. 2007).

Liver tumors were also evaluated by respiratory breath-holding versus respiratory-triggered imaging in a study of 92 lesions showing the mean contrast-to-noise ratio (CNR) of metastases, hepatocellular carcinomas, and abscesses was better using the respiratory-triggered approach (Kandal et al. 2009).

9.4.2 Pulmonary Metastases

The common finding of a pulmonary solitary nodule on chest x-rays leads to CT and PET/CT studies with attendant patient stress, radiation exposure, and false positives and negatives. Nodules smaller than 5 mm are likely to be benign (Goodman 2005). In a study of 54 biopsy-proven solitary nodules greater than 5 mm, malignant nodules showed a mean DWI score of 4.03 while benign nodules approached a score of 2.50 with an accuracy of 79.6 %. While useful for evaluation of large nodules, small nodules remain a diagnostic problem (Satoh et al. 2008).

9.5 Imaging Bone Metastases

Metastases prefer to site in areas of red bone marrow usually found in the axial skeleton (Scher 2003). Conventional bone scintigraphy has been used since 1970 and still is used to detect the osteoblasis in the bone matrix commonly associated with osteoblastic-forming tumors like prostate cancer. However, false-positive findings seen in degenerative disease, inflammatory disorders, and trauma degrade the sensitivity of this modality (Eustace et al. 1997). Conventional x-ray and CT show abnormal findings in the boney cortex rather than bone marrow invasion and represent late-stage disease.

MRI has been used for two decades to detect marrow disease; however, findings often lack specificity and 18F PET/CT has been improving

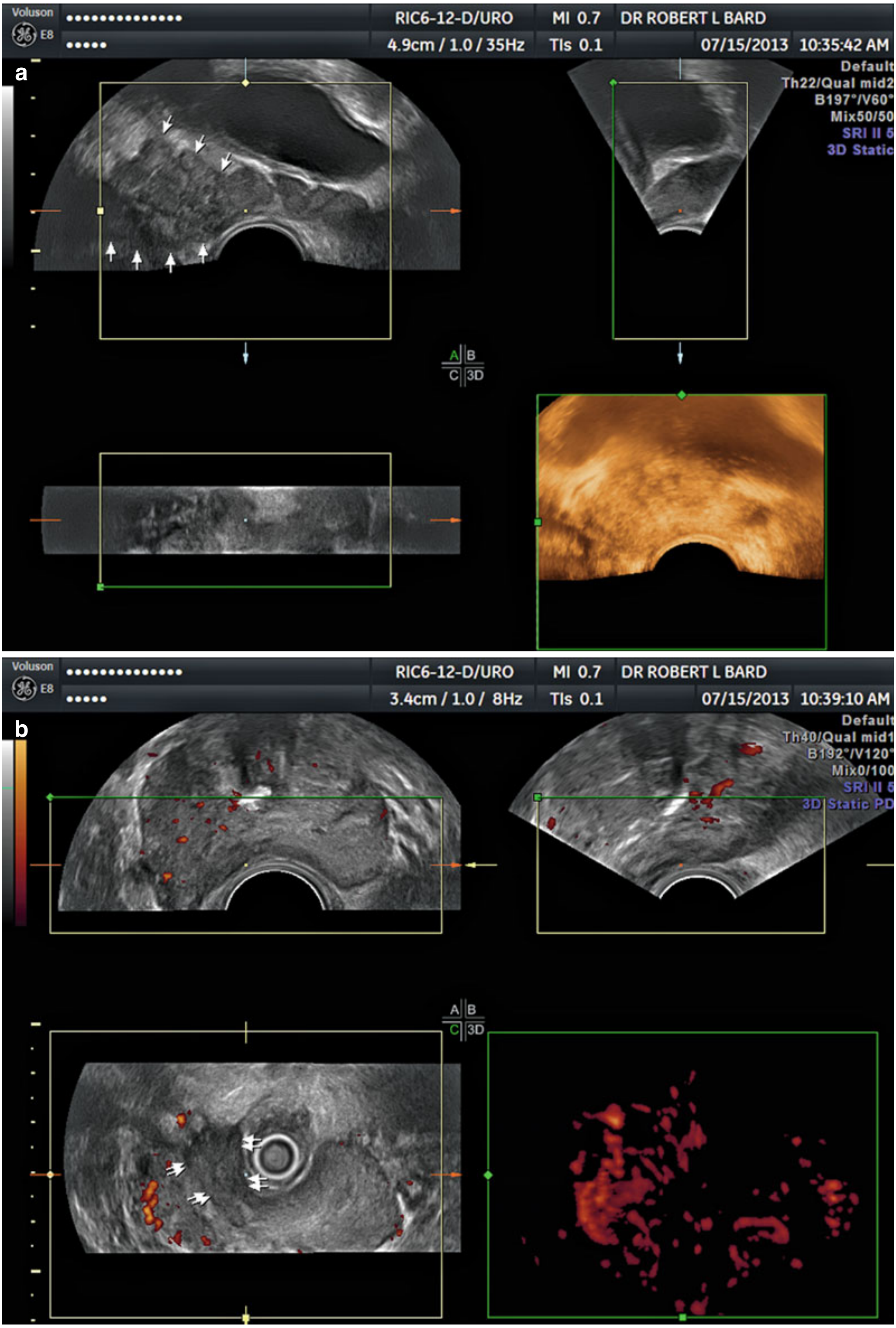

Fig. 9.1 (**a**) 3D patient with Gleason 7 shows dilated right seminal vesicle. (**b**) 3D coronal view shows direct invasion. (**c**) 3D coronal view shows lateral indirect invasion. (**d**) 3D Doppler confirms vascular invasion. (**e**) MRI shows indirect invasion. (**f**) Coronal MRI shows direct invasion. (**g**) DCE-MRI confirms invasion. (**h**) Sagittal MRI confirms direct invasion. (**i**) Sagittal MRI confirms indirect invasion. (**j**) T1 MRI shows right obturator lymph node. (**k**) T2 MRI shows right obturator lymph node. (**l**) Diffusion MRI shows right obturator lymph node

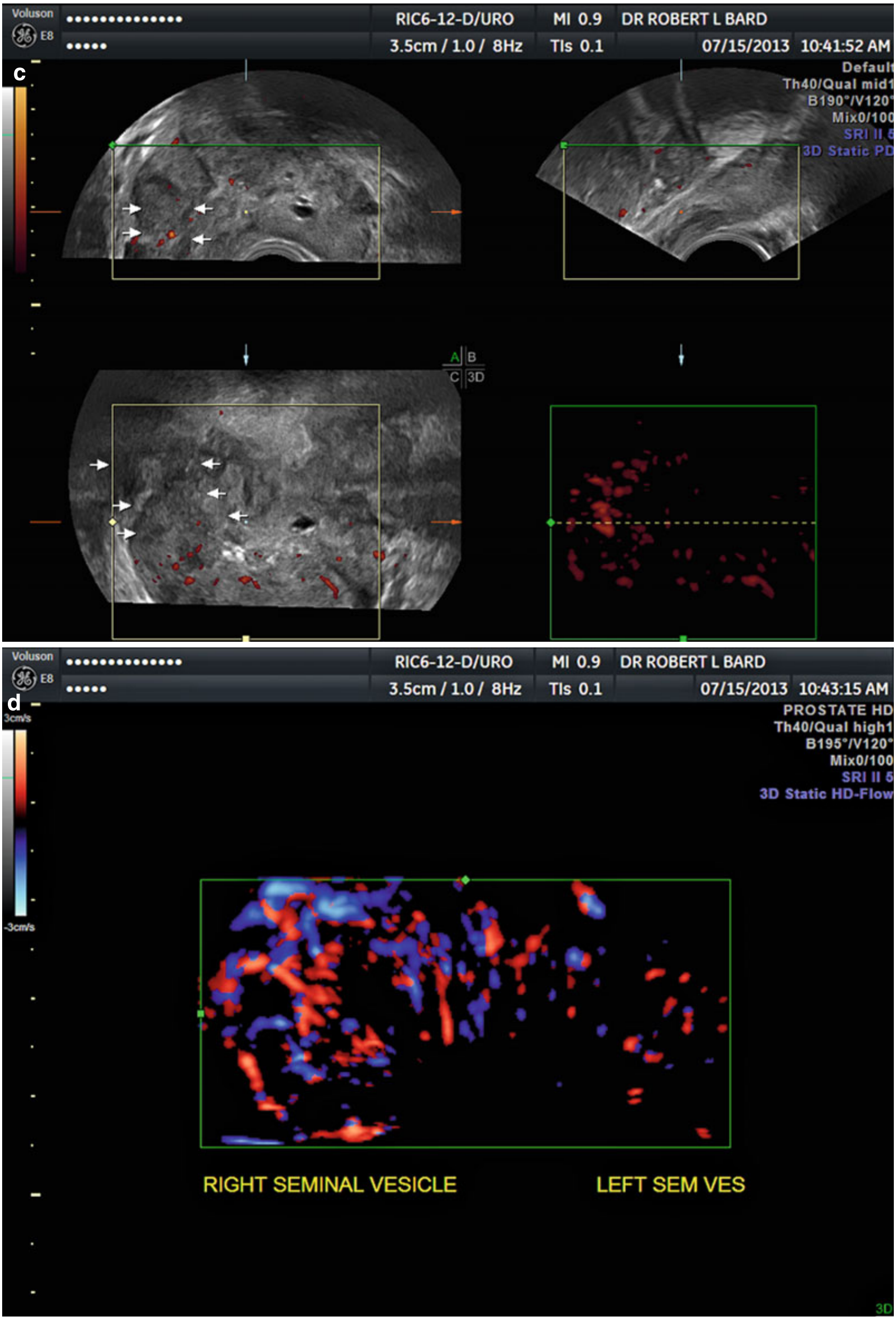

Fig. 9.1 (continued)

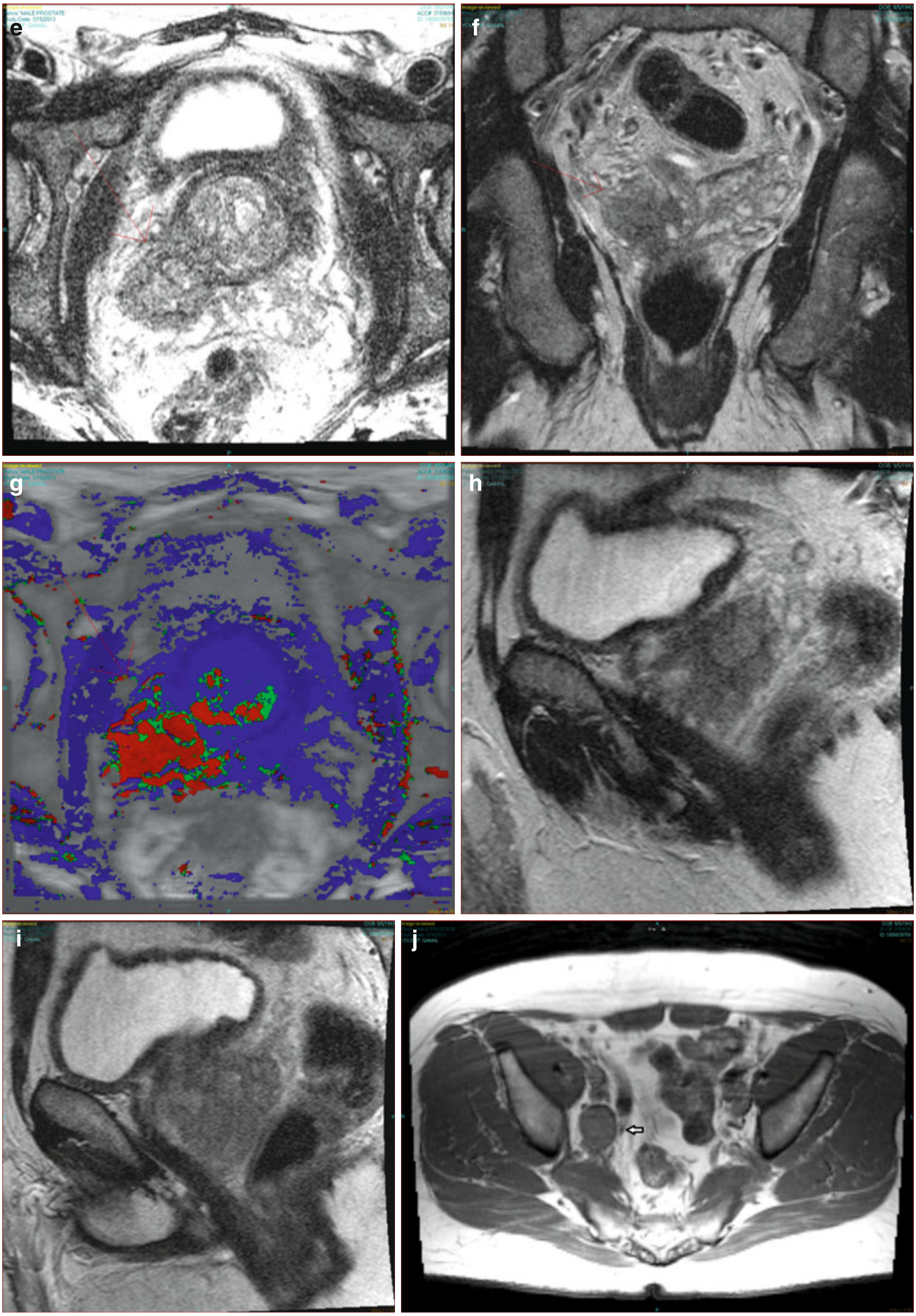

Fig. 9.1 (continued)

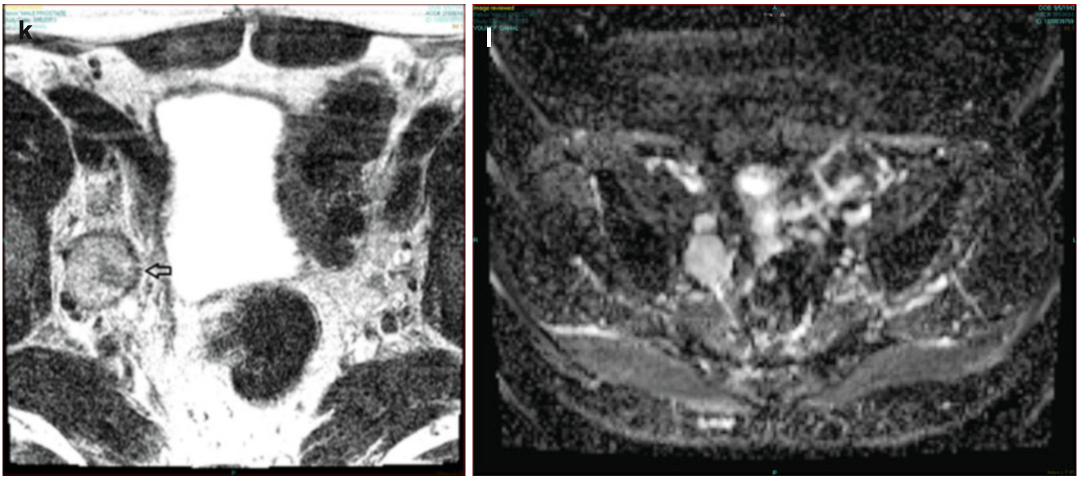

Fig. 9.1 (continued)

accuracy (Bard 2009). WbDWI provides anatomic and functional imaging of solid tumors that experience restricted diffusion possibly due to high cellular density and/or breakdown of the Na+/K+ (sodium/potassium) pump occurring from apoptosis.

WbDWI was evaluated against the current gold standard of 18F PET CT in a study of Gleason score 8 tumors. The study showed the pelvis and spine were the most common sites and there were no solitary metastases outside these locations. wbMRI showed a higher specificity and 18F PET/CT showed a higher sensitivity for detection of bone metastases from prostate cancer. False-positive findings are more common with 18F PET /CT than wbDWI since it is not tumor specific, and its uptake in bone lesions reflects elevated local blood flow in association with increased osteoblastic activity (Mosavi et al. 2012).

9.5.1 Principles of Bone Marrow Imaging

Since bone metastases cause great morbidity, a noninvasive modality is preferred. WbDWI is showing greater acceptance since it is highly sensitive to cellular density changes in the marrow space. Yellow bone marrow is low in cell density due to fatty tissue predominance, and red bone marrow has higher cell density and water content providing a higher b value in wbDWI; therefore patients with higher marrow fat content (elderly, postmenopausal women, and patients with drug-induced osteoporosis) are better candidates for DWI. Younger patients and patients receiving bone marrow stimulators are less well suited for evaluation (Padhani et al. 2013).

9.5.2 Imaging Bone Metastases from Prostate Carcinoma

Bone scintigraphy, widely used to confirm metastatic foci, has a sensitivity of 70 % and a specificity of 57 %. This has led to the preference for 18F-NaF PET/CT for confirmation; however, this lacks specificity due to a 100 % sensitivity (Even-Saphir et al. 2006).

wbMRI poorly depicts tumors in the skull and ribs; however, studies have shown that metastases outside the pelvis and spine are rare (Costelloe et al. 2012). A scientific panel at the 60th Journees Francaises de Radiologie (JFR2012, Paris) concluded that standard MRI of the pelvis and lumbar spine was sufficient screening to rule out metastatic disease to the axial skeleton.

9.6 Imaging Artifacts in wbMRI

3 T imaging has the intrinsic advantage of higher SNR which improves lesion detection. Artifacts such as dielectric effects and tissue

absorption rates generally noted at 3 T are less common at 1.5 T. Eddy currents induced by the rapid switching of the magnetic gradient field with echo planar imaging cause residual magnetization that results in geometric distortion and image shearing (Koh and Collins 2007) which makes DW image alignment with T2WI more difficult. Greater B1 field inhomogeneity at 3 T fails to achieve uniform fat suppression across large fields of view causing chemical shift and ghosting artifacts. MR frequency offsets applied can differ between anatomic stations, and voxel shift can occur in the phase encoding direction producing structural misalignment (i.e., spinal nonalignment) between imaging stations. Further technical considerations may be found in the MRI scientific literature (Koh et al. 2012) and go beyond the scope of this book.

Conclusion

The value of diffusion-weighted imaging for prostate cancer staging and whole-body imaging for metastatic workup of other tumors is now well established. It will prove valuable in other cancers especially in liver imaging where uveal melanoma metastases are routinely not imaged by PET/CT. When applied to the prostate, it brings value in its ability to distinguish and grade prostate tumors. It can provide both qualitative and quantitative image-based functional analysis of prostate cancer, and the information from DWI integrates well with that from other imaging sources. DWI offers certain advantages, including the lack of necessity for contrast agents or exposure to ionizing radiation and reduced imaging time compared with PET/CT. Whole-body DWI may be performed at the same time as mpMRI for the prostate when an index lesion is identified and staging workup is indicated. The high specificity and lack of ionizing radiation will lend it to further use in staging other malignancies since it is more specific in detecting boney metastases that 18 NaF PET/CT.

References

Bard R. DCE MRI atlas of prostate cancer. Springer-Verlag Berlin Heidelberg; 2009. p. 61.

Buchbender C, Hartung-Knemeyer V, et al. Does positron emission tomography data acquisition impact simultaneous diffusion-weighted imaging in a whole-body PET/MRI system? Eur J Radiol. 2013;82(2):380–4. doi:10.1016/j.ejrad.2012.11.018.

Costelloe CM, Kundra V, et al. Fast Dixon whole body MRI for detecting distant cancer metastases: a preliminary clinical study. J Magn Reson Imaging. 2012;35(2):399–408.

Eustace S, Tello R, et al. A comparison of whole body MRI imaging and 99m Tc scintigraphy in the examination of patients with suspected skeletal metastases. AJR Am J Roentgenol. 1997;169:1655–61.

Even-Saphir E, Metser U, et al. The detection of bone metastases in patient with high risk prostate cancer: 99m Tc scintigraphy, SPECT and 18F-fluoride PET. J Nuc Med. 2006;47:287–97.

Goodman LR. Small pulmonary emboli: what do we know? Radiology. 2005;234:654–8.

Goudarzi B, Kishimoto R, et al. Detection of bone metastases using diffusion weighted magnetic resonance imaging: comparison with (11)C-methionine PET and bone scintigraphy. Magn Reson Imaging. 2010;28:372–9.

Kandal H, Sharma R, et al. Respiratory triggered versus breath hold DWI of liver lesions. AJR Am J Roentgenol. 2009;192(4):915–22.

Kim CK, Park BK, Lee HM, et al. Value of diffusion-weighted imaging for the prediction of prostate cancer location at 3T using a phased-array coil. Invest Radiol. 2007;42:842–7.

Kim C, Park BK, Kim B. Diffusion-weighted MRI at 3T for the evaluation of prostate cancer. AJR Am J Roentgenol. 2010;194:1461–9.

Koh DM, Collins DJ. Diffusion weighted MRI in the body: applications and challenges in oncology. AJR Am J Roentgenol. 2007;188:1622–35.

Koh DM, Blackledge M, et al. Whole body diffusion-weighted MRI: tips, tricks and pitfalls. AJR Am J Roentgenol. 2012;199(2):252–62.

Le Bihan D, Breton E, et al. MR Imaging of intravoxel incoherent motions : application to diffusion and perfusion in neurologic disorders. In: Annual meeting of the RSNA, Chicago, 1985.

Le Bihan D, Breton E, Lallemand D, et al. MR imaging of intravoxel incoherent motions: application to diffusion and perfusion in neurologic disorders. Radiology. 1986;161:401–7.

Lenz C, Klarhofer M, Scheffler K, et al. Assessing extracranial tumors using diffusion-weighted whole-body MRI. Z Med Phys. 2011;21:79–90.

Lichy MP, Aschoff P, et al. Tumor detection by diffusion weighted MRI and ADC-mapping. Proc Intl Soc Mag Reson Med. 2007;15:283–4.

Luboldt W, Kufer R, et al. Prostate carcinoma: diffusion-weighted imaging as a potential alternative to conventional MR and 11C-choline PET/CT for detection of bone metastases. Radiology. 2008;249:1017–25.

Mosavi F, Johansson S, et al. Whole-body diffusion-weighted MRI copared with 18GNaF PET/CT for detection of bone metastases in patients with high-risk prostate carcinoma. AJR Am J Roentgenol. 2012;199:1114–20.

Ohba Y, Nomori H, Mori T, et al. Is diffusion-weighted magnetic resonance imaging superior to positron emission tomography with fludeoxyglucose F 18 in imaging non-small cell lung cancer? J Thorac Cardiovasc Surg. 2009;138(2):439–45.

Ohno Y, Koyama H, Yoshikawa T, et al. Diffusion-weighted MRI versus ^{18}F-FDG PET/CT: performance as predictors of tumor treatment response and patient survival in patients with non-small cell lung cancer receiving chemoratiotherapy. AJR Am J Roentgenol. 2012;198(1):75–82.

Padhani AR, van Ree K, et al. Assessing the relation between bone marrow signal intensity and ADC in diffusion-weighted MRI. AJR Am J Roentgenol. 2013;200:163–70.

Pledger T, Sakaie K, et al. Diffusion-weighted magnetic resonance imaging. Eradimaging. 2011. Epub at http://www.eradimaging.com/site/article.cfm?id=768.

Reiner CS, Fischer MA, et al. Molecular imaging of malignant tumor metabolism: whole-body image fusion of DWI/CT vs. PET/CT. Acad Radiol. 2011;18(8):040–6. doi:10.1016/j.acra/2011.03.010.

Satoh S, Kitazume Y, et al. Can malignant and benign pulmonary nodules be differentiated with diffusion weighted MRI? AJR Am J Roentgenol. 2008;191(2):464–74.

Scher HI. Prostate carcinoma; defining therapeutic objectives and improving overall outcome. Cancer. 2003;97:758–71.

Soussan M, Des Guetz G, et al. Comparison of FDG-PET/CT and MR with diffusion-weighted imaging for assessing peritoneal carcinomatosis from gastrointestinal malignancy. Eur Radiol. 2012;22:1479–87.

Stehling MK, Turner R, Mansfield P. Echo-planar imaging: magnetic resonance imaging in a fraction of a second. Science. 1991;254:43–50.

Takahara T, Imai Y, Yamashita T, et al. Diffusion weighted whole body imaging with background body signal suppression (DWIBS): technical improvement using free breathing, STIR and high resolution 3D display. Radiat Med. 2004;22:275–82.

Turkbey B, Shah VP, et al. Is apparent diffusion coefficient associated with clinical risk scores for prostate cancers that are visible on 3-T MR images? Radiology. 2011;258(2):488–95.

Woodfield C, Tung G, Grand D, et al. Diffusion-weighted MRI of peripheral zone prostate cancer: comparison of tumor apparent diffusion coefficient With Gleason score and percentage of tumor on core biopsy. AJR Am J Roentgenol. 2010;194(4):W316–22.

Yang RM, Li L, Wei XH, et al. Differentiation of central lung cancer from atelectasis: comparison of diffusion-weighted MRI with PET/CT. PLoS One. 2013;8(4):e60279. doi:10.1371/journal.pone.0060279.

10

MRI-Guided Biopsy

Jurgen J. Fütterer

10.1 Introduction

In Europe and the USA, prostate cancer is the most commonly diagnosed form of cancer among males (Siegel et al. 2013). One out of six males will die from the disease. In the USA, prostate cancer is the second leading cause of death next to lung cancer (Siegel et al. 2013). Early diagnosis of clinically significant prostate cancer is of utmost importance.

In patients with an elevated or rising prostate-specific antigen (PSA) test and/or abnormal digital rectal examination, random systematic transrectal ultrasound (TRUS)-guided biopsy is the most commonly used technique to further investigate the prostate. However, like PSA, which is a sensitive but unspecific marker (specificity of 36 %), TRUS-guided biopsy also has its shortcomings (Schroder et al. 1998, 2008). Histopathology of the biopsy ultimately confirms the presence and the Gleason score of prostate cancer.

The term TRUS-guided biopsy is misleading because grayscale TRUS is unable to discriminate between prostate cancer and other benign diseases of the prostate. A TRUS-guided biopsy session includes an ultrasound probe that is inserted in the rectum of the patient for biopsy guidance. The ultrasound images are used to guide the biopsy needle towards the different areas within the prostate. Ten to twelve biopsy samples are obtained from the prostate according to a standardized scheme (depending on prostate volume). More than 20 % of the cancers are not detected in the first TRUS-guided biopsy session due to sampling error (Djavan et al. 2001). Reported prostate cancer detection rates for repeat TRUS-guided biopsy are in the order of 7–17 % (Roehl et al. 2002; Djavan et al. 2005; Lujan et al. 2004). Consequently, a large number of patients with a persistently elevated or increasing PSA and one or more negative TRUS-guided biopsy sessions are subject to diagnostic uncertainty.

The in-office TRUS-guided biopsy is the most common method used for prostate cancer diagnosis. It is fast, cheap, and easily accessible. However, with the current TRUS-guided biopsy protocol, clinically significant tumors are missed. Clinically insignificant tumors are identified by chance, and there is undergrading of the true Gleason score (34–38 %) when the less aggressive part of a tumor is sampled or the index lesion is missed (Kvale et al. 2009; Lattouf and Saad 2002; Divrik et al. 2007; Berglund et al. 2008).

10.2 Multiparametric Prostate MR Imaging

Multiparametric prostate MR (mpMRI) imaging is currently the most accurate technique for detection, localization, and staging of prostate

---

J.J. Fütterer, MD, PhD
Department of Radiology,
Radboud University Nijmegen Medical Centre,
9101, Nijmegen 6500 HB, The Netherlands
e-mail: j.futterer@rad.umcn.nl

R.L. Bard et al. (eds.), *Image Guided Prostate Cancer Treatments*,
DOI 10.1007/978-3-642-40429-0_10, © Springer-Verlag Berlin Heidelberg 2014

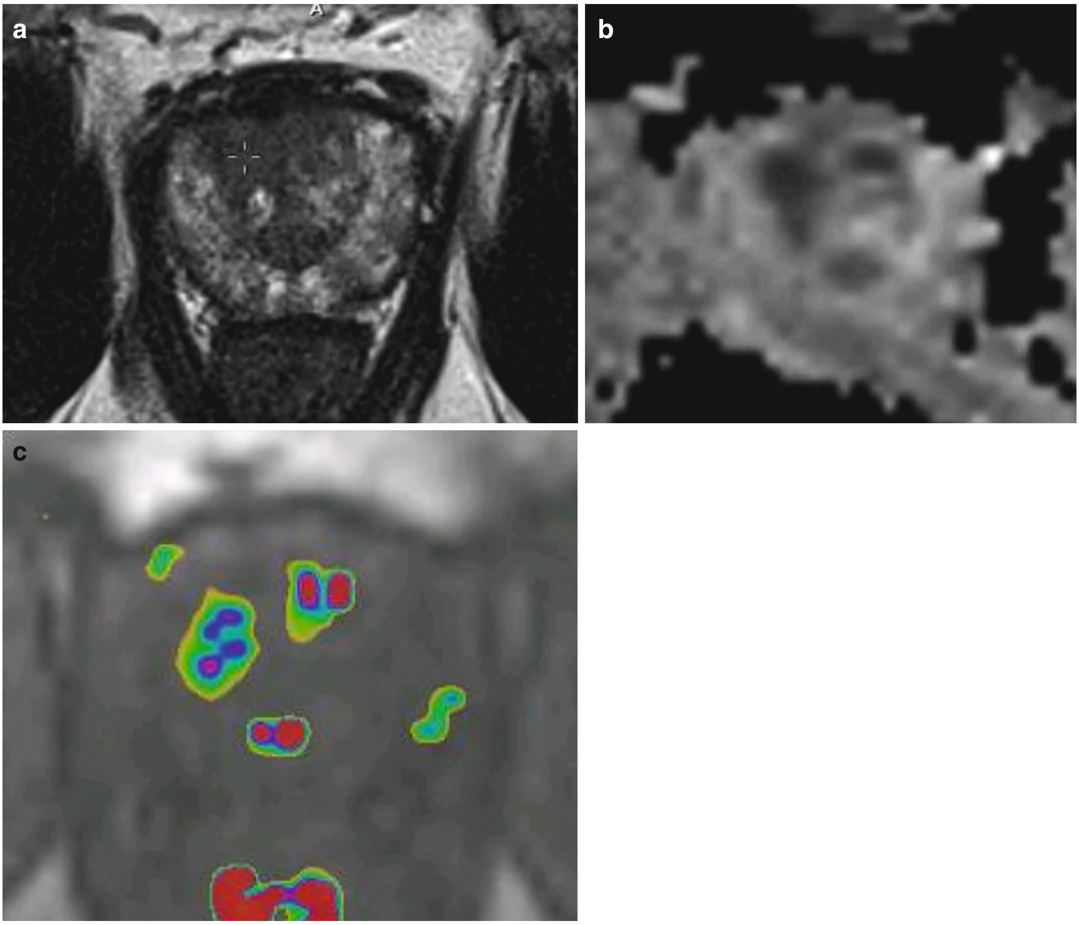

Fig. 10.1 A 64-year-old male with biopsy-proven prostate cancer (Gleason 7 and PSA 6.7 ng/mL). The axial T2-weighted anatomical MR image (**a**) shows a lesion in the ventral area of the transition zone (midprostate). This is confirmed on the ADC map showing restricted diffusion (**b**). The Ktrans map demonstrates an increased Ktrans compared to the contralateral site (**c**)

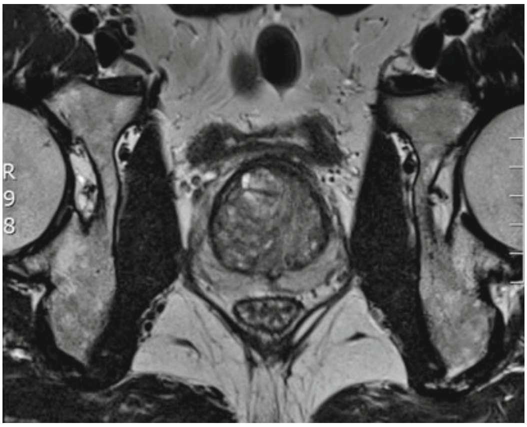

Fig. 10.2 Axial T2-weighted MR imaging demonstrating a high signal intensity in the healthy peripheral zone. No lesions can be appreciated in the peripheral zone

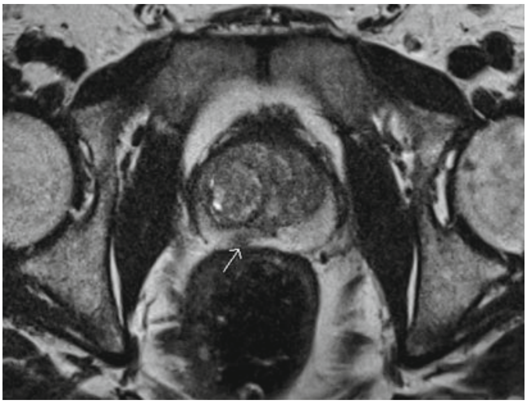

Fig. 10.3 A 63-year-old male with MR-guided biopsy-proven prostate cancer in the right peripheral zone. The T2-weighted image demonstrates a low-signal-intensity area in the right peripheral zone (*arrow*)

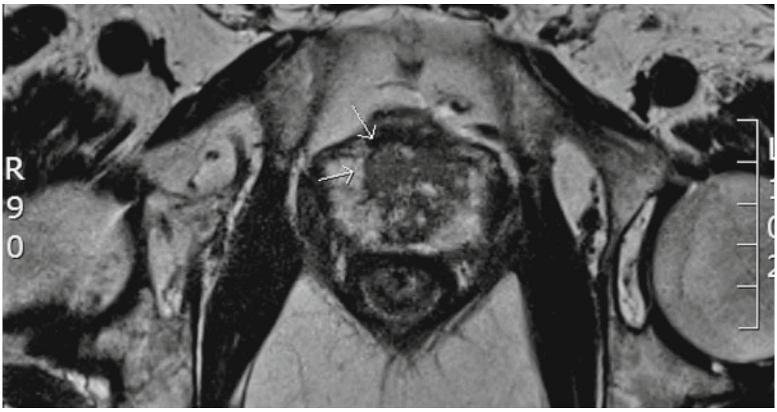

Fig. 10.4 A 71-year-old male with MR-guided biopsy-proven prostate cancer in the right transition zone. The T2-weighted image demonstrates a low-signal-intensity area (erased charcoal sign) in the right transition zone (*arrows*)

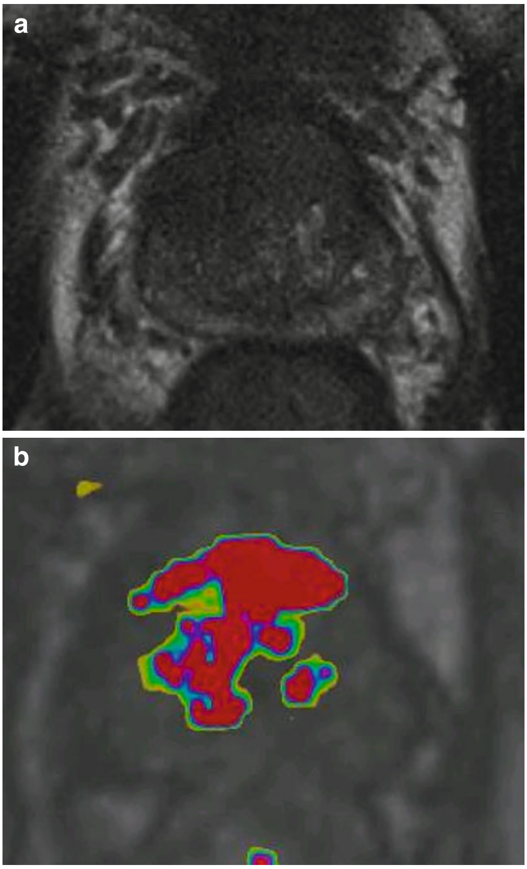

Fig. 10.5 A 72-year-old male with a PSA of 18 and two negative TRUS biopsy sessions underwent MR-guided biopsy. (**a**) The T2-weighted MR image demonstrates a large area of low signal intensity in the transition zone. (**b**) The perfusion MRI demonstrates washout in this area

cancer (Fig. 10.1) (Hoeks et al. 2011). With the available MR imaging techniques, it is possible to obtain anatomical and functional information from the prostate. MR-guided prostate biopsy is mainly used to detect prostate cancer in patients with rising or elevated PSA. For this purpose, high-resolution prostate MR examinations are best suited to produce optimized biopsies and are termed a "detection MRI study."

The detection MR examination includes at least two functional MR imaging techniques in addition to the anatomical information (Barentsz et al. 2012). Anatomical information can be obtained from T2-weighted imaging sequences (Figs. 10.2, 10.3, and 10.4), which are acquired in at least two planes (Barentsz et al. 2012). Preferably, axial and sagittal planes are chosen. T2-weighted MR imaging provides the best depiction of the prostate's zonal anatomy and is the cornerstone of prostate MR imaging. Dynamic contrast-enhanced (DCE) MR imaging provides information about the perfusion and neovascularization of the prostate (Figs. 10.5 and 10.6). In both peripheral and transition zones, prostate cancer often demonstrates neovascularization; however, not all enhancing lesions are potential cancers. DCE-MR imaging is a very sensitive technique and lacks specificity. Benign prostatic hyperplasia, prostatitis, and scar tissue demonstrate similar enhancement patterns (Figs. 10.7, 10.8, and 10.9). Especially, prostatitis and low-grade prostate cancers are difficult to discern based on the DCE-MR imaging parameters (Fig. 10.10). Diffusion-weighted MR imaging (DWI) is a measure for the diffusion of water molecules. Restricted diffusion is seen in tissues with a high cellular density, such as prostate cancer. Apparent diffusion coefficient (ADC) values

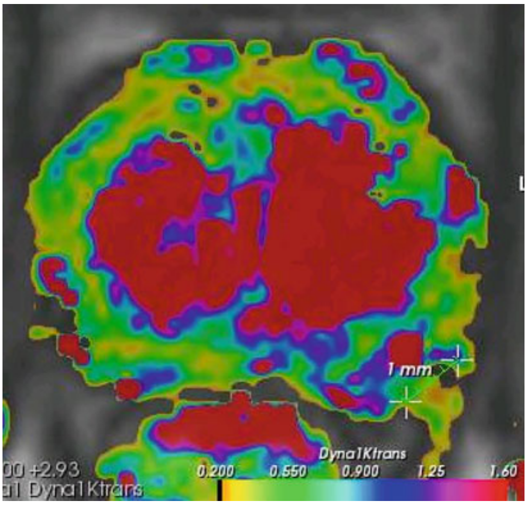

Fig. 10.6 A 69-year-old-male with an elevated PSA of 13 underwent MR-guided biopsy of the left peripheral zone. The perfusion MRI showed washout

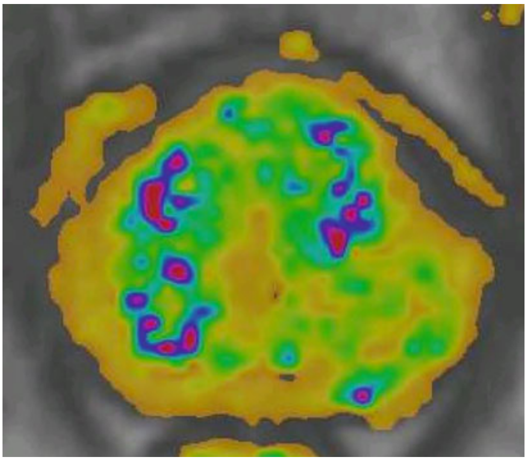

Fig. 10.7 The perfusion images demonstrate symmetric popcorn enhancement and washout in the transition zone. The pathology specimens revealed BPH

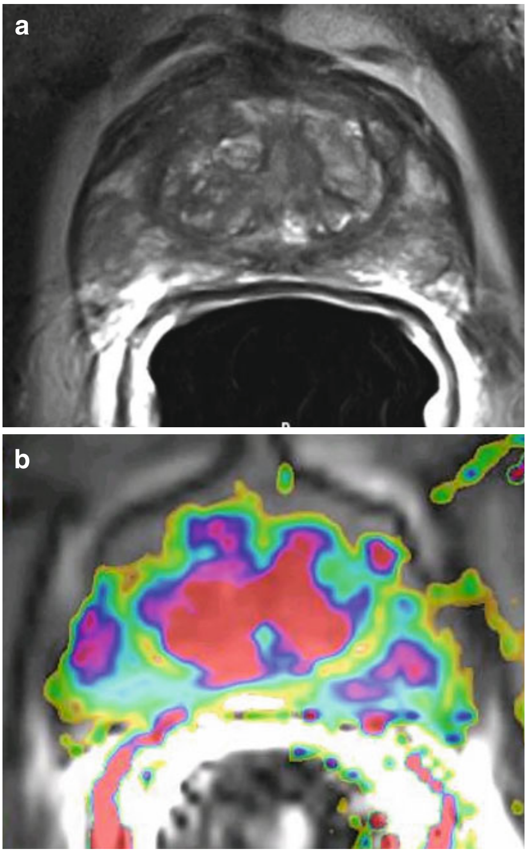

Fig. 10.8 A 73-year-old male with a PSA of 8.9 underwent MR imaging of the prostate and subsequent biopsy. (**a**) The T2-weighted MR image demonstrates triangular areas of low signal intensity and bilateral washout (**b**). Biopsy revealed chronic prostatitis

derived from DWI are related to prostate cancer aggressiveness (Hambrock et al. 2011; Kobus et al. 2011; Vargas et al. 2011; Turkbey et al. 2011). Considerable overlap in ADC values is seen in normal and cancerous tissue. Diffusion-weighted imaging shows differences between prostatitis and prostate cancer in both the peripheral zone and central gland, although its usability in clinical practice is limited as a result of significant overlap in ADCs (Nagel et al. 2013). Magnetic resonance spectroscopic imaging (MRSI) can be used to predict the presence or absence of prostate cancer; however, there is significant overlap in choline + creatine over citrate ratios between benign and malignant tissue. MRSI is performed with a three-dimensional chemical shift imaging technique (Fig. 10.11).

The optimal strength of multiparametric MR imaging is achieved by combining the information obtained with the various techniques. For the detection of prostate cancer with multiparametric MR imaging, areas under the curve of

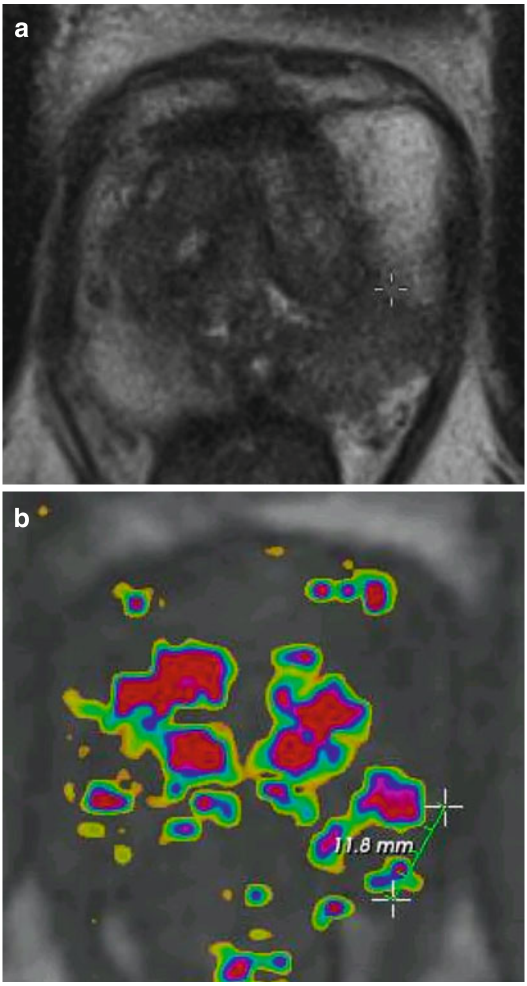

Fig. 10.9 A 61-year-old male with a Gleason 7 tumor in the left peripheral zone. (**a**) The T2-weighted MR images demonstrate a PI-RADS 4 lesion in the left peripheral zone. (**b**) DCE map shows an increased contrast uptake in the left peripheral zone (also note the popcorn enhancement in the transition zone)

0.94–0.98 have been reported (Tanimoto et al. 2007; Chen et al. 2008; Futterer et al. 2006; Langer et al. 2009). Recently, the PI-RADS scale was introduced for structured reporting. MR-guided biopsy is performed in case of a PI-RADS 4 or 5 score (i.e., clinically significant cancer is likely to be present or clinically significant cancer is highly likely to be present, respectively).

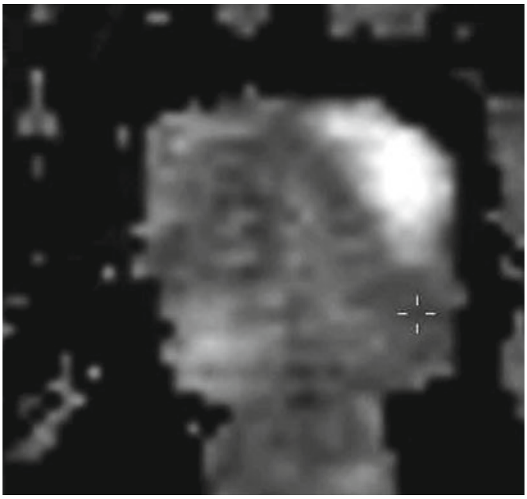

Fig. 10.10 A 61-year-old male with rising PSA and two negative biopsy sessions. The ADC map shows restricted diffusion in the left peripheral zone. MR-guided biopsy revealed a Gleason 7 cancer

10.3 MR-Guided Prostate Biopsy

Currently, the most commonly used transrectal MR-guided prostate biopsy device is a manually adjustable positioning device for needle guide positioning. A needle guide is inserted in the rectum of the patient (Fig. 10.12). Based on the acquired MR images, the needle guide is manually positioned in the direction of the clinical suspicious lesion (Fig. 10.13). In order to manipulate needle guide direction, the patient has to be withdrawn from the scanner bore and positioned inside the scanner bore for imaging. Consequently, the physician repeatedly moves between the scanner room and the control room to adjust needle-guided direction and interpret needle-guided direction on the MR images, respectively. To overcome the human element of interaction, MR-compatible robotic manipulators are being developed. The robotic manipulator needle guide direction is controlled outside the magnet room with real-time MR imaging guidance. Consequently the patient does not need to be continually moved in and out of the magnet bore during the needle guide positioning.

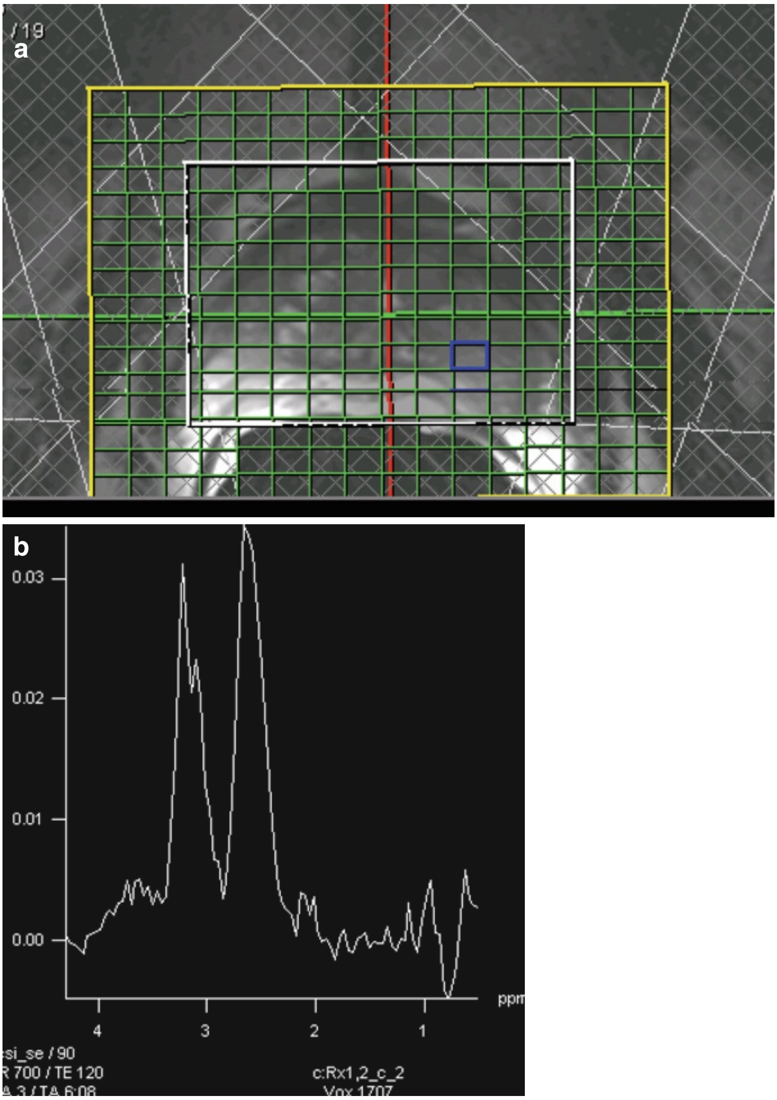

Fig. 10.11 Three-dimensional chemical shift imaging of the prostate. (**a**) A grid with saturation bands around the prostate is superimposed on the T2-weighted axial image. The blue voxel represents a cancerous voxel (**b**) with an increase choline and creatine level and decreased citrate. This is a typical voxel for prostate cancer

A limitation of MR-guided biopsy is that a multiparametric MR imaging and the MR-guided biopsy need to be performed in separate sessions because image postprocessing and exact tumor spatial localization demand time. Another disadvantage is movement of the prostate during the biopsy procedure (Pondman et al. 2008). New developments in the direction of TRUS-MR fusion platforms are currently being explored. Promising results have been reported. In the near future, large lesions (>1 cm) can be targeted using fusion systems. Patients with small lesions or TRUS-MR-negative biopsies can undergo MR-guided prostate biopsy.

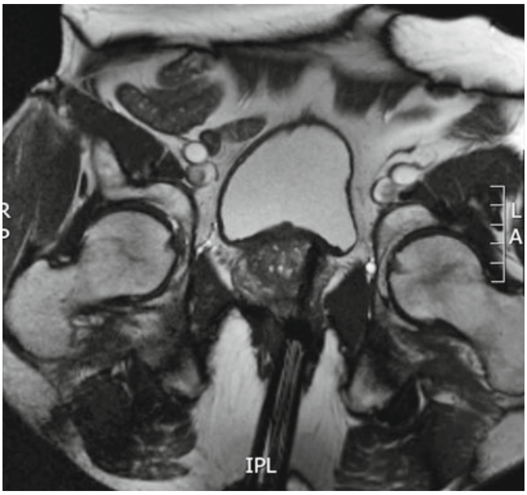

Fig. 10.12 Semi-axial TrueFISP image through the needle guide

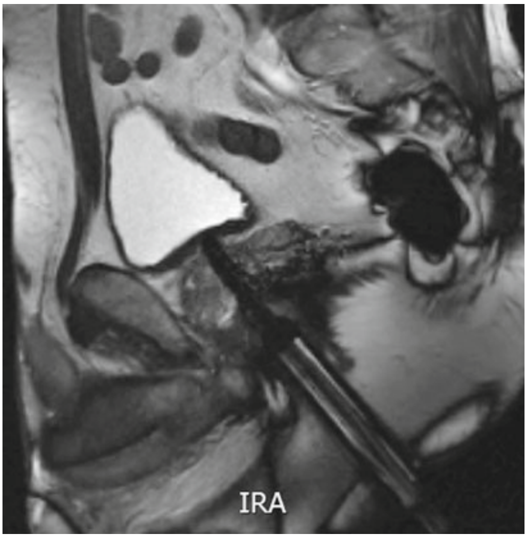

Fig. 10.13 Sagittal TrueFISP image through the needle guide confirming correct positioning

References

Barentsz JO, Richenberg J, Clements R, et al. ESUR prostate MR guidelines 2012. Eur Radiol. 2012;22(4):746–57.

Berglund RK, Masterson TA, Vora KC, et al. Pathological upgrading and up staging with immediate repeat biopsy in patients eligible for active surveillance. J Urol. 2008;180(5):1964–7; discussion 7–8.

Chen M, Dang HD, Wang JY, et al. Prostate cancer detection: comparison of T2-weighted imaging, diffusion-weighted imaging, proton magnetic resonance spectroscopic imaging, and the three techniques combined. Acta Radiol. 2008;49:602–10.

Divrik RT, Eroglu A, Sahin A, et al. Increasing the number of biopsies increases the concordance of Gleason scores of needle biopsies and prostatectomy specimens. Urol Oncol. 2007;25(5):376–82.

Djavan B, Ravery V, Zlotta A, et al. Prospective evaluation of prostate cancer detected on biopsies 1, 2, 3 and 4: when should we stop? J Urol. 2001;166(5):1679–83.

Djavan B, Milani S, Remzi M. Prostate biopsy: who, how and when. An update. Can J Urol. 2005;12:44–8.

Futterer JJ, Heijmink SW, Scheenen TW, et al. Prostate cancer localization with dynamic contrast-enhanced MR imaging and proton MR spectroscopic imaging. Radiology. 2006;241:449–58.

Hambrock T, Somford DM, Huisman HJ, et al. Relationship between apparent diffusion coefficients at 3.0-T MR imaging and Gleason grade in peripheral zone prostate cancer. Radiology. 2011;259:453–61.

Hoeks CMA, Barentsz JO, Hambrock T, et al. Prostate cancer: multiparametric MR imaging for detection, localization, and staging. Radiology. 2011;261:46–66.

Kobus T, Hambrock T, Hulsbergen-van de Kaa CA, et al. In vivo assessment of prostate cancer aggressiveness using magnetic resonance spectroscopic imaging at 3 T with an endorectal coil. Eur Urol. 2011;60:1074–80.

Kvale R, Moller B, Wahlqvist R, et al. Concordance between Gleason scores of needle biopsies and radical prostatectomy specimens: a population-based study. BJU Int. 2009;103(12):1647–54.

Langer DL, Van der Kwast TH, Evans AJ, Trachtenberg J, Wilson BC, Haider MA. Prostate cancer detection with multi-parametric MRI: logistic regression analysis of quantitative T2, diffusion-weighted imaging, and dynamic contrast-enhanced MRI. J Magn Reson Imaging. 2009;30:327–34.

Lattouf JB, Saad F. Gleason score on biopsy: is it reliable for predicting the final grade on pathology? BJU Int. 2002;90(7):694–8.

Lujan M, Paez A, Santonja C, et al. Prostate cancer detection and tumor characteristics in men with multiple biopsy sessions. Prostate Cancer Prostatic Dis. 2004;7:238–42.

Nagel KN, Schouten MG, Hambrock T, et al. Differentiation of prostatitis and prostate cancer by using diffusion-weighted MR imaging and MR-guided biopsy at 3 T. Radiology. 2013;267(1):164–72.

Pondman KM, Fütterer JJ, ten Haken B, et al. MR-guided biopsy of the prostate: an overview of techniques and a systematic review. Eur Urol. 2008;54(3):517–27.

Roehl KA, Antenor JA, Catalona WJ. Serial biopsy results in prostate cancer screening study. J Urol. 2002; 167(6):2435–9.

Schroder FH, van der Maas P, Beemsterboer P, et al. Evaluation of the digital rectal examination as a screening test for prostate cancer. Rotterdam section of the European Randomized Study of Screening for Prostate Cancer. J Natl Cancer Inst. 1998;90(23): 1817–23.

Schroder FH, Carter HB, Wolters T, et al. Early detection of prostate cancer in 2007. Part 1: PSA and PSA kinetics. Eur Urol. 2008;53(3):468–77.

Siegel R, Naishadham D, Jemal A. Cancer statistics, 2013. CA Cancer J Clin. 2013;63:11–30.

Tanimoto A, Nakashima J, Kohno H, Shinmoto H, Kuribayashi S. Prostate cancer screening: the clinical value of diffusion-weighted imaging and dynamic MR imaging in combination with T2-weighted imaging. J Magn Reson Imaging. 2007;25:146–52.

Turkbey B, Shah VP, Pang Y, et al. Is apparent diffusion coefficient associated with clinical risk scores for prostate cancers that are visible on 3-T MR images? Radiology. 2011;258(2):488–95.

Vargas HA, Akin O, Franiel T, et al. Diffusion-weighted endorectal MR imaging at 3 T for prostate cancer: tumor detection and assessment of aggressiveness. Radiology. 2011;259:775–84.

11

MRI-Ultrasound Fusion Imaging

Dan Sperling

11.1 Background and Motivation

The sheer number of images being acquired daily by clinicians such as radiologists is staggering. These include magnetic resonance imaging (MRI), transrectal ultrasound (TRUS), and computerized tomography (CT) to name a few. Frequently, multiple imaging sequences are acquired from the same patient. In the case of MRI, multiple different parameters are acquired in the same scanning session, resulting in a plethora of images acquired within minutes of each other. Each type of imaging sequence may contain orthogonal information. For example, a T2-weighted MRI contains structural information, while dynamic contrast-enhanced (DCE) MRI contains the rate of contrast dye uptake by various vascularized regions within the body.

The amount of imaging information being acquired opens up an exciting possibility for doctors, as information from multiple sources can be used to make a more informed diagnostic or treatment decision. For example, a prostate tumor may not be clearly visible on T2-weighted MRI and yet can appear vivid on an apparent diffusion coefficient (ADC) MRI image.

However, a problem arises in that the various images are not necessarily spatially aligned. To make an informed decision as to whether a tumor is visible in a certain region of the prostate, the corresponding region must be realized on all the images (Fig. 11.1). The process of bringing multiple images (from the same patient or different patients) into spatial alignment is the task known as "registration" and is performed with the help of sophisticated computer vision algorithms.

Fig. 11.1a ADC MRI	Fig. 11.1b DCE MRI
Fig. 11.1c T1-weighted MRI	Fig. 11.1d T2-weighted MRI
Fig. 11.1e Registered result	

For multiparametric MRI, an accurate registration can allow the clinician to make a more informed diagnosis, but the result of image registration is not limited to diagnosis. The following sections discuss the current state-of-the-art computerized registration algorithms, specifically in how they relate to medical imagery.

D. Sperling, MD
Sperling Prostate Center, Alpha 3T MRI,
145 E. 32nd St., New York, NY 10016, USA
e-mail: dan.sperling@sperlingmedical.com

R.L. Bard et al. (eds.), *Image Guided Prostate Cancer Treatments*,
DOI 10.1007/978-3-642-40429-0_11, © Springer-Verlag Berlin Heidelberg 2014

11.2 Clinical Advantages of MRI-Ultrasound Fusion Images

MRI offers significant diagnostic capabilities, and prostate cancer can frequently be detected using MRI (Turkbey and Choyke 2012). In addition, there is evidence that MRI can even be used to stage the aggressiveness of prostate cancer by being correlated with Gleason scores (Turkbey and Choyke 2012; Rastinehad et al. 2011; Rais-Bahrami et al. 2013).

However, when performing prostate biopsies for detecting cancer, an ultrasound image is utilized and is the current clinical standard due to its cost, ease of use, and widespread use by urologists. However, it is rife with problems such as low spatial resolution, ultrasound artifacts, and extremely low signal-to-noise ratio.

MRI-TRUS fusion devices aim to overcome these issues by utilizing MRI to target the lesion and incorporating this information with a TRUS biopsy to yield more precise biopsies (Pinto et al. 2011; Sonn et al. 2013; Natarajan et al. 2011; Zogal

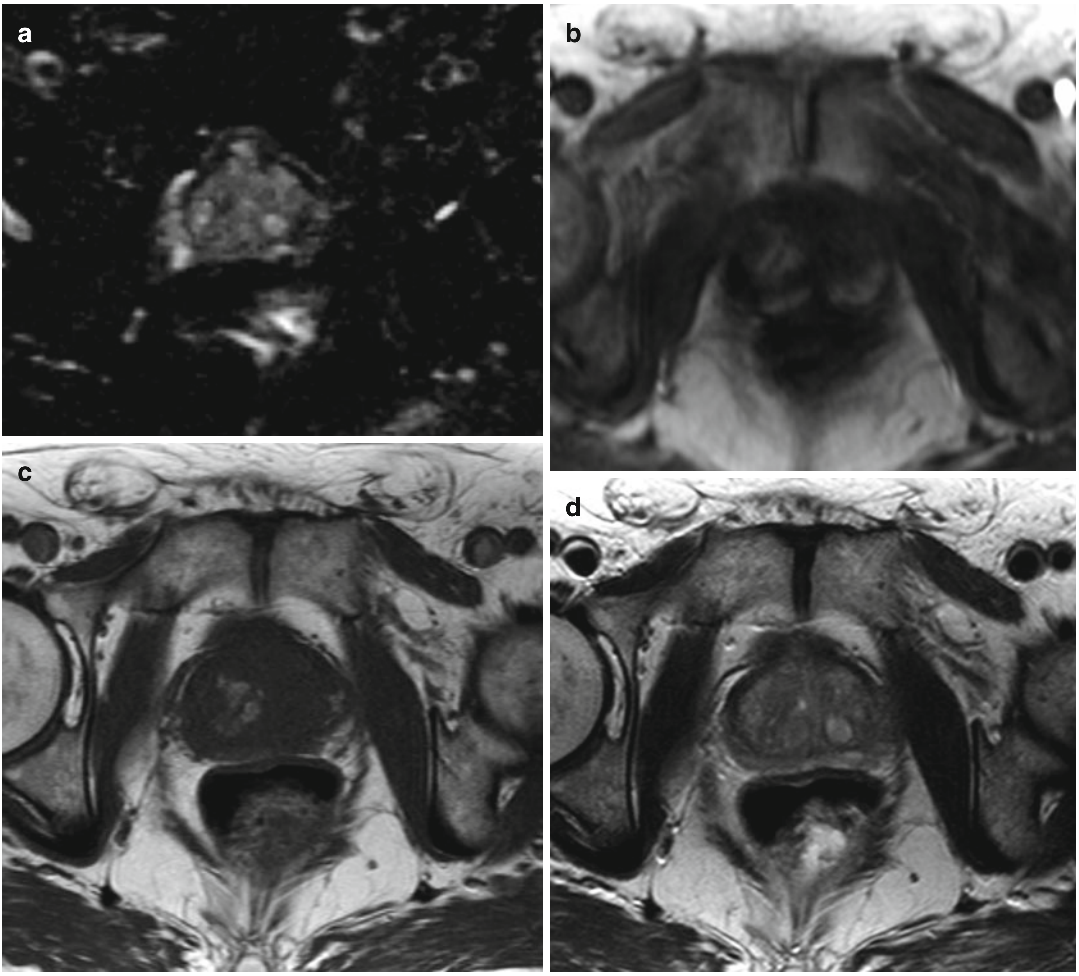

Fig. 11.1 Various MRI images (**a**–**d**) are acquired for a single patient. A computer registration algorithm brings these various images into spatial alignment (**e**), so orthogonal information from the various parameters can be used simultaneously to make an informed diagnosis

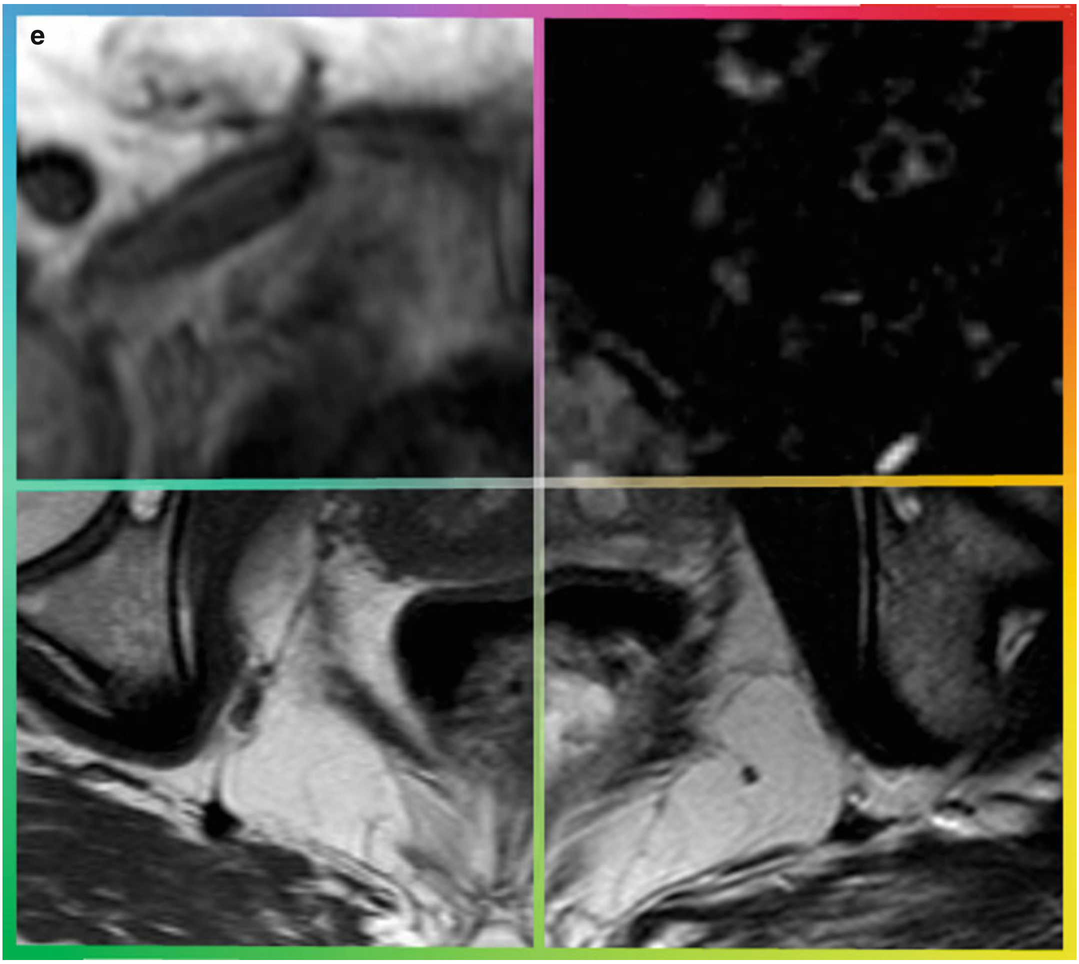

Fig. 11.1 (continued)

et al. 2011; Ukimura et al. 2012; Fiard et al. 2013; Marks et al. 2013). When performing a TRUS biopsy, a fusion system may wish to overlay the MRI information on top of the TRUS image, to help guide the biopsy. This requires that the MRI image be registered live with the TRUS image (Fig. 11.2).

Once the MRI and TRUS images are fused via image registration, a urologist can use the information derived from the MRI (such as the tumor outlined by an experienced radiologist) and guide the biopsy needle to that precise region within the prostate (Pinto et al. 2011; Sonn et al. 2013; Natarajan et al. 2011; Zogal et al. 2011; Ukimura et al. 2012; Fiard et al. 2013; Marks et al. 2013).

11.3 Devices That Offer MRI-TRUS Fusion

There are several examples of commercial systems for MRI-TRUS fusion and prostate biopsy guidance, some of which employ computerized registration algorithms, outlined below.

- *BiopSee*®: This device can only be used for transperineal biopsies. It has reported a guidance accuracy of 1.7 mm (Zogal et al. 2011), although explicit MRI-TRUS registration accuracy is not reported. The probe automatically rotates to the next target, but the needle guide requires manual adjustments.

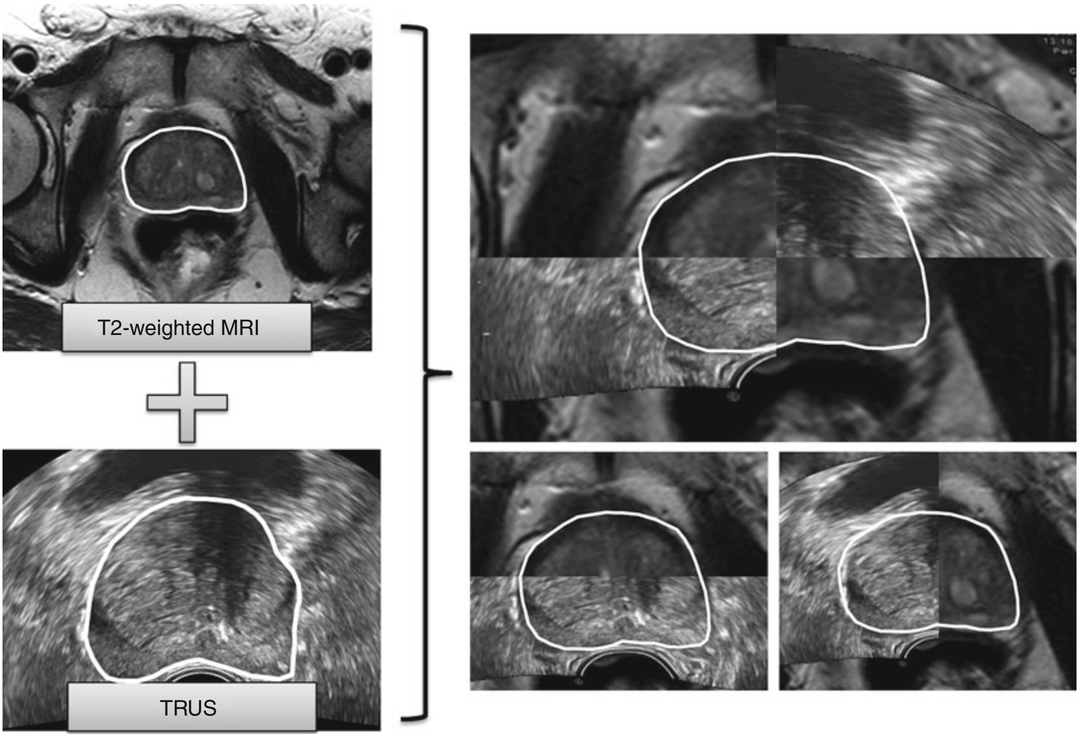

Fig. 11.2 A computerized registration algorithm brings a prostate MRI image in spatial alignment with a transrectal ultrasound (TRUS) image, which is necessary for guided biopsies

- *GeoScan BioJet*™: This system is relatively inexpensive, yet is also limited to transperineal biopsies and not compatible with many ultrasound systems. As of July 2013, the guidance and fusion accuracies are not reported and clinical validation is still required.
- *UC-Care Navigo*™: This system is relatively inexpensive, although it is compatible with only a few ultrasound systems. While it is an image-guided biopsy system with the ability to integrate pathology lab findings, it currently offers no MRI fusion capabilities.
- *Biobot Mona Lisa*: This is a robotic 3D prostate biopsy system with an accuracy guidance within 1.5 mm. However, it is limited to transperineal biopsies, offers no MRI fusion, and is currently awaiting regulatory approval.
- *Koelis Urostation*: This is a software system which attaches to an existing ultrasound machine. It uses image registration to track, via computer algorithms, the location of the probe within the prostate. MRI fusion targeting accuracy was reported to be 84 % in phantoms (Ukimura et al. 2012). Initial feasibility studies (with 20 cases) show a 91 % sensitivity to significant cancer (Fiard et al. 2013), although systematic clinical validation is still required.
- *In vivo UroNav*: This system from In Vivo/Philips offers MRI-TRUS fusion and has an easy to use freehand transducer for tracking. It was found to have approximately a 90 % detection rate for highly suspicious targets on MRI (Pinto et al. 2011). The system utilizes a rigid registration technique (no deformable registration, see Sect. 11.5) and is costlier than several other comparable systems, although it has been extensively clinically validated at the NCI.
- *Eigen Artemis*: This system from Eigen was the first commercial MRI fusion-guided biopsy system. It utilizes both rigid and non-rigid registration algorithms (see Sect. 11.5) and uses a robotic arm to hold and maneuver

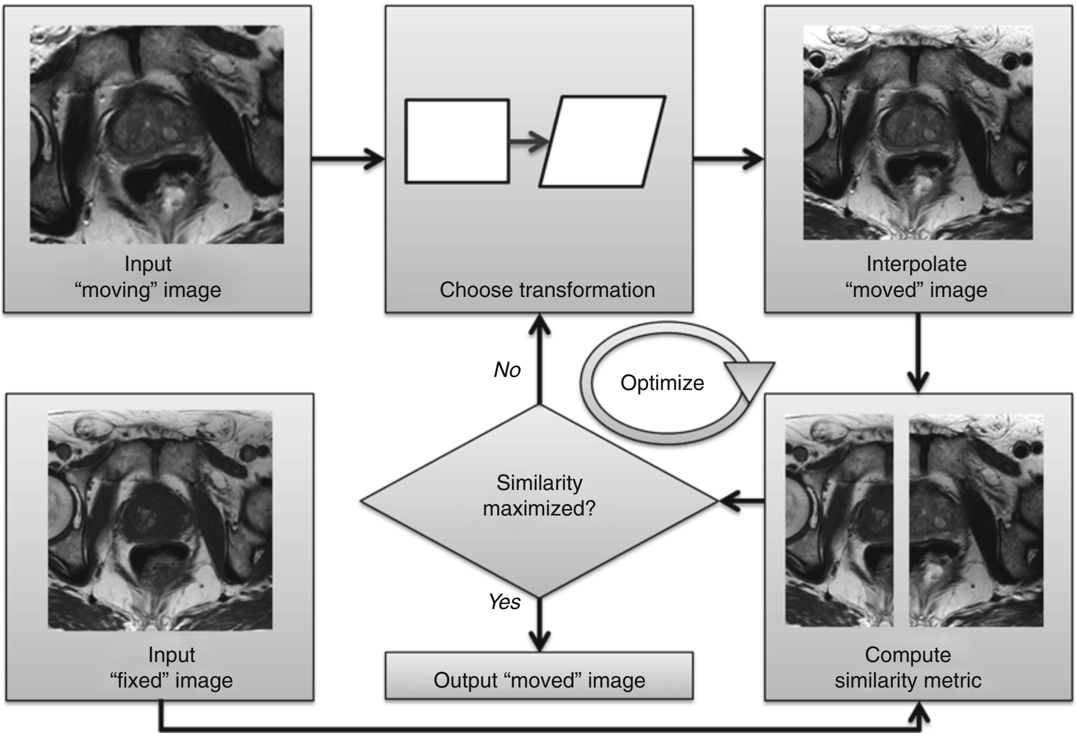

Fig. 11.3 Computerized registration workflow. A “moving” image is transformed until a similarity with a “fixed,” reference image is maximized

the transducer to the target. It has validated in a number of clinical studies (Sonn et al. 2013; Natarajan et al. 2011; Marks et al. 2013) and is approximately two to three times more sensitive for detecting prostate cancer compared to traditional biopsies.

- *MIMviewer*®: This software package from MIM Software, Inc. offers TRUS-MRI fusion by plugging into existing ultrasound systems’ video feeds and performing software-based registration. It is significantly less costly than alternative devices since it does not require a new dedicated fusion ultrasound machine to be purchased.

11.4 Registration Overview

As stated previously, registration is the process of bringing multiple images into spatial alignment. The images are typically either 2D or 3D, although 4D time-series data is sometimes available. The goal of any registration algorithm is to determine a transformation which best aligns the images. This transformation can be as simple as translating the image (moving up/down or left/right) or as sophisticated as warping certain spots within the images (called “deformable registration”).

A computer algorithm essentially tries various transformations and finds the “optimal” one which best aligns the images. The workflow of a registration algorithm is illustrated in Fig. 11.3. There is always a reference “fixed” image which does not move, and a “moving” image, to which the transformations are applied. Various transformations are tried, and an “interpolator” generates a “moved” image for each of those transformations. The “moved” image which most closely matches the “fixed” image is chosen (via the use of an “optimizer”) and output. The following sections describe each of these processes in detail.

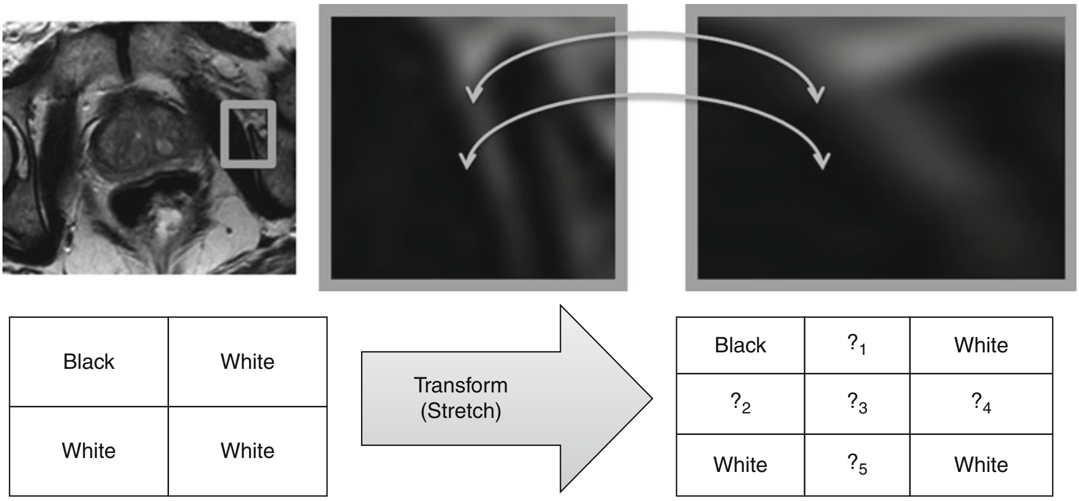

Black	White
White	White

Black	$?_1$	White
$?_2$	$?_3$	$?_4$
White	$?_5$	White

Fig. 11.4 An interpolator is used to decide what colors to make pixels in the new image, based on the transformation, and the color of nearby pixels. Essentially the goal is to fill in the "?'s" in the above

11.5 Transformations

A transformation is an integral component to any registration algorithm. It defines how to move, or deform, a given image. The two general categories of transformations are "linear" and "deformable" transformations.

A linear transformation is any translation, rotation, scaling, or shearing which is applied to the image as a whole. Figure 11.3 represents a linear transformation applied to a rectangle, creating a sheared rectangle. A transformation which only allows translation and rotation is considered "rigid." When incorporating scaling and shearing, the transformation is considered "affine." Rigid registration was used to fuse MRI and CT prostate images in Greene et al. (2009).

A deformable registration allows warping of an image at specific locations. Essentially, in its most general form, every single pixel (or tiny location within the image with an intensity value) is allowed to move anywhere else in the image. There are various types of deformable transformations including B-splines, thin plate splines, and finite element model transformations. Examples of algorithms which use splines to register prostate images can be found in Ogura and Mitra (Ogura et al. 2009; Mitra et al. 2012). Examples of algorithms which use finite element models to register prostate images can be found in Chi et al. (2006), Boubaker et al. (2009), Hensel et al. (2007), and Brock et al. (2008).

Whether using a linear or deformable registration, a series of numbers is used to represent the given transformation. In the case of linear transformations, these numbers may represent the amount to translate the image (in mm) or the magnitude of rotation (in degrees). In the case of deformable registration, these numbers may represent how certain regions of the image should warp relative to other regions.

11.6 Interpolators

A given transformation is defined by a set of numbers, and an interpolator uses those numbers to generate a "moved" image (Fei et al. 2003). When stretching the image, for example, you do not want "holes" or "tears" to appear in the moved image. As such, the computer algorithm needs to decide how to stretch two adjacent regions of the image and how to deal with regions which lie between two pixels or result from stretching a pixel.

An example is shown in Fig. 11.4, in which a transformation attempts to stretch a part of an image. The goal of the interpolator is to fill in the question marks with the correct colors.

The following are the most common interpolators:

- *Nearest neighbor*: The "nearest-neighbor" interpolator is the simplest (and fastest) interpolator, in which the closest point on the moving image is chosen when deforming the image (Fei et al. 2003). In the example in Fig. 11.4, a nearest-neighbor interpolator could choose either "white" or "black" for the question marks "$?_1$, $?_2$, $?_3$" and would choose "white" for question marks "$?_4$, $?_5$" since only white pixels surround them.
- *Linear*: The "linear" interpolator uses a linear blending of nearby pixel values to decide the color (Fei et al. 2003). In the example in Fig. 11.4, "$?_4$ and $?_5$" would be white, "$?_1$ and $?_2$" would be mid-grey, and "$?_3$" would be a light grey.
- *Spline*: A "spline" interpolator, similar to a linear interpolator, performs a blending of nearby pixel values. However, it fits a curve to the pixels and uses that to decide "how grey" to make the interpolated pixels. A spline interpolator may consider not just neighboring pixels but also pixels a few mm away to make a more informed decision of the color. This interpolator typically takes much longer to compute than a linear interpolator, and may not necessarily yield a more accurate interpolation.

There are more sophisticated interpolators, but a tradeoff between computational time and accuracy leads most algorithms to employ a linear interpolator, as the marginal benefit of sophisticated interpolators rarely lead to a significant increase in registration accuracy.

11.7 Metrics

After interpolating a "moved" image (see Fig. 11.4), the algorithm then needs to compare this to the reference "fixed" image. This is done using a similarity metric, which yields a large number in the case of high similarity and a low number in the case of a low similarity. This similarity is used to evaluate the correctness of a transform in registering the images. There are a plethora of similarity measures which could be employed, and merits and issues with each. The most common ones in use for image registration are outlined below (Xu et al. 2008; Zhang et al. 2011; Wells et al. 1996; Maes et al. 1997; Viola and Wells 1997), although additional, more sophisticated measures have been developed for prostate registration (e.g., Chappelow et al. 2011).

- *Intensity differences*: The differences in image intensity values are computed and summed over the entire image or a region of the image (Xu et al. 2008). For example, black may be given a value of 0, and white may be given a value of 1. If two pixels are spatially aligned and both have a value of white, then the difference could be 0. The algorithm typically will sum the absolute differences over all the pixels to output a final value and negate that value (since we want to maximize, not minimize, the similarity). A value of 0 would indicate a perfectly spatially aligned image, and a large negative value would indicate an extremely dissimilar pair of images.
- *Normalized cross correlation* (*NCC*): Using intensity differences is subject to various imaging artifacts such as changes in brightness and contrast which could throw off the accuracy of the measure. In addition, one image may represent black with a value of 0, while another image may represent black with a value of 50, and as such the intensity differences may not be an accurate measure. The NCC between two images is a normalized measure calculated by fitting a line through a collection of pixel values in two images (Zhang et al. 2011). Essentially if one image had intensity values of $\{20, 30, 40\}$ at 3 pixels and a second image had intensity values of $\{80, 90, 100\}$ at those same 3 pixels, that would be considered perfectly aligned. This is mathematically similar to the intensity differences but less prone to artifacts such as brightness and contrast.
- *Mutual Information* (*MI*): MI is a more sophisticated measure derived from information theory (Wells et al. 1996; Maes et al. 1997; Viola and Wells 1997). It essentially models how well the intensity values in one image can "predict" the intensity values in another image. MI quantifies

the information content shared between two images, such that two images which share a lot of “information” get a high value (such as two prostate images from the same patient) and two images which share no information (such as a prostate and breast image) get a low value.

11.8 Optimizers

As shown in Fig. 11.4, after computing the similarity of the moved and fixed images and calculating the accuracy of the given transformation via the similarity metric, the algorithm must decide whether to try another transformation or output the result.

The role of the optimizer is to (a) decide when the transformation is “good enough” and (b) decide what new transformation to try next. There are many different types of optimizers, and optimization is an area of active research. A few common optimizers employed in image registration are described below (Holia and Thaker 2009; Salvi et al. 2007; Maintz and Viergever 1998; Wachowiak et al. 2004):

- *Simplex*: A simplex optimizer (Holia and Thaker 2009) takes the previous transformation and slightly modifies it based on the magnitude of the similarity error. It is one of the simplest optimizers, and may be useful in honing in on a transformation, but may not perform well in choosing an initial transformation.
- *Genetic algorithm* (*GA*): A GA optimizer for image registration (Salvi et al. 2007; Maintz and Viergever 1998) considers each transformation as an “individual” in a population. It decides the relative “fitness” of each individual by the image similarity. Individuals (i.e., transformations) with low image similarity have a higher chance of dying out. Individuals with a high image similarity will mate and evolve over several generations. The underlying hypothesis is that only the fittest individuals (i.e., transformations with high image similarities) will remain after several generations.
- *Particle swarm*: A particle swarm optimizer for image registration (Wachowiak et al. 2004) considers each transformation as a particle in space. A collection of particles represent various transformations and will have velocities proportional to their image similarities and ideally converge on the optimal transformation.

Several common problems with optimizers is that (a) they may require a lot of parameters to tune, (b) may not necessarily know when to stop, and (c) can take a significant amount of computational time to arrive at a solution. This last issue is extremely important when one needs real-time registration, as in the case of MRI-TRUS fusion biopsy. Current research is attempting to address these issues in terms of both algorithmic improvements and properly utilizing increases in computational power.

11.9 Concluding Remarks and Future Directions

Overall, the task of computerized registration for medical image fusion is a nontrivial task which has gained much traction in the computer vision community over the past several decades. Yet it is still very much an unsolved problem, and significant research is still required.

A problem arises when one wishes to (a) evaluate registration accuracy and (b) decide if an algorithm is “good enough.” To evaluate registration, one may wish to use manual fiducials identified within the image and evaluate the displacement, determine the overlap of the objects of interest, or determine how well an algorithm performed in a specific task, such as accurately sampling a tumor in the case of MRI-TRUS fusion biopsies.

In terms of commercial systems, “good enough” may also require one to take into account cost of development and the speed of the system. A real-time registration algorithm which has an error of 3 mm may be sufficient to consistently sample a tumor in terms of a biopsy and may be considered “better” than an algorithm which takes 1 h yet has an error of 1 mm.

It truly depends on one’s goal for the registration algorithm, and in the future many more fusion systems will likely employ more sophisticated and advanced registration algorithms.

References

Boubaker M, Haboussi M, et al. Finite element simulation of interactions between pelvic organs: predictive model of the prostate motion in the context of radiotherapy. J Biomech. 2009;42:1862–8.

Brock K, Nichol A, et al. Accuracy and sensitivity of finite element model-based deformable registration of the prostate. Med Phys. 2008;35(9):4019–25.

Chappelow J, Bloch BN, et al. Elastic registration of multimodal prostate MRI and histology via multiattribute combined mutual information. Med Phys. 2011;38(4): 2005–18.

Chi Y, Liang J, Yan D. A material sensitivity study on the accuracy of deformable organ registration using linear biomechanical models. Med Phys. 2006;33(2): 421–33.

Fei B, Lee Z, et al. Image registration for interventional MRI guided procedures: Interpolation methods, similarity measurements, and applications to the prostate. In: Biomedical image registration. Berlin/Heidelberg: Springer; 2003. p. 321–9.

Fiard G, Hohn N, et al. Targeted MRI-guided prostate biopsies for the detection of prostate cancer: initial clinical experience with real-time 3-dimensional transrectal ultrasound guidance and magnetic resonance/transrectal ultrasound image fusion. J Urol. 2013;81(6):1372–8.

Greene W, Chelikani S, et al. Constrained non-rigid registration for use in image-guided adaptive radiotherapy. Med Image Anal. 2009;13:809–17.

Hensel J, Menard C, et al. Development of multiorgan finite element-based prostate deformation model enabling registration of endorectal coil magnetic resonance imaging for radiotherapy planning. Int J Radiat Oncol Biol Phys. 2007;68(5):1522–8.

Holia M, Thaker V. Image registration for recovering affine transformation using Nelder Mead Simplex method for optimization. Int J Image Process. 2009;3(5):218–29.

Maes F, Collignon A, et al. Multimodality image registration by maximization of mutual information. IEEE Trans Med Imaging. 1997;16(2):187–98.

Maintz JBA, Viergever MA. A survey of medical image registration. Med Image Anal. 1998;2(1):1–36.

Marks L, Young S, Natarajan S. MRI-ultrasound fusion or guidance of targeted prostate biopsy. Curr Opin Urol. 2013;23(1):43–50.

Mitra J, Martí R, et al. Prostate multimodality image registration based on B-splines and quadrature local energy. Int J Comput Assist Radiol Surg. 2012;7(3):445–54.

Natarajan S, Marks LS, et al. Clinical application of a 3D ultrasound-guided prostate biopsy system. Urol Oncol. 2011;29(3):334–42.

Ogura S, Tokuda J, et al. MRI signal intensity based B-spline nonrigid registration for pre- and intraoperative imaging during prostate brachytherapy. J Magn Reson Imaging. 2009;30(5):1052–8.

Pinto P, Chung PH, et al. Magnetic resonance imaging/ultrasound fusion guided prostate biopsy improves cancer detection following transrectal ultrasound biopsy and correlates with multiparametric magnetic resonance imaging. J Urol. 2011;186(4):1281–5.

Rais-Bahrami S, Siddiqui M, et al. Utility of multiparametric MRI suspicion levels in detecting prostate cancer. J Urol. 2013. doi:10.1016/j.uro.2013.05.052.

Rastinehad A, Baccala AA, et al. D'Amico risk stratification correlates with degree of suspicion of prostate cancer on multiparametric magnetic resonance imaging. J Urol. 2011;185(3):815–20.

Salvi J, Matabosch C, et al. A review of recent range image registration methods with accuracy evaluation. Image Vision Comput. 2007;25(5):578–96.

Sonn GA, Chang E, et al. Value of targeted prostate biopsy using magnetic resonance–ultrasound fusion in men with prior negative biopsy and elevated prostate-specific antigen. Euro Urol. 2013. doi:10.1016/j.eururo.2013.03.025.

Turkbey P, Choyke PL. Multiparametric MRI and prostate cancer diagnosis and risk stratification. Curr Opin Urol. 2012;22(4):310–5.

Ukimura O, Desai MM, et al. 3-dimensional elastic registration system of prostate biopsy location by real-time 3-dimensional transrectal ultrasound guidance with magnetic resonance/transrectal ultrasound image fusion. J Urol. 2012;187(3):1080–6.

Viola P, Wells III WM. Alignment by maximization of mutual information. Int J Computer Vision. 1997; 24(2):137–54.

Wachowiak M, Smolikova R, et al. An approach to multimodal biomedical image registration utilizing particle swarm optimization. IEEE Trans Evol Comput. 2004;8(3):289–301.

Wells III W, Viola P, et al. Multi-modal volume registration by maximization of mutual information. Med Image Anal. 1996;1(1):35–51.

Xu S, Kruecker J, et al. Real-time MRI-TRUS fusion for guidance of targeted prostate biopsies. Comput Aided Surg. 2008;13(5):255–64.

Zhang B, Arola DD, et al. Three-dimensional elastic image registration based on strain energy minimization: application to prostate magnetic resonance imaging. J Digit Imaging. 2011;24(4):573–85.

Zogal P, Sakas E, et al. BiopSee® – transperineal stereotactic navigated prostate biopsy. J Contemp Brachyther. 2011;3(2):91–5.

Part II

Clinical Applications

12

Clinical Applications of Ultrasound, Doppler Ultrasound, MRI, and DCE-MRI

Robert L. Bard

12.1 Multimodality Imaging

Screening for prostate cancer with DRE and PSA has met with controversy the past two decades. The 2008 position statement of the American College of Preventive Medicine concludes: "…there is insufficient evidence to recommend routine population screening with DRE or PSA" (Lim and Sherin 2008).

Medical imaging with high-resolution ultrasound, elastography, contrast-enhanced ultrasound (CEUS), and spectral, power, or color Doppler has proved clinically useful. 3D sonography differentiates between cancer and inflammation in documenting the capsular effacement/penetration that occurs with malignant tumors. The combination of ultrasound technologies with MRI sequences is called multimodality imaging and provides the highest accuracy.

Tumors may show up better in one plane on both ultrasound and MRI. Some lesions are delineated much better on one modality than the other. Optimally, the same imager performs and interprets all studies sequentially the same day. The imaging group conferring on the multiple exams will reach a diagnostic conclusion and suggest other examinations, such as targeted biopsy, bone scan, or whole-body diffusion imaging as a next step.

As with many imaging modalities, the early use of MRI to detect prostate cancer was met with initial euphoria (Schnall et al. 1991) followed by wise reticence. Dr. F. May (May et al. 2001) stated "treatment should not be altered based on endorectal coil (EC) MRI findings." Presentations of dynamic contrast-enhanced (DCE) MRI showed improved results for diagnosis of local disease and extension of tumor for staging purposes. Difficulties in grayscale perception of abnormalities led to the introduction of computer-aided diagnosis with colorized representations of malignant findings that significantly improved detection of major pathologies with subtle imaging features imperceptible to the human eye.

12.1.1 Current Clinical MRI Techniques

Following is a brief presentation of current clinical MRI techniques, including dynamic contrast-enhanced (DCE-MRI) and spectroscopic (MRS or S-MRI) with their respective advantages and disadvantages (Bard 2009):

Standard MRI at 1.5 Tesla

(a) T1-weighted in axial plane with 4 mm slices with large field of view (FOV).
(b) T1-weighted is necessary to detect hemorrhage in the prostate bed which will appear as a signal loss on T2.
(c) T2-weighted in 3 planes with thickness 2.5–4.0 mm with small FOV.

R.L. Bard, MD
Bard Cancer Center, Biofoundation for Angiogenesis
Research and Development, 121 E. 60th St,
New York, NY 10022, USA
e-mail: rbard@cancerscan.com

R.L. Bard et al. (eds.), *Image Guided Prostate Cancer Treatments*,
DOI 10.1007/978-3-642-40429-0_12, © Springer-Verlag Berlin Heidelberg 2014

(d) T2-weighted shows tumor as signal loss; however, false positives occur in hemorrhage, calcification, fibrosis (postinflammatory, postoperative, post-hormonal (ADT), post-radiation or post-thermal ablation treatment), and inflammation. False negatives occur in the presence of infiltrating non-focal tumors and benign hyperplasia. While some tumors (20 %) are not visible, cancer may be differentiated from prostatitis by focality of signal loss and distinctness of border. Small tumors (less than 0.5 cc) are not imaged and transitional zone tumor is difficult to distinguish from benign hyperplasia.

Extracapsular extension is denoted by focal growth beyond the capsule infiltration of the periprostatic fat and asymmetry of the neurovascular bundles. Seminal vesicle invasion is detected as enlargement and loss of signal.

DWI-MRI

DWI-MRI uses diffusion-weighted imaging analysis of Brownian movement of water. Apparent diffusion coefficient (ADC) is a variation of this sequence. Initial results were mixed in its application to prostate disorders. This older technology was replaced by DCE-MRI imaging and recently has been refined to add significant information on anterior tumor verification and correlate with tumor grade. Recent improvements have made this a useful indicator of tumor in the presence of inflammatory disease.

DWI-MRI including whole-body DWI will be addressed fully in other chapters.

EC-MRI

EC-MRI uses an endorectal receiver coil which improves the signal-to-noise ratio and spatial resolution. However, patient discomfort and deformation of the prostate alter the information gathered. Also, motion artifacts due to the E-coil (patient or bowel) may increase.

MR Spectroscopy

MR spectroscopy (MRS) measures the in vivo levels of the metabolites citrate, creatine, and choline. Cancer has high choline content. The large sample field means small tumors will not be sampled and thus missed in the final data. It is inoperative in the fat limiting the potential diagnosis of extracapsular extension. Inflammation and posttreatment artifact produce false positives. Users at the *Journees Francaises de Radiologie* (JFR) 2007 reported an overall specificity of 44 %.

3 Tesla MRI (3 T MRI)

Higher field strength of 3 T MRI improves signal to noise as well as spatial resolution and may decrease imaging time and allow for imaging without an EC coil. However, increased magnetic and chemical artifacts and lack of signal detection from tissue distant from the E-coil antennae may limit the accuracy. High magnetic field strength may pose danger to patients with metallic devices. Indeed, patients with unrecalled ophthalmic injuries or postoperative metallic implants are forced to stop the high field exam due to pain in the affected area. Special 1.5 T protocols are often as accurate as 3.0 T images with the possible exception of the posterior prostatic capsule and rectal wall. However, this region is well visualized by 18 MHz sonography.

12.1.2 Perfusion or DCE-MRI

DCE-MRI uses intravenously injected Gadolinium chelate contrast which has few side effects and the presence of intravenous flow reduces patient movement. Tumor angiogenesis induces immature blood vessels that are both heterogeneous and leaky. These characteristics can be demonstrated by measuring the perfusion parameters with MRI with T1-weighted dynamic imaging.

Signal enhancement with time is measured qualitatively and quantitatively. Visually on T1-weighted imaged, this appears as increased white on the dark background. Many variables include time of appearance of enhancement (enhancement delay), time to peak, slope of enhancement, intensity of peak, and washout.

Pharmacokinetic parameters are permeability surface area product per unit volume of tissue, lesion leakage space (extravascular-extracellular space per unit volume of tissue), contrast exchange rate, etc. Acquisition time should be 10–30 s. There has been no consensus in use of protocol and trials with whole mount pathology have been designed to correlate imaging findings with tumor volume and aggression. Standard DCE-MRI has limited resolution but most vascular homogeneous tumor nodules enhance early and discretely.

Perfusion can also be assessed without injecting a contrast agent using arterial spin labeling techniques, diffusion MRI, or BOLD (blood oxygen level-dependent) MRI. However, these latter methods are limited by a low signal-to-noise ratio and problems with quantification.

The main indication for perfusion MRI is assessment of antiangiogenic and antivascular treatments (Huward et al. 2007) since the blood flow of a successfully treated tumor decreases before the morphology and size changes. While it may take 6–12 weeks for PSA to drop below 1 ng/mg, hyperemia reduction may be observed immediately post thermal treatments and within days with other therapies. Tumor recurrence in a treated gland is often missed with MRI without contrast enhancement due to the overall signal loss directly related to the tissue changes of the therapeutic modality.

DCE-MRI was developed to improve on the limitations of MRS and standard DCE-MRI by affording better visual conspicuity and more useful pharmacokinetic data. Also called “cartographic” MRI, this modality has increased the yield of positive biopsies, improved staging, and facilitated success of image-guided therapies, as presented by Rouviere et al. during the 2007 *Journees Francaises de Radiologie*. The Harvard Medical School team reported 96 % accuracy with this technology at the 2007 NY Roentgen Ray Meeting at the NY Academy of Medicine. While lymph node metastases are best diagnosed by Combidex lymph node MRI (LNMRI), hypervascular foci that responded to treatment with decreased vascularity have been documented by standard DCE-MRI on nodes measuring 3 × 3 mm and greater in size. DCE imaging has highlighted bladder cancers found incidentally during prostate imaging allowing for life-saving early intervention in patients with low-grade prostate cancers.

12.2 Multiplanar Multimodality Imaging of Benign Pathology

Benign disorders are common and unusual presentations of innocuous lesions may mimic tumors. Careful attention to imaging characteristic is necessary to provide optimal diagnosis.

12.2.1 Normal Prostate, Bladder, Urethra, and Seminal Vesicles

MRI imaging of the prostate may be done supine or prone with or without an endorectal coil. Sonography may be performed transabdominal, transrectal (TRUS), or transperineal, which is often used to biopsy or place radioactive seeds. Generally, for diagnostic purposes, transrectal US with Doppler is followed by 1.5 T or 3 T MRI with contrast and without an endorectal coil. The TRUS imaging planes will match the MRI planes depending on the type of US probe. Biplane probes more closely align with the MRI while endfire probes see the apex and base better, although the actual plane is an oblique plane between the coronal and transverse. The endfire probe is rotated 90 to produce a true orthogonal image.

The normal MRI and sonographic dimensions of the prostate are length 20–40 mm, thickness 21–34 mm, and width 39–53 mm for a total volume ranging from 13 to 37 cc.

The base lies cranially against the bladder and the apex lies caudally near the pelvic floor muscles (Fig. 12.1a–d).

The rectum is posterior to the prostate and separated by Denonvillier’s fascia in which part of the neurovascular plexus is located as it extends anterolaterally. For practical reasons of symmetry analysis, most images will be exhibited in the transverse sonographic plane and the transverse or axial MRI plane.

The urethra is centrally located within the longitudinal axis and receives the ejaculatory ducts in the midgland structure of the verumontanum. These areas are not imaged unless diseased.

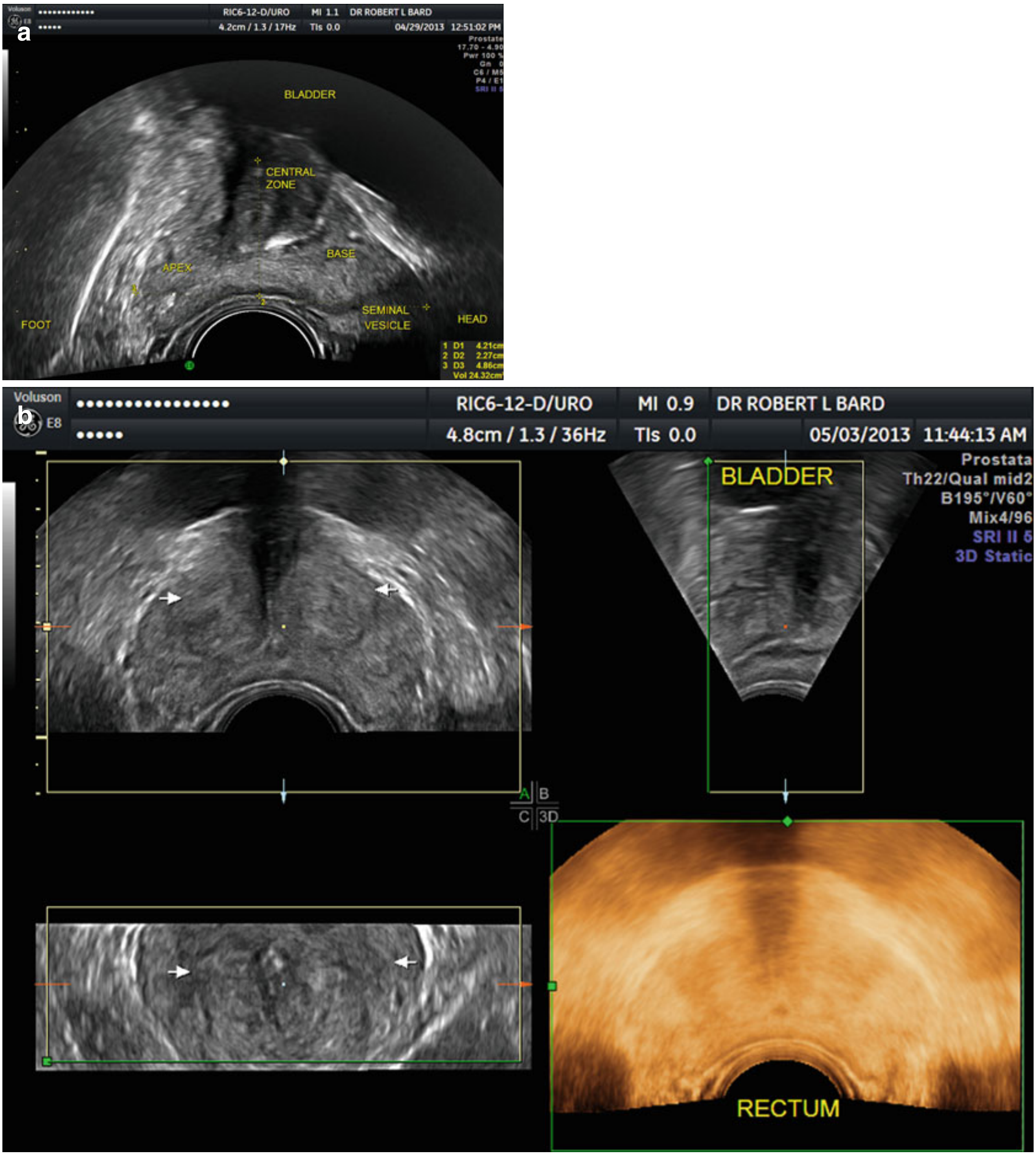

Fig. 12.1 (**a**) Sagittal plane. Base is cephalad between bladder and seminal vesicles. (**b**) Transverse plane. Central zone abuts bladder base. (**c**) Transverse plane. Peripheral zone (*white*). Bladder anterior to central zone (*gray*). (**d**) Transverse plane. Prostate homogeneously blue (no enhancement). (**e**) Urethra (*double arrows*) ejaculatory duct (*arrows*). (**f**) Verumontanum (*double arrows*) peripheral-central zone border (*arrows*)

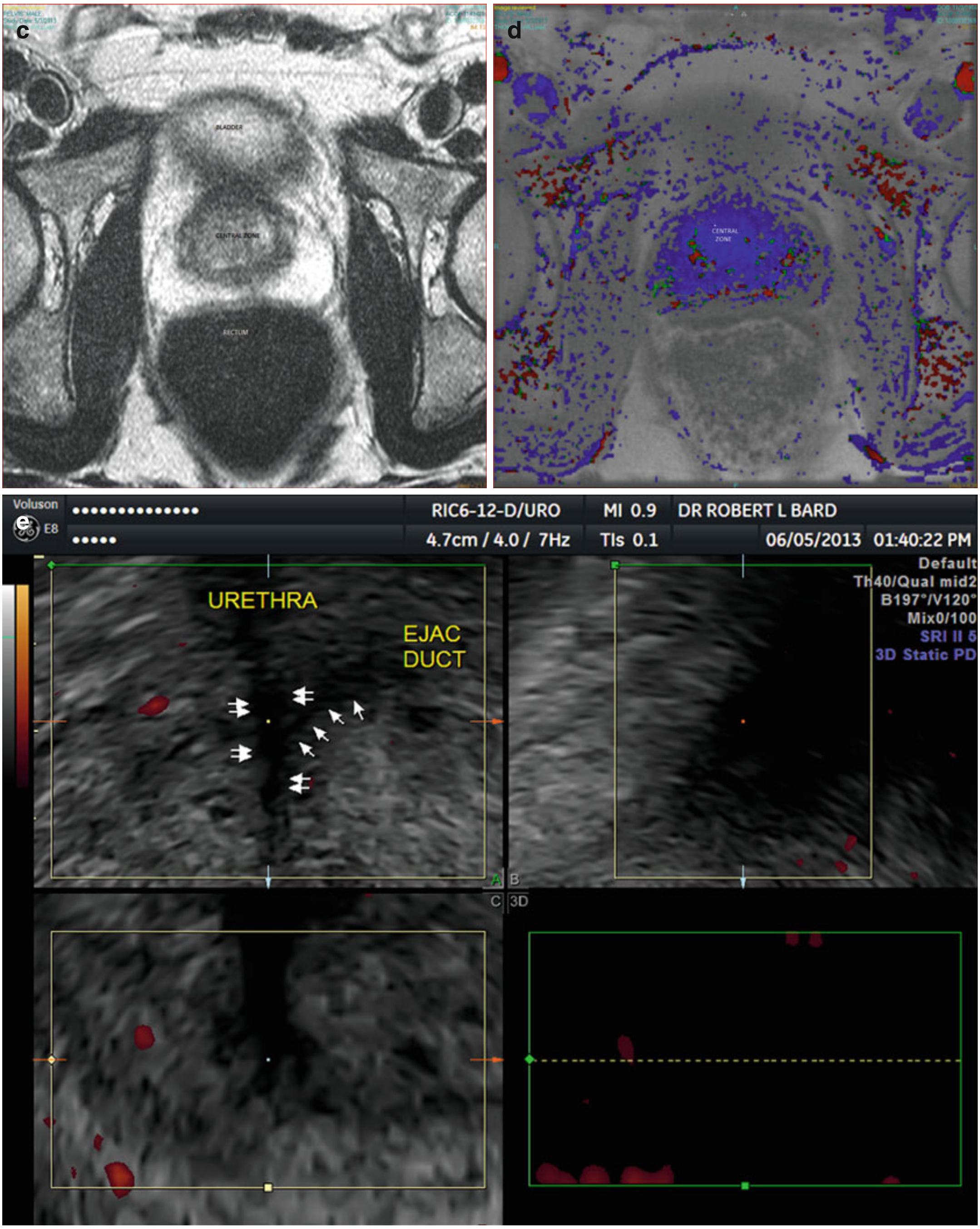

Fig. 12.1 (continued)

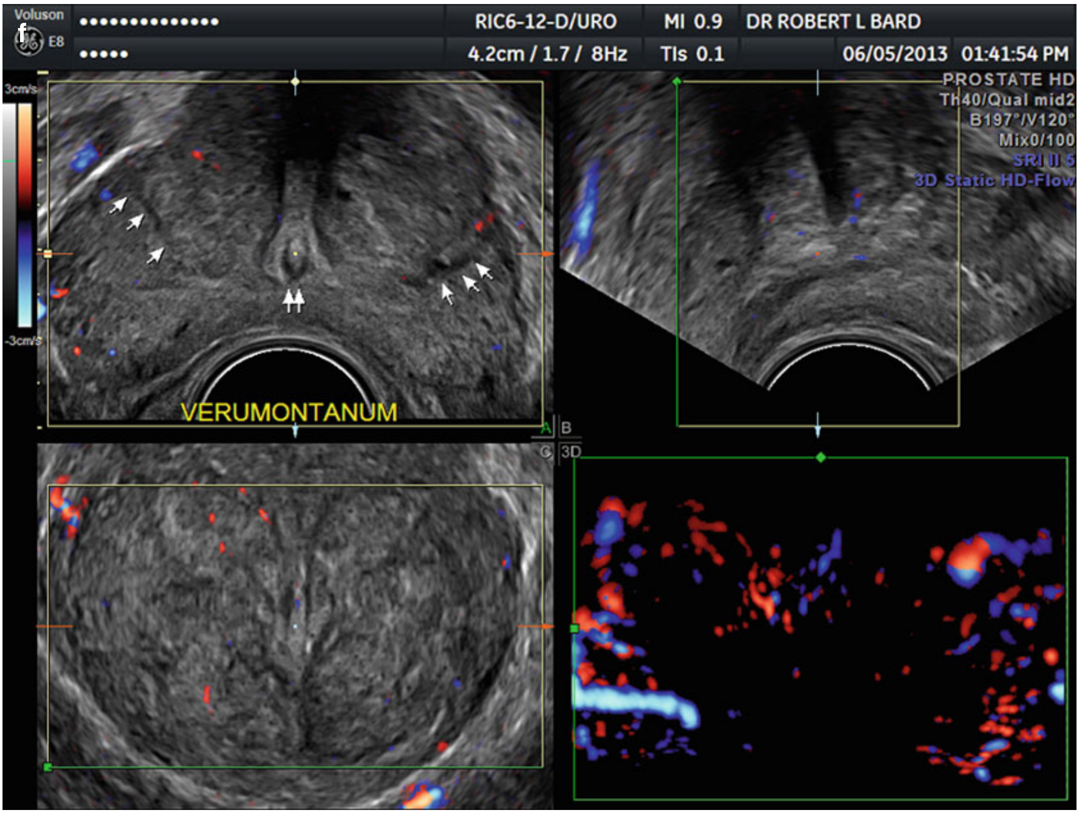

Fig. 12.1 (continued)

The paired seminal vesicles and vas deferens ducts are located posterior and superior to the prostatic base. The seminal vesicles are readily imaged if ejaculation is postponed for 3 days (Fig. 12.2a–e).

12.2.2 Congenital Anomalies and Cysts

Congenital cysts are usually midline and thin-walled regions. Mullerian duct cysts are pear shaped and occur near the prostate base with the neck of the cyst extending to the verumontanum. In chronic cysts, the walls may thicken or calcify (Figs. 12.3a–c and 12.4a–d).

Ultrasound findings of a complex cyst wall may be missed by MRI. Utricle cysts or congenitally enlarged prostatic utricles are not true cysts although they are imaged as such and project from the posterior wall of the prostatic urethra as a diverticulum. This entity is associated with hypospadias and undescended testes allowing clinical differentiation of these cystic entities.

Ejaculatory cysts are diagnosed when the cystic areas are bilateral. Urethral diverticula, usually symptomatic in females, are difficult to distinguish from other cystic areas.

On occasion cysts can bleed producing internal echoes on US and T1 findings on MRI-chronic cysts may simulate tumors (Bard 2009).

Acquired cysts are the most common finding in older men. These are generally no larger than 10 mm and tend to be irregular in outline. These are usually off the midline, most common in the hyperplastic inner gland of benign prostatic hypertrophy and are not easily mistaken as congenital cysts (Landes and Ransom 1949). Rarely are periprostatic cysts noted on the periphery (Hamper et al. 1990).

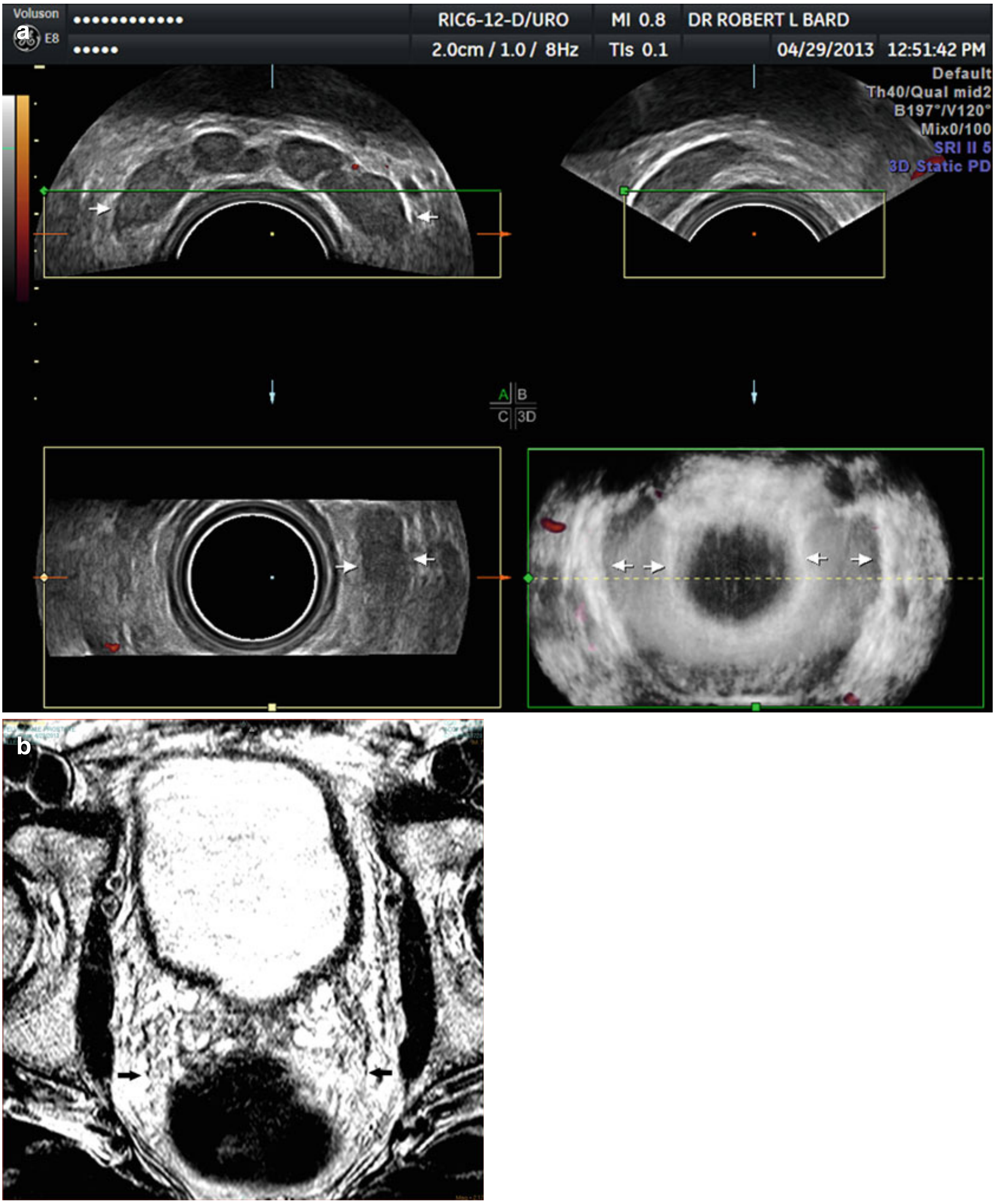

Fig. 12.2 (**a**) Transverse plane. Seminal vesicles (*arrows*). (**b**) Seminal vesicles between rectum (*black*) and bladder (*white*). (**c**) 3D image of seminal vesicles (3 orthogonal views + composite). (**d**) MRI. Septations in both seminal vesicles. (**e**) DCE-MRI. Scattered trace enhancement

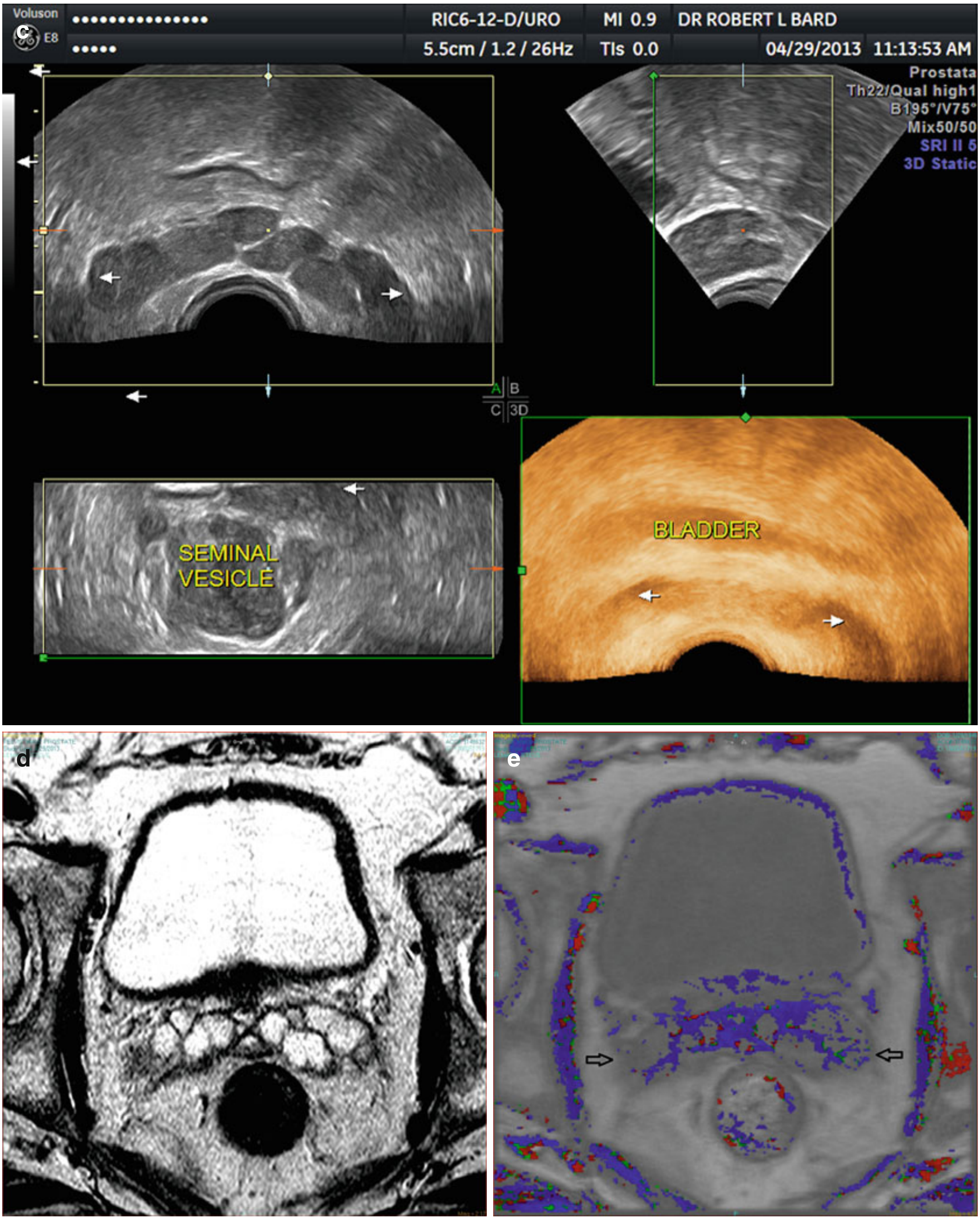

Fig. 12.2 (continued)

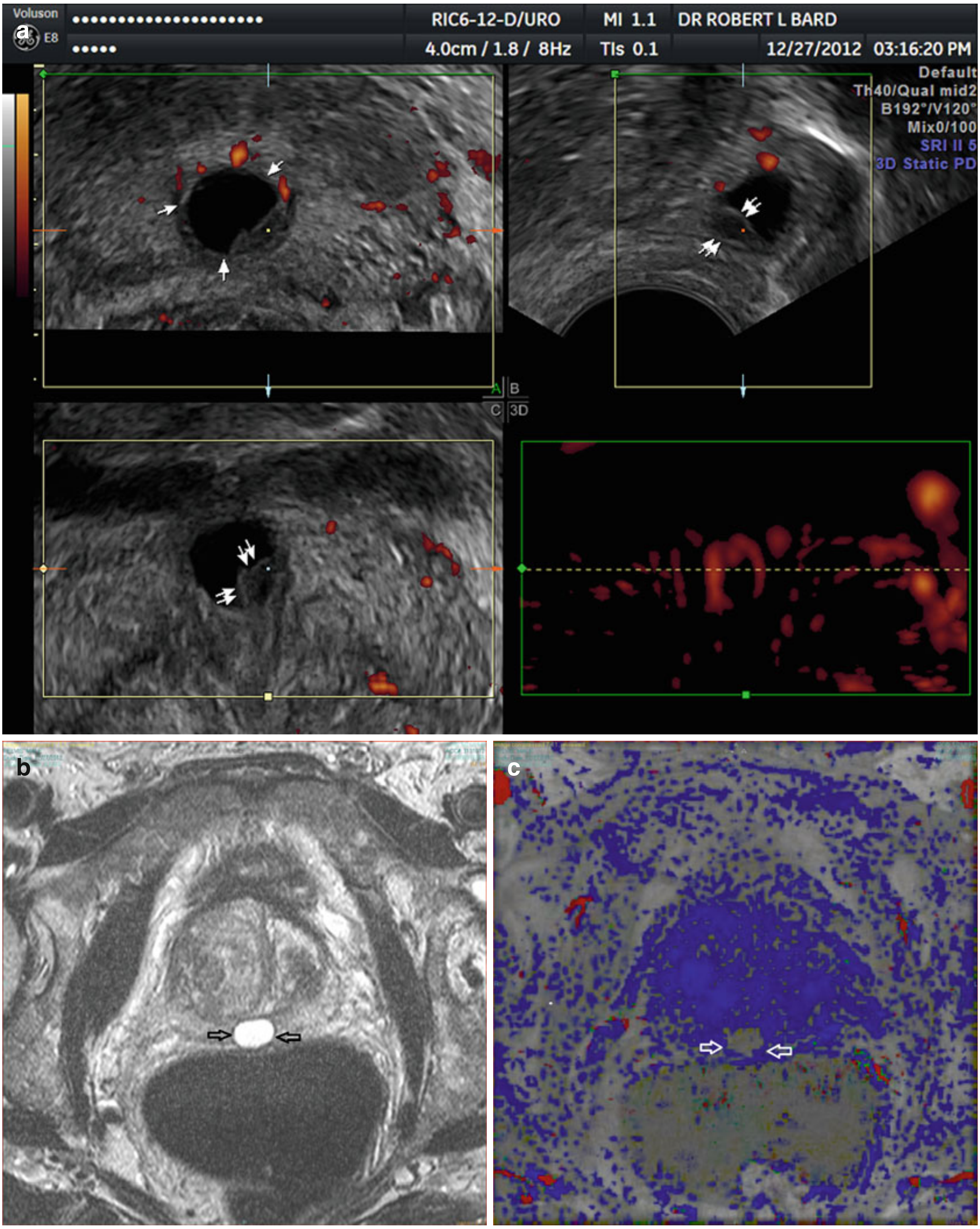

Fig. 12.3 (**a**) Midline cyst with solid wall elements. (**b**) MRI. Cyst (*white*) without wall irregularity. (**c**) DCE-MRI. No enhancement in cyst

12.2.3 Benign Prostatic Hypertrophy (BPH)

This common clinical entity occurs in the transition zone (TZ) (central region on MRI) thinning and compressing the peripheral zone (PZ) to variable degrees. Rarely, benign nodules appear in the peripheral zone and may mimic malignant lesions (Figs. 12.5a–c and 12.6a, b). Calculation of prostate volume, length × height × width × 0.52, is important for certain treatments, especially whole-gland HIFU, since the ablation is 10 cc/h. The symptoms of bladder outlet obstruction are only weakly related to the volume of glandular hypertrophy (Denis et al. 1998). In determining enlargement, the urologist looks at the median lobe of the central gland from the urethra so the hypertrophy appears lateral to the urethra, whereas the imager sees the entire gland and correctly observes the central enlargement, which is descriptively called lateral lobe.

Bladder changes, such as wall thickening and trabeculation, inferior mass effect on the base,

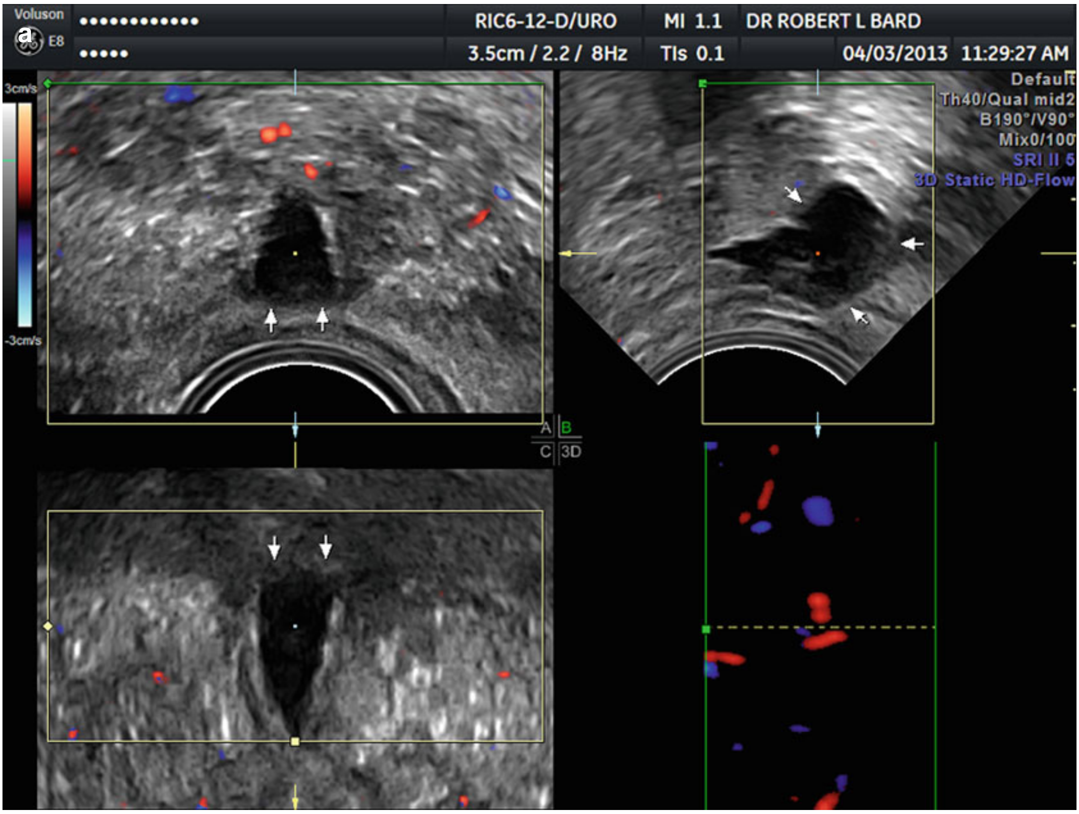

Fig. 12.4 (**a**) 3D. Pear-shaped nature of cyst. (**b**) 3D. Note thick cystic wall. (**c**) MRI. Well-marginated cyst. (**d**) DCE-MRI with no cyst enhancement

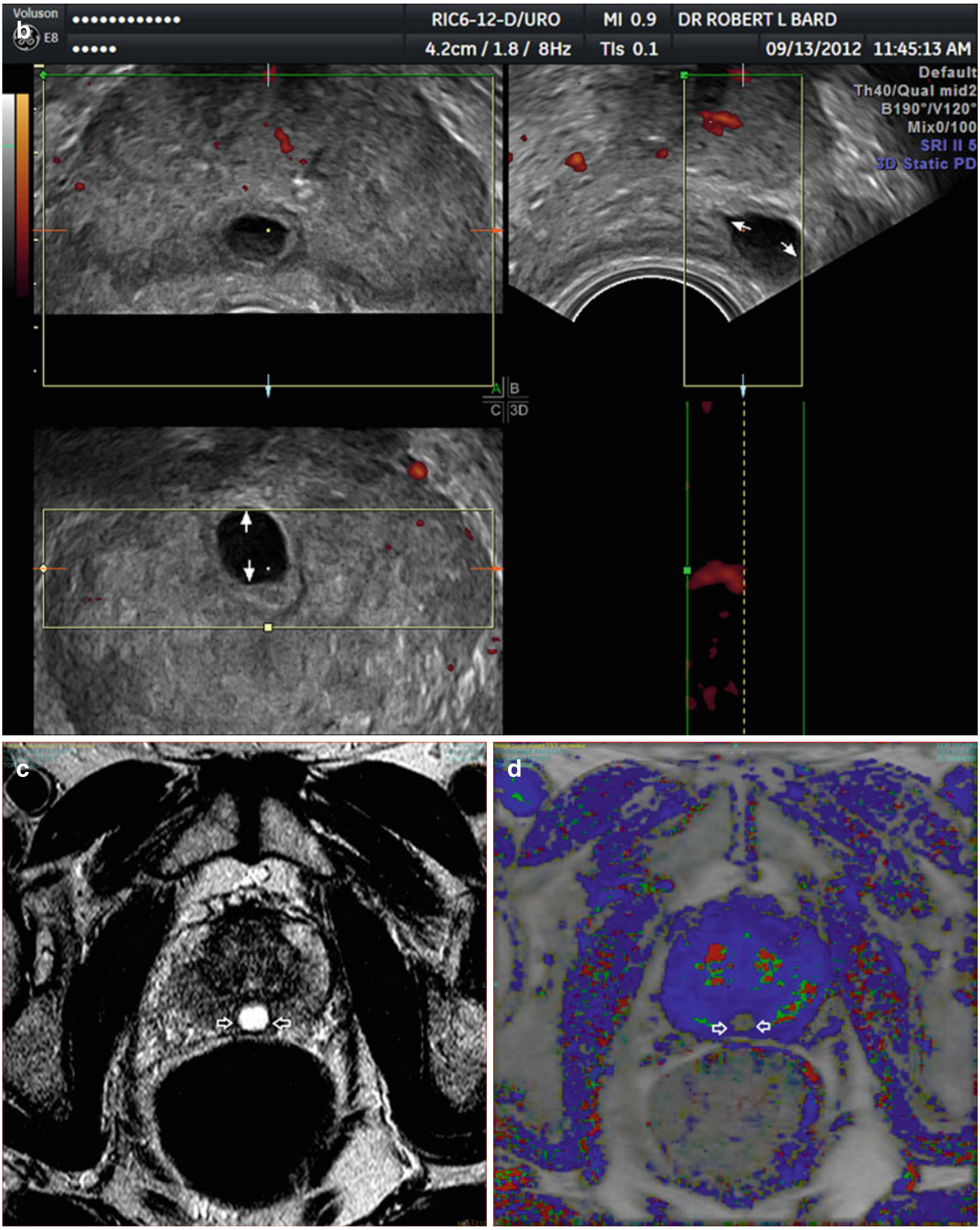

Fig. 12.4 (continued)

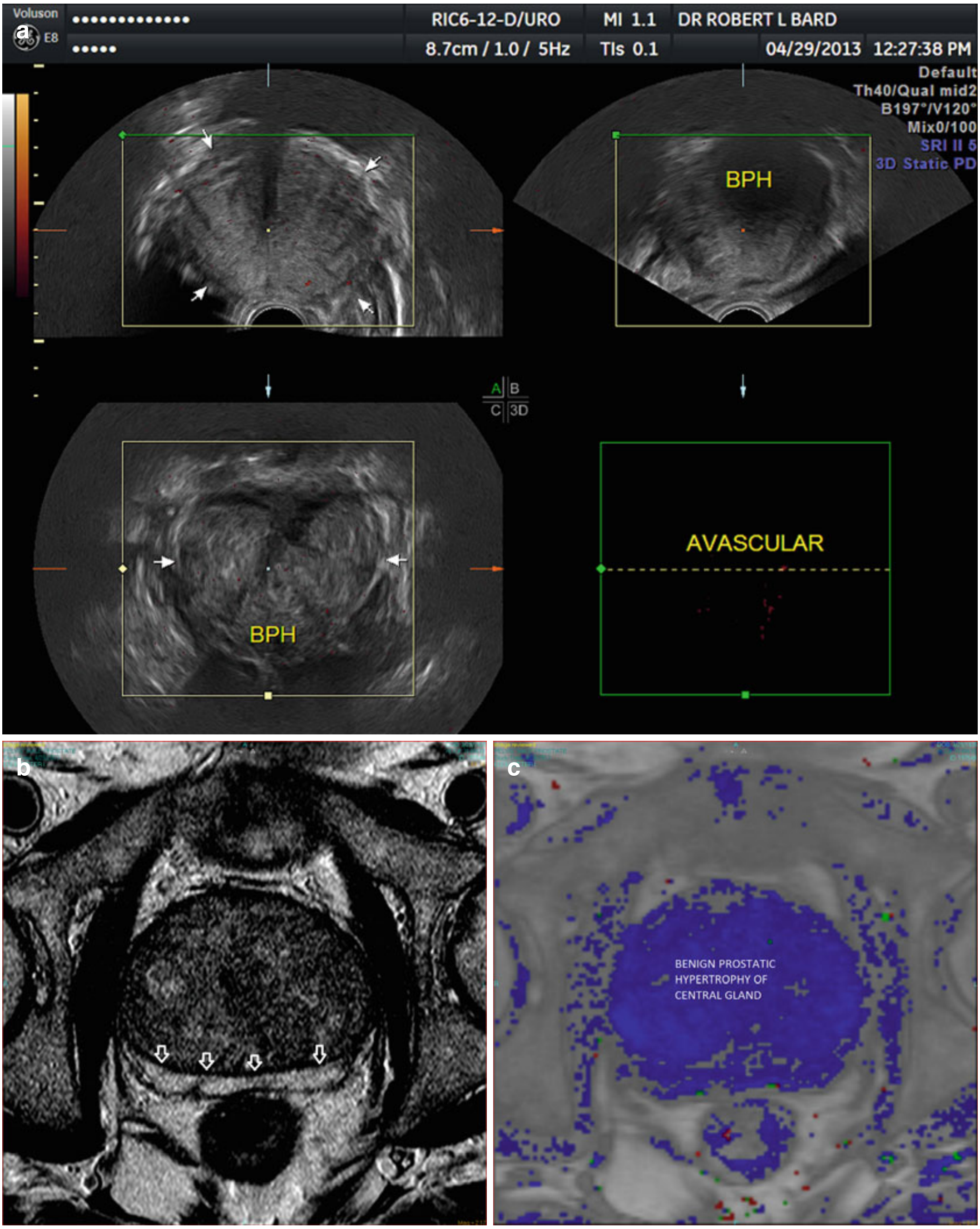

Fig. 12.5 (**a**) 3D. Central gland avascular benign hypertrophy. (**b**) MRI. Homogeneous central gland enlargement. (**c**) DCE-MRI. BPH shows no enhancement

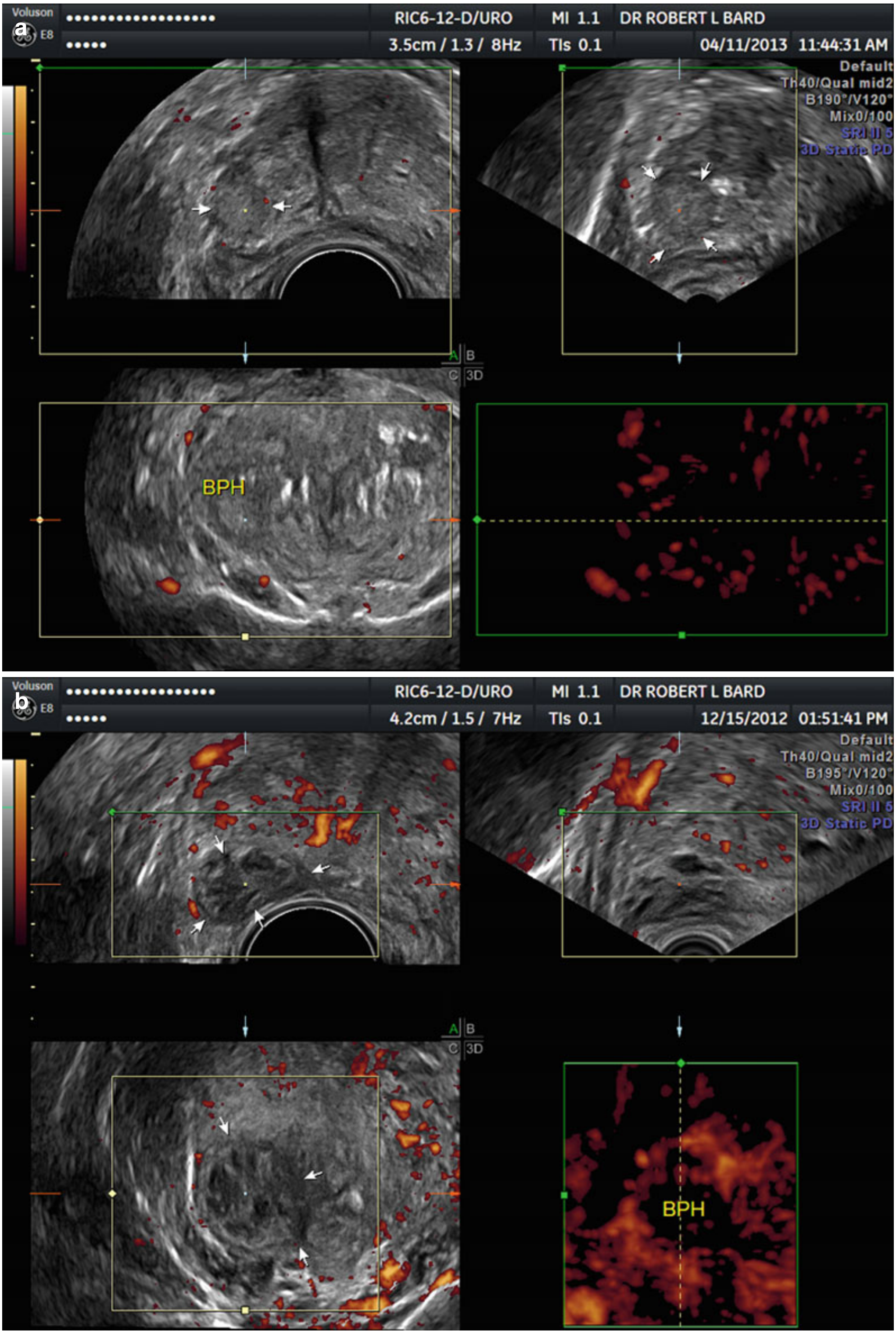

Fig. 12.6 (**a**) 3D. Peripheral zone benign hypertrophic nodule. (**b**) 3D. Avascular BPH nodule in peripheral zone

and diverticula, are readily observed on both TRUS and transabdominal US. BPH nodules on MRI and TRUS are generally smoothly rounded although great variety in echodensity and MRI signal occur including blood flow and contrast studies. Contrast-enhanced US seems more accurate in demonstrating malignant neovascular enhancement although elastography in certain centers has been useful.

12.2.4 Prostatitis

Prostatitis is generally classified into three categories:

1. Bacterial: acute and chronic TRUS may be nonspecific, with small and/or confluent microcalculi noted. Doppler and DCE-MRI often show symmetric increased flow, sometime with a characteristic butterfly pattern.
2. Nonbacterial: granulomatous prostatic disease is chronic and may simulate cancer on all modalities – biopsy is necessary.
3. 3-prostadynia patients with prostatic pain usually have normal imaging studies.

Prostatitis is clinically important because it may simulate cancer on ultrasound and MRI imaging (Figs. 12.7a, b and 12.8a–d).

12.2.5 Prostatic Calculi and Calcifications

These are classified into two patterns: primary in a non-diseased gland and secondary due to disease processes. Calculi form in hollow/tubular structures whereas calcification occurs in solid tissue. Calcium on MRI appears as signal loss or may cause artifact if large. TRUS is exquisitely sensitive in finding microcalculi.

Primary calculi form commonly in older men the periurethral glands forming corpora amylacea and appear as linear strings alongside the urethra above the verumontanum.

Secondary calculi are a sequel of chronic prostatitis, especially chronic prostatitis. Calcification in cancer, like stippled calcium in breast cancers, is finely particulate occurring rarely as an imaging finding with standard imaging (Meares 1987). High-resolution US will find malignant microcalculi in 5 % of cancers, so it is essential to biopsy these clusters. Heavily calcified glands may obscure central gland disease and MRI examination is mandatory.

12.2.6 Seminal Vesicle Disease

The seminal vesicles are best investigated when ejaculation has been postponed for 3 days. Biplane transducers have limited access when the prostate is enlarged, displacing the vesicles superiorly, and an endfire probe may image better. Dilation may be easily measured and ejaculatory stone investigated as a possible cause.

The appearance of the normal seminal vesicle varies with age and dilation with semen. Cysts, fibromas, and calcifications are rare (Fig. 12.9a, b).

The seminal vesicles in cancer may be invaded internally or externally, in whole or in part. Invasion is best delineated by MRI as loss of normal high signal in the lumen although 3D PDS has imaged neovascularity in cases with gross invasion of high-grade disease. Primary adenocarcinoma of the seminal vesicle is quite rare followed by sarcomas (Okada et al. 1992).

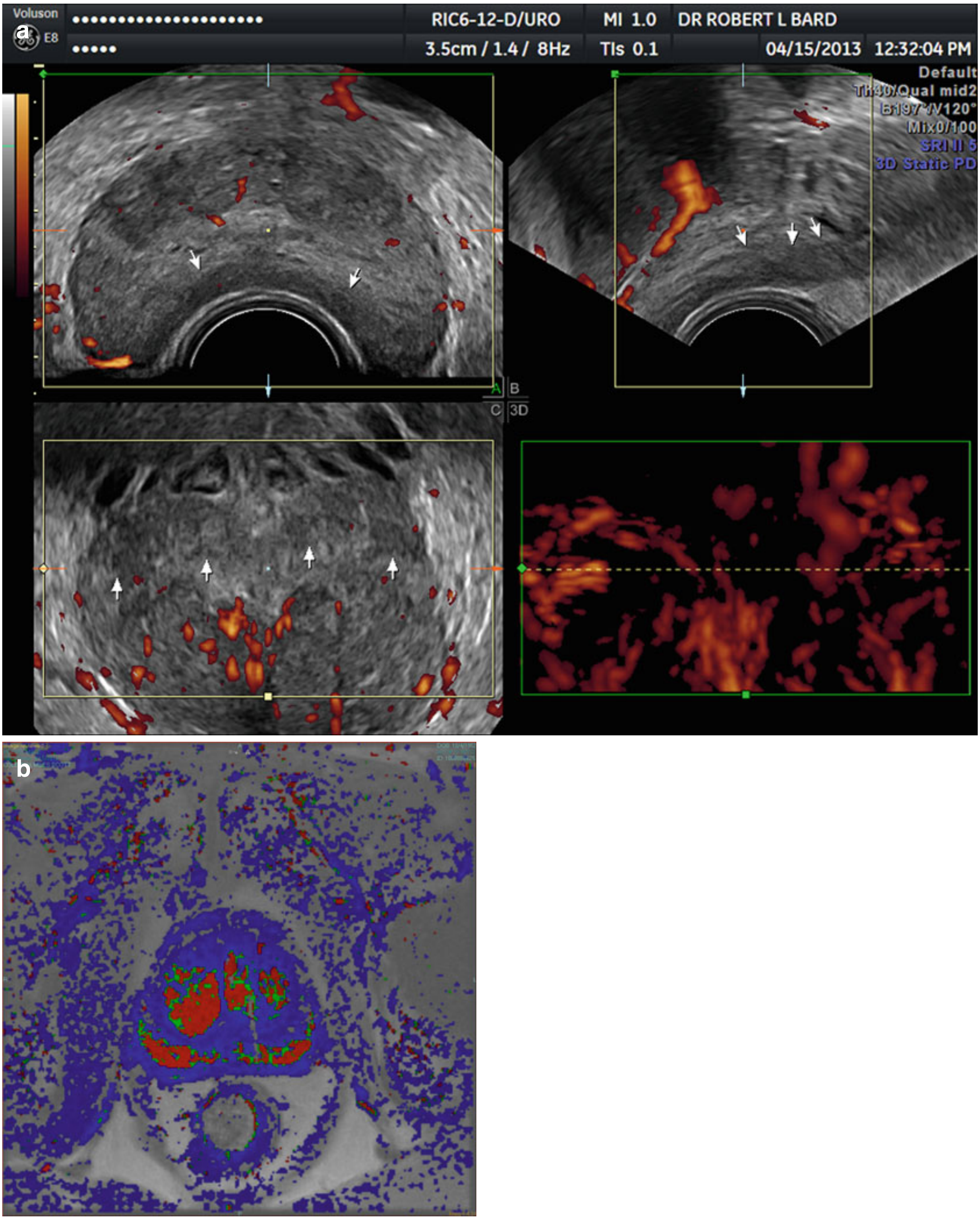

Fig. 12.7 (**a**) 3D. Prostatitis. Echo poor peripheral zone (PZ). (**b**) DCE-MRI. Symmetric peripheral zone perfusion

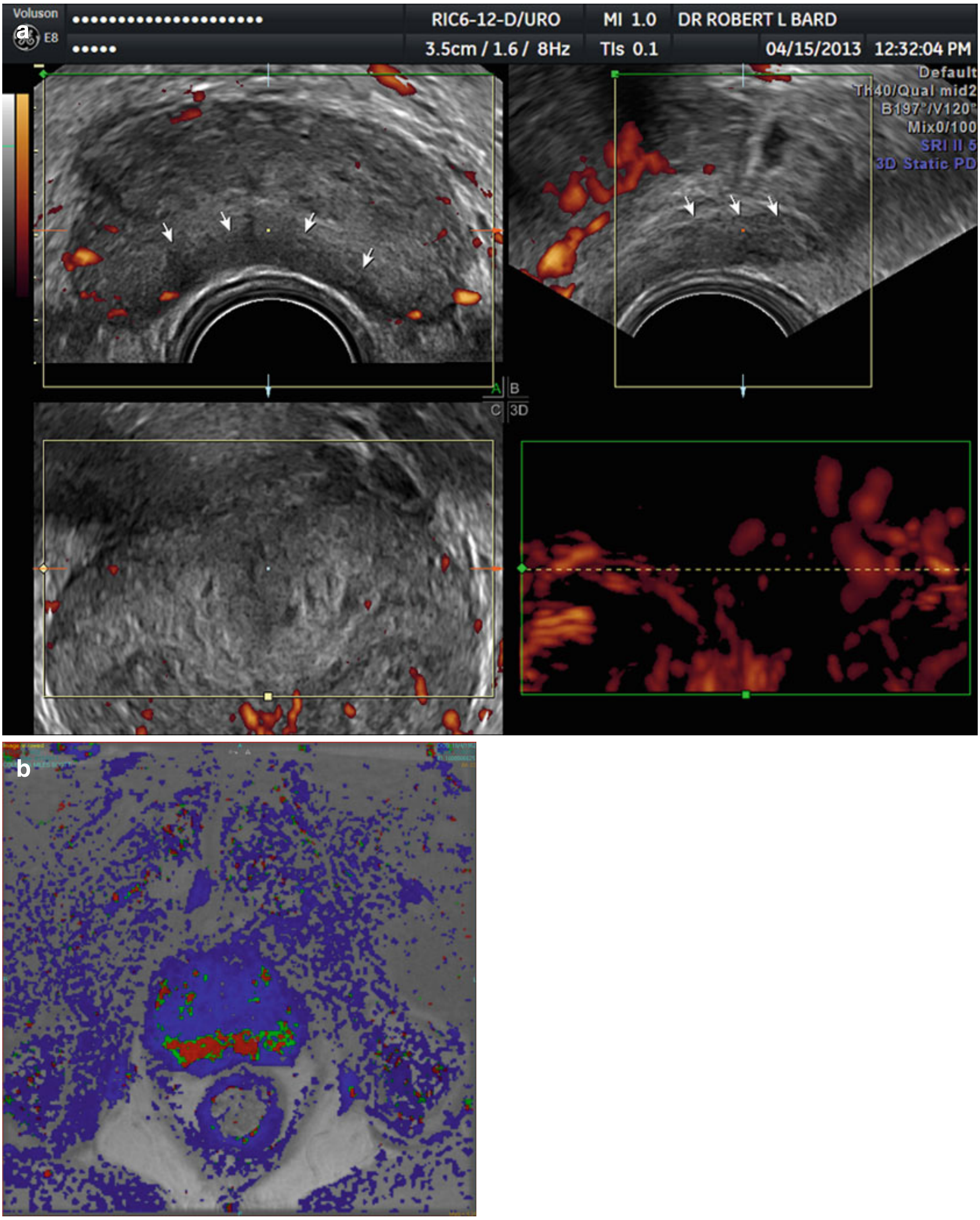

Fig. 12.8 (**a**) 3D. Prostatitis. PZ signal loss (*arrows*). Capsule intact. (**b**) DCE-MRI. Symmetric PZ perfusion. Common pattern BPH enhancement. (**c**) 3D. Anterior bilateral areas with bulging capsule. (**d**) MRI. Nonspecific non-focal signal loss. (**e**) DCE-MRI. Bilateral PZ perfusion of prostatitis

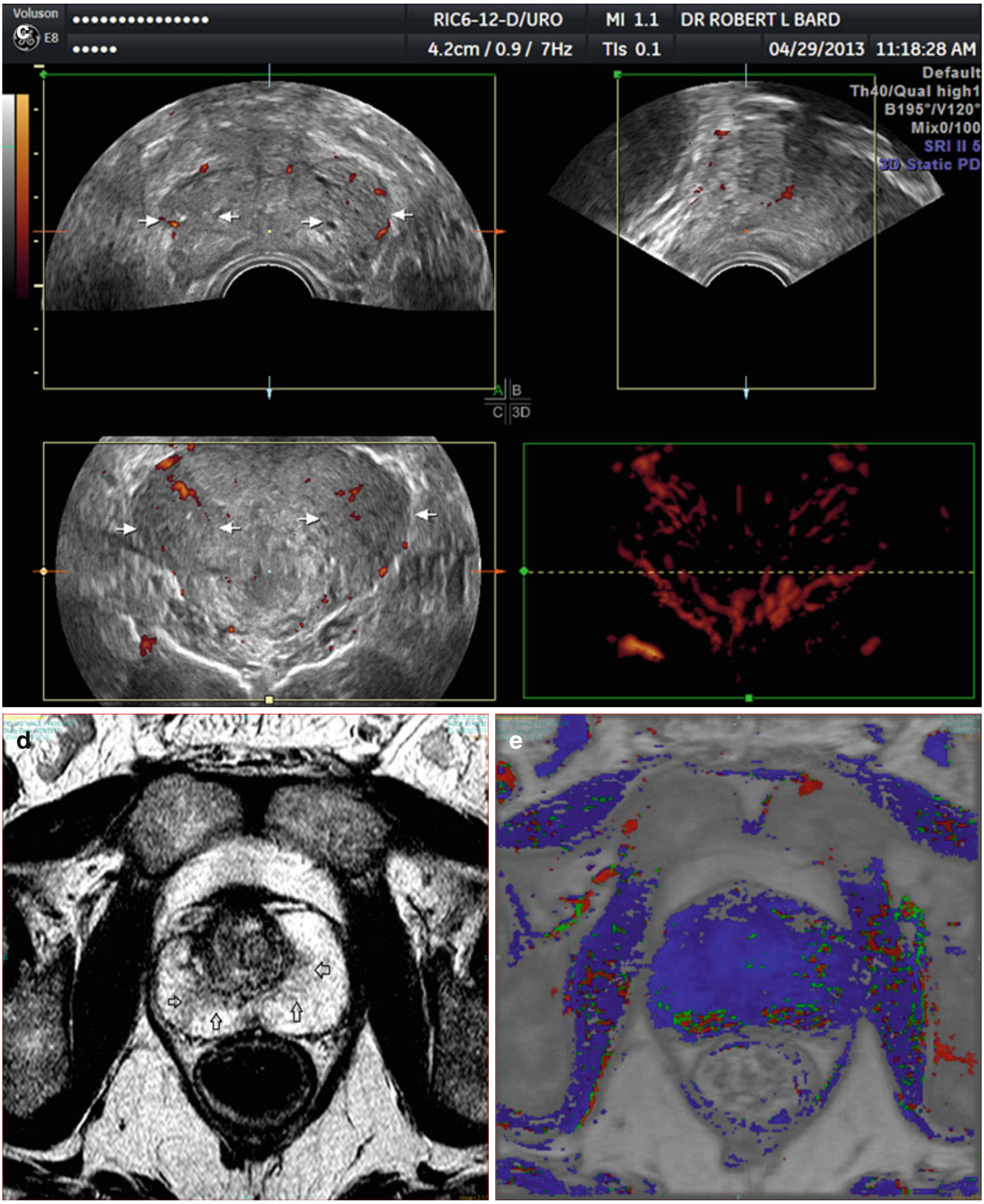

Fig. 12.8 (continued)

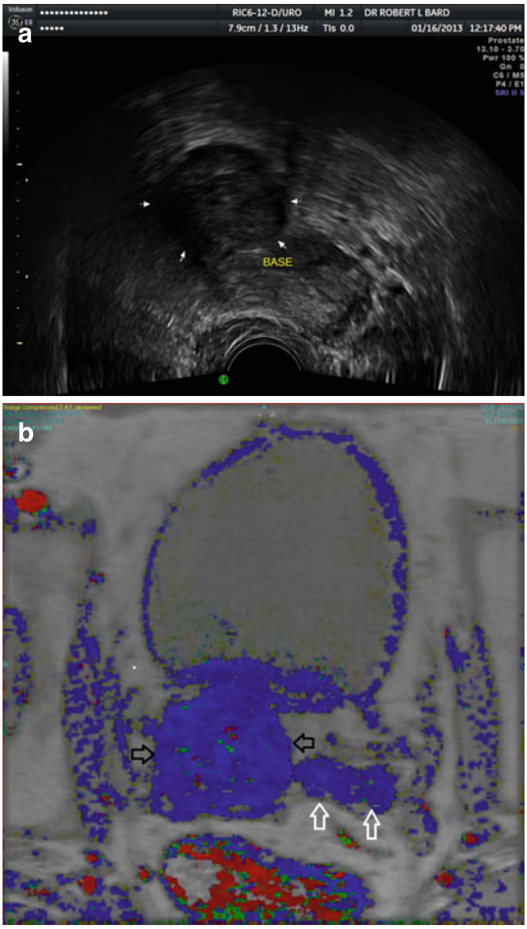

Fig. 12.9 (**a**) 3D. Right avascular seminal vesicle mass (fibroma). (**b**) DCE-MRI. Non-enhancing right round mass (*blue*)

References

Bard R. Dynamic contrast-enhanced MRI atlas of prostate cancer. Berlin: Springer; 2009. p. ix–xi.

Denis L, Griffiths K, Khoury S, et al. Proceeding of fourth international consultation on BPH, Paris, July 1997. Plymouth: Health Publications; 1998.

Hamper UM, Epstein J, Sheth S. Cystic lesions of the prostate. J Ultrasound Med. 1990;9:395.

Huward L, et al. Magnetic resonance imaging of angiogenesis in tumors. J Radiol. 2007;88(3 Pt 1):331–8.

Landes RR, Ransom CL. Mullerian duct cysts. J Urol. 1949;61:1089.

Lim LS, Sherin K. ACPM Prevention Practice Committee. Screening for prostate cancer in U.S. men ACPM position statement on preventive practice. Am J Prev Med. 2008;34(2):164–70.

May F, Treumann T, et al. Limited value of endorectal magnetic resonance imaging and transrectal ultrasonography in the staging of clinically localized prostate cancer. BJU Int. 2001;87(1):66–9.

Meares EM. Acute and chronic prostatitis: diagnosis and treatment. Infect Dis Clin North Am. 1987;1(4):855–73.

Schnall MR, Imai Y, et al. Prostate cancer: local staging with endorectal surface coil MR imaging. Radiology. 1991;178:797–802.

Okada Y, Tanaka H, et al. Papillary adenocarcinoma in a seminal vesicle. J Urol. 1992;148:1543–5.

Intraprostatic Cancer

13

Robert L. Bard

13.1 Multimodality Imaging of Focal Prostate Cancer

13.1.1 Focal Tumors: Intraprostatic

Intraprostatic tumors on US and MRI can be divided into a central zone and a peripheral zone or outer zone. About 70 % of clinically significant tumors occur in the outer zone (Byar and Mostofi 1972). The TNM classification of tumors:

T1 lesions—not palpable.
T1c lesions—discovered on biopsy.
T2 lesions—palpable and confined to prostate.
T3 lesions—extension beyond the gland.
N or nodal replacement by tumor is best imaged by MRI.
M or metastatic foci are imaged by MRI, whole-body diffusion MRI, PET/CT, and bone scans.

While prostate cancer is a multifocal disease in over 86 % of patients, the concept of a significant index lesion is the rationale for focal treatment, with the idea that early local treatment will prevent the need for radical surgery or radiation with the possibility of impotence and incontinence. While a single tumor may occur in 24 % of cases, an index tumor with smaller, secondary tumors less than 0.5 cc was found in 39 % of patients in a radical prostatectomy series (RP) (Noguchi et al. 2003).

Tumor volume of the index lesion is an independent factor in predicting biochemical failure after radical prostatectomy (Stamey et al. 1999). Gleason grade also represents a negative outcome factor in that the higher the grade, the worse the prognosis (Jones 2008). Extracapsular extension of tumor disease (ECE) is another independent factor of later tumor reoccurrence (Ohori and Scardino 2002).

On TRUS, sonographically visible tumor appears echo poor or hypoechoic to the surrounding parenchyma. A small percentage of tumors are isoechoic and are depicted by abnormal vessels on 3D PDS. Rarely, echogenic cancers are found with extensive fibrosis from chronic inflammation or microcalculi in necrotic areas. Prostatitis may form similar patterns and often has spared hyperemia which will distinguish this entity from cancer. Focal bulging, contour abnormality, or invasion of the capsule should be assessed. The postoperative prostate is best imaged in the sagittal plane for recurrence, appearing usually as a solid nodule but sometimes as a complex cystic area. The post radiation seed prostate will often show a characteristic reverberation artifact from the metallic inserts. The externally radiated gland will lose the normal echogenicity and PDS must be used to detect vascular recurrences. Tumors may image better on one modality than another, in one plane better than another, and Doppler flow and/or perfusion may coincide or not, especially in cases of low flow conditions (Figs. 13.1, 13.2, and 13.3).

R.L. Bard, MD
Bard Cancer Center, Biofoundation for Angiogenesis Research and Development, 121 E. 60th St,
New York, NY 10022, USA
e-mail: rbard@cancerscan.com

R.L. Bard et al. (eds.), *Image Guided Prostate Cancer Treatments*,
DOI 10.1007/978-3-642-40429-0_13, © Springer-Verlag Berlin Heidelberg 2014

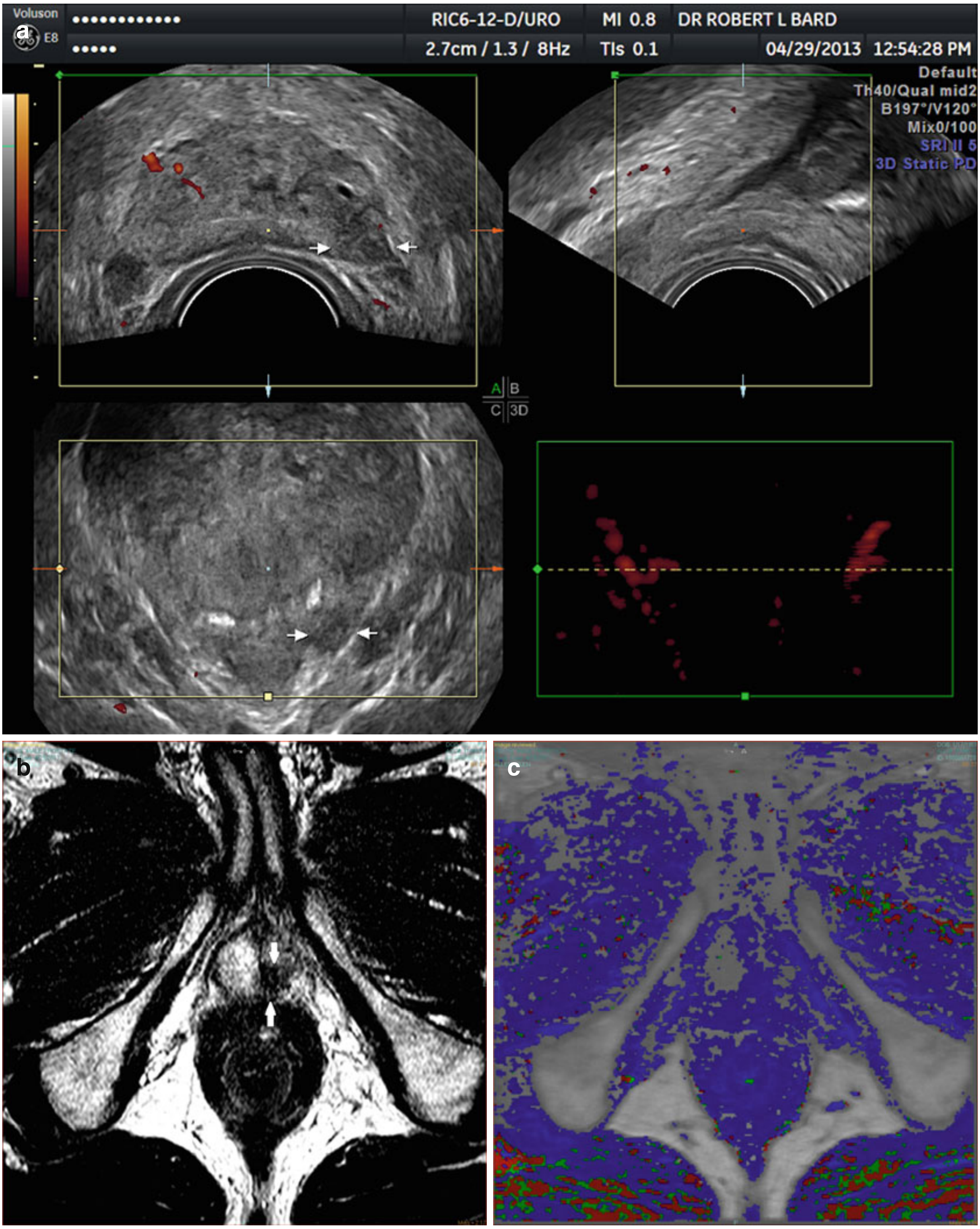

Fig. 13.1 (**a**) 3D apical tumor (*arrows*) with capsule intact. (**b**) MRI irregular focal tumor (*arrows*). (**c**) DCE-MRI no enhancement is noted

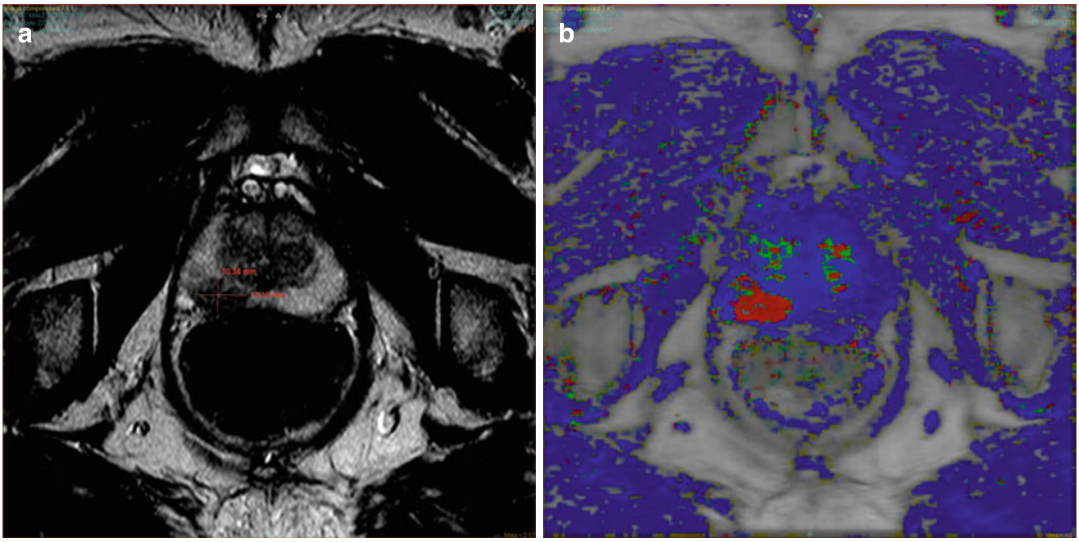

Fig. 13.2 (**a**) MRI focal midgland tumor right. (**b**) DCE-MRI homogeneous enhancement

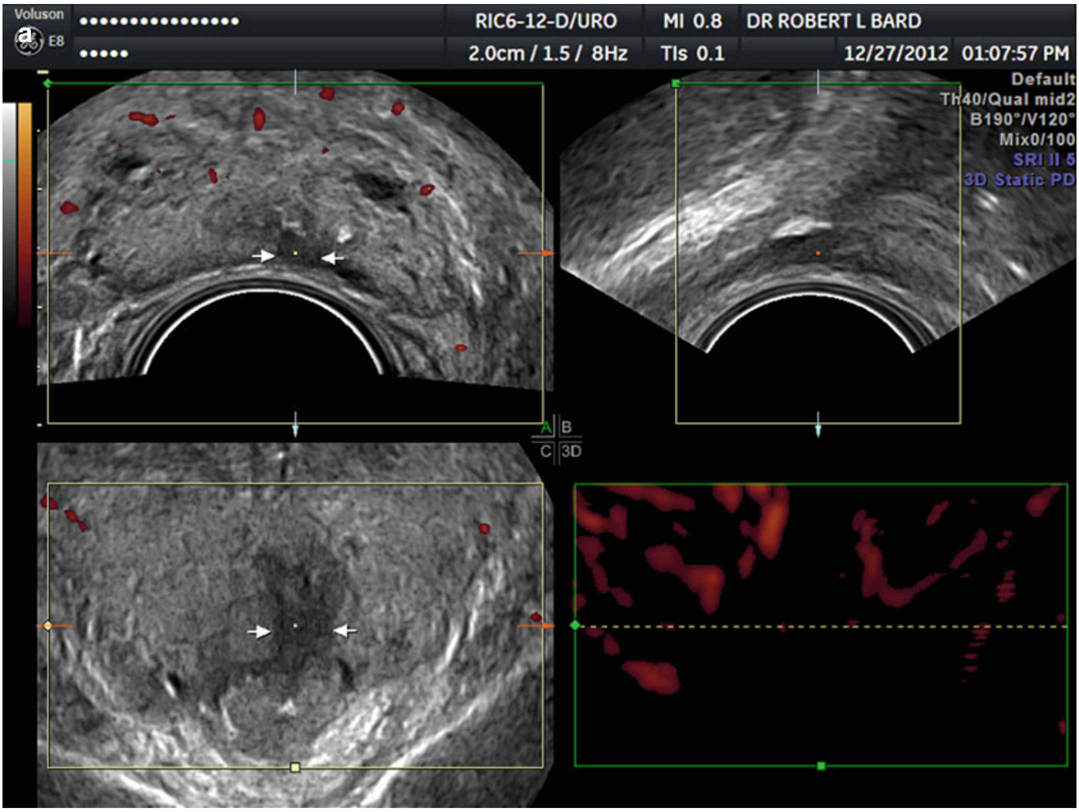

Fig. 13.3 (**a**) 3D 4 mm avascular apical tumor (*arrows*). (**b**) MRI tumor poorly visualized (*arrow*). (**c**) DCE-MRI no tumor enhancement

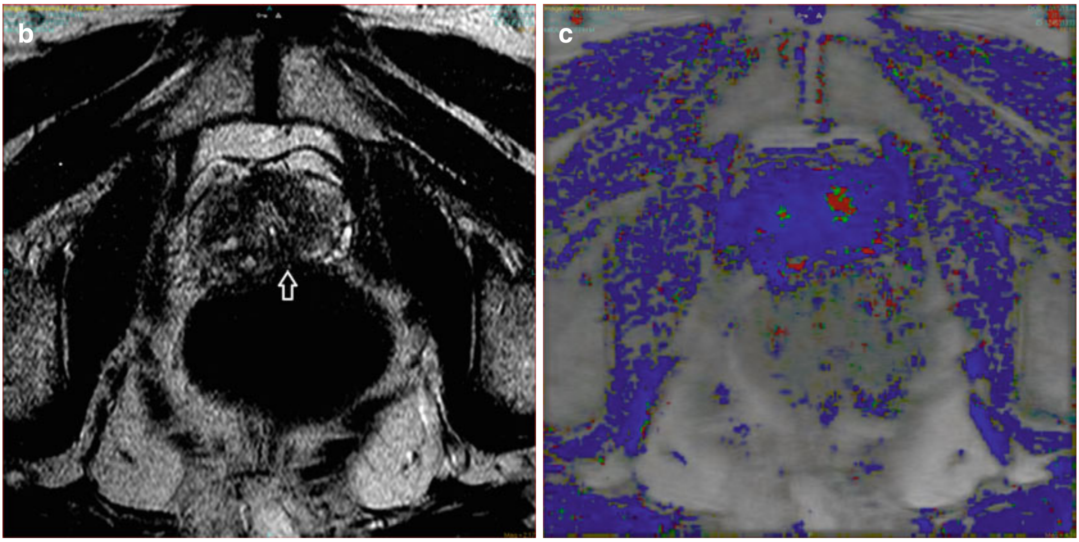

Fig. 13.3 (continued)

MRI appearance of prostate cancer will be extensively covered in other chapters; however, T2-weighted imaging sequences (T2WI) produce the best results showing hypointense regions that are usually focal or curvilinear. In this chapter, transverse T2-weighted images are used as the standard to correlate with other imaging options. The traditional role of MRI for local staging has been replaced as a localizer of index lesions for focal treatments. Limitations of T2-weighted imaging include similar appearances of benign processes such as inflammation, atrophy, hemorrhage, and posttreatment change.

A multiparametric MRI (MP-MRI) approach is more accurate, using initial sagittal T2WI images to set up coronal T2WI to set up axial or transverse T2WI sequences. This is followed by axial or transverse diffusion-weighted imaging (DWI), showing tumor foci as dark on the ADC map. Next DCE-MRI imaging contrast is injected and images are recorded using T1WI technology. A scoring system is set up for each modality from 1 to 5, 5 being the highest suspicion for cancer and 1 being the lowest. Thus a score of 3 (score of 1 for T2WI, 1 for DWI, and 1 for DCE-MRI) indicates benign disease. A score of 15 (5 for T2WI, 5 for DWI, and 5 for DCE-MRI) would imply strong suspicion for malignancy.

References

Byar DP, Mostofi FK. Carcinoma of the prostate: prognostic evaluation of pathologic features. Cancer. 1972;30(1):5–13.

Jones JS. Prostate cancer: are we over diagnosing or underthinking? Eur Urol. 2008;53(1):10–2.

Noguchi M, Stamey TA, et al. Prognostic factors for multifocal prostate cancer in radical prostatectomy specimens. J Urol. 2003;170(2 Pt 1):459–63.

Ohori M, Scardino PT. Localized prostate cancer. Curr Probl Surg. 2002;39(9):833–957.

Stamey TA, McNeal JE, et al. Biologic determinants of cancer progression in men with prostate cancer. JAMA. 1999;281(15):1395–400.

Focal Tumors: Extraprostatic

14

Robert L. Bard

14.1 Prostatic Capsule

The prostatic capsule is a thin layer of compressed fibrous tissue and not a true epithelial capsule. Imaging with US depicts the pericapsular fat as a strongly echogenic structure while MRI appearance is that of a dark envelope. Thinning of the capsule is often noted in benign hyperplasia. The capsule tends to be incomplete around the apex which accounts for more extraprostatic spread from tumors at the apex. Similar to focal tumor diagnosis, capsular erosion must appear in 2 of the 3 orthogonal views.

14.2 Capsular Invasion

Capsular invasion occurs with infiltration of the cancer into the fibrous capsule. Capsular penetration is tumor invasion that extends beyond the capsule that produces bulging, irregularity of the capsule, and gross tumor noted invading the fascial planes. Perineural invasion, a microscopic diagnosis, cannot be inferred from diagnostic imaging at this time. However, the nerve supply of the gland tends to follow the major arterial network which can be imaged with color Doppler sonography (CDS) or power Doppler sonography (PDS). Capsular lateral wall erosion is often best imaged in the coronal view on 3DPDS, while posterior erosion usually is best depicted on the transverse 3DPDS. MRI, with its inferior capsular resolution (including endorectal coil scans), may not always confirm extracapsular disease clearly exhibited on high-resolution sonography (Bard 2009) (Figs. 14.1, 14.2, 14.3, 14.4, 14.5, and 14.6).

Small areas of extracapsular disease may be successfully treated focally. It has been reported that ECE (also known as extraprostatic extension or EPE) occurs in over 19 % of RP specimens in patients with low risk, clinically focal and low grade intraprostatic lesions (Mouraviev et al. 2007).

14.3 Extraprostatic Nonfocal Tumors

Imaging will confirm the presence of other index or non-index tumors. The option for focal treatment depends on the characteristics of the initial tumors and their response to treatment over time (Figs. 14.7, 14.8, 14.9, and 14.10).

R.L. Bard, MD
Bard Cancer Center, Biofoundation for Angiogenesis
Research and Development, 121 E. 60th St,
New York, NY 10022, USA
e-mail: rbard@cancerscan.com

R.L. Bard et al. (eds.), *Image Guided Prostate Cancer Treatments*,
DOI 10.1007/978-3-642-40429-0_14, © Springer-Verlag Berlin Heidelberg 2014

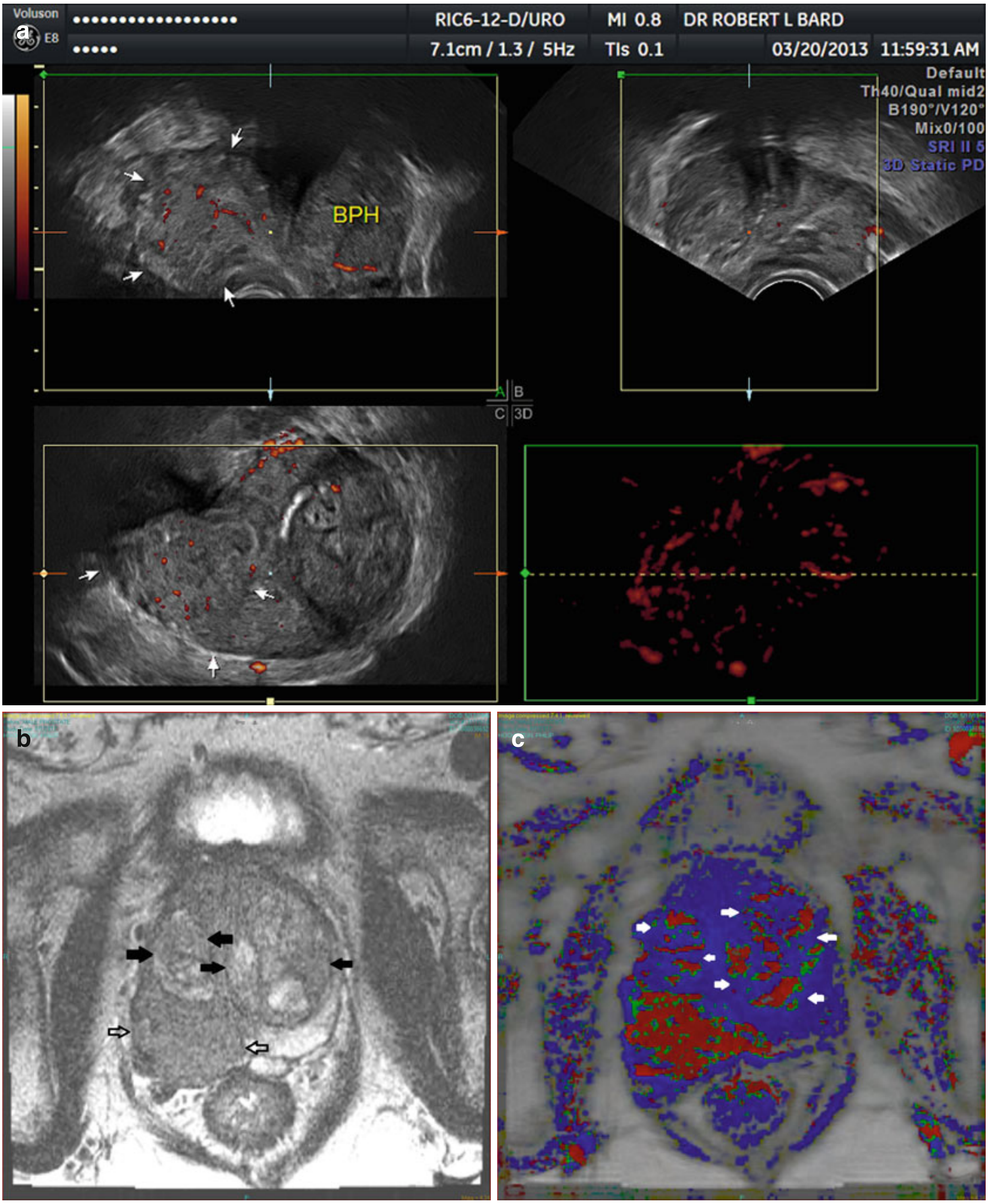

Fig. 14.1 (**a**) 3D. Right solid tumor (*arrows*) has irregular borders and internal tortuous vascularity compared to left BPH nodule. (**b**) MRI. Homogeneous signal loss in right tumor (*open arrows*). Inhomogeneous left and right midgland well-circumscribed nodules (*closed arrows*). (**c**) DCE-MRI. Homogeneous enhancement of tumor. BPH nodules (*arrows*)

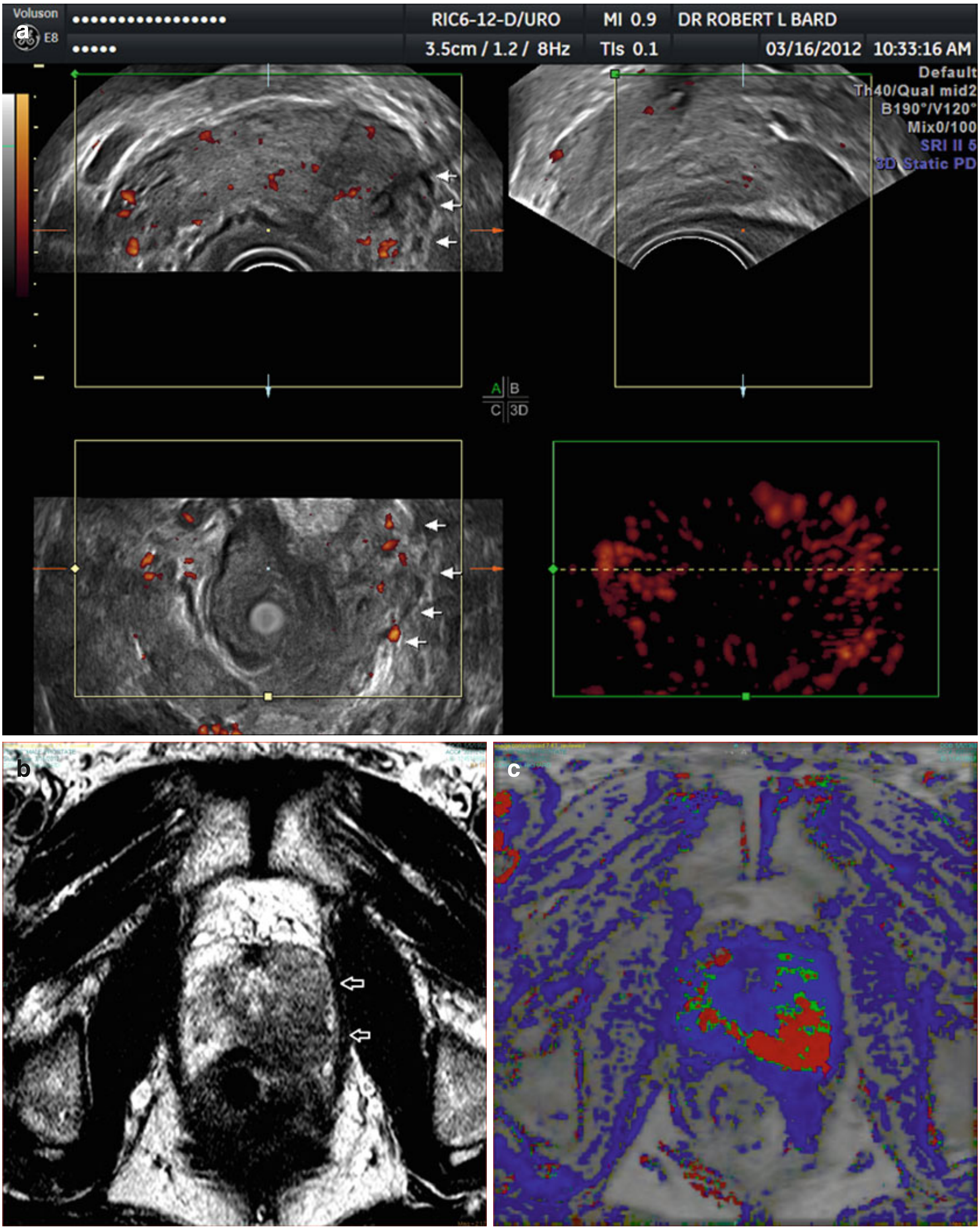

Fig. 14.2 (**a**) 3D. Tumor with left capsular erosion (*arrows*). (**b**) MRI. Tumor (*arrows*) with mixed signal and intact capsule. (**c**) DCE-MRI. Homogeneous enhancement of tumor

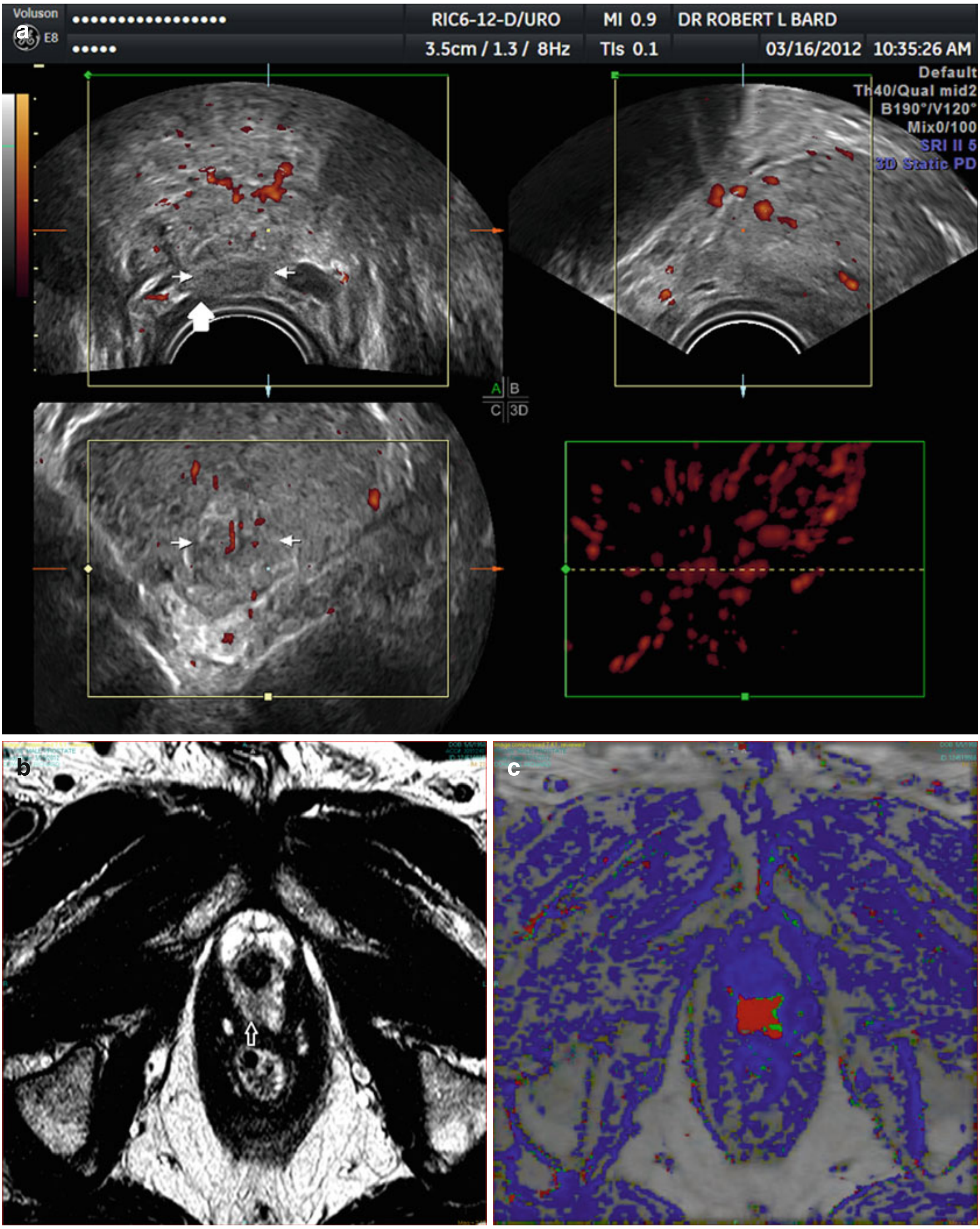

Fig. 14.3 (**a**) 3D. Apical tumor (*arrows*) with posterior erosion. (**b**) MRI. Apical tumor (*arrows*) without erosion. (**c**) DCE-MRI. Homogeneous enhancement

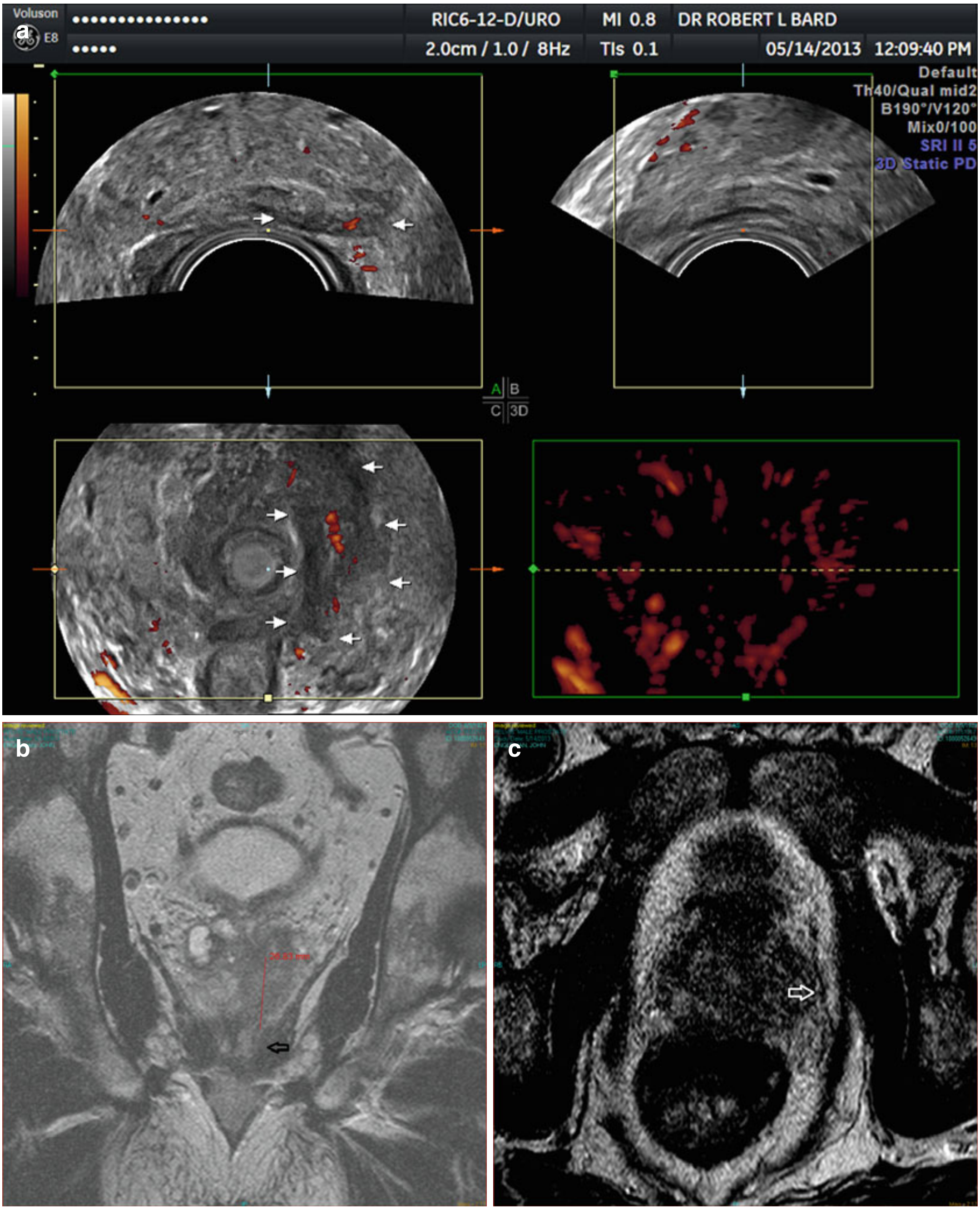

Fig. 14.4 (**a**) 3D. Midgland tumor with erosion (*arrows*) best on coronal plane. (**b**) MRI. Coronal plane. Capsular erosion (*arrows*). (**c**) MRI. Left capsular erosion (*arrows*). (**d**) DCE-MRI. Tumor eroding capsule has minimal perfusion

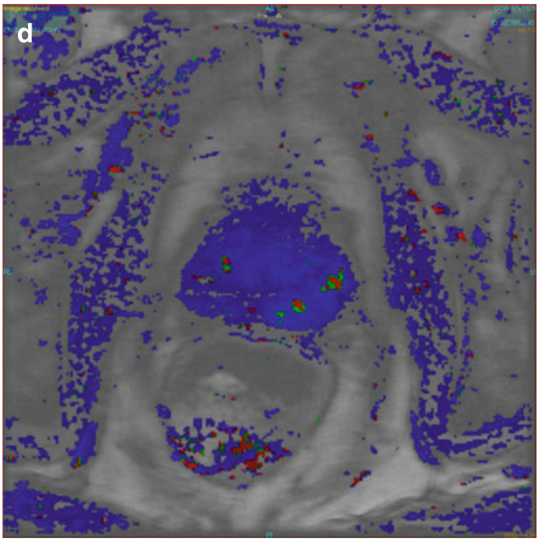

Fig. 14.4 (continued)

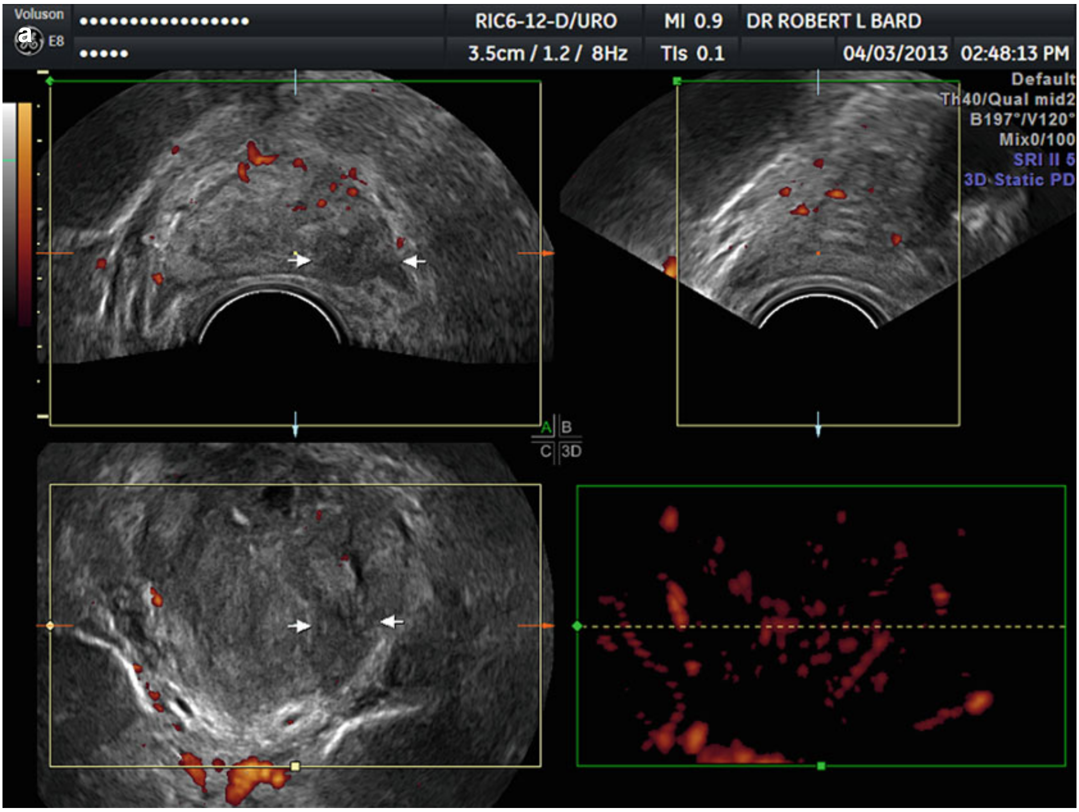

Fig. 14.5 (**a**) 3D. Avascular apical tumor (*arrows*) eroding capsule. (**b**) MRI. Capsular erosion (*arrows*) questionable. (**c**) DCE. Tumor missed on perfusion study

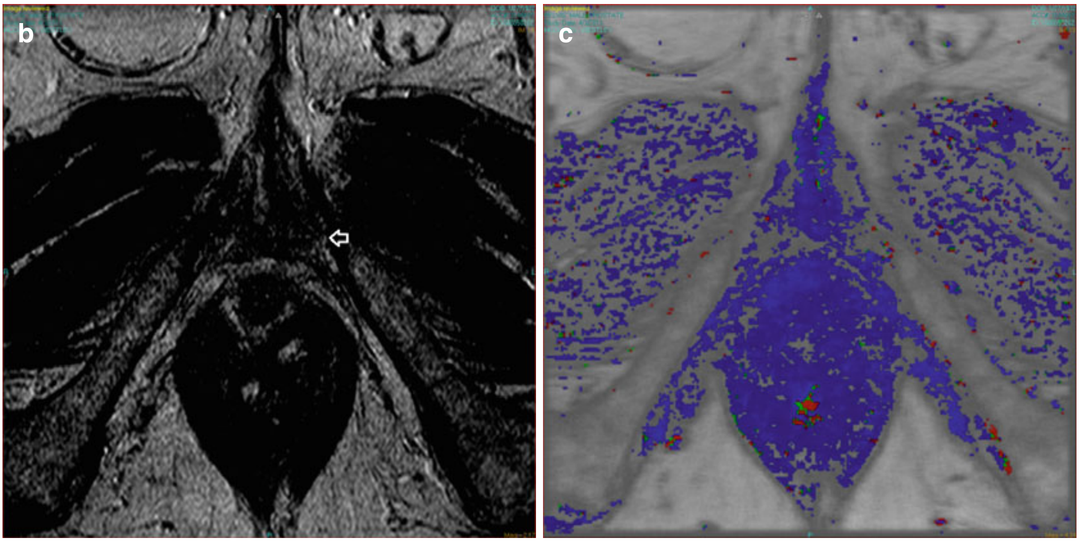

Fig. 14.5 (continued)

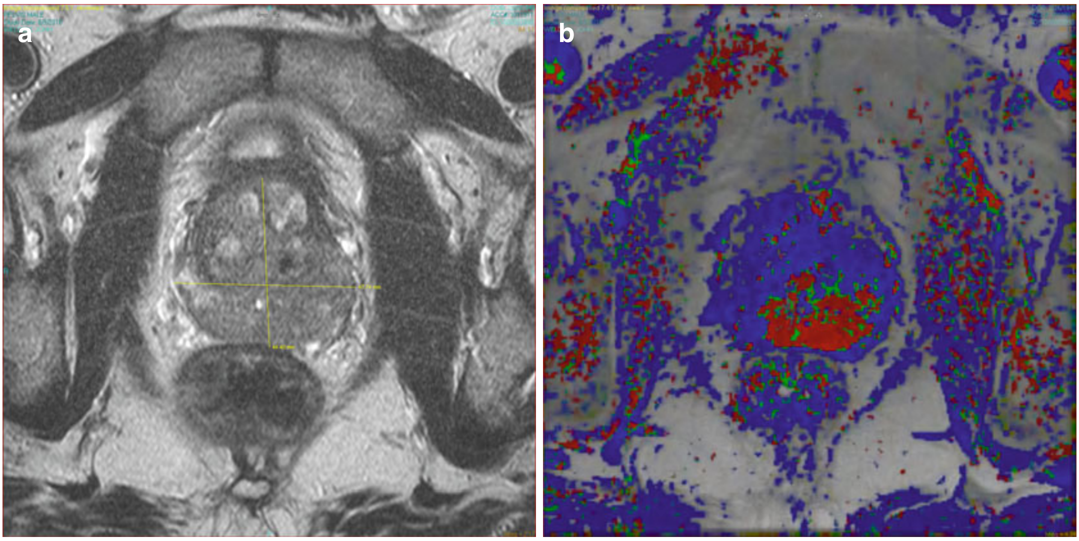

Fig. 14.6 (**a**) MRI. Tumor involving both halves of gland. (**b**) DCE-MRI. Gleason 9 tumor perfusion matches T2 study

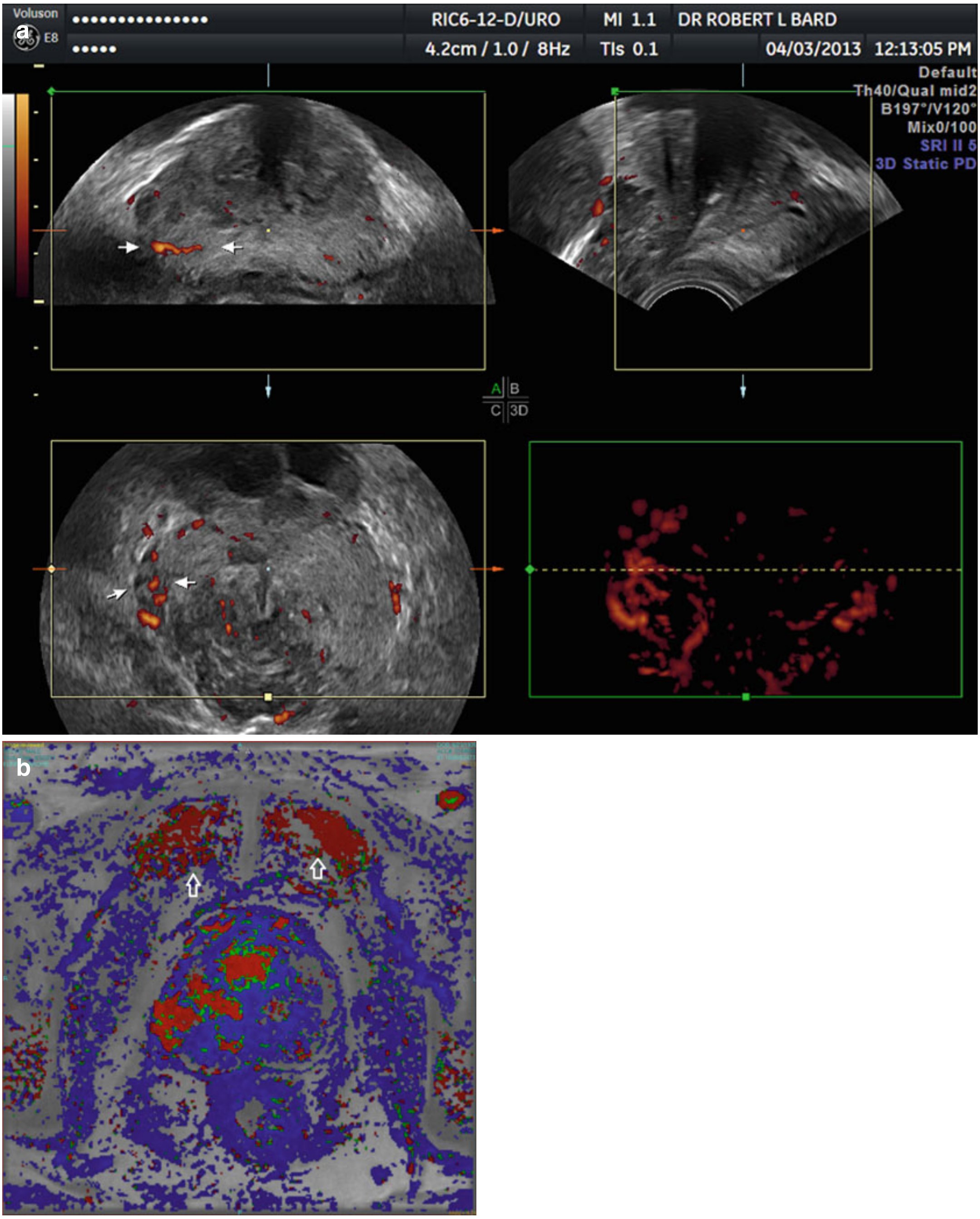

Fig. 14.7 (**a**) 3D. Isoechoic midgland vascular lesion (*arrows*) erodes capsule. (**b**) DCE-MRI Erosion and symphysis pubis boney metastases (*arrows*)

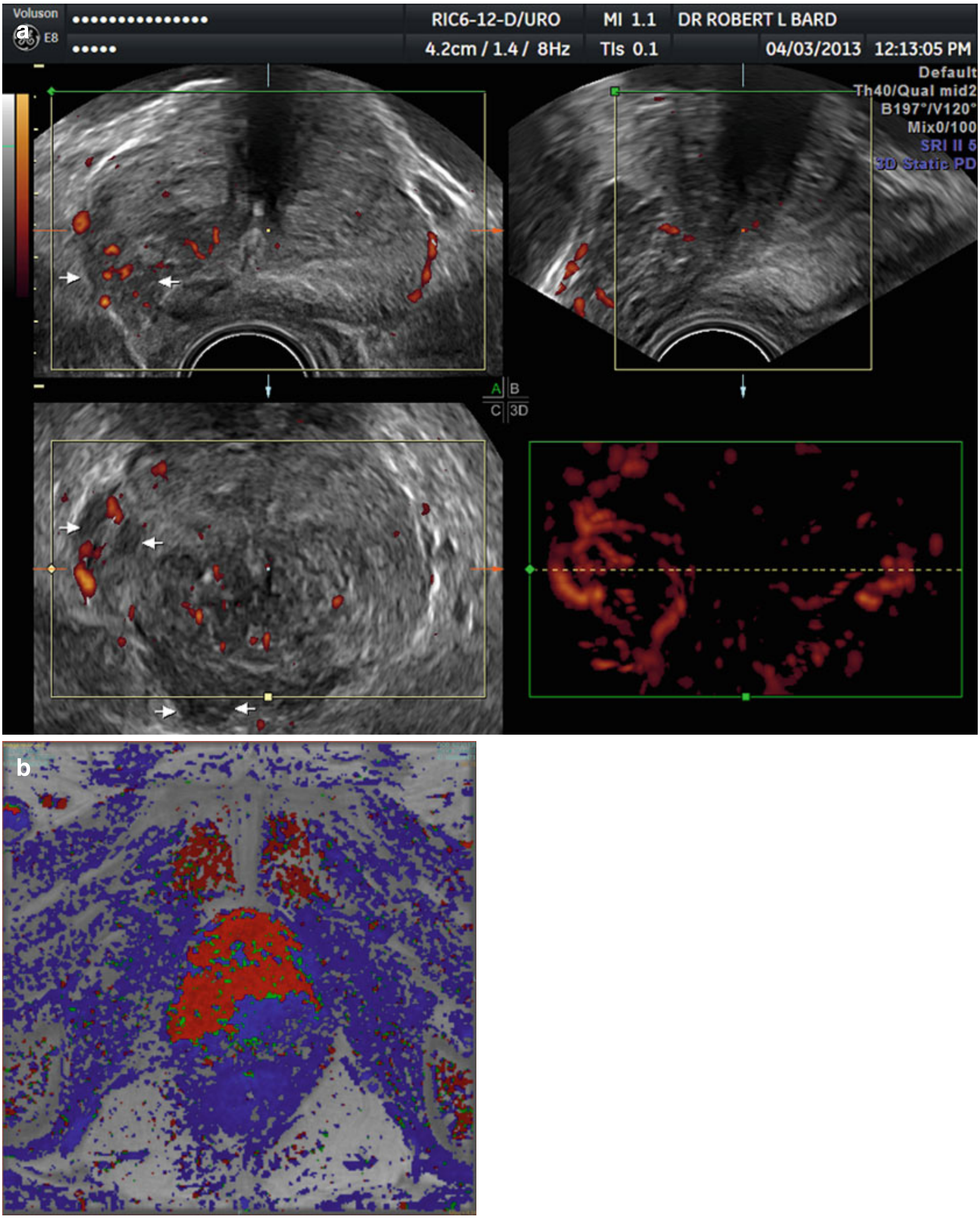

Fig. 14.8 (**a**) 3D. Vascular tumors (*arrows*) with erosion lateral and anterior. (**b**) DCE-MRI. Erosion extends anteriorly

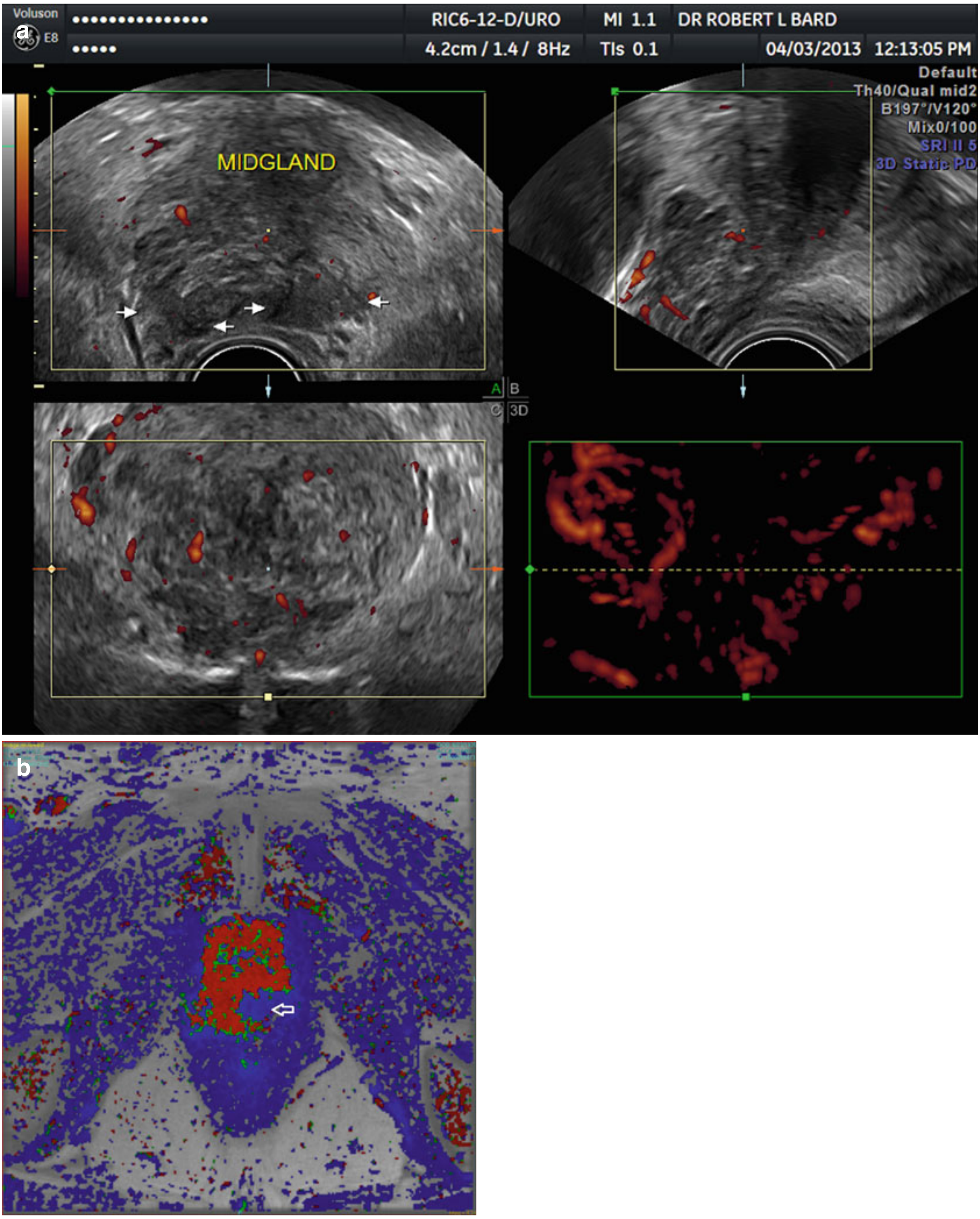

Fig. 14.9 (**a**) 3D. Bilateral tumors (*arrows*) with right posterior erosion. (**b**) DCE-MRI. Left tumor (*arrow*) is low grade without erosion

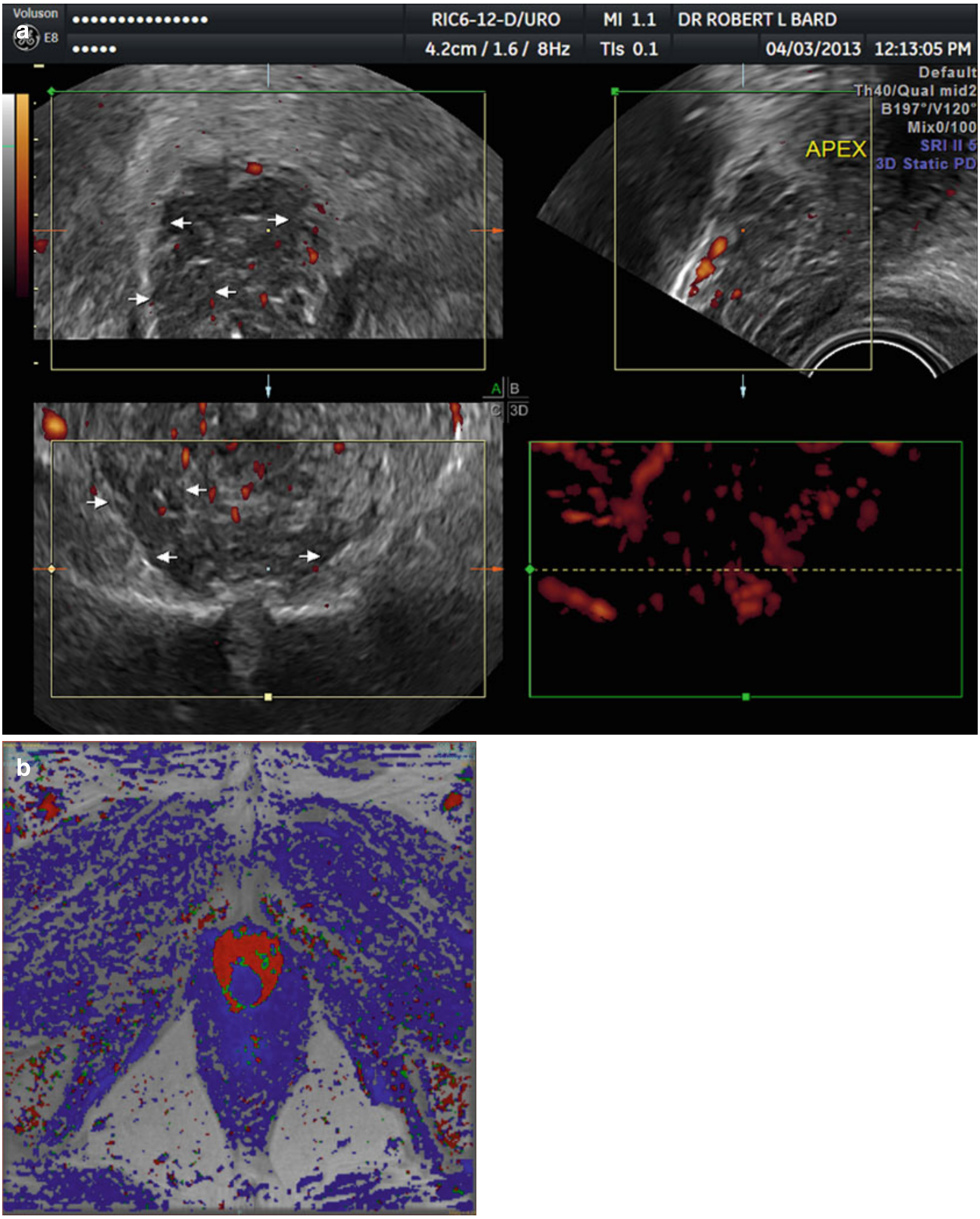

Fig. 14.10 (**a**) 3D. Apex bilateral tumor (*arrows*) with erosion. (**b**) DCE-MRI. Bilateral apical enhancement

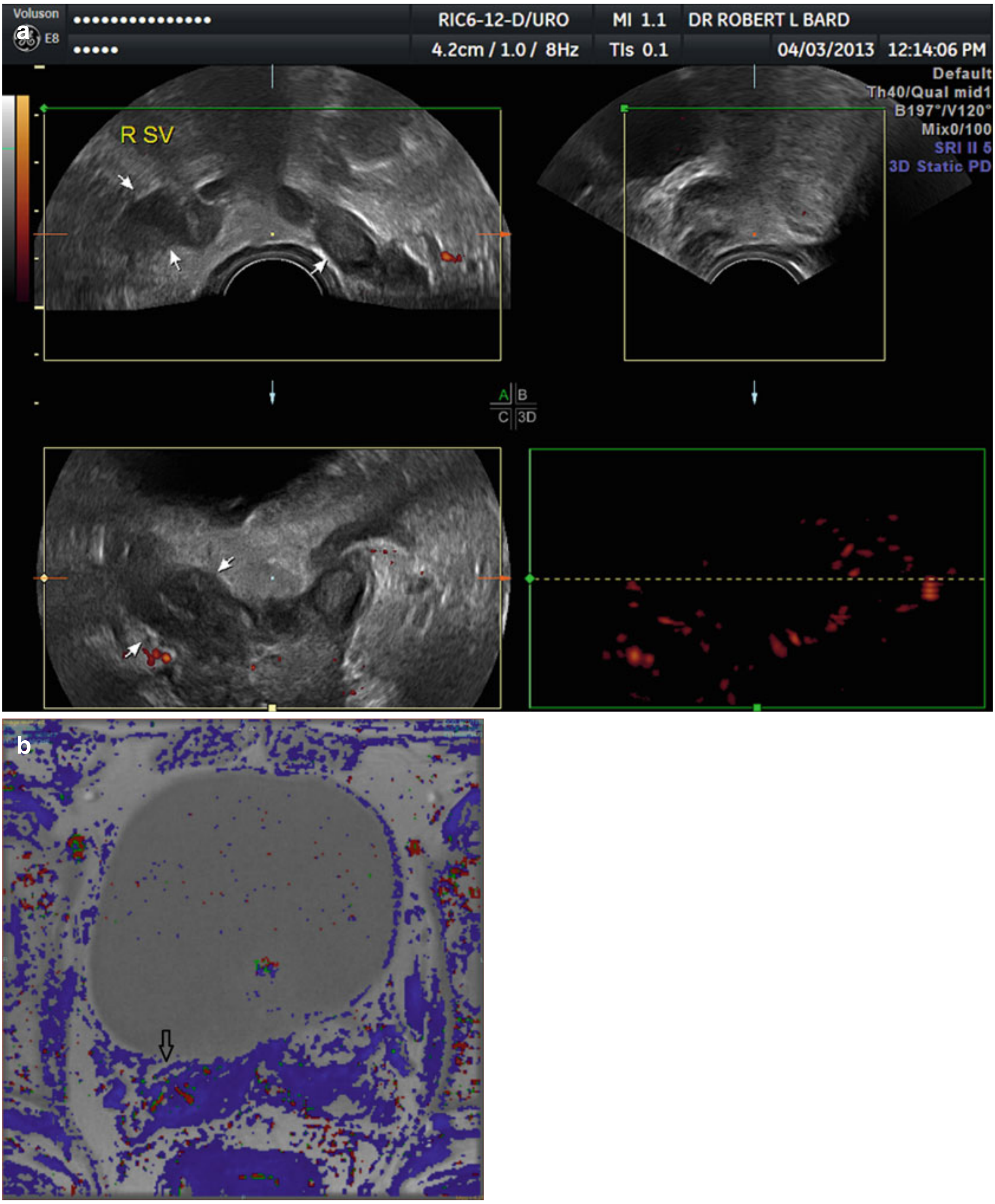

Fig. 14.11 (**a**) 3D. Dilated distal right seminal vesicle (*arrows*) compared to left. (**b**) DCE-MRI. Slight enhancement of distal seminal vesicle (*arrow*)

14.4 Seminal Vesicle Invasion

The seminal vesicles are primarily infiltrated from tumors of the base extending by direct invasion or through the ejaculatory ductal system (Halpern and Strup 2000). Tumor spread along the ejaculatory duct may result in thickening of the narrowed duct with obstruction of the seminal vesicles, producing asymmetry of the proximal structure with loss of its normal tapering as it enters the midline base of the

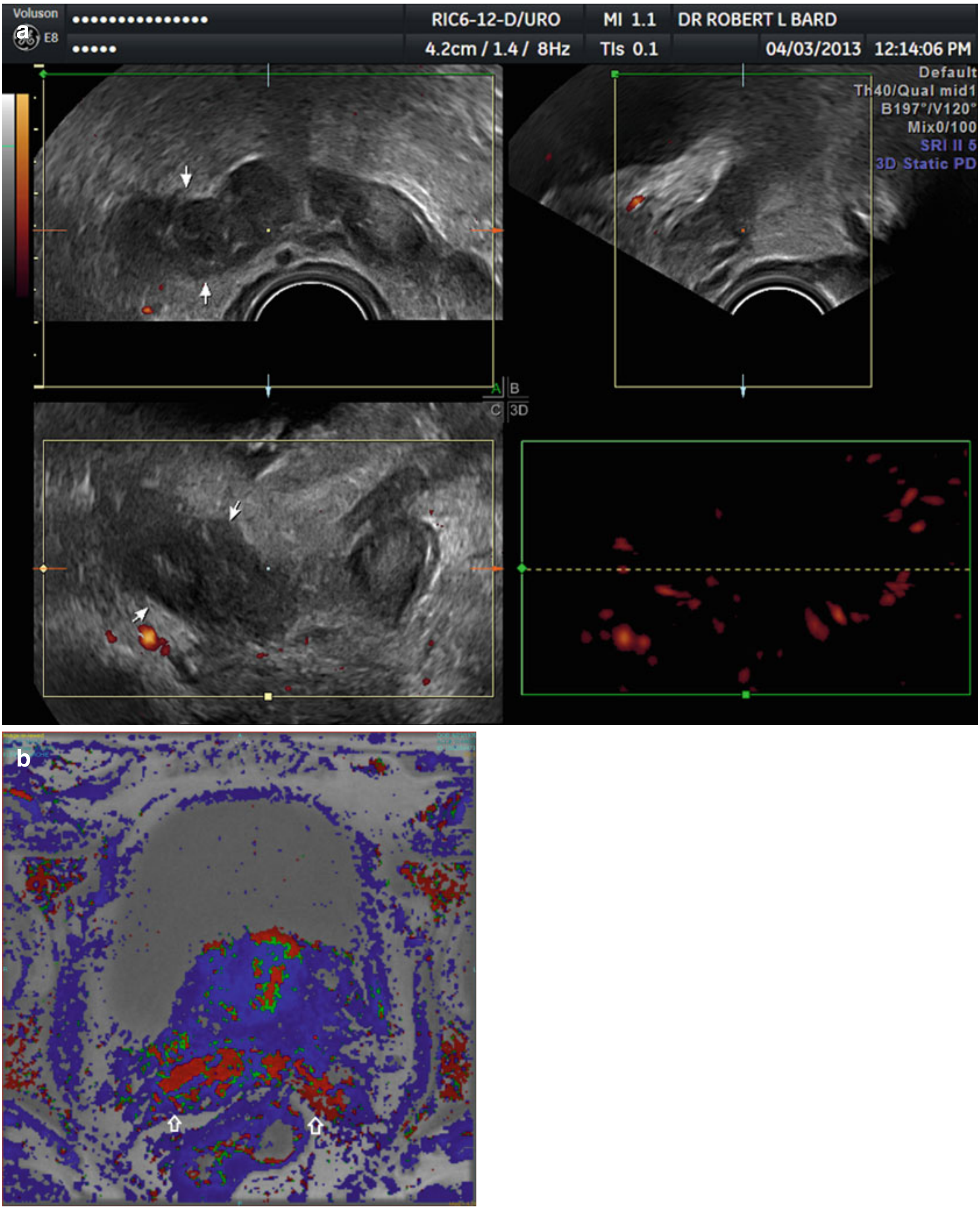

Fig. 14.12 (**a**) 3D. Dilated proximal seminal vesicles (*arrows*) $r>1$. (**b**) DCE-MRI. Marked enhancement of proximal seminal vesicles (*arrows*)

prostate gland. The appearance of ductal dilation and ectasia may be noted in the distal fundal regions. They are secondarily invaded by lateral midgland or base tumors invading extraductally by growing cephalad in a lateral manner (Cornud et al. 2000) (Figs. 14.11, 14.12, 14.13, and 14.14).

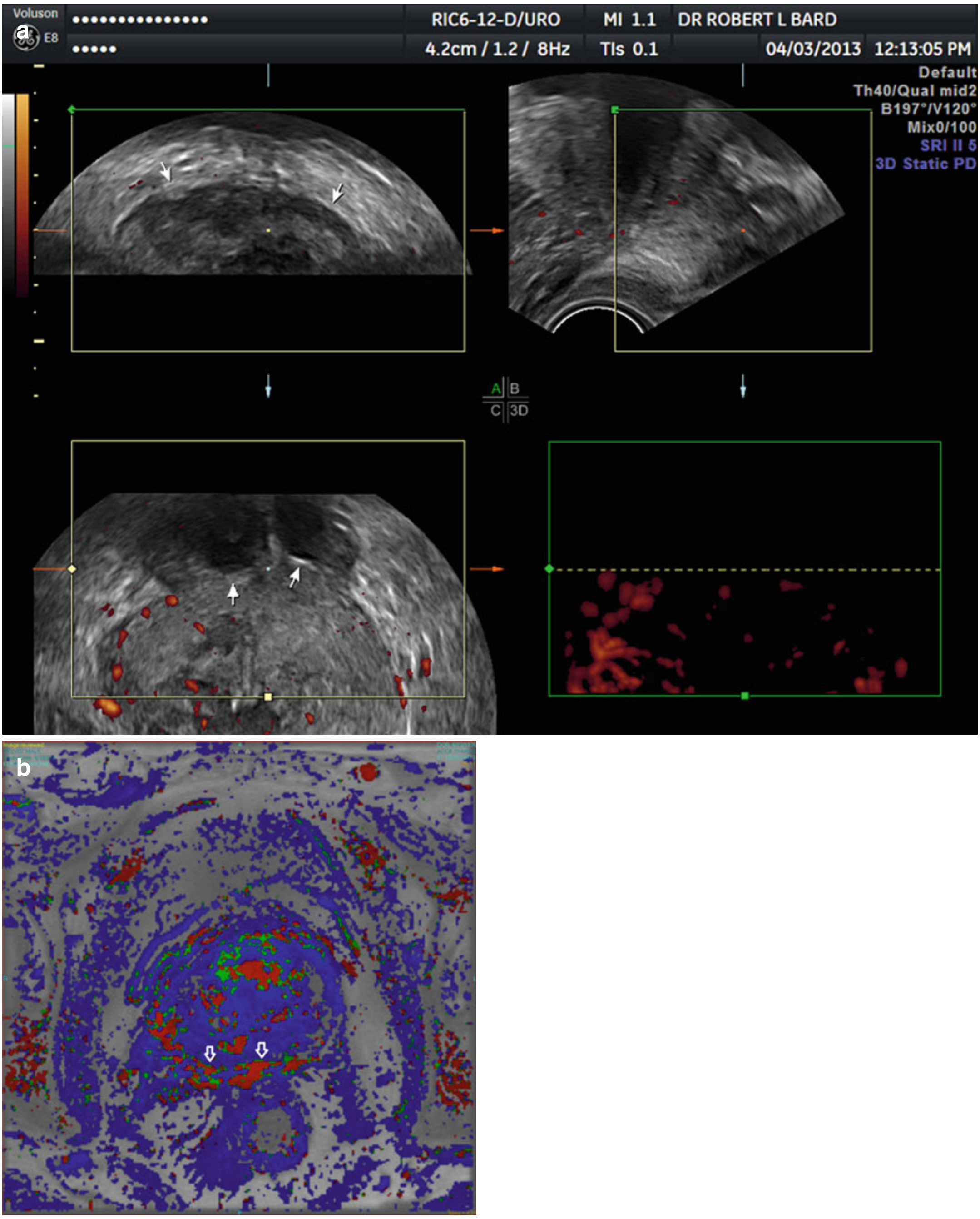

Fig. 14.13 (**a**) 3D. Ampullary portion of vas deferens (*arrows*) at prostate base. (**b**) DCE-MRI. Enhancing vas deferens (*arrows*) medial to seminal vesicles

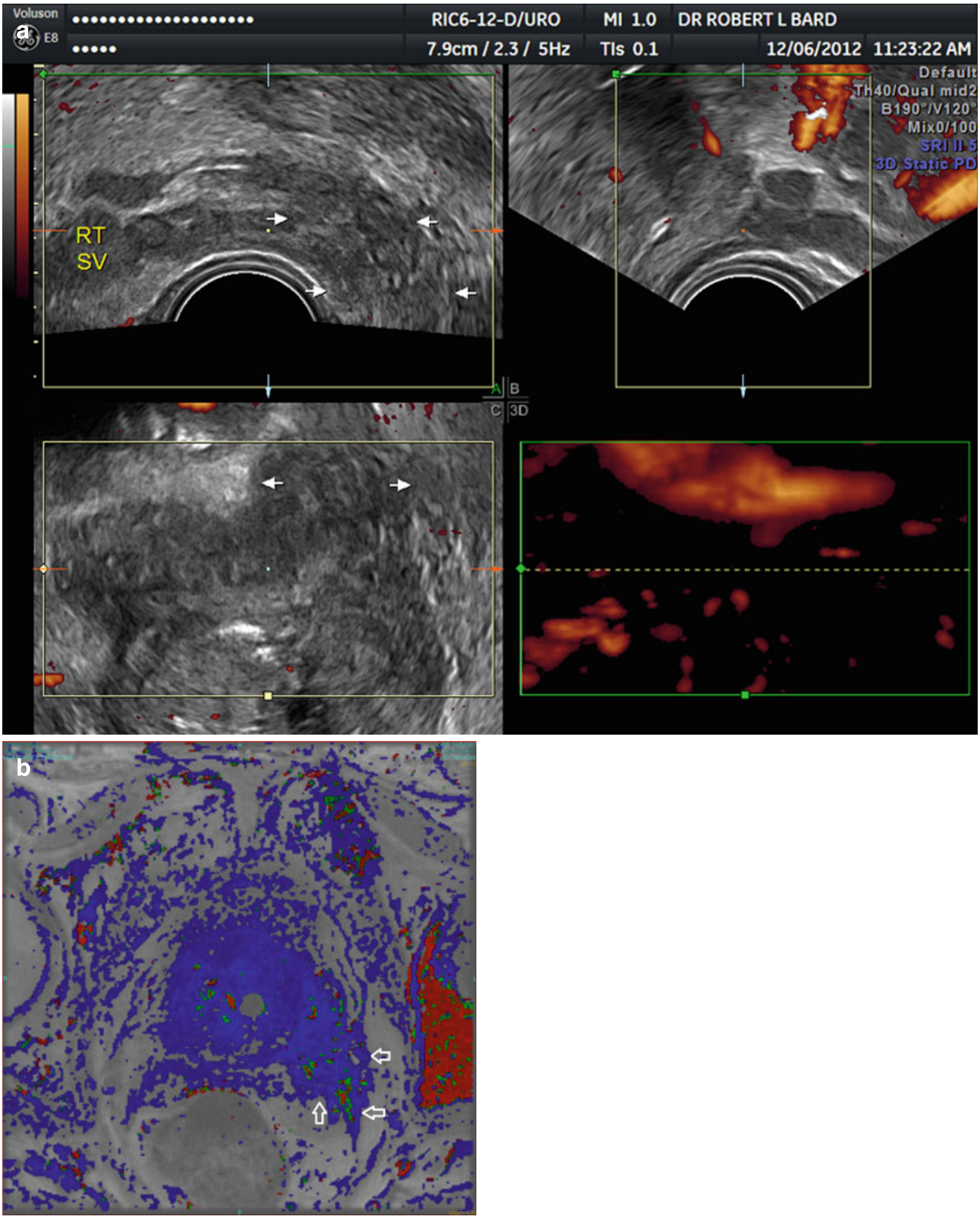

Fig. 14.14 (**a**) 3D. Dilated irregular left seminal vesicle (*arrow*) (sv). (**b**) DCE-MRI. Enhancing left sv (*arrows*) with left acetabular metastasis indicating patient is not focal therapy candidate

References

Bard R. DCE MRI, atlas of prostate cancer. Berlin: Springer; 2009. p. 41.

Cornud F, Hamida K, et al. Endorectal color Doppler sonography and endorectal MR imaging features of prostate cancer: correlation with radical prostatectomy findings. AJR Am J Roentgenol. 2000;175(4):1161–8.

Halpern EJ, Strup SE. Using grey scale, color and Doppler sonography to detect prostate cancer. AJR Am J Roentgenol. 2000;174:623–7.

Mouraviev V, Mayes JM, et al. Prostate cancer laterality as a rationale of focal ablative therapy for the treatment of clinically localized prostate cancer. Cancer. 2007; 110(4):906–10.

15 Metastatic Disease

Robert L. Bard

15.1 Pelvic Lymphadenopathy

Prostate cancers have four possible routes of spread within the pelvis: (a) anterior pelvic route, (b) lateral route, (c) internal iliac (hypogastric) route, and (d) presacral route.

The anterior pelvic route uses lymphatic drainage from the anterior wall of the bladder along the obliterated umbilical artery into the internal iliac (hypogastric) nodes. This is an uncommon pathway for prostate cancers. The lateral route draining lymph from the prostate to the medial chain of the external iliac nodal group is a common pathway. The internal iliac group (includes the anteriorly located obturator area) formerly called the hypogastric pathway receives prostate cancer cells commonly along the visceral branches of the internal iliac lymph ducts to the junctional lymph glands (this is the junction of the internal and external iliac vessels). The presacral route which causes perirectal lymphadenopathy includes the nodal plexus anterior to the coccyx and sacrum which then ascends upward to the common iliac nodal system. Perirectal nodes, which are first filled with micrometastases, indicate a late stage of prostate malignancy. This lymphatic involvement may be by direct extension of a large tumor or by spread by the lymphatic system (Harisinghani 2013).

Pelvic lymph node dissection (PLND) is used to provide accurate staging information about small metastatic foci and commonly involves the external iliac, internal iliac, and obturator areas, with the obturator region being most commonly involved in metastatic foci (Godoy et al. 2012). The presacral and perirectal areas are generally not included due to location and associated tissue damage.

Imaging with lymph node-specific contrast agents using ultrasmall superparamagnetic particles of iron oxide (Combidex or USPIO) contrast was most promising but is not approved by the FDA and therefore not clinically available at this time. An alternative contrast agent gadofosveset has shown a sensitivity and specificity of 85 and 97 % in detecting benign lymph nodes that enhance from cancerous nodes in patients with rectal carcinomas (Lambregts et al. 2012) and may have application in prostate cancer staging.

The application of 3DPDS vascular density histogram analysis may be applied to lymph nodes detected on wide-field TRUS. This is used commonly in assessing benign from malignant foci in nodal abnormalities in the staging of cancer of the breast, skin (melanoma and nonmelanoma), bladder, ophthalmic retina, thyroid, and liver. This is discussed in Chapter 6 since it allows focal targeting of the most aggressive part of a large lesion.

R.L. Bard, MD
Bard Cancer Center, Biofoundation for Angiogenesis
Research and Development, 121 E. 60th St,
New York, NY 10022, USA
e-mail: rbard@cancerscan.com

R.L. Bard et al. (eds.), *Image Guided Prostate Cancer Treatments*,
DOI 10.1007/978-3-642-40429-0_15, © Springer-Verlag Berlin Heidelberg 2014

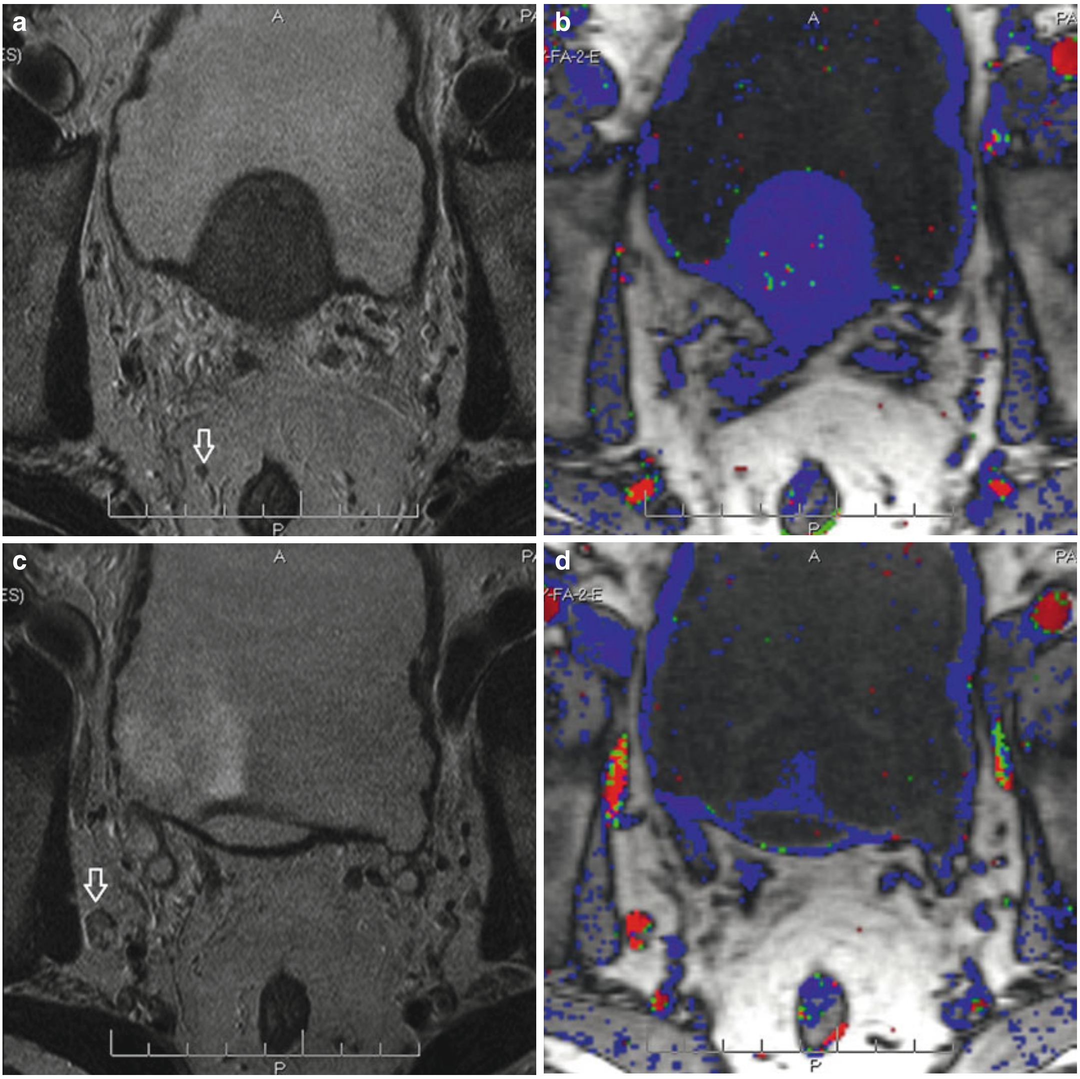

Fig. 15.1 (**a**, **b**) Right perirectal node 3 mm (*arrow*) with homogeneous signal. (**c**, **d**) Right obturator node 9 mm (*arrow*) with inhomogeneous signal

The presence of capsular erosion is associated with two times greater risk of perirectal lymphadenopathy and three times greater risk of bone metastases (Sperling et al. 2013). The presence of capsular irregularity on 3DPDS will focus increased attention to the perirectal area on MRI and boney landmarks. The presence of perirectal adenopathy is associated with higher risk of boney metastases (Bard 2013). A large multicenter study showed that 30 % of patients with intermediate to high risk have nodal metastases exclusively found outside the area of routine PLND (Heesakkers et al. 2009) including 8 % in the pararectal and/or presacral region (Figs. 15.1a–d, 15.2a–l, 15.3a–d, 15.4a, b, 15.5a, b, 15.6a, b, 15.7a–d, and 15.8a–d).

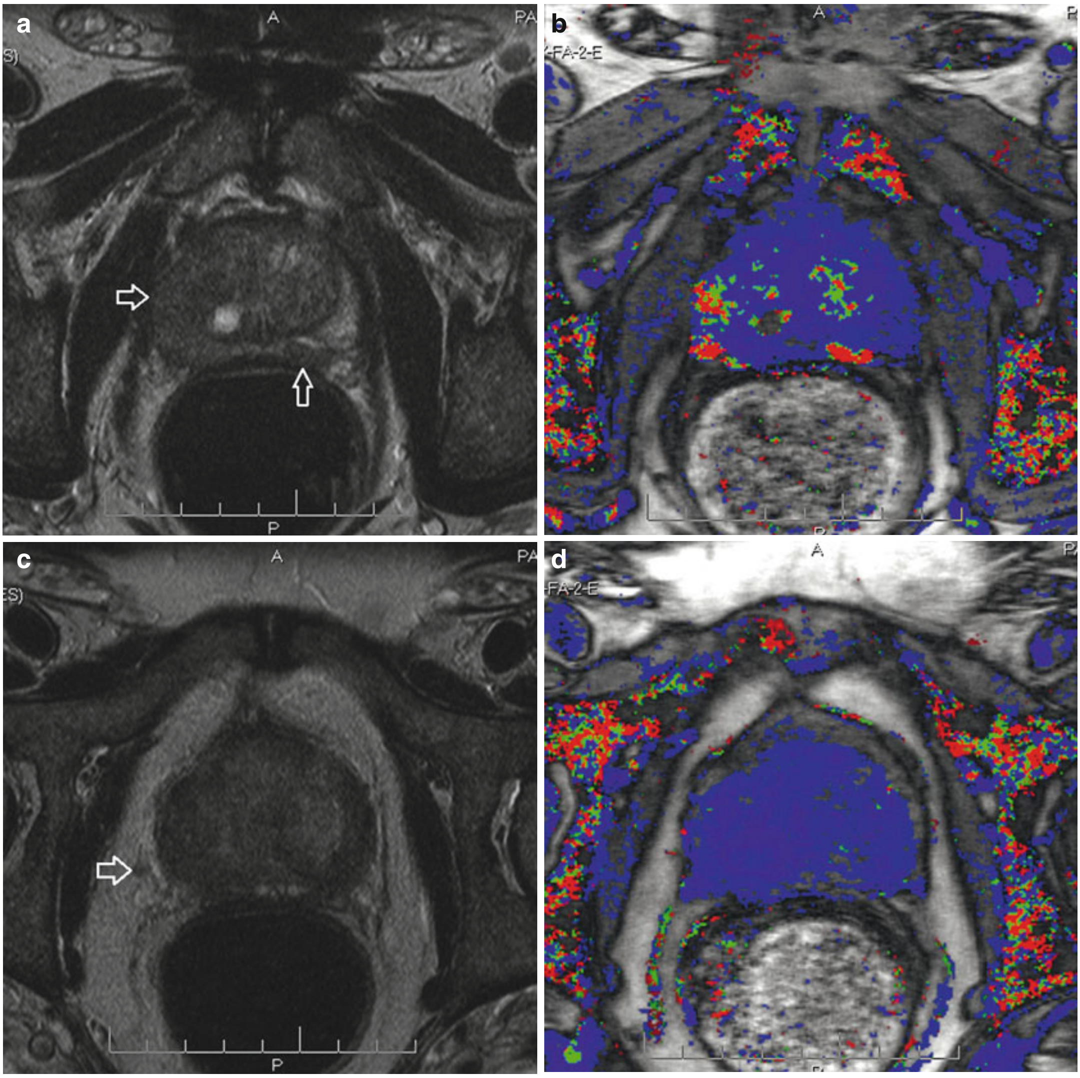

Fig. 15.2 (**a**, **b**) Gleason 4 left base (*arrows*) and Gleason 5 right base. (**c**, **d**) Right periprostatic 3 mm node (*arrow*). (**e**, **f**) Right perirectal node and left obturator nodes (*arrow*). (**g**, **h**) Bilateral vascular obturator nodes (*arrows*) and bone metastases. (**i**, **j**) Bilateral vascular internal iliac nodes (*arrows*) and bone metastases. (**k**, **l**) Bilateral vascular external iliac nodes (*arrows*) and bone metastases

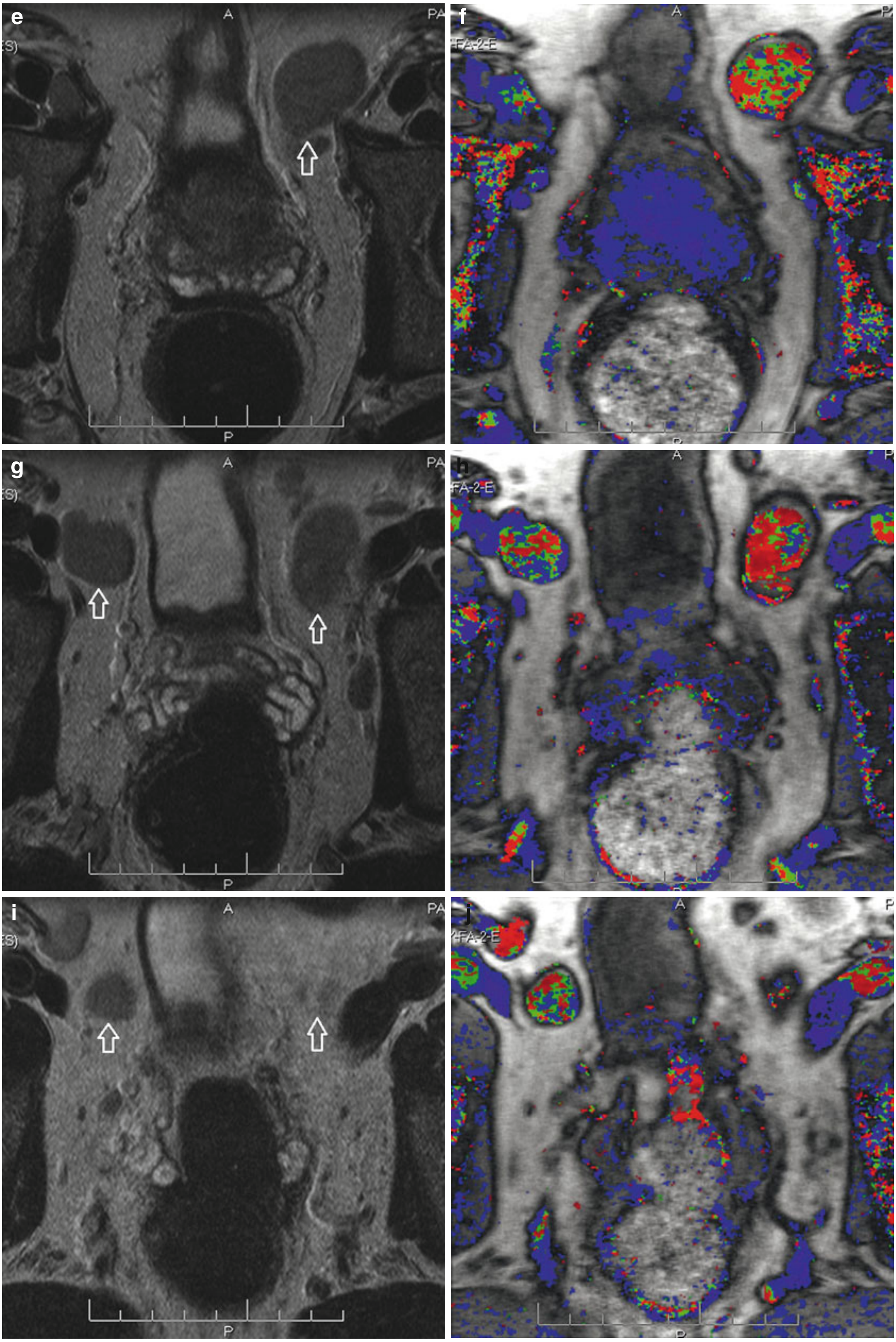

Fig. 15.2 (continued)

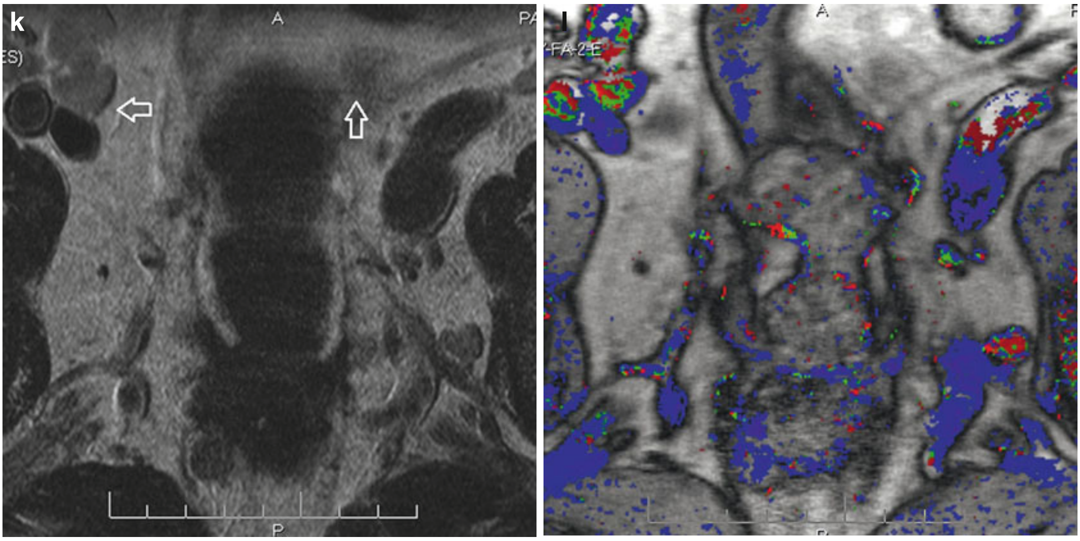

Fig. 15.2 (continued)

15.2 Bladder Invasion

The bladder may be involved by direct invasion of cancers in the base of the prostate gland or rarely by hematogenous spread. It is important to verify if the bladder mass is a calculus (attached to the wall or mobile), a blood clot, or a true bladder tumor. Rotation of the patient may demonstrate movement of the lesion confirming a stone or a clot. Stones generally are rounded and a calcific rim or heavy internal microcalculi will often produce a distinct sonic shadow.

Blood clots tend to resolve with time and may have different echo patterns depending on the degree of clot contraction/fibrosis or clot dispersion (Figs. 15.9a, b and 15.10a, b). Rarely, a ureteral tumor will prolapse into the bladder lumen. Oftentimes a dilated ureter or hydronephrosis will be present, entering the base of the prolapsed portion (Figs. 15.11a, b, 15.12a, b, 15.13a, b, 15.14a, b, and 15.15a, b). MRI and 3DPDS may image polypoid lesions 3 mm and larger. Sessile or surface lesions may be missed. This resolution may be used as a screening test for bladder neoplasms that protrude into the lumen. Internal irregularities may be falsely exaggerated with a partially distended bladder.

Computerized tomography (CT), MRI, and 3DPDS will show asymmetry of the bladder outline. Irregularities of the bladder wall are better imaged on MRI and CT than with standard 3DPDS. The common inguinal hernia may pull the bladder wall causing irregularity and thickening. Bladder tumors may be present along with a hernia and may attach to the hernia sac producing herniation of the bladder along with the hernia sac. Clinical correlation of an irregularly thickening muscular wall is appropriate (Fig. 15.16a–f). Since the dome of the bladder is a curved structure, wall thickening and intraluminal lesions must be confirmed in all three orthogonal imaging planes. Bladder polyps and calculi are often noted with obstructive benign hypertrophy of the prostate or obstructive malignant lesions (Fig. 15.17a, b). Bladder wall irregularity may be easily appreciated on the transverse transabdominal sonogram when there is deviation from its classic rectangular shape (Wu et al. 2011).

15.3 Bone Metastases

Prostate cancers commonly metastasize to the boney skeleton by the hematogenous route with multiple, randomly distributed sites mostly in the pelvis (86 %), rib cage 67 %, and spine (57 %) (Lobo et al. 1999). Standard MRI often shows the

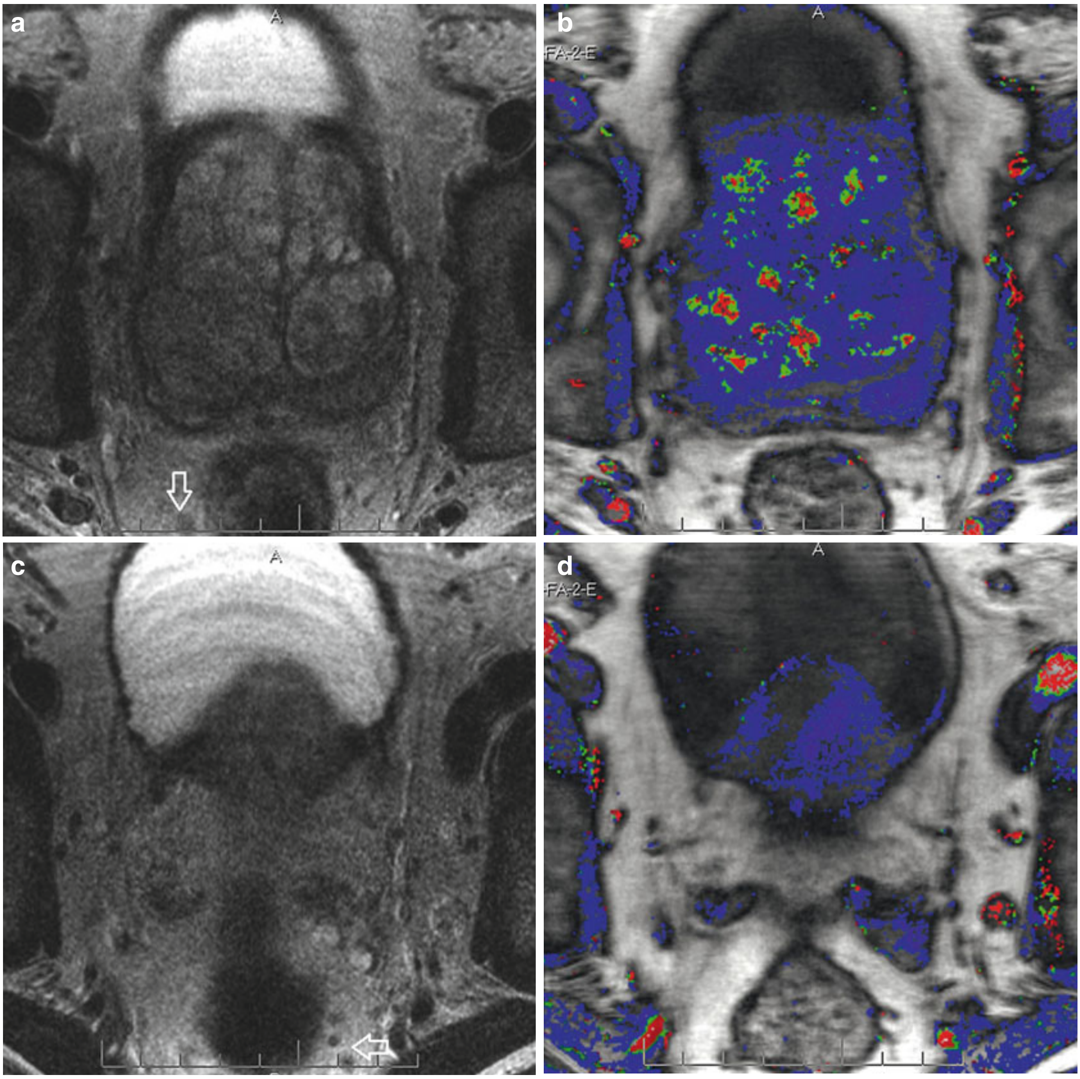

Fig. 15.3 (**a**, **b**) Right perirectal node 6 mm (*arrow*) with homogeneous signal. (**c**, **d**) Left perirectal node 3 mm (*arrow*); note 2 anterior vessels

lesion; however, the specificity is low. Correlation with DCE-MRI enhancing improves the chance that the lesion is cancerous. Commonly a single focus is found in the boney pelvis (Figs. 15.18a, b, 15.19a, b, and 15.20a, b). In highly anaplastic aggressive malignancies, the pelvis may be symmetrically and diffusely involved (Figs. 15.21a, b, 15.22a, b, 15.23a, b, 15.24a, b, and 15.25a, b).

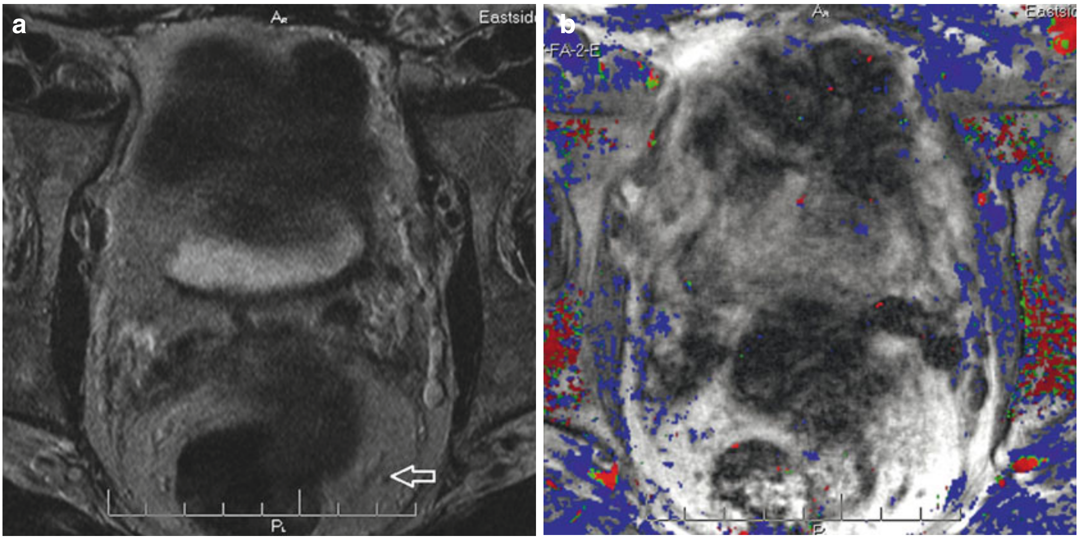

Fig. 15.4 (**a**, **b**) Left 3 mm perirectal node (*arrow*)—avascular

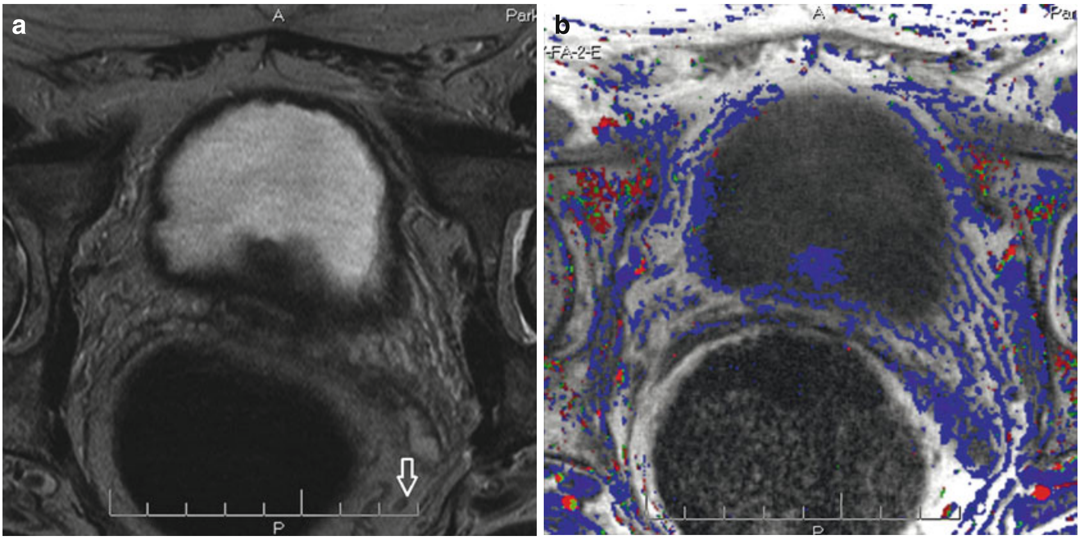

Fig. 15.5 (**a**, **b**) Left 3 × 5 mm perirectal node (*arrow*)—vascular

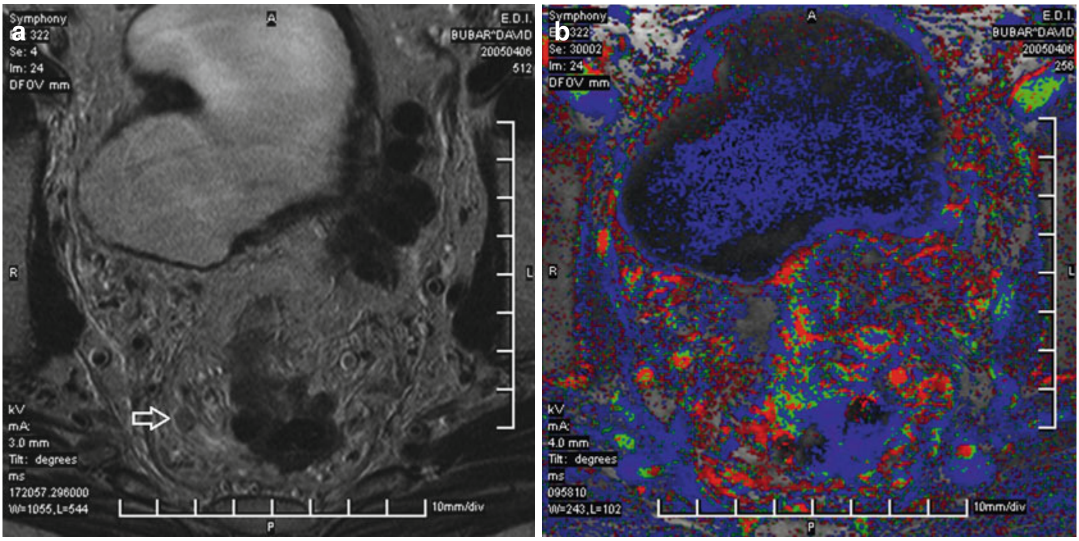

Fig. 15.6 (**a**, **b**) Right perirectal vascular node (*arrow*) from squamous cell carcinoma; note massive rectal invasion

15.4 Rectal Invasion

Subtle rectal invasion is best seen on 3DPDS with loss of the posterior prostatic capsule and tumor vascularity extending into the rectal lumen. The tumor may attach and invade the sigmoid colon on the left directly by extension and rarely the cecum on the right via extensive pelvic lymphadenopathy (Bard 2009).

Primary rectal tumors are better imaged on MRI and DCE-MRI as TRUS is not designed to image this air-filled organ. While there are specifically designed ultrasound units to find and stage anal and rectal tumors, these will not be discussed in this textbook. More frequently, massive hemorrhoid disease will be identified as the dilated vessels are traced from the rectum inferiorly to the anus (Figs. 15.26a, b and 15.27a, b).

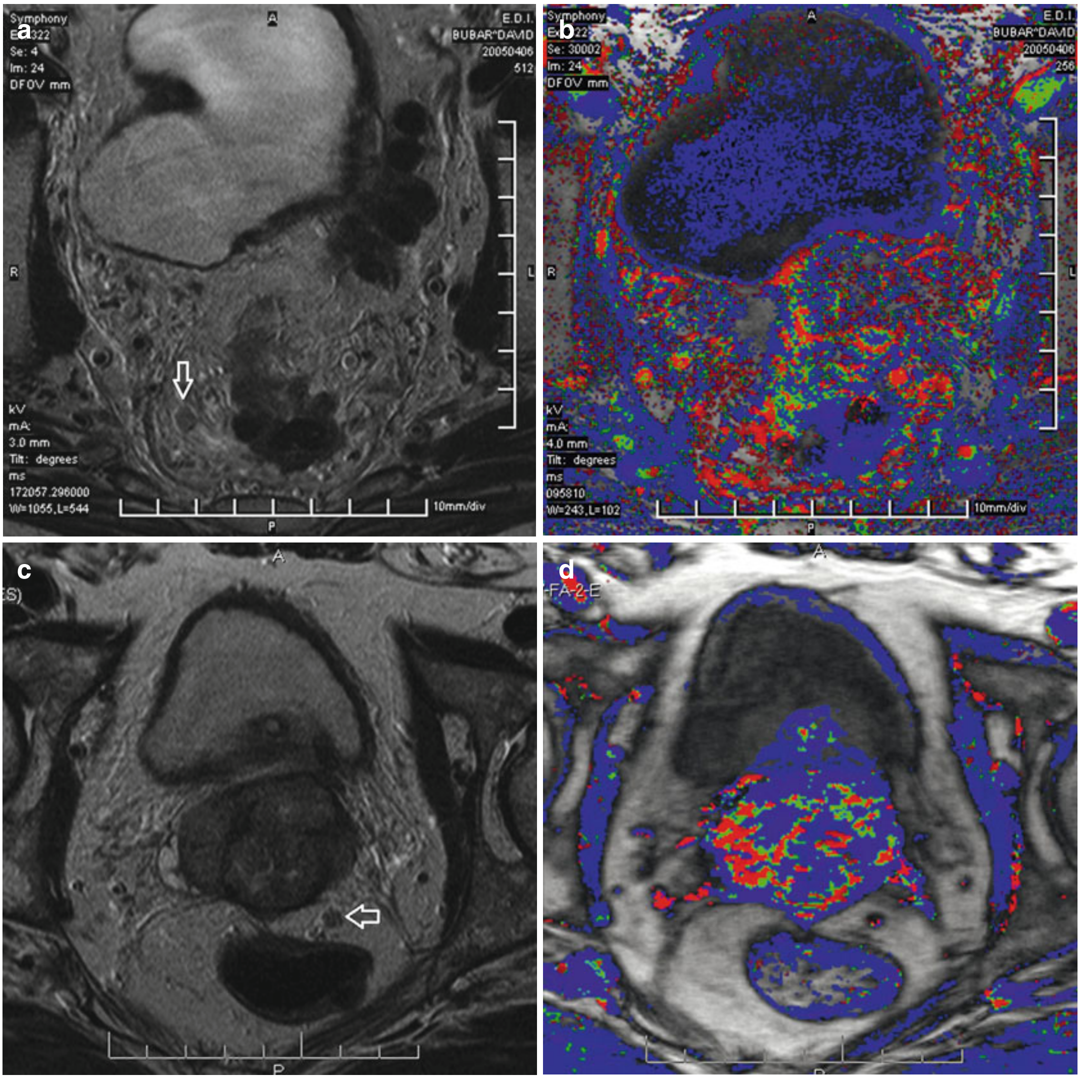

Fig. 15.7 (**a**, **b**) Right perirectal node (*arrow*) with massive rectal invasion. (**c**, **d**) Seminal vesicle invasion with left perirectal node (*arrow*)

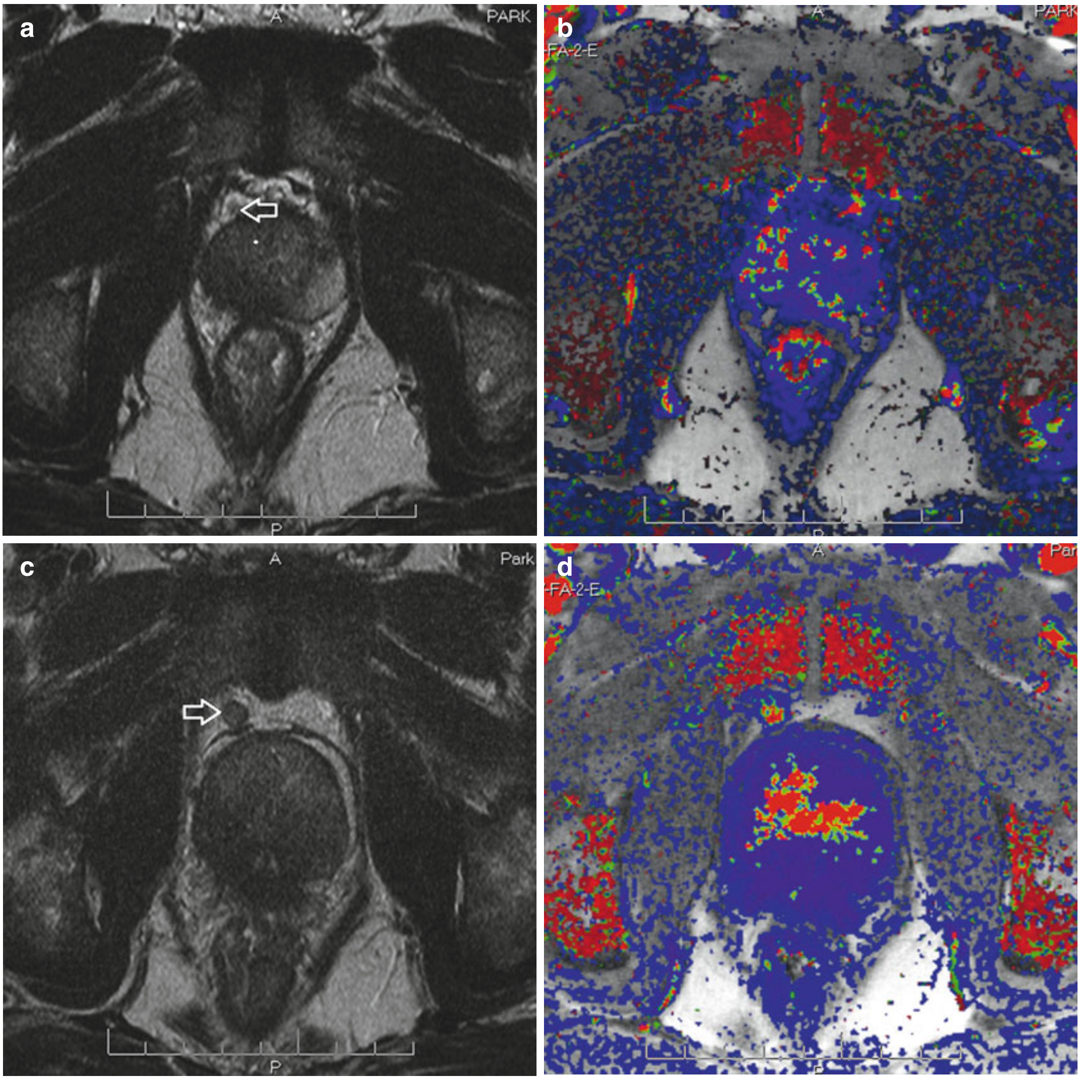

Fig. 15.8 (**a**, **b**) September 2006 avascular retropubic 4 mm right anterior lymph node in the space of Retzius (*arrow*). (**c**, **d**) Nine-month follow-up (June 2008) retropubic node increased to 6 mm (*arrow*) with increased perfusion

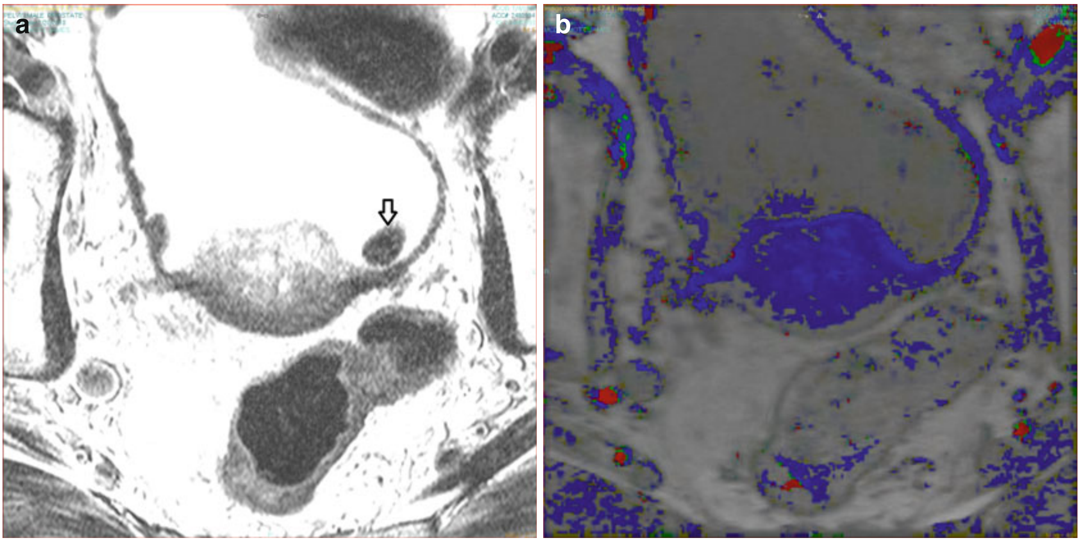

Fig. 15.9 (**a**) MRI dark oval left stone (*arrow*). (**b**) Left bladder stone not imaged on DCE

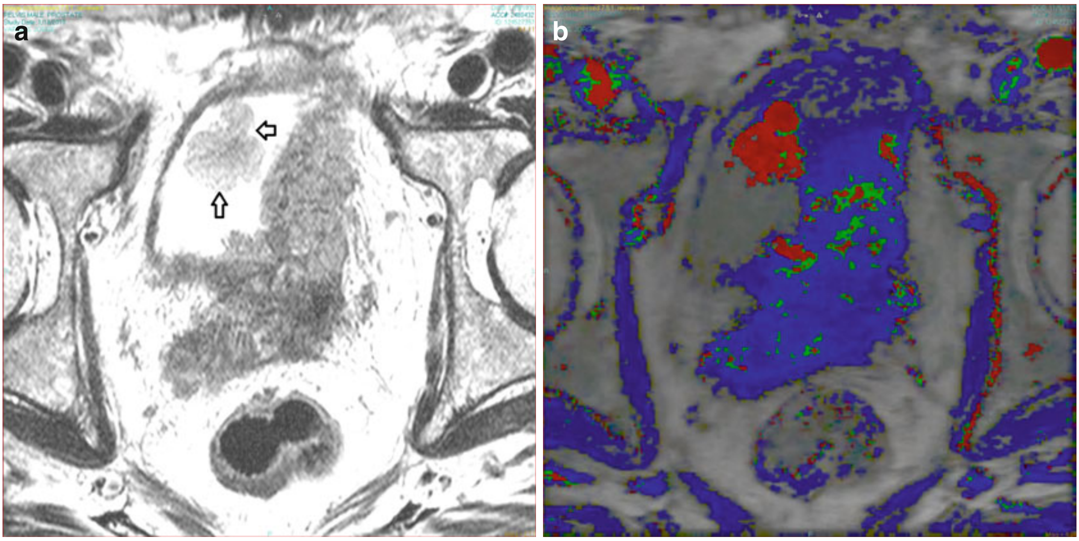

Fig. 15.10 (**a**) MRI Superior bladder tumor (*arrow*) R DOME. (**b**) DCE-MRI enhancing transitional cell carcinoma

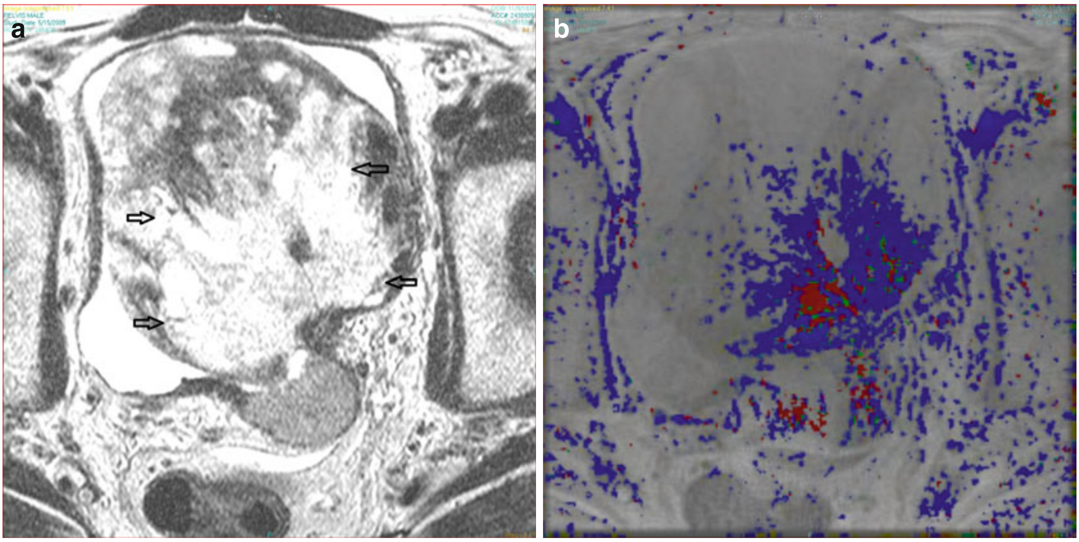

Fig. 15.11 (**a**) MRI necrotic (same signal as bladder) massive bladder tumor (*arrows*). (**b**) DCE-MRI viable tumor enhances

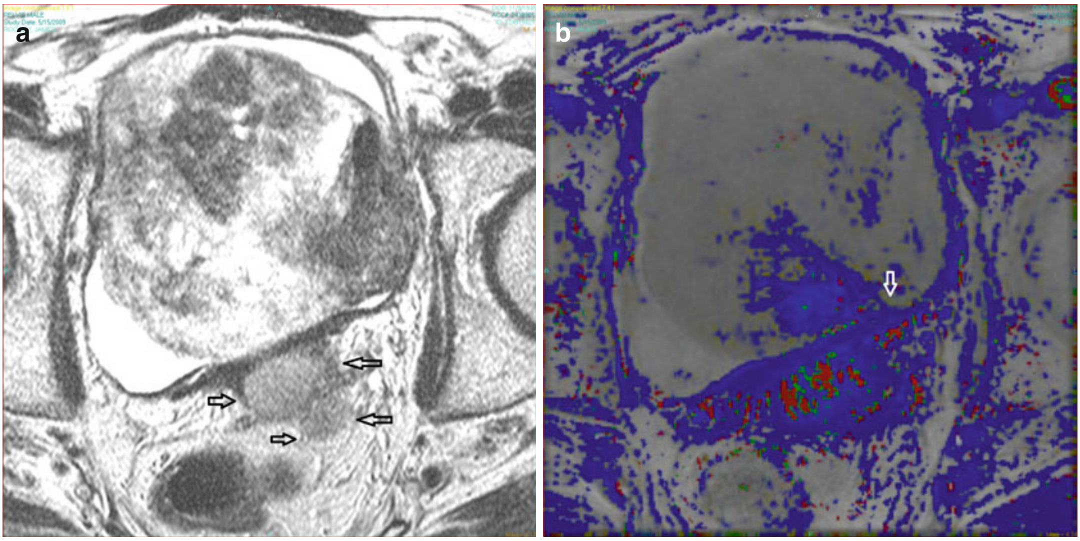

Fig. 15.12 (**a**) Ureterocele (*arrows*) with distal urothelial tumor herniating into bladder. (**b**) Massive necrosis: vessel constriction (*arrows*) and lack of perfusion

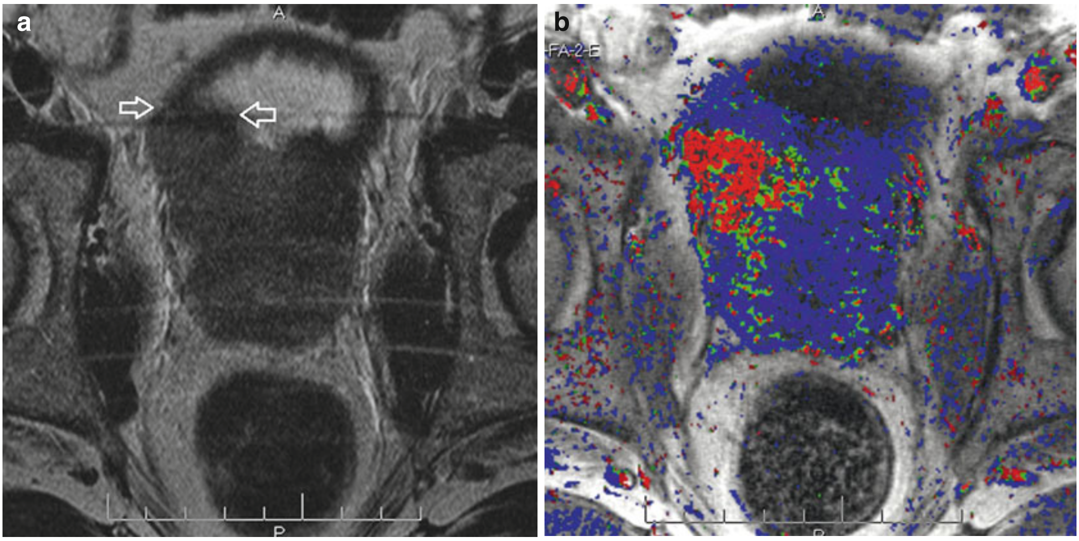

Fig. 15.13 (**a**, **b**) Right tumor (*arrows*) invading bladder with extension through bladder wall

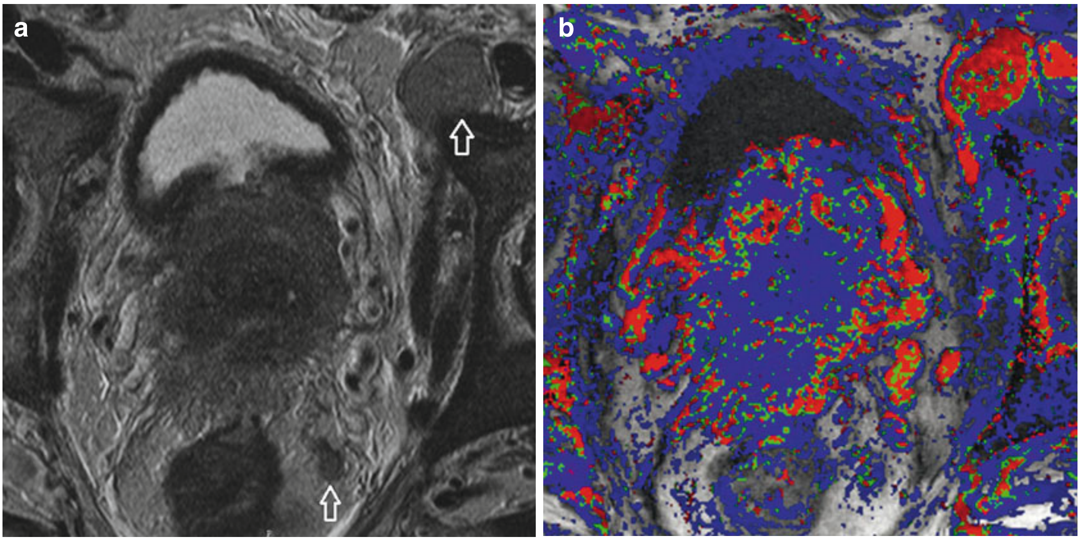

Fig. 15.14 (**a**, **b**) Massive tumor invading bladder base with left perirectal and external iliac adenopathy (*arrows*)

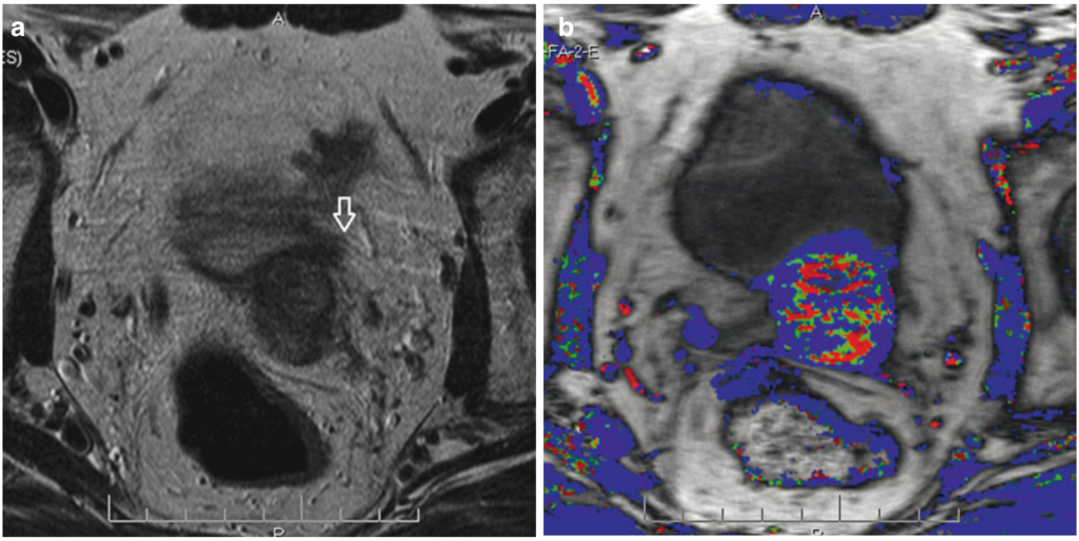

Fig. 15.15 (**a**, **b**) Gleason 5 invading bladder lumen (*arrows*)

Fig. 15.16 (**a**) T2 MRI; note irregular thickened bladder wall tapering towards left inguinal hernia (*arrows*); note normal right bladder wall (*open arrows*). (**b**) DCE-MRI; note left weakly enhanced bladder wall. (**c**) T2 caudal section shows left dome of bladder thickening (*arrows*). (**d**) T2 coronal view, midline-wall thickening (*arrows*) confirmed in orthogonal view. (**e**) T2 coronal view, anterior thickened dome of bladder (*arrows*). (**f**) 3D transverse sonogram shows loss of expected symmetric oval or rectangular appearance of distended bladder outline on the left superolateral wall

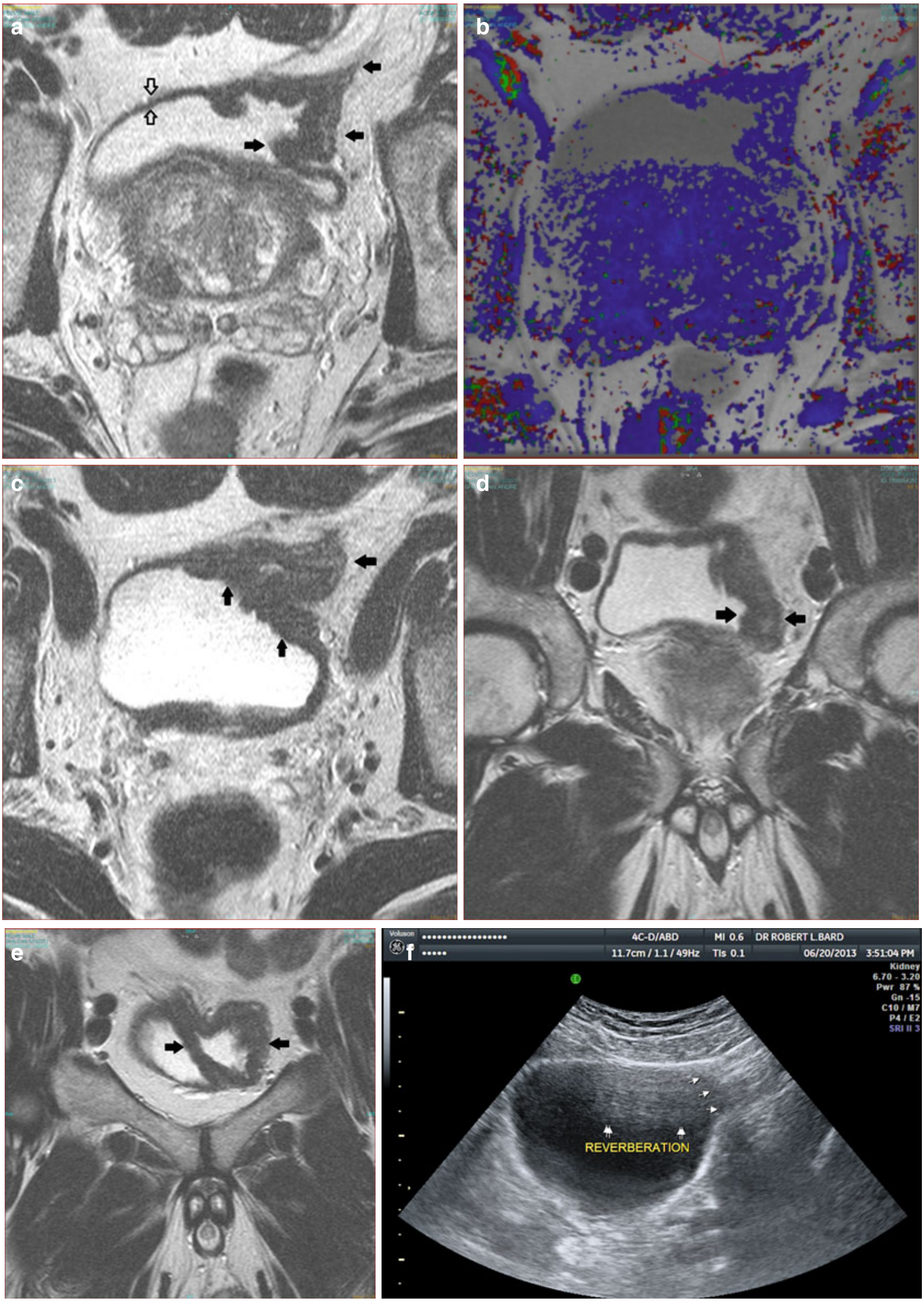
a
b
c
d
e
f
Voluson
4C-D/ABD
MI 0.6
DR ROBERT L.BARD
11.7cm / 1.1 / 49Hz
TIs 0.1
06/20/2013
3:51:04 PM
Kidney
6.70 - 3.20
Pwr 87 %
Gn -15
C10 / M7
P4 / E2
SRI II 3
REVERBERATION

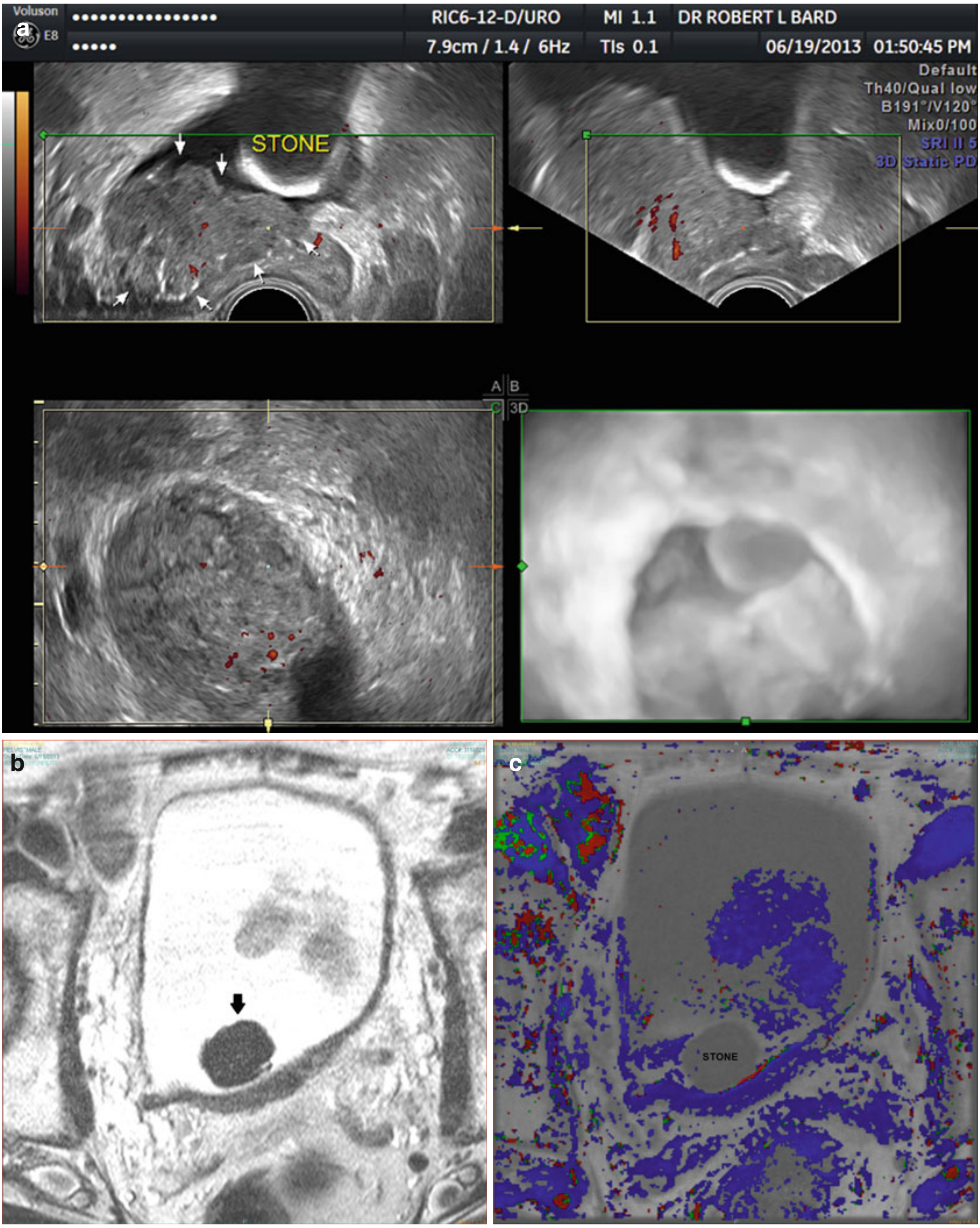

Fig. 15.17 (**a**) 3D right prostate tumor (*arrows*) invading bladder. (**b**) Left calculus due to obstruction. (**c**) Large stone shows no enhancement

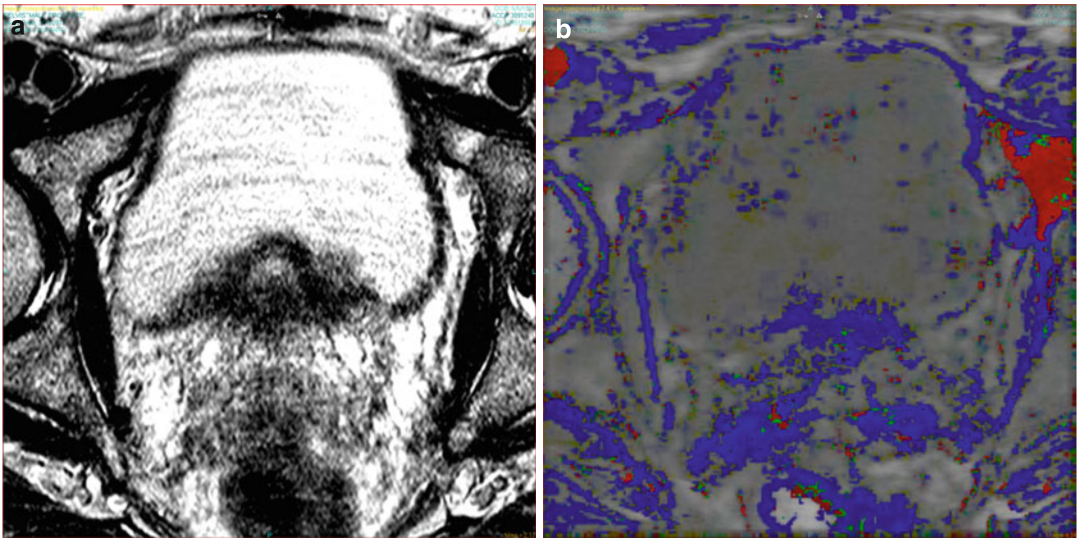

Fig. 15.18 (**a**) MRI bone met not identified on T2. (**b**) Anterior left acetabular met well defined

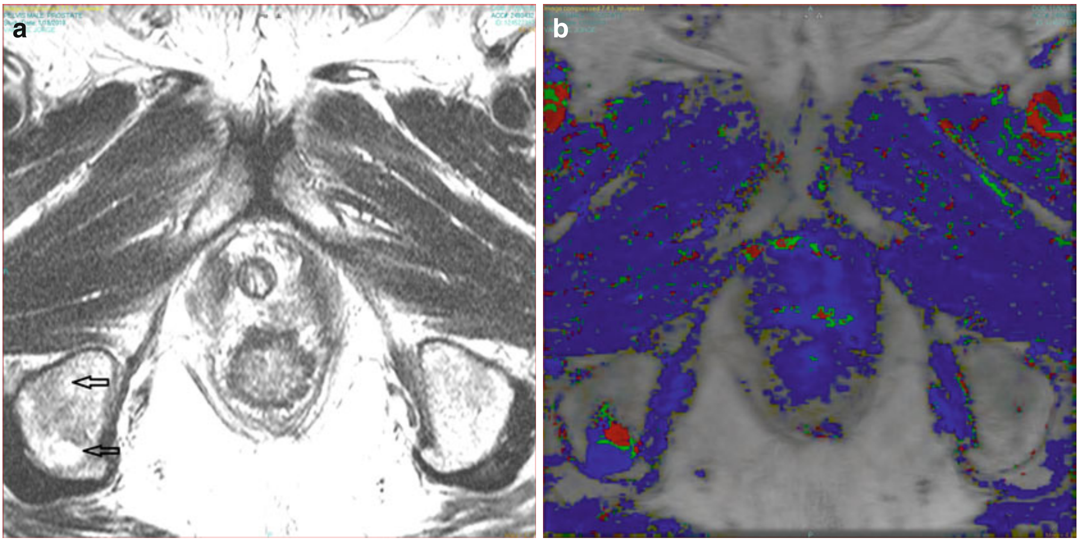

Fig. 15.19 (**a**) MRI right ischial metastasis (*arrows*) poorly defined. (**b**) DCE-MRI right ischial met well perfused

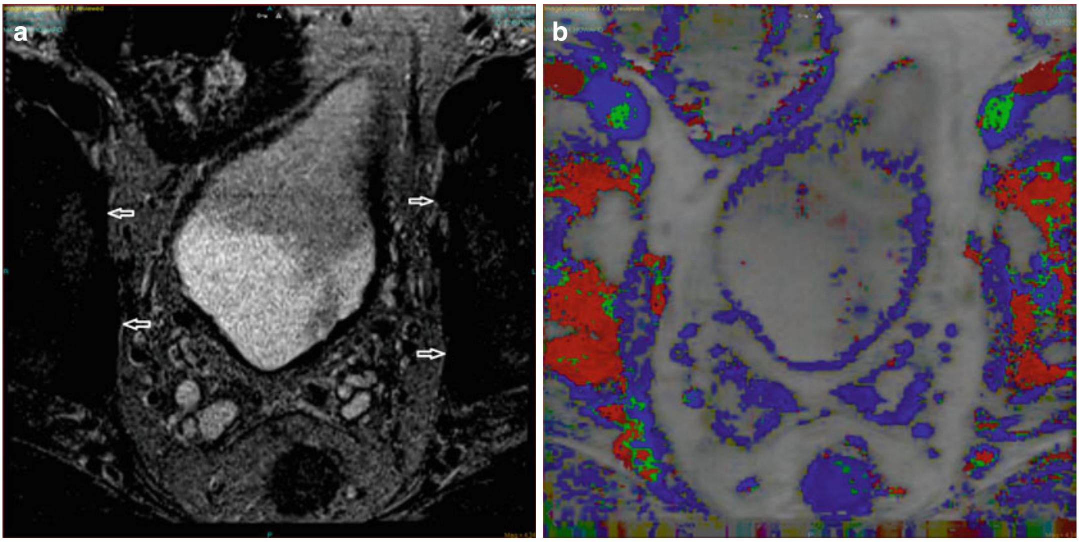

Fig. 15.20 (**a**) MRI bilateral iliac boney metastases (*arrows*). (**b**) DCE-MRI metastatic foci enhancing

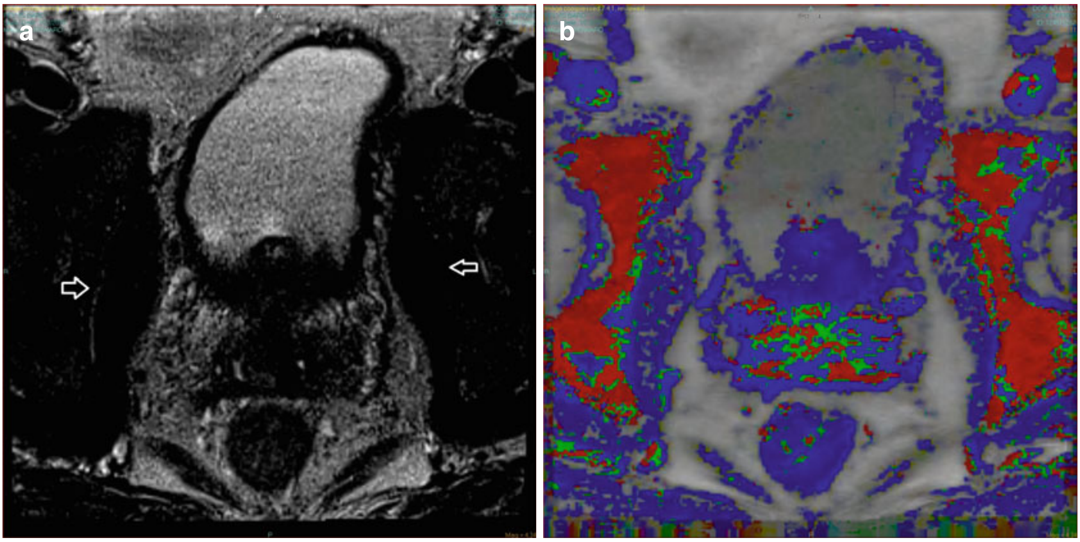

Fig. 15.21 (**a**) MRI upper acetabular metastases (*arrows*). (**b**) DCE-MRI boney lesions well perfused

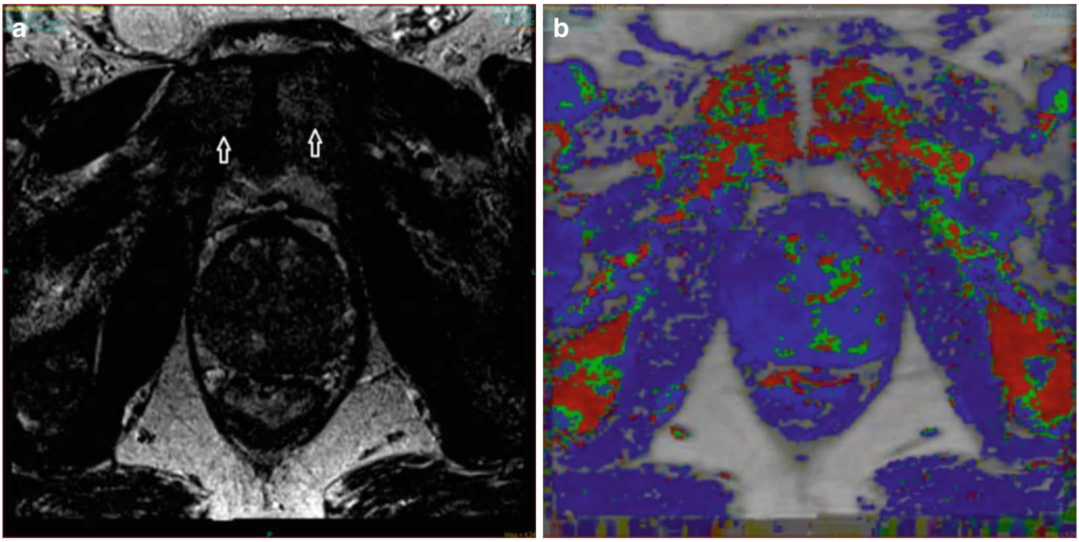

Fig. 15.22 (**a**) MRI lower acetabular and symphysis pubis (*arrows*) metastases. (**b**) DCE-MRI boney lesions well perfused

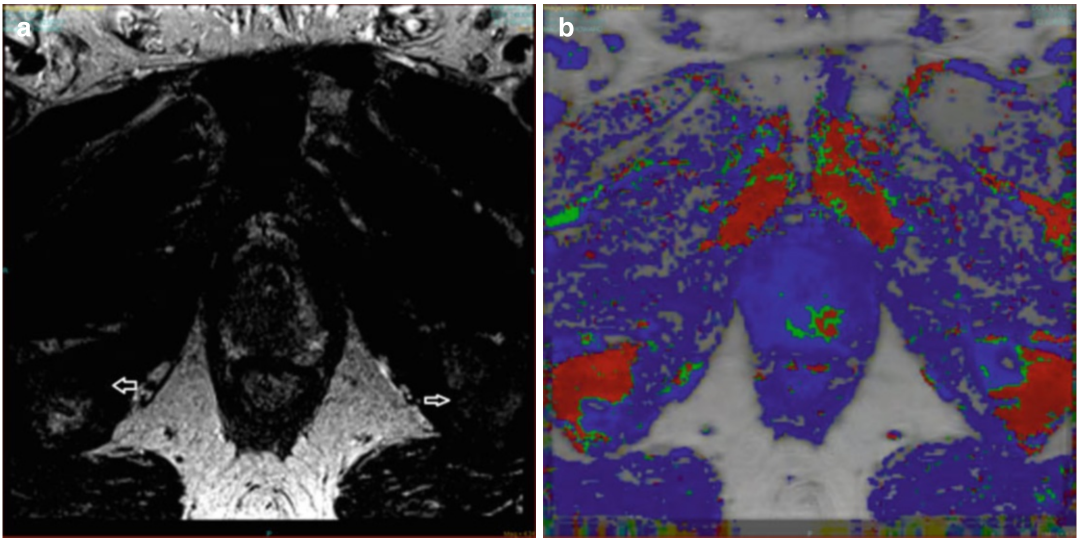

Fig. 15.23 (**a**) MRI symphysis pubis and ischial (*arrows*) metastases. (**b**) DCI-MRI bilateral lesions enhance well

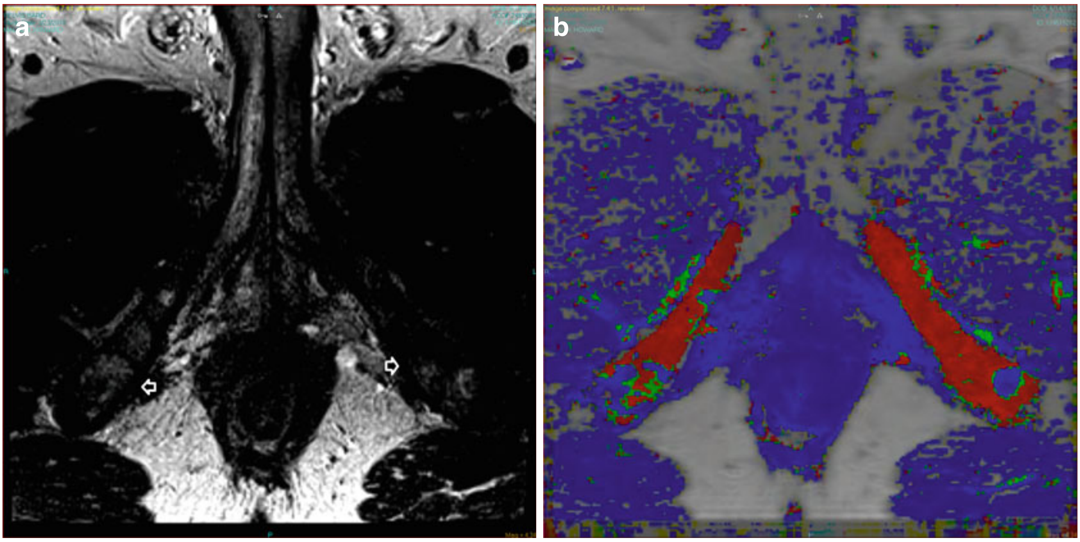

Fig. 15.24 (**a**) MRI inferior pubic ramus metastases (*arrows*). (**b**) DCE-MRI bilateral lesions enhance well

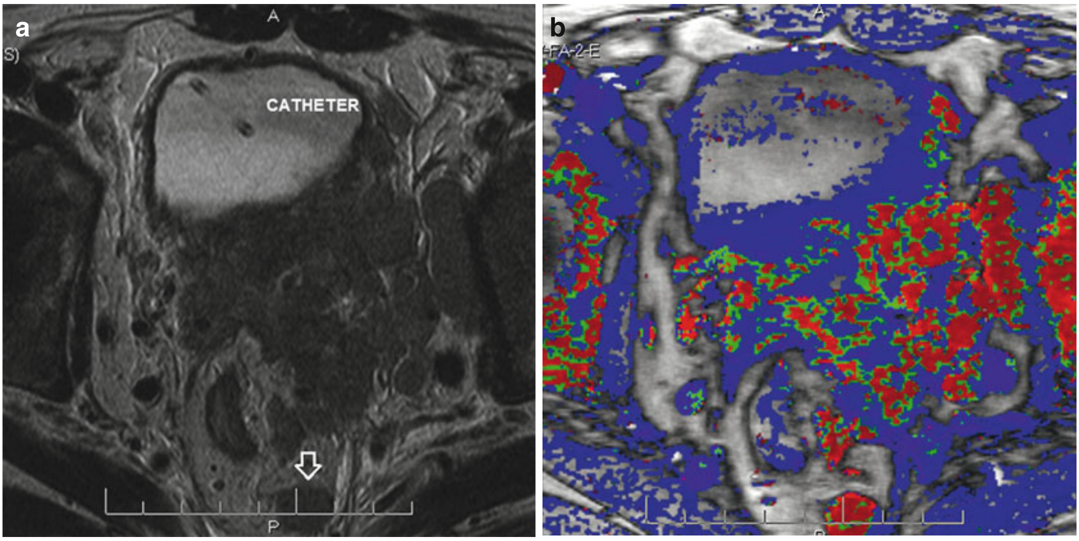

Fig. 15.25 (**a**, **b**) Iliac boney metastases and large left perirectal node (*arrow*)

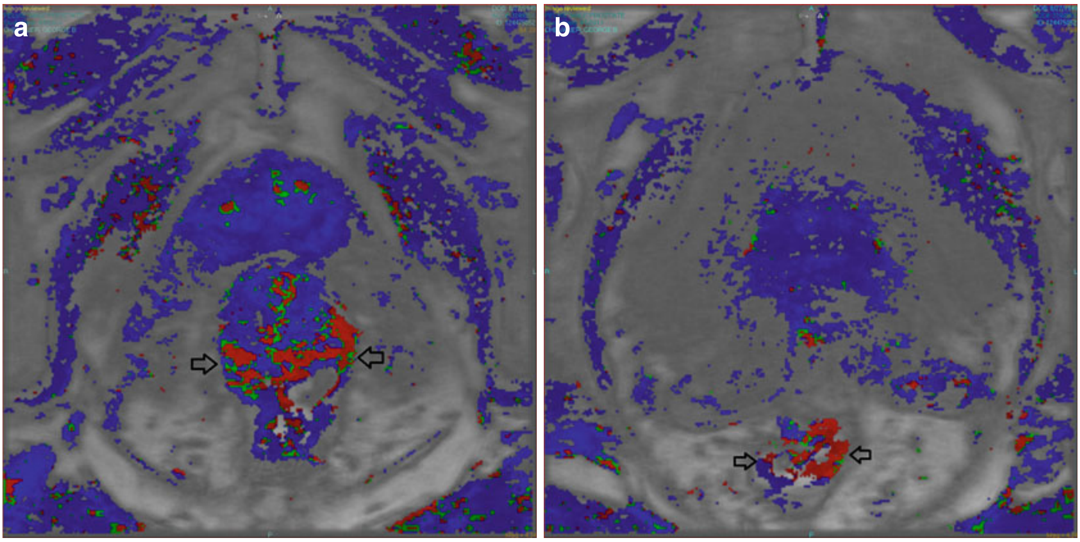

Fig. 15.26 (**a**) DCE-MRI midpelvis image rectal hemorrhoids (*arrows*). (**b**) DCE-MRI caudal image confirms anal hemorrhoids (*arrows*)

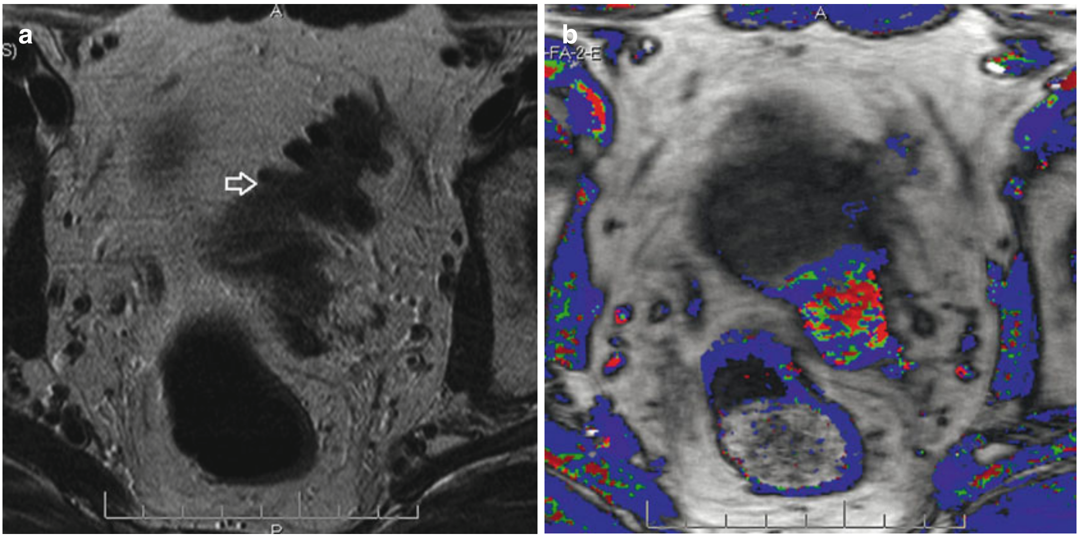

Fig. 15.27 (**a**, **b**) Tumor invading distal sigmoid colon (*arrow*)

References

Bard R. DCE-MRI atlas of prostate cancer. Berlin: Springer; 2009. p. 1.

Bard R. Vascular imaging of lymph nodes metastases. In: 2013 American Institute of Ultrasound in Medicine Annual Convention, New York, 2013, p. 134.

Godoy G, Bodman C, Daher C, et al. Pelvic lymph node dissection for prostate cancer. J Urol. 2012;187(6):2082–6.

Harisinghani MG, editor. Atlas of lymph node anatomy. New York: Springer; 2013. p. 127.

Heesakkers R, Jager G, et al. Detection of lymph node metastases outside the routine surgical area with ferumoxtran-10-enhanced MRI. Radiology. 2009;251(2):408–14.

Lambregts DM, Heijnen LA, et al. Gadofosveset enhanced MRI for assessment of rectal cancer lymph nodes. Abdom Imaging. 2012;38:720–7.

Lobo G, Ladrón de Guevara D, et al. Bone scintigraphy in prostate cancer: correlation with clinical and laboratory features and with survival. Rev Med Chil. 1999;127:181–8.

Sperling D, Bard R, Futterer J. Prostate capsular erosion increases risk of bone metastases and perirectal adenopathy. In: 2013 American Roentgen Ray Society meeting, Washington, DC, 2013.

Wu S, Tu R, Liu G. Recognition and application of the rectangular sonographic appearance of the urinary bladder. J Ultrasound Med. 2011;30:1215–20.

Diagnosing, Treating, and Reversing Prostate Cancers with Hormonal and Nutritional Intervention

16

Robert L. Bard, Arthur Bartunek,
and Eugene Shippen

16.1 Introduction

A primary goal in the treatment of prostate and other cancers is to identify aggressive cancers that can kill, as opposed to cancers that do not threaten life, and may not even show any symptoms. The current, widely used diagnostic techniques make this identification extremely elusive. The technology to achieve this diagnostic distinction should be noninvasive and provide measures that can be easily and accurately compared to previous exams, making it easy to track changes. At the same time, it should provide a systematic approach to monitoring the patient's response to therapeutic intervention. In this way, the diagnosis, monitoring, and treatment can be tailored to each individual's circumstances and responsiveness.

With recent advances in the technology of Doppler ultrasound and MRI, these goals can and are being achieved. Until recently, this diagnostic technology has required extensive experience and training in interpreting the images. Now, advances in the computerization of the imaging, blood flow, and tumor measures of exact size and density provide for an accurate and repeatable diagnosis and a means to follow the individual's unique pattern of cancer development, progress, and response to treatment. Recent technological advances also make these procedures available to much broader clinical application, without requiring years of very unique training and experience, and these advances are applicable beyond prostate cancer (PCa), the example used here.

In this paper, the noninvasive diagnostic tracking of a patient's standard treatment progress is presented, along with a naturopathic nutritional approach, the β-sitosterol/antioxidant matrix (β-sit/AOX), which provides vital support for cell function and membrane integrity. The β-sit/AOX matrix properly restores essential nutrition that has been systematically removed from our food supply. It systemically supports the body and is especially targeted to naturally restore cell membrane elasticity and permeability and apoptosis, reduce cell proliferation, and reestablish a healthy intracellular environment that naturally protects against metastases. This directly nourishes the body's natural cancer prevention mechanisms and is appropriate for healthy individuals, for individuals during cancer episodes, and for post-episode maintenance. Following men with PCa using Doppler imaging has shown that an appropriate β-sit/AOX formulation is effective and successful for a wide range of men with diagnosed prostate cancer who elect proactive watchful waiting. The evaluation of nearly 10 years of patient records for men opting for proactive

---

R.L. Bard, MD (✉) • A. Bartunek, PhD
Bard Cancer Center, Biofoundation for Angiogenesis
Research and Development, 121 E. 60th St,
New York, NY 10022, USA
e-mail: rbard@cancerscan.com

E. Shippen, MD
Reading Hospital, 9 East Lancaster Avenue,
Shillington, PA 19607, USA
e-mail: ershippen@comcast.net

R.L. Bard et al. (eds.), *Image Guided Prostate Cancer Treatments*,
DOI 10.1007/978-3-642-40429-0_16, © Springer-Verlag Berlin Heidelberg 2014

watchful waiting (Gleason scores ranging from 5 to 9) using the β-sit/AOX matrix has demonstrated the success of this nutritional approach—with the result being approximately 90 % of men showed significant reduction or full stabilization of vascular indices for nonaggressive cancers, and the same improvement was shown in nearly 70 % of men with aggressive cancers, over a 10-year period. Careful monitoring also provides the basis for deciding on other available treatment options, if necessary.

The success of coupling noninvasive monitoring with key nutrition provides a robust basis for tailoring intervention to an individual. This system provides a reliable evaluation of each person on a case-by-case criterion. Thus, we are able to evaluate the individual's ability to respond to nutritional and lifestyle intervention and the potential need for more invasive medical intervention and treatment, while reducing unnecessary invasive treatments. The clinical efficacy of the anti-angiogenetic properties of nutraceuticals is now being followed and compared with the classic pharmaceutical bevacizumab in studies using contrast-enhanced ultrasound (CEUS). Following treatment of liver metastases with bevacizumab, the intranodular tumor vessel flow was decreased slightly and the density of matured blood vessels was decreased significantly (Kitamura et al. 2011).

16.2 Background and Brief History

In 1940, the classic textbook of pathology, Ewing's Neoplastic Diseases noted prostate cancer is a rare disease, accounting for 0.27 % of tumors in the male population of that era. Half a century ago, pathologists found a high percentage of men without "clinical" prostate cancer to have malignant cells in the operative specimens of surgery for relief of benign prostatic obstruction. In addition, the rate of cancer being present in prostates examined during autopsy varies dramatically in different regions of the world, with the food supply being the single variable able to account for the differences. In the absence of demonstrable tumor invasion, perhaps cancer formation should be considered a nonthreatening aspect of normal body aging or, at worst, a chronic disease that is governed by lifestyle and the available food supply.

This leads to a simple clinical question: Is there a way to determine whether a cancer is part of the natural aging process to be watched (inconsequential cancer) or whether the malignancy will have deadly consequences?

This question is being answered by a building body of knowledge that has recently been accelerated by technological advances in diagnostic imaging. In 1994, a prominent British physician, David Cosgrove, published a paper in *Radiology* demonstrating the presence of blood flows in breast cancers (Cosgrove 1994). The new generation of sonogram equipment had the capability to show pictures of blood vessels. The arteries and veins supplying a tumor could be clearly imaged. Moreover, the actual flowing blood in the cancer could be seen and velocity of flow of blood in the vessels accurately measured. At an international conference in Italy in 1994, Dr. Rodolfo Campani, an Italian radiologist specializing in studying the blood flows of cancers at the University of Pavia Medical Center, showed the criteria to differentiate malignant cancer vessels from benign tumor blood vessels. Benign vessels are few in number, smoothly outlined, follow straight courses, and branch regularly. Malignant vessels are many in number, irregularly outlined, irregular in course, and crooked in branching patterns (Campani 1994). These findings have been confirmed by other investigators and presented at the 2006 World Congress of Interventional Oncology. Today, malignant blood vessels may be accurately and noninvasively detected by newer Doppler sonography techniques and advanced blood flow MRI protocols.

16.3 Sonography

16.3.1 Doppler Ultrasound Has Wide Application for Improving Cancer Therapy

The physical principle of ultrasound, the piezoelectric effect where sound is created from electrical energy, was discovered by Pierre and

Marie Curie 10 years before the recognition of the X-ray. Early medical uses included imaging disorders of the eye, heart, and the developing fetus. As computers grew in sophistication, so did the applications of ultrasound, and now, it is often used as the first diagnostic test for many medical disorders. Doppler sonar created in 1972 gives pictures of flow movement in the human body in the same way it shows motion in the weather patterns (Doppler radar) that one sees on television weather reports. Doppler technology has been around for years.

Urologists in Japan, oncologists in England, surgeons in the Netherlands, chemotherapists in Belgium, ultrasonographers in Norway, and radiologists in France, seeing the success of sonograms in diagnosing malignant tumors in the breast, turned their attention to the study of the prostate. They concluded that the vascular pattern shown by the Doppler technique held the key to the degree of malignancy. In 2000, German cancer surgeons at the University of Ulm, the largest bone tumor center in Europe, showed bone tumors that were highly malignant had high blood flows (Shulte 2002). The current clinical use of Doppler equipment in Europe is keeping patients from unnecessarily losing their arms and legs to surgery. Historically, the standard treatment for bone cancer has been amputation of the entire limb. Current surgical intervention has become more conservative, often removing a limited portion of the bone so the tumor can be removed with a rim of normal bone without the need for an amputation. However, by distinguishing cancer aggressiveness, Doppler techniques have refined this even more, since bone tumors that demonstrate no vascularity or low blood flows are now watched or treated more conservatively.

Dr. Nathalie Lassau, an interventional radiologist at the Institut de Cancerologie Gustave Roussy, an internationally known cancer center in Paris, published similar findings on the deadly skin cancer, melanoma. Her *American Journal of Radiology* article (Lassau et al. 2002) revealed lethal skin cancers to be highly vascular and skin cancers that could be watched were not vascular. Dr. Lassau is currently investigating medicines to reduce blood flows to cancers in hope of lessening their malignant consequences and has presented this work at numerous international meetings. Her finding that 3-D Doppler sonography correlates best with the pathologic process was highlighted at the 2011 Eighth International Symposium on Melanoma. Now, newer MRI imaging protocols are currently being fine-tuned based on the proven high accuracy of the Doppler sonography data.

16.3.2 Clinical Application of 3-D Doppler and MRI Diagnostic Technology

Imaging Tumor Aggression

The blood flow patterns depicted by Doppler sonography provide a way to quantitatively measure and serially monitor the severity of malignancy, as well as the response to therapy throughout the treatment course. Blood flow analysis can show which cancers are aggressive, since these have many vessels, and which are responding to treatment, or nutritional intervention, or both, since the number of tumor vessels decreases with successful therapies (Cornud et al. 2000).

Monitoring Intervals

Because it is a noninvasive procedure, the 3-D Doppler exam can be performed as often as necessary. Our experience has shown that cancers are more variable in their response to intervention than generally believed. During early stages of diagnosis and intervention for PCa, a 3-month follow-up exam is warranted. Once the cancer shows signs of regressing, based primarily on measures of vascularity and density, a 6- to 9-month follow-up schedule is more appropriate. MRIs should be repeated when the tumor has not responded to treatment by 6 months. Routine ultrasound follow-up should be on a 6-month basis and MRI yearly for 3 years.

Tumor Size Alone Can Be Misleading

The routine use of tumor size decrease has been shown to be less reliable than blood flow analysis, since the edema of cell death may cause dying cancers to enlarge. Although this concept was described in the early 1990s in Europe, it was first mentioned in the American literature in 1996. Dr. Edmund Louvar (Henry Ford Hospital, Detroit, MI) combined radiology and pathology studies to determine that the power Doppler flows in malignancies were related to the vessels that fed aggressive tumors (Louvar et al. 1996).

High Correlation to Gleason Scores

Significantly higher Gleason scores were seen in cancer biopsies of high Doppler flow areas compared to cancers with no Doppler flows. Dr. D. Downey (John Robarts Research Institute, University Hospital, Ontario, CN) examined vascular imaging techniques and 3-dimensional imaging of blood vessels. Blood vessels can be rendered in 3-D with angiography (high-intensity dye injected into arteries), CT scanning (medium-intensity dye), MR angiography (low-intensity dye), 3-D color Doppler imaging, and 3-D power Doppler imaging. He noted that in prostate cancers, power Doppler better delineated abnormal vessel architecture than color Doppler techniques (Downey 1995). Indeed, computer analysis of malignant vessel density is now being used as a substitute for Gleason grading, which is solely based on randomly obtained histologic microscopic findings.

16.4 Clinical Advantage of Doppler Technologies

16.4.1 3-D Doppler Ultrasound Overcomes Diagnostic Problems Caused by Treatments

Treatment Alters Standard Diagnostic Accuracy

A 2004 newsletter from the Prostate Cancer Research Institute reported that hormone therapy may change the way the pathologist interprets a cancer (Bostwick 2004). Androgen deprivation therapy (ADT) and similar medicines such as Proscar (finasteride), Avodart (dutasteride), and certain hair maintenance formulations make it more difficult to grade the tumor with microscopic analysis. Dr. Pam Unger, a prostate cancer pathology specialist at Mount Sinai Hospital in New York, mentioned in a personal communication that radiation changes also caused difficulties in reading the microscopic slides (2012). Furthermore, pathologists generally do not look for blood vessels, and thus, do not routinely evaluate the vascular pattern in the specimens they interpret.

Blood Flow, Measured by Doppler Sonogram, Is Not Disrupted by Treatments

The diagnostic accuracy of 3-D Doppler, based on blood flow analysis, is not altered by the treatments noted above. Men who have been on ADT should have a Doppler sonogram study to confirm the absence of residual disease. If there are areas of abnormal blood vessels, biopsy may be considered. Many patients who have been treated for cancer accept the presence of abnormal blood flows as proof of recurrence and choose treatments accordingly without further biopsies. Most patients use the amount of decrease in number of the visible blood vessels to represent the degree of success.

16.5 MRI Complements Doppler Imaging of the Prostate

MRI routinely refers to the image of signal intensity in the gland with the patient in the tube of the unit. Three primary MRI formats have proven useful for prostate examination: EC-MRI uses an endorectal coil (EC) to improve resolution in the prostate; S-MRI or spectroscopic MRI involves analysis of the chemical composition of the prostate tissues, with emphasis on the compound *choline*; and DCE-MRI, or dynamic contrast-enhanced MRI, is the most useful format to complement 3-D Doppler for a complete diagnosis. DCE-MRI uses the injection of a contrast agent *gadolinium* that reveals the blood flow within tumorous prostatic tissue (Bard 2009b). A fourth type, diffusion-weighted imaging (DWI-MRI) is discussed below.

MRI shows cancer as a loss or decrease of the normal glandular prostatic tissue signal; however, other benign pathologies, such as calculi, hemorrhage (bleeding from recent biopsy), stones, BPH, and inflammation, may also produce this effect. Some infiltrating types of cancer will not produce any visible changes. Data from the 2009 American Roentgen Ray Meeting shows a 75 % sensitivity (25 % false negatives) and 95 % specificity (5 % false positives). MRI was originally used to stage the spread of cancer outside the prostate gland also denoted as ECE (extracapsular extension). The data showed ECE medium specificity (74 %) and sensitivity (71 %) (Bard 2009a).

16.5.1 Each MRI Format Has a Unique Purpose

Each of the different MRI formats has its own characteristics and can refine the diagnosis.

1. By using the endorectal coil inflated as a balloon, EC-MRI was designed to better define the capsule of the gland and the seminal vesicles.
2. S-MRI was designed to detect intraglandular cancer and shows the aggression. The spectroscopic chemical analysis of cancer shows higher levels of choline and citrate than in normal prostatic tissues. The analyzed sections of the prostate are divided into a grid pattern of such a size that small cancers could be missed. Currently S-MRI is practiced at few US medical centers and is losing popularity at many international academic facilities. A 2012 presentation by Dr. O. Rouviere from Lyon, France, at the French Radiology Meeting highlighted the problem that S-MRI was not effective in analyzing tumor extension into the fatty tissues adjacent to the prostate gland (Rouviere 2012).
3. DCE-MRI is widely used and has improved specificity by about 80 % according to Drs. J. Futterer and J. Barentsz (personal communication, 2013). DCE-MRI provides noninvasive analysis of prostate vascularization as well as tumor angiogenesis and capillary permeability characteristics in prostate cancers.
4. DWI-MRI utilizes diffusion-weighted imaging. It is a process that shows molecular motion inside a tumor. The more motion, the more likely a lesion is benign, as in a fluid-filled cyst. Several articles now assert that this technology may be used to predict Gleason scores (e.g., Shigemura et al. 2013; Rajakumar et al. 2012; Woodfield et al. 2010). As protocols have improved, this technology is gaining wider use and clinical acceptance.

16.5.2 Comparing Doppler and MRI

An MRI exam shows the extent of cancer but not the activity. In patients successfully treated by radiation or hormones, the abnormality may still persist on the MRI picture; on the other hand, the Doppler test has the advantage of showing that blood flows are greatly reduced or completely absent. S-MRI is also designed to show activity, but has not been shown to be as sensitive as physicians had hoped. Diffusion-weighted MRI has not been successful in finding small lesions and the EC-MRI study distorts the anatomy by the balloon inflation process. Most MRI fails to show small areas of extracapsular disease. Fortunately, the latest generation of 3-D 18 mHz ultrasound probes has a resolution 5 times greater than the MRI and can verify capsule integrity. MRI is used to find spread of the prostate tumor into the boney structures, seminal vesicles, and lymph nodes. It may also confirm extension of malignancy into the rectum.

16.6 Applications of 3-D Doppler Imaging

The ultrasonographic physician or specially trained imaging technician looks at the instantaneous video appearing on the screen, taking pictures and measuring images according to a standard protocol, and notes and documents abnormalities. Two-dimensional pictures are taken in “real time,” which are similar to the images of the inside of the pregnant mother’s womb, showing moving babies or the fetal heart beating. The same 3-D technology that shows the face of the baby in the womb is now being successfully applied to the prostate. 3-D is different, in that it is faster, and contains more information than the standard 2-D sonogram.

16.6.1 3-D Data Analysis

Essentially, the 3-D machine takes a volume of pictures and stores this data inside the unit's computer banks. The data may be analyzed immediately or later reviewed and reconstructed in various angles or planes. In comparing 2-D with 3-D imaging, one can say the sonographer looks and then takes pictures with the 2-D system; whereas, with the 3-D technology, pictures are taken which are then looked at and formally evaluated later. If a significant problem is seen and annotated with the 2-D exam, it cannot be later observed except by completely re-scanning the patient. The 3-D rendition may be reviewed over and over without recalling and reexamining the patient. 3-D imaging has made exam time shorter, providing more patient comfort. The images are then analyzed on a special computer work station, allowing optimal rendering of the prostate in multiple planes as required.

16.6.2 Imaging Invasive Cancer

This special view, available only on 3-D equipment, allows one to see invasion of cancer more easily. Specifically, the spread of cancer outside the prostate gland or extracapsular extension is well seen with this technique. This is most apparent in extension to the seminal vesicles noted on the transverse plane and penetration of the capsule in the coronal plane. As the three orthogonal images are displayed in real time, the observation of seminal vesicle or capsular abnormality will focus attention to a significant cancer immediately adjacent to the initially observed finding(s).

16.6.3 Individualized Assessment and Follow-Up

The patient's own vascular pattern that determines aggression can be overlaid on the 3-D scan. This adds greatly to the assessment of the disease and the feasibility of treatment possibilities unique to each individual. This is notably useful in men with low-grade cancers who wish to be followed with watchful waiting, with or without nutritional or alternative therapies, thereby avoiding surgery or radiation. Most low-grade tumors remain localized and may be watched or controlled with noninvasive or minimally invasive treatments. (The standard MRI cannot demonstrate tumor aggression in the moment, although comparison from previous exams shows progress and interval changes. 3-D PDS can be repeated as often as needed to objectively follow an individual.) The 3-D PDS information also sets a basis for ongoing evaluation, with follow-on imaging appropriate for each individual, depending upon aggression and expectations of change, and the ability to repeat exams as often as necessary to adjust treatment based on real-time results.

16.6.4 2-D Standard Sonogram vs. 3-D Doppler

The regular 2-D sonogram may miss low-grade cancers that have the same appearance as the normal gland, which account for up to 40 % of prostate tumors. The overall accuracy is about 50 %. The accuracy is better in glands that have never been subjected to a biopsy, inflamed or treated in any way. The accuracy is lower in prostate glands that have been biopsied multiple times or in persons who have been treated with radiation or hormones.

16.6.5 Power Doppler Sonography

The power Doppler study adds about 30 % more accuracy, since the abnormal blood vessels provide a road map to the tumor; however, detours on the road may occur with older 3-D systems in the presence of stones or calculi. Indeed, a US patent, number 5,860,929, was obtained by Norwegian scientists to determine power Doppler blood flows in optimally diagnosing prostate cancers. When a stone is identifiable, the sound waves bounce back so strongly that they create a false color pattern. This pattern to the trained clinician will not be mistaken for a tumor vessel.

16.6.6 Uniquely 3-D Power Doppler Formats

Fortunately, the Doppler technology has other formats that correctly identify the artifactual or spurious colors, distinguishing it from a true cancer. In Dr. Bard's practice combining 3-D PDS with focused computer-aided vascular MRI exams, we have achieved a 97 % overall accuracy in diagnosing and staging prostate cancers. An important exception occurs in the seminal vesicles, which sit on top of the prostate gland generating the fluid that produces the ejaculation. Early cancer spread to these paired vesicles may be missed by the 3-D PDS. When a tumor is found near or adjacent to the seminal vesicles at the base of the prostate, MRI scans are mandatory. Another important advantage of 3-D PDS is the ability to accurately measure tumor volume and density.

16.6.7 3-D PDS and Tumor Volume

A meaningful use of 3-D technology is the determination of tumor volumes. Clinically "insignificant prostate cancer" is generally defined as a volume less than 0.5 cc which means the cancer is less than 7 × 8 mm. Gleason score must be less than or equal to 7. No extracapsular extension implying no tumor beyond the prostate capsule, no invasion of seminal vesicles, no boney metastases, and no lymphadenopathy (Ewing 1940).

16.6.8 3-D PDS and Tumor Density

Tumor density is an important factor in determining both the grade of the tumor and response to treatment. As explained elsewhere, some tumors may remain the same size or actually increase in volume while responding to treatment. Density, accurately measured by recent software advances in 3-D PDS, is a principal indicator of both grading, especially aggressiveness, and response to treatment on a real-time basis. (The system with this capability is FDA approved.)

16.6.9 The Future Potential for MRI and 3-D Doppler Ultrasound

When you look around the world at advances and innovation in MRI and 3-D Doppler technology, software, and utilization, it is evident that this technology will become an important part of cancer practice, especially in this age of cost containment. Some of these techniques are not new and are in practice outside the USA. Here are just two very promising examples:

1. Contrast Doppler: In 1999, at the University of California San Diego campus, a French medical researcher, Dr. Olivier Lucidarme, developed a highly sensitive technique to improve Doppler ultrasound. Special bubbles injected intravenously greatly improved imaging of small vessels. To date, our FDA has not approved this technology and Dr. Lucidarme now practices this methodology in Paris at the Pitie-Salpetriere Hospital, the largest teaching center in Europe. Italian researchers at the University of Rome, Drs. Vito Cantisani and Francesco Drudi, have shown this technology to show cancers unsuspected by other means. While this technology is approved for Doppler echocardiography, it can be used as a nondiagnostic (off-label use) adjunct in cancer diagnosis in the prostate.
2. Lymph node MRI: Advanced MRI scans performed in Europe are not available in the USA, nor are certain sophisticated radioactive bone scans, or techniques for evaluating lymph node involvement, allowed in the States at this writing. For example, in 2004, Dr. Jelle Barentsz et al. described a new technique to evaluate cancer spreading to the lymph nodes at the International Congress of Radiology (Barentsz et al. 2004). This uses MRI with ferumoxtran-10, a novel contrast agent called "Combidex" in the USA. The lymph node technique is termed MRL (magnetic resonance lymphangiography), and ferumaxtran-10 is

being used in a wide range of MRI procedures throughout Europe, as it has shown a very good safety record, especially as it does not induce nephrogenic systemic fibrosis (NSF), a recently recognized severe complication associated with gadolinium (Gd)-based contrast agents (GBCAs) when used with patients who have compromised kidney function. GBCA is standardly used in the USA.

This technology is extremely important since MRI is the best way to image abnormal glands that are hidden or inaccessible at surgery. The imaging shows the size and location of the lymph nodes as well as the presence of cancerous tissue as small as 1/5 in. This critical piece of information that pinpoints cancer infiltration tells where the spread occurs, and allows for accurate treatment planning. The current "gold standard" for lymph node evaluation is surgery called *pelvic lymph node dissection* (*PLND*). Clearly this invasive exploratory operation, where the surgeon searches with his hand for hard lumps in the abdomen, cannot find all the tiny disease sites to which cancer spreads. Moreover, the metastases to nodes are generally subcentimeter so they are likely to be missed clinically and radiographically. In addition, the most reliable sign of metastatic adenopathy is finding abnormal nodes in the perirectal and/or presacral space. This area is not routinely examined at surgical dissection due to the risk of major surgical trauma. The MRL exam is so accurate that a negative exam translates into a 96 % chance that there is no metastatic disease to the lymph nodes. In addition to sparing patients from the risk and pain of surgery, this methodology reduces health-care costs. As this technology is not FDA approved, it is not widely practiced. Other lymph node MRI technologies are discussed in later chapters.

16.6.10 Ultrasound/MRI Image-Guided Biopsy and Laser Ablation

The ability to image a tumor with ultrasound and/or MRI permits the image-guided placement of a biopsy needle and/or treatment laser fiber into the area of disease. Laser physics outline the volume of heat damage to a millimeter of a vital structure and heat sensors prevent tissue damage to nearby organs. These topics are covered in detail in other chapters.

16.7 ProActive Monitoring: A Model Made Possible by 3-D Doppler Technology

The monitoring approach presented here is based on Dr. Bard's 39 years experience in the field of diagnostic ultrasound, 15 years of imaging the prostate with power Doppler blood flows, and 6 years of performing 3-D power Doppler sonograms (3-D PDS) and comparing the results with high-resolution MRI scans of the pelvis with special sequences formulated specifically for the prostate. Dr. Bard has diagnosed, observed, and shared in the treatment of some 5,900 patients. Through nutritional support, medical treatment when appropriate, and 3-D monitoring on a schedule dictated by each individual's current situation, only 5 of these 5,900 men have died from their prostate cancer in a 10-year time period. This compares very favorably to the expected 239 deaths from PCa within 4 years of diagnosis, based on figures from the Health Professionals Follow-Up Study for men diagnosed with nonmetastatic PCa observed from 1990 to 2008 (Kenfield et al. 2011).

ProActive Monitoring couples 3-D Doppler and MRI imaging at regular intervals, with the β-sitosterol/antioxidant matrix (β-sit/AOX) nutritional support. The β-sit/AOX approach was first developed out of Arthur Bartunek's early work with CoEnzyme Q10 and cofactors that improved Q10 outcomes, especially for cancers. The formulations and protocols used during ProActive Monitoring were further refined with feedback from the progressive 3-D Doppler monitoring of men with varying stages of prostate cancer. During the 10 years of this process, improvements in imaging have allowed changes to be tracked more accurately and to make appropriate nutritional adjustments based on this. In addition, the use of several nutritional items, notably curcumin and tocotrienols, has been independently developed for use with cancer and is reaching phase II and phase III clinical trials. These have been included in the protocol and are discussed here.

16.7.1 β-Sitosterol/Antioxidant Matrix (β-Sit/AOX) Nutritional Support

One way of phrasing the question we posed about 10 years ago was: What could happen when essential nutrition for cell membrane integrity and healthy cell reproduction was returned to the diet through supplementation? This is a quintessential naturopathic nutritional intervention. This was based on more casual observations of improvement in PCa in men following a rigorous program of lifestyle and dietary change. From another realm, it was observed by Dr. William V. Judy, and related to me in a personal communication, that CoEnzyme Q10 was proving more efficacious for PCa for subjects who were also taking β-sitosterol-rich foods; however, this was based primarily on change in PSA and not direct exam of the prostate (Judy W, Bartunek A, personal communication 2003). After reviewing diets of populations with extremely low cancer, cardiovascular, and hypertension rates, a high-β-sitosterol-based supplement was produced, with antioxidants derived from these same diets. The combination provides nutrition that is integral to cell membrane health and a healthy cell environment. Combining the β-sit/AOX formulation with appropriate CoQ10, and a highly rated multi-supplement with high vitamin B complex, became the basis for ProActive intervention. With this, watchful waiting became ProActive Monitoring.

The 3-D color power Doppler sonogram provides a means to track changes and progress in the condition of the prostate and PCa. By correlating the 3-D exam with state-of-the-art DCE-MRI grading of the cancer, Dr. Bard was able to both evaluate procedures for optimal timing of reexam and provide feedback for modification of an individual's nutrition program, and in increasingly rare circumstances, recommendations for procedures such as HIFU (high-intensity focused ultrasound), and more recently MRI-guided focal laser ablation. Routine feedback also gave the information needed to further develop the core protocol, based primarily on changes in prostate size, tumor size, location and density, vascularity, and capsule integrity.

16.7.2 Background: Prostate Nutrition

The walnut-sized prostate gland is a mucus-producing organ in males that lies just below the bladder. Growth to functional size is triggered by puberty and continues until about age 30 when equilibrium is established between cell growth and apoptosis. Normal midlife hormone changes, when coupled with diets that do not provide adequate nutrition for prostate cell integrity and hormone balance, can trigger benign enlargement (BPH) and set the stage for other prostate conditions including prostatitis and prostate cancer. The typical hormone pattern leading to BPH is elevated estradiol combined with elevated DHT and typically estrogen dominance. This also sets up the circumstances for chronic prostatitis. While there is substantial evidence that BPH does not develop into cancer, the same underlying factors of cellular environment and integrity set the stage for PCa, and therefore, both can be considered nutritional in origin.

The key factors that influence the development of PCa include:

1. *Inflammation*: While only a relatively small percent of prostatitis—any form of inflammation of prostate tissue—is caused by bacterial infection, increasing evidence indicates a link to an imbalance in sex steroid hormones in all chronic prostatitis. Elevated levels of inflammatory cytokine IL-8 is a second and critical inflammation factor. IL-8 promotes stromal and epithelial cell proliferation. It is upregulated in both BPH and PCa, and it is also implicated in angiogenesis. IL-8 has been shown to have a pervasive role in promoting tumor cell survival and proliferation for all cancers. Although BPH is not a causal factor

for PCa, any form of chronic inflammation of the prostate can now be considered a risk factor for prostate cancer. (Some nutritional approaches have gone further, declaring inflammation the single "driving force" behind PCa and rely on nonnutritive supplements in an attempt to address this issue. However, this does not restore underlying nutritional imbalances which can redress the inflammation and adds an extra, mostly unnecessary, layer of complexity.)

2. *Prostate Cell Membrane Elasticity*: There is substantial evidence from two sides that disruption in the cell membrane's elasticity, increasing rigidity, is a precursor for the development of cancer cells. It is also a factor in insulin resistance. On one side, there is evidence that suggests rigidity leads to focal adhesions and aberrant growth [cancer] by increasing tension in the cell that is normally generated by elevated Rho (GTP-binding protein family) (Alexander et al. 2008; Choi 2005). On the other, ultrasound units that can read the elasticity of cell membranes are now being shown to accurately be able to detect cancer. The primary dietary reason for alteration to a cell's elasticity and fluidity is an imbalance between β-sitosterol (β-sit) and cholesterol in the cell membrane (Endress et al. 2002; Henriksen et al. 2004).

16.7.3 Membrane Permeability and Intracellular Environment

There are many cell functions dependent upon normal cell membrane permeability. Of interest, here is an alteration in the isoprenoid pathway, the alteration of the balance of calcium and magnesium with excessive entry of Ca2+ and the release of calcium stores, which is a critical factor in cancer metastasis, which can be triggered when this imbalance is accompanied by critically low CoEnzyme Q10 levels in the immediate intracellular fluids.

The same nutritional protocol described here, that addresses the above issues, also increases PCa cell apoptosis, reduces proliferation, reduces excess estrogen production, supports/restores normal cell reproduction and differentiation, and reestablishes several mechanisms of homeostasis, especially for copper homeostasis. In other words, the β-sit/AOX matrix provides the nutritional substructure missing from today's food supply for the body's normal, dynamic anticancer functions and when the nutritional components are balanced properly accomplishes this at physiological levels.

16.7.4 Diet and Prostate Cancer

A great deal of research has been published attempting to isolate dietary factors for cancer in general, and for PCa specifically. At best, this has yielded a limited picture and conflicting recommendations. When you step back and examine the diets and food supplies of regions where cancer rates are low, a different picture emerges. For example, when the PCa rates for Greece (pre-2006) are compared to USA rates, based upon autopsy examination of the prostate, you find that men between 50 and 59 years old in Greece have a rate of 5.2 % vs. 30+% in the USA. For men between 60 and 69 years old in Greece, the rate is 13.8 % while the US rate is 65+%, or 4.7 times the Greek rate (Stamatiou et al. 2006). This period was selected because at that time, the Greek people still ate from a locally grown, heirloom food supply, unaltered in seed line and growing methods for hundreds of years (it has since changed to comply with EU requirements and their health profile appears to be rapidly changing). This pre-2006 food supply represents a healthy variant of the Mediterranean diet.

In areas of Spain, where cancer rates are also extremely low, again the diet consists of locally grown heirloom foods. From this region, we have a measure of the phytosterol content of the diet, which shows that average consumption of total phytosterols is about 400 mg/day, of which 67 % is β-sitosterol (US Patent 8,394,425 2013). From here if we move to Germany, where cancer rates are approximately those of the USA, again we find that the total phytosterol consumption is about 350–400 mg/day; however, the β-sitosterol content is only in the 35–43 % range (US Patent 8,394,425 2013).

One conclusion from this literature, especially when it is looked at in a broader context, is that it is not just the diet, but the nutritional composition of the food consumed in that diet that makes a critical difference, and that β-sit is essential for health in general and our body's anticancer mechanisms in particular.

Another way to look at this is to look at the effects of high levels of dietary and circulating β-sitosterol. A partial list of the effects produced with high levels of β-sit includes normalizing cholesterol, a reduction in insulin resistance, support for normal weight control and fat metabolism, a reduction in asthma incidents, acting as an anti-inflammatory and an immune modulator, a reduction in cardiovascular disease and arteriolosclerosis, and reduced rates of lung, prostate, and other cancers.

16.7.5 Natural Synergism and Potentiation

One explanation for the wide-ranging effects of adequate dietary β-sit, which can be measured by blood levels, is that it acts in synergy with other substances and also acts as a catalyst that potentiates antioxidant activity, as well as other antioxidant responses, especially for herb-based antioxidants, which in turn potentiate the efficacy of vitamin D3 (Vivancos and Moreno 2005; Wang et al. 2005). It also is involved in a variety of processes throughout the body, from cell membrane structure to regulation of estrogen and DHT production, elimination of excess estrogens, apoptosis, and immune regulation, among others.

16.7.6 The Ideal Phytosterol Composition

Based upon the available literature and our clinical observations, the ideal balance of phytosterols is comprised of β-sitosterol being greater than 62 %, campesterol being less than 25 %, stigmasterol being less than 10 %, and brassicasterol being less than 3 %. The following is a brief summary of the evidence for this composition.

(Note: Most phytosterol supplements contain a maximum of 43 % β-sitosterol. This is due to it being derived from currently available soy. The problem with using this material as a supplement is that it merely provides the same balance found in the food supplies that are associated with higher rates of cancer, cardiovascular disease, obesity, and type II diabetes. Both population studies and clinical observation show that the balance of the sterols, from supplement and diet, is more important than the absolute amount. Therefore, higher supplemental amounts of properly balanced phytosterols are needed to offset the low β-sitosterol content and ratio from the food supply.)

β-sitosterol (*β-sit*) (at least 62 %; absorption rate about 4 %)

1. Reduces absorption of dietary cholesterol.
2. High plasma concentrations are associated with a markedly reduced risk of coronary heart disease ($n = 1{,}242$, >65 year-old) (Escurriol et al. 2010).
3. Increases apoptosis in cancer cells (4–6 times baseline) (Awad and Fink 2000).
4. High levels in diet correlate with lower levels of cancer (prostate, lung, breast, colorectal, etc.).
5. Anti-inflammatory (Awad and Fink 2000).
6. Current healthy Mediterranean food supplies provide phytosterols with over 65 % β-sitosterol/sitostanol content, while geographical areas with high cancer and CV disease rate have about 43 % or less β-sit (with about the same amounts of total phytosterols, about 400 mg/day) content in their food (Jiménez-Escrig et al. 2006). US intake is estimated at between 80 and 250 mg/day, (Muti et al. 2003) with 43 % or less β-sit.
7. Immune system modulator.
8. β-sitosterol and campesterol also reduced alpha-tocopherol oxidation in liposomal membranes.
9. Decreases plaque formation in arteries.
10. Reduces estradiol production and carries excess estradiol from the gut.

Campesterol (*CS*) (not exceeding 20 %; absorption rate about 13 %)

1. Increases apoptosis in cancer cells (estimated to be about 4–6 times baseline).
2. *Increases* plaque formation in arteries.

Note: *Statin drugs increase CS concentrations in muscle tissue*, reducing β-sit content and disrupting membrane balance (Päivä et al. 2005).

Stigmasterol (not exceeding 10 %; absorption rate about 4 %)

1. Stigmasterol, but not β-sit or CR, inhibited SREPB-2 processing and reduced cholesterol synthesis.
2. Stigmasterol activated the Liver X receptor. (Liver X receptor alpha (LXR-alpha), an oxysterol-activated nuclear hormone receptor, regulates the expression of genes involved in lipid and cholesterol homeostasis and inflammation.) This may improve glucose tolerance (Laffitte et al. 2003).
3. However, stigmasterol is a prooxidant and inflammatory (Moraa-Ranjeva et al. 2006).
4. Lowers Q10 levels (β-sit and campesterol do not).
5. Stigmasterol can cause damage to adrenal glands by disrupting normal cholesterol homeostasis (β-sit and CS do not).
6. And stigmasterol is a potent in vitro antagonist of the NR for bile acids FXR, critically involved in hepatoprotection from cholestasis (*inhibition of bile flow*). (β-sit does not have any inhibitory effect.)

Brassicasterol (not exceeding 3 %; absorption rate not known). The European Union does not allow in supplements any amount greater than normally found in nature, which is a maximum of 3 %.

1. Brassicasterol can cause damage to adrenal glands by disrupting normal cholesterol homeostasis (β-sit and CS do not).
2. May lower Q10 levels (β-sit and CS do not).

Note: Brassicasterol is significantly increased during the processing of canola oil. However, despite the problems with brassicasterol for the human body, this is considered to be good, since brassicasterol helps stabilize the oil and contributes to overall cholesterol lowering (#1 above).

16.7.7 Phytosterols Require Complementary Antioxidants

Two of the overlooked aspects of increasing dietary β-sit is that it stimulates both the sphingomyelin cycle through increased ROS activity, increasing proliferation as demonstrated in prostate cancer cells, and also high levels of both cholesterol and β-sit, which can cause lipid peroxidation. For these reasons, β-sit needs to always be administered in a composition that includes complementary antioxidants, countering the ROS activity and supporting its action in the cell membrane and intracellular environment. Regarding the effects on cancer, the practical effects of inadequate or incompatible antioxidants with β-sit would be a leveling off at a balance between increased apoptosis and increased proliferation.

The β-Sit/AOX Matrix

The β-sit/AOX matrix interaction is complex, requiring multi-ingredient supplement support. In some ways the relationship is as symbiotic as it is synergistic. For example, β-sitosterol potentiates antioxidant activity and activates other antioxidant responses. β-sit and plant-based antioxidants work together to protect cell membranes from lipid peroxidation (Moraa-Ranjeva et al. 2006; Hernandez et al. 2000; Toda and Shirataki 1999). In addition, targeted antioxidants support activities of β-sit, i.e., Astragalus root and β-sit work together to increase the activities of antioxidant enzymes, including SOD and GSH-Px (Toda 1999; Wang et al. 1996).

A natural pairing of β-sit and select antioxidants, forming a supportive nutritional matrix, is fundamental to a wide range of biological processes, so the components of the matrix need to be selected to fit the desired outcome. In this case, the matrix is comprised of β-sit and antioxidants that work with it to improve membrane integrity and function, reestablish a healthy intracellular fluid environment, as well as support healthy cell reproduction and the body's mechanisms for controlling improperly reproduced cells—cancer cells.

A select group of antioxidants that form the β-sit/AOX matrix for natural anticancer support are Astragalus, ellagic acid, Gynostemma pentaphyllum, Ligustrum fruit, lutein, lycopene, quercetin, resveratrol, Rhodiola, Rosemary officinalis, Schisandra fruit, trans-e-viniferin, Wasabia japonica, and zinc.

Synergy Within the Matrix

Just like the components that make up foods, to be efficient the matrix needs to be comprised of nutrients that work together, for example:

- Quercetin + resveratrol work together to naturally reduce iNOS gene expression and nitric oxide production, providing cardiovascular support and other benefits (Chan et al. 2000).
- Resveratrol + ellagic acid aid the cell's structural ability to repair efficiently (Chakraborty et al. 2004).
- Ellagic acid + quercetin synergistically support normal reproduction rates and proper apoptosis when balanced at dietary-level concentrations (Mertens-Talcott et al. 2003, 2005).
- β-sit + resveratrol combine to provide a balanced ROS 1 level and synergistically inhibit inappropriate cell growth. In addition, the systemic presence of β-sit enhances resveratrol activity (Vivancos and Moreno 2008).

This nutritional formulation is further advanced in this matrix by what is in essence a *potentiation chain*, with the interaction of components comprising and improving the effectiveness of the overall matrix. For example, β-sit, as previously mentioned, potentiates rosemary and carnosic acid, which in turn is synergistic with curcumin to inhibit the growth of ER-negative human breast cancer cells (Einbond et al. 2012). No one component is responsible for the outcome. It is the combination and interaction of the nutritional components of the β-sit/AOX matrix that becomes biologically effective.

Curcumin and β-Sit/AOX Matrix Synergy

There is growing investigation into the use of curcumin for treatment of cancer. One of the drawbacks is the diminished effect of curcumin with increased levels of insulin. At the same time, an increased level of insulin and insulin resistance is a known risk factor for developing prostate and breast cancer, as well as other cancers, and is often a cofactor with cancer patients. β-sit reduces insulin resistance, most likely by restoring membrane function, especially selective permeability, and regulates insulin production through several mechanisms, one of which is by supporting normal cholesterol homeostasis. In addition, curcumin inhibits cell membrane cholesterol accumulation, furthering the effects of β-sit, via a different mechanism.

An ideal curcumin will be naturally absorbed, maintain effective serum levels for at least 12 h, allowing for 24-h effective blood levels without frequent dosing, and stored in the liver for release throughout the day. In this way, doses of as little as 1,000–4,000 mg are recommended.

CoEnzyme Q10 and the β-Sit/AOX Matrix

There are a number of key reasons why CoQ10 should always be included in the matrix. First, it is essential for proper cell reproduction. Second, it has been shown that when the circumstances for metastases are set up, the process is not triggered if there is adequate CoQ10 present. CoQ10 has been demonstrated to reduce IL-8 to normal levels. As noted above, IL-8 is the primary inflationary mechanism that drives the formation and survival of tumor cells for all cancers. Reducing IL-8 also works with the other components of the matrix to reduce, and even eliminate, cancer angiogenesis, as demonstrated with follow-up 3-D PDS and focused computer-aided vascular MRI exams. The efficiency of CoQ10's function in the cell membrane and for overall cell function is restored in cancer cells through the reestablishment of membrane elasticity and permeability by β-sit.

An ideal CoQ10 is highly absorbable and 100 % of what is supplemented needs to be available for absorption. The circulating Q10 needs to be readily able to cycle from the ubiquinone to ubiquinol forms and be orthomolecular in nature, allowing it to be cellularly bioavailable. Preferably, the Q10 used should have a long clinical track record and have research demonstrated efficacy with cancer, cardiovascular health, and mitochondrial energy. Recommended dose range is from 300 to 800 mg/day, in divided doses of no more than 200 mg/dose.

The above forms the basis for the nutritional support we use. As appropriate for each individual, a more complete program is developed including: vitamin D3 to bring the D3 levels to a range of 65–90 ng/ml, mixed tocopherols with high gamma-tocopherol (taken in the morning) and 125–500 mg of a high-delta-tocotrienol supplement taken in the evening, a balanced calcium and magnesium supplement, vitamin K2, vitamin B complex, and 5 g of vitamin C.

Using β-Sit/AOX Matrix Nutrition

Given that the basis of the matrix is to restore essential missing nutrients, it can be used in a general nutrition program, during treatment, and for anyone who has developed cancer as lifelong maintenance nutrition.

16.7.8 Monitoring and Follow-Up

The nutritional program outlined above, the *β-sit/AOX matrix*, has been used for more than 7 years, and the results reported in the first section are based on this use. Visually, this can be seen in the following imaging of the same prostate, initially diagnosed as a Gleason 7 (Fig. 16.1a) and upon a follow-up examined after daily use of the above supplement regime (Fig. 16.1b).

The results shown here illustrate both the efficacy of restoring fundamental nutritional support that has been systematically removed from our diets by alterations in the food supply, and the need for a means to monitor, on a regular basis, each individual's response to treatment. Given the number of factors involved in nutritional support, this is the only way to know that this individual's body is capable of restoring its anticancer functions. The same monitoring approach can be applied to any therapeutic intervention, especially since the 3-D sonogram is not compromised by the treatment itself.

When establishing a monitoring schedule for an individual, two additional areas need to be kept in mind, interval cancers and evaluating successful treatment.

Interval Cancers

The concept of fast-growing cancers called "interval cancers" has led to routine biannual screening of male and female high-risk patients. It is recognized that mammography misses invasive breast cancers with great frequency, so there is a half-year time period in which health-conscious women should alert themselves to the possibility of early breast cancer as they routinely undergo ultrasound breast screening twice a year. In practice, about 5 % of men develop aggressive interval cancers within half a year from their last normal or stable evaluation. A presentation entitled "Interval Cancers Of The Prostate: Evaluation By 3-T MRI And 3-D Power Doppler Ultrasound" was made at the 2011 meeting of the Societe Francaises de Radiologie in Paris, demonstrating that new aggressive tumors may occur more rapidly than clinically expected and may, in part, explain the failure of certain treatments (Bard 2011).

When a man has not had a biopsy or has had a negative biopsy and a vascular tumor is demonstrated on the 3-D PDS, an MRI exam is recommended, which shows the prostate gland, the capsule of the prostate, the regional lymph glands, seminal vesicles, and boney pelvis. Other bones, to which cancer frequently spreads such as the lower spine and hip, may also be imaged for abnormalities. While the MRI exam is not as good an indicator of cancer aggression, it shows spread of the tumor outside the prostate capsule to the lymph nodes better than the 3-D PDS and better than the CT scan, which is currently used as the standard test for staging.

Assessing Response to Prostate Cancer Therapy

The value of medical imaging is to:

- Localize volume of disease including extracapsular extension
- Assess bone metastases, seminal vesicle invasion, and lymphadenopathy

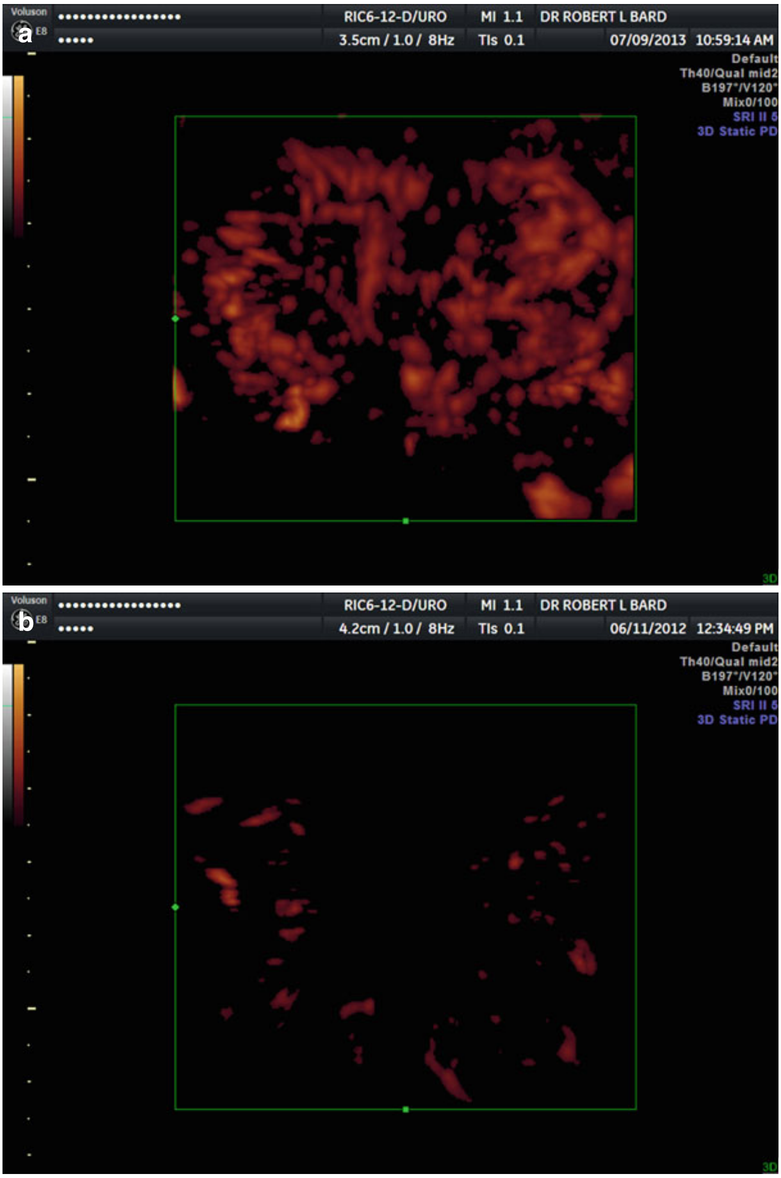

Fig. 16.1 Prostate cancer subject treated with **β**-sit/AOX supplement program. (**a**) DCE-MRI of Gleason 8 diffuse prostate cancer (vascular enhancement is *red*). (**b**) Posttreatment scan of same area showing marked reduction of vascular enhancement

- Estimate degree of aggressivity (similar to Gleason grading)
- Determine efficacy of therapy
- Monitor changes
- Tailor future therapy
- Determine tumor recurrence
- Identify new tumor

One of the problems of evaluating cancer treatment is that the tumor may be rendered harmless or even dead but the volume of the tumor remains the same or even enlarges. That is, the cancer cells may be killed off and scar tissue replaces the dead cells, leaving the size of the original malignancy unchanged, or edema and necrotic fluid buildup enlarges the region, simulating tumor growth. This lesson was learned 19 years ago in treating liver tumors. The therapy would render the cancer harmless, but the size of the mass on the isotope scans, sonogram, CT, and MRI would remain unchanged or even enlarge. The same is true of some prostate cancers that are inactivated but still feel like cancer on the digital rectal exam and show a mass effect on the sonogram and MRI. There needs to be a way to monitor changes and determine the efficacy of treatment. Fortunately, the blood flows in malignancies that have been inactivated decrease or disappear and can be quickly and accurately measured in the moment. Thus, with 3-D PDS, there is a simple tool to quantify blood flow patterns to demonstrate therapeutic response.

16.8 Hormonal Treatment Options for Prostate Cancer

Testosterone has not been implicated as the cause of prostate cancer. Environmental and dietary factors are likely major contributors of the development of aggressive, invasive cancers. Despite these factors, androgens—testosterone and DHT—are thought to be the major source of PCA growth. Yet androgen ablation therapy, ABT, is a failed approach in many cases. Over time, most prostate cancer cell lines become more and more resistant to androgen receptor activities or growth suppression due to the development of androgen resistant cell lines. Initial suppression by ABT is frequently followed by rapid progression of poorly differentiated, hormone-independent cell lines within 12–36 months. Newer approaches have aimed at increasing the antiandrogen blockade. However, since androgens have significant systemic benefits, this treatment approach can have serious progressive adverse effects and QOL decrements. These antiandrogen approaches or adjunctive chemotherapy may extend the remission temporarily, but all these options have highly significant adverse effects associated with prolonged use and few individuals are able to achieve full remissions. Those cases that seem to achieve stable “remissions” have low-grade cell types that might do better with intermittent hormone blockade or alternative approaches. The primary focus on the role of androgens in the growth, progression, and suppression of PCA cell lines has limited the development of other potential endocrine approaches. Still there are no good options available when ABT failures occur.

16.8.1 The Role of Estrogens and Estrogen Receptors

One area that is reemerging is the newer scientific understanding of the role of estrogens in regulating PCA growth and progression as well as inhibition and induction of apoptosis. Earlier use of potent estrogens, such as diethylstilbestrol, were associated with some success but also serious side effects that resulted in switching to newer approaches, including androgen deprivation therapy (ADT).

The majority of PCA cell lines, including those that have developed androgen resistance after ADT, have active estrogen receptors as modulators of cell growth and apoptosis. This option opens up various newer interventions with the use of various estrogens, phytoestrogens, or SERMs with selective estrogen receptor effects. These approaches have been greatly underutilized or lacked popularity due to past side effects of high doses of oral estrogens.

At the ages we begin to see PCA becoming more prevalent/active, after age 50, there is an upward shift in estrogen production within the prostate and a downward shift in androgens, DHEA, and testosterone. Intraprostatic hormone levels do not necessarily parallel serum levels due to local intracrine production.

There is a well-described forward feedback loop that involves increased aromatase activity that results in increased estrogen production. Increased estrogen stimulates pro-inflammatory cytokines and prostaglandins that further stimulate aromatase activities and higher intraprostatic estrogen levels. This has been well described in association with intracrine estrogen production in endometriosis, uterine fibroids, and in breast, ovarian, and endometrial cancers. Local intra-tumoral aromatase activity may be greatly increased over normal tissue levels, resulting in huge increases in estrogen production by cancer cells.

What is now becoming better appreciated is the role of estrogens and estrogen receptors in regulating growth or suppression in many tissues throughout the body as well as within the prostate. Estrogens activate specific estrogen receptors, ERa and ERb, which have opposing effects on promotion of growth or inhibition of growth, control of inflammation, and induction of apoptosis within various tissues, including the prostate. ERa has pro-growth, pro-inflammatory, and antiapoptotic effects. ERb has the opposite effects and might be viewed as an anticancer receptor activating cell cycle arrest and apoptosis. Increased intraprostatic estrogens and ERa activation may play important roles in the development of BPH.

Genetic changes within cancer cells may increase or reduce ERa and ERb that may result in positive benefits or failures with estrogen treatments. In PCA, predominance of ERa over ERb results in pro-cancerous changes, growth, cell cyclic activation, and inflammation. Increased intraprostatic estradiol production leads to a vicious cycle upward that may promote cancer cell activities. So it appears that estrogens are part of the problem or part of the resolution depending on the ERa/ERb activities. The newer approaches are aimed at decreasing ERa activities and shifting to ERb dominance. Interestingly, most plant estrogens, phytoestrogens, have greater ERb activation than ERa that should reduce cancer cell activities. In fact, countries that have predominantly vegan diets have very low prostate cancer rates.

Another interesting aspect of testosterone/DHT metabolism is that one of the major metabolites of DHT, 3 Adiol, is primarily an ERb activator with suppressive cancer effects. 5AR inhibitors that suppress DHT will also suppress 3 Adiol. This leads lack of ERb effects, such as apoptosis, and results in gradual promotion of more aggressive, undifferentiated cell lines as has been reported with long-term use of 5AR inhibitors.

16.8.2 New Approach to Prostate Cancer Utilizing Estrogen Receptors

A new approach to the treatment of PCA, particularly androgen-independent failures or cases where secondary recurrence has occurred, is treatment to control estrogen receptors. It may prove to be useful in conjunction with other modalities, i.e., radiation, surgery, cryotherapy, or HIFU, or as a treatment where watchful waiting is the best option. It is less likely to result in serious side effects as was seen in earlier high-dose estrogen treatments with diethylstilbestrol.

Since estrone and estradiol activate both ERa and ERb, the best way to decrease ERa and increase ERb activities is to reduce local and systemic estrogen production. This can be easily accomplished with the use of available aromatase inhibitors, anastrozole, letrozole, or exemestane or possibly natural aromatase inhibitors like chrysin or trans-resveratrol. Additionally, aromatase can be downregulated by inhibition of COX-2 and NF-Kappa B pro-inflammatory pathways.

Once intraprostatic and systemic estrogens are significantly reduced, an ERb agonist should be added to selectively increase the anticancer mechanisms that this receptor activates. There are a number of partial or more complete ERb SERMs—raloxifene or the natural estrogen metabolite estriol (E3). E3 is primarily ERb active, has fewer general side effects, and can be given topically that would negate the prothrombic oral route. It also has the benefit of vasodilation and other positive cardiovascular effects that would antagonize the effects of aromatase inhibitors. Induced E2 deficiency may have adverse cardiovascular effects as has been demonstrated in genetic aromatase deficiency. In general, the use of long-term aromatase inhibitors is associated with relatively mild, well tolerated side effects. Like antiandrogen treatments, aromatase treatments may also result in bone loss and osteoporosis.

This approach should be utilized with other positive anticancer modalities such as adequate vitamin D and providing other antioxidants that have been shown to have complimentary, pro-apoptotic, and anti-inflammatory effects. Vitamin D3 has many promising benefits that include maintenance of cellular differentiation that includes hormone receptor activities and induction of several anticancer genes. Natural COX 2 inhibitors, like curcumin, reduce inflammation and the stimulation of aromatase activity. It also reduces NF-Kappa B pathway that regulates many inflammatory cytokines. Pomegranate juice or extracts have diverse anticancer effects. Resveratrol is an aromatase inhibitor and inducer of apoptosis. Green tea extracts contain proapoptotic compounds, like EGCG with additional anti-angiogenesis effects that limit tumor growth. Most of these compounds are phytoestrogens and mild ERb agonists.

There are a number of combined complementary medicine treatments that have shown significant successes in treatment of PCA. They might further benefit from the addition of aromatase inhibitors to reduce intraprostatic ERa estrogens. Further research with controlled trials of these approaches is warranted.

Summary of new estrogen treatment approach as a primary or secondary treatment or for ABT failures:

1. Use of an aromatase inhibitor to reduce intraprostatic and systemic estrogens to reduce ERa stimulation
2. Use of a selective ERb agonist, such as estriol or raloxifene, to induce apoptosis and cell cycle arrest
3. Correction of vitamin D3 deficiency with high doses of D3 to maintain high normal levels of 25(OH)D3
4. Use of phytoestrogens with ERb and various anti-inflammatory benefits, as well as specific anticancer effects, such as induction of apoptosis or anti-angiogenesis

References

Alexander NR, Branch KM, et al. Extracellular matrix rigidity promotes invadopodia activity. Curr Biol. 2008;18(17):1295–9.

Awad AB, Fink CS. Phytosterols as anticancer dietary compounds: evidence and mechanism of action. J Nutr. 2000;130(9):2127–30.

Bard R. Dynamic contrast enhanced MRI of prostate cancer. Berlin: Springer, Berlin; 2009a.

Bard R. 3D Doppler sonography and DCE MRI of recurrent prostate cancer. In: Annual meeting American Roentgen Ray Society, Boston; 2009b. p. 267.

Bard R. Interval cancers of the prostate: evaluation by 3-T MRI and 3-D power Doppler ultrasound. In: 58th Journees Francaises de Radiologie, Paris; 2011.

Barentsz JO, Harisinghani M, Husband J. MR of lymph nodes. In: 23rd International congress radiology, Montreal; 2004. p. 46.

Bostwick D. Does Finasteride alter the pathology of the prostate and cancer grading? PCRI Insights. 2004;7(1). http://prostate-cancer.org/does-finasteride-alter-the-pathology-of-the-prostate-and-cancer-grading/.

Campani R. Color Doppler imaging of liver metastases. La Radiologica Medica. 1994;87:32.

Chakraborty S, Roy M, Bhattacharya RK. Prevention and repair of DNA damage by selected phytochemicals as measured by single cell gel electrophoresis. Environ Pathol Toxicol Oncol. 2004;23(3):215–26.

Chan MM, Mattiacci JA, et al. Synergy between ethanol and grape polyphenols, quercetin, and resveratrol, in the inhibition of the inducible nitric oxide synthase pathway. Biochem Pharmacol. 2000;60(10):1539–48.

Choi C. Tumor malignancy linked to rigidity. The Scientist 2005;6(1). http://www.the-scientist.com/?articles.view/articleNo/23444/title/Tumor-malignancy-linked-to-rigidity/

Cornud F, Hamida K, et al. Endorectal color Doppler sonography and endorectal MR imaging features of non palpable prostate cancer. AJR Am J Roentgenol. 2000;175:1161–8.

Cosgrove D. Color Doppler signal in breast diseases. Radiology. 1994;192:580.

Downey D, Fenster A. Vascular imaging with a three-dimensional power Doppler system. Am J Radiol. 1995;165:665–8.

Einbond LS, Wu HA, et al. Carnosic acid inhibits the growth of ER-negative human breast cancer cells and synergizes with curcumin. Fitoterapia. 2012;83(7):1160–8.

Endress E, Bayerl S, Prechtel K, et al. The effect of cholesterol, lanosterol, and ergosterol on lecithin bilayer mechanical properties at molecular and microscopic dimensions: a solid-state NMR and micropipet study. Langmuir. 2002;18:3293–9.

Escurriol V, Cofan M, et al. Phytosterol plasma concentrations and coronary heart disease in the prospective Spanish EPIC cohort. J Lipid Res. 2010;51:618–24.

Ewing J. Neoplastic diseases. London: WB Saunders; 1940.

Henriksen J, Rowat AC, Ipsen JH. Vesicle fluctuation analysis of the effects of sterols on membrane bending rigidity. Eur Biophys J. 2004;33:732–41.

Hernandez OM, Discher DJ, et al. Rapid activation of neutral sphingomyelinase by hypoxia-reoxygenation of cardiac myocytes. Circ Res. 2000;86(2):198–204.

Jiménez-Escrig A, Santos-Hidalgo AB, Saura-Calixto F. Common sources and estimated intake of plant sterols in the Spanish diet. J Agric Food Chem. 2006;54(9):3462–71.

Kenfield SA, Stampfer MJ, et al. Physical activity and survival after prostate cancer diagnosis in the health professionals follow-up study. J Clin Oncol. 2011;29(6):726–32.

Kitamura H, Matsumura H, Yokoi K, et al. Correlation of contrast enhanced ultrasonography with histologic assessment of tumor angiogenesis in bevacizumab treated human metastatic liver tumors from colorectal cancer. J Ultrasound Med. 2011;S12.

Laffitte BA, Chao LC, et al. Activation of liver X receptor improves glucose tolerance through coordinate regulation of glucose metabolism in liver and adipose tissue. Proc Natl Acad Sci U S A. 2003;100(9):5419–24.

Lassau N, Koscielny S, et al. Prognostic value of angiogenesis evaluated with high frequency and color Doppler sonography for preoperative assessment of melanomas. AJR Am J Roentgenol. 2002;178:1547–51.

Louvar E, Littrup P, et al. Correlation of color Doppler flow in the prostate with tissue vascularity. First presented at the 96th annual meeting of the American Roentgen Ray Society, San Diego. 5–10 May 1996.

Mertens-Talcott SU, Talcott ST, Percival SS. Low concentrations of quercetin and ellagic acid synergistically influence proliferation, cytotoxicity and apoptosis in MOLT-4 human leukemia cells. J Nutr. 2003;133:2669–74.

Mertens-Talcott SU, Bomser JA, et al. Ellagic acid potentiates the effect of quercetin on p21waf1/cip1, p53, and MAP kinases without affecting intracellular generation of reactive oxygen species in vitro. J Nutr. 2005;135:609–14.

Moraa-Ranjeva MP, Charveron M, et al. Incorporation of phytosterols in human keratinocytes consequences on UVA-induced lipid peroxidation and calcium ionophore-induced prostaglandin release. Chem Phys Lipids. 2006;141(1–2):216–24.

Muti P, Awad AB, et al. A plant food–based diet modifies the serum β-sitosterol concentration in hyperandrogenic postmenopausal women. J. Nutr.2003;133(12): 4252–55.

Päivä H, et al. High-dose statins and skeletal muscle metabolism in humans: a randomized, controlled trial. Clin Pharmacol Ther. 2005;78(1):60–8.

Rajakumar N, Margolis D, et al. Correlation of Gleason scores with diffusion-weighted imaging findings of prostate cancer. Adv Urol. 2012;Article ID 374805:5 p.

Rouviere O. HIFU treatment of prostate cancer recurrence. In: 59th Journees Francaises de Radiologie, Paris; 2012.

Shigemura K, Yamanaka N, Yamashita M. Can diffusion-weighted magnetic resonance imaging predict a high Gleason score of prostate cancer? Korean J Urol. 2013;54(4):234–8.

Shulte M. Color duplex sonography in staging malignant bone tumor. In: 5th Congress of International Society for Musculoskeletal Ultrasonography, Prague; 2000. p. 37.

Stamatiou K, Alevizos A, et al. Frequency of impalpable prostate adenocarcinoma and precancerous conditions in Greek male population: an autopsy study. Prostate Cancer Prostatic Dis. 2006;9(1):45–9.

Toda S, Shirataki Y. Inhibitory effects of Astragali Radix, a crude drug in Oriental medicines, on lipid peroxidation and protein oxidative modification by copper. J Ethnopharmacol. 1999;68(1–3):331–3.

Vivancos M, Moreno JJ. β-Sitosterol modulates antioxidant enzyme response in RAW 264.7 macrophages. Free Radic Biol Med. 2005;39(1):91–7.

Vivancos M, Moreno JJ. Effect of resveratrol, tyrosol and β-sitosterol on oxidised low-density lipoprotein-stimulated oxidative stress, arachidonic acid release and prostaglandin E2 synthesis by RAW 264.7 macrophages. Br J Nutr. 2008;99:1199–207.

Wang D, Shen W, et al. Protective effect of active components extracted from radix Astragali on human erythrocyte membrane damages caused by reactive oxygen species [Article in Chinese]. Zhongguo Zhong Yao Za Zhi. 1996;21(12):746–8, 763.

Wang Q, Salman H, et al. Cooperation between antioxidants and 1,25-dihydroxyvitamin D3 in induction of leukemia HL60 cell differentiation through the JNK/AP-1/Egr-1 pathway. J Cell Physiol. 2005;204(3):964–74.

Woodfield CA, Tung GA, et al. Diffusion-weighted MRI of peripheral zone prostate cancer: comparison of tumor apparent diffusion coefficient with Gleason score and percentage of tumor on core biopsy. Am J Roentgenol. 2010;194(4):W316–22.

Imaging Detection of Regression and Recurrence

17

Robert L. Bard

17.1 Introduction

Traditionally, regression and recurrence following prostate cancer treatment have been screened by rising PSA, biopsy, and other biomarkers. Imaging provides an accurate alternative or complement to these conventional methods by depicting anatomic and functional images.

17.2 The Changing Scope of Prostate Cancer

Optimum imaging sequences and timing spacing for follow-up depend on the tumor grade and the treatment modality. Treatments using surgery or ablative technologies with cryotherapy, radiofrequency ablation, HIFU (high-intensity focused ultrasound), PDT (photodynamic therapy), and laser demonstrate immediate absence of flow by Doppler ultrasound or enhancement by DCE-MRI.

Since tumor recurrence in a previously treated area has the greatest likelihood of occurring within 6 months to 5 years, semiannual screening is an appropriate follow-up guideline. Other modalities, such as radiation or hormone therapies, develop measurable perfusion deficits over varying time intervals and may be initially followed every 2–3 months to document vascular perfusion abatement. This is important since high-grade prostate cancers tend to be radioresistant, and timely change of treatment may be lifesaving if early therapeutic failure is documented.

Another variable is the nonmedical/nonphysician (over the counter or OTC) nutraceutical market in which the quality of the listed ingredients is not controlled. The male public has been taking supplements such as saw palmetto for over 50 years for prostate support. These supplements are generally not reported to physicians and are accordingly not considered in the overall analysis of the imaging studies. Moreover, some noncontrolled supplements are grown in sites containing former toxic waste substances. Hepatitis and other hepatic disorders with subsequent abnormalities of testosterone metabolism and prostate tumor growth may be noted.

17.3 Follow-up of Active Surveillance Protocols

Clinically insignificant prostate cancers are true Gleason Score 6 and do not metastasize. A high-quality sonogram or MRI that is normal has a very high negative predictive value and can be used for longitudinal imaging to ensure that the disease will not become lethal. At major medical centers, men with elevated PSA who are potential

---

R.L. Bard, MD
Bard Cancer Center, Biofoundation for Angiogenesis
Research and Development, 121 E. 60th St,
New York, NY 10022, USA
e-mail: rbard@cancerscan.com

R.L. Bard et al. (eds.), *Image Guided Prostate Cancer Treatments*,
DOI 10.1007/978-3-642-40429-0_17, © Springer-Verlag Berlin Heidelberg 2014

biopsy candidates undergo pre-biopsy MRI and sonography. If the imaging is negative, there is no biopsy unless the risk is high.

Positive imaging studies now lead to co-registration biopsies that fuse the sonogram with the abnormal MRI findings.

The reason for biopsy “optimization” is to detect lethal prostate cancer and avoid over-detection of clinically insignificant tumors. The limitations of current biopsy protocols include: (a) identifying insignificant lesions, (b) under-classification of important cancers, and (c) missing index or significant tumors due to the random nature of the biopsy. Indications for repeat biopsy are rising PSA (especially doubling of the PSA velocity), high-grade PIN (prostate intraepithelial neoplasia), and active surveillance guidelines. Significant index lesions are now being detected by imaging before targeted biopsies. In some cases, strongly suspicious lesions may be assumed to be cancer, and biopsy may be deferred as treatment is based on the sonogram and MRI characteristics.

Since most urologists use TRUS to ensure the biopsy needle targets only the prostate and localizes the biopsy quadrants, few use this modality to look for suspicious areas of cancer. Radiologists and/or urologists with experience will be able to target index lesions better. Centers that use fusion technologies combining TRUS and MRI will have more accurate targeting data (Sonn et al. 2013).

The most effective diagnostic imaging and biopsy performance will be by a uroradiologist, that is, either a radiologist trained in urology or a urologist trained in radiologic imaging using MRI and 3DPDS (Turkbey et al. 2012).

17.4 Minimally Invasive Treatment (MIAT) or Active Surveillance AS

Minimally invasive treatments for localized prostate cancer are an alternative to active surveillance for low-risk disease or radical treatments such as radical prostatectomy or radiation therapy that may cause side effects and even increase mortality. Remember that insignificant disease should not be treated even with a MIAT protocol. One may consider the prostate as two separate and independent halves and offer MIAT or AS based upon the site-specific tumor characteristics and patient comorbidities.

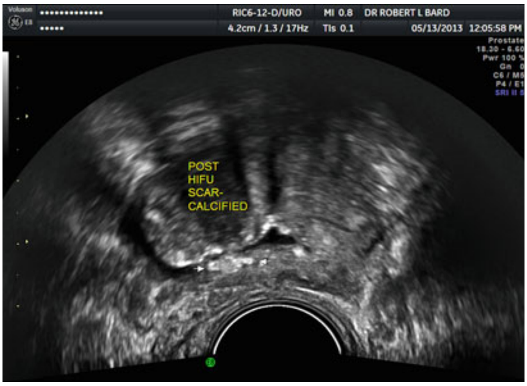

Fig. 17.1 Post HIFU necrotic calcification

17.5 Follow-up of the Treated Prostate

The successfully treated prostate on 3D-PDS may have a normal to irregular echo pattern with absent neovascularity. DCE-MRI will show signal loss (darker) in treated areas and no enhancement in successful therapies. The Doppler studies show medium-sized tumor vessels and may not detect an early recurrence that exhibits microcirculatory anastomotic vessels easily imaged by other contrast-enhancement modalities. The leaking vessels of neovascular arteries will enhance regardless of the tumor grade, whereas the 3D-PDS will show vascular density imaging that will be proportional to the degree of tumor invasiveness or malignant aggression potential. There has been insufficient experience with tumor recurrence characteristics on the DWI-MRI and elastography studies.

The posttreated prostate may show atrophic changes with volume loss. Distal urethral scarring and postnecrotic calcification (Fig. 17.1) or fibrosis with stricture may dilate the intraprostatic urethra (Fig. 17.2a, b).

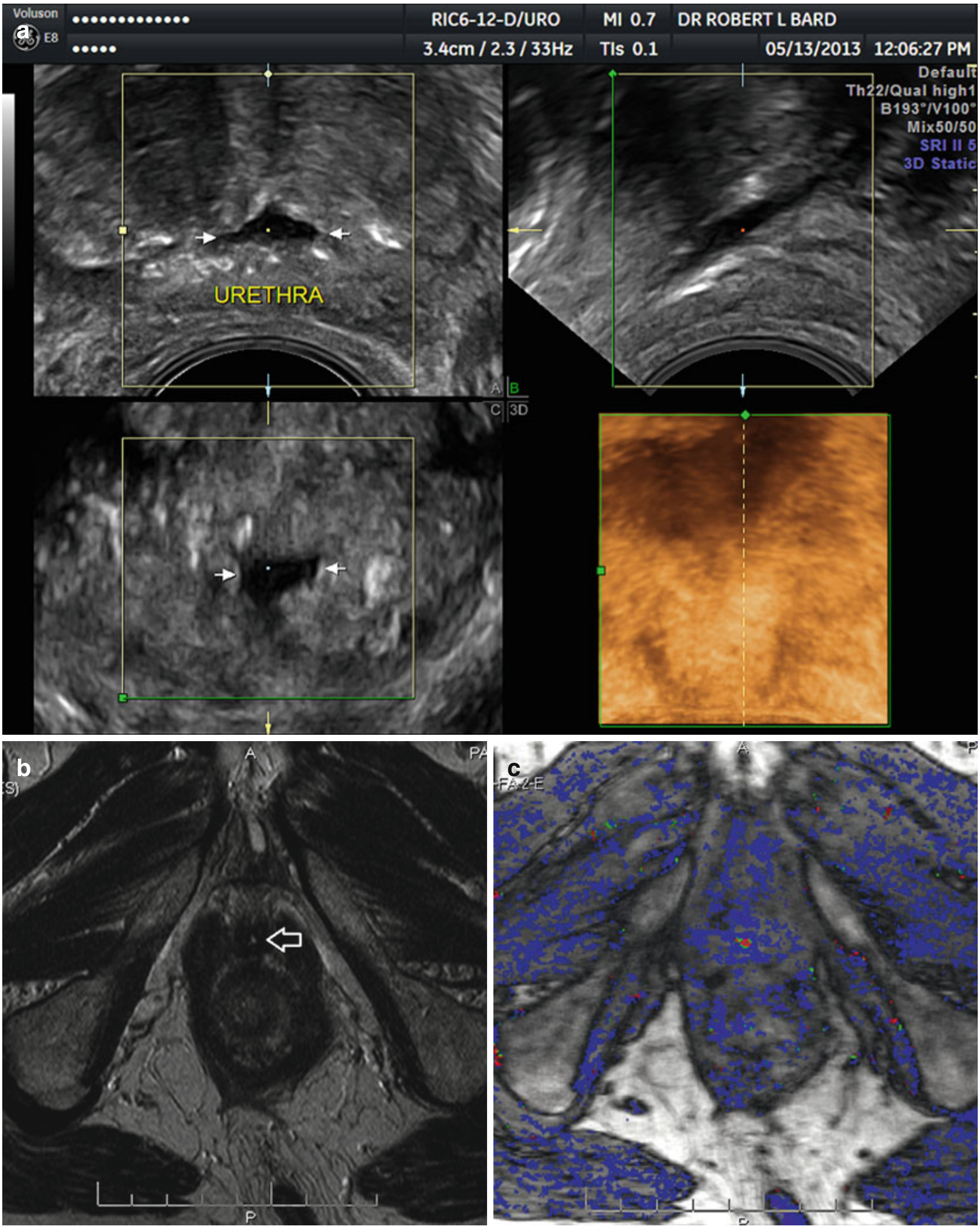

Fig. 17.2 (**a**) Post HIFU urethral dilation. (**b**) T2 MRI with thickened prostatic urethral wall (*arrow*). (**c**) DCE-MRI with periurethral hyperemia and enhancement

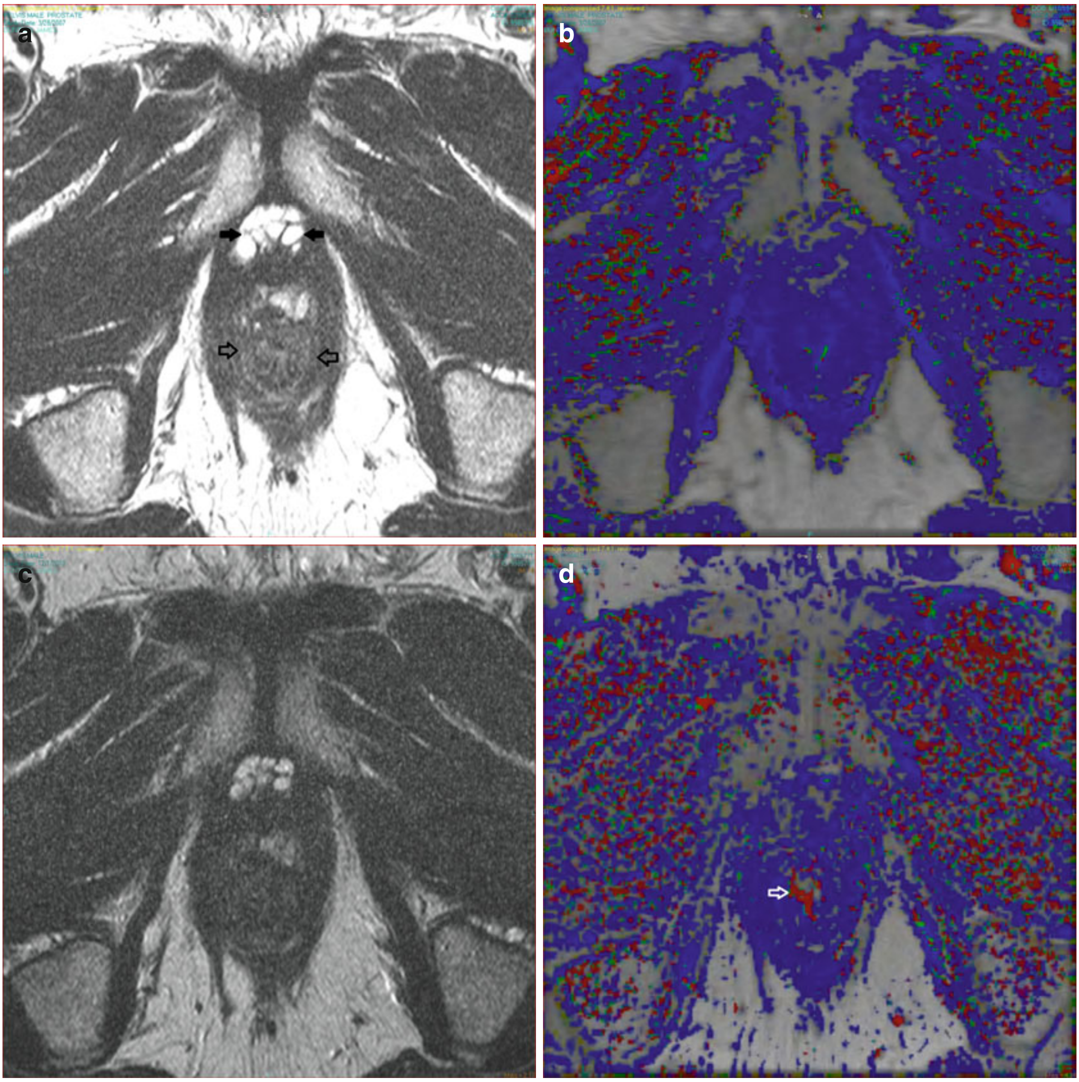

Fig. 17.3 (**a**) A T2 post HIFU signal loss and atrophy (*open arrows*). (**b**) DCE shows no enhancement indicating lack of recurrence. (**c**) T2 six months follow-up with no change. (**d**) DCE no interval change; note periurethral vein on right (*arrow*) which is not to be mistaken for recurrence and is due to vascular reorganization or recanalization following treatment changes

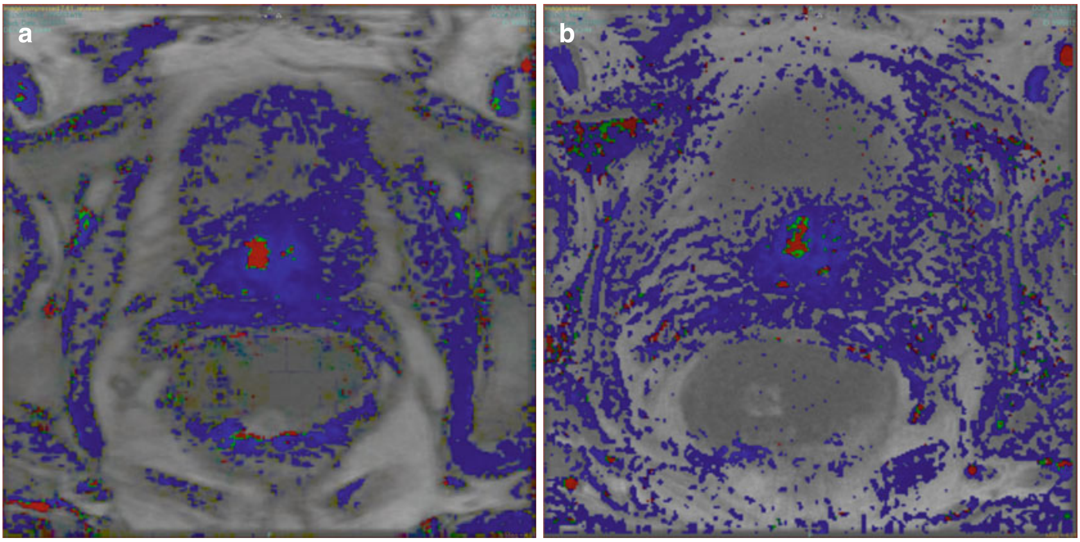

Fig. 17.4 (**a**) DCE-MRI focal HIFU recurrence. (**b**) DCE-MRI improved on antioxidant treatments

Tumor recurrence in the posttreatment prostate generally requires functional imaging for evaluation. 3D-PDS and DCE-MRI are usually sufficient to make a determination in the absence of a biopsy. Increased vessel density and irregular vessels in prostate cancer are present in 69 % of cases with Gleason 7 or greater tumors (Sauvain et al. 2006). External beam radical radiotherapy remains the primary treatment for patients with locally advanced or high-grade tumors in the USA as is associated with a 5-year failure rate of 35 % with Gleason scores of 6 or higher (Sartor 2002). The usual test is a PSA follow-up to determine biochemical failure (BF). This failure rate predicting tumor recurrence is less reliable than thought, and elevated PSA levels may be due to local recurrence or distant metastases. BF evaluation may be replaced by other functional parameters such as DCE-MRI and tumor vascular endothelial growth factor (VEGF) expression (Green et al. 2007). The addition of in vivo real-time volume density measurements of tumor neovascularity may prove to be of value in determining the risk of tumor recurrence noninvasively (Figs. 17.3a–d, 17.4a, b, 17.5a, b, 17.6a, b, 17.7a, b, 17.8a, b, 17.9a, b, and 17.10a, b).

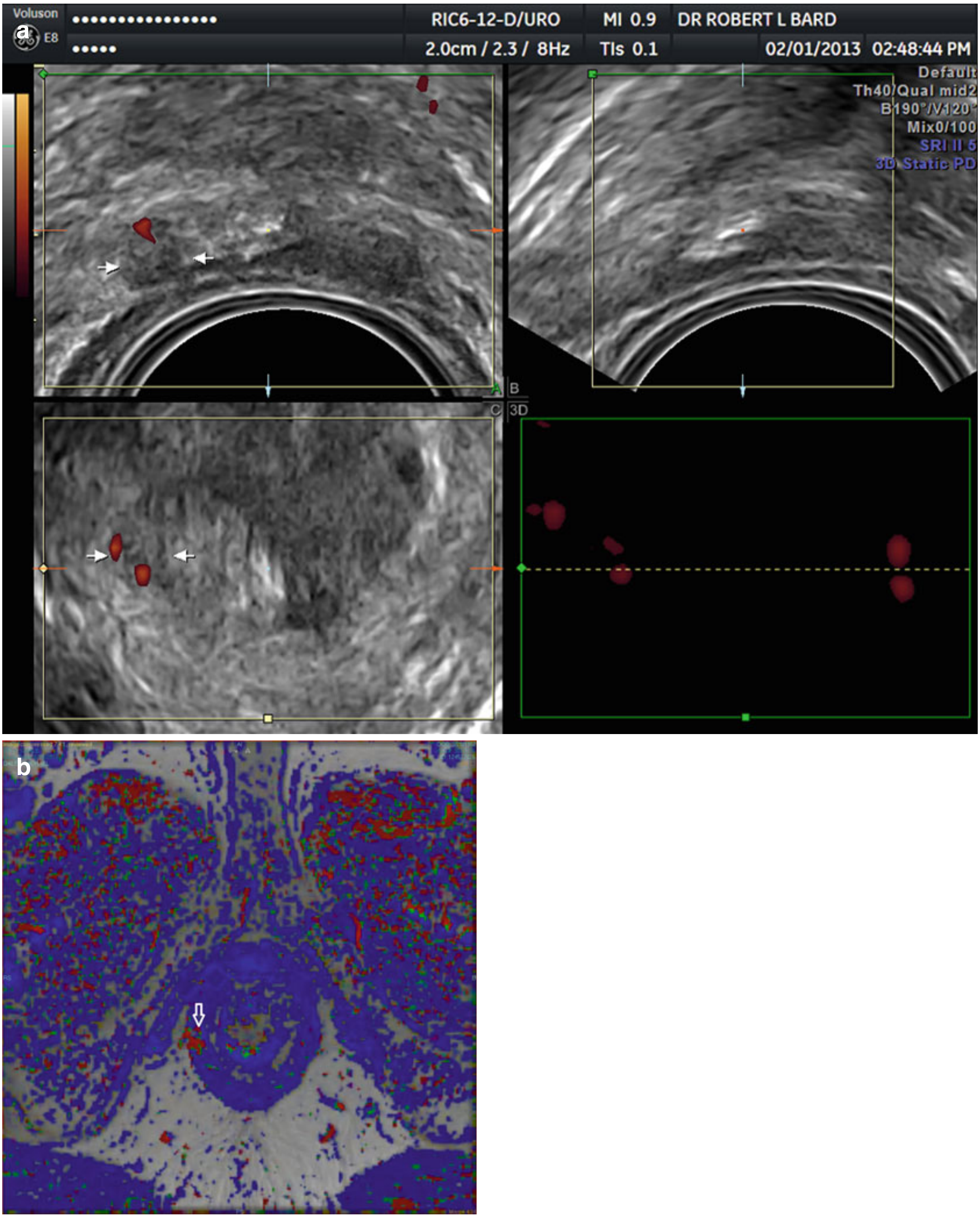

Fig. 17.5 (**a**) 3D right vascular 3 × 4 mm post HIFU recurrence in 3 cc treated gland (*arrows*). (**b**) T2 focal recurrence HIFU (*arrow*)

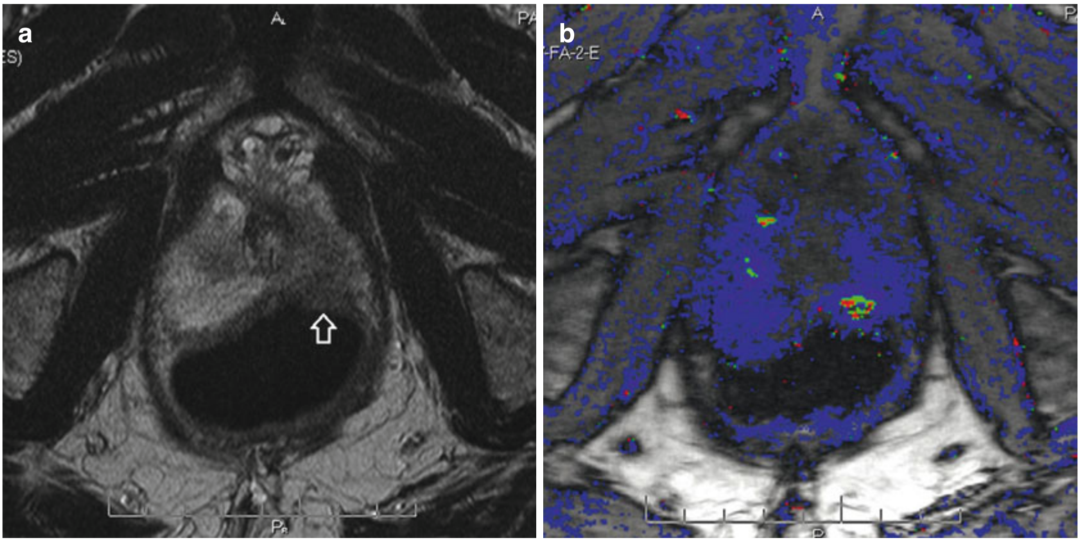

Fig. 17.6 (**a**) T2 post left cryotherapy with atrophy (*arrow*). (**b**) Local recurrence in treatment zone

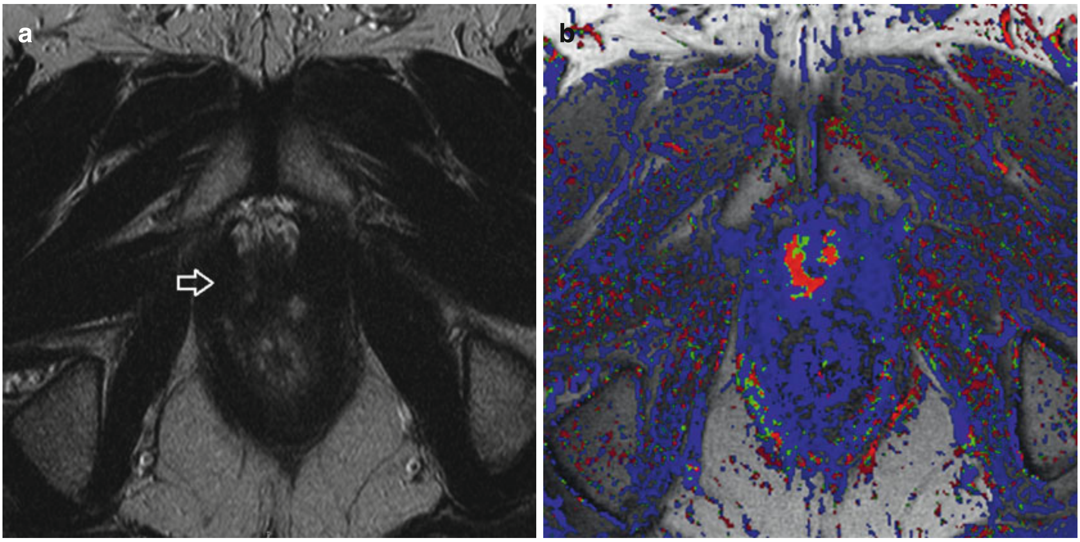

Fig. 17.7 (**a**) T2 post HIFU Gleason 5 right apex (*arrow*). (**b**) DCE-MRI focal apical recurrence noted

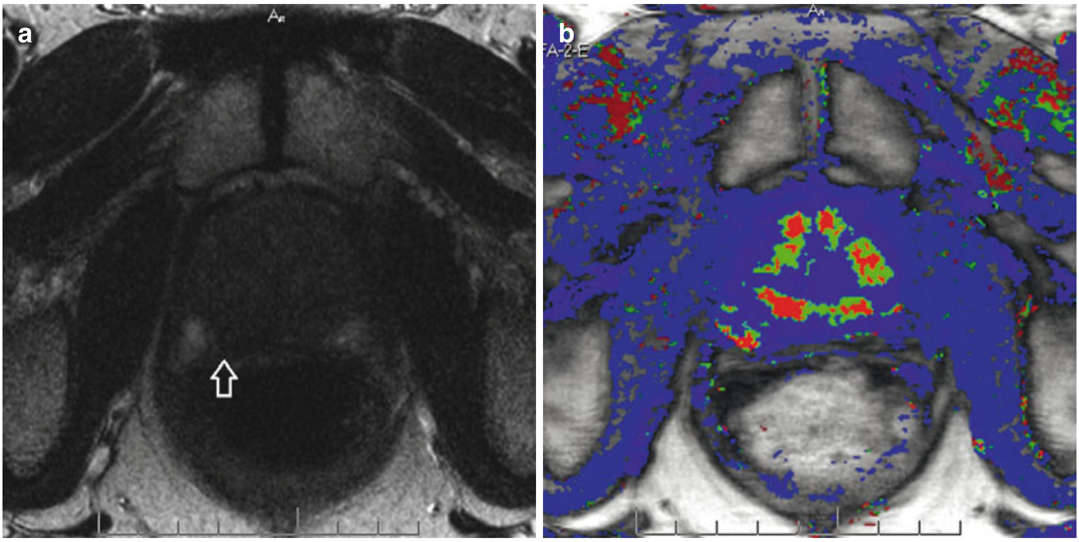

Fig. 17.8 (**a**) T2 post radiation with diffuse signal loss as dark gland (*arrow*). (**b**) Right peripheral and central recurrence noted

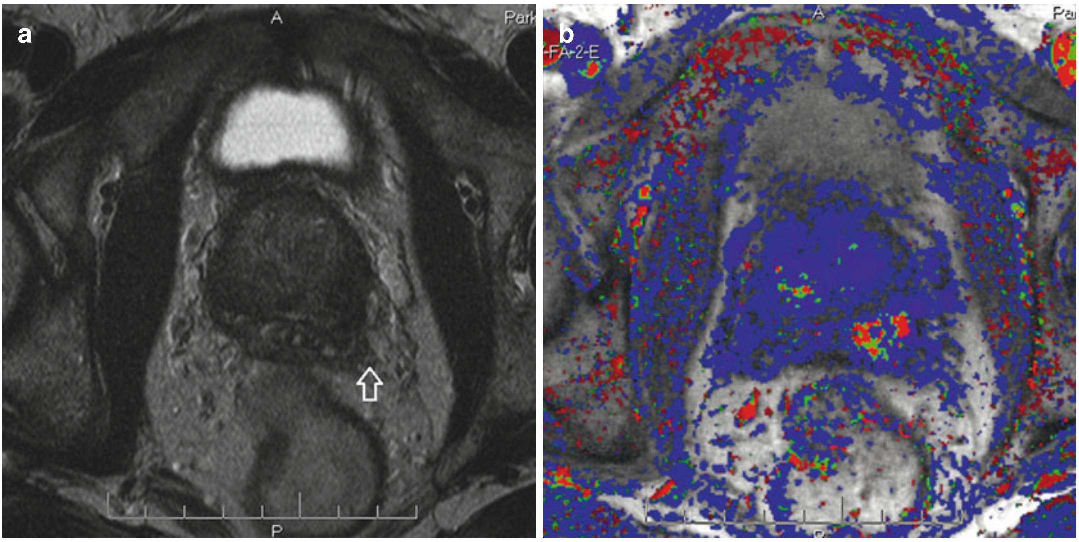

Fig. 17.9 (**a**) T2 post hormone treatment with diffuse signal loss (*arrow*). (**b**) Left seminal vesicle recurrence noted

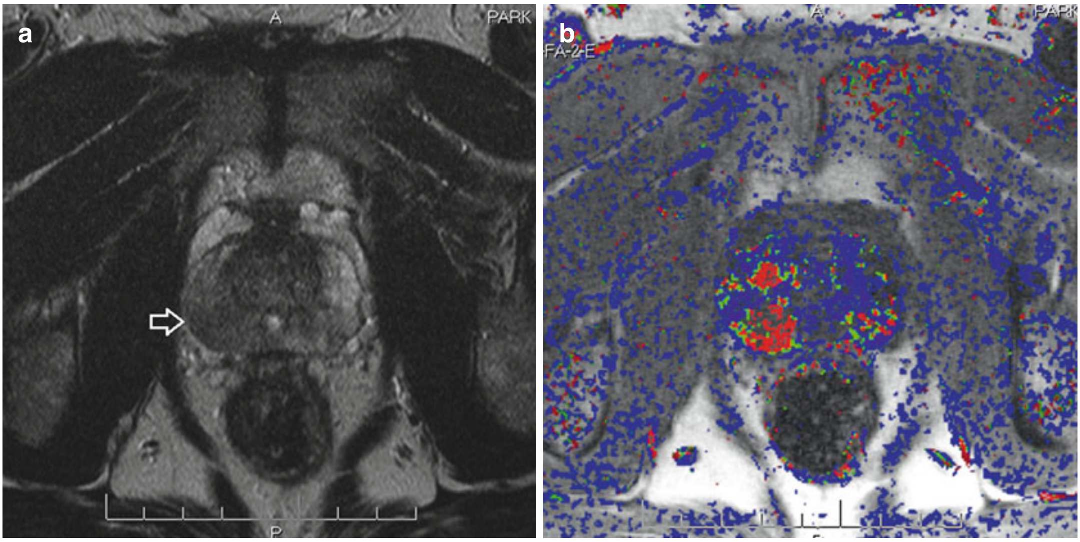

Fig. 17.10 (**a**) Eleven months post hormone treatment with $r>1$ signal loss in peripheral zone (*arrow*) and right anterior region. (**b**) Right anterior and left midgland recurrence confirmed

Conclusion

Anatomic and functional imaging provides valuable additional information in detecting, tracking, mapping, and staging recurrence.

References

Green MM, Hiley CT, et al. Expression of vascular endothelial growth factor in locally invasive prostate cancer is prognostic for radiotherapy outcome. Intl J Radiat Oncology Biol Phys. 2007;67(1):84–90.

Sartor O. Endpoints in prostate cancer clinical trials. Urology. 2002;60 Suppl 1:101–7.

Sauvain JL, Palascak P, Nader N. Power Doppler imaging and prostate cancer: optional or necessary technique? [translated from French]. J Radiol. 2006;87(9):1063–72.

Sonn GA, Nataraian S, et al. Targeted biopsy in the detection of prostate cancer using an office based magnetic resonance ultrasound fusion device. J Urol. 2013;189(1):86–91.

Turkbey B, Mani H, et al. Correlation of MRI tumor volume with histopathology. J Urol. 2012;188(4):1157–63.

Part III

Advanced Image Guided Procedures

Laser Principles

18

Arif Aslam and David J. Goldberg

18.1 History of laser

Albert Einstein first conceived the concept of laser radiation long before the first laser was invented. In 1917, he published his theory of stimulated light energy based on the original model of the atom provided by Bohr. He hypothesised that a photon of electromagnetic energy could stimulate the emission of another identical photon from atoms or molecules in an excited state (Einstein 1917).

Theodore Maiman, a physicist, invented and developed the first working laser in California, USA, in 1959 (Maiman 1960). He used a flash-lamped-pumped ruby crystal which produced a red light with a wavelength of 694 nm. This device was called a laser, an acronym for ‘light amplification by the stimulated emission of radiation’.

Some of the lasers commonly used today, including the neodymium, CO_2, organic dye and argon lasers appeared in the following years. Their availability opened up a wide range of applications that were subsequently developed. The defence, communication and music industries have all benefitted. The expansion of lasers in medicine began in the 1960s, and since there has been a plethora of new devices which provide novel methods of treating difficult conditions.

18.2 Electromagnetic Radiation

Electromagnetic radiation (EMR) is a fundamental form of energy that exhibits properties of both waves and photons. All forms of light are represented in the EMR. The electromagnetic spectrum encompasses all energy sources that travel through space in the form of waves. It ranges from the shorter wavelengths of x-rays and gamma rays to the long wavelengths of microwaves and radio waves (Fig. 18.1). The interaction of EMR and matter is mainly characterised by the absorption of energy and excitation of absorbing particles by photons.

18.3 Spontaneous and Stimulated Emission of Radiation

Electrons surrounding an atom or molecule can exist in more than one energy level but are usually found at the lowest energy level or resting state where they are stable. Energy can be

A. Aslam (✉)
The Dermatology Centre, Salford Royal NHS
Foundation Trust, The University of Manchester,
Manchester Academic Health Science Centre,
Manchester, UK
e-mail: a.aslam@doctors.org.uk

D.J. Goldberg
Skin Laser and Surgery Specialists of New York
and New Jersey, New York, 10016 NY, USA

Mount Sinai School of Medicine,
New York, NY, USA
e-mail: drdavidgoldberg@skinandlasers.com

R.L. Bard et al. (eds.), *Image Guided Prostate Cancer Treatments*,
DOI 10.1007/978-3-642-40429-0_18, © Springer-Verlag Berlin Heidelberg 2014

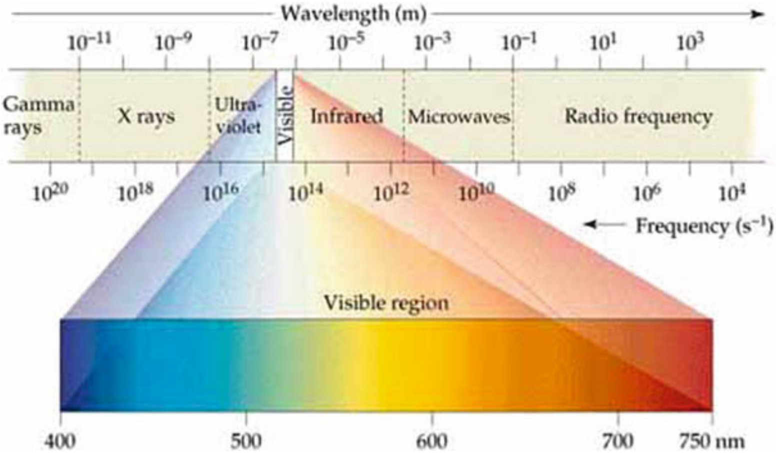

Fig. 18.1 The electromagnetic spectrum (EMR)

absorbed or lost from a molecule by a photon resulting in a change of the energy level of the electron. An electron in the resting state can absorb a photon of light of the correct wavelength changing it into an excited state. It is unstable in the excited state and will usually drop back down to the resting state, releasing a photon of energy. This process is called spontaneous emission (Fig. 18.2a). If another photon of the appropriate wavelength collides with the electron while it is still excited, the electron will return to its resting state by emitting two photons which are synchronised in time and space and are of the same energy. This is called stimulated emission of radiation (Fig. 18.2b). The emitted photons may stimulate further emissions from excited atoms of the same type. Stimulated emission is rare as normally the majority of electrons are in a resting state. To increase the likelihood of stimulated emission there must be 'population inversion'. This is a state when photons have a higher probability of encountering excited electrons and stimulating further emissions of photons with the same energy. An external source of energy must be used to increase the proportion of excited atoms in the population to a level where stimulated emission is a frequent occurrence. This process is called 'pumping'.

Constructing a laser device consists of three basic elements: a pumping system, lasing medium and an optical cavity. The pumping system or the external source of energy creates a population inversion for the excited electrons in the laser chamber. For example, the high-powered flashlamp is used in some dye lasers. The lasing medium or gain is the source of laser radiation and supplies the electrons needed for the stimulated emission of radiation. The wavelength of the emitted light is determined by the distinctive energy transitions of the molecules of the medium. The medium can be gaseous (argon, CO_2, copper vapour), liquid (organic dye) or solid (ruby, alexandrite, Er:YAG, Nd:YAG and diode). The optical cavity is a chamber consisting of two parallel mirrors enclosing the laser medium which is excited by the pumping system. Photons of energy in the axis of the chamber are reflected off the mirrors at either end, stimulating further emissions in the same axis. One mirror in the chamber is partially reflective, and this allows some of the stored photons to escape and form a laser beam.

18.4 Properties of Laser Light

Laser light has several unique properties which distinguish it from other types of light such as sunlight. These properties are monochromaticity, coherence and collimation (Stratiagos and Dover 2000).

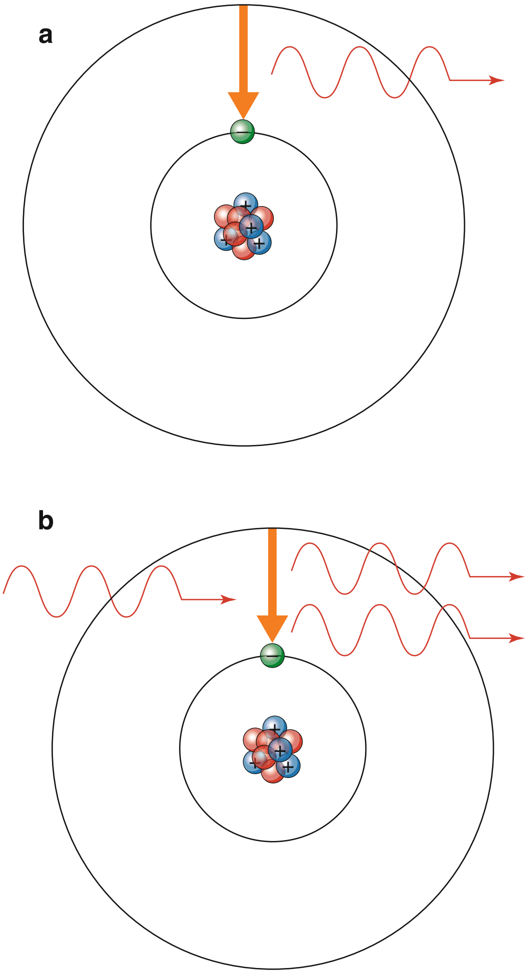

Fig. 18.2 (**a**) Spontaneous emission. (**b**) Stimulated emission

18.4.1 Monochromaticity

Laser light contains a single wavelength of light or a very narrow band of wavelengths. The wavelength is determined by the lasing medium used in the laser. Other sources of light emit a wide spectrum of wavelengths.

18.4.2 Coherence

Laser radiation waves are in phase with respect to space and time with minimal degree of divergence. This is based on the principle of stimulated emission.

18.4.3 Collimation

Laser waves are highly ordered and parallel which allow the beam to travel long distances without spreading and to be focused on a small spot with very high-power density.

18.5 Radiometry

It is important to understand *energy, fluence, power and irradiance*. This will help to understand laser physics and laser-tissue interactions. *Energy* is the capacity to do work and is measured in joules. The energy of laser light refers to the number of photons delivered in a single pulse and is measured in joules and is most suitable to describe the energy of pulsed lasers. *Fluence* is the energy per area and is also known as energy density which is expressed as joules per cm^2. *Power* is the amount of energy released over time and is measured in watts (J/s). Watts are mainly used to describe continuous wave lasers. *Irradiance* describes the power density, i.e. the watts per square centimetre. It describes the intensity of a continuous wave laser.

18.6 Laser-Time Dependence

Laser light can be divided into three main types: continuous wave, quasi-continuous wave and pulsed. Continuous wave lasers emit a continuous beam at a constant power (Fig. 18.3a). CO_2, argon, krypton and argon dye lasers are examples of continuous wave lasers. Copper vapour is an example of a quasi-continuous wave laser. It delivers a beam with a train of pulses closely spaced together (Fig. 18.3b). Pulsed laser beams are either short pulse with nanosecond (10^{-9} s) pulse durations or long pulse with pulse durations

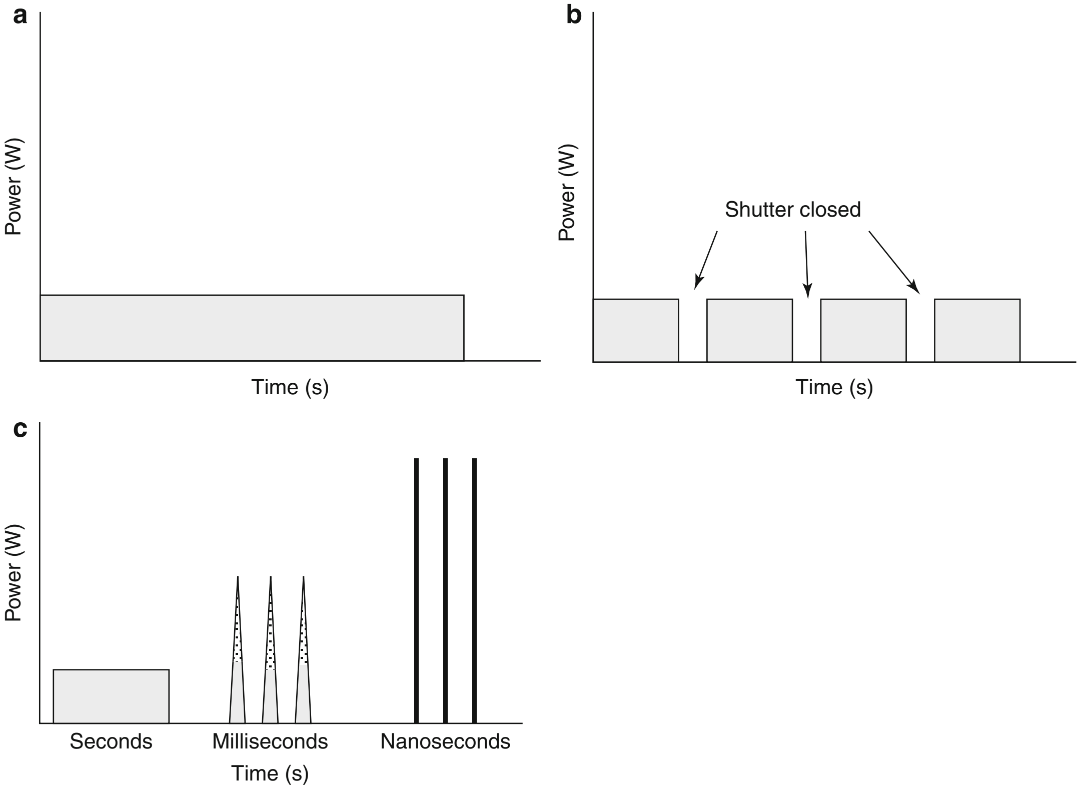

Fig. 18.3 (**a**) continuous wave lasers. (**b**) quasi continuous wave lasers. (**c**) pulsed lasers

within milliseconds (10^{-3} s). Pulse lasers are high-power lasers which emit ultrashort single pulses with extremely high energies (Fig. 18.3c). Quality switching or (Q-switched) lasers contain a photooptical switch or shutter within the laser cavity. This creates a sudden population inversion in the lasing medium and allows the release of extremely short powerful bursts of high energy light within the nanosecond range.

18.7 Laser Parameters

18.7.1 Wavelength

The wavelength of the laser light must correspond to the absorption spectrum of the intended target chromophore.

18.7.2 Pulse Duration

The pulse duration is also called the pulse width. This must be equal to or shorter than the thermal relaxation time (TRT) which is directly proportional to the square size of the chromophore.

18.7.3 Energy Density

The energy density, also known as the fluence, must be high enough to destroy the target chromophores within the defined pulse duration.

18.7.4 Spot Size

The spot size of a laser is an important parameter. It is not simply based on the size of targeted area.

It has a significant impact on the depth of the penetration of a laser despite the wavelength. The spot size directly influences the fluence and the irradiance of the laser beam as well as the depth of penetration and the scattering of the laser light. Fluence and irradiance are inversely proportional to the square of the radius (r) of the spot size (energy = πr^2). For example, if a pulsed dye laser with an energy of 10 J/pulse is focused on at a spot size of 10 mm, then the area of the spot will be $\pi r^2 = \pi(0.5)^2$ and the energy density will be 12.7 J/cm^2. If the same light source at the same energy level is focused on a spot size of 5 mm, the calculated energy density is 50.9 J/cm^2. Therefore, halving the spot size increased the energy density by a factor of 4. Conversely, to achieve the same energy density with a spot size half the diameter, the laser energy output would need to be reduced by 4.

18.7.5 Beam Profile

The beam profile represents how the intensity of the light produced by a laser is distributed across the beam diameter. This special distribution of power is also referred to as transverse electromagnetic mode (TEM). Most commercial lasers used in dermatology produce a beam profile with a Gaussian profile. This beam profile is called the fundamental mode or TEM00 of the laser. In this beam profile, the intensity is not the same across the beam diameter but it peaks in the centre of the diameter. Approximately 86 % of the power is contained at that impact spot. From the centre of peak intensity, the intensity falls off to both sides with a Gaussian (bell-shaped) distribution.

18.7.6 Cooling

Cooling is important in order to protect the surrounding tissue which is not the intended target from the effects of laser light. It also helps to reduce pain and oedema. It can be performed before, during or after treatment. It is usually performed by a cryogen spray built into the laser hand piece, an air cooling device, contact cooling or ice. Parallel cooling is performed simultaneously with laser treatment using cooled sapphire tips within the hand piece. Post cooling helps extract excess heat from the treated tissue and prevent side effects such as post inflammatory hyperpigmentation. However, too much cooling can result in ineffective treatments, and the balance of laser energy and cooling is critical.

18.8 Laser Tissue Interaction

The biological effects of laser can are separated into thermal and mechanical.

18.8.1 Photothermal

Laser light imposes a tissue effect when it is absorbed and converted into heat energy. The induced biological effect is determined by the temperature reached within the tissue (Herd et al. 1997). Further increases in temperature of only 5–10 °C lead to cell injury and subsequent inflammation and repair. Proteins and DNA molecules become denatured at high temperatures, and temperatures greater than 100 °C water exceed its boiling point resulting in vaporisation. The steam produced causes a rapid increase in pressure which damages cellular elements and blood vessels. If the heating continues at these temperatures, desiccation and charring occurs. In order to determine the tissue effect of laser, heat conduction must be taken into account. When light is absorbed by a target, heat loss occurs immediately by conduction to all adjacent tissues. This process is called thermal relaxation. The speed of thermal relaxation varies depending on the thermal relaxation time (TRT) of the tissue. This is defined as the time necessary for the targeted tissue to cool down to half the temperature to which it was heated. The TRT varies according to the size of the targeted structure. Small objects cool much faster than larger ones.

The tissue effect of lasers is primarily affected by two parameters: the heating of chromophores and the secondary spread of heat to the adjacent tissues. The degree of thermal damage is influenced first by the temperature reached within the target which relates to the energy density and secondly by the length of time that the target remains at that temperature, which depends on the pulse duration.

18.8.2 Photomechanical

Lasers can also cause photomechanical effects. When the pulse duration is less than the TRT, there is sudden thermoelastic expansion due to spatially localised heating. This sudden change creates acoustic waves that evidently damage the absorbing tissue (Watanabe et al. 1988). An example of photomechanical destruction of tissue is the purpura induced by the high-fluence short-pulse-width pulsed dye laser.

18.8.3 Photochemical

Photodynamic therapy is an example of a photochemical reaction. This reaction occurs when endogenous or exogenous photosensitisers elicit a selective photochemical reaction by absorbing light. Porphyria can also be considered to be a photochemical reaction.

18.9 Selective Photothermolysis

The theory of selective photothermolysis was introduced by Anderson and Parrish in 1983 (Anderson and Parrish 1983). It was a significant breakthrough towards understanding complex laser-tissue interactions. In light-absorbing targets or chromophores, the competition between active heating and passive cooling determines how high the temperature rises within the target. Selective photothermolysis occurs when the energy is delivered at a rate faster than the rate of cooling of the targeted structures. If the pulse duration of the emitted wavelength is longer than the TRT, heat diffuses from the target before the latter is irreversibly thermally damaged. On the other hand, if the pulse duration is too short, then in the case of vascular lesions, insufficient damage is caused and the targeted tissue is not successfully destroyed. However, if the laser exposure duration is just less than the TRT, the target cannot get rid of its heat during laser exposure and irreversible thermal damage is confined within the target.

Three basic parameters are mandatory in order to achieve selective photothermolysis. These are wavelength, fluence or energy density and pulse duration. A wavelength must be absorbed more by the targeted structure compared to the surrounding tissue. Secondly, the energy density or fluences delivered to the target should be high enough to cause sufficient thermal damage and destroy the target. Finally the pulse duration should be less than the time needed for the target to cool in order to achieve confinement of thermal damage.

For instance, damage can be confined to a blood vessel with limited collateral damage to nearby structures by choosing a wavelength absorbed by haemoglobin such as 585 nm and a laser pulse duration shorter than 1–3 ms which is the TRT of blood vessels with diameters of 10–100 μm. The flashlamp pulsed dye laser, the first laser developed based on selective photothermolysis, was designed to emit a yellow light at 585 nm with a pulse duration of 450 μs; there is sufficient energy absorption by haemoglobin to cause blood vessel coagulation. Very short pulse durations of 1 μs causes microvascular rupture and haemorrhage, whereas a long exposure time increases the risk of damage to the surrounding tissue with unacceptable perivascular damage.

18.10 Laser Safety

Laser can pose a significant hazard, and these are divided into beam and nonbeam hazards. Beam hazards inflict ocular and cutaneous injury, and nonbeam hazards arise from the laser device or its interaction with other materials. Plume, fire and electrical hazards are examples of nonbeam hazards.

Eye injury is a very serious complication arising from using a laser. A laser beam usually operates in the millisecond range of pulse duration and so cannot effectively be shielded by the eyelid blink reflex. This reflex takes a tenth of a second to complete (Friedman et al. 1987). Ocular damage resulting from laser surgical procedures is directly related to the laser wavelength being used. Optical radiation emitted by lasers operating in the ultraviolet (200–400 nm), mid-infrared (1,400–3,000 nm) and far-infrared (3,000–10,600 nm) range of wavelengths is absorbed by the anterior eye segment and inflicts injury to the lens or cornea. Light emitted by lasers in the visible light (400–760 nm) and near-infrared (760, 1,400 nm) spectrum penetrates the lens and cornea and is absorbed by the retina and vascular choroid (Youker and Ammirati 2001). Eye protection is of paramount importance when operating a laser device, and everyone that is exposed to the optical radiation must wear protective eyewear including patients and visitors. The two most common eyewear options include those made from coated glass and those made from polymeric materials. Large, clear warning signs should be displayed on the door of laser theatres to inform potential visitors and staff of the potential ocular hazards inside.

Laser fires may result from ignition of combustible material in close vicinity to the laser resulting in burns. Common flammable materials include gauze, surgical drapes and respiratory devices. Hair can also be ignited, and caution should be taken when performing laser procedures at hair-baring sites.

Lasers contain high-voltage electrical energy and pose a significant risk of electrocution.

Lasers are the second most common heat-generating device used by surgeons, second only to electrosurgical units. Surgical smoke or plume is produced when a heat-producing device interacts with treated tissue. Numerous chemical substances some carcinogenic have been detected in laser plume including carbon monoxide, hydrogen cyanide, ammonia, formaldehyde, acrolein, toluene and benzene (Barrett and Garber 2003). Human papillomavirus DNA has been isolated from laser plume generated in the CO_2 laser treatment of verruca plantaris and respiratory papillomatosis (Ferenczy et al. 1990). Human immunodeficiency virus DNA capable of infecting cultured cells has also been recovered from laser plume (Baggish et al. 1991). Laser masks and smoke evacuators should always be used to combat the laser plume hazard. Laser masks filter particles larger than 0.1 μm by means of electrostatically charged synthetic fibres. A high efficiency smoke evacuation device with a powerful vacuum should also be used. They should contain a filter which removes particles up to 0.1 μm in size and a charcoal filter to remove toxic smoke.

References

Anderson RR, Parrish JA. Selective photothermolysis: precise microsurgery by selective absorption of pulsed radiation. Science. 1983;220:524–7.

Baggish MS, Poiesz BJ, Joret D, Williamson P, Refai A. Presence of human immunodeficiency virus DNA in laser smoker. Lasers Surg Med. 1991;11:197–203.

Barrett WL, Garber SM. Surgical smoke: a review of the literature. Is this just a lot of hot air? Surg Endosc. 2003;17:979–87.

Einstein A. Zur Quantentheorie der strahlung. Physik Z. 1917;18:121–8.

Ferenczy A, Bergeron C, Richart RM. Human papillomavirus DNA in C02 laser generated plume of smoke and its consequences to the surgeon. Obstet Gynecol. 1990;75:1140118.

Friedman NR, Saleeby ER, Rubin MG, Sandu T, Krull EA. Safety parameters for avoiding acute ocular damage from the reflected C02 (10.6 microns) laser beam. J Am Acad Dermatol. 1987;17(part 1):815–8.

Herd RM, Dover JS, Arndt KA. Basic laser principles. Dermatol Clin. 1997;15:355–72.

Maiman T. Stimulated optical radiation in ruby. Nature. 1960;187:493–4.

Stratiagos AJ, Dover JS. Overview of lasers and their properties. Dermatol Ther. 2000;13:2–16.

Watanabe S, Flotte TJ, McAuliffe DJ, Jacques SL. Putative photoacoustic damage in skin induced by pulsed ArF excimer laser. J Invest Dermatol. 1988; 90:761–6.

Youker SR, Ammirati CT. Practical aspects of laser safety. Facial Plast Surg. 2001;17:155–63.

Focal Laser Ablation of the Prostate

19

Dan Sperling and Robert L. Bard

19.1 Rationale for Focal Ablative Treatment of Prostate Tumors

Prostate cancer patients presenting with early-stage, low-risk disease face a dilemma. On the one hand, radical treatments (surgery, radiotherapy, cryotherapy, HIFU) address the assumption that prostate cancer is a multifocal disease by treating the entire gland but with varying risks of urinary, sexual, and bowel comorbidities. On the other hand, active surveillance (AS) places on the patient both monitoring and psychological burdens. In fact, monitoring alone may entail repeat biopsies with their accompanying risk rates of false negatives. These are not without risk to patient health and cost to an overburdened healthcare system.

With ever-improving diagnostics through imaging, targeted biopsies, and pathology analytics, the potential exists to identify which patients may best benefit from radial treatment and which may gain cancer control with minimal to no toxicity through direct (focal) treatment of clinically significant prostate lesions. Patients who undergo such therapy are informed that focal treatment entails the risk of future disease progression. However, patients who are clinically qualified and psychologically motivated for focal treatment experience confidence in the positive probability of buying time with high quality of life. For such patients, this offsets the concomitant responsibility of monitoring for progression.

While ongoing research is needed to continually inform risk stratification, patient selection criteria, and treatment protocols (Marchettei and Eggener 2011; Nguyen and Jones 2011), direct focal treatment offers qualified candidates a middle ground between AS and radical therapies while preserving future focal and radical treatment options if needed. Magnetic resonance imaging (MRI) plays an essential role in focal therapies, including laser ablation (Sommer et al. 2013; Lindner et al. 2010).

19.2 Background of Focal Laser Ablation

The term "ablation" has become a common description attached to devices that kill or remodel selective tissue without destroying the major structures themselves. Today, minimally invasive thermal ablation involves diverse technologies such as laser, radiofrequency, microwave, and high-intensity focused ultrasound (HIFU)

D. Sperling, MD (✉)
Sperling Prostate Center, Alpha 3T MRI,
145 E. 32th St, New York, NY 10016, USA
e-mail: dan.sperling@sperlingmedical.com

R.L. Bard, MD
Bard Cancer Center, Biofoundation for Angiogenesis
Research and Development, 121 E. 60th St,
New York, NY 10022, USA
e-mail: rbard@cancerscan.com

R.L. Bard et al. (eds.), *Image Guided Prostate Cancer Treatments*,
DOI 10.1007/978-3-642-40429-0_19, © Springer-Verlag Berlin Heidelberg 2014

and is commonly utilized in technology-driven urologic treatment areas, such as benign prostatic hyperplasia (BPH) or benign nodular thyroid tumors and cancer ablation in the prostate, kidney, and bladder. Ablation is becoming a cost-effective, efficacious alternative to surgery (Medtech Insight Report 2012).

Numerous energy systems have been utilized for thermal tumor ablation (Bozzini et al. 2013), but none has emerged as a dominant technology. However, interstitial laser ablation under MRI guidance is gaining ground (Bomers et al. 2012; Stafford et al. 2010a; Lindner et al. 2010). As early as the 1980s, descriptions of laser interstitial thermal ablation of liver tumors appeared in the literature. During the 1990s, interest in thermal tumor ablation using laser energy was conceived as a way to overcome the challenges to surgical and pharmacological treatment of brain lesions. Early efforts to deliver large doses of laser energy to tissue sites using fiber optics showed promise, but the complexity with which light interacted with tissue made predictable accuracy impossible. In 2000, McNichols et al. announced development of a system using temperature-sensitive MRI images to effect closed-loop feedback control of laser thermal therapy in real time, allowing the user to regulate laser lesion production and a hardware interface to modulate laser delivery parameters based on temperature feedback data (McNichols et al. 2000). Four years later, Kangasniemi et al. published their results using small diffusing laser fiber tips with canine cerebral tumors to better distribute the energy deposition and a computer-controlled feedback system to monitor therapy and prevent excess temperature buildup (Kangasniemi et al. 2004).

Application of laser ablation within the prostate and other organs followed quickly. In 2005, McNichols et al. reported their results with fiber-optically delivered interstitial laser thermal therapy to treat prostate tumors in a canine model. They demonstrated that real-time MRI is useful in computing temperature changes based on the proton resonance frequency (PRF) shift, constructing two-dimensional maps of temperature rise and chronic thermal damage to control laser therapy (McNichols and Gowda 2005). Efficacy and consistency of prostate tumor necrosis have been demonstrated in other animal models (Colin et al. 2012; Stafford et al. 2010b; Marga et al. 2011).

Since 2007, the FDA has cleared numerous devices to apply laser to ablate interstitial tumors in soft tissue, but there is no specific ICD-9 coding for application in the prostate. It is being explored not only for brain, spine, and prostate lesions but also kidney and liver tumors (Stafford et al. 2010a). FLA may be useful in cases of prostate cancer recurrence in the prostate bed following prostatectomy (Woodrum et al. 2011). Prostate FLA is used for the direct treatment of malignant tumors and should not be confused with laser-based vaporization treatments for urethral constriction due to benign prostatic enlargement, such as Green Light Laser.

19.3 Technological and Clinical Description

19.3.1 Technology

Various manufacturers have received FDA clearance to use their laser devices for MRI-guided tumor ablation in neurological and other tissues. Among them are:

- Biotex (Houston, TX) which developed a neurological application
- Visualase® (Houston, TX)
- Monteris, Inc. (Minneapolis, MN) developed Neuroblate and AutoLITT® which are used for brain tumors
- Novian Health (Chicago, IL) offers Novilase® for MRI-guided treatment of benign and malignant breast tumors

Other systems are in research and development.

As with other types of thermal ablation, laser has the ability to be directed by image guidance and applied with minimal invasiveness. It can be performed under local, regional, or general anesthesia, and recovery is quick and virtually pain-free.

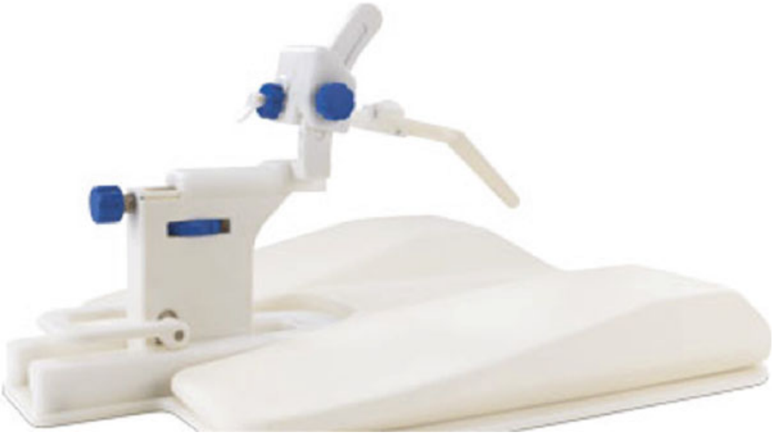

Fig. 19.1 Biopsy guide device used for treatment planning/localization

Saldahna et al. provide an excellent summary of clinical laser technology. The components of a laser include a power source, laser medium, and reflecting mirrors. As with alternative techniques, laser delivery can be performed percutaneously, laparoscopically, or through open surgery. A laser fiber is introduced into a target lesion through a cannula, typically 13–15 gauge for modern quartz fibers. The laser then is set to emit low energy ranging between 3 and 20 W for 2–20 min. As in alternative techniques, carbonization limits the maximal zone of ablation. Attempts to circumvent this limitation are similar to those in RFA, particularly with the creation of water-cooled probes. Water-cooled sheaths have been designed to be paired with higher laser power outputs up to 50 W. Ablational zones up to 80 mm have been produced with the introduction of water-cooled probes (Saldanha et al. 2010).

19.3.2 Clinical Application

In our practice, we currently use the Visualase® device guided by real time, in bore 3T MRI. Multiplanar MRI provides image visualization as well as thermometry to monitor tissue destruction.

Patient Preparation

- Bowel preparation: Fleet enema 2 h prior to procedure
- Antibiotics (IV ceftriaxone; Cedax PO)
- Anesthesia (2 layers: ultrasound guided and MRI guided)

Localization of Target Area

3T MRI is used for placement and real-time monitoring. The patient is positioned prone on the MRI table. The needle sleeve biopsy guide is placed in the rectum. The localization device is attached to the biopsy guide, and preliminary T2 axial and sagittal sequences are acquired. Utilizing prostate CAD (computer-aided design), the lesion is localized to document optimal positioning (Figs. 19.1 and 19.2).

Based on coordinates generated by the software, the device base is adjusted. A confirmation MRI scan is conducted to confirm needle guide trajectory to target, and a 14 Gauge guide catheter with an MR-compatible trochar is placed into the target lesion. The trochar is then removed, and the Visualase laser applicator is inserted through the guide catheter into the lesion. MRI scans are performed to confirm the location of the laser applicator (Fig. 19.3a, b).

Laser Ablation

An imaging plane containing the applicator is chosen and a T1 planning image is acquired. After loading the planning image into the Visualase system, temperature-sensitive fast RF-spoiled gradient-recalled echo images are acquired repeatedly on the MRI and transferred in real time to the Visualase workstation for analysis.

After establishment of baseline, the laser is activated at a reduced power level insufficient to cause thermal injury (Fig. 19.4). This intermediate step is performed to verify proper placement

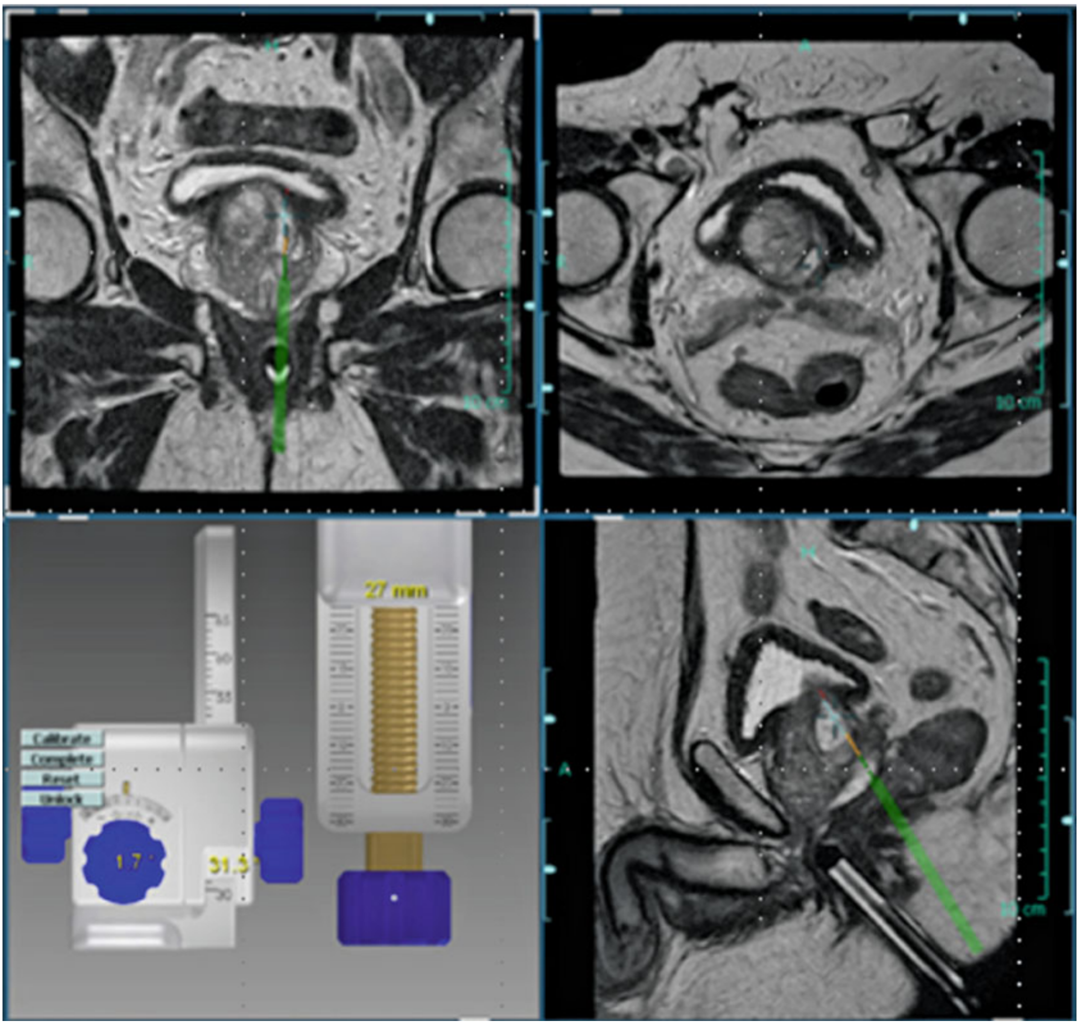

Fig. 19.2 Preliminary sequences obtained to document optimal positioning

of the applicator and proper operation of thermal imaging. Test dosage assists in calculating the irreversible damage estimate for laser firing.

Subsequent to a successful test pulse, laser treatment is initiated. Imaging is continued for approximately 30–60 s after cessation of laser irradiation in order to fully visualize cooling and return to baseline. During each laser treatment, temperatures of the rectal wall, urethra, and other vital structures closest to the area of the prostate being treated are monitored using the Visualase software (Fig. 19.5).

Post Ablation

Following ablation, IV gadolinium is administered. Treatment efficacy is indicated by lack of enhancement to the focus treated by laser ablation (Fig. 19.6).

Once the ablation zone has been validated, the laser applicator is removed and the patient is allowed to ambulate. If the patient is able to void, he is routinely discharged 30 min later or when in satisfactory condition without complaints. He is given Cedax to be taken PO QD for 3 days post procedure.

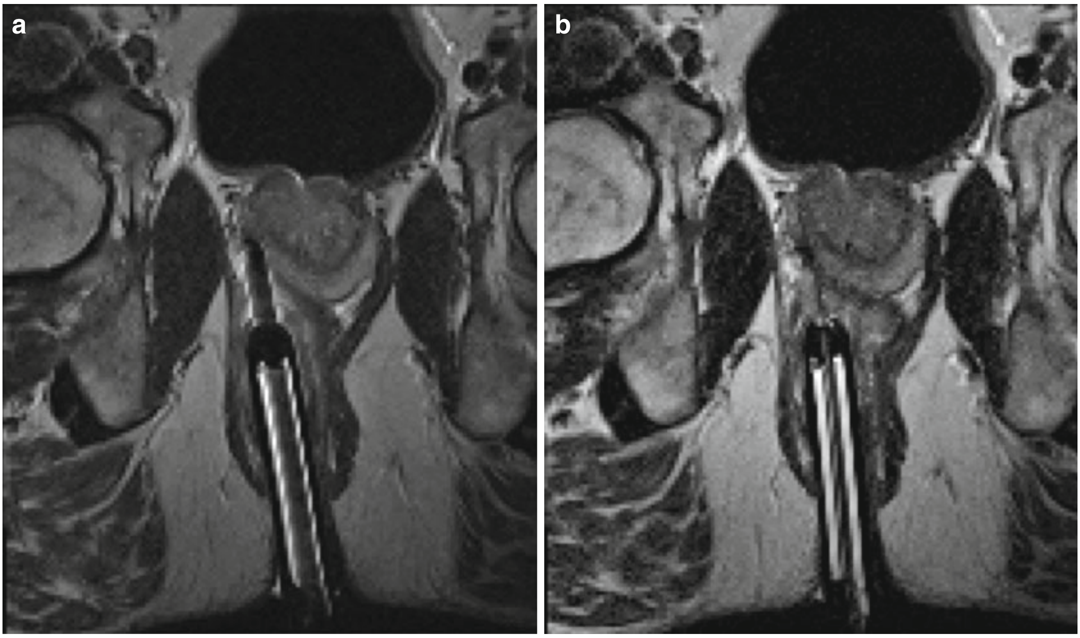

Fig. 19.3 (**a**) Placement of biopsy needle with trajectory confirmed. (**b**) Laser fiber placed within biopsy needle and confirmed on MRI

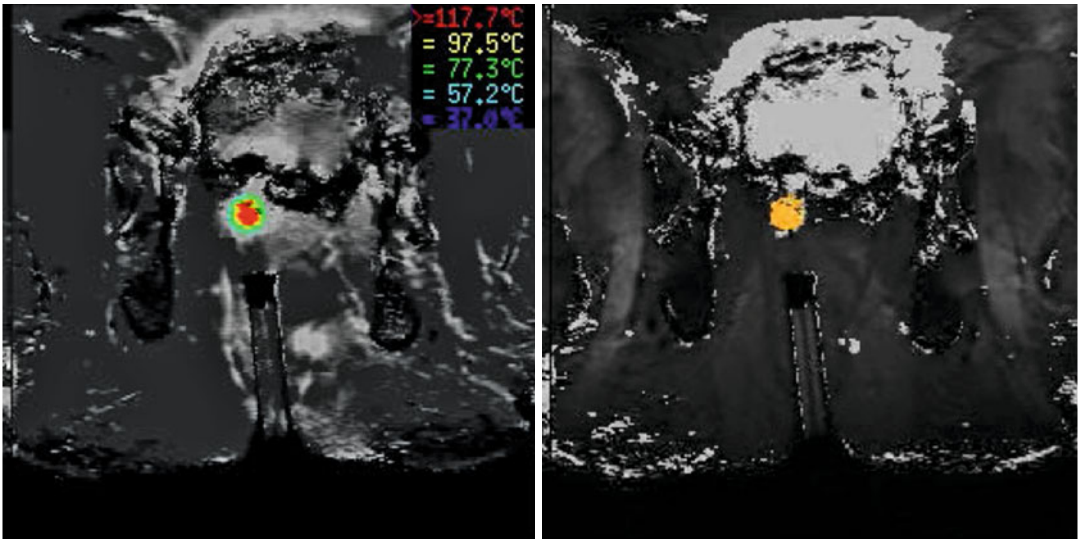

Fig. 19.4 Example of test dose for 34 s (*green*)

Mechanisms

The thermal effect of laser depends on the amount of heat energy delivered and the depth of light distribution. Wavelengths between 590 and 1,064 nm overcome weak absorption by water and hemoglobin. Ablation is accomplished at a target temperature of 60 °C. Laser physics are discussed in the previous chapter in detail.

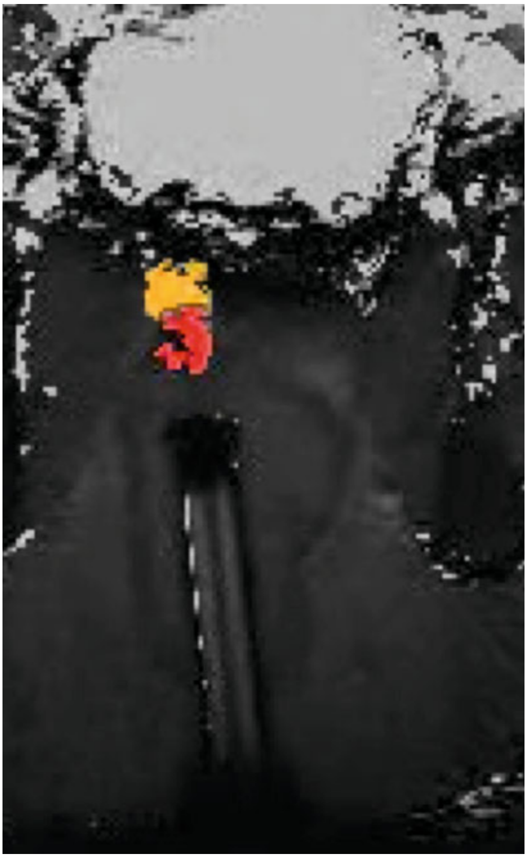

Fig. 19.5 Laser ablation in process (*orange* and *red areas*)

Thermometry

In addition to MRI's superior soft tissue discrimination and ability to image at any angle, it is also sensitive to temperature. During monitoring of an ablation procedure, MRI continuously acquires temperature images throughout heating and provides structure images during and after heating. MRI can continuously acquire temperature images derived from gradient echo MR images (Breen et al. 2007). In fact, MRI is ideal for temperature mapping as well as target identification and definition and, as demonstrated above, can reflect a virtually immediate assessment of laser treatment efficacy (Quesson et al. 2000).

In our case, MRI thermometry software allows us to monitor temperature at specific points in tissue. It provides effective monitoring and feedback to control laser. Not only are we confident of achieving lethal temperatures in and around the entire lesion, but we can also maintain temperatures at a safe level at the borders of the bladder, seminal vesicles, rectal wall, and urethra.

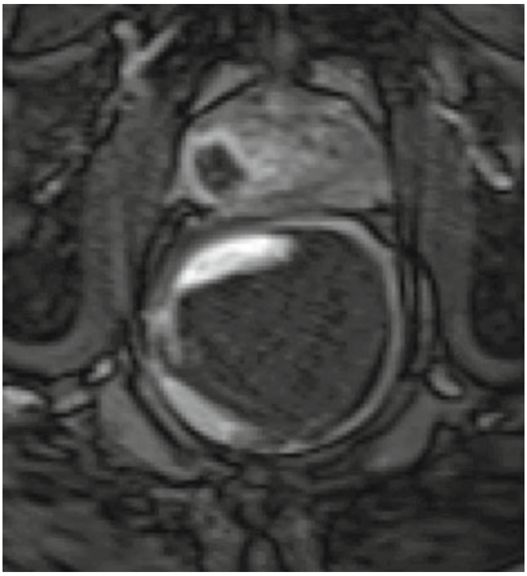

Fig. 19.6 Posttreatment lack of enhancement in same location confirms ablation

Follow-Up Protocol

Patients who undergo laser treatments are expected to comply with our follow-up protocol:

1. Receive a multiphasic MRI at 3–6 months post ablation with a targeted in-gantry or MRI-US fusion-guided biopsy in the ablation zone.
2. At 1 year follow-up, undergo a 12-core MRI-US fusion-guided biopsy.

19.4 Clinical Results

To date there are no large-scale, randomized, prospective clinical trials. Much clinical study is warranted.

Oto et al. reported the results of a small, phase I study out of the University of Chicago. Transperineal MR-guided focal laser ablation for clinically low-risk prostate cancer was performed in nine patients with clinically low-risk prostate cancer, defined as a Gleason score of 7 or less in three or fewer cores limited to one sextant obtained with transrectal ultrasonography (US)-guided biopsy and a concordant lesion at MR imaging. At follow-up MR-guided biopsy, 78 % (7 out of 9) showed no signs of cancer. At follow-up, average posttreatment IPSS and SHIM score changes were not significantly different from baseline. The results of this preliminary study indicate that focal laser ablation "appears to be a feasible and safe focal therapy option for clinically low-risk prostate cancer" (Oto et al. 2013).

The authors reported a follow-up study of 59 low-risk (Gleason grade 3 or 4) patients whose treatment efficacy was assessed at 6 months posttreatment using 3D power Doppler ultrasound (3D-PDS) and dynamic contrast-enhanced MRI (DCE-MRI). Imaging showed the tumor vascularity absent in 21/21 patients who demonstrated significant neovascularity. Patients returned to work immediately without catheter. No complications were noted at 6 months, except for one patient who experienced mild bleeding from rectal hemorrhoids. However, long term efficacy and disability rates are not established (Bard et al. 2013).

As of this writing, MR-guided FLA in North America is in clinical trial at these locations:

- National Institute of Health/National Cancer Center
- Princess Margaret Hospital (Toronto, ONT)

An increasing number of US centers are performing FLA of the prostate. To name just a few: Sperling Prostate Center (NY), Smilow Comprehensive Prostate Cancer Center (NY), Memorial Sloan-Kettering Cancer Center (NY), Emory University Hospital (GA), University of Chicago Comprehensive Cancer Center (IL), and others.

Conclusion

Focal laser ablation has advantages on many levels. It is relatively easy and efficient, and the cost of FLA is low. The laser work station is configured to take up minimum space in the MRI suite. FLA can be done under local or general anesthesia. Patients do not need a catheter. Recovery is rapid, and posttreatment quality of life is generally high. In addition, FLA is FDA-cleared. While much research needs to be done, FLA is a promising contribution to prostate cancer treatment.

References

Bard R, Sperling D, Futterer J. Focal laser ablation of prostate cancer: a prospective study of 59 patients. Boston: American Society of Lasers in Surgery and Medicine Annual Meeting; 2013.

Bomers JG, Sedelaar JP, et al. MRI-guided interventions for the treatment of prostate cancer. AJR Am J Roentgenol. 2012;199(4):714–20.

Bozzini G, Colin P, et al. Focal therapy of prostate cancer: energies and procedures. Urol Oncol. 2013;31(2): 155–67.

Breen MS, Breen M, Butts K, et al. MRI-guided thermal ablation therapy: model and parameter estimates to predict cell death from MRI thermometry images. Ann Biomed Eng. 2007;35(8):1391–403.

Colin P, Nevoux P, et al. Focal laser interstitial thermotherapy (LITT) at 980 nm for prostate cancer: treatment feasibility in Dunning R3327-AT2 rat prostate tumour. BJU Int. 2012;109(3):452–8.

Kangasniemi M, McNichols RJ, et al. Thermal therapy of canine cerebral tumors using a 980 nm diode laser with MR temperature-sensitive imaging feedback. Lasers Surg Med. 2004;35(1):41–50.

Lindner U, Lawrentschuk N, Trachtenberg J. Image guidance for focal therapy of prostate cancer. World J Urol. 2010;28(6):727–34.

Marchettei P, Eggener S. Focal therapy for clinically localized prostate cancer. Arch Esp Urol. 2011;64(8): 815–22.

Marga MR, Colin P, et al. Focal laser ablation of prostate cancer: numerical simulation of temperature and drainage distribution. Biomed Eng Online. 2011; 10:45.

McNichols RJ, Gowda A. Percutaneous MRI-guided laser thermal therapy in canine prostate. Proc SPEI. 2005;5686:214–25.

McNichols RJ, Gowda A, Wright SM. MR-guided feedback control of laser thermal therapy. Denver: Proceedings of the ISMRM; 2000.

Medtech Insight. U.S. thermal devices ablation market. 2012. http://www.medtechinsight.com/ReportA562.html.

Nguyen CT, Jones JS. Focal therapy in the management of localized prostate cancer. BJU Int. 2011;107(9): 1362–8.

Oto A, Sethi I, et al. MR imaging-guided focal laser ablation for prostate cancer: phase I trial. Radiology. 2013;267(3):932–40.

Quesson B, de Zwart J, Moonen C. Magnetic resonance temperature imaging for guidance of thermotherapy. J Magn Reson Imaging. 2000;12:525–33.

Saldanha D, Khiatani VL, et al. Current tumor ablation technologies: basic science and device review. Semin Intervent Radiol. 2010;27(3):247–54.

Sommer G, Bouley D, et al. Focal ablation of prostate cancer: four roles for magnetic resonance imaging guidance. Can J Urol. 2013;20(2):6672–81.

Stafford RJ, Fuentes D, et al. Laser-induced thermal therapy for tumor ablation. Crit Rev Biomed Eng. 2010a; 38(1):79–100.

Stafford RJ, Shetty A, et al. Magnetic resonance guided, focal laser induced interstitial thermal therapy in a canine prostate model. J Urol. 2010b;184(4):1514–20.

Woodrum DA, Mynderse LA, et al. 3.0T MR-guided laser ablation of a prostate cancer recurrence in the postsurgical prostate bed. J Vasc Interv Radiol. 2011;22(7):929–34.

Focal Therapy for Prostate Cancer Using Irreversible Electroporation

20

Gary Onik

20.1 Introduction

Irreversible electroporation (IRE) is a new nonthermal ablation modality that uses short pulses of DC electric current to create irreversible pores in the cell membrane thus causing cell death. This method has been shown by Onik et al. to have significant advantages in ablating prostatic tissue, rapid lesion resolution, sparing of structures such as vessels, nerves and urethra, and uniform destruction throughout the IRE lesion (Rubinsky et al. 2007).

The focal therapy of prostate cancer, i.e., a "male lumpectomy," is gaining interest as a potentially new prostate cancer management strategy, falling between watchful waiting on the one hand and morbid whole-gland treatments such as radical prostatectomy on the other. Onik et al. introduced the concept of using focal therapy for treating prostate cancer using cryoablation in 2002 (Onik et al. 2002). Other clinical series using cryoablation to focally treat prostate cancer have shown excellent cancer control rates with extremely low morbidity (Onik et al. 2007; Bahn et al. 2006; Lambert et al. 2007). Cryoablative lesions, however, have some distinct limitations, such as variable damage at the cryoablation lesion's margin, injury to adjacent structures such as rectum, urethra and neurovascular bundle (NVB), and long procedure time due to the need for multiple freeze thaw cycles. These characteristics could limit the widespread acceptance of this modality despite certain demonstrated advantages over the more traditional treatments of radiation and radical prostatectomy (Bahn et al. 2002). In this chapter, we will explore the principles of electroporation and its application to focal therapy for prostate cancer.

20.2 Principles of Irreversible Electroporation (IRE)

IRE, rather than causing destruction through coagulative necrosis such as in RFA or through cellular and microvascular disruption as in cryoablation, causes cell death by the mechanism of irreversible electroporation. When cells are exposed to a pulsed electrical field with the proper parameters, holes are created in the cell membrane increasing its permeability. Depending mainly on the magnitude of the transmembrane potential the cell is exposed to, the holes may close (reversible electroporation) or remain open (irreversible electroporation).

Reversible electroporation occurs within a narrow range of parameters roughly between 300 and 600 V/cm^2 although cell size, pulse duration, and number of pulses can affect these ranges. The application of reversible electroporation to tissues has found important applications in

---

G. Onik, MD
Department of Engineering,
Carnegie Mellon University,
Pittsburgh, PA, USA
e-mail: onikcryo@gmail.com

R.L. Bard et al. (eds.), *Image Guided Prostate Cancer Treatments*,
DOI 10.1007/978-3-642-40429-0_20, © Springer-Verlag Berlin Heidelberg 2014

biotechnology and medicine. Electrogenetherapy (EGT) is the in vivo insertion of genes into cells in tissue through reversible electroporation and presents an alternative to viral vectors (Neumann et al. 1982). Electrochemotherapy is accomplished by injecting drugs or macromolecules into a targeted area. Electrodes are placed into or around that area to generate a reversible permeabilizing electric field in the tissue, thereby introducing the drugs or macromolecules into the cells of the affected area (Mir et al. 1991). In addition, potent but normally impermeable anticancer drugs such as bleomycin are used with electroporation to ablate tissue.

In the above applications, the electroporation has to be reversible and irreversible electroporation is consciously avoided. Therefore, the electrical parameters that induce irreversible electroporation were studied only as an upper limit to the range of electrical parameters that induce reversible electroporation. Irreversible electroporation, however, has been studied extensively in in vitro cellular systems. For instance, IRE has been considered an effective means for killing both gram-negative and gram-positive bacteria responsible for water contamination. Davalos et al were the first to suggest that irreversible electroporation could be used for surgical tissue ablation without the inherent limitations of chemotherapeutic injection or the narrow window of parameters associated with reversible electroporation (Davalos et al. 2005). They speculated that this could result in significant advantages over the currently used thermal ablation methods. This was later confirmed with the first animal study creating liver lesions (Rubinsky et al. 2007).

Some of the parameters that can be manipulated with IRE to create larger tailored ablation zones include the use of multiple needle arrays as in cryosurgical ablation, increased exposure of the active zone to increase lesion length, increasing the pulse number, and an increase in pulse voltage. Much work remains to be carried out in determining what approach is best for creating and shaping the ablation zones needed for a whole-gland prostate ablation.

Of course ablating normal prostate tissue is not equivalent to ablating tumors. It is very possible that the parameters needed to destroy tumor cells may be different than that needed to destroy a normal prostate. In addition, it is very likely that different tumor cells will have lesser or greater sensitivity to destruction by electroporation. Rather than a single parameter (i.e., temperature) that determines cell destruction in the thermal ablation techniques, IRE has multiple parameters that can be manipulated to optimize cell death. These include voltage gradient, pulse duration, pulse number, and pulse polarity.

Miller et al. have shown that in vitro testing can be a valuable tool in determining the optimal IRE protocol for a given tumor type (Miller et al. 2005). Using an in vitro IRE testing technique, they were able to quickly determine an optimal IRE protocol which resulted in 100 % destruction of a highly malignant hepatocellular carcinoma cell line.

20.3 Advantages of IRE Over Thermal Ablation

20.3.1 Rapid Resolution of the IRE Lesion

A major limitation to the monitoring of the efficacy of thermal ablation procedures is the many months both heat- and cold-based lesions take to show decrease in size and years to show complete resolution. The determination of an adequate treatment by imaging, therefore, becomes a matter of assessing continued tumor growth at the margins of the treated lesion or stability of the size of the lesion, signs of which take time to determine treatment failures. Our work shows that an IRE lesion exhibits extremely rapid resolution, with the treated tissue showing marked diminution in size 2 weeks after the creation of the lesion (Fig. 20.1).

We believe the underlying basis for this phenomenon is the preservation of the microvasculature, down to the arteriolar level, throughout IRE lesion. IRE lesions are therefore able to heal throughout their volume whereas cryoablation and RFA lesions, which are completely devascularized shortly after lesion creation, must resolve from the edges of the lesion inwards.

In the prostate this has major implications other than just lesion monitoring. Many older patients with prostate cancer have some measure of BPH causing significant urinary flow symptoms. The immediate and midterm effect of cryoablation, therefore, can often be to initially increase the patient's urinary flow problems. With an IRE lesion and its rapid decrease in the volume of the prostate, in a matter of weeks we might expect actually an improvement in symptoms over the short and long term. This also raises the possibility that IRE might be an excellent treatment for BPH where cryoablation has not been used with success due to the unfavorable characteristics of its lesion resolution.

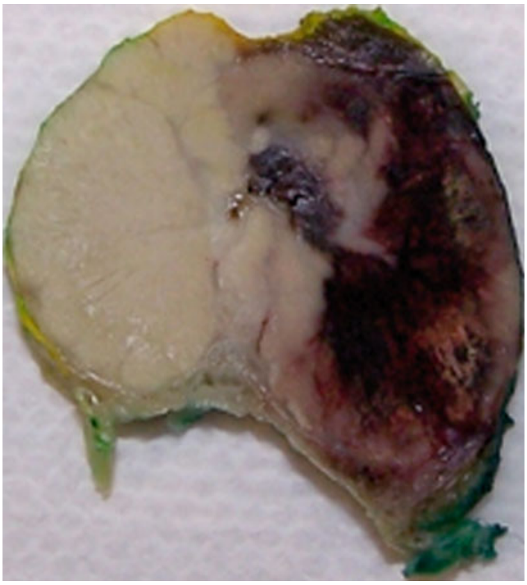

Fig. 20.1 Gross pathology of the IRE lesion at 24 h. The right side of the gland is hemorrhagic (pulses = 8, Kv = 1)

20.3.2 Uniform Necrosis Within the IRE Lesion

IRE produces a lesion within the prostate with uniform necrosis throughout and to the very margin of the lesion (Fig. 20.2). Since the pulse occurs in microseconds the variability of blood flow has no effect on the destruction within the lesion. The field effect is uniform within the lesion, and therefore the necrosis is uniform, making a distinct margin where the magnitude of the field falls below the irreversible electroporation range.

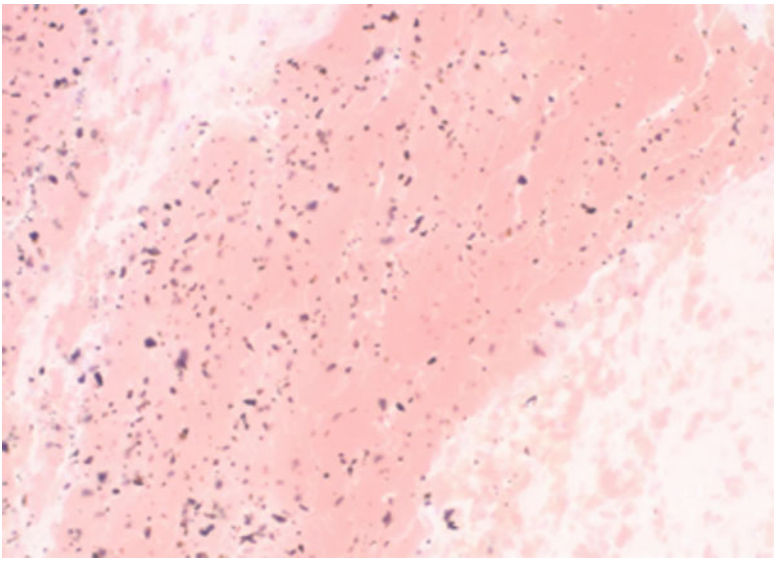

Fig. 20.2 Photomicrograph of prostate tissue that has been electroporated at 24 h. No glandular elements are visible (pulses = 8, Kv = 1)

This is in marked contrast to cryoablation lesions, which have a zone of variable destruction as the lesion margin is approached. In the prostate, where so many important structures are packed closely together, this creates a situation in which greater freezing may have to be carried out in order to insure tumor destruction. However, this sets up a potential dilemma: either stop the freeze prematurely to avoid injury to the rectum (possible undertreatment) or risk complications such as impotence when the NVB is included in the cryoablation lesion in order to assure destruction of a nearby cancer (possible overtreatment).

20.3.3 Lack of Heat Sink Effect

All thermal ablation methods have a significant limitation due to the vessel heat sink effect. This vessel heat sink effects protects cancer adjacent to major vessels resulting in high local recurrence rates in this clinical setting. In contrast, IRE lesions show complete destruction of tissue extended directly up to the vessel wall, without sparing of tissue adjacent to the vessel. In addition, this is accomplished without vessel destruction or occlusion. This characteristic has major implications, particularly in the prostate, where preservation of blood flow is a critical component of maintaining potency. Based on this characteristic, tumor infiltrating the NVB area should be treatable without damage to the associated vessels (Fig. 20.3).

20.3.4 Preservation of Collagenous and Neural Structures

Another major limitation of thermal ablation technologies has been the nonselective nature of the destructive process. RFA and to a somewhat lesser extent cryoablation cause complications to normal structures that are encompassed within the ablation zone. Gross and microscopic pathology of IRE lesions, however, show preservation of the prostatic urethra (Fig. 20.4) as well as the periprostatic nerves (Fig. 20.5). Unlike thermal ablation technologies, IRE will destroy the cellular components of a tissue such as the mucosal cells of the urethra but does not affect the underlying collagen network of tissue, thereby preserving the basic tissue structure. This allows certain tissue with regenerative capacities such as the urethra to replace its mucosal cells over time. If successfully translated into clinical practice, this lack of effect on the supporting collagen network of tissue could have major implications by markedly decreasing the incidence of urethral and rectal complications that were associated with prostate cryoablation. The finding that both nerves and vessels appear to survive IRE raises the possibility of a treatment for prostate cancer with minimal effect on patient potency.

20.3.5 Possible Immunological Effect

Another unique and unexpected pathologic finding with IRE lesions is evidence for an immunologic reaction in the lymph nodes draining the area of the ablation. With the rapid resolution of large areas of ablated tissue, reaction in draining lymph nodes would be understandable particularly since there is no denaturing of proteins associated with IRE. In relation to tumor ablation, this raises the possibility of whether there might be a tumor-specific immunological reaction to be harnessed in association with IRE. Such a reaction has been found to occur in association with cryoablation (Tanaka 1982), another modality in which proteins are not denatured by the ablation process and are theoretically still able to be recognized by the host's immune system. If a tumor-specific reaction in draining lymph nodes can be harnessed, it could have tremendous implications for patients who at the time of diagnosis already demonstrate lymph node involvement or that are diagnosed with it after failed radiation therapy. Such a reaction in lymph nodes draining an area of cancer could result in destruction of micrometastasis in the affected lymph nodes. In turn, this could significantly affect survival in patients at high risk for recurrence.

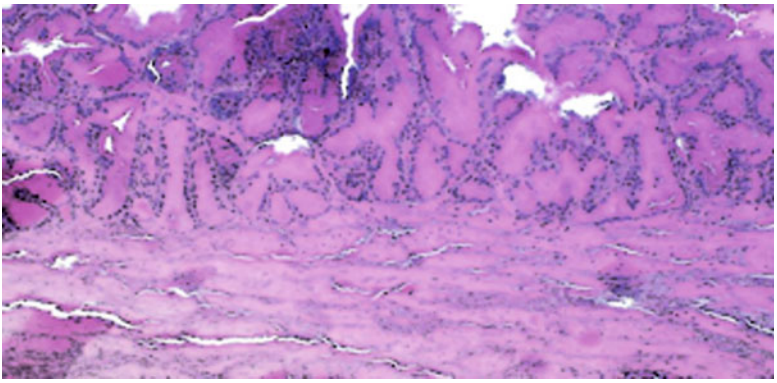

Fig. 20.3 Photomicrograph at the margin of the IRE lesion. A very narrow zone of transition between normal and necrotic tissue is noted at the margin (pulses = 8, Kv = 1)

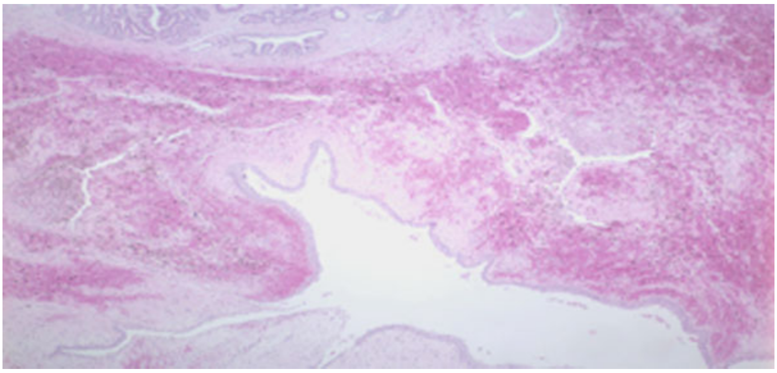

Fig. 20.4 The urethra is noted at the center of the micrograph as the open space at 24 h. Submucosal hemorrhage is noted but the integrity of the urethra is still intact (pulses = 8, Kv = 1)

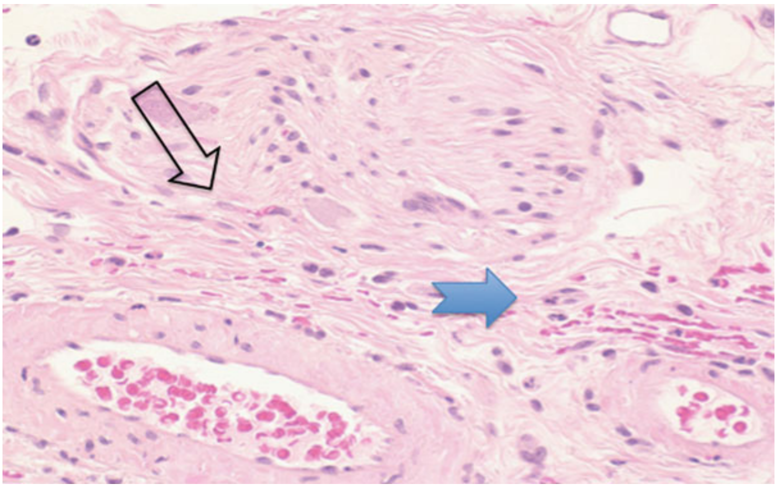

Fig. 20.5 Photomicrograph of the neurovascular bundle after electroporation at 2 weeks (pulses = 80, Kv = 1.5). It can be seen that both the vessel (*arrowhead*) and the nerve trunk (*open arrow*) show no evidence for necrosis

20.3.6 Speed of the Procedure

From a technical point of view, IRE has some interesting differences compared to previous thermal ablation techniques. For instance, the speed of the procedure is impressive with the ablation occurring in seconds rather than minutes. The time needed therefore to complete an IRE procedure is almost solely determined by the time needed to properly place the ablation probes. In the majority of our experiments, ablations were carried out in a bipolar fashion with at least two needles needed for lesion generation. IRE however is a rather flexible technology allowing both elements, active and ground electrodes, to be placed on a single probe.

20.3.7 Decreased Trauma Due to Decreased Probe Size

Another difference with thermal ablations is the size of the ablation probes needed to create adequate size lesions. Unlike both cryoablation and RFA, the size of the probes has little effect on the ability to create an IRE lesion. In our experiment an 8 gauge needle was used. Calculations indicate, however, that very little capability would be lost by using an even smaller 20 or 22 gauge needle.

20.3.8 Predictability of Lesion and Lack of Blood Flow Effects

In addition, since blood flow is not a factor in determining the size and shape of an IRE lesion, IRE is particularly amenable to predictive modeling. Previous experiments in liver have shown lesion size and shape to have a close correlation with predictions made by a method of mathematical modeling previously described (Rubinsky et al. 2007). We anticipate that this will be true for the prostate although these experiments were not designed to confirm this. Practically speaking, incorporation of these models into clinical application software, to be used for procedure planning, could add a greater degree of procedure reproducibility than that which is seen with thermal ablation techniques.

Lastly, experience has to be gained with the radiographic imaging and monitoring of IRE. In the liver, there appears to be excellent correlation of the post-IRE ultrasound image, as evidenced by a hypoechoic zone corresponding to the IRE lesion. This needs to be confirmed in the prostate as well. Other modalities such as CT and MRI also need to be investigated as possible monitoring modalities for IRE.

20.3.9 Clinical Usage

At the present time, there are no clinical series published in the literature relating to IRE and the treatment of prostate cancer. It stands to reason that with the compelling advantages demonstrated by the theoretical work already accomplished, patient experience should be available soon.

Conclusions

When considered as a whole, the pathologic data now available indicates that the advantages IRE has over thermal ablation technologies in the prostate are significant. Improved procedure planning, monitoring, and lesion resolution could have a significant impact on the field of tumor ablation. The ability to do in vitro testing for various cell types should allow the development of optimal procedure protocols from the outset of patient treatment. The improved safety profile should facilitate physician acceptance, and the possibility of harnessing a positive immunologic reaction offers numerous research and development opportunities.

References

Bahn DK, Lee F, Badalament R, et al. 7-year outcomes in the primary treatment of prostate cancer. Urol. 2002;60(2 Suppl 1):3–11.

Bahn DK, Silverman P, Lee Sr F, Badalament R, Bahn ED, Rewcastle JC. Focal prostate cryoablation: initial results show cancer control and potency preservation. J Endourol. 2006;20(9):688–92.

Davalos RV, Mir LM, Rubinsky B. Tissue ablation with irreversible electroporation. Annals Biomed Eng. 2005;33(2):223–31.

Lambert EH, Bolte K, Masson P, Katz AE. Focal cryosurgery: encouraging health outcomes for uni-focal prostate cancer. Urol. 2007;69(6):1117–20.

Miller L, Leor J, Rubinsky B. Cancer cells ablation with irreversible electroporation. Technol Cancer Res Treat. 2005;4(6):1–6.

Mir LM, Belehradek M, Domenge C, Luboniski B, Orlowski S, Belehradek J, et al. Electrochemotherapy, a novel antitumor treatment: first clinical trial. C R Acad Sci. 1991;Ser III(3113):613–8.

Neumann E, Schaefer-Ridder M, Wang Y, Hofschneider PH, et al. Gene transfer into mouse lyoma cells by electroporation in high electric fields. J Embo. 1982;1:841–5.

Onik G, Narayan P, Vaughan D, et al. Focal nerve sparing cryoablation for the treatment of primary prostate cancer: A new approach to preserving potency. Urol. 2002;60(1):109–14.

Onik G, Vaughan D, Lotenfoe R, Dineen M, Brady J. “Male lumpectomy”: focal therapy for prostate cancer using cryoablation. Urol. 2007;70(6 Suppl):16–21.

Rubinsky B, Onik G, Mikus P. Irreversible electroporation: a new ablation modality–clinical implications. Technol Cancer Res Treat. 2007;6(1):37–48.

Tanaka S. Immunological aspects of cryosurgery in general surgery. Cryobiology. 1982;19(3):247–62.

Photodynamic Therapy

21

Ashley J. Ridout and Caroline M. Moore

21.1 Introduction

The use of light for the treatment of disease has been documented since ancient times. 'Heliotherapy' (whole body sun worship) was used by those in ancient Greece and other cultures for treatment of skin diseases such as psoriasis and was reportedly used by Hippocrates to treat wasted muscles. Photochemotherapy, defined as drug activation by light, was used in ancient India to treat vitiligo—patients sat in sunlight after eating leaves of the *Psoralea corylifolia* plant. It is now known that these leaves contain furocoumarins, the active ingredient now used clinically for treatment of psoriasis. Photodynamic therapy (PDT) involves activation of a photosensitizing agent with light of a particular wavelength, in the presence of oxygen. This was first documented by the medical student Oscar Raab and his supervisor Hermann von Tappeiner, who noticed that paramecia exposed to the biological dye acridine survived for ten times longer in a thunderstorm (when exposed to lower light levels, reducing the PDT effect) than in identical conditions in the presence of light, and it was later realised that oxygen was also required for this process (Ackroyd et al. 2001). Niels Ryberg Finsen was awarded a Nobel Prize in 1903, for the use of carbon arc phototherapy in the treatment of cutaneous tuberculosis (lupus vulgaris) (Ackroyd et al. 2001). Finsen set up the Medical Light Institute in Copenhagen and provided the foundations for modern photodynamic therapy. The Light Department in the London Hospital in Whitechapel was subsequently set up after Queen Alexandra brought Finsen's work to England. The therapeutic use of light currently takes various forms, including UVA light exposure for skin diseases, phototherapy for neonatal jaundice and photodynamic therapy.

The first urological use of PDT was for superficial bladder cancer, using an intravenous hematoporphyrin derivative photosensitizer agent (Kelly and Snell 1976). This was associated with allergic reactions and skin photosensitivity, requiring light protection for weeks after the procedure. Due to these side effects, the acceptance of PDT in urological diseases was slow. However, technical improvements, including improvements in laser technology and advances in photosensitizer agents, have resulted in clinical work to assess the use of PDT for prostate cancer, both as whole-gland and focal treatment in primary and

---

A.J. Ridout
Division of Surgical and Interventional Science,
Department of Urology, University College London,
London, UK

Department of Radiology, University College London
Hospitals NHS Foundation Trust, 3rd Floor,
Charles Bell House, 67-73 Riding House Street,
London W1W 7EJ, UK

C.M. Moore, MD, FRCS (Urol) (✉)
Department of Radiology, University College London
Hospitals NHS Foundation Trust, 3rd Floor,
Charles Bell House, 67-73 Riding House Street,
London W1W 7EJ, UK
e-mail: caroline.moore@ucl.ac.uk

R.L. Bard et al. (eds.), *Image Guided Prostate Cancer Treatments*,
DOI 10.1007/978-3-642-40429-0_21, © Springer-Verlag Berlin Heidelberg 2014

radio-recurrent disease. The procedure has become more acceptable for patients, with one visit required for the treatment, and only a short period of light protection. Targeted light treatment offers the potential for focal treatment of prostate cancer as well as whole-gland treatment, with the potential for reduced side effects.

21.2 Mechanism of Action

Photodynamic therapy (PDT) involves activation of a photosensitizer agent, with light of a particular wavelength, in the presence of oxygen. The activated photosensitizer agent interacts with molecular oxygen to form reactive oxygen species, resulting in local cell and tissue damage and destruction. The photosensitizer agent is promoted to a higher energy state by the appropriate wavelength of light, followed by production of reactive oxygen species (ROS). Energy is subsequently released in three potential ways—as heat, light or conversion to an intermediate (triplet) state, which produces reactive oxygen species and has a local cytotoxic effect.

21.3 Photosensitizer Agents

The ideal photosensitizer agent would be pharmacologically stable at a range of temperatures, administered intravenously or orally, would selec tively accumulate in malignant cells and, once activated, have selective cytotoxicity against cancer cells, sparing other tissues. Activation by multiple light wavelengths would increase its treatment potential, with shorter wavelengths activating the drug at shorter distances from the light fibre and longer wavelengths used for interstitial treatments requiring greater depth of light penetration. The agent should ideally be washed out of the body rapidly after treatment, reducing the side effects associated with residual photosensitivity.

Specific targeting of the photosensitizer to the target cells or tissue increases the potential for cancer-specific therapy. This could be associated with reduced collateral damage and fewer side effects than a nontargeted therapy. Cellular targeting methods may include linkage to serum proteins such as albumin and uptake into cells via receptor-mediated endocytosis. This could be done with monoclonal antibody linkage—the use of prostate-specific membrane antigen (PSMA) has generated interest for both imaging and therapeutic purposes. In vitro studies have shown that photosensitizer-conjugated PSMA inhibitors may allow focal-targeted treatment of prostate cancer (Liu et al. 2010). However, there may be significant disadvantages associated with this technique, including the reduced photosensitivity of the combination agent as compared to the photosensitizer agent alone, and the heterogeneity of antibody expression in prostate cancer that may lead to incomplete targeting, and consequently incomplete treatment, of the targeted tissue. To counteract these limitations, other methods have been suggested, including intracellular delivery of the photosensitizer agent through linkage to molecules such as serum proteins, annexins, bisphosphonates, steroids, toxins and lectins, epidermal growth factor, insulin and nuclear localisation signals and adenovirus and adenoviral proteins (Sharman et al. 2004).

photosensitizer agents may be activated either in the tissue or the vasculature. Tissue-activated agents require a delay of hours to days between drug administration and treatment (the 'drug-light' interval) as the agent reaches optimal concentration in the targeted tissue. During this period the photosensitizer accumulates in other tissues, conveying a sensitivity to light which requires protection, such as of the skin and eyes. This protection may be required for up to 6 weeks after the procedure, and as such these agents have not been widely attractive to patients with other treatment options available. Vascular-activated agents reach optimal concentration within minutes, so the drug-light interval is very short, enabling drug and light to be given in a single session. Furthermore, these agents do not persist in the vasculature, tissue or other organs (such as the skin) for long after activation, so a much shorter period of light protection is required. The prototype photosensitizer agent for vascular-targeted PDT (VTP) was WST-09, a palladium bacteriopheophorbide molecule, made from the bacteriochlorophyll molecule (Schreiber et al. 2002).

21.4 Preclinical Studies

The canine prostate provides the closest anatomical model to the human prostate and so has commonly been used in preclinical studies. Although there is not a specific-induced prostate cancer model, much work has been done on the benign canine prostate, and a few have used spontaneously occurring canine prostate cancers. Selman et al demonstrated the feasibility of interstitial prostate treatment, demonstrating haemorrhagic necrosis, subsequent fibrosis and overall reduction in prostate volume after treatment (Selman et al. 1996). Feasibility studies have been performed in the animal model with various photosensitizer agents: tin ethyl etiopurpurin dichloride (Selman et al. 2001), motexafin lutetium (Hsi et al. 2001), porfimer sodium (Lee et al. 1997), disulfonated aluminium phthalocyanine, meso-tetra-(m-hydroxyphenyl) chlorin (Chang et al. 1996) and 5-aminolevulinic acid-induced protoporphyrin IX (Chang et al. 1997). The vascular-activated agent WST-09 was developed from a bacteriochlorophyll derivative, with the addition of palladium conveying photostability (Fiedor et al. 2002). Once its cytotoxic effect was demonstrated in vitro, initial animal studies used implanted gliomas to show that photodynamic treatment of the implanted tumours was associated with a greater chance of cure than surgery (Schreiber et al. 2002) thought to be due to an immune reaction resulting in prolonged antitumour activity (Preise et al. 2011). Subsequent canine studies were done, using a laparotomy approach for fibre insertion and interstitial prostate light delivery, with additional light delivery to the bladder and colon, in order to determine the clinical effect of light delivery on other organs. Prostates of 16 animals were studied, exposed to light either superficially or interstitially, and the local light fluence rate and temperature were monitored with interstitial probes placed in the prostates. This revealed a maximum temperature rise of 0.9 °C, further confirming that the tissue effect was not due to thermal damage. There were no demonstrable side effects, and there was no significant histopathological evidence of the effect of light on the colon or bladder at exposure levels that would be in keeping with collateral light delivery during prostate treatment. This formed the basis of subsequent animal work using the photosensitizer agent WST-09. Huang et al studied the effect of VTP in 4 dogs which had been pretreated with 20 fractions of ionising radiation (total 70 Gy) to the prostate (Huang et al. 2004). After 20–23 weeks the animals were treated with WST-09 PDT at 2 mg/kg, at escalating light doses of 50, 100 and 200 J/cm. There was no acute urinary retention, and even when within the treatment field, there was no evidence of urethral necrosis. Histopathological lesion size correlated with light dose, easily distinguishable from the underlying effect of previous radiation exposure and with similar appearance to previously treated dogs without prior radiation exposure. The lesions were variably longer than the length of light fibre used, especially at higher light doses.

Canine studies have also been used to investigate the role of magnetic resonance imaging (MRI) in posttreatment assessment. It was shown that gadolinium contrast-enhanced MRI demonstrated the most accurate correlation to volume of PDT effect on whole mount histopathology specimens, when compared with diffusion-weighted and T2-weighted imaging at 1 week after treatment (Huang et al. 2006). Subsequent clinical studies used contrast-enhanced scans to demonstrate the PDT effect at 1 week after treatment. Imaging revealed a central, non-enhancing core of haemorrhagic necrosis, surrounded by an enhancing area of atrophic glandular tissue, patchy mononuclear cell infiltrate, fibromuscular hyperplasia, neovascularisation, oedema and dilated glandular structures. The same group also showed a dose-dependent effect upon peripheral nerves in response to PDT treatment, with apparent resistance compared to prostate tissue (Huang et al. 2007). This could translate clinically into a ‘nerve-sparing’ approach, similar to that often attempted with the radical surgical approach aiming to reduce erectile dysfunction.

21.5 Clinical Studies

The first clinical report of PDT in prostate cancer was published in 1990—two patients were treated transurethrally with a different tissue-based photosensitizer agent (haematoporphyrin derivative and porfimer sodium), 6 weeks after transurethral resection of the prostate (Windahl et al. 1990). After treatment, both individuals demonstrated decreasing PSA, and prostate biopsies at 3 months after treatment identified no histological evidence of residual prostate cancer.

21.5.1 Salvage Treatment of Recurrent Prostate Cancer

Nathan et al reported the first formal study of patients with radio-recurrent prostate cancer (Nathan et al. 2002). They used the photosensitizer agent meso-tetra hydroxyl phenyl chlorin (mTHPC/'Foscan'/temoporfin) to treat 14 patients with histologically proven recurrent prostate cancer after radiotherapy. 9/13 patients who received a higher light dose demonstrated a reduction in PSA in the first 3–6 months after treatment, and prostate biopsies were negative in 4 of these individuals. All eventually demonstrated a rising PSA, and 10 required systemic hormone treatment. Motexafin lutetium (mLu/LuTex) was also used for treatment of radio-recurrent disease, and after initial feasibility studies (Du et al. 2006), work was done to identify the dose requirements for prostate treatment (Verigos et al. 2006). Oncological outcomes were better in those treated with higher doses—the group treated with 2 mg/kg photosensitizer, fluence 150 J/cm^2 and drug-light interval 3 h showed the longest time to biochemical relapse.

Trachtenberg et al reported the first study of WST-09 (TOOKAD/Padoporfin) for histologically proven, organ-confined, radio-recurrent prostate cancer in humans (Trachtenberg et al. 2007). This study was in two parts—the first group was treated with a drug dose-escalation protocol, in which cohorts of men were treated with increasing drug doses, up to 2 mg/kg, and received a fixed light dose of 100 J/cm. A total of 24 patients were treated, with no significant drug-related adverse effects reported at the highest dose of 2 mg/kg, although there were episodes of transient hypotension shortly after photosensitizer drug administration in 12 men, which responded rapidly to intravenous fluids and/or vasopressors. Most men reported some initial urinary symptoms, although urinary and bowel function were not significantly different between baseline assessment and at 6 months after treatment. The second part of the study involved treatment of 28 individuals with a light dose-escalation protocol up to 360 J/cm, with all men treated at a drug dose of 2 mg/kg (Trachtenberg et al. 2008). Prior to treatment, individualised drug doses and treatment plans were calculated. Results were reported for those men who completed the study (25 underwent all imaging investigations and 26 underwent all prostate biopsy requirements). Post-operative MR imaging demonstrated variability in treatment between patients, despite exposure to the same light dose. There were irregular treatment margins in 22/25 men, with discontinuous treatment effects in some. Treatment effect upon the urethra was not always predictable, with pretreatment plans predicting urethral treatment in 24/25 men, but posttreatment imaging demonstrating urethral sparing in 10 individuals. Evidence of treatment outside the prostate included involvement of the puborectalis and levator ani muscles (22/25), obturator internus (3/25) and anterior rectal wall (9/25). By 6-months posttreatment, these changes had resolved in at least two-thirds of patients. Despite 9 men showing some degree of anterior rectal wall changes, only one clinically presented with symptoms suggestive of a rectal fistula, although this was never formally identified with imaging or endoscopy and symptoms resolved with conservative management. This group concluded that a complete response (defined as prostate biopsy negative for prostate cancer at 6 months after treatment) required a light dose of at least 23 J/cm^2 to at least 90 % of the prostate volume.

However, in the study, 13 men received this dose, but only 8 had negative prostate biopsies, also associated with significant PSA reductions. Imaging at 1 week after treatment revealed that in those who demonstrated a >60 % VTP effect at 1 week, all went on to have a biopsy negative for prostate cancer, but this relationship was not always exclusive, as some men who showed a lesser treatment effect also went on to have negative biopsies. This could either be explained due to a sampling bias, whereby prostate cancer was missed at biopsy or that the true treatment effect was incompletely demonstrated with post-operative MR imaging. Most patients in these studies reported a deterioration of urinary (particularly storage) symptoms after treatment, but this showed a return to baseline level at 6 months after treatment and in the interim were controlled with medical therapy.

The same group formally assessed the skin photosensitivity reactions associated with the treatment (Weersink et al. 2005a). After photosensitizer administration, men were kept in a light-dimmed environment, and a solar simulator (using both UV-positive and UV-negative light) was used to test skin photosensitivity at 3, 12 and 24 h after drug administration, with no skin responses demonstrated with either UV or non-UV light. Consequently, light protection requirements after PDT treatment with WST-09 were reduced, allowing patients to be discharged on the day of procedure without the need for significant light protection measures.

21.5.2 Primary Treatment of Prostate Cancer

After the first clinical report from Windahl et al, a series of 6 patients treated with 5-aminolevulinic acid (5-ALA) at 20 mg/kg was reported by Zaak et al (2003). The first treatment was carried out during radical prostatectomy, with the photosensitizer agent administered 4 h before the procedure and light delivered with a fluence of 140 J/cm^3. Subsequent treatments were carried out transurethrally after TURP and then transperineally with ultrasound guidance. There were no reported side effects, and average PSA reduction was between 30 % (for those treated transperineally) and 55 % (transurethral treatment).

Moore et al reported their Phase I study of a series of 6 men with previously untreated, histologically proven organ-confined Gleason 3+3 prostate cancer (Moore et al. 2006). Men were treated with temoporfin (mTHPC) at 0.15 mg/kg^2, with drug-light intervals from 2 to 5 days, and post-operative assessment included MR imaging. MRI demonstrated patchy necrosis and oedema, and PSA fell by up to 67 %. 4/6 patients subsequently underwent a second PDT treatment, resulting in a total of 10 separate PDT treatments in this group. By 2–3 months after treatment, overall prostate volume reduction ranged from 21 to 35 %, and there was an overall average PSA reduction of 43.8 % for 8/10 treatments (1 individual was excluded from PSA analysis due to prior hormone treatment). Reported side effects included irritative urinary symptoms for 2 weeks after treatment, 2 episodes of acute urinary retention requiring catheterisation and one episode of sepsis.

Due to potentially serious side effects associated with WST-09, subsequent trials have used the water-soluble agent WST-11 (TOOKAD-Soluble/padeliporfin). Two men experienced adverse cardiac events with WST-09—one developed an acute coronary syndrome requiring coronary revascularisation, and another had a myocardial infarction and subsequent CVA within 24 h of the procedure (this individual was found to have a patent foramen ovale). As a result of these events, the study was stopped and a safety investigation initiated. PCM201 was a dose-escalation study and PCM203 a fixed-dose study using 4 mg/kg activated by light dose 200 J/cm with computer-assisted planning. In a cohort of 40 men, good correlation between energy and volume of prostate necrosis was seen—200 J at dose 4 mg/kg produced necrosis of approximately 1 cm^3 (Arumainayagam et al. 2010). Reports from the PCM203 study demonstrated mean percentage of ablated tissue as 77 % for all patients and 87 % for those who had unilateral treatment at photosensitizer dose 4 mg/kg (Azzouzi 2013). A European Phase III randomised trial is currently in progress (PCM301), with 400 men included by May 2013. This compares VTP with active surveillance (with a follow-up period of 3 years for each participant) in men with low-risk localised prostate cancer diagnosed on transrectal ultrasound-guided prostate biopsy (Table 21.1).

21.6 Treatment Technique

21.6.1 Light Delivery

Most photosensitizers absorb light at a specific wavelength which produces maximal photodynamic effect and can be delivered from a laser directed along optical fibres. The use of fibres has allowed treatment of both superficial lesions, and interstitial treatments, as the fibres can be inserted directly to the target organ. The patient is placed in the lithotomy position, under general anaesthetic, in a darkened operating theatre with eye and skin protection. The optical fibres are inserted transperineally using a brachytherapy template on a stepper device, guided with transrectal ultrasound imaging (see Fig. 21.1). Fibres may be either bare ended, with light directly emitted from the end of the fibre, or cylindrical, with a diffusing end. For bare-ended fibres, light is distributed in all directions from the end of the fibre, like a torch or flashlight, and the light dose is measured in J/cm^2. The dose from the active length of cylindrical fibres is measured in J/cm, comparable to a ‘strip light’. Bare-ended fibres allow light delivery along a given length at the distal end of the fibre and can be used for superficial treatments using endoscopic access to hollow organs or on the skin itself. Cylindrical diffusers are more commonly used for treatments in solid organs, such as the prostate.

In preclinical studies, optical fibres were also inserted either with an open technique at laparotomy. Although technically feasible for human treatments, open fibre insertion would be inappropriate considering the other available options (transurethral/transperineal). In animal studies, the transurethral approach was associated with urethral strictures and has not been clinically evaluated for use in treatment of prostate cancer (Selman and Keck 1994). In current clinical trials, treatment is delivered using a transperineal template and transrectal ultrasound guidance.

21.6.2 Treatment Planning

Treatment planning may be either done prior to treatment with a ‘rule-based’ approach or with a ‘real-time’ approach during treatment itself, using feedback from light, drug and oxygen measurements (Moore et al. 2011). With individualised pretreatment planning, account can be made for anatomical variations, with predetermination of the number and position of treatment fibres and light characteristics. The first reported clinical demonstration of patient-specific treatment planning for photodynamic therapy was in the TOOKAD study of recurrent prostate cancer (Davidson et al. 2009). The largest studies of this vascular-targeted PDT for prostate cancer used MR imaging to determine prostate anatomy prior to treatment, with subsequent planning of fibre placement. A retrospective review of patients treated with the water-soluble WST-11 was used to produce a model for treatment planning, with demonstration of correlation between the treatment plan and posttreatment MR imaging (Betrouni et al. 2011). In the TOOKAD study currently underway, a study committee remotely determines the treatment plan, which is sent to the treating centres prior to the scheduled treatment.

Pretreatment planning has some disadvantages, including the anatomical deformation due to the effect of the rectal ultrasound probe and intraoperative swelling of the prostate due to fibre insertion and treatment effect. Even for a pretreatment MR-based plan, it may well be necessary to alter the grid positions and add or exclude light delivery fibres once the prostate is seen under real-time ultrasound guidance.

Canine studies have demonstrated the feasibility of real-time treatment planning modified according to light dose received (Jankun et al. 2005), and it has been reported in a small cohort of patients (Swartling et al. 2010) based upon

Table 21.1 Summary of clinical work for prostate PDT

Study	Number of patients	Entry criteria	photosensitizer	Summary of results	Reported adverse effects
Recurrent disease treatment					
Nathan (2002)	14	Phase I/II study—patients with rising PSA and biopsy-proven local recurrence after radiotherapy	Meso-tetra hydroxyl phenyl chlorin; mTHPC (temoporfin/ 'Foscan')—0.15 mg/kg—high light doses used in 13/14 patients	9/13 patients who received the higher light dose showed a PSA reduction 3–6 months after treatment, and biopsies were negative in 4. All men eventually showed PSA rise—10 required androgen therapy	Acute urinary retention-3; stress urinary incontinence-2; recto-urethral fistula (after rectal biopsy)-1; photosensitivity reactions-5; erectile dysfunction-4/7 with previously acceptable function; irritative urinary symptoms-all
Verigos (2006); Patel (2008)	17	Phase I study—locally recurrent prostate cancer	Motexafin lutetium	Greatest delay to biochemical progression in the cohort treated with 2 mg/kg, fluence 150 J/cm^2 and drug-light interval 3 h	Urinary urgency-1; irritative urinary symptoms
Weersink (2005b); Trachtenberg (2007, 2008)	24 (2 fibres) 28 (multiple fibres—up to 6)	Phase I/II clinical trials—radio-recurrent prostate cancer Gleason >6, life expectancy >5 years, no evidence of metastases, PSA <20 ng/ml and prostate volume <50 cm^3	WST-09 (Padoporfin/TOOKAD)—drug dose-escalation protocol (0.1–2 mg/kg) with light dose 100 J/cm and light dose escalation with 2 mg/kg drug dose at 230–360 J/cm	Feasibility of whole-gland treatment demonstrated—for complete response at 6-month biopsy they suggest light doses of ≥23 J/cm^2 in ≥90 % prostate	Recto-urethral fistulae-2; intra-operative hypotension; irritative urinary symptoms
Primary disease treatment					
Windahl (1990)	2	First clinical use of PDT in prostate cancer—patients underwent TURP 6 weeks prior to treatment	Each treated with different agent—haematoporphyrin derivative and porfimer sodium	Both showed decreasing PSA and had negative biopsy at 3 months after treatment	None reported
Moore (2006)	6 (total 10 treatments)	Phase I study—localised prostate cancer	Meso-tetra hydroxyl phenyl chlorin; mTHPC	After 8/10 sessions PSA reduced by up to 67 %, early MRI showed patchy necrosis and oedema	Sepsis-1; recatheterisations-2; temporary erectile dysfunction-1; irritative urinary symptoms-all

(continued)

Table 21.1 (continued)

Study	Number of patients	Entry criteria	photosensitizer	Summary of results	Reported adverse effects
Zaak (2003)	6	1st treatment during radical prostatectomy, then transurethrally after TURP and then transperineally with US guidance	5-aminolevulinic acid (5-ALA)—20 mg/kg	Average PSA reduction at 6/52 after treatment: 55 % (transurethral) and 30 % (transperineal)	None reported
Azzouzi (2011; 2013)	PCM201—40 PCM203—86	Multicentre Phase II, 6-month open label trials in patients with localised prostate cancer eligible for active surveillance, to determine optimal treatment conditions for tumour ablation (using dose, power and light escalation) and to assess the effects of WST-11 mediated VTP	WST-11 (TOOKAD-soluble/padeliporfin)	The technique is well tolerated and reproducible—good efficacy demonstrated when optimal treatment conditions were used	Prostatitis-2; haematuria-1; epididymo-orchitis-1; optic neuropathy-1; urethral stricture-1
PCM301	400 (recruited May 2013)	Multicentre Phase III, open label, randomised controlled study in subjects with low-risk prostate cancer on TRUS-biopsy Patients randomised to VTP underwent IV administration of WST-11 with 753 nm laser light at 150 mW/cm and 200 J/cm through transperineal interstitial optical fibres with US guidance	WST-11 (200 AS/200 VTP)	Awaited	Awaited

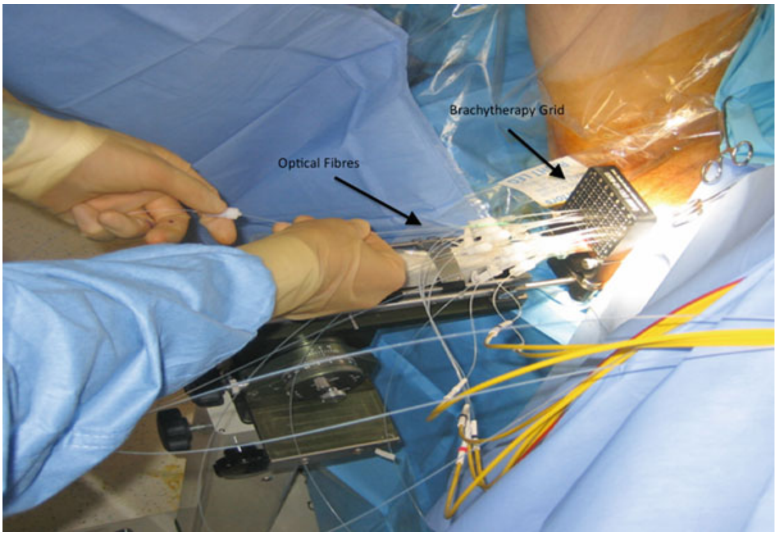

Fig. 21.1 PDT – Brachytherapy grid and fibres labelled

3-dimensional tissue models from ultrasound imaging. In this small series, residual cancer was present in 3 out of 4 patients treated; however, the authors suggest that this was due to inadequate light doses.

Conclusion

The opportunity exists to offer increasingly focal treatments to malignant lesions within the prostate. There has also been interest in the use of PDT for treatment of disease outside the prostate, including solitary bone metastases and for treatment of recurrence in the prostate bed after radical prostatectomy. As with other focal treatments, this aims to provide good cancer control, while minimising potential side effects associated with whole-gland treatment, including effects on urinary and erectile function. Whether this aim can be achieved needs to be proven in large multicentre clinical studies. While still under investigation, techniques such as conjugating the photosensitizer with a monoclonal antibody specific for the targeted malignant cells provide hope that tumour-specific targeted treatment will be possible. Furthermore, improvements in pre-procedure treatment planning, combined with the opportunity for real-time adjustment based on feedback during the procedure, provide the opportunity for more specific and individualised treatments, adapting for changes which may occur during the procedure, such as oedema and prostate deformation.

We await the results of larger studies, which will provide more mature data of both ontological control and functional outcomes. By improving the selectivity of photosensitizer agents, we aim to increase opportunities for focal treatment and so reduce the potential side effects associated with photodynamic therapy. There is some evidence to challenge the role of radical interventions in improving survival for low-risk prostate cancer (Wilt et al. 2012), and, with the broad range of treatment options available for these patients, it is increasingly important that we aim to provide a minimally invasive treatment method, with excellent oncological control and minimal side effects.

References

Ackroyd R, Kelty C, Brown N, Reed M. The history of photodetection and photodynamic therapy. Photochem Photobiol. 2001;74(5):656–69.

Arumainayagam N, Moore CM, Ahmed HU, Emberton M. Photodynamic therapy for focal ablation of the prostate. World J Urol. 2010;28(5):571–6.

Azzouzi AR. Results of TOOKAD soluble vascular targeted photodynamic therapy (VTP) for low risk localised prostate cancer (PCM201/PCM203). In: 26th annual EAU congress, Vienna, 2011; Extended Abstract Session 6 (Abstract 86).

Azzouzi AR, Barret E, Moore CM, Villers A, Allen C, Scherz A, et al. TOOKAD(®) Soluble vascular-targeted photodynamic (VTP) therapy: determination of optimal treatment conditions and assessment of effects in patients with localised prostate cancer. BJU Int. 2013;112(6):766–74. doi: 10.1111/bju.12265.

Betrouni N, Lopes R, Puech P, Colin P, Mordon S. A model to estimate the outcome of prostate cancer photodynamic therapy with TOOKAD soluble WST11. Phys Med Biol. 2011;56(15):4771–83.

Chang SC, Buonaccorsi G, MacRobert A, Bown SG. Interstitial and transurethral photodynamic therapy of the canine prostate using meso-tetra-(m-hydroxyphenyl) chlorin. Int J Cancer. 1996;67(4):555–62.

Chang SC, Buonaccorsi GA, MacRobert AJ, Bown SG. Interstitial photodynamic therapy in the canine prostate with disulfonated aluminum phthalocyanine and 5-aminolevulinic acid-induced protoporphyrin IX. Prostate. 1997;32(2):89–98.

Davidson SR, Weersink RA, Haider MA, Gertner MR, Bogaards A, Giewercer D, et al. Treatment planning and dose analysis for interstitial photodynamic therapy of prostate cancer. Phys Med Biol. 2009;54(8):2293–313.

Du KL, Mick R, Busch TM, Zhu TC, Finlay JC, Yu G, et al. Preliminary results of interstitial motexafin lutetium-mediated PDT for prostate cancer. Lasers Surg Med. 2006;38(5):427–34.

Fiedor J, Fiedor L, Kammhuber N, Scherz A, Scheer H. Photodynamics of the bacteriochlorophyll-carotenoid system. 2. Influence of central metal, solvent and beta-carotene on photobleaching of bacteriochlorophyll derivatives. Photochem Photobiol. 2002;76(2):145–52.

Hsi RA, Kapatkin A, Strandberg J, Zhu T, Vulcan T, Solonenko M, et al. Photodynamic therapy in the canine prostate using motexafin lutetium. Clin Cancer Res. 2001;7(3):651–60.

Huang Z, Chen Q, Trncic N, LaRue SM, Brun PH, Wilson BC, et al. Effects of pd-bacteriopheophorbide (TOOKAD)-mediated photodynamic therapy on canine prostate pretreated with ionizing radiation. Radiat Res. 2004;161(6):723–31.

Huang Z, Haider MA, Kraft S, Chen Q, Blanc D, Wilson BC, et al. Magnetic resonance imaging correlated with the histopathological effect of pd-bacteriopheophorbide (tookad) photodynamic therapy on the normal canine prostate gland. Lasers Surg Med. 2006;38(7):672–81.

Huang Z, Chen Q, Dole KC, Barqawi AB, Chen YK, Blanc D, et al. The effect of tookad-mediated photodynamic ablation of the prostate gland on adjacent tissues–in vivo study in a canine model. Photochem Photobiol Sci. 2007;6(12):1318–24.

Jankun J, Keck RW, Skrzypczak-Jankun E, Lilge L, Selman SH. Diverse optical characteristic of the prostate and light delivery system: implications for computer modelling of prostatic photodynamic therapy. BJU Int. 2005;95(9):1237–44.

Kelly JF, Snell ME. Hematoporphyrin derivative: a possible aid in the diagnosis and therapy of carcinoma of the bladder. J Urol. 1976;115(2):150–1.

Lee LK, Whitehurst C, Chen Q, Pantelides ML, Hetzel FW, Moore JV. Interstitial photodynamic therapy in the canine prostate. Br J Urol. 1997;80(6):898–902.

Liu T, Wu LY, Berkman CE. Prostate-specific membrane antigen-targeted photodynamic therapy induces rapid cytoskeletal disruption. Cancer Lett. 2010;296(1):106–12.

Moore CM, Nathan TR, Lees WR, Mosse CA, Freeman A, Emberton M, et al. Photodynamic therapy using meso tetra hydroxy phenyl chlorin (mthpc) in early prostate cancer. Lasers Surg Med. 2006;38(5):356–63.

Moore CM, Emberton M, Bown SG. Photodynamic therapy for prostate cancer–an emerging approach for organ-confined disease. Lasers Surg Med. 2011;43(7):768–75.

Nathan TR, Whitelaw DE, Chang SC, Lees WR, Ripley PM, Payne H, et al. Photodynamic therapy for prostate cancer recurrence after radiotherapy: a phase I study. J Urol. 2002;168(4 Pt 1):1427–32.

Patel H, Mick R, Finlay J, Zhu TC, Rickter E, Cengel KA, et al. Motexafin lutetium-photodynamic therapy of prostate cancer: short- and long-term effects on prostate-specific antigen. Clin Cancer Res. 2008;14(15):4869–76.

Preise D, Scherz A, Salomon Y. Antitumor immunity promoted by vascular occluding therapy: lessons from vascular-targeted photodynamic therapy (VTP). Photochem Photobiol Sci. 2011;10(5):681–8.

Schreiber S, Gross S, Brandis A, Harmelin A, Rosenbach-Belkin V, Scherz A, et al. Local photodynamic therapy (PDT) of rat C6 glioma xenografts with pd-bacteriopheophorbide leads to decreased metastases and increase of animal cure compared with surgery. Int J Cancer. 2002;99(2):279–85.

Selman SH, Keck RW. The effect of transurethral light on the canine prostate after sensitization with the photosensitize tin (II) etiopurpurin dichloride: a pilot study. J Urol. 1994;152(6 Pt 1):2129–32.

Selman SH, Keck RW, Hampton JA. Transperineal photodynamic ablation of the canine prostate. J Urol. 1996;156(1):258–60.

Selman SH, Albrecht D, Keck RW, Brennan P, Kondo S. Studies of tin ethyl etiopurpurin photodynamic therapy of the canine prostate. J Urol. 2001;165(5):1795–801.

Sharman WM, van Lier JE, Allen CM. Targeted photodynamic therapy via receptor mediated delivery systems. Adv Drug Deliv Rev. 2004;56(1):53–76.

Swartling J, Axelsson J, Ahlgren G, Kälkner KM, Nilsson S, Svanberg S, et al. System for interstitial photodynamic therapy with online dosimetry: first clinical experiences of prostate cancer. J Biomed Opt. 2010;15(5):058003.

Trachtenberg J, Bogaards A, Weersink RA, Haider MA, Evans A, McCluskey SA, et al. Vascular targeted photodynamic therapy with palladium-bacteriopheophorbide photosensitize for recurrent prostate cancer following definitive radiation therapy: assessment of safety and treatment response. J Urol. 2007;178(5):1974–9. discussion 1979.

Trachtenberg J, Weersink RA, Davidson SR, Haider MA, Bogaards A, Gertner MR, et al. Vascular-targeted photodynamic therapy (padoporfin, WST09) for recurrent prostate cancer after failure of external beam radiotherapy: a study of escalating light doses. BJU Int. 2008;102(5):556–62.

Verigos K, Stripp DC, Mick R, Zhu TC, Whittington R, Smith D, et al. Updated results of a phase I trial of motexafin lutetium-mediated interstitial photodynamic therapy in patients with locally recurrent prostate cancer. J Environ Pathol Toxicol Oncol. 2006; 25(1–2):373–87.

Weersink RA, Forbes J, Bisland S, Trachtenberg J, Elhilali M, Brún PH, et al. Assessment of cutaneous photosensitivity of TOOKAD (WST09) in preclinical animal models and in patients. Photochem Photobiol. 2005a;81(1):106–13.

Weersink RA, Bogaards A, Gertner M, Davidson SR, Zhang K, Netchev G, et al. Techniques for delivery and monitoring of TOOKAD (WST09)-mediated photodynamic therapy of the prostate: clinical experience and practicalities. J Photochem Photobiol B. 2005b; 79(3):211–22.

Wilt TJ, Brawer MK, Jones KM, Barry MJ, Aronson WJ, Fox S, et al. Radical prostatectomy versus observation for localized prostate cancer. N Engl J Med. 2012; 367(3):203–13.

Windahl T, Andersson SO, Lofgren L. Photodynamic therapy of localised prostatic cancer. Lancet. 1990; 336(8723):1139.

Zaak D, Stroka R, Hoppner M. Photodynamic therapy by means of 5 ALA induced protoporphyrin IX in human prostate cancer e preliminary results. Med Laser Appl. 2003;18:91–5.

22

High-Intensity Focused Ultrasound for the Treatment of Prostate Cancer

John C. Rewcastle and Inderbir S. Gill

22.1 Introduction

High-intensity focused ultrasound (HIFU) is an emerging noninvasive, local treatment for prostate cancer with, as of 2013, 17 years of clinical experience during which approximately 50,000 HIFU treatments have been performed worldwide. The premise behind HIFU is the destruction of tissue by depositing large amounts of energy into it. Ultrasound waves deposit energy as they travel through tissue, but the amount of energy deposited during traditional, diagnostic ultrasound imaging is insignificant (Woodward and Warwick 1970). Ablating with ultrasound is accomplished by doing two things: increasing the intensity of the waves and focusing the waves on a focal point. When performed appropriately, it will raise the temperature of tissue to a level sufficient to cause irreversible damage (cell kill) in a discrete volume of tissue (Wu et al. 2001).

During HIFU, a reproducible small volume of ablation is created by each pulse of energy. The geometry of each ablated volume is an ellipsoid, and the size of the ellipsoid is a function of crystal geometry. Treatment of cancer of the prostate is accomplished by systematically pulsing energy throughout the target volume at different locations until the entire volume has been ablated. Several authors have recently reported encouraging, 10-year survival rates following whole-gland HIFU (Ganzer et al. 2013; Thüroff et al. 2013; Crouzet et al. 2013).

22.2 Technology Foundation

A piezoelectric crystal vibrates at a frequency characteristic of the crystal when an electric current passes through it. A vibrating piezoelectric crystal initiates the propagation of sound waves through adjacent media. Ultrasound is a sound that is at a frequency in excess of the upper range that is detectable by the human ear, around 20,000 hertz (Hz). Medical applications of ultrasound typically use frequencies ranging from a few MHz to about 10 MHz.

The ability of different mediums to transmit ultrasound waves varies widely. Air, for example, is a relatively very poor transmitter of ultrasound with a sound speed of approximately 350 m/s. The speed of sound in soft tissue is approximately 1,500 m/s and varies upon the density of specific tissues. When a propagating ultrasound wave encounters boundaries between structures of different density, some of the wave will be echoed (reflected) and some will continue propagating away from the crystal. This leads to the first clinical application of ultrasound which is built upon the fact piezoelectric crystals also create electricity when vibrated. The return of an echo vibrates the crystal creating a pulse of electric current. Analysis of the current created

---

J.C. Rewcastle, PhD (✉) • I.S. Gill, MD
USC Institute of Urology, Keck School of Medicine,
University of Southern California,
Los Angeles, CA, USA
e-mail: rewcastle@shaw.ca

R.L. Bard et al. (eds.), *Image Guided Prostate Cancer Treatments*,
DOI 10.1007/978-3-642-40429-0_22, © Springer-Verlag Berlin Heidelberg 2014

by all the echoes makes it possible to construct an image in real time. A higher ultrasound frequency yields a higher resolution image. However, penetration decreases with increasing frequency. Thus, a high-frequency ultrasound crystal allows for high-resolution images proximal to the crystal; a lower-frequency crystal allows for deeper imaging but with lower resolution.

As with all medical imaging technologies, the goal is to image without, or at least with minimal, perturbation of the subject. This is acutely important in neonatal imaging applications. Certainly benign at low intensities, ultrasound is a safe imaging technology (Woodward and Warwick 1970). However, the propagation of ultrasound is the propagation of energy, and the attenuation of ultrasound waves as they pass through tissue is the deposition of energy which is absorbed by the tissue. It is these facts that lead to the application of HIFU.

22.3 Mechanisms of Action

HIFU results in the thermal ablation of tissue by depositing large amounts of energy into it in a controlled manner. This is accomplished by increasing the intensity of the waves and focusing the waves on a single physical location. It is possible to raise the temperature of predictable volume of tissue and cause physical disruption to it to induce irreversible damage (Linke et al. 1973).

The ablative mechanism of action of HIFU is from one of two physical phenomena: thermal and cavitational (Hill and ter Haar 1995). Elevation of temperature leads to the melting of lipid membranes and protein denaturation resulting in coagulative necrosis of tissue and vessels (Yang et al. 1993). This is the desired effect of HIFU. The temperature rise is quick and brief, so heat diffusion into adjacent tissues beyond target area is minimal. The boundary between ablated and adjacent viable tissues is sharp; thermo-lesions in intervening tissue are not observed.

If significant deposits of energy occur, mechanical damage may result in gas bubble formation and/or cavitation (Barnett et al. 1994). Gas bubbles can form inside tissue during HIFU as a result of several mechanisms. The first mechanism is simple boiling which will create air pockets that have the potential of disrupting the ultrasound signal and modifying the ablation volume in an uncontrollable way. This phenomenon is always avoided during HIFU.

The second mechanism is cavitation and can be either inertial cavitation or stable (non-inertial) cavitation. During inertial cavitation, gas microbubbles form within tissue due to the negative pressure caused by HIFU. Upon subsequent collapse due to the higher pressure of the surrounding medium, the temperature and pressure inside the microbubble will increase rapidly. This can lead to the dissipation of the gas into the surrounding medium in the form of a shock wave. Inertial cavitation is relatively unpredictable in terms of formation and dissipation of energy and is avoided during HIFU.

Stable cavitation is the oscillation of existing microbubbles in the tissue, and it is not associated with a violent collapse and dispersion of energy. Microbubble oscillations can result in sheering forces and viscous-damping heating. Although stable cavitation is currently avoided during the procedure, there is some experimental evidence that stable cavitation may be able to enhance tissue ablation during HIFU (Curiel et al. 2004). The following are the time evolutionary microscopic changes following HIFU (Wu et al. 2001):

- *Days 1–7*: Homogeneous areas of irreversible cell death (pale coagulative necrosis, distorted tumor cells, pyknotic shrunken nuclei, indistinct cell borders, cellular debris). No residual viable tumor cells. Clear, extremely sharp border comprising only several cell layers between treated-untreated areas, with a ring of congestion at the margin of ablation.
- *Day 7*: Small amount of granulation tissue, immature fibroblasts, inflammatory cells, and new capillaries in the boundary region.

- *Days 10–14*: Destroyed tumor cells are disaggregated, no distinct cytoplasm or nucleus. HIFU-damaged area partially absorbed and replaced with new proliferative repair tissue. Margin area replaced by mature fibrous tissue.

22.4 Prostate Cancer

Incidence of prostate cancer has increased significantly over the last three decades. Currently, it is the most frequently occurring cancer in men over 50 years of age, and it represents the second most common cause of death in men in the developed world, after lung cancer (American Cancer Society 2013). These increases are undoubtedly related to cancer screening by plasma PSA levels, (Soloway and Roach 2005), as well as to the increase in life expectancy and the more frequent recognition of prostate cancer as a leading cause of death (Rebillard et al. 2002).

In the USA, the number of new prostate cancer cases and deaths in 2013 are estimated to be 238,590 and 29,720, respectively (American Cancer Society 2013). Its incidence increases with age. The average age of men with prostate cancer is somewhere around 68 years but some men are affected at an earlier age.

Prostate cancer is a disease that spans a wide prognostic spectrum, from indolent to lethal with everything in between. However, standard treatments for localized disease have remained binary: "do nothing" (active surveillance) or "destroy the entire prostate" with radical whole-gland treatment (surgery or radiation – in all their permutations). The current range of available treatment options does not fully match the spectrum of the disease.

Focal treatment of prostate cancer, loosely defined as anything less than complete ablation of the prostate, is flexible in extent and has the advantage that it can be tailored to the individual patient. It may prove to be a welcome addition to the existing armamentarium of prostate cancer treatments.

22.5 Commercially Available Devices

Several HIFU devices are commercially available but those currently in clinical practice were primarily designed for whole-gland ablation. There are two HIFU manufacturers of transrectal HIFU devices for the treatment of localized prostate cancer. Until recently, these devices were designed exclusively for whole-gland ablation. The first to be available was the Ablatherm® (EDAP-TMS, Lyon, France). Subsequently, Sonacare (Charlotte, NC) developed a system called the Sonablate®. The foundation science and technology of both systems is identical, but there are several technological differences between the two devices. These differences, for the most part, arise from different schools of thought with regard to how best design the optimal HIFU treatment system.

Three generations of the Ablatherm have been manufactured by EDAP-TMS. The first-generation HIFU device was introduced in 1995 as a prototype (Gelet et al. 1996), with the first commercial device, the Ablatherm Maxis, introduced into clinical use in Europe in 2000. The third-generation Ablatherm Integrated Imaging device was introduced in 2005 and incorporates advances over previous models that include TRUS-based real-time visualization through a new electronic probe, probe fixation that limits patient movement, in-built controls that automatically correct or stop treatment and adjust the endorectal probe position for optimal distance from the rectal wall, an external motion sensor, and internal safety circuits that halt the procedure if technical malfunction or patient movement is detected. To avoid rectal injury the rectum is cooled throughout the procedure. All Ablatherm devices treat the prostate with a single pass as the anterior-posterior height of an elementary lesion is 19–26 mm in anterior-posterior height.

The Sonablate 500 is the most recent offering from Sonacare which treats the prostate in multiple passes with an elementary lesion height of 10 mm. Safety features incorporated into this device include active cooling of the rectum during the procedure as well as reference to real-time image comparisons to detect movement. Additionally, the Sonablate has the ability to have the HIFU power adjusted intraprocedure.

It is possible to do less than total ablation with either whole-gland device. Although arbitrary targeting of a HIFU lesion at a given location within the prostate is not always possible. It is feasible to perform a relatively non-precise focal treatment with the current devices. Typically a hemi-ablation approach is taken, wherein one entire lobe of the prostate is completely ablated.

Focal-One is a new-generation HIFU device manufactured by EDAP-TMS that creates small 5 mm lesions which can be targeted virtually anywhere within the prostate. The device incorporates all the safety features of the Ablatherm. To specifically facilitate focal ablation, the device can fuse of real-time ultrasound and pretreatment MR images. This offers the potential for unprecedented accuracy in tissue targeting and ablation and opens the door for true focal ablation: lesion plus margin. Additionally, contrast-enhanced ultrasound can be performed immediately after the completion of a planned ablation to ensure complete devascularization of the treated tissue.

22.6 Clinical Outcomes

As of 2013, approximately 50,000 HIFU procedures for prostate cancer have been performed worldwide. Many publications have appeared reporting outcomes of HIFU for treatment of localized prostate cancer, as recently reviewed by Chaussy and Thuroff (2011). Importantly, in 2013 already, three independent single-center studies reporting 10-year outcomes of HIFU for localized prostate cancer have been published (Table 22.1).

Ganzer et al. (2013) reported a retrospective single-center study of 538 consecutive patients undergoing primary HIFU for clinically localized prostate cancer and followed over a 14-year period. Measures of efficacy included overall, metastasis-free, and prostate cancer-specific survival rates. Morbidity was also assessed. Per D'Amico stratification, patients included 229 men with low-risk disease and 211 men with moderate-risk disease. On average, 1.22 HIFU sessions were performed per patient. For the low- and intermediate-risk groups, 10-year cancer-specific survival was 100 and 96.2 %, and metastasis-free rate was 99.6 and 94.3 %, respectively. No rectal fistulae were observed following first HIFU and 4 (0.7 %) were observed following repeat HIFU. Post-HIFU urinary tract infection (UTI) was observed in 10 % of patients, with 28.3 % having an episode of bladder outlet obstruction. At most recent follow-up, grade I incontinence (defined as loss of urine under heavy exercise requiring 0–1 pad per day) was observed in 14 % of subjects and grade II and III was reported by 2.4 and 0.7 % of patients, respectively. Potency was assessed 12 months following HIFU. Of men potent prior to HIFU, 65 % resumed intercourse following HIFU, including 25 % without and 40 % with oral pharmaceutical assistance (Viagra) (Note: in North America, standard potency reporting includes men potent with or without oral pharmaceutical assistance).

Thuroff and Chaussy (2013) from Munich, Germany, reported long-term cancer control and morbidity of HIFU; in their study, transurethral resection of prostate (TURP) was performed to downsize the prostate prior to HIFU. Patients underwent primary HIFU for localized disease (T1-2, N0, M0, PSA <50 ng/ml) and were followed prospectively in their database. Patients with shorter follow-up (<15 months), locally advanced prostate cancer, and previous long-term androgen deprivation or any PSA-influencing therapy were excluded. All patients underwent whole-gland HIFU. Of 704 study patients, 78.5 % had intermediate- or high-risk disease. Follow-up was up to 14 years. Ten-year cancer-specific survival was 99 %, metastasis-free survival was 95 %, and 10-year salvage treatment-free rates were 98 % in low-risk, 72 % in intermediate-risk, and 68 % in high-risk patients. Side effects were moderate. HIFU re-treatment rate was 15 % since 2005.

Morbidity was assessed and stratified according to the generation of device used: *Cohort 1*: prototype device; *Cohort 2*: Maxis device (the first commercially available device launched in 2000) and *Cohort 3*: Ablatherm Integrated Imaging

Table 22.1 Long-term outcomes of whole-gland HIFU

	Risk group	*N*	Ten-year cancer-specific survival (%)	Ten-year metastases-free survival (%)
Ganzer et al.	Low	229	100	99.6
	Intermediate	211	96.2	94.3
Thuroff et al.	All localized (72 % Int or high)	704	99	95
Crouzet et al.	Low	357	99	99
	Intermediate	452	98	95
	High	174	92	86

device (became available in 2005). Perioperative complications (Clavien classification) occurred in 16 % of the entire sample, with a decrease over time noted between Cohorts 1, 2, and 3 (29 %/10 %/14 %). No perioperative complication was severe, all were short-lasting, and no Clavien IV or V complications were observed. Short-intermediate term morbidity included incontinence (4 %), obstruction (4.6 %), infection (2.1 %), rectourethral fistula (0.23 %), perineal pain (0.7 %), and others (4.4 %). No patient developed a fistula since 2005 when the Ablatherm Integrated Imaging was introduced. The morbidity profile, but not the overall rate, changed significantly in the recent cohorts. Overall rate of urinary incontinence (grade II or III) >3 months was 3.3 %, with rates of 5.1, 3.1, and 1.5 % in Cohorts 1, 2, and 3, respectively. Overall rate of secondary obstruction (from necrotic or scar tissue that resulted in bladder neck or intraprostatic stenosis) was 23, 19, and 23 % in Cohorts 1, 2, and 3, respectively. Recurrent UTI occurred in 2.5, 1.9, and 3.1 % of the sample. Although comprehensive data on erectile function with validated questionnaires were not available, the post-HIFU clinical potency rate in previously potent patients was approximately 55 %; of these patients, roughly two thirds were taking PDE-5 inhibitors.

Crouzet et al. (2013) reported a single-center experience with HIFU from Lyon, France. A total of 1,002 patients were included, 63 % of whom had moderate- or high-risk disease. One, 2, and 3 HIFU sessions were required in 60, 38, and 2 % of patients, respectively. Ten-year overall and prostate cancer-specific survival rates were 80 and 97 %, respectively. Cancer-specific survival rates were 99 % for low-risk (D'Amico) patients, 98 % for intermediate-risk patients, and 92 % for high-risk patients. Ten-year metastasis-free survival rates were 94 % for the entire population and 99, 95, and 86 % for low-, intermediate-, and high-risk patients, respectively. Incontinence was assessed using the Ingelman-Sundberg score, and potency was assessed using the five-item version of the International Index of Erectile Function (IIEF-5) scores between 12 and 24 months after HIFU. All adverse effects, such as bladder outlet obstruction (BOO) (obstruction of the outflow of urine from necrotic debris or urethral stricture), were prospectively recorded. Severe incontinence (Grade II or III) and bladder outlet obstruction decreased with refinement in technology, from 6.4 and 34.9 %, respectively, in patients treated with the prototype device, to 3.1 and 5.9 %, respectively, for those treated with the Ablatherm Integrated Imaging device.

Potency was evaluated in 187 patients treated after 2005 with the latest generation of device. Median IIEF-5 score decreased from 17 (range: 5–25) to 5 (range: 1–22) ($p < 0.001$). Potency was preserved (IIEF ≥17) without pharmaceutical aid in the 42.3 % of patients with a baseline IIEF score ≥17 (<70 years: 55.6 %; ≥70 years: 25.6 %; $p < 0.001$). Return to intercourse rate was not reported but would likely be significantly higher based on the observations of Ganzer et al. (2013).

From an oncologic prospective, these outcomes are impressive in comparison with radical prostatectomy, surgical removal of the entire prostate: the gold standard treatment for prostate cancer. Boorjian et al. (2008) published 10-year cancer-specific survivals and freedom from metastasis rates from patients undergoing prostatectomy at the Mayo Clinic in Rochester, MN. This study included over 7,000 men. Stephenson

Table 22.2 Comparison of HIFU and prostatectomy 10-year cancer-specific survival and freedom from metastasis rates

	10-year cancer-specific survival		10-year metastasis-free survival	
	Prostatectomy	HIFU	Prostatectomy	HIFU
Low	99^{b}–100^{a} %	99–100 %	99^{a} %	99–100 %
Intermediate	96^{b}–97^{a} %	96–98 %	94^{a} %	94–95 %
High	92^{b}–95^{a} %	92 %	89^{a} %	86 %

[a] Boorjian et al. (2008)
[b] Stephenson et al. (2009)

et al. (2009) published a multicenter study of over 10,000 men treated at Memorial Sloan Kettering (New York, NY), the Cleveland Clinic (Cleveland, OH), and the University of Michigan (Ann Arbor, MN). A comparison of the recent HIFU outcomes to the results of these studies is presented in Table 22.2.

Ahmed et al. (2012) reported a focal trial with such a device wherein patient selection utilized multiparametric magnetic resonance (MR) imaging (T2-weighted, dynamic contrast-enhanced, diffusion-weighted) and template transperineal prostate mapping biopsies. This series included low-risk (27 %), intermediate-risk (63 %), and high-risk (10 %) prostate cancer in 41 patients. Of 39 patients undergoing follow-up biopsy, 27 (69 %) showed no evidence of cancer, 8 (23 %) had no evidence of clinically significant cancer, and 3 (8 %) has clinically significant cancer. No detailed PSA stability data were presented. Return of potency, as determined by IIEF questionnaire, was observed in 95 % of the 20 patients and pad-free continence rate was 95 %. Erectile dysfunction (defined as men with satisfactory function for penetration before treatment and not 12 months after treatment) was observed in 11 % and no incontinence (defined as men leak free before treatment and not 12 months after treatment) was observed. These are impressive results as they were obtained with a device designed for whole-gland treatment of the prostate.

Conclusions

HIFU emerged as a novel therapy for prostate cancer 17 years ago. Rigorous study and patient follow-up have resulted in the emergence of multiple 10-year outcome papers with results comparable to radical prostatectomy for low-, moderate-, and high-risk localized disease. With such outcomes, the procedure can no longer considered investigational or experimental. Whole-gland HIFU offers men definitive local therapy options that will be attractive to many. Focal therapy in general, and focal HIFU specifically, represents a shifting paradigm in prostate cancer management. Certainly issues of patient's selection and follow-up strategy remain to be resolved but initial outcomes are encouraging. Continued research regarding focal therapy will likely change the way prostate cancer is managed in the relatively near future.

References

Ahmed HU, Hindley RG, Dickinson L, Freeman A, Kirkham AP, Sahu M, Scott R, Allen C, Van der Meulen J, Emberton M. Focal therapy for localised unifocal and multifocal prostate cancer: a prospective development study. Lancet Oncol. 2012;13(6):622–32.

American Cancer Society. Cancer facts & figs. 2013. Atlanta: American Cancer Society; 2013.

Barnett SB, ter Haar GR, Ziskin MC, Nyborg WL, Maeda K, Bang J. Current status of research on biophysical effects of ultrasound. Ultrasound Med Biol. 1994;20(3):205–18.

Boorjian SA, Karnes RJ, Rangel LJ, Bergstralh EJ, Blute ML. Mayo Clinic validation of the D'amico risk group classification for predicting survival following radical prostatectomy. J Urol. 2008;179(4):1354–60.

Chaussy CG, Thüroff SF. Robotic high-intensity focused ultrasound for prostate cancer: what have we learned in 15 years of clinical use? Curr Urol Rep. 2011;12(3):180–7.

Crouzet S, et al. Whole-gland ablation of localized prostate cancer with high-intensity focused ultrasound: oncologic outcomes and morbidity in 1002 patients. Eur Urol. 2013;91:66–79. In press.

Curiel L, Chavrier F, Gignoux B, Pichardo S, Chesnais S, Chapelon JY. Experimental evaluation of lesion prediction modelling in the presence of cavitation bubbles: intended for high-intensity focused ultrasound prostate treatment. Med Biol Eng Comput. 2004;42:44–54.

Ganzer R, Fritsche HM, Brandtner A, Bründl J, Koch D, Wieland WF, Blana A. 14-year oncologic and functional outcome of high-intensity focused ultrasound (HIFU) in localized prostate cancer. BJU Int. 2013; 112(3):322–9.

Gelet A, Chapelon JY, Bouvier R, Souchon R, Pangaud C, Abdelrahim AF, Cathignol D, Dubernard JM. Treatment of prostate cancer with transrectal focused ultrasound: early clinical experience. Eur Urol. 1996;29(2):174–83.

Hill CR, ter Haar GR. High intensity focused ultrasound–potential for cancer treatment. Br J Radiol. 1995;68(816):1296–303.

Linke CA, Carstensen EL, Frizzell LA, Elbadawi A, Fridd CW. Localized tissue destruction by high-intensity focused ultrasound. Arch Surg. 1973;107(6): 887–91.

Rebillard X, Villers A, et al. Comité de Cancérologie de l'AFU. Recommandations 2002 sur le cancer de prostate. Prog Urol. 2002;12:31–67.

Soloway M, Roach III M. Prostate cancer progression after therapy of primary curative intent. A review of data from the prostate-specific antigen era. Cancer. 2005;14(11):2310–22.

Stephenson AJ, Kattan MW, Eastham JA, Bianco Jr FJ, Yossepowitch O, Vickers AJ, Klein EA, Wood DP, Scardino PT. Prostate cancer-specific mortality after radical prostatectomy for patients treated in the prostate-specific antigen era. J Clin Oncol. 2009;27(26):4300–5.

Thüroff S, Chaussy C. Evolution and outcomes of 3 MHz high intensity focused ultrasound therapy for localized prostate cancer during 15 years. J Urol. 2013;190(2): 702–10.

Woodward B, Warwick R. How safe is diagnostic sonar? Br J Radiol. 1970;43(514):719–25.

Wu F, Chen WZ, Bai J, Zou JZ, Wang ZL, Zhu H, Wang ZB. Pathological changes in human malignant carcinoma treated with high-intensity focused ultrasound. Ultrasound Med Biol. 2001;27(8):1099–106.

Yang R, Sanghvi NT, Rescorla FJ, Kopecky KK, Grosfeld JL. Liver cancer ablation with extracorporeal high-intensity focused ultrasound. Eur Urol. 1993;23 Suppl 1:17–22.

Index

A
Ablatherm®, 257, 258
Acoustic radiation force impulse (ARFI) imaging, 36–37
Acoustic shadowing, 17
Acquired cysts, 132
Active surveillance (AS) protocols, 5–6, 207–208
Anatomic T2-weighted MR imaging, 84, 85
Androgen deprivation therapy (ADT), 13
Anecdotal observation, 6–7
Anterior pelvic route, for prostate cancers, 165
Apical tumor, 146–148
Apparent diffusion coefficient (ADC), 85–86, 98, 109–110
ARFI imaging. *See* Acoustic radiation force impulse (ARFI) imaging
Attenuative sonic shadowing, 17
AutoLITT®, 228

B
Benign prostatic hypertrophy (BPH), 86, 136, 138–140, 195
β-sitosterol/antioxidant matrix (β-sit/AOX), 187–188
Biobot Mona Lisa, 118
BiopSee®, 117
Biotex, 228
Bladder
  invasion, 169
    bladder wall, 178, 179
    blood clots, 169, 175
    Gleason 5, 178
    iliac adenopathy, 177
    necrosis, 176
    necrotic massive bladder tumor, 176
    ureterocele, 176
  multiplanar multimodality imaging, 129, 130
Bleomycin, 236
Bone metastases, 169–170
  acetabular, 182, 183
  imaging, 99, 103
  inferior pubic ramus, 184
  ischial metastasis, 181
  symphysis pubis, 183
Broadband transducers, 15

C
Capacitive microma-chined ultrasonic transducer (CMUT), 42
Capsular arteries, 56
Chronic prostatitis, 86
Comet tail sign, 17
Complementary and alternative medicine (CAM), 8–9
Congenital anomalies and cysts, 132, 135–137
Continuous wave lasers, 221, 222
Contrast agents, 25, 48
Contrast-enhanced ultrasound (CEUS), 31, 188
  biopsies, 48–51
  detection, 48, 49
  examination, 48, 50
  and MRI, 51, 52
Cryotherapy, 6

D
Dall'Era's criteria, 63, 67
D'Amico's criteria, 63, 67
Deformable registration, 119
Diffusion-weighted imaging (DWI), 84–86, 109–110
  bone metastases, 99, 103
  development of, 97
  mechanisms, 98
  prostate tumors, 98–103
  whole-body, 97–98 (*see also* Whole-body DWI (wbDWI))
    imaging artifacts, 103–104
    liver and pulmonary metastases, 99
Digital rectal exam examination (DRE)
  definition, 19
  prostate elastography, 32
  tumor localization, 94
Doppler histogram vessel density analysis
  3D sonography and power Doppler angiography
    color-coded signal, 72
    resistive index, 71
    spectral waveform analysis, 72
  histogram analysis
    Gleason grading, 73, 75, 76
    power Doppler image, 73

R.L. Bard et al. (eds.), *Image Guided Prostate Cancer Treatments*,
DOI 10.1007/978-3-642-40429-0, © Springer-Verlag Berlin Heidelberg 2014

- Doppler histogram vessel density analysis (*cont.*)
  - tumor volume VOCAL reconstruction
    - ROC curves, 77
    - vascular area, for grading, 74, 81
    - vascular index, 74, 78, 79
  - volume analysis
    - tumor flow review, 73
    - VOCAL histogram, 71, 74
- Doppler ultrasound
  - applications
    - assessment and follow-up, 192
    - contrast Doppler, 193
    - data analysis, 192
    - *vs.* 2-D sonogram, 192
    - image-guided biopsy and laser ablation, 194
    - invasion of cancer, 192
    - power Doppler sonography, 192–193
    - tumor volume and density, 193
  - clinical advantages, 190
  - 3-D and MRI
    - Gleason scores, 190
    - monitoring intervals, 189
    - tumor aggression imaging, 189
    - tumor size, 189–190
  - Gleason scores, 190
  - monitoring intervals, 189
  - piezoelectric effect, 188
  - proactive monitoring
    - assessing response, 200–202
    - β-sit/AOX, 195
    - diets, 196–197
    - interval cancers, 200
    - membrane permeability and intracellular environment, 196
    - natural synergism and potentiation, 197
    - phytosterol composition, 197–200
    - prostate nutrition, 195–196
  - regression and recurrence, 208, 211
  - tumor
    - aggression imaging, 189
    - size, 189–190
- Dynamic contrast-enhanced MRI (DCE-MRI), 86–88, 128–129
  - bladder invasion, 175, 176, 178–179
  - bone metastases, 181–184
  - capsular invasion
    - Gleason 9 tumor, 155
    - homogeneous enhancement, 150–152
    - tumor eroding capsule, 153
  - enhancement patterns, 109–111
  - extraprostatic nonfocal tumors
    - bilateral apical enhancement, 159
    - boney metastases, 156
  - perfusion and neovascularization, of prostate, 109, 110
  - rectal invasion, 185
  - regression and recurrence, 208–211, 213
  - seminal vesicle invasion
    - distal seminal vesicle, 160
    - proximal seminal vesicles, 161
    - vas deferens, 162

E

- Edge shadowing, 17
- Eigen Artemis, 118–119
- Ejaculatory cysts, 132
- Electrochemotherapy, 236
- Electrogenetherapy (EGT), 236
- Electromagnetic radiation (EMR), 219, 220
- European Randomized Study of Screening for Prostate Cancer (ERSSPC), 4
- Extracapsular extension (ECE), 60–61, 149
- Extraprostatic focal tumors
  - capsular invasion
    - apical tumor, 152
    - avascular apical tumor, 154
    - bilateral tumors, 158
    - capsular erosion, 151
    - ECE, 149
    - Gleason 9, 155
    - homogeneous signal loss, 150
    - midgland tumor, 153
    - perineural, 149
    - posterior erosion, 152
    - signal and intact capsule, 151
    - solid tumor, 150
  - nonfocal tumors, 149, 156–159
  - prostatic capsule, 149
  - seminal vesicle invasion
    - 3D, 160–163
    - DCE-MRI, 160–163
    - ductal dilation and ectasia, 161
    - ejaculatory ductal system, 160
- Extraprostatic nonfocal tumors, 149, 156–159

F

- Focal laser ablation (FLA), 6
  - clinical application
    - follow-up protocol, 232
    - localization, 229–231
    - mechanisms, 231
    - patient preparation, 229
    - post ablation, 230, 232
    - thermometry, 232
    - Visualase system, 229–232
  - clinical results, 232–233
  - description, 227–228
  - rationale for, 227
  - technological description, 228–229
- Focal tumors
  - extraprostatic (*see* Extraprostatic focal tumors)
  - intraprostatic, 145–148

G

- Genetic algorithm (GA) optimizer, 122
- GeoScan BioJet™, 118

H

- High-intensity focused ultrasound (HIFU), 6
  - clinical outcomes
    - focal trial, 260
    - morbidity assessement, 258, 259

    - oncologic prospective, 259, 260
    - potency, 259
    - retrospective single-center study, 258, 259
    - TURP, 258
  - devices
    - Ablatherm, 257
    - focal-one, 258
    - Sonablate 500, 257, 258
  - ellipsoid, 255
  - incidence of, 257
  - mechanisms of action
    - cavitation, 256
    - thermal phenomena, 256
    - time evolutionary changes, 256, 257
  - piezoelectric crystal vibrates, 255, 256
  - regression and recurrence, 208–213
- Hormonal and nutritional intervention
  - ABT failures, 204
  - antiandrogen approaches, 202
  - bevacizumab, 188
  - β-sit/AOX, 187–188
  - environmental and dietary factors, 202
  - ERa and ERb, 202–203
  - estriol, 203
  - estrogens, 202–203
  - history, 188
  - monitoring, 188
  - sonography, 188–190
  - vitamin D, 203
- Hypervascular lesion, 58, 61
- Hypoechoic lesion, 27, 62, 63

I

- Inferior vesical arteries, 56
- Internal iliac route, for prostate cancers, 165
- Interpolators, 120–121
- Intraprostatic cancer, 145–148
- In vivo UroNav, 118
- Irreversible electroporation (IRE), 6
  - ablation zones, 236
  - advantages
    - blood flow effects, 240
    - clinical usage, 240
    - collagenous and neural structures, 238, 239
    - decreased trauma, 240
    - heat sink effect, 238, 239
    - immunological effect, 238
    - lesion predictability, 240
    - probe size, 240
    - rapid resolution, 236–237
    - procedural speed, 239–240
    - uniform necrosis, 237–238
  - cryoablation, 235
  - electrochemotherapy, 236
  - electrogenetherapy, 236
  - reversible electroporation, 235, 236
- Isoechoic lesion, 58, 61

K

- Koelis Urostation, 118

L

- Laparoscopic radical prostatectomy (LRP), 7
- Laser principles
  - biological effects
    - photomechanical and photochemical, 224
    - photothermal, 223–224
  - continuous wave lasers, 221, 222
  - electromagnetic radiation, 219, 220
  - history, 219
  - parameters
    - beam profile, 223
    - cooling, 223
    - energy density, 222
    - pulse duration, 222
    - spot size, 222–223
    - wavelength, 222
  - properties
    - coherence and collimation, 221
    - monochromaticity, 221
  - pulsed laser, 221, 222
  - quality switching lasers, 222
  - quasi-continuous wave laser, 221, 222
  - radiometry, 221
  - safety of
    - beam and nonbeam hazards, 224, 225
    - eye injury, 225
    - fires, 225
    - masks, 225
  - selective photothermolysis, 224
  - spontaneous and stimulated emission, 221
    - energy level, 219, 220
    - lasing medium, 220
    - optical cavity, 220
    - pumping process/system, 220
- Lateral route, for prostate cancers, 165
- Linear interpolator, 121
- Linear transformation, 120
- Liver metastases, 99

M

- Magnetic resonance imaging (MRI)
  - benign prostatic hypertrophy, 136, 138–140
  - bladder invasion, 175, 176, 178–179
  - bone metastases, 99, 181–184
  - capsular invasion, 150–152
  - and CEUS, 51, 52
  - clinical techniques
    - DWI-MRI, 128
    - EC-MRI, 128
    - MR spectroscopy, 128
    - 1.5 tesla, 127–128
    - 3 tesla MRI, 128
  - congenital anomalies and cysts, 132, 135–137
  - DCE-MRI, 190–191
  - description, 83–84
  - detection
    - high-b-value diffusion-weighted imaging, 93
    - multiparametric MRI, 92
  - *vs.* Doppler imaging, 191
  - drawbacks of, 84

Magnetic resonance imaging (MRI) (*cont.*)
    DWI (*see* Diffusion-weighted imaging (DWI))
    EC-MRI, 190–191
    FLA (*see* Focal laser ablation (FLA))
    Gleason scores, 190
    lymph node MRI, 193–194
    monitoring intervals, 189
    MRI-TRUS fusion devices
        Biobot Mona Lisa, 118
        BiopSee®, 117
        clinical advantages, 116–117
        Eigen Artemis, 118–119
        GeoScan BioJet™, 118
        interpolators, 120–121
        In vivo UroNav, 118
        Koelis Urostation, 118
        metrics, 121–122
        MIMviewer®, 119
        optimizers, 122
        registration, 119
        transformations, 120
        UC-Care Navigo™, 118
    perfusion, 128–129
    prostatic calculi and calcifications, 140
    prostatitis, 140–143
    role of, 83
    S-MRI, 190–191
    technique
        DCE-MRI, 86–88
        diffusion-weighted imaging, 84–86
        mpMRI, 89
        T1-weighted imaging, 84
        T2-weighted imaging, 84, 85
    tumor
        aggression imaging, 189
        localization, 94–95
        size, 189–190
        staging, 94, 95
Magnetic resonance lymphangiography (MRL), 14, 194
Magnetic resonance spectroscopic imaging (MRSI), 110, 112
Metastatic disease
    bladder invasion, 169, 175–180
    bone metastases, 169–170, 181–184
    pelvic lymphadenopathy (*see* Pelvic lymphadenopathy)
    rectal invasion, 172, 185
Microcalculi scattered sound waves, 16
MIMviewer®, 119
Minimally invasive treatment (MIAT), 208
mpMRI. *See* Multiparametric prostate MR imaging (mpMRI)
MR-guided prostate biopsy, 111–113
Mullerian duct cysts, 132
Multimodality imaging, 127
Multiparametric prostate MR imaging (mpMRI), 89, 148
    description, 107, 109
    Ktrans map, 108, 109
    T2-weighted MR imaging, 108, 109
Mutual information (MI), 121–122

N
Nearest-neighbor interpolator, 121
Neovascularization, tumor, 22–23
Non-palpable hypoechogenic leison, 64
Normalized cross correlation (NCC), 121
Novilase®, 228

O
Optoacoustic imaging. *See* Photoacoustic imaging (PA)

P
Particle swarm optimizer, 122
Pelvic lymphadenopathy, 165–166
    iliac nodes and bone metastases, 167–169
    obturator node, 166–168
    perirectal node, 167–168
        avascular and vascular, 171
        with homogeneous signal, 166, 170
        with massive rectal invasion, 173
Pelvic lymph node dissection (PLND), 14, 165, 166
Photoacoustic imaging (PA)
    description, 32, 38–39
    preclinical applications in prostate, 40–42
    principles of, 39–40
Photodynamic therapy (PDT), 6
    canine studies, 245–246
    clinical studies
        primary treatment, 247–250
        salvage treatment, 246–247
    definition, 243
    mechanism of action, 244
    photosensitizer agents, 244–245
    treatment technique
        light delivery, 248, 251
        planning, 248, 251
        TOOKAD study, 248
    urological use, 243
Photosensitizer agents, 244–245
Phytosterol
    β-sit/AOX matrix, 198–200
    CoEnzyme Q10, 199–200
    composition, 197–198
    curcumin, 199
    synergy, 199
Piezoelectric crystals, 255, 256
Power Doppler sonography (PDS)
    advantages of, 18
    and biopsy decision, 65, 68
    Doppler modes, 56–57
    prostate cancer diagnosis, 19–21
    prostate vascular anatomy, 56
    prostatic inflammatory disease, 65, 68
    transrectal power Doppler sonography, 58, 59
        extracapsular extension, 60–61, 67
        low-risk prostate cancer detection, 61–63
        results, 60
        semiology and power Doppler, 58, 60, 61

- tumor location, 58–60, 65, 66
- vascular tumor types, 58, 62–64
- vascular types, 27

Presacral route, for prostate cancers, 165

Proscar®, 6

Prostate cancer
- clinical trial and anecdotal observation, 6–8
- complementary and alternative medical therapies, 8–9
- description, 3
- dualistic *vs.* integrative thinking, 8
- focal therapy, 6
- prostate-specific antigen testing
  - active surveillance and protocols, 5–6
  - prostate imaging, 5
- screening, 4
- statistics, 9–10

Prostate elastography
- elasticity principles, 32–34
- elastic properties, of prostate, 34
- elastographic methods
  - ARFI, 36–37
  - shear wave imaging, 37–38
  - strain imaging, 34–36
  - vibration amplitude sonoelastography, 38
  - vibro-elastography, 38

Prostate-specific antigen (PSA) testing, 107
- active surveillance and protocols, 5–6
- prostate imaging, 5

Prostatitis
- acute, 65
- chronic, 86
- multiplanar multimodality imaging, 140–143

Pulmonary metastases, 99

Pulsatility index (PI), 22

Pulsed laser beam, 221, 222

Pulse-echo imaging, 14–16

Q

Quality switching lasers, 222

Quantitative approach, DCE-MRI, 87

Quasi-continuous wave laser, 221, 222

R

Radiofrequency ablation (RFA), 6

Radiometry, 221

Rectal invasion, 172, 185

Regression and recurrence
- active surveillance protocols, 207–208
- biochemical failure, 211
- cryotherapy, 213
- Doppler studies, 208
- dynamic contrast-enhanced MRI, 208–211, 213
- Gleason 5, 214
- Gleason score 6, 211
- high-intensity focused ultrasound, 208–213
- hormone treatment, 207, 215
- local recurrence, 213
- minimally invasive treatment, 208
- postnecrotic calcification, 208
- prostate-specific antigen level, 211
- radiation therapies, 207, 214
- saw palmetto supplement, 207
- seminal vesicle recurrence, 214
- 3D power Doppler ultrasound, 208, 211
- T2 MRI, 209
- treatments, 207
- urethral dilation, 209

Rigid transformation, 120

S

Salvage treatment, PDT, 246–247

Selective photothermolysis, laser, 224

Seminal vesicle disease, 140, 144

Seminal vesicle invasion (SVI)
- detection of, 28–29
- focal tumors
  - 3D, 161–163
  - DCE-MRI, 161–163
  - ductal dilation and ectasia, 161
  - ejaculatory ductal system, 160

Semiology, ultrasound, 58

Semiquantitative approach, DCE-MRI, 87

Shear wave elastography, 37–38

Simplex optimizer, 122

Sonablate®, 257, 258

Sonography, 11
- Power Doppler, 19–22 (*see also* Power Doppler sonography (PDS))
- three-dimensional, 71

Spline interpolator, 121

Spontaneous emission, 219–221

Stimulated emission, 219–221

Strain imaging, prostate elastography, 34–36

Subtle hypoechoic and hypervascular lesion, 58, 60

T

Thermometry, 232

Three-dimensional chemical shift imaging, of prostate, 110, 112

3 tesla MRI, 128

TOOKAD study, PDT, 248

Transabdominal approach, 17

Transgenic adenocarcinoma mouse prostate (TRAMP) model, 40

Transrectal approach, 17

Transrectal ultrasound (TRUS), 19, 145
- MRI-TRUS fusion devices
  - Biobot Mona Lisa, 118
  - BiopSee®, 117
  - clinical advantages, 116–117
  - Eigen Artemis, 118–119
  - GeoScan BioJet™, 118
  - interpolators, 120–121
  - In vivo UroNav, 118
  - Koelis Urostation, 118

Transrectal ultrasound (TRUS) (*cont.*)
        metrics, 121–122
        MIMviewer®, 119
        optimizers, 122
        registration, 119
        transformations, 120
        UC-Care Navigo™, 118
    TRUS-guided biopsy, 107
T2-weighted imaging (T2WI) sequences, 84, 85, 148
T1-weighted MR imaging, 84

U
UC-Care Navigo™, 118
Ultrasonic contrast agents (UCA), 48
Ultrasound (US)
    advanced (*see* Photoacoustic imaging (PA); Prostate elastography)
    blood flow, 12–13
    CEUS (*see* Contrast-enhanced ultrasound (CEUS))
    color and power Doppler applications, 18–19
    contrast agents, 25
    digital rectal exam examination, 19
    Doppler flow imaging, 25–29
    Doppler technologies, 13
    gray-scale appearance, of prostate cancer, 18
    harmonic imaging, 25
    HIFU (*see* High-intensity focused ultrasound (HIFU))
    high-frequency scanning
        artifacts, 16–17
        attenuation, 15
        pulse-echo method, 14–16
        scan planes, 17–18
    medical progress and government regulation, 13–14
    physical principle of, 11
    prostatic calculi and calcifications, 140
    TRUS, 19, 20
    tumor
        angiogenesis, 22–23
        metastases, 23–24
Urethra, 129, 131
U.S. Preventive Services Task Force (USPSTF), 4
Utricle cysts, 132

V
Velocity artifacts, 17
Vibration amplitude sonoelastography, 38
Vibro-elastography, 38
Visualase®, 228–230
VOCAL program, 71, 74

W
Watchful waiting (WW), 5
Whole-body DWI (wbDWI), 97–98
    imaging artifacts, 103–104
    liver and pulmonary metastases, 99
WST-09, PDT, 245, 247

Y

Young's modulus, 33–34